FLUID MECHANICS, ACOUSTICS,

AND DESIGN

OF TURBOMACHINERY

Part I

A symposium held at

THE PENNSYLVANIA STATE UNIVERSITY

University Park, Pennsylvania

August 31–September 3, 1970
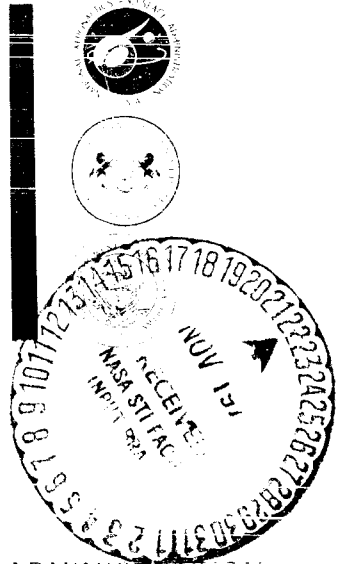
NATIONAL AERONAUTICS AND SPACE ADMINISTRATION

FLUID MECHANICS, ACOUSTICS, AND DESIGN OF TURBOMACHINERY

Part I

A symposium held at The Pennsylvania State University,

University Park, Pennsylvania, August 31 to September 3, 1970,

and sponsored by the National Aeronautics and Space Administration,

The Pennsylvania State University, and the U.S. Navy

Edited by

B. LAKSHMINARAYANA
The Pennsylvania State University

W. R. BRITSCH
NASA Lewis Research Center

W. S. GEARHART
The Pennsylvania State University

FLUID MECHANICS, ACOUSTICS, AND DESIGN OF TURBOMACHINERY

Part I

GENERAL CHAIRMAN

B. LAKSHMINARAYANA .... The Pennsylvania State University

SESSION CHAIRMEN

J. H. HORLOCK .... Cambridge University, England
H. MARSH .... Cambridge University, England
J. P. JOHNSTON .... Stanford University
J. W. HOLL .... The Pennsylvania State University
M. SEVIK .... The Pennsylvania State University
L. H. SMITH .... General Electric Company
M. J. HARTMANN .... NASA Lewis Research Center
R. E. HENDERSON .... The Pennsylvania State University

ORGANIZING COMMITTEE MEMBERS

W. R. BRITSCH .... NASA Lewis Research Center
W. S. GEARHART .... The Pennsylvania State University
R. E. HENDERSON .... The Pennsylvania State University
J. W. HOLL .... The Pennsylvania State University
J. H. HORLOCK .... Cambridge University, England
M. SEVIK .... The Pennsylvania State University
L. H. SMITH .... General Electric Company
N. F. WOOD .... The Pennsylvania State University

PREFACE

The present status of fluid mechanics, in particular the fluid mechanics of turbomachines, is much like a flexible montage: It consists partly of derived theoretical expressions and partly of expressions obtained through insight, but to a far greater degree the montage consists of the empirical results derived from the hard-earned experimental data that also serve as the bond for the montage. This montage stems from our inability to solve the complex equations governing real fluid flow for all but the simplest problems. The nature of their nonlinearity in the general case precludes any closed-form solution. Unfortunately, the flow of fluids in turbomachines requires the solution to these equations in their most complex form. Even with our modern computers, the time required to solve this set of equations is prohibitive from the monetary viewpoint. Their manual solution has never been considered practical.

Engineers, physicists, and mathematicians have all imposed many simplifying assumptions to gain some knowledge of the behavior of fluids. Engineers and physicists found this approach necessary to solve practical flow problems confronting them. Mathematicians used this approach to obtain a whole series of elegant *closed-form* solutions to simplified, usually steady state, inviscid and incompressible, fluid-flow problems. These mathematical solutions are in many cases excellent approximations to the real flows and are used as the starting point for analysis of most real flow problems. But now our needs extend far beyond these simplified solutions and also beyond the ability of the theorist to provide a true solution within the imposed limitations of time and cost. The need for speed on the one hand and for precision on the other has created separated branches for the experimental and the theoretical approaches to fluid mechanics.

The need for the rapid development of modern gas turbines and rocket engines to satisfy our expanding needs for communication and transportation has necessitated quick answers, whether approximate or exact, to many questions long extant and some new ones. The need for answers has been on the one hand useful in narrowing the gap between the mathematician and the fluid dynamicist, but on the other hand it has forced a division of fluid dynamics into several disciplines and subgroups within

them. Research is now being conducted on specialized problems in the realms of subsonic, transonic, supersonic, and hypersonic flows; viscous, boundary-layer, and secondary flows, two-phase flow and cavitation; laminar and turbulent flows and flow stability; steady and nonsteady flows and noise; and flows in cascades, compressors, and turbines. Solutions to any of the specialized problems in each of these disciplines are certainly contributing to a better understanding of fluid flow. The superposition of all these separate solutions cannot describe the flow of real fluids in a complex flow field because in many instances the assumptions as to flow conditions and boundary conditions will be inconsistent and incompatible.

In the development of a turbomachine, the fluid dynamic designer must sift through the results obtained in the various disciplines and determine which are applicable. All his knowledge and skills are required to reassemble these separate flow pictures artfully in an iterative process to define the desired blade shapes. He is painfully aware that all his efforts can at best give him only reasonable assurance that his design goal can be met and that final blade adjustments or even the need for some redesign will be determined in the laboratory. The theorist is in a similar position. He must use the empirical results first to guide and justify the simplifying assumptions to obtain a tractable set of equations and then again to check the accuracy of his solutions against the experimental results.

Obviously, theory, design, and experiment are interdependent; so too are the several disciplines of fluid mechanics. Major advances in the design of turbomachines can only be obtained through constant interchange of knowledge among specialists in all these facets of fluid mechanics. This conference was designed to promote just such an exchange of ideas. Its dedication to Dr. George F. Wislicenus is in recognition of his continuing efforts to narrow the gaps between those interested in the theoretical, the design, and the experimental phases of flow in turbomachines and of his efforts to make us all aware of developments in the other disciplines.

Credit for the conception, structure, and organization of this conference goes primarily to Dr. Lakshminarayana, who devoted considerable time and effort beyond his normal duties to bring this meeting to a successful conclusion. Arrangements for the symposium were efficiently handled by Professors N. F. Wood and W. S. Gearhart, Betty Beckwith, and Maude Gagorik.

Many thanks to Jack Suddreth, Nelson Rekos, and Dr. Robert Levine of NASA Headquarters, to Irving Johnsen of the NASA Lewis Research Center, and to Dr. Ralph D. Cooper of the Office of Naval Research for their considerable effort and support toward making this conference possible.

The committee extends its thanks to The Pennsylvania State University for hosting this conference; to the Office of Naval Research for providing travel for the overseas participants; and to NASA for its financial support. We wish to thank Dean N. J. Palladino for his continued encouragement of this conference and Dr. A. O. Lewis for his enjoyable and enlightening after-dinner presentation "From Bakewell to Buxton—The Engineer A Humanist." Above all many thanks and much credit are due the session chairmen, who had the primary responsibility for inviting the papers for their sessions, and to the authors and the discussors without whose contribution this conference would not have been possible.

WERNER R. BRITSCH

CONTENTS

Part I

SESSION I

THEORETICAL PREDICTION OF TWO-DIMENSIONAL AND THREE-DIMENSIONAL FLOWS IN TURBOMACHINERY

Chairmen: J. H. Horlock and H. Marsh

SESSION II
TWO- AND THREE-DIMENSIONAL VISCID FLOWS
Chairman: J. P. Johnston

SESSION III
CAVITATION
Chairman: J. W. Holl

Part II*

* *Sessions IV, V, VI, and VII are presented under separate cover.*

SESSION VI
PUMPING MACHINERY FOR
AEROSPACE APPLICATIONS
Chairman: M. J. Hartmann

SESSION VII
TURBOMACHINERY FOR
MARINE PROPULSION
Chairman: R. E. Henderson

INDEX OF AUTHORS AND DISCUSSORS

Keynote Address

J. H. Horlock

Cambridge University, England

Professor Lakshminarayana has asked me to provide the technical introduction to this conference, and it is a pleasure and an honor for me to do so.

The idea for this meeting on the fluid mechanics and design of turbomachinery was born at The Pennsylvania State University during the last year of Professor George Wislicenus' distinguished term of office as head of the aerospace engineering department and as director of the Garfield Thomas Water Tunnel. It was felt that there was a need in the United States for a wide-ranging discussion of turbomachinery aerodynamics and hydrodynamics and that it would be most appropriate to link this discussion with a tribute to Professor Wislicenus, in view of his own broad interests in the field. There have been two recent conferences on turbomachinery in Europe—the Royal Society Conference at Cambridge in 1967 (ref. 1) and the Brown Boveri Conference at Baden in 1969 (ref. 2), but I think it is true to say that they did not range as widely as this conference, which will cover basic fluid mechanics, propulsion aspects of the field, and design applications to turbomachines using gases and liquids.

The reason for the wide range of subjects at this conference is the breadth of Professor Wislicenus' interests. Each of us who has organized a session has been closely associated with him and benefited from his experience and wisdom; and each of us has tended to concentrate in a different specialist area. Yet Professor Wislicenus has made his mark in most of them—the design of one of the first supersonic compressors at Worthington; studies of the performance of the bypass engine (ref. 3); the work of Smith, Trangott, and Wislicenus (ref. 4) (perhaps the first essential statement of the streamline curvature calculation method); the mean streamline method for design of two-dimensional blading (ref. 5) (widely used in the turbomachinery designed here at Pennsylvania State and elsewhere); the contributions to design taking account of cavitation (refs. 6, 7, 8); basic thinking on marine propulsion (ref. 9); and a survey

1

of noise generation (ref. 10). In passing, we may note that not the least of Wislicenus' achievements has been the establishment of his own "school" of research workers, many of whose names appear as joint authors of the publications I have quoted.

It is the hope of the organizing committee that this meeting will provide a unifying environment for workers in turbomachinery aerodynamics. Indeed, we have invited several people not directly in the field to contribute so that we may get a wider view of a difficult subject, for, if there is one area that has almost every difficulty and complication built in, it is turbomachinery fluid mechanics. It is unsteady; it may be incompressible but with cavitation; it may be compressible—mixed supersonic, transonic, and subsonic; it is certainly viscous—including laminar, transitional, and turbulent flows; it is highly three-dimensional and rotational; it may contain large separated regions; it is noisy; and it is closely linked with the thermodynamics of the working fluid. From this complicated fluid mechanics the designer must make his decision, taking into account overall cycle and/or propulsive efficiency. Professor Wislicenus' keen interest in the design aspects of turbomachinery is reflected in a special session we have devoted to this subject.

It is perhaps useful briefly to review some recent developments in the field of turbomachinery fluid mechanics to set the scene for this Conference. In referring to recent developments I would distinguish three phases.

First of all, in the era during and following World War II, the application of classical aerodynamics to turbomachinery design allowed the gas turbine to become a reality and steam turbines to be further developed. I have in mind developments such as the analysis of free vortex flows (which has been associated with the names of Whittle, Griffith, Tietjens, and von Kármán), which enables a rational design of long turbine blades to be undertaken; the analysis of potential flow in cascades by Howell (ref. 11), Kraft (ref. 12), Merchant and Collar (ref. 13), and others; and the application of aeronautical standards in experimental testing of turbomachines and their components. This led to the compressor cascade correlations of Howell (ref. 14) and Erwin *et al.* (ref. 15; see also ref. 16), which provided a sound base for the design of compressor blading. The careful analysis of experimental data from turbines and cascades similarly led to the blading design methods of Söderberg at Westinghouse (ref. 17), Ainley at N.G.T.E. (ref. 18), and Zweifel at Brown Boveri, for axial flow turbine blade sections (ref. 19; see also ref. 20).

Concentrated aerodynamic work continued for a substantial period with the actuator disc theory of Marble (ref. 21); the general equations of Wu (ref. 22); the secondary flow work of Mager (ref. 23), Hawthorne (ref. 24), Smith (ref. 25), Johnston (ref. 26), and Taylor (ref. 27). The

diffuser work of Kline and his collaborators (ref. 28) and the work of Emmons (ref. 29) and others on rotating stall are some later examples. This period perhaps culminated in the outstanding review by NACA on axial flow compressor design (ref. 30).

The second major development over the last 10 years or so has been in the massive use of computers to analyze internal flows. Use of the computer has led to the rapid solution of the incompressible cascade flow (usually using the Martensen (ref. 31), Schlichting (ref. 32), and Stanitz (ref. 33) methods); of the three-dimensional meridional or axisymmetric flow (for example, Marsh's numerical solution (ref. 34) of Wu's general through flow equations; of flutter problems (for example, Whitehead (ref. 35)); of the flow past propellers or fans with widely spaced aerofoils (where we may not smear out the vorticity over the complete annulus); and of off-design performance. Perhaps in this stage we may not have continued sufficiently the careful aerodynamic experiments of the first stage, and we may have put too much emphasis on uncorroborated computer solutions. It is very often experimental work from the earlier era that we refer back to in making comparisons between theory and experiment.

I think perhaps we are now in a third era where we are absorbing new aerodynamic knowledge from other fields—the theory of boundary layers and acoustics—but at the same time making maximum use of the computer. This is particularly true in the general area of unsteady fluid mechanics, which is so obviously of vital importance in turbomachinery.[1] Here we see the application of established aerodynamic theory—the work of von Kármán and Sears before the war (ref. 37), for example, together with new questioning of established ideas (witness Giesing's work on the Kutta condition in unsteady flow (ref. 38), something of which you will see in a film to be shown during the symposium).

If there is a main challenge remaining—a fourth stage of development—it appears to me that it lies in the synthesis of all this developing fluid mechanics into the design process. For example, although we know the pressure distribution on the blades is unsteady, no designers are as yet calculating this pressure distribution together with the unsteady boundary layer development and optimizing design as a result. Although estimates of annulus wall boundary layer growth are made, predictions of angle variation through the boundary layer due to secondary flow are not included in the design—at least not to my knowledge. To include all these effects is a vast undertaking, principally in the education of designers and in the integration and management of design and research teams.

---

[1] Professor Dean (ref. 36) pointed out some years ago that we would not get any change in stagnation enthalpy in reversible flow through a turbomachine unless the flow were basically unsteady.

So although great progress has been made in the understanding of the internal fluid mechanics of turbomachines, and in establishing this field as a recognized technological discipline, much remains to be done, particularly in the application of the results of research. It is to further this end that this conference has been initiated jointly by The National Aeronautics and Space Administration, The Pennsylvania State University and The Department of the Navy.

References

1. Internal Aerodynamics (Turbomachinery). *Inst. Mech. Eng. (London)*, 1970.
2. DZUNG, L. Z., ed., *Flow Research in Blading*. Elsevier Press, 1970.
3. WISLICENUS, G. F., Principles and Applications of By-Pass Turbo-Jet Engines. *Trans. SAE*, Vol. 64, p. 486, 1956.
4. SMITH, L. H., S. C. TRAMGOTT, AND G. F. WISLICENUS, A Practical Solution of a Three-Dimensional Flow Problem of Axial-Flow Turbomachinery. *Trans. ASME*, Vol. 8, No. 3, p. 789, 1941.
5. WISLICENUS, G. F., *Fluid Mechanics of Turbomachinery*. McGraw-Hill Book Co., Inc., 1947.
6. WISLICENUS, G. F., Critical Considerations on Cavitation Limits of Centrifugal and Axial Flow Pumps. *Trans. ASME*, Vol. 78, No. 8, p. 1707, 1956.
7. HOLL, J. W., AND G. F. WISLICENUS, Scale Effects in Cavitation. *Trans. ASME, J. Basic Eng.*, Vol. D83, pp. 386–398.
8. HENDERSON, R. E., J. F. MCMAHON, AND G. F. WISLICENUS, *A Method for the Design of Pump-Jets*. Penn. State U. Ordnance Res. Lab Report NOw 63–0209–c–7, 1964.
9. WISLICENUS, G. F., Hydrodynamics and Propulsion of Submerged Bodies. *J. Am. Rocket Soc.*, Vol. 30, No. 12, pp. 1140–1148, 1960.
10. WISLICENUS, G. F., AND M. SEVIK, *A Survey of Hydrodynamic Generation of Noise*. Penn. State U. Ordnance Res. Lab Report TM 504, 2461–04, 1964.
11. HOWELL, A. R., Theory of Arbitrary Aerofoils in Cascades. R.A.E. Note E3859, A.R.C. Report 5095, 1941, *Phil. Mag.*, Ser. 7.39, p. 913.
12. KRAFT, H., The Development of a Laminar Wing Type Turbine Bucket. *Z. angew. Math. Phys.*, IXb (Fasc. 5/6), 1958, p. 404.
13. MERCHANT, W., AND A. R. COLLAR, *Flow of an Ideal Fluid Past a Cascade of Blades: Part II*. A.R.C. R & M 1893, 1941.
14. HOWELL, A. R., *The Present Basis of Axial Flow Compressor Design: Part I, Cascade Theory and Performance*. A.R.C. R & M 2095, 1942.
15. HERRIG, L. J., J. C. EMERY, AND J. R. ERWIN, *Systematic Two-Dimensional Cascade Tests of NACA 65-Series Compressor Blades at Low Speeds*. NACA R.M. L51G31, 1951.
16. HORLOCK, J. H., *Axial Flow Compressors*. Butterworth Scientific Publications, 1958.
17. SÖDERBERG, C. R., Unpublished notes. MIT Gas Turbine Lab, 1949.
18. AINLEY, D. G., The Performance of Axial Flow Turbines. *Proc. Inst. Mech. Engrs.*, Vol. 159, 1948, p. 230.
19. ZWEIFEL, O., *Die Frage der optimalen Schaufelteilung bei Beschaufelungen von Turbomaschinen, insbesondere bei grosser Umlenkung in den Schaufelreihen.* Brown Boveri Mitteilungen, December 1945.
20. HORLOCK, J. H., *Axial Flow Turbines*. Butterworth Scientific Publications, 1966.

21. MARBLE, F. E., The Flow of a Perfect Fluid Through an Axial Turbomachine With Predescribed Blade Loading. *J. Aeron. Sci.*, Vol. 15, p. 473, August 1948.

22. WU, C. H., A General Theory of Three-Dimensional Flow in Subsonic and Supersonic Turbomachines of Axial, Radial and Mixed Flow Types. *Trans. Am. Soc. Mech. Engrs.*, November 1952, NACA T.N. 2604, 1952.

23. MAGER, A., *Generalization of the Boundary Layer Momentum-Integral Equations to Three-Dimensional Flows, Including Those of Rotating Systems.* NACA Report 1067, 1951.

24. HAWTHORNE, W. R., Secondary Circulation in Fluid Flow. *Proc. Roy. Soc.* (London), Series A, Vol. 206, p. 374, 1951.

25. SMITH, L. H., Secondary Flow in Axial Flow Turbomachinery. *Trans. Am. Soc. Mech. Engrs.*, Vol. 77, p. 1065, 1955.

26. JOHNSTON, J., Three-Dimensional Turbulent Boundary Layers. MIT Gas Turbine Lab, Report No. 35, October 1962.

27. TAYLOR, E. S., The Skewed Boundary Layer. *Trans. ASME, J. Basic Eng.*, Series D, Vol. 81, 1959, pp. 297–304.

28. KLINE, S., D. E. ABBOTT, AND R. W. FOX, Optimum Design of Straight Walled Diffusors. *Trans. ASME, J. Basic Eng.*, Series D, Vol. 81, 1959, pp. 321–331.

29. EMMONS, H. W., C. E. PEARSON, AND H. P. GRANT, Compressor Surge and Stall Propagation. *Trans. ASME*, Vol. 77, No. 4, pp. 455–469, 1955.

30. NACA: Members of Compressor and Turbine Research Division, *Aerodynamic Design of Axial Flow Compressors.* NACA R.M.E. 56 B O 3 b, 1956 (Revised), NASA SP–36.

31. MARTENSEN, E., Calculation of Pressure Distribution Over Profiles in Cascade in Two-Dimensional Potential Flow, by Means of a Fredholm Integral Equation. *Arch. for Rat. Mech. and Anal.*, Vol. 3, No. 3, 1959.

32. SCHLICHTING, H., AND N. SCHOLTZ, Uber die theoretische Berechnung der Strömungsverluste eines ebenen Schaufelgitters. *Ing.-Arch.*, Bd.XIX, Heft I, 1951.

33. STANITZ, J. D., *Approximate Design Method of High-Solidity Blade Elements in Compressors and Turbines.* NACA T. N. 2408, 1951.

34. MARSH, H., *A Digital Computer Program for the Through-Flow Fluid Mechanics in an Arbitrary Turbo-Machine Using a Matrix Method.* Aero. Research Council R & M 3509, 1966.

35. WHITEHEAD, D. S., Aerodynamic Aspects of Blade Vibration. *Proc. Inst. Mech. Engrs.*, Vol. 180, No. 3(i), 1965–6, pp. 49–60.

36. DEAN, R. C., On the Necessity of Unsteady Flow in Fluid Mechanics. *Trans. ASME, J. Basic Eng.*, Series D, Vol. 81, 1959, p. 24.

37. VON KÁRMÁN, T., AND W. R. SEARS, Aerofoil Theory for Non-Uniform Motion. *J. Aero. Sci.* Vol. 5, No. 10, 1938, pp. 379–390.

38. GIESING, J. P., Vorticity and Kutta Condition for Unsteady Multi-Energy Flows. *Trans. ASME, J. Appl. Mech.*, p. 609, 1969.

N75 11176

Turbomachinery Design Described by Similarity Considerations

George F. Wislicenus

The dimensionless representation of the *operating conditions* of turbomachinery by the specific speed and the suction specific speed is well known, although specific speed and suction specific speed are often not used in truly dimensionless form. It is also known that these expressions of operating conditions are related to the design of the machine. This paper presents first an extension of this approach, particularly in the direction of mechanical design characteristics. Secondly, the paper attempts to establish a reasonably comprehensive picture of the dimensionless field of turbomachinery design. This attempt results in the concept of a "space of dimensionless operating conditions." Every point in this space can be associated with a set of dimensionless *design* parameters such as diameter ratios, flow coefficients, head coefficients, and the like, provided certain "design choices" regarding the fluid and the machine have been made. The core of the design process then relates such sets of design parameters to the dimensionless design form of the machine. This part of the design process is not described in this paper but only "located" relative to other parts of the overall design process.

For over half a century, the design of turbomachines has been related to a principally dimensionless expression of operating conditions, the "specific speed," which is defined by the statement that any fixed value of the specific speed describes that combination of operating conditions which permits similar flow conditions in geometrically similar turbomachines. Figure 1 depicts the well-known relation between the runner design of hydrodynamic pumps and the specific speed.

The specific speed, called in this paper the "basic specific speed," is here used in strictly dimensionless form:

$$n_s = \frac{n\sqrt{Q}}{(g_o H)^{3/4}} \tag{1}$$

A list of symbols is provided at the end of this paper. Metric or any other units may also be used, as long as consistent units are employed for length and time. This is often not the case, as for example with the pump specific speed usually used in the United States. There the speed of rotation, n,

$n_s = 0.06$
(1000)

$n_s = 0.12$
(2000)

$n_s = 0.25$
(4300)

$n_s = 0.37$
(6400)

$n_s = 0.60$
(10 000)

$n_s = 0.85$
(15 000)
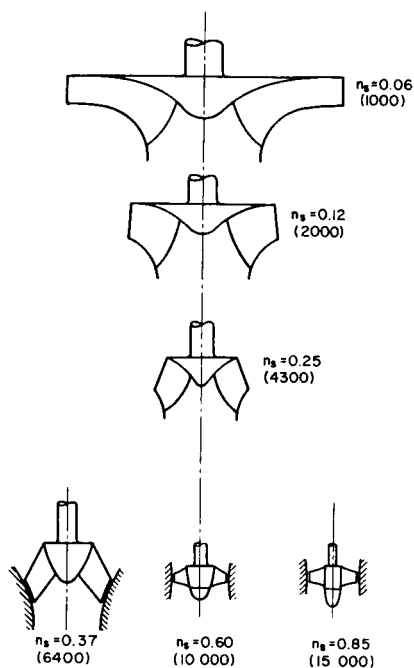
FIGURE 1.—*Pump runner profiles as a function of basic specific speed.*

is measured in revolutions per minute (rpm), Q in gallons per minute (GPM), and H in feet (ft), omitting the standard acceleration, g_o. This dimensional specific speed is related to the dimensionless specific speed n_s given by equation (1) as follows:

$$\frac{n\,(\text{rpm})\,\sqrt{Q\,(\text{GPM})}}{H\,(\text{ft})^{3/4}} = 17{,}200\ n_s$$

The dimensional values of the pump specific speed are given in figure 1 (and in fig. 18) in parentheses.

The relation between the design form of the machine and the dimensionless specific speed is easily obtained by putting

$$n = \frac{U_o}{D_o\,\pi} \quad \text{and} \quad Q = V_{m_i} \cdot \frac{D_i^2\,\pi}{4}\left(1 - \frac{D_h^2}{D_i^2}\right)$$

The notations used are defined in figure 2 and are given in the list of symbols. Substituting these expressions into equation (1) leads to the following equation:

$$n_s = \frac{n\sqrt{Q}}{(g_oH)^{3/4}} = \frac{1}{2^{1/4}\pi^{1/2}} \left(\frac{U_o^2}{2g_oH}\right)^{3/4} \left(\frac{V_{mi}}{U_i}\right)^{1/2} \left(\frac{D_i}{D_o}\right)^{3/2} \left(1 - \frac{D_h^2}{D_i^2}\right)^{1/2} \quad (2)$$

By assuming fixed values for the flow coefficient V_{mi}/U_i and for the maximum head coefficient $2g_oH/U_{omin}^2$, it is not difficult to derive the runner forms shown in figure 1. However, one can, by using the condition of continuity for incompressible fluids, relate the basic specific speed also to other form characteristics of the runner or of stationary flow passages adjacent to the runner.

About 35 years ago the concept of specific speed was extended to include cavitation conditions, leading to the now well-known concept of "suction specific speed." Suction specific speed can be expressed in exactly the same form as the basic specific speed (eq. (2)) simply by replacing the total head of the machine (H) by the total suction head of the machine above the vapor pressure (H_{sv}). A more useful expression of the suction specific speed (in dimensionless form) is

$$S = \frac{nQ^{1/2}}{(g_oH_{sv})^{3/4}} = \frac{1}{2^{1/4}\pi^{1/2}} \left(\frac{V_{mi}^2}{2g_oH_{sv}}\right)^{3/4} \frac{U_i}{V_{mi}} \left(1 - \frac{D_h^2}{D_i^2}\right)^{1/2} \quad (3)$$

because it is concerned only with conditions at the low-pressure side of the runner, and $2g_oH_{sv}/V_{mi}^2$ is approximately constant for a wide range of S values.
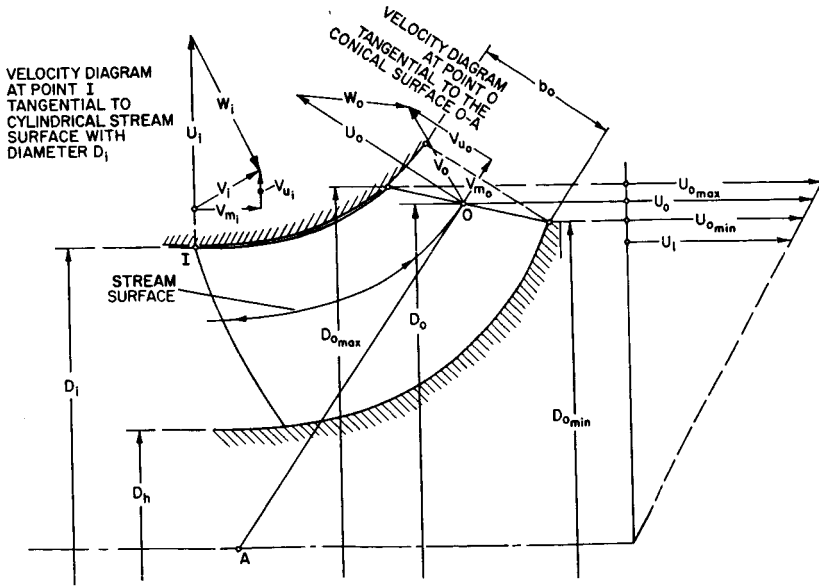

FIGURE 2.—Profile of a turbomachine runner, defining notations.

During the last few years it has become apparent that the basic specific speed and the suction specific speed are only examples of a much wider range of dimensionless expressions of operating conditions. References 1 and 2 demonstrate the application of this type of consideration to a variety of engineering design problems. The "power factor" $B_P = n\sqrt{P}/V^{5/2}$ is a "specific speed" that has been used in marine engineering for many years.

This paper represents an attempt to present the relation between the dimensionless operating conditions of turbomachines, expressed here in the form of various specific speeds, to the design form of turbomachines. A *design form* shall be defined as the three-dimensional, geometric form of an engineering device (i.e., a device conceived and judged by functional, not artistic, criteria). The term "design" is broader, including properties of the structural materials. Furthermore, the word "design" denotes a plan (like drawings, specifications, or a computer program) for an object as well as the action of creating such a plan.

It shall be understood that all geometrically similar machines represent only *one* design form so that the entire field of all possible design forms of turbomachines is dimensionless. Since the corresponding field of all possible, continuously variable operating conditions can also be presented in dimensionless form (the specific speeds), it is seen that the relation between operating conditions and design forms is a relation between two fields of dimensionless technical informations.

It is hoped that a presentation of the physical facts involved in this relation will stimulate a mathematically competent engineer or a mathematician to formulate this subject in a theoretically more satisfactory fashion. In view of this possibility, it should be mentioned that the terminology used in this paper is that of an engineer, not that of a mathematician. For example, the word "field," when used here, does not have its mathematical meaning. In some cases the mathematicially inclined reader might substitute "class" for "field."

OPERATING CONDITIONS EXPRESSED IN THE FORM OF SPECIFIC SPEEDS

There are, of course, many other operating conditions besides n, Q, H, and H_{sv} that determine the design of a turbomachine. These operating conditions may be expressed in dimensionless form in many different ways. It is merely for reasons of tradition that this writer has chosen the form of the specific speed for this purpose.

Table I presents the operating conditions and corresponding specific speeds that have been considered by this writer. No doubt other operating conditions could be considered. The right sides of the equations presented

can be expressed in as many ways as the rate of volume or mass flow may be related to the fluid velocities in various parts of the machine (see table II).

It is evident that all dimensionless operating conditions (i.e., all specific speeds) follow the same general scheme. In all cases, the kinematically determined velocity $(n\sqrt{Q})^{2/3}$, raised to the $\frac{3}{2}$ power, is divided by the $\frac{3}{2}$ power of a velocity expressing some forces that determine the action of the machine; for example, $(\sqrt{2g_oH})^{3/2}$, $(\sqrt{2g_oH_{sv}})^{3/2}$, the acoustic velocity $a^{3/2}$, $(\sqrt{\sigma/\rho})^{3/2}$, and so on. Designating this general, force-describing velocity by v, tables II and III present the form of all specific speeds considered here and its relations to various parts of the machine.

TABLE I.—*Partial List of Dimensionless Operating Conditions (Specific Speeds)*

Basic specific speed:

$$n_s = \frac{nQ^{1/2}}{(g_oH)^{3/4}} = \frac{1}{2^{1/4}\pi^{1/2}} \left(\frac{U_o^2}{2g_oH}\right)^{3/4} \left(\frac{V_{mi}}{U_i}\right)^{1/2} \left(\frac{D_i}{D_o}\right)^{3/2} \left(1-\frac{D_h^2}{D_i^2}\right)^{1/2} \qquad \text{(a)}$$

Suction specific speed:

$$S = \frac{nQ^{1/2}}{(g_oH_{sv})^{3/4}} = \frac{1}{2^{1/4}\pi^{1/2}} \left(\frac{V_{mi}^2}{2g_oH_{sv}}\right)^{3/4} \frac{U_i}{V_{mi}} \left(1-\frac{D_h^2}{D_i^2}\right)^{1/2} \qquad \text{(b)}$$

Compressibility specific speed:

$$n_a = \frac{nQ^{1/2}}{a^{3/2}} = \frac{1}{2\pi^{1/2}} \left(\frac{w_i}{a}\right)^{3/2} \frac{(V_{mi}/U_i)^{1/2}}{\left(1-2\frac{V_{ui}}{U_i}+\frac{V_{ui}^2}{U_i^2}+\frac{V_{mi}^2}{U_i^2}\right)^{3/4}} \left(1-\frac{D_h^2}{D_i^2}\right)^{1/2} \qquad \text{(c)}$$

Viscosity specific speed:

$$n_\nu = \frac{nQ^{1/2}}{(n\nu)^{3/4}} = \frac{\pi^{1/4}}{2} \left(\frac{U_oD_o}{\nu}\right)^{3/4} \left(\frac{D_i}{D_o}\right)^{3/2} \left(\frac{V_{mi}}{U_i}\right)^{1/2} \left(1-\frac{D_h^2}{D_i^2}\right)^{1/2} \qquad \text{(d)}$$

Stress specific speed:

$$n_\sigma = \frac{nQ^{1/2}}{(\sigma/\rho)^{3/4}} = \frac{1}{2^{1/4}\pi^{1/2}} \left(\frac{\rho U_o^2}{2\sigma}\right)^{3/4} \left(\frac{D_i}{D_o}\right)^{3/2} \left(\frac{V_{mi}}{U_i}\right)^{1/2} \left(1-\frac{D_h^2}{D_i^2}\right)^{1/2} \qquad \text{(e)}$$

Gravity specific speed:

$$n_g = \frac{nQ^{1/2}}{(g/n)^{3/2}} = \frac{1}{2\pi^2} \left(\frac{U_o^2}{gD_o}\right)^{3/2} \left(\frac{D_i}{D_o}\right)^{3/2} \left(\frac{V_{mi}}{U_i}\right)^{1/2} \left(1-\frac{D_h^2}{D_i^2}\right)^{1/2} \qquad \text{(f)}$$

Vibration specific speed:

$$n_v = \frac{nQ^{1/2}}{(E/\rho_s)^{3/4}} = \frac{1}{2^{1/4}\pi^{1/2}} \left(\frac{\rho_s U_o^2}{2E}\right)^{3/4} \left(\frac{D_i}{D_o}\right)^{3/2} \left(\frac{V_{mi}}{U_i}\right)^{1/2} \left(1-\frac{D_h^2}{D_i^2}\right)^{1/2} \qquad \text{(g)}$$

TABLE II.—*Specific Speeds Based on the Representative Velocity (v) Defined in Table III*

$$\frac{nQ^{1/2}}{(v)^{3/2}}=\frac{1}{2\pi^{1/2}}\left(\frac{U_o}{(v)}\right)^{3/2}\left(\frac{D_i}{D_o}\right)^{3/2}\left(\frac{V_{mi}}{U_i}\right)^{1/2}\left(1-\frac{D_h^2}{D_i^2}\right)^{1/2}$$

$$\frac{nQ^{1/2}}{(v)^{3/2}}=\frac{1}{2\pi^{1/2}}\left(\frac{U_i}{(v)}\right)^{3/2}\left(\frac{V_{mi}}{U_i}\right)^{1/2}\left(1-\frac{D_h^2}{D_i^2}\right)^{1/2}$$

$$\frac{nQ^{1/2}}{(v)^{3/2}}=\frac{1}{2\pi^{1/2}}\left(\frac{V_{mi}}{(v)}\right)^{3/2}\left(\frac{U_i}{V_{mi}}\right)\left(1-\frac{D_h^2}{D_i^2}\right)^{1/2}$$

$$\frac{nQ^{1/2}}{(v)^{3/2}}=\frac{1}{2\pi^{1/2}}\left(\frac{w_i}{(v)}\right)^{3/2}\frac{(V_{mi}/U_i)^{1/2}}{\left(1-2\dfrac{V_{u_i}}{U_i}+\dfrac{V_{u_i}^2}{U_i^2}+\dfrac{V_{mi}^2}{U_i^2}\right)^{3/4}}\left(1-\frac{D_h^2}{D_i^2}\right)^{1/2}$$

$$\frac{nQ^{1/2}}{(v)^{3/2}}=\frac{1}{\pi^{1/2}}\left(\frac{U_o}{(v)}\right)^{3/2}\left(\frac{V_{mo}}{U_o}\right)^{1/2}\left(\frac{b_o}{D_o}\right)^{1/2}$$

$$\frac{nQ^{1/2}}{(v)^{3/2}}=\frac{1}{\pi}\left(\frac{U_o}{(v)}\right)^{3/2}\left(\frac{V_{u_o}}{U_o}\right)^{1/2}\left(\frac{D_o}{D_{th}}\right)^{1/2}\frac{A_{th}^{1/2}}{D_o}N^{1/2}$$

One may also compare the general velocity (v) with the head of the machine in the form $(v)^2/g_oH$.

TABLE III.—*Definitions of the Representative Velocity (v)*

$v = (g_oH)^{1/2}$ for the basic specific speed
$v = (g_oH_{sv})^{1/2}$ with respect to cavitation
$v = a =$ the velocity of sound, with respect to compressibility
$v = (n\nu)^{1/2} = (U \cdot \nu/\pi D)^{1/2}$ with respect to viscosity
$v = (\sigma_c/\rho_s)^{1/2}$ with respect to centrifugal stresses
$v = (\sigma_f/\rho_f)^{1/2}$ with respect to fluid-induced stresses
$v = g/n = g\pi D/U$ with respect to any general acceleration g of the system as a whole
$v = (E/\rho)^{1/2} = D \cdot f$ with respect to vibrations of the machine at a frequency f

The foregoing comments raise the question whether the $\frac{2}{3}$ power of the specific speeds would not be a better dimensionless expression of operating conditions than the specific speeds used here, as the $\frac{2}{3}$ power would be a velocity ratio. Since any power of such a ratio serves essentially the same purpose, this writer prefers not to depart from the conventional specific speed more than to use it in its dimensionless form, recognizing that raising the specific speeds to *any* power does not make any essential difference.

PHYSICAL SIGNIFICANCE OF THE DESIGN PARAMETERS

The various dimensionless ratios appearing on the right sides of the specific speed equations (tables I and II) are here denoted as "design parameters." This does not require any explanation regarding the simple ratios of linear dimensions D_i/D_o, b_o/D_o, D_h/D_i, etc., as these ratios have clear meanings regarding the *form* of the "profile" of the machine to be designed (see fig. 2). *The flow coefficient V_{m_i}/U_i and the head coefficient $2g_oH/U_o^2 = 2\eta_hV_{u_o}/U_o$ (for zero rotation of the fluid at the suction side of the runner) determine the velocity vector diagrams at the inlet and discharge edges of the impeller vanes,* using the condition of continuity. By some extensions, this is true also for the nearby stationary vane systems, provided the general form of the machine has been selected, as will be discussed later. Figure 3 depicts the information that can be derived from equations (2) and (3) regarding the design of a radial- or mixed-flow runner, considering that the direction of the vane ends is closely related to the direction of the relative velocity of flow (w). (It illustrates that this relation exists also if the flow on the suction side of the runner has a circumferential component (V_{u_i}, V_u, V_{u_h}).) With the information given in figure 3 the true design process starts, connecting these pieces of information to a geometrically, hydrodynamically, and mechanically consistent structure.
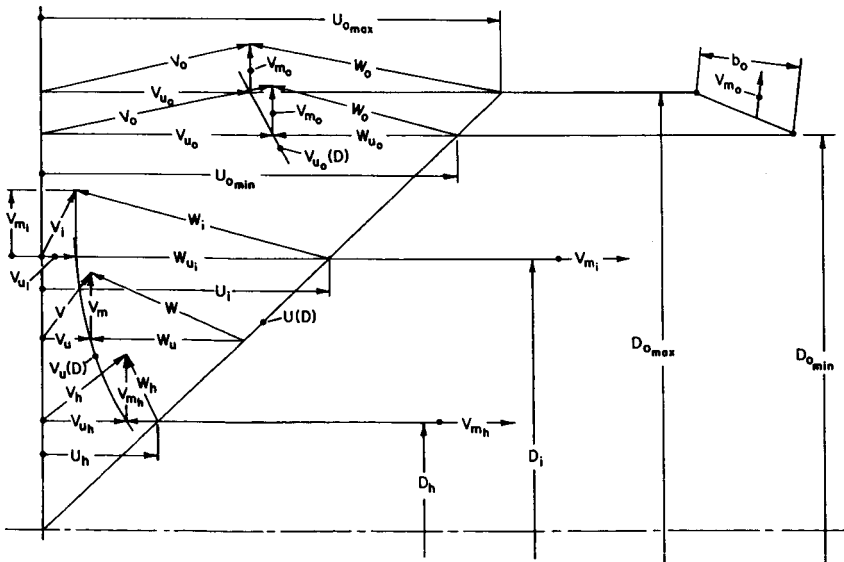

FIGURE 3.—*Information on runner design derived from basic and suction-specific speeds.*

With respect to mechanical design characteristics, the "stress specific speed"

$$n_\sigma = \frac{nQ^{1/2}}{(\sigma/\rho)^{3/4}} = \frac{1}{2^{1/4}\pi^{1/2}} \left(\frac{\rho U_o^2}{2\sigma}\right)^{3/4} \left(\frac{D_i}{D_o}\right)^{3/2} \left(\frac{V_{m_i}}{U_i}\right)^{1/2} \left(1 - \frac{D_h^2}{D_i^2}\right)^{1/2} \quad (4)$$

is of particular interest. The stress (σ) is here an *allowable* stress and is therefore known from the properties and the working conditions of the structural material. The stress coefficient $\rho U_o^2/2\sigma$ is of the most direct significance regarding the centrifugal stress σ_c of a structural rotating element having the mass per unit volume ρ_s. For example, a thin, freely rotating hoop has the centrifugal stress coefficient $\rho_s U_o^2/2\sigma_c = 1/2$.[1]

For a radial strut of constant cross section, the maximum stress coefficient at the center of rotation is $\rho_s U_o^2/2\sigma_c = 1$.[1] Straight radial structural members are of importance for runner blades (as shown in fig. 4), having radial blade elements to achieve maximum resistance against centrifugal forces. This condition is fulfilled almost automatically for axial-flow runners. In such cases the radial blade elements usually do not have constant cross sections, but radially diminishing cross sections. Figure 5 shows the cross-section distribution of straight radial struts having
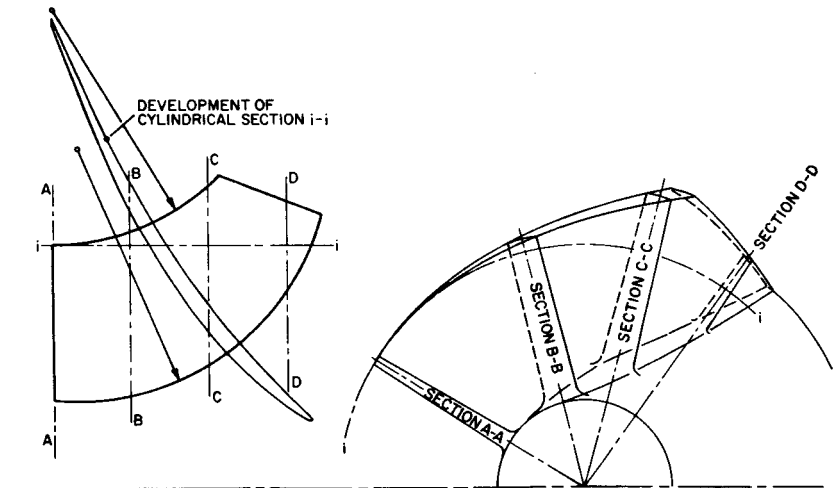

FIGURE 4.—*Turbomachinery runner with radial blade elements.*

---

[1] If the fluid rotates at the same angular velocity as the solid, rotating parts, then the difference between the mass-density of the structural material and the fluid should be used in these expressions.
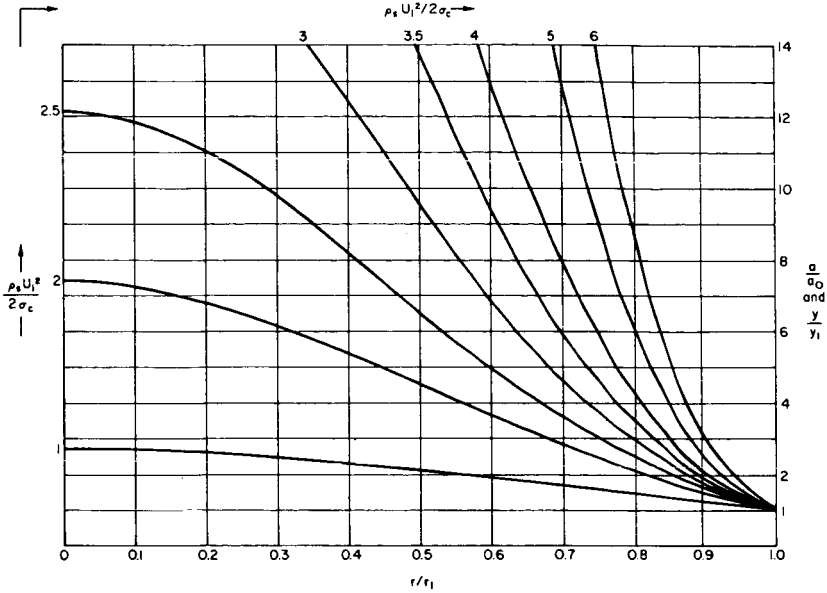
FIGURE 5.—*Area distribution of a rotating radial strut (vane element) of constant stress, and thickness distribution of a rotating disc of constant stress.*

radially constant centrifugal stress including their outer cross section at radius r_1, where such a stress might be imposed by an outer shroud or by an extension of the radial element with nonuniform, radially diminishing stress. The curves shown in figure 5 describe also the thickness distribution y/y_1 of a rotating disc of constant stress. In this case the radial stress at the outer periphery is generated by the vanes and vane-holding rim, considering a standard axial-flow turbine or compressor runner as shown in figure 6. If the stress coefficient is calculated with the maximum peripheral velocity U_o at radius $r_o > r_1$, its value will be higher than shown in figure 5. For radial blade elements, the stress at radius r_1 permits a constant area radial extension of the blade beyond r_1, say to $r_o > r_1$. The resulting cross-section distribution and stress coefficients $\rho_s U_o^2/2\sigma_c$ are given in figure 7.

Axially extending, nonradial vanes (as used, for example, with standard centrifugal pump or compressor runners with backward-bent vanes) obviously lead to bending stresses in the vanes. The resulting centrifugal stress coefficient referred to the peripheral velocity at the vane section considered is

$$\frac{\rho_s U^2}{2\sigma_c} = \frac{q}{12} \frac{h}{b} \frac{r}{b} \frac{1}{\sin \beta} \tag{5}$$
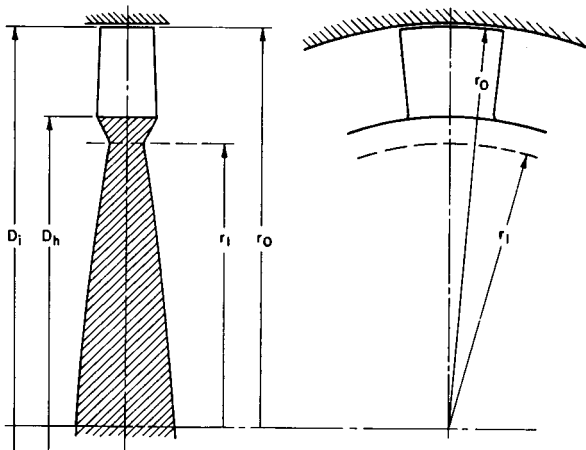
FIGURE 6.—*Axial-flow runner of high stress-specific speed, defining notations.*
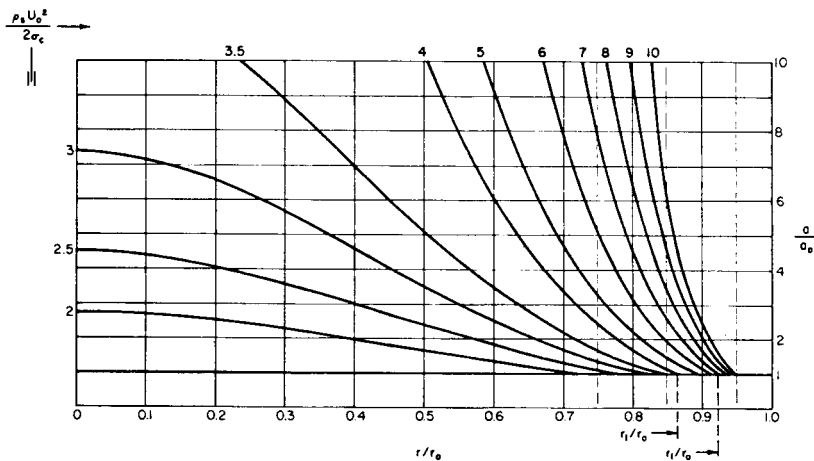
FIGURE 7.—*Area distribution of a rotating radial element with zero stress at* r_0 *and constant stress from* $r = r_1$ *to* $r = 0$.

The notations used are defined by figure 8, except q, which varies from 8 for no bending stiffness at the axial end supports of the vanes (i.e., very thin shrouds) to 32 for completely rigid end supports; q is 2 for vanes cantilevered axially from a single shroud.

From the above, one can readily draw some conclusions regarding the centrifugal stress coefficients of runners of various forms. For example, an axial-flow runner as shown in figure 6 will have a centrifugal stress coefficient of $\rho_s U_o^2 / 2\sigma_c = 4$ *if* $r_o/r_1 = \sqrt{2}$, if the disc thickness ratio $y/y_1 = 7$ at
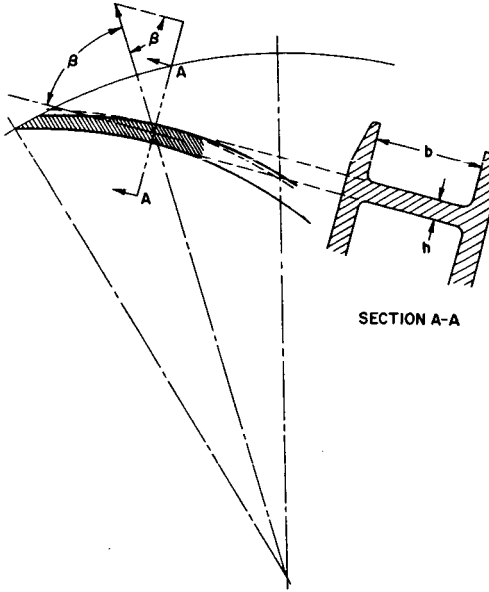
FIGURE 8.—*Bending stress configuration of nonradial vanes, defining notations.*

$r = 0$, and if the blade cross-section ratio $a/a_o = 2.5$ at a blade root-to-tip radius ratio of $r/r_o = 0.75$. This may well be close to a maximum for turbomachinery runners. The corresponding stress-specific speed would be, according to the equation given for n_{σ_c} in table I:

$$\frac{nQ^{1/2}}{\sigma_c/\rho_s} = n_{\sigma_c} = 0.487 \tag{6}$$

where it was assumed that $D_h/D_i = 0.75$, $V_{mi}/U_i = 0.3$, and, of course, $D_o = D_i$.

For a runner with axially extending nonradial vanes, one finds from equation (5) that $\rho_s U_o^2/2\sigma_c = 1.52$, where it was assumed that $h/b = \frac{1}{4}$, $r/b = 4.2$, and $\beta = 60°$. The coefficient q was assumed to be 15. The corresponding centrifugal stress specific speed was found to be in the neighborhood of $n_{\sigma_c} = 0.17$, where the basic specific speed was assumed to be about 0.12 (2060). The fact that this stress specific speed is only about one-third that previously calculated for an axial flow runner of very favorable proportions (in terms of stress) reflects correctly the less favorable design form of a centrifugal runner with backward-bent vanes. Nevertheless, even this runner form does not come close to representing a minimum of centrifugal

stress specific speed. Comparable runners of higher specific speeds would have lower stress specific speeds than 0.17.

The most important fluid-dynamically generated stresses σ_f are probably the bending stresses in the vanes, and are therefore proportional to the average vane-pressure difference $C_L \rho_f w^2 / 2$. A corresponding bending-stress coefficient would be

$$\frac{\rho_f U_o^2}{2\sigma_f} = q \frac{U_o^2}{C_L w^2} \frac{m_s}{b^2 l} \tag{7}$$

where m_s is the root section modulus of the vane, b the vane span, l the vane length, and $q = 2$ for cantilevered vanes; or $q = 8$ to 32 for vanes supported on both ends.

It is of interest to compare the fluid-dynamically induced stress (σ_f) with the centrifugal stress (σ_c). This comparison is most direct for centrifugal bending stresses in axially extending, nonradial vanes. One finds

$$\frac{\sigma_f}{\sigma_c} = \frac{\rho_f}{\rho_s} \cdot \frac{r}{2h} \frac{C_L w^2}{U_o^2 \sin \beta} \tag{8}$$

with the additional notations defined by figure 8.

Evidently $C_L w^2 / U_o^2 \sin \beta$ is of the order *one*. $r/2h$ is for geometric reasons much larger than one, usually in the neighborhood of ten. For gases, ρ_s / ρ_f is about 1000 so that $\sigma_c > \sigma_f$. For liquids with densities in the neighborhood of that of water, ρ_s / ρ_f lies between 2 and 10 so that $\sigma_f \geqq \sigma_c$. For liquid hydrogen, $\rho_s / \rho_f > 10$ so that $\sigma_c > \sigma_f$.

It should be evident that next to the basic specific speed, the suction specific speed, and (perhaps) the compressibility specific speed, the stress specific speeds have the best defined influence on the design of turbomachines. It is for this reason and because this specific speed and coefficient are not yet used extensively that this type of stress consideration has been given a prominent place in this paper.

RELATION BETWEEN VELOCITY DIAGRAMS AND VANE SHAPE

Figure 3 presented an example of the information on design form represented by the design parameters derived from the flow-determined specific speeds. It was pointed out that the complete design form of the vane system has to be derived from this information by what may well be considered as the core of the design process. This derivation requires the entire knowledge and experience available in the field and is a problem far too extensive to be explored here. Two considerations will be presented because they describe the nature of the design problem: A real-flow limita-

tion of the velocity diagrams and the relation between the velocity diagrams and the shape of cylindrical, coaxial vane sections through axial-flow runners.

The limitation of the velocity diagrams results from the "separation" or "stall" limits of the flow of a real fluid in vane systems. It has been found by approximate theoretical considerations, supported by test results, that the mean relative velocity of flow cannot be reduced in a single vane system to less than about 60 percent of its initial mean value (i.e., $w_2/w_1 \geqq 0.6$ for rotating vane systems and $V_2/V_1 \geqq 0.6$ for stationary vane systems). The reason for this limitation is outlined in chapters 12 and 25 of reference 3 and does not lie within the scope of this paper. However, the *existence* of such a limitation is important for the present considerations. It means that there *is* a limitation on the velocity vector diagrams (i.e., on the conditions of design) before the design process is started. This limitation is different from other limitations such as cavitation limitations insofar as it is not a function of a continuously varying operating condition, because the dependence of this limit on the Reynolds number (and thereby on the viscosity specific speed) is not known.

With this limitation of the velocity vector diagrams in mind, these diagrams will now be related to the vane shapes as appearing in coaxial, cylindrical sections through axial-flow vane systems. Figure 9 shows the
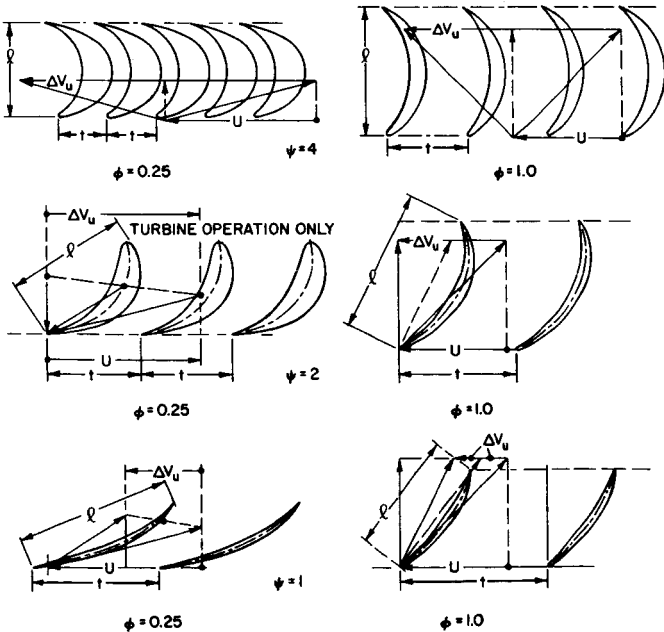

FIGURE 9.—*Family of axial-flow vane systems.*

vane shape as a function of the flow coefficient $\phi = V_{m_i}/U_i$ and of the head coefficient $\psi = 2g_oH/U^2$. The velocity vector diagrams are shown for pump (or compressor) flow (vertically up) except for the case $\phi = 0.25$, $\psi = 2$, where this condition leads to $w_2/w_1 < 0.6$ for pump operation. Thus this system is shown for turbine operation (flow from top to bottom) only.

The family of axial-flow vane systems indicated diagrammatically in figure 9 is not uniquely related to the flow and head coefficients ϕ and ψ as the *rate* of changing the angular momentum along the blade; i.e., the *distribution* of blade pressure difference affects the blade shape for given inlet and discharge conditions. However, for some given (say, optimum) pressure distribution, the (optimum) blade shape may well become a unique function of the inlet and discharge conditions, or of ϕ and ψ.

Before closing this discussion it is necessary to say something about the vane *spacing*. Its determination is theoretically included in criteria concerning a satisfactory vane pressure *distribution*. However, a more practical approach is one by way of the blade lift coefficient, which should for this purpose be expressed in the following form:

$$C_L = \frac{2\Gamma}{w_\infty l}$$

where Γ is the circulation per blade. For axial-flow machines, this reduces to the simple form

$$C_L = 2\,\frac{\Delta V_u}{w_\infty}\frac{t}{l} \tag{10}$$

and, for radial-flow machines,

$$C_L = 2\,\frac{V_{u_o}}{w_\infty}\left(1 - V_{u_i}\,\frac{D_i}{D_o}\right)\frac{t_o}{l} \tag{11}$$

One can only estimate that, for vane systems with very little change in mean static pressure, C_L has about the same maximum value as for a single airfoil in an infinitely extended stream (say, $C_{L_{max}} = 1.5$). For systems with retarded relative flow ($w_2 < w_1$), $C_{L_{max}}$ is lower (say, between 1 and 1.5), whereas, for accelerated relative flow, $C_{L_{max}}$ may be chosen higher than 1.5 (say, 2, and perhaps still higher, although a true maximum value of C_L has never been established).

For any estimated value of C_L, equations (10) or (11) determine the vane spacing t or t_o for a given vane length l.

"DESIGN CHOICES" AND THE RELATION BETWEEN OPERATING CONDITIONS AND DESIGN FORMS

Assuming the relation between the velocity diagrams and the vane shape is extended into the field of radial-flow runners, including the three-dimensional relation between vane shape and profile shape of the runner, one can imagine a complete line of connections between the operating conditions (the specific speeds), the design parameters (which determine certain elementary design form characteristics and the velocity vector diagrams), and, finally, the complete design form of a turbomachine. This connection is as complete as the given operating conditions and the knowledge available regarding the design of such machines.

However, even under the most ideal circumstances this relationship is not unique. Certainly there is a vast difference in design between machinery handling liquids and machinery handling gases. There is another fundamental difference between pumps (and compressors) on one hand and turbines on the other. Distinctions of this type will be called "design choices," although many of them are obviously not made by the design engineer but by the customer. Obviously design choices of such fundamental nature have to be made before the design process can start. However, even regarding what many may consider as design details, certain choices must be made before one can start with the most elementary analytical procedures. For example, it is well known that the runner forms given in figure 1 are not the only forms by which the given specific speed values can be satisfied.

Figure 10 shows a series of *axial-flow* runners covering essentially the same range of basic specific speeds as figure 1, but agreeing in design form
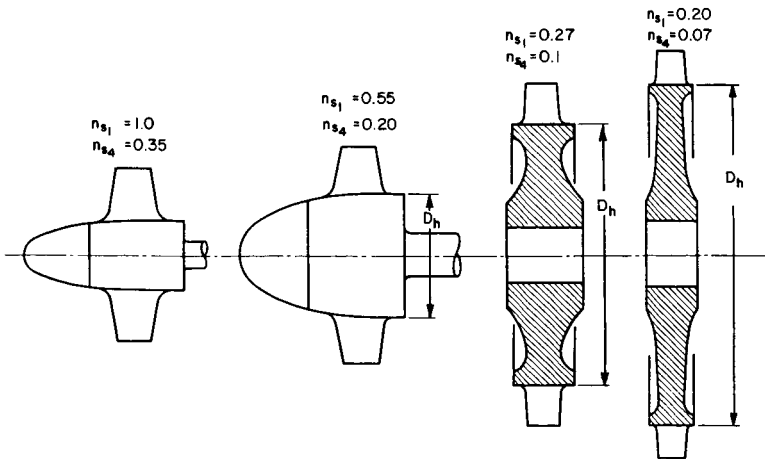
FIGURE 10.—*Axial-flow runner profiles as a function of basic specific speed.*

with figure 1 only in the region of high specific speeds. (n_{s_1} denotes the basic specific speed achieved with a root head coefficient $\psi = 1$, and n_{s_4} with a blade root head coefficient $\psi = 4$. For the axial vane sections, see fig. 9.) On the other hand, figure 11 shows the same range covered entirely by radial- and mixed-flow runners. It is thus apparent that a *choice* between radial- and axial-flow design must be made before the design form can be determined from the specific speeds. Figure 11 also shows diagrammatically the stationary parts encasing the runner, indicating that for the highest specific speeds only a diffuser with axial discharge is a practically useful solution, thus demonstrating why in this range of n_s axial-flow machines are usually preferred.

Figure 12 describes the design choice between a single-stage, radial-flow pump and a multistage, axial-flow pump. Here the choice is often debatable. Both types of machines have about the same volume and weight, and, for medium basic specific speeds (about 0.12), about the same efficiency. The radial-flow pump has a wider stable operating range (at constant speed). The axial-flow pump has a mechanically much better casing with respect to high internal pressures, and, by virtue of its large number of vanes, probably lower amplitudes of pressure fluctuations at the discharge. In the aircraft gas turbine field, the lower "frontal area" was decisive for the choice of the axial-flow design.

Another design choice is that between "single-suction" and "double-suction" machines shown in figure 13. The double-suction machine has the advantage of a higher suction specific speed or (for gases) a lower Mach
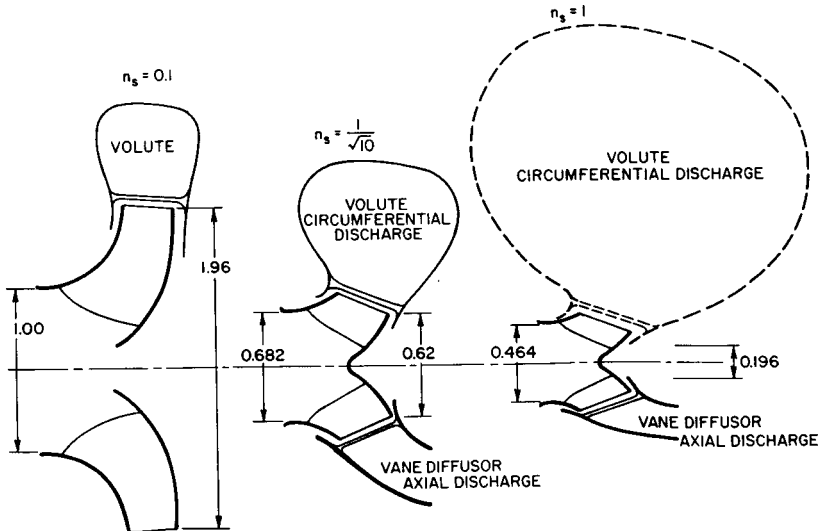
FIGURE 11.—*Radial- and mixed-flow pump profiles as a function of basic specific speed.*
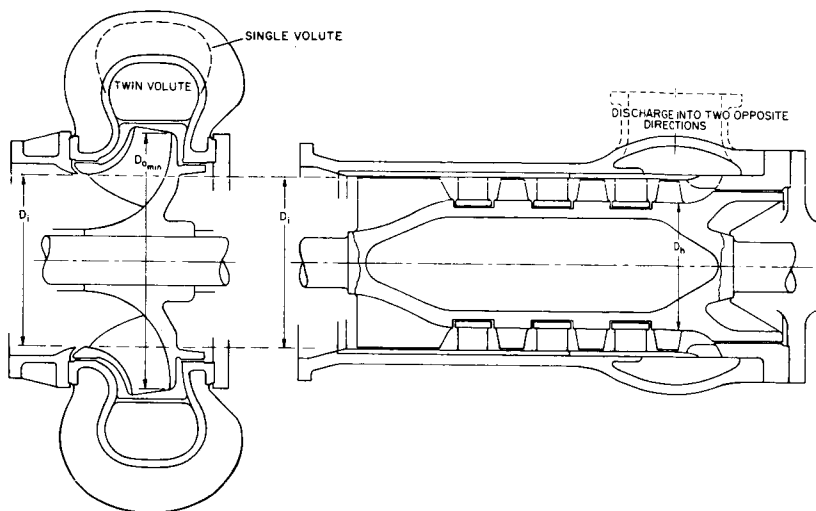
FIGURE 12.—*Design choice between a single-stage radial-flow and a multistage axial-flow turbomachine.*
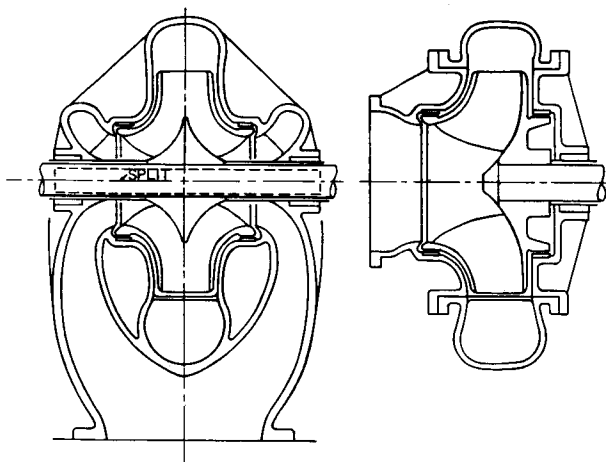
FIGURE 13.—*Design choice between double-suction and single-suction turbomachines.*

number of the relative flow entering the runner, or higher compressibility specific speed. The single-suction machine has the advantage of greater mechanical simplicity.

Figure 13 also demonstrates still another design choice; namely, that between the so-called horizontally split and vertically split casing construction. "Horizontally split" actually means that the casing is divided along a plane containing the axis of rotation; "vertically split" means the

casing is divided along planes normal to the axis of rotation. Figures 14 and 15 show the principle of this distinction with respect to multistage machines.

Horizontally split machines are much easier to assemble or disassemble than vertically split machines, particularly multistage machines. This construction is mostly used for commercial multistage pumps and compressors and large steam turbines. The vertically split construction has the advantage of greater reliability and is therefore preferred in rocket pumps; pumps for highly corrosive, toxic, or otherwise dangerous fluids; aircraft turbine engines; etc.

There are other design choices; examples include choices regarding number of stages and "volute" versus "diffuser" pumps. From the examples given, it will be clear that the term "design choice" is used here whenever one is concerned with a very limited number of *alternates*—often only two. In contrast, operating conditions are understood to be given in terms of *continuous variables* (speed, rate of flow, head, allowable stress, density, etc.).
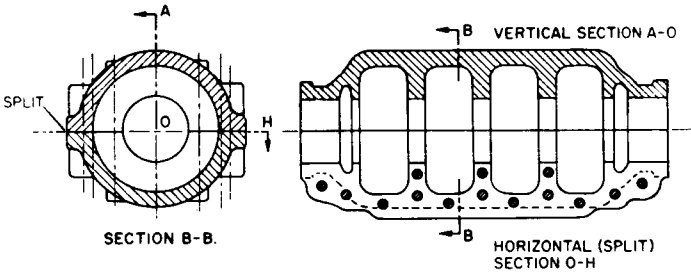
FIGURE 14.—*"Horizontally split" multistage pump casing.*
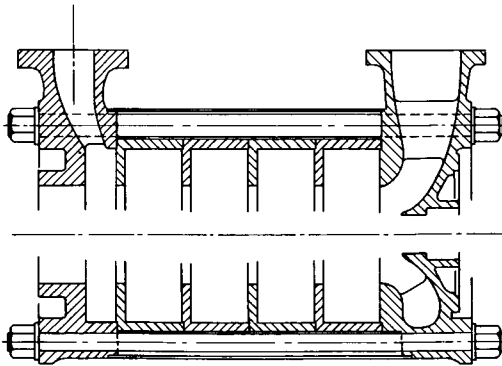
FIGURE 15.—*"Vertically split" multistage pump casing.*

It has been mentioned before that under idealized conditions of knowledge one can imagine a definite relation between the continuously varying operating conditions and the corresponding continuously varying design forms. Furthermore, it was stated that this relationship is not unique even under the idealized assumption that for completely given conditions there is only one optimum design form. *It can now be stated that the multivalued character of the relation between operating conditions and design forms is dictated by the discrete design choices described in this section.*

REPRESENTATION OF THE FIELD OF TURBOMACHINERY DESIGN

The last step in this presentation of turbomachinery design is the construction of a mental picture or scheme representing what was said before

The field of all possible dimensionless operating conditions—here presented as a number of specific speeds (the *left* sides of the equations in tables I and II)—is imagined as a multidimensional space, each coordinate being one of the dimensionless, continuously variable operating conditions (one specific speed). A point in this space represents one complete set of dimensionless operating conditions.

According to what was said before, every specific speed can be related to a number of design parameters as expressed by the *right* sides of the equations in tables I and II. This relation is multivalued, every particular solution depending on a number of design choices. However, after all pertinent design choices have been made, one can imagine that every point in the space of dimensionless operating conditions can be associated with a set of numerical values of the design parameters appearing on the right sides of the specific-speed equations. Accordingly one can draw in the multidimensional space of operating conditions the loci (lines, surfaces, etc.) of constant values of the design parameters concerned.

It is somewhat difficult to demonstrate this situation, not only because of the multidimensional nature of this space, but also because the design information available for most of the specific speeds is as yet far too incomplete to permit such a demonstration in definite terms. Therefore a highly simplified case will be considered for this demonstration.

Only two specific speeds will be considered as being variable. The best design information available today falls in the hydrodynamic field, represented by the basic specific speed and the suction specific speed. These two specific speeds shall therefore be the variable operating conditions considered in this demonstration, with all other specific speeds having fixed values in ranges where sufficient design information is available. One may consider this example as a plane section through the multidimensional

space of operating conditions, this section being parallel to the n_s and S axes, and normal to all other coordinate axes of this space.

The next step is that of making the necessary design choices. These choices shall be the following:

(a)   The machine is a pump (not a turbine).

(b)   The fluid is a liquid of low viscosity; this determines a sufficiently low value of the compressibility specific speed and a sufficiently high value of the viscosity specific speed to make the effects of changes in compressibility and changes in viscosity (and size) negligible.

(c)   The peripheral velocities are sufficiently low and the strength-to-weight ratio of the structural material sufficiently high to practically eliminate stress considerations; specifically, the centrifugal stress specific speed shall be well below $\frac{1}{10}$.

(d)   The gravity specific speed is sufficiently high and the vibration specific speed sufficiently low to practically eliminate gravity and vibration effects from the design consideration.

(e)   The runner design form will be single-suction and will vary continuously from radial (outward) flow for low basic specific speeds to axial flow for high basic specific speeds.

These design choices are not yet sufficient to solve the equations for the basic specific speed and the suction specific speed for the design parameters. However, certain design parameters can be chosen on theoretical and empirical grounds, as follows.

On theoretical grounds, one can select the inlet velocity head ratio $2g_oH_{sv}/V_{m_i}{}^2 = 3.5$, and, on empirical grounds, the hub diameter ratio $D_h/D_i = 0.25$. With these assumptions, the equation for the suction specific speed is reduced to

$$S = \frac{1}{5.585} \frac{U_i}{V_{m_i}} \tag{12}$$

With the flow coefficient V_{m_i}/U_i so determined by the suction specific speed alone, the basic specific speed equation can be solved for D_i/D_o if one can make a rational assumption about the head coefficient. It will be assumed empirically that the maximum value of this head coefficient, which exists at the minimum discharge diameter ($D_{o_{\min}}$), is $2g_oH/U_{o_{\min}}^2 = 1$. With this assumption and equation (12), one finds:

$$n_s = 0.4585 \left(\frac{V_{m_i}}{U_i}\right)^{1/2} \left(\frac{D_i}{D_{o_{\min}}}\right)^{3/2} = \frac{0.4585}{(5.585S)^{1/2}} \left(\frac{D_i}{D_{o_{\min}}}\right)^{3/2} \tag{13}$$

Figure 16 shows a graphical evaluation of equations (12) and (13); this evaluation indeed represents the beforementioned "section" through the multidimensional space of operating conditions. In this section appear
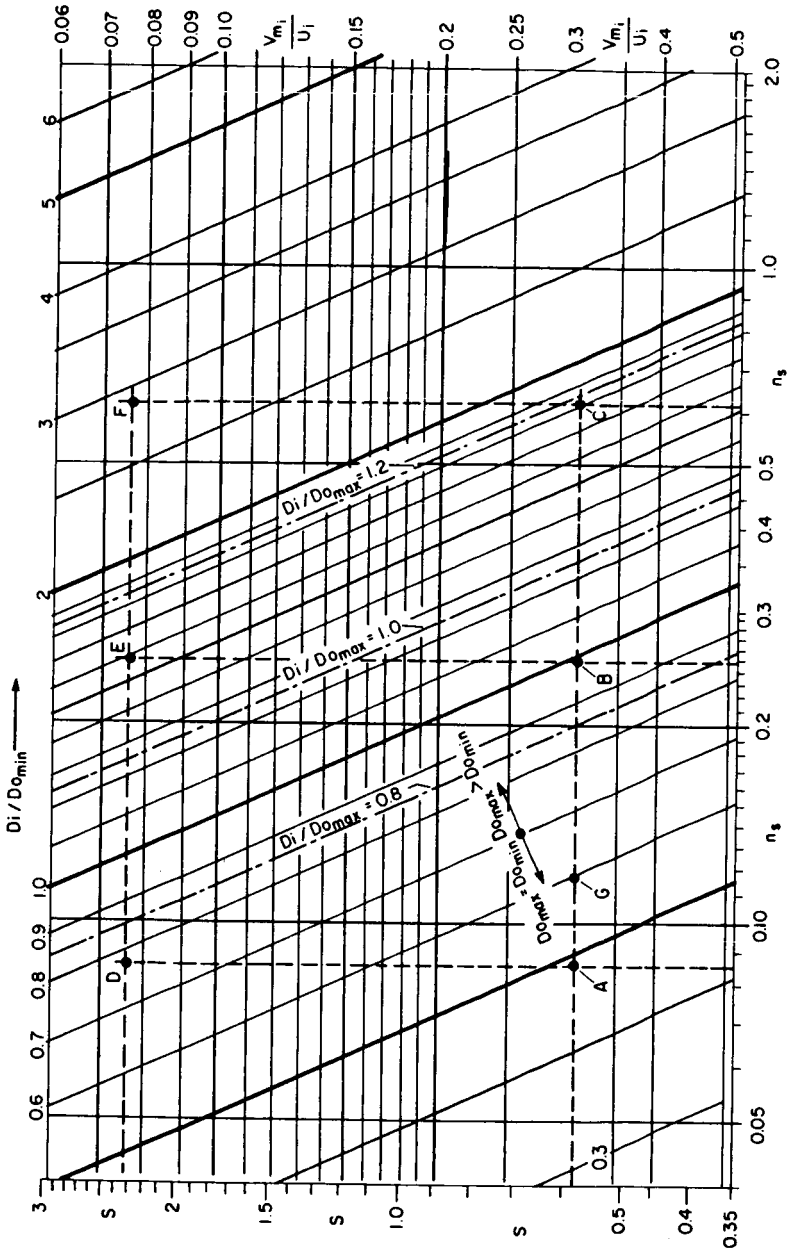
FIGURE 16.—*Design parameters as functions of n_s and S for $2g_0H/U_{0\,min}^2 = 1$.*

two systems of lines—lines of constant values of the inlet flow coefficient V_{mi}/U_i and lines of constant values of the diameter ratio $D_i/D_{o\min}$. It is quite proper to use, for dimensionless coordinates, logarithmic scales, which give this section the qualities of a computation chart. Thus this initially somewhat abstract concept of a section through the space of dimensionless operating conditions appears in a practically useful form, giving hope that the concept of a space of dimensionless operating conditions may have eventually some practical usefulness.

The diameter ratio $D_i/D_{o\min}$ and the flow coefficient V_{mi}/U_i are of course not the only design parameters that are of interest and can be related to the specific speeds. Of particular significance is the maximum outside diameter, $D_{o\max}$. Often this diameter must be larger than $D_{o\min}$ because of the previously mentioned limit of the retardation of the relative flow. To arrive at a simple solution, it was here assumed that the circumferential component of the relative flow should not be retarded more than according to $w_{u_o}/w_{u_i} \geq 0.65$.

Using Euler's turbomachinery momentum equation as well as $w_{u_i} = -U_i$ (for zero rotation of the absolute flow at the impeller inlet), and with $(2g_oH/U_{o\min})^2 = 1$, one arrives at

$$\frac{D_{o\max}}{D_i} \geqq \left[\frac{1}{2\eta_h}\left(\frac{D_{o\min}}{D_i}\right)^2 + 0.325^2\right]^{1/2} + 0.325 \qquad (14)$$

where η_h is the so-called hydraulic efficiency of the machine, accounting only for head losses, not for leakage or parasite torque increases. Figure 17 shows the evaluation of equation (14) under the assumption that $\eta_h = 0.90$, and using only the equality sign, so that $D_{o\max}/D_i$ has its minimum value. Evidently it would be possible to enter this information into the section through the space of operating conditions represented by figure 16. This has been done only for $D_i/D_{o\max} = 0.8$, 1.0, and 1.2. These values are represented in figure 16 as dash-and-dot lines to indicate this family of lines diagrammatically. Since, according to equation (14), the lines $D_i/D_{o\max} =$ constant are parallel to the lines $D_i/D_{o\min} =$ constant, it would be difficult to distinguish the $D_i/D_{o\max}$ family of lines clearly from the $D_i/D_{o\min}$ family. However, only such practical considerations of visibility prevent one from showing other parameters such as $D_i/D_{o\max}$, or $2g_oH/U^2_{o\max}$, in the section (fig. 16). The minimum head coefficient $2g_oH/U^2_{o\max}$ is derived easily from the assumed value of the maximum head coefficient $2g_oH/U^2_{o\min} = 1$ by the relation:

$$2g_oH/U^2_{o\max} = (2g_oH/U^2_{o\min})\frac{D^2_{o\min}}{D^2_{o\max}} \qquad (15)$$

with $D_{o\max}/D_{o\min}$ given in figure 17.
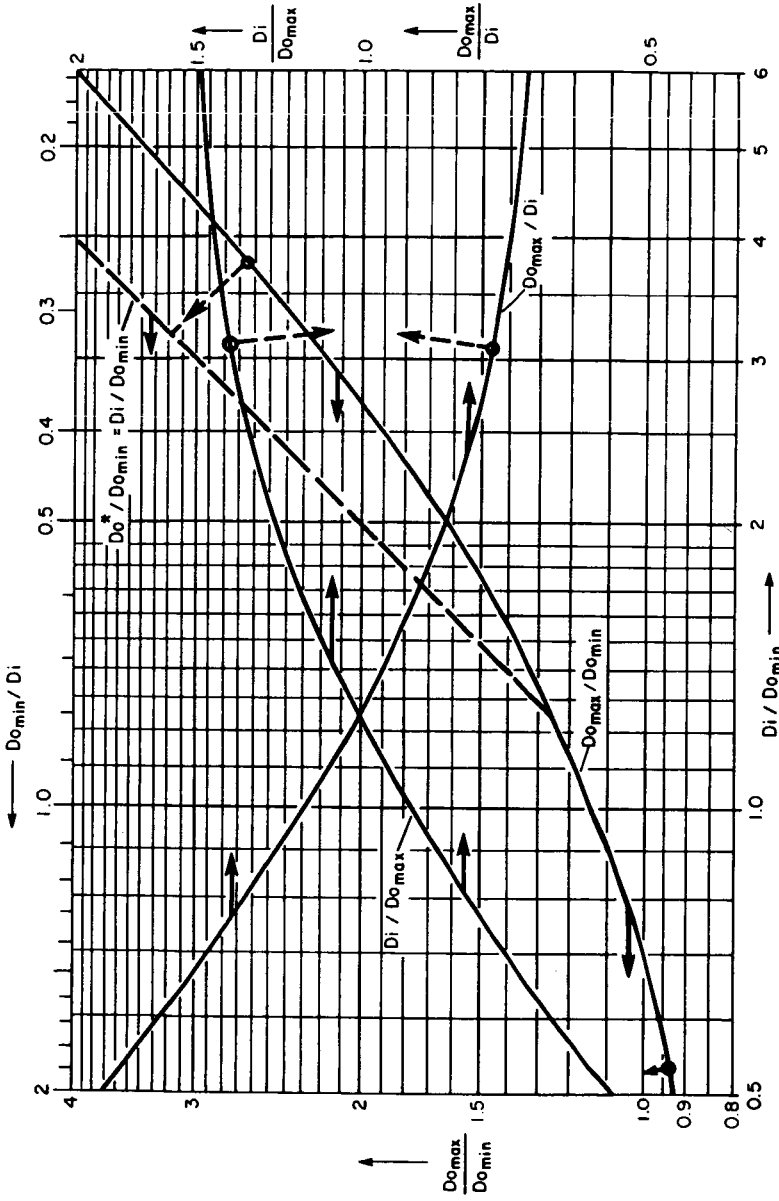
FIGURE 17.—*Maximum pump discharge diameters* $D_{o_{max}}$ *and* D_o^* *as functions of* $D_{o_{min}}/D_i$.

Additional design coefficients can easily be calculated by the elementary laws of turbomachinery design (as for example the discharge width ratio $b_o/D_{o_{min}}$ (see fig. 2) from the condition of continuity, or dimensions of stationary vane passages adjacent to the impeller), primarily on the basis of the law of constant angular momentum. Every point in the section shown in figure 16 therefore represents in principle the whole set of dimensionless design parameters as completely as permitted by the state of knowledge available. Figure 3 depicts the type of information represented by every point in this section (fig. 16), in this case with respect to the design form of the impeller only.

Before returning to multidimensional considerations on the space of operating conditions, it is desirable to illustrate the last step; i.e., *the establishment of a complete design form from the design parameters.* At present this step can be demonstrated (under many simplifying assumptions) only for the relatively well established field of hydrodynamic runners, represented in an only two-dimensional "space" of the operating conditions, n_s vs. S.

Ideally every point in this space, or section, should be associated with a complete design form. This can be demonstrated here only for a very limited number of points A, B, C, D, E, and F in figure 16. Figure 18 illustrates diagrammatically the corresponding design forms by showing the impeller profiles only. The various profiles are correlated with the six points in figure 16 by the same letters, as well as by the values of the basic specific speed (n_s) and the suction specific speed (S). (Values of the specific speeds in conventional pump units are given in parentheses.)

Since the impeller design forms actually include the vane shapes as derived from the velocity diagrams (shown in fig. 3), it is evident that this last step is a very major step, demanding all the knowledge, experience, and skill available in the pump design field. It is the core of the design process. Hopefully, what has been said shows this process in its proper position within the overall design procedure.

Since $D_{o_{max}}/D_i$ given by figure 17 is a minimum value of this ratio, it is permissible, even desirable, to show in figure 18 a larger ratio $D_o^*/D_i = 1$ whenever $D_{o_{max}} \leqq D_i$.

It is now time to return to the original, multidimensional picture of the space of dimensionless operating conditions. To aid our imagination, we will consider at one time the interaction of the n_s vs. S section (shown in fig. 16) with only *one* of the other coordinates (specific speeds) of this space. This particular coordinate axis is of course normal to the n_s vs. S plane, giving a three-dimensional picture of this "interaction" with a third specific speed.

The lines in figure 16 represent in this picture surfaces intersecting the n_s vs. S plane. Under the design choices (or assumptions) made at the
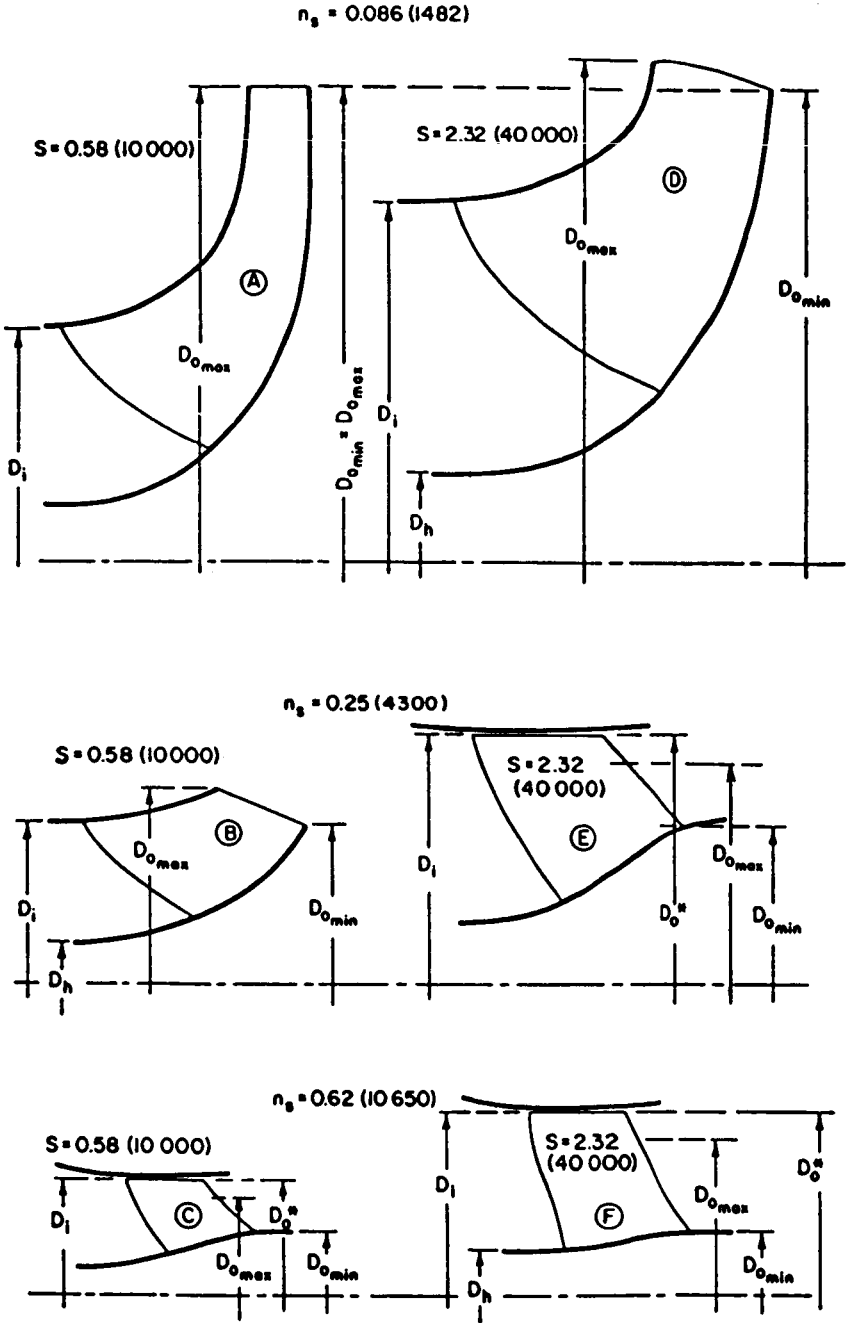
FIGURE 18.—*Runner profiles as functions of* n_s *and* S.

beginning of this example, these surfaces will intersect the particular n_s vs. S plane at right angles if the third specific speed is either the compressibility specific speed or the viscosity specific speed, the stress, the gravity, or the vibration specific speed, because it was assumed that the effects of small changes in the compressibility, viscosity, stress, gravity, and vibrations characteristics should be negligible. This set of assumptions or design choices therefore eliminates (as intended) the multidimensional character of this space, leaving n_s and S as the only significant variables.

As soon as one extends considerations to large changes in compressibility, viscosity, stress characteristics, etc., the picture becomes quite different. The surfaces, represented in the n_s vs. S plane by lines $D_i/D_{o\min}=$ constant and $V_{mi}/U_i=$ constant, *curve* in planes *normal* to the n_s vs. S plane. For example, at low viscosity specific speeds (low Reynolds numbers) the lines in the n_s vs. S plane have different positions, and the surfaces they represent intersect the n_s vs. S plane at angles substantially different from 90°. This is just a geometric way of saying that the viscosity of the fluid (the viscosity specific speed), and changes thereof, have substantial effects on the design parameters of the machine.

The very same type of statement can be made for other specific speeds as the third coordinate, for example, the stress specific speed. It is to be expected that at high stress specific speeds the surfaces of constant design parameters, such as $D_i/D_{o\min}$ or V_{mi}/U_i, will intersect an n_s vs. S plane not at right angles and at a substantially different place than at the low stress specific speed assumed before. To describe this three-dimensional space of the three operating conditions n_s, S, and n_σ, one could investigate relations in planes normal to the n_s vs. S plane, for example, in several n_σ vs. n_s planes at different constant values of S. A series of diagrams, analogous to figure 16, representing n_σ vs. n_s, n_σ vs. S, and n_s vs. S planes at different, constant values of S, n_s, and n_σ, respectively, would describe the field of single-suction centrifugal and axial-flow pump design forms rather completely and would be of great practical value, particularly for preliminary design. Unfortunately, presently available information on the design of such pumps is not nearly sufficient for arriving at an answer for such a representation that is even approximately unique.

To avoid the impression that the foregoing mental pictures are merely abstract speculations, figure 19 presents a somewhat qualitative picture of the final results that might be obtained from a step in the direction of the n_{σ_c} axis at constant values of n_s and S. The step is taken from the point G in figure 16, from a centrifugal stress specific speed $n_{\sigma_c}<0.1$ to a value between $n_{\sigma_c}=0.2$ and $n_{\sigma_c}=0.3$. (It would require a fairly detailed stress analysis to arrive at more definite figures.) As mentioned previously with respect to hydrodynamic design, it will take the entire available knowledge, experience, and skill in hydrodynamic and mechanical
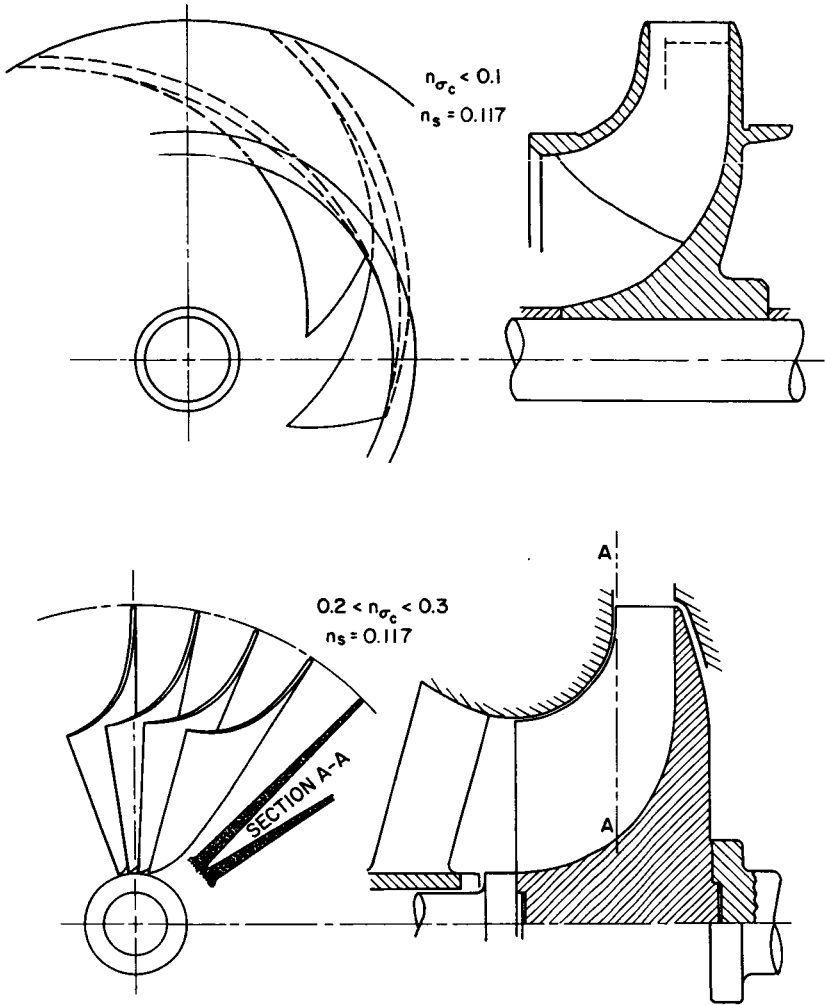
FIGURE 19.—*Radial-flow runner design as a function of stress-specific speed.*

design, and more, to make a reasonably useful attack on the design problems of the n_s, S, and n_{σ_c} space. This situation can hardly be better in the n_s, n_a, and n_{σ_c} space of gas-dynamic machines, and it appears to be much farther from a practically useful solution when the viscosity, gravity, or vibration specific speeds are involved.

SUMMARY

The field of turbomachinery design is first represented by a number of analytical relations among various dimensionless operating conditions, the "specific speeds," and dimensionless design parameters such as ratios of important linear dimensions and flow and head coefficients. Every set of operating conditions is associated with a corresponding set of design parameters that can be reasonably unique only after certain design choices have been made regarding the nature of the fluid, purpose and type of the machine, and so on.

This situation can be represented as a space of dimensionless operating conditions, every coordinate representing one of these operating conditions (i.e., one "specific speed"). Every point in this space represents a complete set of dimensionless operating conditions (as complete as possible within the present state of knowledge).

After all pertinent design choices have been made, every point in this space can be associated with a corresponding set of design parameters, so that one can locate in this space the loci of constant values of all design parameters appropriate for the design choices made. A two-dimensional section through this space shows these loci as lines of constant values of a design parameter (fig. 16). Such sections may thus be charts from which one can read values of the design parameters. *Modern means of computation may not restrict this possibility to the use of two-dimensional, graphical charts.*

The core of the form design process consists in associating with points in this space—i.e., with complete sets of design parameters (as complete as permitted by the state of knowledge)—corresponding *design forms* (see figs. 18 and 19). This process requires all the knowledge, experience, and skill available in the field of design and is not described, only located, in this paper relative to other aspects of the *overall* design process.

Persons qualified in mathematical or computational matters should take over at this juncture.

ACKNOWLEDGMENT

of the Naval Undersea Research and Development Center, San Diego, for their interesting comments and suggestions.

The writer feels greatly indebted to the Committee chaired by Dr. B. Lakshminarayana which initiated and organized the Symposium on Turbomachinery at The Pennsylvania State University and the publication of its proceedings.

LIST OF SYMBOLS

A, a	area	ft²
a	velocity of sound	ft/sec
b	width of impeller, vane span	ft
C_L	lift coefficient	
D	diameter	ft
E	Modulus of Elasticity	lbs/ft²
g	acceleration of the whole system	ft/sec²
g_o	standard gravitational acceleration	ft/sec²
H	head ft lbs/lb = ft	
H_{sv}	total suction head above vapor pressure	ft
h	vane thickness	ft
l	vane length	ft
m_s	section modulus	ft³
n	speed of rotation	rps
$n_a, n_v, n_\sigma, n_g, n_v$	See table I	
n_s	basic specific speed	
N	number of vanes	
p	pressure in a fluid	lbs/ft²
Q	rate of volume flow	ft³/sec
r	radius	ft
S	suction specific speed	
t	circumferential vane spacing	ft
U	circumferential velocity of solid rotating parts	ft/sec
V	absolute fluid velocity	ft/sec
w	relative fluid velocity	ft/sec
w_∞	vectorial mean relative fluid velocity between inlet and discharge of a vane system	ft/sec
y	axial thickness of a rotating disc	ft
y/y_1	ratio of axial thickness of a rotating disc to its thickness at outer radius r_1	
β	angle from the meridional direction	
Γ	circulation, vane circulation	ft²/sec
η	efficiency: η_h "hydraulic efficiency"	

ν	kinematic viscosity	ft²/sec
ρ	mass density	lbs-sec²/ft⁴
σ	stress	lbs/ft²
ϕ	flow coefficient V_m/U	
ψ	head coefficient $2g_oH/U^2$	

Subscripts Not Listed in Connection With Symbol

f	fluid, fluid-induced
h	hub, measured at hub diameter
i	inside, inlet of pumps or compressors
m	meridional
o	outside, measured at outside diameter
s	structural, solid material
th	"throat," discharge cross section of the volute
U	circumferential, in direction of velocity U

REFERENCES

1. LANG, THOMAS G., *A Generalized Engineering Design Procedure*. Naval Undersea Warfare Center, NUWC TP 137 (San Diego).
2. WERNER, R. A., AND G. F. WISLICENUS, *Analysis of Airplane Design by Similarity Considerations*. AIAA Paper 68–1017.
3. WISLICENUS, G. F., *Fluid Mechanics of Turbomachinery*. Dover Publications (New York), 1965.

DISCUSSION

T. G. LANG (Naval Undersea Research and Development Center). This paper is a refreshing and enlightening new approach to the design of turbomachines. By utilizing a nondimensional approach it collapses a large number of design problems into a basic set of design problems, leading to a better understanding of the field of turbomachinery design. The fundamental operating conditions which determine most design problems are listed and the steps leading to the design solutions are described.

It is pointed out that certain design choices must be made which depend largely upon the specific design situation. The design solution is then that form which "best" satisfies the problem in view of both theoretical relationships and empirical design results which have lead to highest efficiency, ease of manufacture, etc.

New operating conditions are introduced, such as the stress, gravity, compressibility, and vibration specific speeds. The latter might be more generally called the elasticity specific speed. The use of this approach should be helpful to the designer who is designing a complete system, since this paper indicates how the turbomachine design might vary as the inlet pressure, shaft speed, flow rate, head, strength of the material, etc., vary. Consequently, this approach could help in selecting the power source, gearing, and other aspects of a complete design problem by quickly showing how the resulting turbomachinery form would vary.

The design example of relating the design form with variations in n_s and S clearly demonstrates the usefulness of this procedure.

J. H. HORLOCK (Cambridge University): Professor Wislicenus' paper gives me much food for thought. My own use of the concept of specific speed has been limited to the basic specific speed, which means the ratio (flow coefficient)/(head coefficient)$^{3/2}$ to me. A low basic specific speed means (relatively) a machine with a small hole at the front for the flow to go through, but a machine with a strong capacity for changing tangential momentum and doing work. Hence the geometry of the first diagram of figure 1, and hence my preference for the term "shape parameter" instead of "basic specific speed." But Professor Wislicenus' introduction of other specific speeds greatly widens visual concepts for the designer.

My main contribution to discussion of his paper must be to add a complication. In the multidimensional space of specific speeds, room should be found for one or more (dependent, not independent) coordinates that give the performance of the machine. For example, in figure 16, the probable efficiency of each of the eight machines should be plotted perpendicular to the paper so that the designer can be assisted in his design choice. (Fig. 1.15 of ref. D-1 was a crude attempt to go in this direction.)

May I also add a philosophical point, or rather a question? Why is it that pump designers and consulting engineers are the widest users of the concept of specific speeds in turbomachinery design? Is it in fact that the gas turbine or steam turbine designer is wallowing in Professor Wislicenus' multidimensional space and cannot cope with the complexities of the problem? Or is it that he has been forced by long experience very close to one point in that multidimensional space, and he cannot get away from it? I suspect the consulting engineer faced with continuously new pump designs can get good estimates of where to design from a graph such as Prof. Wislicenus' figure 16. The situation is more quickly understood because of the effective elimination of many variables (or extra specific speeds)—hence the ready use of the concept.

One final reaction. My first thought on reading this paper was that the designer could turn to the computer to obtain the answer within the multidimensional space of specific speeds. But I think he will get little advantage in doing so. Any "solution" of a design point in that space must be associated with an empirical knowledge of performance for such a design. He may have obtained the geometry (design parameters) that meets the requirement of a dozen specified specific speeds, but it may be a poor machine. He will have to compromise to meet his design point. The computer cannot eliminate the designer's judgment based on experimental observation.

WISLICENUS (author): The writer should like to express his appreciation to all who took the time to discuss this paper. Not every comment can be explicitly recognized here.

Dr. Lang may be interested to hear that in a report to the National Science Foundation entitled "Form Design in Engineering" this writer used in 1967 the term "elastic specific speed" for what he has called now "vibration specific speed." The reason for this change in name is that the writer is as yet not certain that this specific speed is given here in the best form with respect to *steady* elastic deformations. The parameter $U/\sqrt{E/\rho_s}$ on the right side of this specific speed equation is, for simple elastic systems, proportional to n/f, where n is the frequency of excitation (e.g., the speed of rotation or a blade-passing frequency) and f a natural or "critical" frequency of the system. Thus $U/\sqrt{E/\rho_s}$ has a clear *dynamic* significance.

The writer is not sure that he agrees with Dr. Horlock's term "shape factor" for the basic specific speed. Any specific speed is primarily a dimensionless expression of operating conditions. Its relation to the form of the machine is derived, and it is multivalued, depending on several "design decisions."

The space of dimensionless operating conditions has, indeed, "room" for performance characteristics such as efficiency, stall margins, and others. However, most performance characteristics of this type are not rigorously determined by the specific speeds even after the necessary design decisions have been made. The lines, surfaces, etc., of constant efficiency, etc., that can be drawn into the space of dimensionless operating conditions are empirically, not rigorously located, compared with the loci of constant design parameters such as diameter ratios considered in this paper. Of course, this distinction may be only temporary if one assumes that efficiencies, stall margins, etc., will be predictable under some future state of knowledge and design of turbomachinery. With a more complete knowledge than available at present it should certainly be possible to draw (for example) lines of constant efficiencies (at design flow conditions) into figure 16 of the paper.

The basic specific speed is not generally used with machines for compressible fluids because the rate of volume flow (Q) does not have one single value. However, if Q is measured always at the same place in the machines compared, say at their low-pressure ends, then n_s can be defined and employed advantageously. In principle one can use the basic specific speed, the compressibility specific speed, and the stress specific speed for compressible fluids just as effectively and in the same manner as the basic, the suction, and the stress specific speeds for machines handling liquids.

Computers can do, of course, much more accurately what is done by computation charts such as that shown in figure 16, and the computer is not restricted to two (or three) dimensions, as are graphical charts. However, whether graphical or computerized, the results can only represent the knowledge, experience, and skill that originally went into the construction of the charts or into the programming of the computer.

REFERENCES

D-1.—*Axial Flow Turbines*. Butterworth Scientific Publications, 1968.

Theoretical Prediction of Two-Dimensional and Three-Dimensional Flows in Turbomachinery

Chairmen: J. H. HORLOCK AND H. MARSH

Computer Solutions of Wu's Equations for Compressible Flow Through Turbomachines

D. J. L. Smith

National Gas Turbine Establishment
Hampshire, England

Two computer programs, known as Matrix Through-Flow and Matrix Blade-To-Blade, for analyzing the meridional and blade-to-blade flow patterns are described. The numerical solutions are obtained by finite difference approximations to the governing Poisson-type differential equations for the stream function. Solutions for several turbomachines, giving flow patterns and velocity distributions, are included.

The flow through a modern gas turbine or compressor is an extremely complicated three-dimensional phenomenon. The flow has strong gradients in the three physical dimensions—axial, radial, and circumferential—as well as time and viscosity effects. The observation that the flow problem was not easily amenable to numerical solution led early investigators to search for a design system having ease of application. The computational difficulties were resolved by making approximations which permitted the use of two-dimensional techniques. These approximations were based on two flow models,

(1) Blade element flow
(2) Axially symmetric flow.

The blade element approach assumes that the flow in the blade-to-blade or circumferential plane can be described by considering the flow around blade profiles formed by the intersection of a cylindrical flow surface and the blading.

Axial symmetry assumes that an average value can be utilized to represent the state of the fluid in the blade-to-blade plane.

On the basis of these two flow models, several investigators developed analysis and design methods for the axial-flow compressor and turbine. In the case of the compressor, one of the earliest design methods appeared in Howell's classic papers in 1945 (refs. 1 and 2). Using the blade element

43

flow model, Howell correlated experimental linear cascade data to establish a limit that has to be placed on the allowable deflection in any one blade row and determined empirical rules for the deviation and flow loss. In estimating the overall performance of the compressor, the flow is analyzed along a "mean" or "reference" diameter and the gas state is estimated at planes between adjacent blade rows, making use of the axially symmetric flow model. Similar methods were developed for the axial-flow turbine and, of these, the method of Ainley and Mathieson (ref. 3) is one of the best known. These relatively simple, albeit one-dimensional methods for analyzing the overall properties of the flow field, developed when the digital computer was in its infancy and the development of methods suitable for hand desk machines was one of the prime goals, are still, in principle, used widely throughout the aircraft industry and are likely to remain in use for some time.

More recently, with the advent of the large, high-speed digital computer, techniques (refs. 4 and 5) have been developed for analyzing the subsonic fluid motion in the meridional or hub-to-tip plane of axial-flow machines at stations other than the mean diameter (which was used in the early days) both inside the blade rows and in the duct regions. Similar methods have been developed for centrifugal and mixed-flow impellers by Hodskinson (ref. 6) and Wood, et al. (ref. 7). In parallel, several investigators (refs. 8, 9, and 10) have been working on the problem of generating a computer solution for the subsonic blade-to-blade flow with allowances for radial acceleration imposed by the curvature of the streamlines in the meridional plane and for the effects of Coriolis forces.

The purpose of this paper is to present an outline of two advanced computer solutions that have been developed at the National Gas Turbine Establishment (NGTE) for the meridional and blade-to-blade flow patterns. Solutions for several turbomachines, giving flow patterns and velocity distributions, are included.

MATHEMATICAL ANALYSIS

The mathematical analysis is based on the earlier work of Wu (ref. 11) who developed a general theory for the three-dimensional, inviscid, steady flow through an arbitrary turbomachine. The equations of motion are satisfied on two intersecting families of stream surfaces known as the first kind, $S1$ (blade-to-blade), and the second kind, $S2$ (meridional), the complete flow solution being obtained by an iterative process between the flows in the two stream surfaces.

Stream Function Equation for $S1$ Surface

In the real blade-to-blade flow, the $S1$ stream surface would be twisted. To permit computations of the potential flow in the blade-to-blade plane

of a stationary or rotating blade row, Smith (refs. 10 and 12) assumed the stream surface was a surface of revolution.

The shape of the $S1$ surface is obtained by rotating a streamline in the meridional plane (fig. 1) about the axis of rotation.[1] In order to analyze the flow through any type of turbomachine, it is convenient to rotate the r,z axes through an angle θ. Using x and ϕ as the two independent variables, the continuity equation and the equations of motion can be manipulated to arrive at a Poisson-type differential equation for the stream function.

$$\frac{\bar{\partial}^2\psi}{\partial x^2}+\frac{1}{r^2}\frac{\bar{\partial}^2\psi}{\partial\phi^2}=F(x,\phi) \tag{1}$$

where the stream function ψ is defined by

$$\left.\begin{aligned}\frac{1}{r}\frac{\bar{\partial}\psi}{\partial\phi}&=b\rho W_x\\[2em]\frac{\bar{\partial}\psi}{\partial x}&=-b\rho W_\phi\end{aligned}\right\} \tag{2}$$

and the velocity components W_x and W_y are related by

$$W_y=-W_x\tan\lambda \tag{3}$$

Equation (3) is the geometrical condition that the flow follows the stream surface. The derivatives in equations (1) and (2) are those which Wu
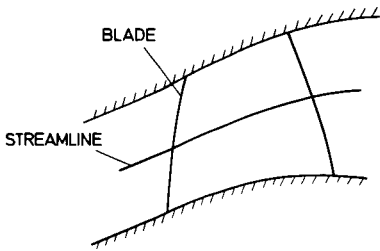
FIGURE 1.—*Meridional plane.*

---
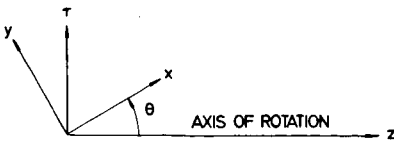
[1] For two-dimensional cascade flow the stream surface is a cylinder.

refers to as special derivatives taken on the stream surface, and the integrating factor b is proportional to the local thickness of a thin stream sheet whose mean stream surface is the $S1$ surface considered.

Stream Function Equation for $S2$ Surface

To analyze the flow in the meridional plane of an arbitrary turbomachine, Marsh (ref. 4) developed a matrix through-flow method. Inside the blade rows, the flow is analyzed in an $S2$ stream surface and for the duct regions between adjacent blade rows, the flow is assumed to be axially symmetric.

As in the case of the $S1$ surface, the r,z axes (fig. 1) are rotated through an angle θ and x,y are the two independent variables. In a manner similar to the $S1$ solution, an equation for the stream function can be derived.

$$\frac{\bar{\partial}^2\psi}{\partial x^2}+\frac{\bar{\partial}^2\psi}{\partial y^2}=f(x,y) \tag{4}$$

where the stream function satisfies

$$\left.\begin{aligned}\frac{\bar{\partial}\psi}{\partial x}&=-rB\rho W_y\\[2em]\frac{\bar{\partial}\psi}{\partial y}&=rB\rho W_x\end{aligned}\right\} \tag{5}$$

The integrating factor B in equation (5) is proportional to the local angular thickness of the $S2$ stream surface and in the through-flow analysis it is assumed to be proportional to the width of the blade passage. In formulating the stream function equation—equation (4)—the viscosity terms were omitted in the equations of motion but the entropy terms were included, and Marsh introduced the effects of irreversibility into the flow calculation by defining a local polytropic efficiency for expansion and compression.

For the flow to follow the stream surface, within the blade rows, the three components of velocity are related by

$$W_\phi=-W_y\tan\lambda-W_z\tan\mu \tag{6}$$

In the duct regions there is no change of angular momentum along a streamline and the circumferential velocity satisfies the relationship

$$rV_\phi=\text{constant} \tag{7}$$

NUMERICAL SOLUTION

The equations for the stream function—equations (1) and (4)—are nonlinear, but they can be solved iteratively using finite difference techniques.

Finite Difference Approximations

In conventional finite difference analysis the domain is covered with a square or rectangular grid and a five-point star is used since this leads to a simple approximation for the Laplacian operator. However, for analyzing the flow in the $S1$ and $S2$ stream surfaces such a simple grid is not accurate enough, owing to the irregular boundaries of the flow domain giving rise to boundary finite difference stars with short limbs and consequently a large truncation error. A good example of this, in fluid mechanics, is the recent blade-to-blade method developed by Katsanis (refs. 8 and 9) in which the flow domain is covered with a square grid. It is clear that the truncation error is significant since the boundary condition of zero velocity normal to the blade surfaces is not satisfied.

In the NGTE methods, use is made of the powerful software of present-day digital computers by adopting an asymmetric finite difference grid. The grid (fig. 2) consists of straight lines normal to the x direction, each line having the same number of equally spaced grid points. In the case of the $S1$ surface, the blade suction and pressure surfaces form curved grid lines, and for the $S2$ surface, the inner and outer annulus walls form curved grid lines so that there are no additional difficulties for grid points close to the boundaries. The spacing of the straight lines need not be uniform and where necessary can be varied locally (in the blade leading and trailing edges, for instance) in order to obtain a detailed picture of the flow.
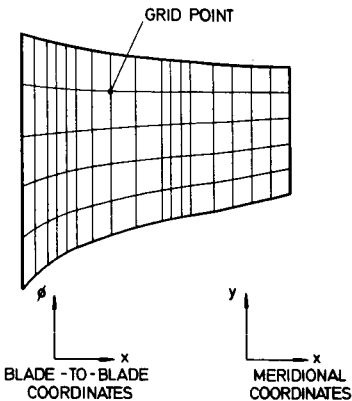
FIGURE 2.—*Asymmetric grid.*

To formulate a finite difference approximation for the Laplacian operator having an error of k^2, where k is the local grid spacing, equations (1) and (4) were modified by adding the term $E(\bar{\partial}\psi/\partial x)$ to both sides. Thus, for the $S1$ surface the stream function equation becomes

$$\frac{\partial^2\psi}{\partial x^2}+\frac{1}{r^2}\frac{\bar{\partial}^2\psi}{\partial\phi^2}+E\frac{\bar{\partial}\psi}{\partial x}=F(x,\phi)+E\frac{\bar{\partial}\psi}{\partial x}$$

or

$$\nabla^2\psi+E\frac{\bar{\partial}\psi}{\partial x}=q(x,\phi) \tag{8}$$

where E is a function of the grid spacing in the x direction and is zero for uniform spacing. The operator $\nabla^2\psi+E(\bar{\partial}\psi/\partial x)$ is approximated by a ten-point star for the interdependence of the function values at neighboring grid points. To maintain an overall accuracy of order k^2, the derivative $\bar{\partial}\psi/\partial x$ is also approximated by the use of a ten-point star.

Boundary Conditions

Considering first the $S2$ surface, the boundary conditions are relatively simple. At inlet to the turbomachine, the flow conditions are known; therefore, the stream function distribution is defined for the first straight line of the grid. The inner and outer annulus walls form limiting streamlines, so that for grid points on the walls the stream function is known. For the far downstream boundary, it is assumed that the shape of the exit duct is such that the stream function distribution is the same on the last two straight lines of the grid.

The blade-to-blade problem—$S1$ surface—poses quite complex boundary conditions. Far upstream of the blade row the gas state and flow angle are known and it is assumed that the flow is uniform. The gradient of stream function is defined, therefore, for the first straight line of the grid. Thus, from equation (2)

$$\left(\frac{\bar{\partial}\psi}{\partial x}\right)_u=-\frac{Q}{r_u}\Delta\phi\tan\alpha_u$$

where $\Delta\phi=2\pi/N$ and N is the number of blades in the row. For the blade region the suction and pressure surfaces form, by definition, limiting streamlines so that for grid points on the blade surfaces the stream function is known. Upstream and downstream of the blade the locations of the streamlines are not known until the problem is solved. For these regions, the boundary condition is that there is a circumferential periodicity of the flow. The final condition is that for the far downstream boundary. In a real blade-to-blade flow the circulation, and consequently

the outlet flow angle, is largely controlled by viscosity. In a potential flow model a criterion has to be adopted for fixing the circulation. In the method developed at NGTE, it is assumed that the flow is uniform and the flow angle is known far downstream of the blade row. These conditions fix the gradient of stream function on the last straight line of the grid which, from equation (2), is

$$\left(\frac{\bar{\partial \psi}}{\partial x}\right)_d = \frac{Q}{r_d}\,\Delta\phi\,\tan\alpha_d$$

Solution of Banded Equations and Convergence

By making use of the finite difference approximations and the boundary conditions, the modified stream function equations—equation (8) for the $S1$ surface—can be written in matrix form:

$$[M]\cdot[\psi]=[q] \tag{9}$$

where $[\psi]$ and $[q]$ are column vectors formed by ψ and q at each grid point and $[M]$ is a band matrix of the influence coefficients of the finite difference approximations. The method of solving equation (9) for the stream function is to solve for a given vector $[q]$, to correct $[q]$ using the new flow pattern, and then to repeat the cycle of calculation until the solution has converged to a specified tolerance. Since the matrix $[M]$ is "banded," only the band of nonzero elements is formed and stored in the computer and a very efficient direct method (ref. 13) is used to solve equation (9) for a given vector $[q]$. This method is better than the alternative indirect or relaxation method, as used by Katsanis, for the simple reason that it is very stable numerically.

Numerical stability can be a major problem with any iterative method. In the matrix through-flow and blade-to-blade methods, the iterative process has been made stable by introducing a relaxation factor R; thus,

$$\psi_p = \psi_{p-1} + R(\psi - \psi_{p-1}) \tag{10}$$

where

ψ calculated value for the pth iteration
ψ_p value taken for the pth iteration
ψ_{p-1} value taken for the $(p-1)$th iteration.

Additional stability was obtained in the through-flow method by limiting the percentage change in ψ between successive iterations, a restriction which is automatically removed as the solution converges. For the blade-to-blade method, the stability was further improved for compressible flow by adopting a "marching" process of increasing the inlet Mach number gradually to the required value.

When the stream function is known, it is possible to calculate the products ρW_x, ρW_ϕ and ρW_y. To calculate the density and hence the velocity components a tabular method, as developed by Wu, is used in the through-flow method. For the blade-to-blade problem, an alternative method, suggested by Gelder (ref. 14), is used. In this method, the calculation of density is allowed to lag the stream function calculation by one iteration. This has the effect of improving stability and for compressible flow, the relaxation factor R—equation (10)—is a function of the maximum Mach number.

BLADE-TO-BLADE FLOW PATTERNS

Eight examples are given to illustrate the use of the blade-to-blade computer program.

(1)   Impulse turbine cascade
(2)   Seventy-degree camber blade
(3)   Axial turbine rotor tip section
(4)   Axial turbine rotor root section
(5)   Axial turbine stator blade
(6)   Turbine stator cascade
(7)   Three-dimensional flow past turbine stator blade
(8)   Radial cascade diffuser

Impulse Turbine Cascade

The first example is the incompressible flow past a 112-degree camber blade in cascade. The blade profile (fig. 3) is an impulse-type turbine blade having a pitch/chord ratio of 0.59 and 101 degrees flow deflection.
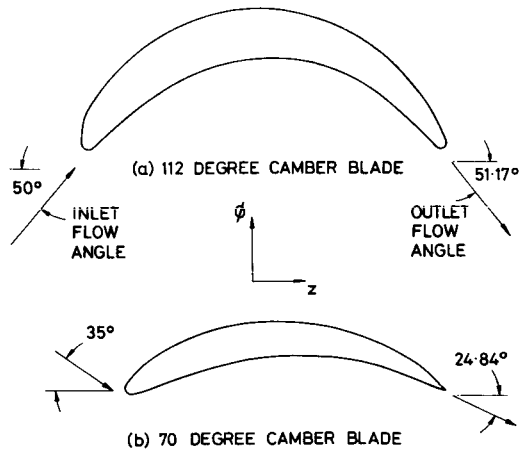
FIGURE 3.—Blade profile-exact solutions.

The velocity ratios are plotted in figure 4. (Velocity ratio is defined as the ratio of local surface velocity to far downstream velocity.) Also shown is an exact solution obtained by Gostelow (ref. 15). The matrix solution is in very good agreement with the exact solution.

Seventy-Degree Camber Blade

This blade profile (fig. 3) has a pitch/chord ratio of 0.9 and 70 degrees of camber. The two-dimensional, incompressible velocity distribution for −70 degrees of incidence is compared with an exact Gostelow solution in figure 5. In general, the matrix solution is in excellent agreement with the

FIGURE   4.—*Velocity   distribution   for impulse-type blade.*
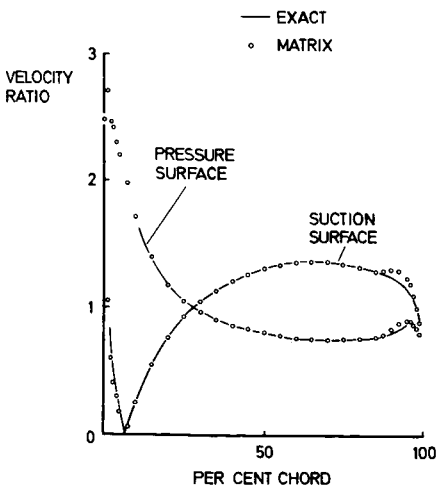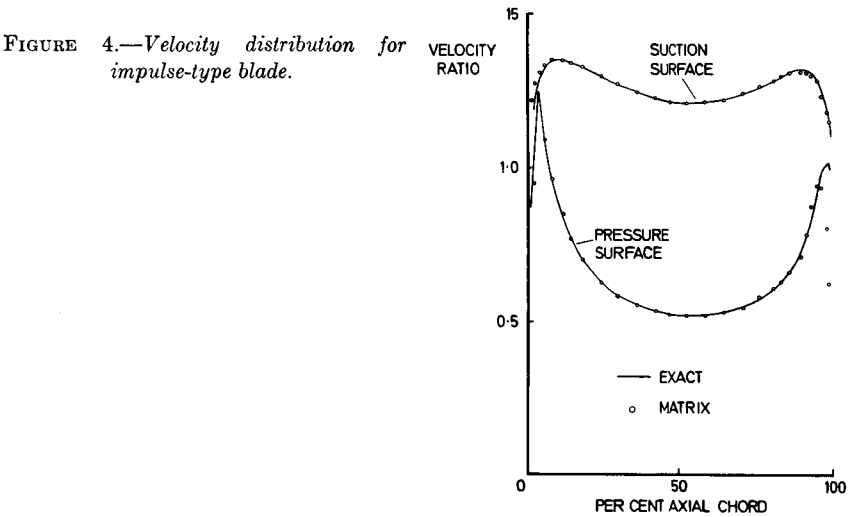
FIGURE 5.—*Velocity distribution for 70-degree camber blade.*

exact solution. It is noticeable that the main discrepancies are in the region of the blade trailing edge on the suction surface. For this region, the exact profile coordinates are a long way apart and it is probable that errors in interpolating the coordinates for the matrix solution have caused the discrepancies. There seems no reasonable doubt that complete agreement would have been obtained if the exact airfoil shape had been more fully defined. This example shows that there is no problem in analyzing high-incidence flows. The streamline pattern, calculated by the matrix method, is shown in figure 6. It may be seen that the leading edge stagnation point is well round on the suction surface.

Axial Turbine Rotor Tip Section

This example of two-dimensional, incompressible flow past a rotor tip section is given to illustrate the type of detailed flow pattern that can be calculated. The blade section is typical of a high pressure ratio turbine stage and is formed by a parabolic camber line and an analytical thickness distribution (ref. 16). Initially, the profile was designed so that the blade inlet angle was equal to the gas inlet angle of 18 degrees, a condition often referred to as zero geometric incidence. Figure 7 shows the blade profile. The surface velocity distribution around the blade leading edge is plotted in figure 8. It may be seen that it has the undesirable characteristic of a high peak on the suction surface. Such effects have been found by Hall (ref. 17). This is due to the large induced incidence which can be seen from the streamline pattern in figure 9a. The high suction peak was reduced by effectively drooping the nose of the blade (fig. 7) by 10 degrees so that the profile was operating at −10 degrees geometric incidence. The resulting velocity distribution is shown in figure 8 and, from the streamline pattern (fig. 9b), it may be seen that the induced incidence was considerably reduced. These results serve to show that computer methods can be very powerful in analyzing detailed aspects of the flow which would probably be very difficult to find experimentally.
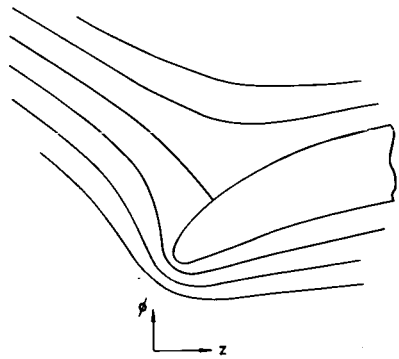
FIGURE 6.—*Streamline pattern for leading edge of 70-degree camber blade.*
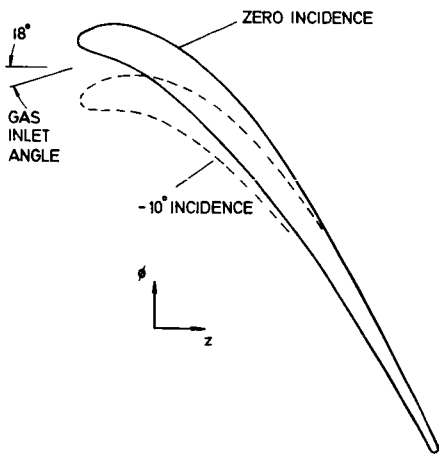
FIGURE 7.—*Turbine rotor tip sections.*

FIGURE 8.—*Velocity distributions for turbine rotor tip sections.*
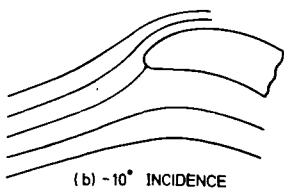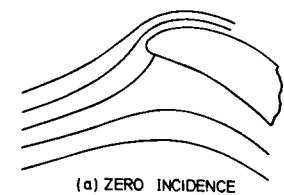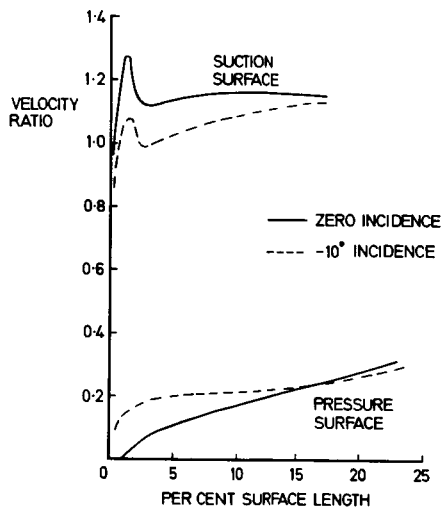
FIGURE 9.—*Streamline patterns for leading edge of turbine rotor tip sections.*

Axial Turbine Rotor Root Section

This blade section is typical of a high pressure ratio turbine stage. The basis for the design is the same as that of the previous example. The gas inlet angle was 48.9 degrees and the blade geometry at inlet was chosen so that the geometric incidence was zero. At outlet, the blade passage was adjusted to satisfy the gas outlet angle of −63.9 degrees by the empirical rule of Ainley and Mathieson (ref. 3). The blade surface velocity for two-dimensional, incompressible flow (fig. 10) shows that a detailed solution can be obtained in the region of the leading edge stagnation point. A particularly interesting feature of this blade section is that, according to the Ainley and Mathieson rule, the deviation[2] is 2.87 degrees negative. The velocity distribution for the trailing edge region is shown, enlarged, in figure 11 for an outlet flow angle of −64.15 degrees—a difference of only 0.25 degrees from the Ainley and Mathieson value. It is seen that on both the suction and pressure surfaces there is a rapid rise in velocity as the flow passes around the trailing edge. At the blade cutoff points, the velocities are equal, a criterion often used for fixing the outlet flow angle (ref. 18). Also, if the two surface velocity distributions are extrapolated then the loading at the blade trailing edge is zero, thus satisfying Preston's theorem (ref. 19) that equal and opposite vorticity should be shed from

FIGURE 10.—*Velocity distribution for turbine rotor root section.*

---
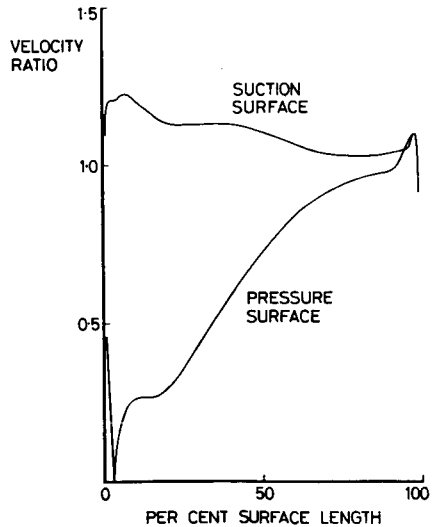
[2] Deviation is the difference between the fluid and blade outlet angles.
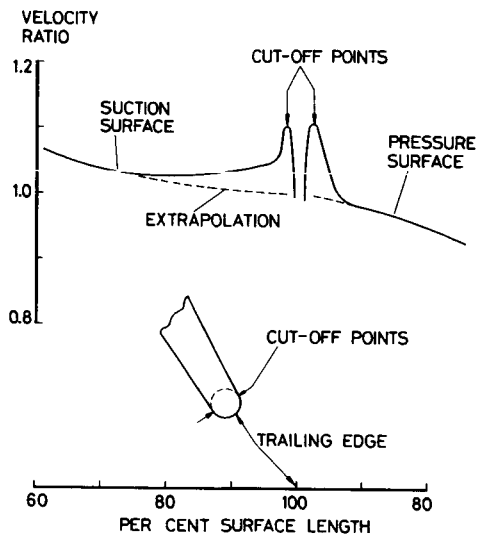
FIGURE 11.—*Trailing edge velocity distribution for turbine rotor root section.*

the two blade surfaces. The streamline pattern is shown in figure 12. It is seen that the flow leaves the trailing edge smoothly. This example shows that, applying existing velocity distribution criteria, the potential flow model gives an outlet flow angle in good agreement with well-established empirical rules, although it is perhaps surprising to find that the deviation is negative.

Axial Turbine Stator Blade

This example of two-dimensional, compressible flow is for the mean diameter section of a stator for a NASA turbine (ref. 20) operating at the design mass flow. The theoretical and experimental distributions of blade surface Mach number are compared in figure 13. In general, the computed Mach numbers agree well with experimental data. As mentioned earlier, Katsanis has developed a similar blade-to-blade method. In his recent paper (ref. 21) mention was made of an attempt to analyze the flow past this blade. He found that it was not possible to obtain an exact solution[3] and he had to resort to an approximate solution.

Turbine Stator Cascade

This turbine cascade was fitted with blades having the same profile as the mean diameter section of the second-stage stator blades of the turbine

───────────

[3] The term "exact" has been used as meaning a numerical solution from the computer program.
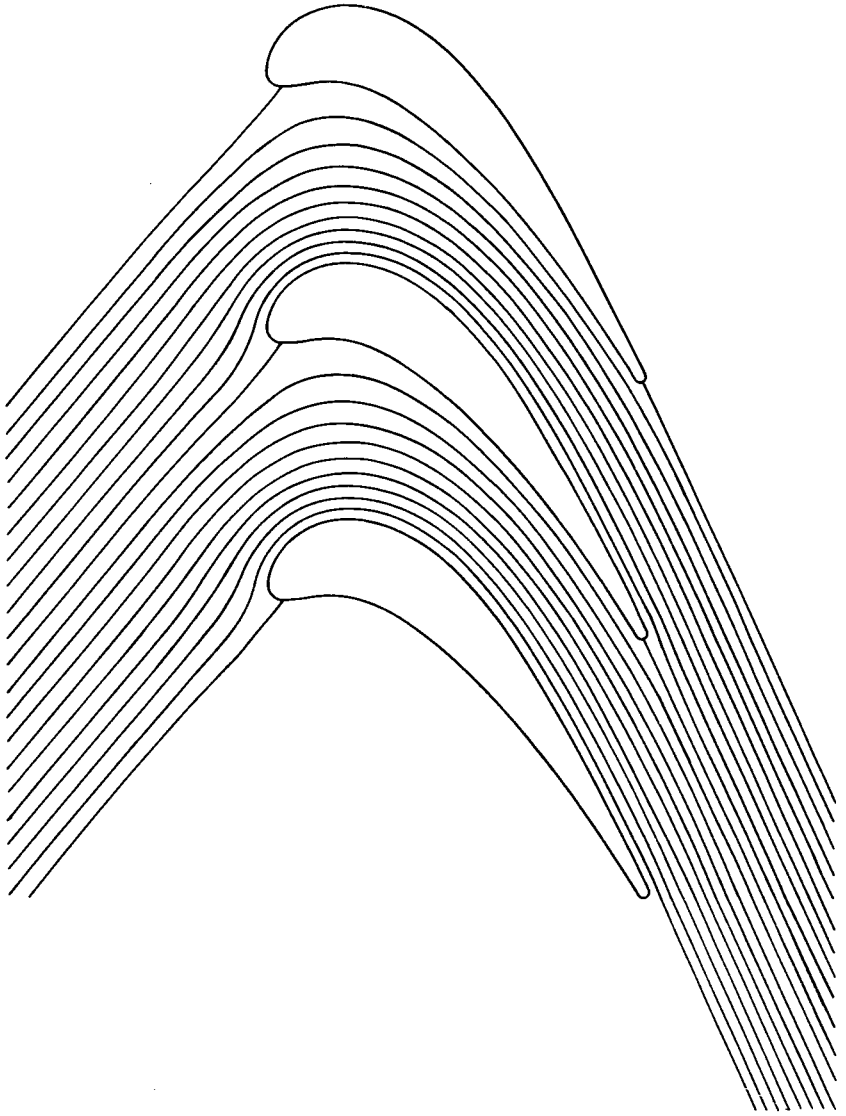
FIGURE 12.—*Computer output—streamline pattern for turbine rotor root section.*

described in reference 22. Two compressible flow solutions for the blade surface Mach number distribution are compared with experimental data in figure 14. The computed Mach numbers agree well with experimental data for this example.

• EXPERIMENT
—— MATRIX
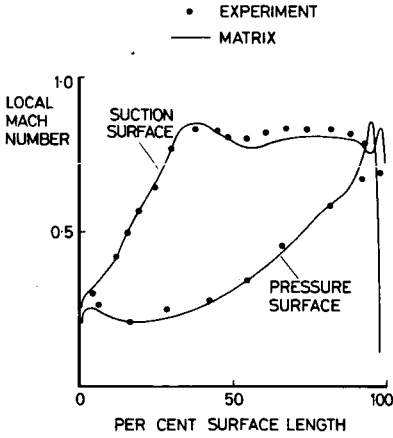
FIGURE 13.—*Mach number distribution for NASA axial-flow turbine.*

FIGURE 14.—*Turbine cascade.*
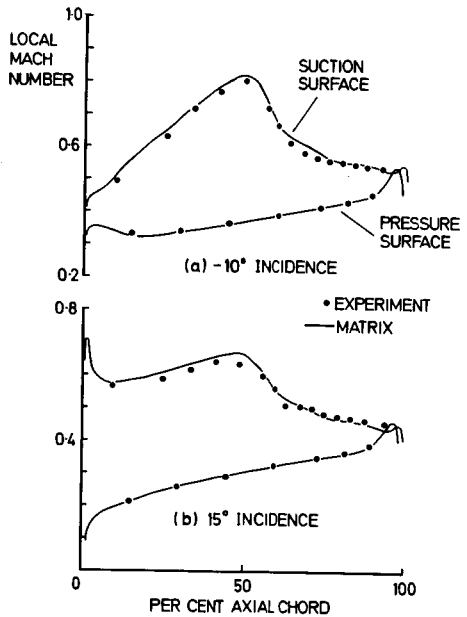
Three-Dimensional Flow Past Turbine Stator Blade

The flow through the two-stage turbine mentioned in the previous example has been analyzed using both the blade-to-blade and through-flow programs. The results of the through-flow analysis are presented in a later section of this paper.

Two matrix blade-to-blade solutions for the flow past the second-stage stator blades were computed. The first solution was for two-dimensional flow (i.e., cylindrical stream surface of constant thickness) and the outlet

flow angle was calculated from the Ainley and Mathieson empirical rule. The second or quasi-three-dimensional solution is a refinement in that the stream surface thickness was varied. The variation of thickness was determined from a solution for a meridional flow pattern using the through-flow program and the outlet flow angle was determined by applying the condition of zero trailing edge loading.

A comparison of observed blade surface Mach numbers with the theoretical calculations, for the mean diameter section, is shown in figure 15. The most striking point here is that when some of the interactions between the meridional and blade-to-blade flow patterns are introduced the quasi-three-dimensional solution is in good agreement with experimental data. As mentioned earlier, this mean diameter section has been tested in cascade. The cascade Mach number distribution shown in figure 14a corresponds to the turbine flow conditions given in figure 15. By comparing the cascade and turbine results, it may be seen that the three-dimensional flow effects are significant on the peak surface Mach number.

Radial Cascade Diffuser

To illustrate the types of turbomachines to which the matrix blade-to-blade method can be applied, the last example is a radial cascade diffuser. The initial calculations were made for incompressible flow with the cascade operating at zero geometric incidence and the outlet flow angle equal to the blade outlet angle (i.e., zero deviation). The theoretical velocity distribution is shown in figure 16. The peak near the trailing edge is due to the potential flow model picking up the rapid change in blade surface curvature in this region. In real flow, such peak velocities would be removed by the presence of boundary layers. By extrapolating the suction
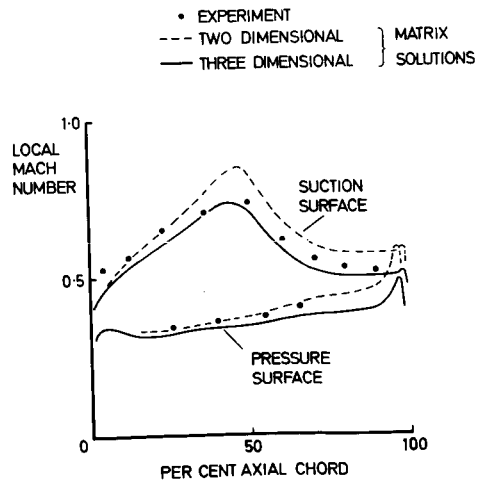
FIGURE 15.—*Blade surface Mach numbers for two-stage turbine stator blade.*
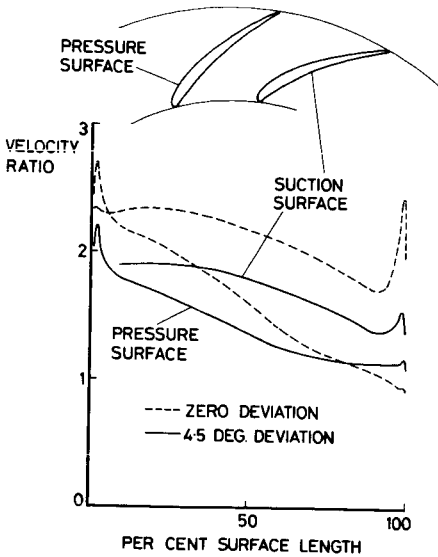
FIGURE 16.—*Velocity distribution for a radial cascade diffuser.*

surface velocity distribution from 90 percent of the way along the surface (i.e., just upstream of the rapid acceleration in the trailing edge region), it is seen that the condition of zero trailing edge loading is not satisfied. By increasing the outlet flow angle such that the deviation is 4.5 degrees, it is seen that the loading at the trailing edge satisfies Preston's theorem.

MERIDIONAL FLOW PATTERNS

In this section, four examples are given of meridional flow patterns obtained from the matrix through-flow program.
(1)   Two-stage axial-flow turbine
(2)   Single-stage axial-flow turbine
(3)   Low pressure ratio centrifugal compressor
(4)   High pressure ratio centrifugal compressor

Two-Stage Axial Flow Turbine

This turbine (ref. 22) is the one referred to in the previous section. In applying the matrix through-flow program, the effects of irreversibility were taken into account by assuming that the local polytropic efficiencies were constant throughout the flow field. From the comparison of the experimental and predicted profiles of axial velocity at the turbine exit shown in figure 17, it is seen that the through-flow theory gives a fair estimate of the axial velocities. Recent work by Gregory-Smith (ref. 23)

FIGURE 17.—*Axial velocity profiles far downstream of two-stage turbine.*

(a) 87·5% DESIGN SPEED

VELOCITY ft./s.

• EXPERIMENT
—— MATRIX THROUGH FLOW

(b) 50% DESIGN SPEED

VELOCITY ft./s.

RADIUS ft.
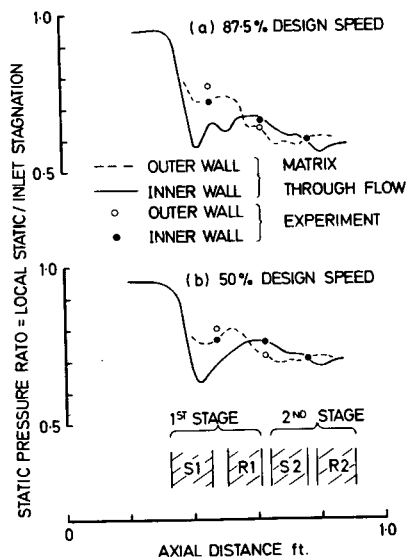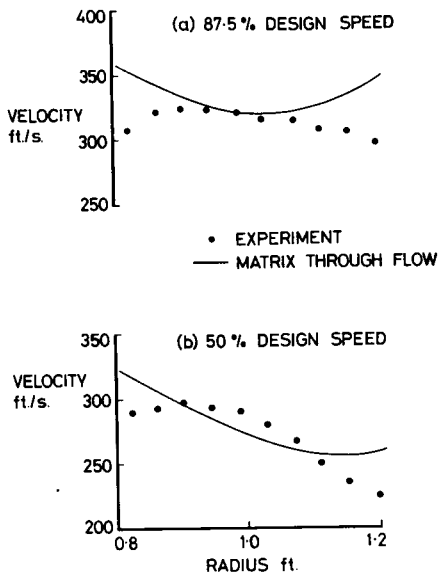
FIGURE 18.—*Static pressure for two-stage turbine.*

(a) 87·5% DESIGN SPEED

- - - OUTER WALL ⎫ MATRIX
——— INNER WALL ⎬ THROUGH FLOW
o OUTER WALL ⎫ EXPERIMENT
• INNER WALL ⎭

(b) 50% DESIGN SPEED

STATIC PRESSURE RATIO = LOCAL STATIC/ INLET STAGNATION

1ST STAGE 2ND STAGE
S1 R1 S2 R2

AXIAL DISTANCE ft.

on annulus wall boundary layers shows that it should be possible to improve the predictions in the region of the end walls.

The turbine was fitted with static pressure tappings in the annulus walls. Figure 18 shows comparisons of observed pressure distributions with the theoretical calculations. The static pressure ratio is defined as the ratio of local static pressure to turbine inlet stagnation pressure. The main

point to note is the presence of an inverse pressure gradient in the region of the second-stage stator blade—static pressure on the inner wall greater than that at the outer wall—which was successfully reproduced by the through-flow analysis. An alternative to the through-flow method is what is known as the streamline curvature duct flow method (ref. 5). Frost (ref. 24) has found that this method, which is widely used throughout the aircraft industry, did not predict the inverse pressure gradient. This example serves to show that when calculating the detailed internal aerodynamics, the flow inside the blade rows must be analyzed if a fairly accurate solution of the flow pattern is required.

Single-Stage Axial Flow Turbine

This single-stage, lightly loaded turbine was designed and tested at NGTE (ref. 25). In the initial through-flow analysis, no allowance was made for annulus wall boundary layers and the local polytropic efficiencies were assumed to be constant throughout the flow field. The predicted velocities (fig. 19) at turbine exit were in fair agreement with the observed values. Some measure of improvement in the region of the outer annulus wall was obtained by Herbert et al. (ref. 26) by allowing for the blockage caused by the boundary layers on the annulus walls. Improved matching of the experimental and predicted velocity profile would require a detailed boundary-layer analysis along the lines suggested by Gregory-Smith.
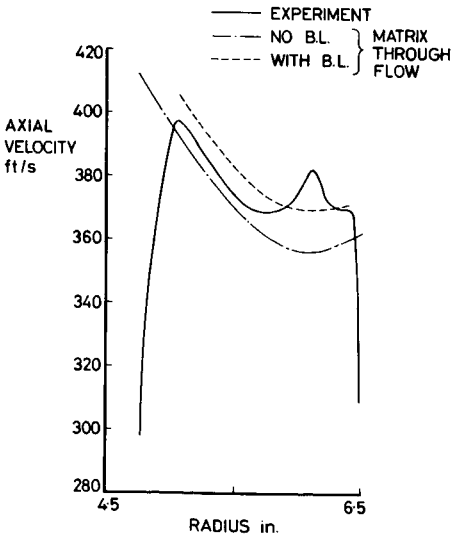
FIGURE 19.—*Axial velocity profile far downstream of single-stage turbine.*

Low Pressure Ratio Centrifugal Compressor

This centrifugal compressor was designed and tested by a firm in the United Kingdom. The results shown in figure 20 are the experimental and theoretical distributions of static pressure ratio along the shroud. The static pressure ratio is defined as the ratio of local to inlet static pressure. In performing the initial calculations, the values of local polytropic efficiency were assumed to be constant throughout the flow field and the slip factor equal to unity. The solution, although giving the correct trend, is in poor agreement with the observed pressures. By assuming a non-uniform distribution of local polytropic efficiency and a slip factor of 0.91, the matching between experiment and theory was improved. This example shows that if a scientifically based model for the flow loss can be formulated then the through-flow theory might eventually be used to provide a quantitative picture of the flow pattern.

High Pressure Ratio Centrifugal Compressor

This example of a centrifugal compressor has been included to illustrate the use of the through-flow program at the design stage of a machine. The initial and modified (final) hub-shroud profiles are shown in figure 21. The only difference between the two impellers is that for the modified machine, the inducer extends beyond the leading edge of the splitter vanes, thus giving a deeper inducer section. The relative Mach number distributions along the hub and shroud profiles are shown in figure 22. It will be seen that the severe velocity gradient in the region of the inducer
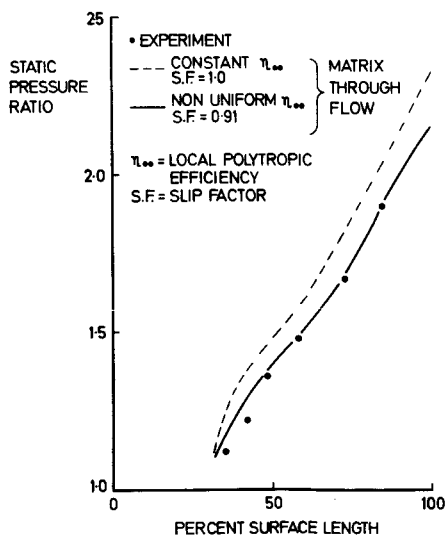
FIGURE 20.—*Static pressure distribution along the shroud of a low pressure ratio centrifugal compressor.*

FIGURE 21.—*Hub-shroud profile of high pressure
ratio centrifugal compressor.*

—— ORIGINAL
- - - MODIFIED
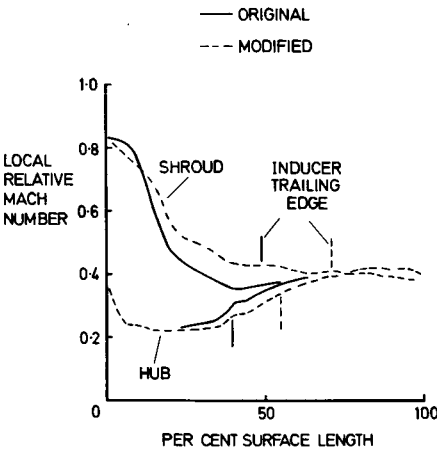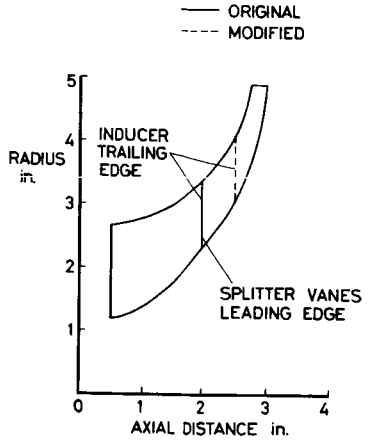
—— ORIGINAL

- - - MODIFIED

FIGURE 22.—*Hub-shroud Mach num-
ber distributions for high pressure
ratio centrifugal compressor.*

leading edge for the original impeller is to some extent alleviated in the modified impeller. This example demonstrates the effects of modifications that are possible within the limits of the same inlet and outlet areas and overall length of the machine. A new design may, of course, permit variations on all these factors and the use of a computer method helps in choosing the best combination.

CONCLUSIONS

Computer solutions for the meridional and blade-to-blade flow patterns in turbomachines have been described. The theory is based on the earlier work of Wu (ref. 11) and the numerical solution is obtained by finite

difference approximations to the governing equations. The main conclusions are the following.

Blade-to-Blade Flow

(1)   Comparisons with exact cascade solutions show that the blade-to-blade program gives an accurate solution for incompressible flow.

(2)   Analysis of turbine rotor blade sections shows that detailed flow patterns can be obtained which would probably be very difficult to find experimentally.

(3)   A comparison with experimental data for a turbine stator blade shows that the method gives a good estimate of high subsonic flow. This analysis demonstrates that the asymmetric finite difference grid developed here is an advancement over the conventional square or rectangular grid.

(4)   An example of a two-stage turbine illustrates that the three-dimensional pressure distributions can be predicted quite well.

Meridional Flow

(1)   The matrix through-flow theory has enabled significant advances to be made in calculating meridional flow patterns. An analysis of a two-stage turbine shows that the theory gives a good estimate of annulus wall static pressure distributions.

(2)   An example of a centrifugal compressor shows that small modifications to the impeller can have significant effects on the flow field. This analysis demonstrates that computer methods can help in selecting the "best" geometry.

(3)   A simple calculation of annulus wall boundary layers for a single-stage turbine enables the through-flow predictions to be improved by allowing for the blockage caused by the boundary layers.

(4)   Improved matching between experimental and predicted flow profiles depends on finding a better loss model and an accurate solution for the boundary-layer development along the annulus walls.

ACKNOWLEDGMENT

LIST OF SYMBOLS

Q Mass flow

r, z, ϕ Radial, axial, and circumferential coordinates

V Absolute velocity

W Relative velocity

x, y Coordinates with tilted axes

λ, α, μ Flow angles

ψ Stream function

Subscripts

d Far downstream of blade row

u Far upstream of blade row

x x-component

y y-component

ϕ Circumferential component

REFERENCES

1. HOWELL, A. R., Fluid Dynamics of Axial Compressors. *Proc. Inst. Mech. Engrs.*, Vol. 153, 1945, p. 441.
2. HOWELL, A. R., Design of Axial Flow Compressors. *Proc. Inst. Mech. Engrs.*, Vol. 153, 1945, p. 452.
3. AINLEY, D. G., AND C. G. R. MATHIESON, *A Method for Performance Estimation for Axial Flow Turbines.* British Aeronautical Research Council, R & M 2974, 1957.
4. MARSH, H., *A Digital Computer Program for the Through-Flow Fluid Mechanics in an Arbitrary Turbomachine Using a Matrix Method.* British Aeronautical Research Council, R & M 3509, 1966.
5. NOVAK, R. A., Streamline Curvature Computing Procedures for Fluid Flow Problems. *Trans. ASME, J. Eng. Power*, Ser. A, Vol. 89, 1967.
6. HODSKINSON, M. G., *A Procedure for Calculating the Axisymmetric Velocity and Pressure Distribution in Centrifugal and Mixed Flow Impellers.* Liverpool U., Dept. Mech. Eng., Reports ULME/B10, 1965, and ULME/B17, 1966.
7. WOOD, M. D., AND A. V. MARLOW, The Use of Numerical Methods for Investigating the Flow in Water Pump Impellers. *Proc. Inst. Mech. Engrs.*, Vol. 181, Part I, No. 29, 1966–67.
8. KATSANIS, T., *A Computer Program for Calculating Velocities and Streamlines for Two-Dimensional Incompressible Flow in Axial Blade Rows.* NASA TN–D3762, 1967.
9. KATSANIS, T., *A Computer Program for Calculating Velocities and Streamlines on a Blade-to-Blade Stream Surface of a Turbomachine.* NASA TN–D4525, 1968.
10. SMITH, D. J. L., AND D. H. FROST, *Calculation of the Flow Past Turbomachine Blades.* Paper 27, Inst. Mech. Eng. Thermodynamics and Fluid Mechanics Convention, Glasgow, 1970.
11. WU, CHUNG HUA, *A General Theory of Three-Dimensional Flow in Subsonic and Supersonic Turbomachines of Axial, Radial and Mixed Flow Types.* NACA TN–2604, 1952.

12. SMITH, D. J. L., *Flow Past Turbomachine Blades*. Ph.D. dissertation, London U., 1970.
13. WILKINSON, J. H., *The Algebraic Eigenvalue Problem*. Oxford U. Press, 1965.
14. GELDER, D., private communication, 1969.
15. GOSTELOW, J. P., *The Accurate Prediction of Cascade Performance*. Ph.D. dissertation, Liverpool U., 1965.
16. EDWARDS, J. P., Unpublished report, Ministry of Technology.
17. HALL, W. S., private communication, 1969.
18. WILKINSON, D. H., *A Numerical Solution of the Analysis and Design Problems for the Flow Past One or More Aerofoils or Cascades: Part I, Analysis Problem; Part II, Design Problem*. British Aeronautical Research Council, R & M 3545, 1967.
19. PRESTON, J. H., *The Calculation of Lift Taking Account of the Boundary Layer*. British Aeronautical Research Council, R & M 2725, 1949.
20. WHITNEY, W. J., M. E. SZANCA, P. T. MOFFITT, AND D. E. MONROE, *Cold Air Investigation of a Turbine for High-Temperature Engine Application: I, Turbine Design and Overall Stator Performance*. NASA TN D-3751, 1967.
21. KATSANIS, T., *Fortran Program for Calculating Transonic Velocities on a Blade-to-Blade Stream Surface of a Turbomachine*. NASA TN D-5427, 1969.
22. JOHNSTON, I. H., AND D. E. SMART, *An Experiment in Turbine Blade Profile Design*. British Aeronautical Research Council, C.P. 941, 1967.
23. GREGORY-SMITH, D. G., *An Investigation of Annulus Wall Boundary Layers in Axial Flow Turbomachines*. ASME Paper 70GT92, 1970.
24. FROST, D. H., *A Computer Program for Analyzing the Flow Through Axial Flow Turbomachines Using the Streamline Curvature Method*. British Aeronautical Research Council, R & M 3687, 1972.
25. SMITH, D. J. L., I. H. JOHNSTON, AND D. J. FULLBROOK, *Investigations on an Experimental Single-Stage Turbine of Conservative Design: Part I, A Rational Aerodynamic Design Procedure; Part II, Test Performance of Design Configuration*. British Aeronautical Research Council, R & M 3541, 1968
26. HERBERT, M. V., AND D. J. L. SMITH, *Investigations on an Experimental Single-Stage Turbine of Conservative Design: Part III, Comparison Between Test Performance and Computer Predictions Using a Through-Flow Analysis*. Unpublished report, Ministry of Technology, 1968.

DISCUSSION

T. KATSANIS (NASA Lewis Research Center): Mr. Smith has shown that approximate three-dimensional solutions for flow through a turbomachine can be obtained by a combination of meridional and blade-to-blade solutions. This is fairly well known. However, we have here a fair number of examples showing both the strengths and weaknesses of these methods in applications.

Limitations of the method should be clearly stated. It appears that the flow must be absolutely irrotational, steady relative to the rotating blades, and nonviscous, and that the flow must be complete subsonic. There must be other assumptions. Certain advantages are stated for the method and the program, but the basic assumptions and limitations are not specified.

The author should specifically state how his method differs from those currently available. For example, a nonorthogonal mesh is used, but the corresponding finite difference equation is not given. Another example is equation (8), where a term has been added, but no explanation of its significance or why $q(x,\phi)$ is not also a function of $\bar{\partial}\psi/\partial x$.

Some comments must be made on one error. This is the statement that the boundary condition of zero velocity normal to the blade is not satisfied in references 8 and 9. This statement is not true. Further, the statement is made that finite difference stars with short limbs leads to large truncation errors. It is true that the standard finite difference equation for unequal spacing has a larger truncation error than with equal spacing. However, this does not mean that the error in the solution will be larger. In fact, with a rectangular mesh, there is theoretically no loss in the accuracy of the solution due to an irregular boundary. This has been amply demonstrated by extensive use and experimentation with the programs of references 8 and 9.

Mr. Smith does not discuss the reason for the use of iterative or relaxation methods for solving matrix equations. There are two main reasons, one being the numerical stability which can be controlled by using a suitable rigorously calculated overrelaxation factor, which assures numerical stability with an optimum rate of convergence. The other reason is economy of storage, which is not shared by most direct methods. Certainly numerical stability cannot be improved with a direct method. The advantage of a direct method would be in reducing the computer calculation time. This reduction in computer time could conceivably be a real advance, provided that storage requirements are not significantly

increased, and that, as indicated, numerical stability is achieved. I would be very much interested in seeing a comparison of computer times for Mr. Smith's program with the times for a method using optimum over-relaxation.

M. D. WOOD (Cambridge University): The paper indicates the magnitude of the recent advances made in calculating fluid flow in turbo-machines. The examples given show that compressible flow in turbine configurations can be predicted to a high degree of accuracy. However, as soon as compressor-type machinery is considered, the position is not so satisfactory. No one is really surprised, because the influence of boundary-layer growth and separation in compressor flow is likely to introduce effects which are of dominant importance. These effects are only recognized in the Wu equations through the presence of losses, and in general even these losses represent average or "smeared" values taken over appropriate computing planes.

It is clear that there are few shortcomings in the equations of motion which Wu manipulates—the shortcomings are only in the simplifications we impose in order to obtain quick gains in current predictive accuracy. I therefore suggest that we should now have the courage to involve our-selves in combining the currently developing detailed calculations of the viscous effects in turbomachinery with the type of basic Wu program described by Mr. Smith. To take examples, we can see how boundary-layer separation in blade corners will lead to warping of stream surfaces. This warping can, in principle, be incorporated in the Smith-type pro-grams. Again, incorporating the predicted development of the boundary layer on blade surfaces would give better understanding of the "slip" factor for use in investigations of centrifugal compressors. Finally, in-clusion of the turbulent diffusion effects between adjacent fluid layers would lead to more realistic representation of the fluid forces in the Wu-type equations.

Although this sounds like a daunting program, it is no more daunting than the thought, 10 years ago, of putting Wu's equations on a computer. Perhaps the author would put my hopes into perspective by explaining what he intends to do next.

A. S. MUJUMDAR (Carrier Corporation): As pointed out by Dr. Katsanis, since the program itself is apparently the major contribution made by the author, it is unfortunate that it cannot be released for publication. Any comparison with the generally available Katsanis programs must, therefore, remain one-sided. The overrelaxation pro-cedure using proper grid spacing and an optimized overrelaxation factor should yield numerically stable results for well-guided geometries. As suggested by Wilkinson (ref. D-1), the maximum relative velocity change

between successive iterations should be taken as the criterion for convergence rather than the maximum streamline deviation chosen by Katsanis.

Since reference 12 in the author's paper is not readily accessible, may I suggest that the finite difference analysis and the numerical scheme be included as an appendix to the paper when it is published. To my knowledge there is no "conventional" finite difference scheme to solve the Poisson-type partial differential equations; a number of variations are possible.

Referring to figure 15 of the paper, could the author explain why the two-dimensional matrix solution appears to give better agreement than the three-dimensional solution with the experimental data for the pressure surface.

Finally, I wish to bring to the author's attention the experimental study of the flow in the blade passages of a radial turbine reported by Glenny (ref. D-2), which may be used to provide further checks for the computer code.

R. C. DEAN (Creare Inc.): I'm a little bit disturbed by perhaps the implications that you suggest about the use of potential analysis in centrifugal compressors. In my experience, the potential analysis usually considerably overpredicts the pressure rise in the wheel and underpredicts or predicts a low relative Mach number at the discharge of the impeller. We have found this through several comparisons between these solutions and data. The potential analysis you are suggesting implies, I think, that the flow follows the blading. I think it is very misleading to think that such a solution would work toward the back of the impeller. The important physics of the flow are not included in the analysis.

L. MEYERHOFF (Eastern Research Group): I have a number of questions.

(1)   Do you have any convergence criteria?

(2)   Are you able to predict the number of iterations for the convergence criteria?

(3)   How do you determine the trailing edge flow angle?

(4)   Did the addition of the E term referred to in your paper still keep the equations set up by Wu, exact? It is not clear whether the equations are still exact after you add these E terms.

(5)   Do you know of any analytical proof of the truncation error for the overrelaxation referred to in your paper?

SMITH (Author): The author thanks the five discussors for their review of this paper.

First, taking the specific points raised by Dr. Katsanis, the purpose of this paper was to present numerical solutions for several turbomachines

to indicate the magnitude of the recent advances made in calculating the fluid mechanics rather than a detailed account of the mathematics of the flow models. The limitations of the methods and the finite difference approximations have been published in references 4 and 10.

On the question of boundary conditions, I have perhaps not made my point clear. In Dr. Katsanis' method (refs. 8 and 9) the flow domain is covered with a rectangular or square grid (fig. D–1). To obtain the blade surface velocity at points such as A, the circumferential component of velocity, W_ϕ, is obtained from the relationship

$$W_\phi = -\frac{1}{b\rho}\frac{\partial\psi}{\partial m}$$

and the resultant surface velocity W is determined so that there is zero velocity normal to the blade; thus,

$$W = \frac{W_\phi}{\cos\beta} \tag{D–1}$$

where β is the local blade surface angle. For points such as B the meridional component of velocity, W_m, is obtained from the relationship

$$W_m = \frac{1}{b\rho r}\frac{\partial\psi}{\partial\phi}$$

and the resultant velocity is given by

$$W = \frac{W_m}{\sin\beta} \tag{D–2}$$

I agree with Dr. Katsanis that these relationships ensure zero velocity normal to the blade. However, a restriction is placed on the resultant velocities; equation (D–1) is limited to $|\beta| \leq 60°$ and equation (D–2) is limited to $|\beta| \geq 30°$. This, I feel, implies an error in the derivatives of the stream function or the stream function values and when the condition of zero normal is imposed gives rise to an error in the resultant velocity.
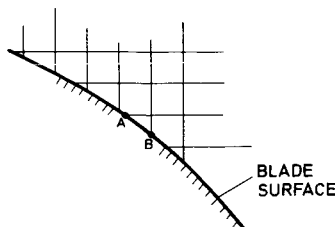
FIGURE D–1.—*Square finite difference grid.*

Turning to the problem of the solution of the matrix equations, I must admit that I have no experience of iterative or relaxation methods. The method I have adopted is a direct method developed by the National Physical Laboratory (NPL), England. This approach, which removes one possible source of divergence, has proved to be very stable numerically and, as I pointed out in my paper, only the band of nonzero elements are formed and stored in the computer. In the recent blade-to-blade computer program, the storage requirements have been further reduced by making use of magnetic tapes as backing store; if the width of the band matrix is W, the core store required is approximately $8W^2$. There is a further point concerned with the basic techniques of the method of solution. Unlike "conventional" direct methods, the NPL procedures do not "invert" the matrix on every iteration; the solution is obtained by a backward and forward substitution process. The matrix equation to be solved is

$$[M] \cdot [\psi] = [q]$$

The first step is a decomposition of the matrix $[M]$; thus

$$[L] \cdot [U] \cdot [\psi] = [q]$$

where the matrices $[L]$ and $[U]$ are lower and upper triangular band matrices, which are only computed on the first iteration. The solution is then obtained by (1) a process of forward substitution, solving for $[Z]$ from

$$[L] \cdot [Z] = [q]$$

and (2) a process of backward substitution, solving for $[\psi]$ from

$$[U] \cdot [\psi] = [Z]$$

The direct method provides an exact solution for the matrix equations and so it could be argued that, since the overall process for finding the stream function distribution is an iterative procedure, it is not necessary to obtain an exact solution on the earlier iterations. It may well be that the best approach is a relaxation method on the earlier iterations, making no attempt to reduce the residuals to zero on each iteration, followed by a direct method on the final iterations.

In answer to Dr. Wood, I would agree that we should now have the courage to extend the type of calculations I have described to include viscous effects. However, as is inevitable with an advanced calculation procedure, my experience of the use of the matrix methods has shown that, for the computer programs to become basic design tools, effort is also required in generating supporting programs for preparing geometric input data and graphical display of output data. This is one aspect I intend to examine.

I am grateful to Mr. Mujumdar for drawing my attention to experimental investigation of a radial turbine. With regard to the solutions for the turbine stator (fig. 15) I am unable to provide an explanation for the two-dimensional solution being in better agreement with the pressure surface experimental data than the three-dimensional solution.

I agree with Mr. Dean that, in the case of centrifugal compressors, some of the important physics of the flow are not included in the analysis. However, I feel that, even with the assumption that the flow follows the blading, the computer tools can help the designer in selecting the best geometry. If a boundary-layer analysis of a potential flow velocity distribution indicates, for example, separation in the inducer of a centrifugal compressor then I am sure Mr. Dean would agree with me that the designer would modify the geometry to overcome this problem. A number of examples illustrating this point are given by Dallenbach (ref. D-3) and Ball et al. (ref. D-4).

In answer to Mr. Meyerhoff, it is difficult to establish a unique convergence criterion. The criteria I have adopted are

$$\text{TOL} = \frac{\psi - \psi_{p-1}}{\psi_{p-1}} \qquad \text{(through-flow method)}$$

$$\text{TOL} = \frac{\psi - \psi_{p-1}}{Q} \qquad \text{(blade-to-blade method)}$$

It has been found that TOL can be reduced to 0.001 in 15 iterations for the through-flow method and 0.0001 in 10 to 30 iterations for the blade-to-blade method.

The calculation of the flow angle is a problem I have avoided by assuming it can be determined from existing empirical rules for the deviation. Clearly this is unsatisfactory, as I have indicated by the turbine example of figure 10. In a real flow the circulation is determined by viscous effects, particularly for compressor-type machinery as illustrated by figure 16. This is one aspect of turbomachinery fluid mechanics that demands research.

The addition of the $E(\partial \psi / \partial x)$ does not change the basic Wu equations. This term was added to keep the width of the band matrix to a minimum.

Finally, on the question of the truncation error for conventional finite difference analysis, which Dr. Katsanis also raised, I can perhaps best illustrate my point by considering a square grid. For such a grid a five point star (refs. 8 and 9) is adopted to represent the Laplacian operator. Consider a star near to a boundary (fig. D-2) with one irregular limb. It will be supposed that for the star center, point 3,

$$\left(\frac{\partial^2 f}{\partial x^2}\right)_3 + \left(\frac{\partial^2 f}{\partial y^2}\right)_3 = \sum_{n=1}^{S} a_n f_n + T \qquad \text{(D-3)}$$
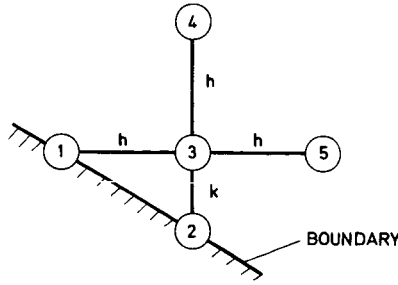
FIGURE   D-2.—*Five-point star with one irregular limb.*

where T is a truncation term and a_1, a_2 are the weightings. The function f can be expanded as a two-dimensional Taylor series about the point 3 at which the function has the value f_3 and derivatives $f_{3,x}, f_{3,y}, f_{3,xx}$, etc. Substituting the Taylor series expressions into equation (D-3), it follows that

$$f_{3,xx}+f_{3,yy}=a_1\left(f_3-hf_{3,x}+\frac{h^2}{2}f_{3,xx}-\frac{h^3}{6}f_{3,xxx}+\ldots\right)$$

$$+a_2\left(f_3-hf_{3,y}+\frac{h^2}{2}f_{3,yy}-\frac{h^3}{6}f_{3,yyy}+\ldots\right)$$

$$+a_3 f_3$$

$$+a_4\left(f_3+kf_{3,y}+\frac{k^2}{2}f_{3,yy}+\frac{k^3}{6}f_{3,yyy}+\ldots\right)$$

$$+a_5\left(f_3+hf_{3,x}+\frac{h^2}{2}f_{3,xx}+\frac{h^3}{6}f_{3,xxx}+\ldots\right)$$

$$+T'$$

Since f is a general function, it follows that the coefficients of f and each of its derivatives may be equated on each side of the above equation. There are five disposable constants $a_i (i=1(1)5)$ and so only the coefficients of f, f_x, f_y, f_{xx} and f_{yy} may be used in order to make the finite difference approximation independent of the low-order derivatives. From the coefficient equations, it is easy to show that the solution for the weightings is

$$a_1=\frac{1}{h^2}$$

$$a_2 = \frac{2}{(\gamma+1)h^2}$$

$$a_3 = \frac{2(\gamma+1)}{\gamma h^2}$$

$$a_4 = \frac{2}{(\gamma+1)\gamma h^2}$$

$$a_5 = \frac{1}{h^2}$$

where $\gamma = k/h$.

The truncation error is

$$T' = \frac{h(\gamma^2-1)}{3(\gamma+1)} f_{3,yyy} + 0(h^2 f_{3,yyyy}) \tag{D-4}$$

It is seen, therefore, that as the irregular limb gets shorter (i.e., γ decreases) the truncation error increases.

REFERENCES

D-1. WILKINSON, D. H., *Stability, Convergence, and Accuracy of Two-Dimensional Streamline Curvature Methods Using Quasi-Orthogonals.* Paper 35, presented at Fluid Mechanics and Thermodynamics Convention, Glasgow U., 1970.

D-2. GLENNY, D. E., *A Theoretical and Experimental Study of the Flow in the Blade Passages of a Radial Turbine.* Mech. Eng. Rept. 120, Aero. Res. Lab., Austr. Dept. Supply, February 1968.

D-3. DALLENBACH, F., *The Aerodynamic Design and Performance of Centrifugal and Mixed-Flow Compressors.* Soc. Automotive Engrs., Technical Progress Series, Vol. 3, 1961.

D-4. BALL, G. A., A. H. BELL, AND L. B. MANN, *The Development of the Chrysler Automotive Centrifugal Compressor.* Soc. Automotive Engrs., Technical Progress Series, Vol. 3, 1961.

Matrix Methods for the Design of Cascades to Prescribed Surface Velocity Distributions and for Fully Compressible Flow

M. E. Silvester and C. M. Fitch

Rolls-Royce, Limited
Derby, England

This paper describes matrix methods that have been developed for calculating compressible flow on a blade-to-blade surface of revolution. The methods have been fully tested to date only for the design of plane cascades to prescribed blade surface distributions; the methods will be illustrated here for that problem only. Similar methods are presently being applied to both the direct and indirect problems and for flow on arbitrary surfaces of revolution in annular cascades with stream sheet thickness variations. It is believed that by such methods, both the direct and indirect calculations can be reduced to about 60 to 90 seconds of computing.

The trend in compressor and turbine design is toward fewer and more highly loaded stages. To do this and maintain high efficiency demands the ability to calculate in ever-increasing detail the gas flow through such a machine. So complex are the equations governing the flow and the geometries involved that practicable solutions can be found only after making simplifying assumptions. The degree of approximation is always a compromise between a realistic description of the physical processes and a mathematical model that can be solved within reasonable time and cost. This has led to design procedures which treat the flow in two stages—a two-dimensional through-flow calculation which neglects circumferential variations, followed by a two-dimensional blade-to-blade calculation in which the flow is assumed to take place on a surface of revolution. Although fully three-dimensional calculations are being attempted, these are slow and costly and have a long way to go before they become design tools.

It seems likely, therefore, that for a few years to come, two-dimensional approaches will remain the basis of most design work and, for this reason, it is worthwhile to make these calculations as realistic and fast as possible.

Methods will be described here for calculations on blade-to-blade surfaces of revolution. These methods are being applied both to the direct problem of calculating blade surface velocities when the blade geometries are prescribed and to the indirect problem of calculating the blade geometry when the blade surface velocities are prescribed. The methods will be illustrated by discussing the indirect problem for compressible flow in a plane cascade. This has been chosen because it is the only problem for which the methods have been fully tested to date and because the authors have seen no other fully compressible solution to this problem. It is believed that the methods described here extend easily to both the direct and indirect problems on surfaces of revolution with stream sheet thickness variations.

MATHEMATICAL ANALYSIS

Assumptions

The following assumptions have been made.

(1) The flow is steady, inviscid and irrotational.
(2) The fluid is a perfect gas.
(3) The total temperature is uniform across the entry to the cascade.
(4) The flow is plane two-dimensional flow and the normal component of velocity is zero on the blade surface.
(5) The cascade contains an infinite number of equally spaced blades of infinite length.

The assumption of irrotationality, together with the finite difference approximations to the differential equations and the boundary-value approach to the solution of the finite difference equations, tacitly assume that the flow is everywhere subsonic. However, the method will formally produce answers with supersonic patches and, where these are small and the peak Mach numbers only a little above sonic, these solutions are probably realistic.

Equations of Motion

In the analysis that follows, x and y are Cartesian coordinates with x measured in the "axial" direction and y in the "pitchwise" direction, as shown in figure 1. Velocities and density are normalized with respect to the stagnation sound speed and stagnation density, respectively.

The equations governing the flow are those of irrotationality and continuity which are, respectively

$$\frac{\partial V_x}{\partial y} - \frac{\partial V_y}{\partial x} = 0 \tag{1}$$

$$\frac{\partial}{\partial x}\,(\rho V_x)+\frac{\partial}{\partial y}\,(\rho V_y)=0 \tag{2}$$

Density is related to velocity through Bernoulli's equation

$$\rho=\left\{1-\frac{\gamma-1}{2}\,(V_x{}^2+V_y{}^2)\right\}^{1/(\gamma-1)}$$

Equations (1) and (2) may be satisfied identically by a potential function ϕ and stream function ψ defined by

$$\frac{\partial\phi}{\partial x}=V_x$$

$$\frac{\partial\phi}{\partial y}=V_y$$

$$\frac{\partial\psi}{\partial y}=\rho V_x$$

$$\frac{\partial\psi}{\partial x}=-\rho V_y$$

It will be convenient also to work in terms of the net velocity V and flow direction θ, related to V_x and V_y by the equations

$$V_x=V\cos\theta$$

$$V_y=V\sin\theta$$
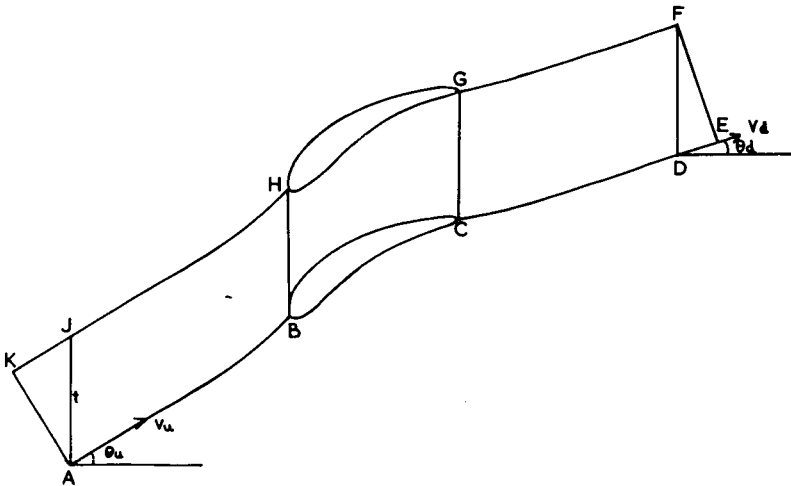
FIGURE 1.—*One strip of the cascade in the physical plane.*

If we now use ϕ and ψ as independent variables instead of x and y, equations (1) and (2) become

$$\rho V \frac{\partial V}{\partial \psi} - V^2 \frac{\partial \theta}{\partial \phi} = 0 \qquad (3)$$

$$V \frac{\partial}{\partial \phi} (\rho V) + (\rho V)^2 \frac{\partial \theta}{\partial \psi} = 0 \qquad (4)$$

and Bernoulli's equation is

$$\rho = \left[1 - \frac{\gamma - 1}{2} V^2 \right]^{1/(\gamma-1)} \qquad (5)$$

At this stage, Stanitz (ref. 1) linearized equations (3) and (4) by approximating equation (5) by

$$\rho = \frac{1}{\sqrt{1 + V^2}}$$

At the equivalent stage in the direct problem, other workers have arranged the equations either in the form of a pseudo Poisson's equation, collecting the terms describing incompressible effects on the left in the form of a Laplacian and the terms describing compressible effects on the right in the form of a source term; or they have arranged the equations in the form of a general partial differential equation in which the coefficients contained derivatives of the density ρ. Finite difference and singularity methods have then been used to solve the equations in these forms iteratively by guessing the source term or coefficients, solving as though the equations were linear, and then re-estimating the terms that had been guessed. Iterative methods based on these forms of arrangements of the equations converge slowly at high Mach numbers because the guessed terms are by no means small perturbations and important contributions are left "trailing" one cycle behind in the iterations.

In order to introduce compressibility effects quickly into an iterative method, the authors consider it better to use Bernoulli's equation to express the derivatives of ρ in terms of those of the dependent variable and then to collect together all terms containing any particular derivative of that variable. The coefficients of these variables then do not contain derivatives of ρ which have to be guessed. For the indirect cascade problem considered here, the term $\partial(\rho V)/\partial \phi$ in equation (4) should not be expressed as $\rho(\partial V/\partial \phi) + V(\partial \rho/\partial \phi)$ with ρ and $\partial \rho/\partial \phi$ being guessed. Instead, equation (5) should be used to obtain

$$d(\rho V) = \rho \left(\frac{1 - [(\gamma+1)/2]V^2}{1 - [(\gamma-1)/2]V^2} \right) dV$$

so that equations (3) and (4) become

$$\frac{\rho}{V}\frac{\partial V}{\partial \psi} - \frac{\partial \theta}{\partial \phi} = 0 \tag{6}$$

$$\frac{1}{\rho V}\left(\frac{1-[(\gamma+1)/2]V^2}{1-[(\gamma-1)/2]V^2}\right)\frac{\partial V}{\partial \phi} + \frac{\partial \theta}{\partial \psi} = 0 \tag{7}$$

If one second-order equation was to be obtained by eliminating between (6) and (7), then, again, the derivatives of ρ introduced should be expressed in terms of those of V. For this problem there is, however, a neater approach. Define F and H by

$$dF = \frac{\rho}{V}\,dV \tag{8}$$

$$dH = \frac{1}{\rho V}\left(\frac{1-[(\gamma+1)/2]V^2}{1-[(\gamma-1)/2]V^2}\right)dV \tag{9}$$

so that equations (6) and (7) become

$$\frac{\partial H}{\partial \phi} + \frac{\partial \theta}{\partial \psi} = 0 \tag{10}$$

$$\frac{\partial F}{\partial \psi} - \frac{\partial \theta}{\partial \phi} = 0 \tag{11}$$

Using equation (5), equation (8) may be integrated directly for some values of γ. Taking $\gamma = \frac{4}{3}$ and writing $z = V^2/6$, we have

$$F(V) = \log V - \frac{3z}{2} + \frac{3z^2}{4} - \frac{z^3}{6} \tag{12}$$

Taking $\gamma = \frac{7}{5}$ and writing $z^2 = 1 - (V^2/5)$, we have

$$F(V) = \log V + \frac{z^5}{5} + \frac{z^3}{3} + z - \log\left(\frac{1+z}{2}\right) - \frac{23}{15} \tag{13}$$

In each case, the constant of integration has been chosen such that $F(V) \to \log V$ as $V \to 0$.

The function F will now be taken as the dependent variable and equation (10) written in the form

$$\frac{dH}{dF}\frac{\partial F}{\partial \phi} + \frac{\partial \theta}{\partial \psi} = 0 \tag{14}$$

where, from (8) and (9),

$$\frac{dH}{dF} = \frac{1}{\rho^2}\left(\frac{1-[(\gamma+1)/2]V^2}{1-[(\gamma-1)/2]V^2}\right)$$

The Potential and Deflection Conditions

In figure 1, which shows one strip of the cascade, AB, CE, GF and KH are dividing streamlines. At any point (x,y) on AB, the flow conditions are the same as at the point $(x,y+t)$ on JH and similarly for CD and GF. The lines KA and FE are far upstream and downstream of the cascade, where flow conditions are uniform. Figure 2 shows the same diagram mapped into the (ϕ,ψ)-plane with A, B, C, D, and E chosen as $\psi = 0$. From the definitions of ϕ and ψ, it follows that

$$d\phi = V\ ds \qquad\qquad (15a)$$

$$d\psi = \rho V\ dn \qquad\qquad (15b)$$

Define

$$\Delta\phi'_L = \phi_H - \phi_B$$

$$\Delta\phi_T = \phi_G - \phi_C$$

$$\Delta\phi_S = \phi_C - \phi_B$$

$$\Delta\phi_P = \phi_G - \phi_H$$

Clearly

$$\Delta\phi_L = \phi_J - \phi_K$$

$$\Delta\phi_T = \phi_E - \phi_D$$

From (15a), remembering that J, K, E and D are far from the cascade,

FIGURE 2. — *One strip of the cascade in the (ϕ,ψ) plane.*

$$\Delta\phi_L = V_u \, t \, \sin \theta_u$$

$$\Delta\phi_T = V_d \, t \, \sin \theta_d$$

It is also clear that

$$\Delta\phi_S - \Delta\phi_P = \Delta\phi_L - \Delta\phi_T$$

so that

$$\Delta\phi_S - \Delta\phi_P = t(V_u \sin \theta_u - V_d \sin \theta_d) \tag{16}$$

Equation (16) will be called the potential condition.

From equation (11), we have

$$\oint_{AEFK} F \, d\phi + \theta \, d\psi = 0$$

from which it follows that

$$\int_B^C F \, d\phi - \int_H^G F \, d\phi = \psi_0(\theta_u - \theta_d) + F_u \Delta\phi_L - F_d \Delta\phi_T \tag{17}$$

where ψ_0 is the value of ψ along KF. Equation (17) will be called the deflection condition.

In the indirect problem, the velocity on the blade surfaces is prescribed as a function of fractional arc length S' measured from $S' = 0$ at the leading edge stagnation point and $S' = 1$ at the trailing edge stagnation point. Let these velocity distributions be $V_S(S')$ and $V_P(S')$ along the suction and pressure surfaces. If L_S and L_P represent the physical lengths of these surfaces, measured between stagnation points, the potential and deflection conditions may be written

$$L_S \int_0^1 V_S \, dS' - L_P \int_0^1 V_P \, dS' = t(V_u \sin \theta_u - V_d \sin \theta_d) \tag{18}$$

and

$$L_S \int_0^1 (VF)_S \, dS' - L_P \int_0^1 (VF)_P \, dS' = \psi_0(\theta_u - \theta_d) + F_u \Delta\phi_L - F_d \Delta\phi_T \tag{19}$$

From the prescribed velocity distributions and upstream and downstream conditions, the corresponding values of F may be found from (12) and (13) and L_S and L_P from (18) and (19). The lengths in the (ϕ,ψ)-plane, $\Delta\phi_S$ and $\Delta\phi_P$, may then be found from

$$\Delta\phi_S = L_S \int_0^1 V_S \, dS'$$

$$\Delta\phi_P = L_P \int_0^1 V_P \, dS'$$

and the diagram of the (ϕ,ψ)-plane constructed. Eliminating θ between equations (11) and (14) gives

$$\frac{\partial^2 F}{\partial \psi^2} + \frac{\partial}{\partial \phi}\left(\frac{dH}{dF}\frac{\partial F}{\partial \phi}\right) = 0 \tag{20}$$

To determine the blade shape corresponding to the prescribed surface velocity distributions and far upstream and downstream conditions, we have to solve equation (20) inside and on the contour $ADFJ$, subject to the boundary conditions:

(1) F is prescribed on BC, HG, AJ and DF
(2)   Along AB and JH

$$F(\phi,0) = F(\phi + \Delta\phi_L, \psi_0) \tag{21a}$$

$$\theta(\phi,0) = \theta(\phi + \Delta\phi_L, \psi_0) \tag{21b}$$

(3)   Along CD and GF

$$F(\phi,0) = F(\phi + \Delta\phi_T, \psi_0) \tag{21c}$$

$$\theta(\phi,0) = \theta(\phi + \Delta\phi_T, \psi_0) \tag{21d}$$

Transformation of the (ϕ, ψ)-Plane

There are a number of possible approaches to a numerical solution of this boundary-value problem. The one given here involves an approximate transformation of the (ϕ,ψ)-plane and some tedious algebra. However, the error in the transformation can be controlled so that it is less than that involved in the numerical methods and leads to a boundary-value problem posed in a form for which this is a quick and elegant method of solution.

First, in order to get a good spacing of points on a finite difference grid and not to map part of the suction surface twice, it is convenient to invert the diagram in the (ϕ,ψ)-plane through a transformation $\psi \to \psi_0 - \psi$. We can achieve this without altering the equations if we make the additional transformation $\theta \to -\theta$. In what follows, this transformation will be assumed to have been made. Define new variables ϕ' and ψ' through the equations

$$\psi = \frac{\psi_0}{\alpha}\psi' \tag{22a}$$

$$\phi = \frac{\Delta\phi_P}{2} + \frac{\Delta\phi_P}{\beta}\left[\phi' + \frac{\psi'}{\alpha}(a_1 + a_2 \tanh \phi')\right] \tag{22b}$$

where

$$a_1 = \frac{\beta}{\Delta\phi_P} \frac{\Delta\phi_T + \Delta\phi_L}{2}$$

$$a_2 = \frac{\beta}{\Delta\phi_P} \frac{\Delta\phi_T - \Delta\phi_L}{2}$$

The constant α is merely a scaling factor which can be chosen freely; β is a constant which, for values of $\phi' \geq \beta/2$, makes $\tanh \phi' \simeq 1$. This transformation approximately maps the contour $ADFJ$ of the (ϕ,ψ)-plane into three rectangular regions in the (ϕ',ψ')-plane as shown in figure 3. If we write

$$a' = \frac{\beta/\Delta\phi_P}{1 + (\psi/\psi_0) a_2 \operatorname{sech}^2 \phi'}$$

$$b' = \frac{-(a_1 + a_2 \tanh \phi')}{\psi_0 [1 + (\psi/\psi_0) a_2 \operatorname{sech}^2 \phi']}$$

then we have

$$\left(\frac{\partial}{\partial\phi}\right)_\psi = a' \left(\frac{\partial}{\partial\phi'}\right)_{\psi'}$$

$$\left(\frac{\partial}{\partial\psi}\right)_\phi = b' \left(\frac{\partial}{\partial\phi'}\right)_{\psi'} + \frac{\alpha}{\psi_0} \left(\frac{\partial}{\partial\psi'}\right)_{\phi'}$$

Writing $\dot{H}$ for dH/dF, equation (20) becomes
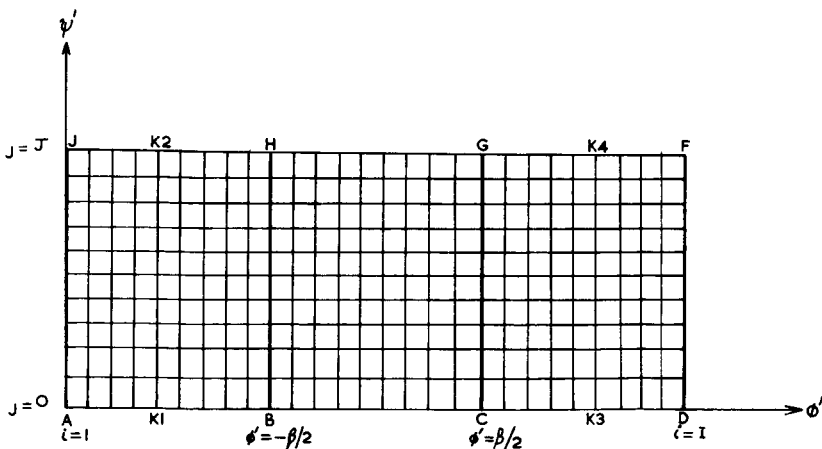
FIGURE 3. — *One strip of the cascade in the (ϕ',ψ') plane.*

$$(a'^2\dot{H}+b'^2)\frac{\partial^2 F}{\partial\phi'^2}+\frac{\partial F}{\partial\phi'}\left[a'\frac{\partial}{\partial\phi'}(a'\dot{H})+b'\frac{\partial b'}{\partial\phi'}+\frac{\alpha}{\psi_0}\frac{\partial b'}{\partial\psi'}\right]$$

$$+\frac{2b'\alpha}{\psi_0}\frac{\partial^2 F}{\partial\phi'\partial\psi'}+\frac{\alpha^2}{\psi_0^2}\frac{\partial^2 F}{\partial\psi'^2}=0 \tag{23}$$

Although this equation looks more complicated than (20), the boundary conditions (21a) and (21b) are simplified to

$$F(\phi',0)=F(\phi',\alpha)$$

$$\theta(\phi',0)=\theta(\phi',\alpha)$$

along AB and JH and similarly along CD and FG.

Numerical Analysis

Equation (23) may now be solved numerically by finite differences on a rectangular grid in the (ϕ',ψ')-plane. The method will be described for a grid with spacing $\delta\phi'$ and $\delta\psi'$ constant in the ϕ' and ψ' directions, respectively. In practice, it is better to use an unequally spaced grid but, to avoid unnecessary complication in the description, a discussion of unequal grid spacing will be left until later. The grid described here is shown in figure 3. Write equation (23) in the form:

$$A(\delta\phi')^2\frac{\partial^2 F}{\partial\phi'^2}+2B\,\delta\phi'\frac{\partial F}{\partial\phi'}+4C\,\delta\phi'\,\delta\psi'\frac{\partial^2 F}{\partial\phi'\,\partial\psi'}+D(\delta\psi')^2\frac{\partial^2 F}{\partial\psi'^2}=0 \tag{24}$$

The method of solution will be to estimate the coefficients A, B, C and D, solve (24) as a linear equation, and re-estimate these coefficients. The process is continued until converged, which usually requires about three or four cycles. Equation (24) may be approximated by finite differences in the form:

$$A_j^i(F_j^{i+1}-2F_j^i+F_j^{i-1})+B_j^i(F_j^{i+1}-F_j^{i-1})+C_j^i(F_{j+1}^{i+1}-F_{j+1}^{i-1}-F_{j-1}^{i+1}+F_{j-1}^{i-1})$$

$$+D_j^i(F_{j+1}^i-2F_j^i+F_{j-1}^i)=0 \tag{25}$$

for $1\le i\le I-1;\qquad 1\le j\le J-1.$

The boundary conditions are (1) that F_0^i and F_J^i are given on BC and HG, together with F_j^0 and F_j^I for $j=0\ldots J$, and (2) that $F_0^i=F_J^i$ and $\theta_0^i=\theta_J^i$ along AB and JH and along CD and GF (eqs. 21(a)–21(d)). The method of solving these finite difference equations is a slight modification of a method suggested to the authors by Stocker (ref. 2). Rewrite equation (25), grouping terms according to superscripts $i+1$, i, and $i-1$.

$$[-C_j{}^i F_{j-1}^{i+1} + (A_j{}^i + B_j{}^i) F_j{}^{i+1} + C_j{}^i F_{j+1}^{i+1}]$$
$$+ [D_j{}^i F_{j-1}{}^i - 2(A_j{}^i + D_j{}^i) F_j{}^i + D_j{}^i F_{j+1}{}^i]$$
$$+ [C_j{}^i F_{j-1}^{i-1} + (A_j{}^i - B_j{}^i) F_j{}^{i-1} - C_j{}^i F_{j+1}^{i-1}] = 0 \qquad (26)$$

Inside the rectangle $BCGH$, augment equation (26) with the equations

$$F_0{}^i = F_0{}^i$$

$$F_J{}^i = F_J{}^i$$

remembering that both $F_0{}^i$ and $F_J{}^i$ are known. In the rectangles $ABHJ$ and $CDFG$, augment equation (26) with

$$F_0{}^i = F_J{}^i$$

$$\theta_0{}^i = \theta_J{}^i$$

The last relation must be expressed in terms of F. This could be done using equation (11), which implies that

$$\left(\frac{\partial F}{\partial \psi'}\right)_0^i = \left(\frac{\partial F}{\partial \psi'}\right)_J^i$$

and approximating this relation by finite differences. This was tried, but it led to small but unacceptable errors. Instead, therefore, equation (11) was integrated along $\phi' = $ constant and the boundary conditions $\theta_0{}^i = \theta_J{}^i$ inserted into the integral. The integral was then approximated by finite differences using Simpson's rule, giving

$$\sum_{j=0}^{J} \left(\dot{H}_j{}^i + \frac{b'^2}{a'^2}\right) K_j (F_j{}^{i+1} - F_j{}^{i-1}) = 0 \qquad (27)$$

where $K_j = 1, 4, 2 \ldots 2, 4, 1$.

Therefore, inside the rectangles $ABHJ$ and $CDFG$, equation (26) is augmented by (27) and $F_0{}^i = F_J{}^i$.

Defining $\mathbf{F}^i$ to be the column vector $(F_0{}^i, F_1{}^i, \ldots, F_J{}^i)$, equation (26), together with the augmenting equations, may be written in the form

$$M^i \mathbf{F}^{i+1} + N^i \mathbf{F}^i + P^i \mathbf{F}^{i-1} = \mathbf{Q}^i \qquad (28)$$

where M^i, N^i and P^i are square matrices and $\mathbf{Q}^i$ is a column vector which contains only zeros inside the rectangles $ABHJ$ and $CDFG$ and is of the form $(F_0{}^i, 0, 0, 0, \ldots 0, F_J{}^i)$ inside the rectangle $BCGH$. To solve equation (28), we begin by estimating $F_j{}^i$ at every mesh point other than those along $i = 0$ and $i = I$ where F is prescribed. From these estimates, the coefficients A, B, C, and D of (24) may be calculated at each point and hence the matrices M^i, N^i and P^i of (28) may be determined. We then look for a solution of (28) of the form

$$\mathbf{F}^i = R^i \mathbf{F}^{i+1} + \mathbf{t}^i \tag{29}$$

where the R^i are square matrices and the $\mathbf{t}^i$ are column vectors. To determine R^i and $\mathbf{t}^i$, we substitute (29) into (28) and, after some re-arrangement, obtain

$$\mathbf{F}^i = -(N^i + P^i R^{i-1})^{-1} M^i \mathbf{F}^{i+1} + (N^i + P^i R^{i-1})^{-1} (\mathbf{Q}^i - P^i \mathbf{t}^{i-1}) \tag{30}$$

Comparing (29) and (30), we obtain by inspection

$$R^i = -(N^i + P^i R^{i-1})^{-1} M^i \tag{31}$$

$$\mathbf{t}^i = -(N^i + P^i R^{i-1})^{-1} (P^i \mathbf{t}^{i-1} - \mathbf{Q}^i) \tag{32}$$

Equations (31) and (32) may be solved recursively for R^i and $\mathbf{t}^i$, for $1 \leq i \leq I-1$, once R^0 and $\mathbf{t}^0$ are known. These are obtained from the prescribed value of $\mathbf{F}^0$, for

$$\mathbf{F}^0 = R^0 \mathbf{F}^1 + \mathbf{t}^0 \tag{33}$$

If (33) is to be satisfied, whatever the value of $\mathbf{F}^1$, we must have

$$R^0 = 0$$

$$\mathbf{t}^0 = \mathbf{F}^0$$

Having determined R^i and $\mathbf{t}^i$, $0 \leq i \leq I-1$, we can now solve for F everywhere, using (29) and commencing from

$$\mathbf{F}^{I-1} = R^{I-1} \mathbf{F}^I + \mathbf{t}^{I-1}$$

where $\mathbf{F}^I$ is the prescribed boundary condition on $i = I$. Having determined $F_j{}^i$ everywhere, the coefficients A, B, C, and D of (24) may be re-estimated and the process repeated until successive estimates of F everywhere converge to within some tolerance. In practical cases, two to four iterations are usually required, depending on the level of Mach number.

There is a further point in the calculation of F which requires discussion; namely, the treatment of the stagnation points, the points B, C, G, and H in figure 3. Near stagnation points, $V \rightarrow 0$ and $F \rightarrow -\infty$. If, when prescribing the velocities along BC and HG, zero velocities are prescribed at the stagnation points, then it is clear that the methods described so far cannot be applied.

A simple and approximate method of overcoming this difficulty, which is equivalent to removing the stagnation points by cusping the blade, is as follows. At the start of each compressibility iteration, a nonzero velocity is assigned to the points B and H and another nonzero velocity to the points C and G. With these values, together with the other prescribed boundary conditions, we can now solve for F everywhere by the methods

already described and this solution will satisfy all the prescribed boundary conditions. However, for arbitrary choices of velocity at the points B and H and C and G, the function F is not constant at upstream and downstream infinity; that is, although $\partial F/\partial \psi'$ is zero there, $\partial F/\partial \phi'$ is not zero. Furthermore, for given boundary conditions, the value of $\partial F/\partial \phi'$ at upstream infinity is primarily controlled by the velocity assigned to B and H, and $\partial F/\partial \phi'$ at downstream infinity by the velocity assigned to C and G. Therefore, at the start of each iteration, as well as recalculating the matrices M^i, N^i, and P^i, new estimates are made of the velocities at B and H and at C and G to make $\partial F/\partial \phi'$ zero at points far upstream and downstream. This additional change does not seriously affect the convergence of the main iteration.

Although this is a rather crude treatment of the stagnation points, it does lead to accurate answers in the following sense. When θ is calculated from F, equation (11) is integrated along a streamline starting from far downstream where θ is prescribed. The closeness of agreement of the calculated and prescribed values of θ far upstream is one measure of the accuracy of the calculation. This agreement is best (about 0.2 percent for 100° of turning) when the adjustments described have converged. Methods such as those of Woods (ref. 3) for dealing with singular points were tried but did not appear to increase the accuracy of the calculation, possibly because the computing grid was coarse compared with the small region over which the velocity is close to zero.

From the converged solution for F, the blade coordinates may be calculated. This is done by first integrating equation (11) along $\psi' = \alpha/2$ to give θ along the center of the blade passage and then integrating equation (10) away from this mean line to give θ on the blade surface. Having found θ, the blade coordinates are found by integrating the equations

$$dx = \frac{d\phi}{V}\cos\theta - \frac{d\psi}{\rho V}\sin\theta$$

$$dy = \frac{d\phi}{V}\sin\theta + \frac{d\psi}{\rho V}\cos\theta$$

The integration is performed in the (ϕ', ψ')-plane and commences from arbitrary values of x and y in the middle of the blade passage, out along the line $\phi' =$ constant to the blade surface and then along the blade surfaces, $\psi' = 0$ and $\psi' = \alpha$. This path of integration avoids the necessity of crossing the stagnation point region. The blade shapes obtained show the cusps over the first and last two points on each surface and the leading and trailing edges are generally rounded by eye.

SIZE AND SPEED OF COMPUTER PROGRAM

The methods described have been programed on an IBM 360/65 computer. Using 40 points of each blade surface, 50 upstream and 50 downstream points, and 11 points across the blade passage, the program size is 162K bytes. For a fully converged solution, three to five cycles are required at an average of 24 seconds per cycle. For a fully compressible calculation on such a large grid, the method is therefore very fast. To obtain this speed of computation, an unequally spaced grid has been used, with the grid becoming more widely spaced far upstream and downstream. The only change required in the methods described is to modify the finite difference approximations to derivatives in the obvious way.

Sample Calculation

The program has been tested on a number of examples, one of which, a NASA blade taken from reference 4, is described here. In figure 4, the circles and triangles represent the measured velocity distribution while the full line is the velocity used in the calculation. The measured outlet angle was changed by about 0.7° to −67.7° because the calculation cannot take into account viscous effects. The true and calculated blade shapes are shown in figure 5, where it will be seen that the agreement is generally good. Agreement is worst near the leading and trailing edges. The shape of the leading edge depends critically on the velocity distribution and this is
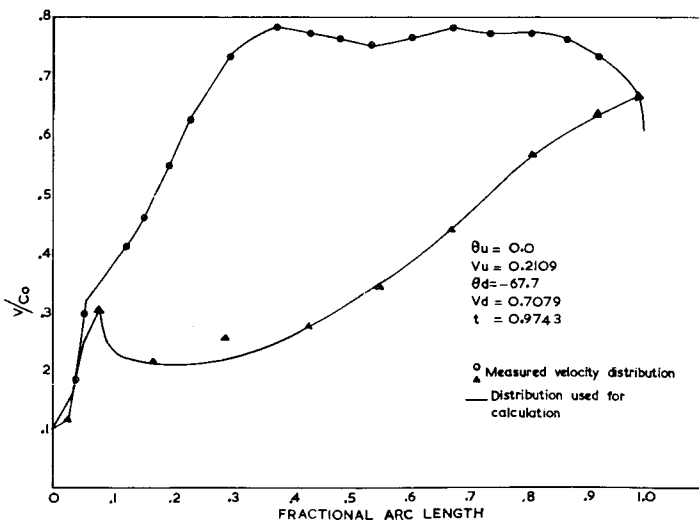
FIGURE 4.—*Velocity distribution of blade of reference 4.*
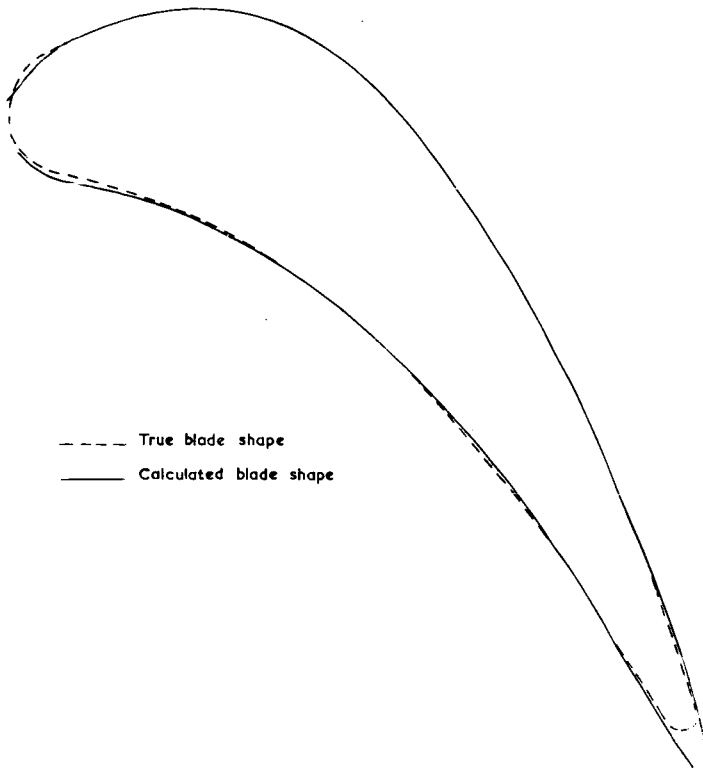
FIGURE 5.—*Comparison of the true and calculated blade shapes.*

impossible to measure at points sufficiently close together to give accurate definition. Also, one of the measured points on the pressure surface has been ignored, for it was found that a smooth velocity distribution through that point did not reproduce the correct blade shape. The velocity distribution used in this region is merely guessed to give a reasonably good blade shape.

LIST OF SYMBOLS

F A function of velocity
H A function of velocity
n Distance normal to a streamline
S Distance along a streamline
S' Fractional length along a blade surface measured between stagnation points
t Pitch

V Velocity, normalized with respect to the stagnation sound speed

V_x The x-component of V

V_y The y-component of V

x Cartesian coordinate measured in the axial direction

y Cartesian coordinate measured in the pitchwise direction

γ Ratio of specific heats

θ Flow direction measured counterclockwise from the positive x direction

ρ Density, normalized with respect to the stagnation density

ϕ Potential function

ϕ' Transformed potential function

ψ Stream function

ψ' Transformed stream function

Subscripts and Superscripts

d Far downstream

i Index referring to the value of ϕ'

j Index referring to the value of ψ'

L Leading edge

T Trailing edge

u Far upstream

REFERENCES

1. Stanitz, J. D., *Design of Two-Dimensional Channels With Prescribed Velocity Distribution Along the Channel Walls.* NACA TN 2595, 1952.

2. Stocker, P., (U. East Anglia, England), private communication with Rolls-Royce, 1967.

3. Woods, L. C., The Relaxation Treatment of Singular Points in Poisson's Equation. Quart. *J. Appl. Math.*, Vol. 6, 1953.

4. Whitney, W. J., E. M. Szanca, T. P. Mollit, and D. E. Monroe, *Cold Air Investigation of a Turbine for High-Temperature Engine Application: I, Turbine Design and Overall Stator Performance.* NASA TN D 3751, 1967.

DISCUSSION

D. PAYNE (Rolls-Royce): The authors are to be congratulated on applying a highly efficient matrix method to the solution of the boundary-value problem which cascade design presents in the compressible flow function plane.

The technique used to solve each iterate of equation (24) (as yet unpublished by Professor Stocker) transmits boundary-value information just once to the right through the vectors **t** and just once to the left through the **F** vectors themselves. This elegant technique thrives on highly rectangular grids, such as the one established here in the (ϕ',ψ')-plane, although the slightly approximate transformation (22b) into this plane could possibly be avoided by the use of a variable skew mesh in the (ϕ,ψ)-plane.

The starting approximation to the coefficients in equation (28), although not explicitly stated, presumably results from taking $H = F$, and this assumption is, in itself, quite accurate for Mach numbers less than about 0.8 (ref. D-1).

The desirability of basing the design of gas turbine blading on a prescribed distribution of surface velocity can be justified by consideration of the mechanical, aerodynamic, and mathematical aspects of the overall design problem (ref. D-2). For the past eight years, all turbine blades designed at the Bristol Engine Division of Rolls Royce Ltd. (previously Bristol Siddeley Engines) have been produced on this basis, using the Bristol Design Transformation (ref. D-3) to generate the necessary cascade geometry. Until now, it has been a rather unfortunate handicap that, while a complete velocity distribution theory (parametric description of velocity distribution, optimization under geometric constraints, wake models, etc.) could be established for an arbitrary density-speed relation (ref. D-1), the actual transformation from the (ϕ,ψ)-plane to the (x,y)-plane was only practical, on a routine basis, for a simplified form of the $\rho(V)$ function (linearized compressible flow, or Chaplygin gas). Although the linearized transformation can be shown to agree closely with plane-flow experiments for Mach numbers up to about 0.85 (ref. D-1), it is to be expected that the methods of Mr. Silvester and Miss Fitch will produce a routine design transformation able to cope with near-sonic and, perhaps, slightly supersonic flow, as well as allowing incorporation of blade-to-blade variations of radial aerodynamic influences, as such variations become better understood.

J. P. GOSTELOW (Cambridge University): The authors introduce their promising new matrix techniques as being suitable for both the direct and the indirect problems of cascade flow prediction. Since it is well known that some considerable effort at their company (ref. D–4) has been invested in iterative solutions of the direct problem, using the Martensen method (ref. D–5) as a basis, it would be of interest to know whether the iterative approach has failed and has therefore been written off. The difficulty with the iterative schemes is that the source distribution contains first derivatives of ρ and, therefore, second derivatives of ψ. It would not be surprising, therefore, if convergence difficulties were experienced at high subsonic Mach numbers where the desired result is masked by rounding-off errors. This question does not concern simply the direct problem since, as Murugesan and Railly (ref. D–6) have shown, the Martensen method can become a successful design tool in solving the indirect problem.

It is interesting to observe that Silvester and Fitch deliberately rearrange the equations so that density-change information is transmitted immediately into the flow solution. It is more conventional for the density calculation to lag the stream function calculation by one iteration, again deliberately to improve stability. This latter approach is employed in Smith's excellent paper (ref. D–7) and in most streamline curvature solutions to the axisymmetric problem. It was clear from Smith's presentation that the trailing density approach is justified for cases where the local Mach number does not exceed 0.85, but even linearized flow models can cope with such examples. It would be interesting to know whether Smith can retain numerical stability, with density lagging by one iteration, when sonic conditions are reached and exceeded on the blade surface.

The kernel of the question is whether one ought to follow Silvester and Fitch in rearranging the equations when local sonic conditions are approached.

L. MEYERHOFF (Eastern Research Group): I have three questions. The first is about trailing edge conditions. I'm curious to know what the author believes would happen if, in our reiteration, the stagnation point of the trailing edge was set right at the trailing edge to zero velocity and the iteration continued with that fact reinserted in each iteration. The other questions are (1) What is meant by the term "cycle" for fully converged solution in your report? Is the word "cycle" meant to be "iteration number"? and (2) What is the total number of mesh points allowed by the program at present?

H. YEH (University of Pennsylvania): You refer to the need for an estimate by the computer for the velocities near the inlet and the trailing edge in order to have the prerequisite velocity at plus and minus infinity. Now, isn't this due to the fact that they really cannot completely describe

the velocities anyway because you must have prerequisite separation for the whole profile to fulfill your inlet and exit conditions at infinity. Furthermore, there is a condition for which you get a closed profile. In other words, the profile may not be closed; this is a so-called conditioned closure. Now, if you had to make use of these conditions beforehand, and if you had considerable freedom in adjusting the velocity distribution and did so, it seems to me that you would not really need a computer to make further adjustments.

J. W. DZIALLAS (General Electric Co.): Here are a few questions which should be of general interest.

(1)   If the flow is assumed everywhere subsonic, how can the field contain "supersonic patches"? If there are these patches, where are they located? Doesn't the authors' selection of the function $F(V)$ near the stagnation points strongly affect these supersonic patches?

(2)   Is the Kutta condition satisfied?

(3)   How close to the sonic velocity can the authors' method go on the profile surface? Does the solution become unstable?

(4)   What useful information can the authors extract from their hodograph?

(5)   Recalling the comparison with the experimental velocity distribution presented in a slide, I ask: How valid is this comparison since, through smoothing of the data, adjustments on the function $F(V)$, and variable grid size it seems possible to arrive at predetermined results. How many trials are necessary to recover the profile?

(6)   It would be interesting to see a comparison with an exact direct-method airfoil computation.

P. N. R. SHEKHAR (University of Liverpool, England): At Liverpool University, we have been concerned with the problem of designing airfoils in two-dimensional cascades. Hence, we would like to raise the following points:

(1)   Equation (17) is valid only for special cases of γ. According to reference D–8, the deflection condition for any γ is (fig. 2)

$$\int (\log q \, d\phi + \theta/\rho \, d\psi) - \int_{\psi=0}^{\pi/2} \int_{\phi=-\infty}^{+\infty} \theta[\partial(1/\rho)/\partial\phi]d\phi \, d\psi = 0$$

This equation can only be solved iteratively. The final solution is consistent with the Price-Martensen theory (ref. D–9).

(2)   In the main paper, the problem is considered as well posed in the (ϕ',ψ')-plane. However, the problem can be well posed in the (ϕ,ψ)-plane itself by Green's function of the second kind as demonstrated in reference D–8. Hence, one wonders if it is not advantageous to work in the (ϕ,ψ)-plane itself?

(3)   Once the boundary conditions are formulated, the problem can be treated as a typical boundary-value problem. The methods available include (i) Green's function, (ii) finite difference scheme, and (iii) variational finite element. Even Stocker's method (ref. 2) could be used advantageously. However, in reference D–8, it is used to get the following matrix:

$$[A][q]=[f]$$

where A is a codiagonal block matrix with submatrices that are also codiagonal. No equation contains more than five nonzero elements and only the nonzero elements are stored; hence, the storage requirement is minimized. This method is attractive compared to the marching procedure for two reasons, at least.

(a)   The distribution of $\log q$ is found at all the interior points of the rectangle in one go.

(b)   The boundary conditions are consistent with the interior solution, whereas in marching procedures this is not so. In our opinion, once the boundary conditions are known, it really does not matter which method is adopted for determining $\log q$ inside the rectangle. We are sure Stocker's method could also be adopted very effectively.

(4)   At stagnation points, $\log q$ has logarithmic infinity and θ is multivalued. According to L. C. Woods, the movement of the front stagnation points by $\frac{1}{1000}$ of chord distance affects the velocity peak by more than 10 percent for isolated airfoils (let alone cascades). What is really important is not so much the presence of the stagnation points as the effect it might have on the rest of the solution. It is probably true that Woods' method needs a very refined mesh. However, Payne has proposed a very attractive method for determining the effect of stagnation points on the rest of the solution by integral equation techniques. A detailed analysis is available in references D–8 and D–1. We find it very difficult to accept the concept that the solution achieved by ignoring four stagnation points is satisfactory. One could even say that the classic channel model proposed by Stanitz is satisfactory for cascades. Stanitz has produced some very realistic profiles in NACA 1116.

(5)   Last, we would like to examine the following two problems:

(a)   Inconsistency with the Price-Martensen theory

(b)   The simplicity of Green's function solution.

The Price-Martensen theory has been used extensively and, to a great extent, satisfactorily. However, we understand from Silvester-Fitch that Smith's solution is consistent with the design problem. Presumably this means that the stagnation points, shape of the stagnation, and other streamlines tie up completely. Hence, it should be pointed out that with the help of design and Smith problem, and treated on an iterative basis, it should be possible to produce a one-to-one correspondence and a closed

profile. The simplicity of Green's function solution can be illustrated very simply by taking the incompressible or linearized flows. The profile shape depends completely on the boundary conditions and it is immaterial what is happening inside the boundary. In the method reported, it is necessary to know what is happening not only on the boundary but inside the boundary as well. The difference between the incompressible and compressible flow lies in the presence of a double integral term and some minor points.

SILVESTER AND FITCH (authors): The authors agree with Dr. Payne about the desirability of being able to design blades to prescribed surface velocity distributions. We believe that both the direct and indirect approaches can be useful to the blade designer and it was for this reason alone that we developed an indirect method alongside our existing direct method based on the work of Martensen and Price.

We have found that the Martensen-Price method converges well for subsonic flow and that convergence can be obtained, although somewhat more slowly, for flows containing supersonic patches, provided these are not too large. We have also been looking at matrix methods for the direct problem because we believe that they can be made faster than singularity methods. We also believe, but have not shown, that the immediate introduction of density change terms into the equations will improve the stability and rate of convergence.

Concerning details of the calculation, we agree with Dr. Payne that we could have worked on a skew mesh in the (ϕ,ψ)-plane. With the method adopted, the algebra is more tedious, but this is compensated for by the fact that the approximation of partial derivatives by finite differences with small truncation error and using only the lines, $i-1$, i, $i+1$ is easier in the (ϕ',ψ')-plane.

We do not commence the calculation by assuming $H = F$. Referring to figure 3, we assume velocities of V_u on AB and JH, V_d on CD and GF, and the prescribed velocities on BC and HG. The velocity elsewhere is assumed to vary linearly with ψ' at constant ϕ'.

In response to the comments of Meyerhoff and Yeh, it is certainly true that for given values of V and θ, far upstream and downstream, not every velocity distribution that the designer may prescribe will give a closed, nonintersecting curve for his blade profile, but only those velocity distributions which satisfy the so-called closure conditions. It is also true that although we have tacitly assumed a closed profile when deriving the equations, we have not placed any restrictions on the velocity distributions that may be prescribed and so may not obtain sensible blade shapes for every velocity distribution. When we use this program, we assume that the designer is able to specify a velocity distribution which nearly satisfies the closure condition and which will require only slight modification within

the program. In practice, we use the program in conjunction with a direct method, so this is usually true. We justify this approach with two arguments. First, when designing a cooled turbine blade, there are factors other than aerodynamic (stressing and cooling considerations) which place restrictions on an acceptable blade geometry. In order to satisfy all these conditions, it is likely that the designer will require three or more runs of the program to achieve a satisfactory blade, modifying his velocity distribution with each successive run. Since the program prints out the modifications to the velocity distributions that it makes internally and these can be fed into the next run, after the first one or two runs, little if any internal modification is required. Second, we know of no method of determining velocity distributions for compressible flow satisfying the closure condition which would involve the designer in any less work than the method we use.

The choice of nonzero velocities at the stagnation points is a necessity since it is impossible to evaluate F or H for zero velocity.

If arbitrary, nonzero values are used and reinserted each cycle, a converged solution may or may not be found. If convergence is obtained, then it will be found that, although the velocity attains the values V_u and V_d far upstream and downstream, $\partial V / \partial \phi$ is not zero there. In addition, integration of $\partial \theta / \partial \phi$ between far upstream and far downstream will not result in the prescribed turning, $\theta_d - \theta_u$. The authors regard the finding of velocities at the stagnation points as a process of finding the shape and direction of cusps which must be added to the rounded profile in order to support the prescribed velocity on the remainder of the profile.

In the paper, the words "cycle" and "iteration" have both been used to denote the process of solving numerically equation (24) for fixed estimates of the coefficients A, B, C, and D at every point and of the velocities of the stagnation points.

The program allows up to 50 points upstream and downstream of the blade, 40 points on each surface of the blade, and 11 points across the blade passage. Best results have been obtained by using a mesh of variable spacing in both the ϕ' and ψ' directions, having points closer together near the blade surfaces and particularly so near the leading and trailing edges.

As to the remarks of Dziallas, it must be made clear that the indirect method described here is intended for use as a design tool in which blade shapes are determined from velocity distributions prescribed by the designer. Although we have tested the program by using it as a direct method (that is, by trying to recover blade shapes from measured velocity distributions) this is not the mode in which it was intended the program should be used. The method described here is not intended as an alternative to the direct methods but as an additional aid to the blade designer. With this intended use of the program in mind, such questions as, "How many trials are necessary to recover a profile?" are not strictly applicable.

Taking the last two questions first, the program has been tested by recovering blade shapes both from measured velocity distributions and from distributions calculated by the singularity method of Martensen and Price, the matrix method of D. J. Smith, and the author's own matrix method, which is still under development. (The method of Katsanis was not available to the authors.) It was found that, for a given blade, the three direct methods gave velocity distributions which differed by small but significant amounts, so that each produced a slightly different blade with the indirect program. Best agreement was with the authors' own direct method. Because of the inconclusive nature of these tests and because it is a more valid test of a program to a designer, most testing of the program has been with measured velocity distributions. In those cases where the tests were two-dimensional and shock-free, blade shapes could be recovered well with velocity distributions close to those measured. There is some freedom in choosing F near the leading and trailing edges because pressure tappings are rarely close enough to give an adequate picture there. Such a test of the program is a useful one, provided one remains close to the measured results (which may include small experimental errors). It simply is not true that one can arrive at predetermined results. Blade shapes are independent of the mesh size, provided it is fine enough.

Although the numerical methods used can be justified only for elliptic equations and hence subsonic flows, even so we can and sometimes do prescribe velocity distributions with supersonic regions. If converged answers are obtained, these must necessarily contain supersonic patches adjacent to the regions of the blade when supersonic velocities have been specified. It can be assumed that in these supersonic regions, small errors due to round-off increase the more distant a mesh point is from the boundary where the velocity is specified. If the patches are small, the errors may not have a chance to grow too large, so it seems possible that sensible answers may be obtained. There is, however, no provision in the program for discontinuous solutions as would be caused by shocks.

The program effectively selects F near stagnation points. We still have some further work to do on this, but we have found that it is more difficult to converge on velocities at the stagnation points when supersonic patches have been prescribed.

As for the Kutta condition, remember that we produce cusped blades. The velocities on the cusps (that is, the velocities which are chosen to satisfy upstream and downstream boundary conditions) are chosen to be equal on both pressure and suction surfaces. In addition, we usually prescribe velocity distributions which become equal on both surfaces close to the leading and trailing edges. This treatment is something like a Kutta condition, although we do not talk specifically in terms of zero velocity.

We have not looked seriously at solutions in the hodograph plane.

In reply to Mr. Shekhar, if the function F is defined by equation (8), then equation (17) is true for all values of γ and for all Mach numbers. Closed analytic forms for F can be found for rational values of γ, and the values of $\frac{7}{5}$ and $\frac{4}{3}$ given by the authors should be quite sufficient for all practical purposes. The error involved in using $\gamma = 4/3$ for the design of a hot turbine blade will be negligible compared with the errors introduced by other assumptions in the mathematical model such as, for example, isentropic inviscid flow. If this is accepted, then it is certainly more convenient and almost certainly more accurate to solve the potential and deflection conditions explicitly by simple numerical integration of the prescribed velocity distribution than iteratively by methods requiring the numerical evaluation of double integrals over the whole flow field with each compressibility cycle. Also, it is worth mentioning that the deflection condition, as we have formulated it, depends only on the boundary conditions. This is useful in two ways. First, it enables the surface lengths to be calculated without any knowledge of the flow field elsewhere and so allows the possibility of abandoning the program before any major computation has been performed if the prescribed velocity leads to unrealistic surface lengths. Second, it allows a check of the accuracy of the solution of equation (24) for fixed boundary conditions, because when the coordinates (x, y) of the blade are eventually found from the solution of (24), the lengths can be calculated and compared against those calculated from the potential and deflection conditions. We have found that for fully converged answers, the lengths calculated by the two methods agree to within less than 0.2 percent.

The relative advantages of the (ϕ, ψ) and (ϕ', ψ') planes have been given in the reply to Dr. Payne.

With reference to question (3), it seems as though Mr. Shekhar believes that the method used by the authors is a marching procedure and one in which, in some way, the solution is inconsistent with the boundary conditions. We do not use a marching procedure; the solution obtained depends at every point upon all the boundary conditions and is completely consistent with them. Moreover, the solution is obtained "all in one go" just as much as in his own method, for (using Mr. Shekhar's own notation), Stocker's method is simply a method of solving the matrix equation

$$[A][q] = [f]$$

Concerning question (4), again, it is not true to say that the authors have neglected the stagnation points. There is a striking similarity between the method used by the authors and the treatment described by Payne as a relaxed treatment. Referring to figure 3, Payne's method consists of the following steps:

(1) Choose nonzero velocity at the stagnation points.

(2) Set the velocity at V_u along AK_1 and JK_2 and V_d on K_4F and K_3D.

(3) Apply the cyclic or repeat conditions to the segments K_2H, K_1B, GK_4 and CK_3.

(4) Set up a variable, but one-parameter, mesh spacing.

(5) Solve as though there were no singularities.

Payne points out that if a solution is now obtained, ignoring the singularities and with an arbitrary mesh parameter, the points B and H, for example, will not be one blade pitch apart in the physical plane—but for a particular choice of the mesh parameter, this can be achieved. Notice that by making the assumptions (2), Payne is, in fact, forcing $\partial V/\partial\phi=0$ far upstream and downstream but, at the same time, relaxing the repeat conditions on θ over the segments on which V is prescribed. Relaxing these conditions permits the streamlines JH and AB to be of different shape when they should be identical, but the error is reduced by forcing B and H to be nearly one pitch apart.

This approach is very similar to that of the authors. We apply the repeat conditions on both V and θ over the whole length of the dividing streamlines, so that the streamlines corresponding to AB and JH, for example, are identical in shape. It then follows that because A and J are one pitch apart in the physical plane, B and H must be. If we were to follow Payne and choose fixed velocities at the stagnation points, then we would have to choose a mesh spacing to make $\partial V/\partial\phi=0$ far upstream and downstream. Instead, we keep the mesh spacing fixed and vary the velocity at the stagnation points. The mesh spacing and the chosen velocity are to some extent interchangeable, for both affect the calculated values of derivatives of V near the leading and trailing edges. Payne also justifies the use of such approximate methods of dealing with stagnation points.

As already stated in reply to Mr. Dzillias, the authors do not obtain complete agreement with any direct method, just as none of the direct methods is in complete agreement with any other. The differences are small, but some further work is needed.

Finally, I would agree that where the equations of motion can be reduced to Laplace's equation (that is, for two-dimensional incompressible flows or flows of sufficiently low Mach number that one could reasonably assume $H=F$) an integral method is probably to be preferred to a differential equation approach. Most practical cases, however, cannot be described adequately by Laplace's equation, either because the Mach number level is too high or because it is necessary to take into account effects such as stream-tube thickness variation or the fact that a turbine blade row does not form a linear two-dimensional cascade. (These effects have yet to be incorporated in the authors' program.) Therefore, in most

practical cases, it is necessary to compute the fluid velocity everywhere (not only on the boundaries), whichever method is used. In such cases, it is debatable whether integral methods are to be preferred to differential methods. It should be pointed out that the double integral to which Mr. Shekhar refers is not simply a minor term in integral methods; apart from increasing the amount of computation to be done (compared with incompressible flow) it does express the difference between incompressible and compressible flow and this can be quite marked when Mach number levels are high. Further, if the other effects referred to were included, the double integral term would express the difference between plane incompressible flow and compressible flow with stream-tube thickness variation and in an annular cascade.

REFERENCES

D–1. PAYNE, D., *Contributions to the Theoretical Aerodynamics of Turbomachinery Blade Rows.* Ph.D. dissertation, London U., 1969.

D–2. PAYNE, D., *Axial Turbine Blading.* Symposium on Gas Turbine Blading Design, Borough Polytechnic, London, March 1970.

D–3. PAYNE, D., *Isolated and Cascade Aerofoils.* Master's thesis, London U., 1964.

D–4. PRICE, D., *Two-Dimensional Compressible Potential Flow Around Profiles in Cascade.* G.T.C.C. Aero Subcommittee Report 547, 1965.

D–5. MARTENSEN, E., *Calculation of Pressure Distribution Over Profiles in Cascade in Two-Dimensional Potential Flow by Means of a Fredholm Integral Equation.* Archive for Rat. Mech. & Anal., Vol. 3, No. 3, 1959, pp. 235–270.

D–6. MURUGESAN, K., AND J. W. RAILLY, Pure Design Method for Aerofoils in Cascade. *J. Mech. Eng. Sci.* Vol. II, No. 5, 1969, p. 454.

D–7. SMITH, D. J. L., *Computer Solutions of Wu's Equations for the Compressible Flow Through Turbomachines.* First paper of this session.

D–8. SHEKHAR, P. N. R., AND J. F. NORBURY, *Design of Aerofoils in Two-Dimensional Cascades to Support Compressible PVD.* To be published; now available as ULME report, 1969.

D–9. PRICE, D. W., Two-Dimensional Compressible Flow Around Profiles in Cascade. *Proc. Seminar on Advanced Problems in Turbomachinery,* Part I, March 29–30, 1965.

A Note on the Influence of Axial Velocity Ratio on Cascade Performance[1]

M. B. Wilson

California Institute of Technology

R. Mani

University of Massachusetts

A. J. Acosta

California Institute of Technology

A thin airfoil quasi-two-dimensional potential flow theory has been used to analyze cascades with axial-flow contraction. Attention is centered on the flow turning of a lattice of foils as measured by the deviation angle. The influence of both axial-flow acceleration and foil thickness on the deviation angle is summarized in plots that should be useful for design purposes. It is shown that the effect of axial-flow contraction is larger when the foils are relatively far apart than when they are close together. The influence of axial velocity ratio across the cascade changes markedly with the stagger angle. These effects are essentially unaltered due to foil thickness.

Design of axial-flow compressors and fans relies heavily on experimental data and simplified empirical rules (see, for example, ref. 1). Concurrent with experimental research, there have been strong advances in theoretical two-dimensional potential flow solutions of cascades (e.g., ref. 2). Within the limitation of assumed two-dimensionality, these theoretical solutions should be very useful in the interpretation and correlation of test data for

---

[1] All graphs, tables, equations and conclusions presented in this revised paper have been corrected from the earlier version presented at the symposium. The work providing the basis for this paper was carried out under Department of the Navy Contract Nonr 220(59).

design purposes. In an actual turbomachine design, of course, there is always a three-dimensional character to the flow, and one of the interesting consequences of this complication is that there is a change in the axial-flow velocity through the cascade. Recent theoretical calculations by Mani (ref. 3) contribute to the possibility of more rationally predicting the potential flow performance of a lattice of airfoils under conditions of a varying axial velocity. A survey of Mani's work appears in reference 4; reference 5 describes the computer techniques used in obtaining numerical results.

The purpose of this note is to outline some further results of computations using Quasi-two-dimensional theory (QTD) and to present these numerical data in the form of graphs and tables useful for design. Primary emphasis is placed on the influence of axial velocity ratio (AVR = Va_2/Va_1) on cascade performance although, as will be seen later, wide ranges of most of the other cascade variables have been considered. In addition, we include some comparisons between existing theoretical results for two-dimensional cascade flows and the present results. The curves presented in the main body of this note are supplemented by the tables of data given in the appendix.

THE QUASI-TWO-DIMENSIONAL CASCADE

The problem under consideration is that of the irrotational incompressible flow through an infinite cascade of airfoils spanning a channel whose width $h(x_1)$ changes slightly along the extent of the blade (figs. 1 and 2). Because $h(x_1)$ is a slowly varying function of x_1 only, the flow is very nearly two-dimensional (hence the term "quasi-two-dimensional"). In the study of plane cascades, the basic flow disturbed by the airfoils is represented by the vector mean V_m of the inlet and outlet flow velocities. In the case of varying axial velocity, for reasons explained in the discussion of this paper, if Va_1 and Va_2 denote the axial velocities at the cascade leading and trailing edges and Vt_1 and Vt_2 the corresponding tangential velocities, the mean velocity representing the basic flow through the cascade (fig. 3) has an axial component $\frac{1}{2}(Va_1+Va_2)$ and a tangential component $V_{t_2}+\frac{1}{2}\Delta V_t(1+\alpha/2E)$, where $\Delta V_t = V_{t_1} - V_{t_2}$ and α and E are contraction parameters shown later in figure 4.

Cascade and Flow Parameters

Performance of a cascade system is usually represented by the amount of flow turning exerted by any one blade $\Delta\beta = \beta_1 - \beta_2$ as a function of all the remaining cascade and flow parameters. To some extent, performance is also indicated by the resulting circulation Γ about an airfoil. In strictly
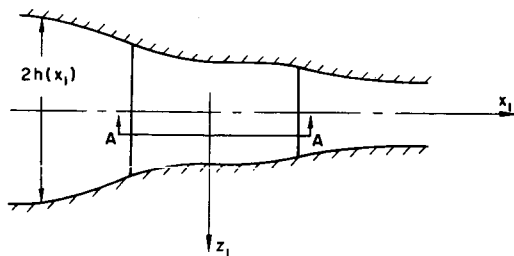
FIGURE 1.—*Schematic of flow through an infinite cascade of airfoils spanning a channel of varying width. Total circulation Γ_t is measured positive counterclockwise (eq. (19)). In plane flow the foil nondimensional lift coefficient is* $C_L = -\Gamma_t = \Gamma$.
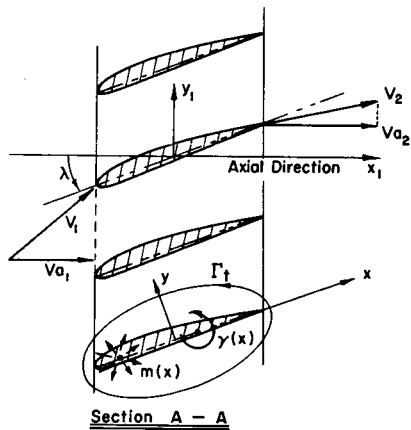
plane flow, the circulation is a direct measure of the lift exerted on the blade.

Figure 2 defines the various parameters of cascade and flow geometry. The notation adopted here differs slightly from that used by Mani in references 3, 4, and 5; it coincides more with Lieblein (ref. 1) and Mellor (ref. 2). In figure 2 all angles are indicated in their positive sense.

The inlet and outlet flow angles are

$$\left.\begin{aligned} \beta_1 &= \lambda + \frac{\theta_1}{2} + i \\[2em] \beta_2 &= \lambda - \frac{\theta_2}{2} + \delta^* \end{aligned}\right\} \tag{1}$$

and the angle $\Delta\beta$ through which the flow is turned is

$$\Delta\beta = \tfrac{1}{2}(\theta_1 + \theta_2) + i - \delta^* \tag{2}$$

In the work to follow, the camber line is symmetric so that $\theta_1 = \theta_2$.
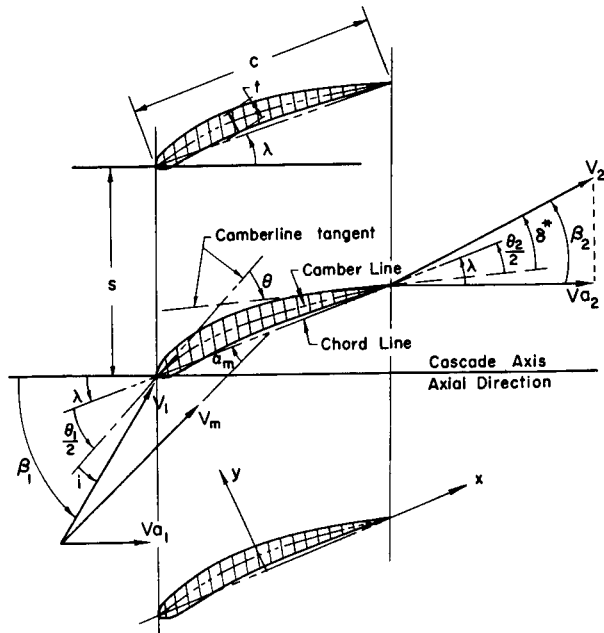
FIGURE 2.—*Definition sketch for the cascade and flow parameters.*

Basic Equations

The quasi-two-dimensional (QTD) flow analysis is modeled after the approach and method of solution for plane flow cascades described in reference 2. There are several notable features of this theory that can be briefly mentioned here. The principal feature is that the governing equation of the strictly three-dimensional flow is reduced to a two-dimensional equation. This simplification can be made only because it is assumed that the channel width $h(x_1)$ is a slowly varying function. Beyond this, for simplicity, a channel contraction shape is adopted which minimizes the requisite calculations yet retains the essential features of the problem. In the present work there is the additional (but not essential) simplification that the thin airfoil approximations can be used. These same approximations have, in fact, been used before for plane cascade flow analysis with good effect (ref. 2) and are believed to be equally useful in the present case.

The key notion in this work is that all relevant quantities can be averaged over the channel height and that any errors that result are much smaller than the effect being sought. This idea is well known, as is indicated in reference 4, and rough estimates of the error involved can even be made (ref. 3). The flow is assumed to be an incompressible, potential
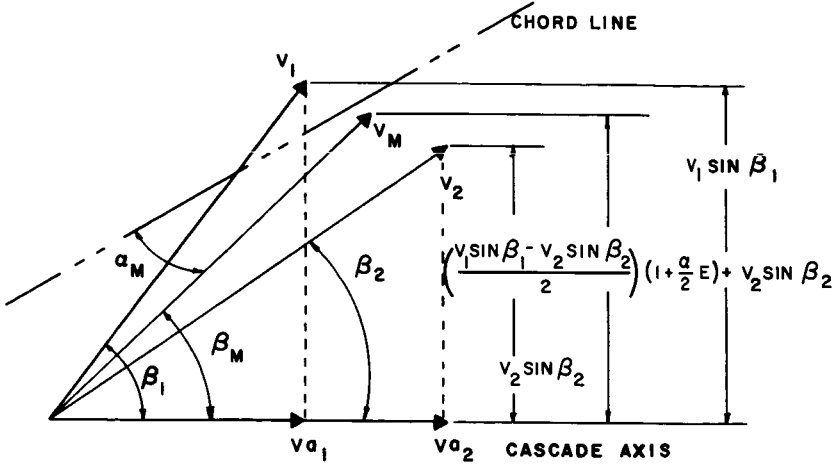
FIGURE 3.—*Velocity vector diagram.*

flow. There will be, accordingly, a velocity potential $\varphi(x,y,z)$ having velocity components $u(x,y,z) = \partial\varphi/\partial x$, etc. We define the following averages

$$\left.\begin{array}{l} \bar{\varphi}(x_1,y_1) = \dfrac{1}{h(x_1)} \displaystyle\int_0^h \varphi(x_1,y_1,z_1)\ dz_1 \\[3em] \bar{u}(x_1,y_1) = \dfrac{1}{h(x_1)} \displaystyle\int_0^h u(x_1,y_1,z_1)\ dz_1, \text{ etc.} \end{array}\right\} \tag{3}$$

It may then be shown (ref. 4) that

$$\left.\begin{array}{l} \bar{u} = \dfrac{\partial\bar{\varphi}}{\partial x_1} \\[2em] \bar{v} = \dfrac{\partial\bar{\varphi}}{\partial y_1} \end{array}\right\} \tag{4}$$

and that a quasi-two-dimensional stream function $\bar{\psi}(x_1,y_1)$ can be defined by

$$h\bar{u} = \frac{\partial\bar{\psi}}{\partial y_1}$$

$$-h\bar{v} = \frac{\partial\bar{\psi}}{\partial x_1}$$

In terms of the averaged flow quantities, the full three-dimensional flow field equations become

$$
\Delta\bar{\varphi}+\frac{h'(x_1)}{h(x_1)}\frac{\partial\bar{\varphi}}{\partial x_1}=0
$$

$$
\Delta\bar{\psi}-\frac{h'(x_1)}{h(x_1)}\frac{\partial\bar{\psi}}{\partial x_1}=0
$$

$$\tag{5}$$

where $h'(x_1)\equiv dh/dx_1$. Fundamental solutions of these equations corresponding to source and vortex flows are clearly dependent on the channel shape through the function $h'(x_1)/h(x_1)$. The principal feature of the quasi-two-dimensional flow theory developed in reference 3 is that it takes explicit account of the fact that the velocity fields of sources and vortices should be calculated on the basis that these singularities themselves are modified by the lack of two-dimensionality.

Even from the equations quoted above for the average potential $\bar{\varphi}$ and stream function $\bar{\psi}$, it is clear that a good choice for the channel shape $h(x_1)$ is one for which the function $h'(x_1)/h(x_1)$ is as simple as possible. For this ratio equal to a constant, $-\alpha$ (a contraction), the result is an exponential channel shape $h(x_1)=h_0\exp(-\alpha x_1)$. A more realistic choice is one which gives a contraction effect and also constant stream velocities far upstream and far downstream. For purposes of the calculations in this report, a channel shape is chosen with a central contraction

$$
\frac{h'(x_1)}{h(x_1)}=-\alpha[H_0(x_1+a)-H_0(x_1-a)]
\tag{6}
$$

where $H_0(x_1)$ is the Heaviside unit step function. This channel is sketched in figure 4a and can be conveniently termed a finite exponential channel.

Calculations of the fundamental source-like and vortex-like singularities of equation (5), even for the case of a finite exponential channel, are very complicated. It is only for the case of small contraction parameter α that the velocity components used for these computations can be approximated to the first order in α; i.e., that the x_1-component of a unit vortex in axially accelerated flow can be expressed in the form

$$
u_{\text{vortex}}=-\frac{1}{2\pi}\frac{y_1}{(x_1{}^2+y_1{}^2)}+\alpha u_{v_1}
\tag{7}
$$

where u_{v_1} is a correction term for the non-two-dimensional character of the flow. Details of the calculations of all the necessary velocity components are contained in reference 3 and are summarized in reference 4. They all have the same form as equation (7), where the resulting formulas

are linear in α. This points to a feature of the final results of the computations described in this note: they can be extended by linear extrapolation to any arbitrary but small α.

The problem is nondimensionalized by putting the chord length $c=2$. The extent of the contraction ($2a$ in fig. 4a) is denoted by E. In the computer computations it is necessary to keep the ratio $E/2 \cos \lambda > 1.0$. Figure 4b indicates the nondimensional channel geometry in the $x_1 - z_1$ plane.

The axial velocity ratio is computed using the axial velocity components Va_1 and Va_2, measured at the leading edge and trailing edge, respectively. From the continuity equation, we have

$$AVR = \frac{Va_2}{Va_1} = \frac{h_0 e^{\alpha \cos \lambda}}{h_0 e^{-\alpha \cos \lambda}} = e^{2\alpha \cos \lambda} \tag{8}$$
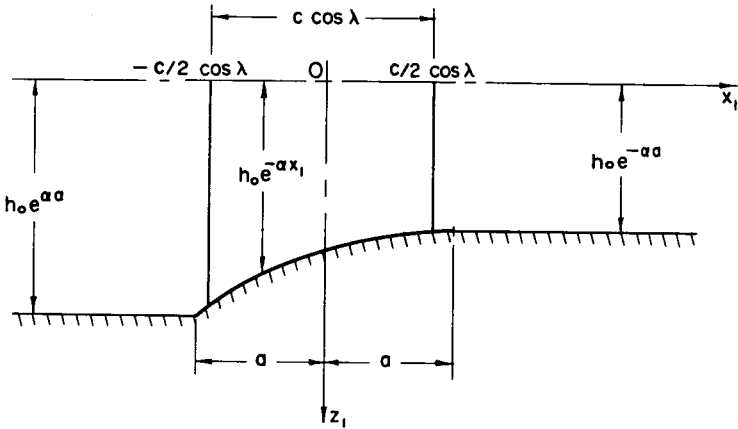
FIGURE 4a.—*Channel shape for a central contraction.*
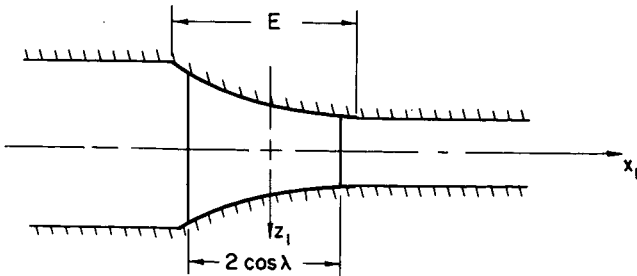
FIGURE 4b.—*Nondimensional contracting flow problem, with a finite length exponential channel and airfoils of chord length* c = 2.

Hence, for the special geometry chosen, the contraction parameter α is related to the axial velocity ratio by the formula

$$\alpha = \frac{1}{2 \cos \lambda} \ln (AVR) \tag{9}$$

Airfoil Sections

The principal geometrical features of any airfoil section are the camber line function $y_c(x)$ and the thickness distribution $y_{th}(x)$.

From figure 2 we see that the camber angle θ is a convenient index for describing the camber line. This is especially true of a symmetrically cambered foil for which $\theta/2$ measured at the leading edge is identical with $\theta/2$ measured at the trailing edge. Now, for design purposes it is often useful to be able to prescribe the section lift coefficient C_b of an isolated airfoil in terms of the camber angle. Two simple camber line functions are of special practical interest: the parabolic arc and the circular arc. They are shown schematically in figure 5, indicating how the camber angle θ is measured for each one. From thin airfoil theory, the section lift coefficient due to camber for the *parabolic* arc is (ref. 6)

$$C_b = \pi \tan \frac{\theta}{2} \doteq \pi \frac{\theta}{2} \left(1 + \frac{1}{12} \theta^2 + \cdots \right) \tag{10}$$

Using the Joukowski transformation, the section lift coefficient for a circular arc camber line at an angle of attack α^* is (ref. 6, p. 69)
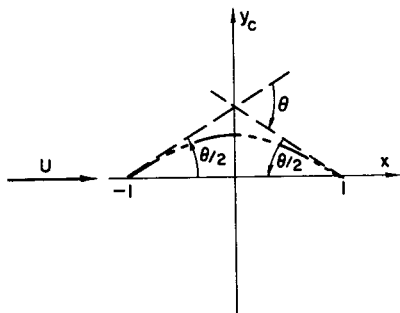
Parabolic Arc Camberline

$$\frac{dy_c}{dx} = A_1 x$$

where: $A_1 = -\frac{C_b}{\pi}$
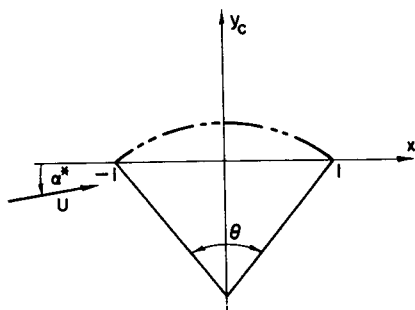
Circular Arc Camberline

$$\frac{dy_c}{dx} = -\frac{x}{\sqrt{\csc^2 \frac{\theta}{2} - x^2}}$$

where: $\theta = \theta(C_b)$

FIGURE 5.—*Parabolic and circular-arc camber lines.*

$$C_b = 2\pi \frac{\sin (\alpha^* + \theta/4)}{\cos \theta/4} \tag{11}$$

Putting $\alpha^* = 0$, the lift coefficient due to camber for a *circular* arc is

$$C_b = 2\pi \tan \frac{\theta}{4} \doteq \frac{\pi\theta}{2} \left(1 + \frac{1}{48} \theta^2 + \cdots \right) \tag{12}$$

Clearly, for reasonably small camber angles, θ, these lift coefficients are nearly the same.

It is convenient to prescribe the camber-line slope in terms of a polynomial

$$\frac{dy_c}{dx} = A_0 + A_1 x + A_2 x^2 \tag{13}$$

The present calculations use a parabolic symmetric camber line with $C_b(\theta)$ from equation (10), so that in equation (13)

$$\left.\begin{array}{l} A_0 = A_2 = 0 \\[1.5em] A_1 = -\dfrac{C_b}{\pi} \end{array}\right\} \tag{14}$$

and

$$\theta = 2 \tan^{-1} \frac{C_b}{\pi} \qquad \text{(parabolic arc)} \tag{15}$$

A circular arc camber line could be only *approximately* represented by equation (13). The camber angle θ, given C_b, is determined from

$$\theta = 4 \tan^{-1} \frac{C_b}{2\pi} \qquad \text{(circular arc)} \tag{16}$$

The present computations were performed using a thickness distribution $y_{th}(x)$ of a symmetrical Joukowski airfoil. The thickness slope is

$$\frac{dy_{th}}{dx} = (0.77) \frac{t}{c} \left(\tan \frac{\varphi}{2} - 2 \sin \varphi \right) \tag{17}$$

where $x = \cos \varphi$.

One of the direct results of the QTD analysis is the determination of the coefficients in the thin airfoil vorticity series

$$\gamma(x) = a_0 \tan \frac{\varphi}{2} + \sum_{n=1}^{N} a_n \sin (n\varphi) \tag{18}$$

For purposes of the calculations, the number of terms N in this series was limited to 5. This is used throughout. However, a higher number of terms might be better, especially for the larger values of the stagger angle λ and for the larger solidities σ.

The total circulation (measured positive counterclockwise; see fig. 1b) for both the two-dimensional and three-dimensional calculations is given by

$$\Gamma_t = \pi \left(a_0 + \frac{a_1}{2} \right) \tag{19}$$

For the two-dimensional cascades, a lift coefficient can be calculated directly from the circulation. Correcting for the sign of Γ_t from equation (19), the lift per unit span is

$$L = -\rho V_m \Gamma_t$$

Then

$$C_L = \frac{L}{\frac{1}{2}\rho V_m^2 c} = -\frac{\Gamma_t}{\frac{1}{2} V_m c}$$

This is nondimensionalized using $c = 2$ and $V_m = 1$. Hence the lift coefficient for an airfoil in the two-dimensional cascade system is

$$C_L = -\Gamma_t \tag{20}$$

Values Used in Present Computations

The results presented in this note have been calculated for a range of stagger angles and solidities with a thickness ratio of 0 and 0.1 and for mean angles of attack of 0 and 0.1 radians. The camber parameter C_b was taken to be unity and the contraction parameter α was taken to be 0 (two-dimensional) and 0.1. The extent of the contraction was always 1.1 times the axial projection of the blade. It was found sufficient to use five terms in the vorticity series. The resulting calculations required a 15-second execution time (per each solidity and stagger angle combination) for the two-dimensional case and 48 seconds for the quasi-three-dimensional case on the IBM 7094 computer.

RESULTS: EFFECT OF FLOW ACCELERATION ON FLOW TURNING

In this section, the main results of this note are presented in the form of nondimensional plots of the deviation angle. As mentioned previously, the calculations were performed assuming parabolically cambered airfoils with a prescribed section lift coefficient C_b. Computations illustrating the

effect of foil thickness (t/c) are presented only for $\sigma = 1$, using the symmetrical Joukowski thickness distribution discussed earlier.

Throughout the ensuing discussion the term "flow turning" will refer to the change in the flow angle $\Delta\beta = (\theta+i) - \delta^*$. This conforms to the usual convention and is the one adopted in references 3, 4, and 5. Comparisons made between two- and three-dimensional flows assume a given inlet condition; so the incidence angle i can be thought of as constant at a given λ and σ. Hence it is actually $(-\delta^*)$ that measures changes in $\Delta\beta$.

Flow turning through a cascade with accelerating flow is influenced by two factors: the magnitude of the circulation Γ_{3D} about the blades and the increase in axial velocity. It has been pointed out (refs. 3 and 4) that the reduced circulation caused by axial-flow acceleration weakens the ability of the cascade to turn the flow, but the speed-up in axial velocity tends to make the flow more axial, and hence acts to increase the flow turning in compressor cascades. The final balance between these effects is complicated and appears to involve all the parameters of the cascade and flow geometry.

Zero Thickness Cascade Blades

Flow turning represented in terms of the nondimensional deviation angle δ^*/θ can be described as a function of the stagger angle λ, the solidity σ, the particular choice of camber-line function $y_c(x)$, and the inlet flow conditions represented by β_1 (or, better, by the incidence angle i).

Figures 6 and 7 are graphs of the change in δ^*/θ due to accelerated flow divided by the quantity (AVR-1), plotted two different ways for convenient use. An important feature of these graphs is that the values of δ^*/θ appearing in the quantity $\Delta[\delta^*/\theta] = (\delta^*/\theta)(2D) - (\delta^*/\theta)(3D)$ have values of two-dimensional minimum loss incidence from Lieblein (ref. 1, Chapter VI). This was accomplished by first establishing the minimum-loss-incidence angles from figure 138 of Lieblein's report. For each of the eight stagger angles λ (see the section on the quasi-two-dimensional cascade) and the prescribed camber angle $\theta = 35.314°$, the appropriate incidence angle i appearing in $\beta_1 = \lambda + \theta/2 + i$ was determined by interpolation. The incidence angles found in this manner are referred to as $i_{ml}^{(2D)}$. From the computer results, values of $(\delta^*/\theta)(2D)$ and $(\delta^*/\theta)(3D)$ are known at two different values of the mean angle of attack α_m (one block of calculations at $\alpha_m = 0$ and another at $\alpha_m = 0.1$). By assuming a straight-line variation of δ^*/θ between the two α_m values, the angles $i_{ml}^{(2D)}$ can be cross-plotted on the same graph to obtain $(\delta^*/\theta)(2D, i_{ml}^{(2D)})$ and $(\delta^*/\theta)(3D, i_{ml}^{(2D)})$ by interpolation. Note that this means that the plane flow δ^*/θ is compared with the accelerated flow δ^*/θ at the *same* inlet condition; namely, minimum loss incidence. From figures 6 and 7, it is clear that the effect of flow acceleration (AVR > 1) is larger when the
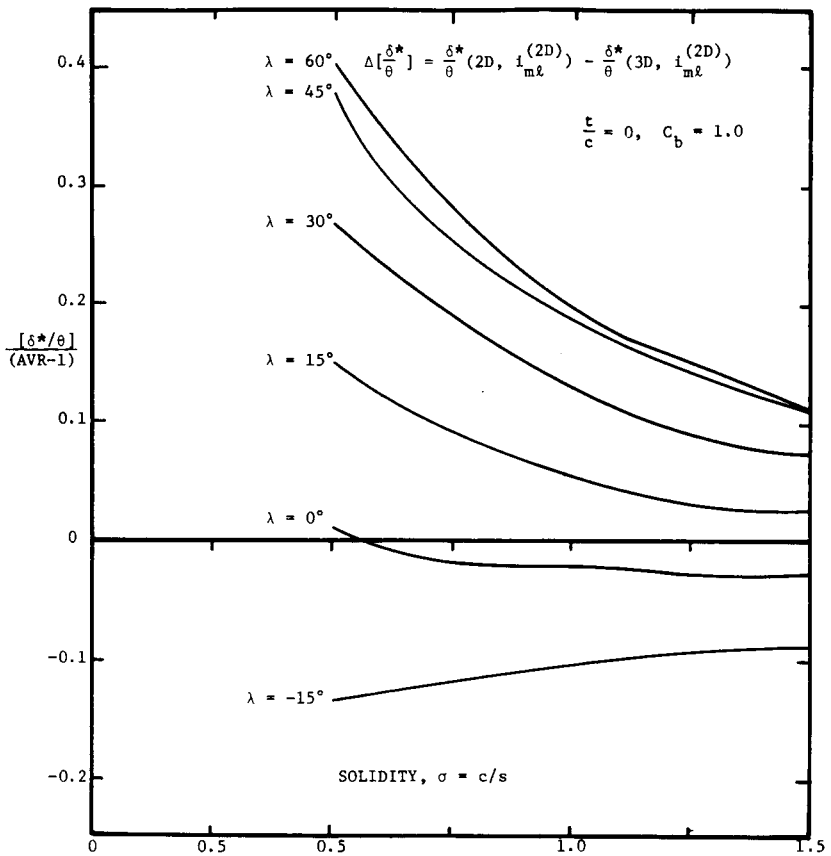
FIGURE 6. — *Effect of flow acceleration on the deviation angle ratio at minimum-loss incidence* $i_{ml}^{(2D)}$.

foils are relatively far apart ($\sigma \to 0$) and that the influence of flow acceleration is diminished as the foils are brought closer together (σ increases). The character of the change in δ^* due to AVR > 1 is also altered as λ increases; i.e., $\Delta[\delta^*/\theta]$ has a steeper curve for the higher λ values. It also changes sign for $\lambda < 0$ (compare the case of $\lambda = -15°$). In the case of $\lambda = 0°$, extremely small values of $\Delta[\delta^*/\theta]$ were obtained and, from a practical design point of view, it would be best to assume $\Delta[\delta^*/\theta] = 0$ for $\lambda = 0°$.

The mean angle of attack α_m is not a constant in figures 6 and 7, but varies with the appropriate minimum-loss-incidence angles $i_{ml}^{(2D)}$.

Several things should be kept in mind concerning the minimum-loss-incidence angles $i_{ml}^{(2D)}$: (1) they were determined experimentally by finding the minimum points on the curves of total pressure loss coefficient
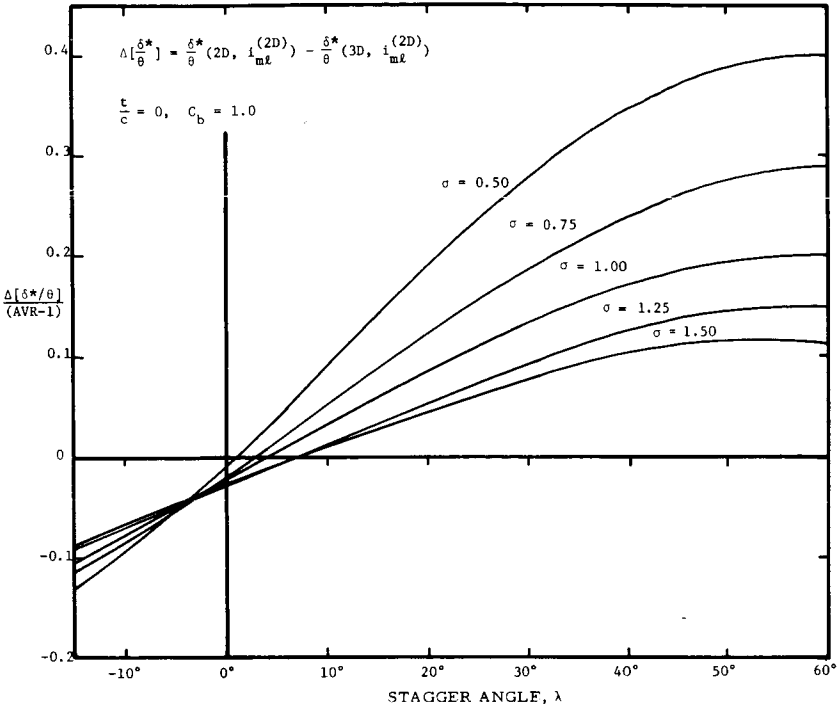
FIGURE 7.—*Effect of flow acceleration on the deviation angle ratio at minimum-loss incidence* $i_{ml}^{(2D)}$.

versus incidence angle i and (2) the experiments that formed the basis for figure 138 of Lieblein's work were performed with NACA 65–(A_{10})-series airfoils, and the results were referred to equivalent circular-arc camber lines.

The impact-free-entry operation of an airfoil is a useful reference condition in design. Large velocity peaks on either foil surface of zero thickness blades are avoided by locating the forward stagnation point exactly at the leading edge. This simple impact-free criterion is not applicable to nonzero-thickness blades with rounded leading edges, but it seems reasonable to apply it to zero-thickness airfoils in a cascade. This was first done by Weining in his approximate theory of a two-dimensional cascade of cambered airfoils (see ref. 1, Chapter VI). For thin airfoil theory, impact-free entry corresponds to arranging the inlet flow angle β_1 so that the coefficient a_0 equals zero in the vorticity series (eq. (18)). The incidence angle i leading to the condition $a_0=0$ can be referred to as an impact-free incidence, $i_{a_0}=0$. Values of this parameter for two-dimensional cases using the present theory were determined by interpolation. Figure 8 is a plot comparing the experimental values of
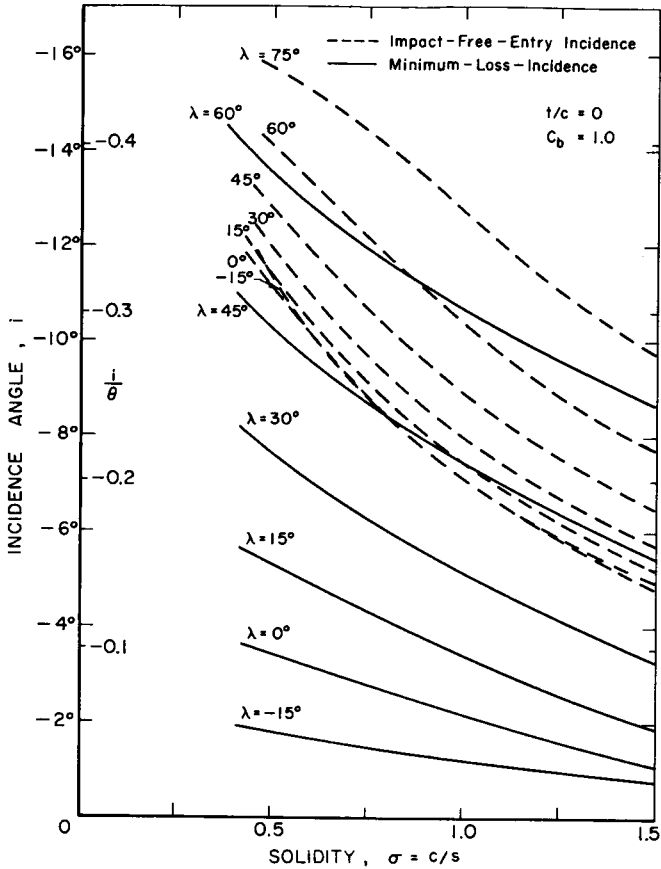
FIGURE 8.—*Comparison between experimental minimum-loss-incidence angles (Lieblein, ref. 1) and potential theory impact-free incidence.*

impact-free incidence $i_{a_0}{}^{(2D)} = 0$ using the QTD theory with $\alpha = 0$. Both are for zero-thickness airfoils. The two sets of curves are seen to agree only somewhat at high values of λ, and disagree completely for the lower and minus values of λ. It is for this reason that we chose inlet conditions corresponding to values of the experimental minimum-loss incidence $i_{ml}^{(2D)}$ in presenting the curves of $\Delta[\delta^*/\theta]$ in figures 6 and 7.

Mutual Influence of Thickness Ratio and Flow Acceleration

To study the effects of thickness, a limited number of computations were carried out for a 0.1-thickness-ratio cascade of parabolic-arc camber-line airfoils of unit solidity and a camber of 35.314°. A range of stagger angles from −15° to 75° was considered. The mean angle of attack was

assumed to be zero. Both quasi-two-dimensional and plane flows were considered, with $\alpha = 0.1$ and $E = 2.2 \cos \lambda$ for the quasi-two-dimensional flows. Thickness, in general, tends to increase deviation angles. In table III of the appendix, we present values of the parameter $\delta^*/\theta(t/c = 0) - \delta^*/\theta(t/c = 0.1)$ for both plane and quasi-two-dimensional flows. The table shows that, in quantitative terms, the effect of thickness in increasing deviation angles is practically identical for plane and QTD flows. Based on these results, it seems reasonable to suggest that the results of figures 6 and 7 will be directly and quantitatively applicable to finite-thickness-ratio cascades as well.

SUMMARY

Flow turning is an important aspect in the design of a compressor row, and it is known that changes in axial-flow velocity through the row can modify cascade performance. In this note, figures 6 through 8 summarize some results concerning the effects on the deviation angle of both axial-flow acceleration and changes in foil thickness. These curves are presented in a fashion that should be useful for design purposes.

The curves of $\Delta[\delta^*/\theta]/(\text{AVR-1})$ versus σ and λ in figures 6 and 7 combine both experimental and theoretical results. Two-dimensional experimental values of minimum-loss-incidence angles from Lieblein were cross-plotted with potential flow results for δ^*/θ from the QTD theory in order to generate values for these graphs. In these two figures, the mean angle of attack α_m is not constant but varies with both λ and σ.

All of the results presented here pertaining to the effects of axial velocity ratio on cascade performance are valid for small contraction parameter $\alpha = \ln (\text{AVR})/2 \cos \lambda$. Whatever trends are evident can be thought of as being linear in terms of this parameter, since the present QTD calculation is essentially a regular perturbation expansion in α. This fact is useful in extrapolating the present results to other small values of the contraction parameter.

We should emphasize that the effects displayed in the graphs of this report are to be taken as trends since they actually apply to a finite exponential contraction and not necessarily to an actual contraction. Also, we have not made a systematic exhaustive numerical study of all the variables at our disposal. For example, variations in the extent of contraction, the camber angle, and the camber-line function are not considered here. However, before further calculations of this type are undertaken, it would be very desirable to have experimental results available from cascade experiments in which the contraction effect and flow geometry are well defined.

LIST OF SYMBOLS

AVR	Axial velocity ratio $= Va_2/Va_1$
A_0, A_1, A_2	Coefficients of the camber line slope (eq. 13))
$a_0, a_1, \ldots, a_N$	Coefficients of the vorticity series (eq. (18))
C_b	Section lift coefficient due to camber
c	Chord length of airfoil
E	Extent of cascade blades along the x_1 direction (fig. 4b)
h	Width function of channel $= h(x_1)$
i	Incidence angle (see fig. 2)
$i^{(2D)}_{a_0=0}, i^{(3D)}_{a_0=0}$	Incidence angles for impact-free entry (for $t/c=0$), for two-dimensional and three-dimensional cascades, respectively
$i^{(2D)}_{ml}$	Incidence angle of minimum-loss operation (2D cascade)
QTD	Quasi-two-dimensional; refers to the spanwise averaged three-dimensional flow developed in reference 3
s	Spacing between foils in a cascade (see fig. 2)
t/c	Thickness/chord ratio
Va_1, Va_2	Axial flow velocity components at the leading edge and trailing edge, respectively
V_1, V_2	Total velocity at the leading edge and trailing edge, respectively
V_m	Mean total velocity, $\frac{1}{2}(V_1+V_2)$
x, y, z	Coordinate system with x_1 taken along the axial direction (cascade axis)
2D	Refers to plane flow cascades, $h(x_1) = $ constant
3D	Refers to three-dimensional (QTD) cascades; for the present calculations, a constant contraction parameter $\alpha = 0.1$ was used
α	Contraction parameter, $\exp(2\alpha \cos \lambda)$
α_m	Mean angle of attack of V_m (see fig. 2)
$\alpha_m^{(2D)}, \alpha_m^{(3D)}$	Mean angle of attack corresponding to minimum-loss incidence for two-dimensional and three-dimensional cascades, respectively
$\alpha_{m a_0=0}^{(2D)}, \alpha_{m a_0=0}^{(3D)}$	Mean angle of attack corresponding to impact-free entry for two-dimensional and three-dimensional cascades, respectively
β_m	Mean flow angle, $\lambda+\alpha_m$
β_1, β_2	Inlet and outlet flow angles, measured with respect to the cascade axis
$\gamma(x)$	Vorticity distribution (eq. (18))
Γ_t	Total circulation (positive counterclockwise); we also use $\Gamma = -\Gamma_t$ for parts of the discussion

$\Delta[\delta^*/\theta]$ Change in δ^*/θ due to axial-flow acceleration, $\delta^*/\theta(2D) - \delta^*/\theta(3D)$

$\Delta_{t/c}^{(2D)}[\delta^*/\theta]$ Change in δ^*/θ due to thickness change for two-dimensional cascade, $\delta^*/\theta(t/c=0) - \delta^*/\theta(t/c=.1)$

$\Delta_{t/c}^{(3D)}[\delta^*/\theta]$ Same as above for three-dimensional cascade

δ^* Deviation angle (see fig. 2)

λ Stagger angle, angle of foil chord with axial direction

σ Solidity, c/s

θ Camber angle, $\frac{1}{2}(\theta_1+\theta_2)$ (see fig. 2)

TABLE I.—Flow Characteristics of Cascades With Parabolic Camber-Line Zero-Thickness Airfoils at Zero Mean Angle of Attack

Stagger angle λ(deg)	Solidity $\sigma = \frac{c}{s}$	Two-dimensional cascades ($\alpha=0$)				Quasi two-dimensional cascades ($\alpha=0.1$)			
		Incidence angle i (deg)	Deviation angle δ^* (deg)	Deviation angle ratio δ^*/θ	—Total circulation $\Gamma = -\Gamma_t$	Incidence angle i (deg)	Deviation angle δ^* (deg)	Deviation angle ratio δ^*/θ	—Total circulation $\Gamma = -\Gamma_t$
−15	0.5	−11.03	11.42	.323	.933	−12.43	12.29	0.348	0.970
	0.75	−8.38	9.11	.258	.864	−9.75	9.88	0.280	0.896
	1.0	−6.31	7.39	.209	.788	−7.66	8.07	0.229	0.816
	1.25	−4.75	6.12	.173	.715	−6.07	6.73	0.191	0.740
	1.5	−3.57	5.19	.147	.649	−4.85	5.74	0.163	0.672
0	0.5	−11.16	11.16	.316	.911	−11.38	11.26	0.319	0.888
	0.75	−8.82	8.82	.250	.829	−9.15	8.98	0.254	0.806
	1.0	−7.1	7.1	.201	.746	−7.5	7.30	0.207	0.724
	1.25	−5.85	5.85	.166	.669	−6.29	6.06	0.172	0.650
	1.5	−4.93	4.93	.140	.602	−5.39	5.14	0.146	0.586
15	0.5	−11.57	11.20	.317	.909	−10.77	10.47	0.296	0.820
	0.75	−9.49	8.82	.25	.824	−8.94	8.30	0.235	0.742
	1.0	−8.0	7.05	.20	.738	−7.63	6.71	0.190	0.664
	1.25	−6.94	5.76	.163	.660	−6.69	5.54	0.157	0.594
	1.5	−6.18	4.83	.137	.592	−6.0	4.66	0.132	0.534

30	0.5	−12.24	11.58	.328	.926	−10.96	10.26	0.290	0.790
	0.75	−10.37	9.13	.258	.850	−9.44	8.13	0.230	0.723
	1.0	−9.04	7.25	.205	.767	−8.34	6.51	0.184	0.652
	1.25	−8.11	5.87	.166	.688	−7.58	5.32	0.151	0.585
	1.5	−7.46	4.87	.138	.618	−7.03	4.44	0.126	0.526
45	0.5	−13.17	12.34	.349	.963	−12.00	10.90	0.308	0.818
	0.75	−11.50	9.83	.278	.911	−10.66	8.70	0.246	0.772
	1.0	−10.28	7.75	.219	.841	−9.67	6.88	0.1945	0.712
	1.25	−9.44	6.18	.175	.764	−8.98	5.51	0.156	0.647
	1.5	−8.87	5.04	.143	.690	−8.50	4.51	0.128	0.585
60	0.5	−14.38	13.57	.384	1.017	−13.67	12.53	0.355	0.906
	0.75	−12.97	11.12	.315	1.02	−12.48	10.26	0.290	0.905
	1.0	−11.84	8.7	.246	.990	−11.52	8.04	0.228	0.878
	1.25	−11.05	6.70	.19	.928	−10.83	6.19	0.1751	0.924
	1.5	−10.55	5.28	.15	.848	−10.39	4.88	0.1381	0.754
75	0.5	−15.89	15.36	.435	1.079	−15.66	14.98	0.424	1.028
	0.75	−14.94	13.45	.381	1.189	−14.79	13.11	0.372	1.128
	1.0	−13.95	10.52	.298	1.319	−13.88	10.27	0.290	1.248
	1.25	−13.22	7.18	.203	1.352	−13.18	6.99	0.198	1.285
	1.5	−12.84	4.87	.138	1.266	−12.82	4.70	0.133	1.206

$t/c=0$ $c_b=1.0$

$\alpha_m=0$ $E/2\cos\lambda=1.1$ $\theta=35.314°$

TABLE II.—*Flow Characteristics of Cascades With Parabolic Camber-line Zero-Thickness Airfoils at 5.73° Mean Angle of Attack*

Stagger angle λ(deg)	Solidity $\sigma = \frac{c}{s}$	Two-dimensional cascades ($\alpha=0$)				Quasi two-dimensional cascades ($\alpha=0.1$)			
		Incidence angle i (deg)	Deviation angle δ^* (deg)	Deviation angle ratio δ^*/θ	—Total circulation $\Gamma = -\Gamma_t$	Incidence angle i (deg)	Deviation angle δ^* (deg)	Deviation angle ratio δ^*/θ	—Total circulation $\Gamma = -\Gamma_t$
—15	0.5	—1.32	13.38	.379	1.472	—2.49	14.08	0.398	1.464
	0.75	2.44	10.09	.286	1.328	1.20	10.77	0.305	1.319
	1.0	5.08	7.84	.222	1.181	3.83	8.47	0.240	1.174
	1.25	6.90	6.33	.179	1.047	5.66	6.91	0.196	1.043
	1.5	8.18	5.28	.15	.933	6.96	5.82	0.1649	0.931
0	0.5	—2.01	13.12	.371	1.431	—1.99	13.01	0.368	1.359
	0.75	1.06	9.79	.277	1.265	0.88	9.85	0.279	1.200
	1.0	3.09	7.56	.214	1.108	2.79	7.71	0.218	1.051
	1.25	4.44	6.06	.172	.973	4.08	6.25	0.177	0.924
	1.5	5.36	5.02	.142	.861	4.98	5.23	0.148	0.819
15	0.5	—3.00	13.28	.376	1.428	—2.12	12.35	0.350	1.292
	0.75	—0.42	9.85	.279	1.258	0.14	9.24	0.262	1.135
	1.0	1.23	7.53	.213	1.097	1.58	7.15	0.202	0.988
	1.25	2.29	5.98	.169	.959	2.52	5.73	0.1625	0.864
	1.5	3.0	4.92	.139	.845	3.15	4.76	0.135	0.762

30	0.5	−4.28	13.93	.394	1.466	−3.10	12.44	0.3530	1.289
	0.75	−2.04	10.30	.292	1.308	−1.26	9.21	0.2610	1.146
	1.0	−0.65	7.77	.220	1.147	−0.10	6.99	0.1980	1.002
	1.25	0.21	6.09	.172	1.003	0.63	5.50	0.1560	1.876
	1.5	0.76	4.96	.140	.883	1.11	4.50	0.1275	0.771
45	0.5	−5.85	15.20	.430	1.546	−4.90	13.66	0.387	1.371
	0.75	−3.92	11.28	.320	1.431	−3.30	10.09	0.286	1.263
	1.0	−2.71	8.33	.236	1.279	−2.29	7.43	0.210	1.126
	1.25	−2.00	6.37	.180	1.126	−1.69	5.70	0.161	0.989
	1.5	−1.57	5.10	.144	.991	−1.32	4.56	0.129	0.871
60	0.5	−7.81	17.35	.491	1.668	−7.22	16.11	0.456	1.539
	0.75	−6.22	13.22	.374	1.665	−5.92	12.32	0.349	1.530
	1.0	−5.17	9.37	.265	1.564	−4.99	8.68	0.246	1.433
	1.25	−4.62	6.81	.193	1.396	−4.50	6.28	0.1775	1.278
	1.5	−4.32	5.26	.149	1.230	−4.24	4.84	0.1370	1.126
75	0.5	−10.22	20.70	.586	1.812	−10.1	20.4	0.576	1.756
	0.75	−9.32	17.49	.495	2.094	−9.25	17.16	0.485	2.023
	1.0	−8.54	11.25	.319	2.304	−8.52	10.98	0.310	2.219
	1.25	−8.25	6.48	.184	2.109	−8.23	6.31	0.1785	2.031
	1.5	−8.15	4.26	.121	1.837	−8.14	4.11	0.116	1.770

$\alpha_m = 0.1\,\text{rad} = 5.73°$ $E/2\cos\lambda = 1.1$ $t/c = 0$ $c_b = 1.0$ $\theta = 35.314°$

TABLE III.—*Values of Parameter* $[\delta^*/\theta\ (t/c=0)-\delta^*/\theta\ (t/c=0.1]$ *as a Function of Stagger Angle* λ *for a Parabolic Arc Camber-Line Airfoil Cascade*[1]

λ degrees	Parameter for Q.T.D. flow	Parameter for T.D. flow
−15	0.000	−0.001
0	−0.011	−0.012
15	−0.025	−0.025
30	−0.040	−0.041
45	−0.0575	−0.057
60	−0.076	−0.075
75	−0.106	−0.107

[1] In the quasi-two-dimensional case, $\alpha = 0.1$ and $E = 2.2 \cos \lambda$. Also, $\alpha_m = 0$, $\sigma = 1$ and $\Theta = 35.314°$ for both cases.

REFERENCES

1. JOHNSON, I. A., AND R. O. BULLOCK, eds., *Aerodynamic Design of Axial-Flow Compressors.* NASA SP–36, 1965 (especially Chapters VI and VII).

2. MELLOR, G. L., An Analysis of Axial Compressor Cascade Aerodynamics. Part I and Errata (December 1962), *Trans. ASME, J. Basic Eng.*, Ser. D, Vol. 81, September 1959.

3. MANI, RAMANI, *Quasi Two-Dimensional Flows Through Cascades.* Ph.D. dissertation, Cal. Tech., December 1966.

4. MANI, RAMANI, AND A. J. ACOSTA, Quasi-Two-Dimensional Flows Through a Cascade. *Trans. ASME, J. Power*, Vol. 90, No. 2, April 1968.

5. MANI, RAMANI, *A Method of Calculating Quasi Two-Dimensional Flows Through Cascades.* Eng. Div., Cal. Tech., Report E–79.10, July 1967.

6. VON KARMAN, T., AND J. M. BURGERS, *Aerodynamic Theory.* Vol. II, Div. E, W. F. Durand, ed., 1934.

7. WILSON, M. B., AND A. J. ACOSTA, *A Note on the Influence of Axial Velocity Ratio on Potential Flow Cascade Performance.* Div. Eng. and Appl. Sci., Cal. Tech., Report E–79.11, January 1969.

DISCUSSION

J. H. HORLOCK AND J. P. GOSTELOW (Cambridge University):
We have followed the work of Mani and Acosta (and now Wilson) with
considerable interest over the past few years since, at Liverpool and
Cambridge, we have been working on the same problem of axial velocity
ratio effects.

On the analytical side, two approaches to the problem have been
described in the discussion of reference 4, referring to papers by Pollard
and Horlock (ref. D–1), and Shaalan and Horlock (ref. D–2). Briefly,
the first approach was to place strip sources across the blade pitch and
solve the potential equations for the flow past thin airfoils in two dimen-
sions. (This is somewhat similar to the approach of Smith, described in
the first paper, in which he allows for the flow in the $S2$ plane in his
solutions for the $S1$ plane.) The second approach made the initial assump-
tion that meridional flow through the midspan section of the blade was on
gently inclined planes, and a potential equation

$$\nabla^2\phi + \frac{h^1(x_1)}{h_1(x_1)}\frac{\partial\phi}{\partial x_1} = 0$$

was derived for the flow *near the center line.* Solution of this equation was
again obtained by using local sources $S = -(h^1/h)(\partial\phi/\partial x)$ varying
linearly across the pitch. No allowance was made for the modification of
the induced velocity due to restricted length of singularities. Essentially,
the problem solved was two-dimensional, but one in which fluid was
introduced uniformly at all values of Z in order to increase the axial
velocity.

Hawthorne (ref. D–3) has since argued that neither the Mani-Acosta-
Wilson nor the Pollard-Horlock-Shaalan approach is strictly valid. If the
Mani-Acosta-Wilson approach is more realistic than the Pollard-Horlock-
Shaalan solution in its allowance for spanwise variation in singularity
strength, then the effects of trailing, or shed, vorticity should also be
included, downstream of the blades. Hawthorne has solved the problem
for closely spaced blades using the type of analysis developed by Honda
for shear flows (ref. D–4).

Another approach is that of Norbury (as yet unpublished) who con-
siders the radial flow through "ring" airfoils. The bound singularities are
then uniform but circular in shape, rather than infinitely long straight

lines (Pollard-Horlock-Shaalan) or lines of finite length (Mani-Acosta-Wilson).

Shaalan has recently provided a summary design manual similar to the current paper. It allows for axial velocity ratio effects and is based on reference D–2. A summary of Shaalan's calculations is given in figures D–1 and D–2 for 20° and 30° camber. We doubt the validity of the thin airfoil analysis, especially for cambers higher than 30°. Also shown is Howell's rule for deviation (ref. D–5), based on experimental cascade data. We expect this rule to be valid for $1.1 < AVR < 1.2$. We have replotted these calculations in figure D–3 (at *zero* incidence, not minimum-loss incidence, which would be roughly −5°) for direct comparison with the Mani-Acosta-Wilson calculations.

We would commend the use of the parameter $\Delta[\delta^*/\theta]/(AVR-1)$ to designers. This is a logical dimensionless group which adequately represents the observed linear dependence of deviation on camber (Howell) and of deviation on axial velocity ratio (Pollard and Gostelow, ref. D–5).
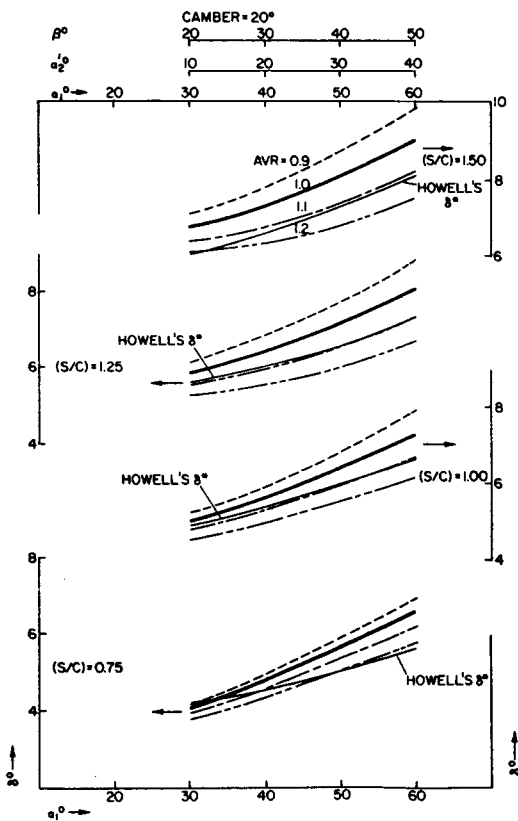
FIGURE D–1.—*Shaalan's prediction for 20° camber.*
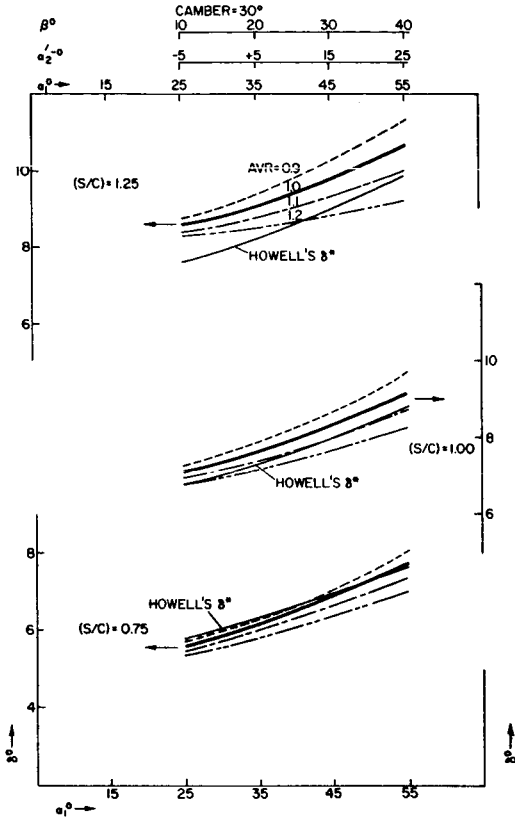
FIGURE D-2.—*Shaalan's prediction for 30° camber.*

The experimental evidence available is that of Pollard and Gostelow (ref. 13), Heilmann (ref. 14) and Masek and Norbury (ref. 15). Pollard and Gostelow used 10/C430 C50 airfoils at 36° stagger, with solidities of unity and 1.15. This resulted in the empirical rule

$$\Delta\delta^* = \delta^*_{3D} - \delta^*_{2D} = 10(\text{AVR}-1)$$

giving

$$\frac{\Delta[\delta^*/\theta]}{\text{AVR}-1} = \frac{10}{30} = +0.33$$

Heilmann tested a NACA 65–(12A2 I8b)10 cascade with 25.5° stagger for minimum-loss incidence and a solidity of 1.5. The slope of the experimental results gives

$$\frac{\Delta[\delta^*/\theta]}{\text{AVR}-1} = +0.15$$

FIGURE D-3.—*Effect of axial velocity change on deviation angle ratio.*
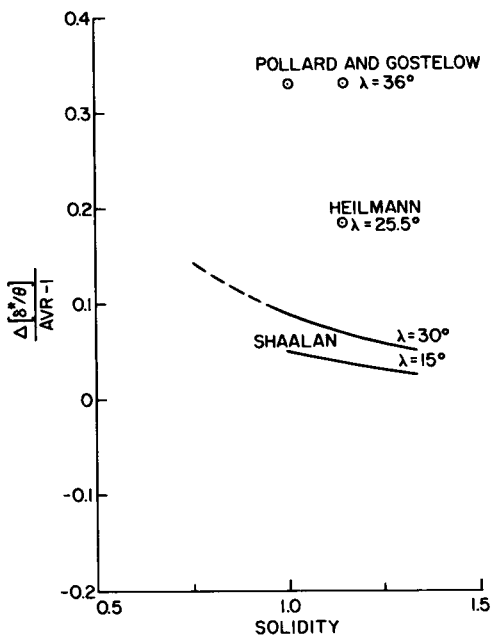
Masek and Norbury tested a specially designed compressor cascade with 35.5° stagger and a solidity of 1.2. The slope of their experimental results, for both zero and minimum-loss incidence, gives

$$\frac{\Delta[\delta^*/\theta]}{\text{AVR}-1} = +0.31$$

We understand that the thin airfoil potential theory used by Mani-Acosta-Wilson for airfoils of finite thickness neglects perturbations of chordwise velocity and of velocity gradient in the equation for source distribution. This may well result in erroneous prediction of lift and deflection. It would be of interest to see the presentation of pressure distributions from the Mani-Acosta-Wilson analysis, for comparison with Shaalan's predictions and with experimental results and for calculation of the blade boundary layers. A disadvantage of all thin airfoil theories is that the Kutta/Joukowski condition again results in erroneous prediction of lift and deflection. Real blading usually has a rounded trailing edge.

It seems that there is much more work to be done. The changes in $\Delta[\delta^*/\theta]/(\text{AVR}-1)$ for off-design incidence have not been assessed either theoretically or experimentally. There may or may not be a significant change in this parameter as incidence is increased. Our own limited evidence is contradictory. The designer also needs information on the

relationship between loss coefficient and axial velocity ratio. This will need a substantial effort with both experimental work and viscous flow calculations.

B. LAKSHMINARAYANA (Pennsylvania State University): I have carried out an approximate analysis for the prediction of the change in deviation angle due to change in axial velocity through the cascade. The predicted change agrees qualitatively with those of the authors and Pollard, Horlock, and Shaalan's theory (refs. D-1 and D-2) and is in good agreement with values measured by Pollard and Gostelow (ref. D-6), Heilmann (ref. D-7), and Schulze, et al. (ref. D-9).

The change in circulation associated with change in axial velocity is given by:[D-1]

$$\Delta \Gamma = S[(V_{x_1} \tan \beta_1 - V_{x_2} \tan \beta_2') - V_{x_1}(\tan \beta_1 - \tan \beta_2)]$$

$$= SV_{x_1}(\tan \beta_2 - \text{AVR} \tan \beta_2') \tag{D-1}$$

where $\beta_2' = \beta_2 - \Delta \delta^*$ and β_2 is the outlet angle for $\text{AVR} = 1$.

$$\Delta \delta^* = \delta_{2d}^* - \delta_{3d}^*$$

For small values of $\Delta \delta^*$,

$$\tan \beta_2' = (\tan \beta_2 - \Delta \delta^*)(1 - \Delta \delta^* \tan \beta_2) \tag{D-2}$$

Substituting equation (D-2) in (D-1) and neglecting the second-order term $(\Delta \delta^*)^2$,

$$\Delta \Gamma / SV_{x_1} = (1 - \text{AVR}) \tan \beta_2 + \text{AVR} \, \Delta \delta^* \sec^2 \beta_2 \tag{D-3}$$

With regard to *change in circulation* ($\Delta \Gamma$), mutual interaction of thickness and axial velocity changes should be small and this has been demonstrated by the authors (table III). Thus, the problem reduces to computation of $\Delta \Gamma$ for a cascade of cambered plates.

The circulation distribution for a cascade of symmetrically cambered (parabolic or circular) plates is given by (ref. D-10),

$$\gamma(x) = KV_m[2\alpha(1 + \cos \theta)/\sin \theta + 8(G/c) \sin \theta] \tag{D-4}$$

where

K is the cascade influence coefficient (see fig. 282.1 in ref. D-10 for values)

$\alpha = i + \theta/2$

$G =$ maximum camber

$x = (c/2)(1 - \cos \theta)$, the coordinate transformation

[D-1] All primed expressions such as β_2^1, V_m^1 refer to values with $\text{AVR} \neq 1$ and V_x refers to axial velocities.

The change in circulation distribution due to axial velocity change (with V_1 and β_1 held fixed) is given by[D-2]

$$d\gamma = 2KV_m \, \Delta\alpha(1 + \cos\theta)/\sin\theta$$

$$+ K\Delta V_m[2\alpha(1 + \cos\theta)/\sin\theta + 8G/c \sin\theta] \qquad \text{(D-5)}$$

where ΔV_m for a cascade (which corresponds to the change in free-stream velocity in the case of an isolated blade) varies from zero at the leading edge to its full value at the trailing edge.

For small changes in axial velocities, the maximum change in V_m can be approximated by

$$(V_m')^2 - V_m{}^2 \cong 2V_m(\Delta V_m)_\text{TE} \qquad \text{(D-6)}$$

where V_m' is the vector mean velocity for a cascade with AVR $\neq 1$ and TE refers to values at the trailing edge.

Using the cascade relationships for V_m and V_m', equation (D-1), and the approximations indicated in equations (D-2) and (D-3), the following expression can be derived

$$\frac{(\Delta V_m)_\text{TE}}{V_{x_1}} = \frac{1}{8}\frac{V_z}{V_m}\left\{(1 + \text{AVR})^2 - 4 - \frac{\Delta\Gamma}{SV_{x_1}}\left[(1 + \text{AVR})\tan\beta_2 + 2\tan\beta_1\right]\right\}$$

$$\text{(D-7)}$$

In equation (D-7), second-order terms such as $\Delta\delta^{*2}$ and $\Delta\Gamma\Delta\delta^*$ have been neglected.

Similarly, the trailing edge of the blade will have an incidence change (for small $\Delta\alpha_\text{TE}$) given by

$$\frac{\tan\beta_1'}{\tan\beta_1} = \frac{1}{\text{AVR}} = \frac{(\tan\beta_1 + \Delta\alpha_\text{TE})(1 + \Delta\alpha_\text{TE}\tan\beta_1)}{\tan\beta_1}$$

Hence,

$$\Delta\alpha_\text{TE} = \frac{1 - \text{AVR}}{\text{AVR}}\frac{\tan\beta_1}{\sec^2\beta_1} \qquad \text{(D-8)}$$

If ΔV_x, $\Delta\alpha$, and ΔV_m vary linearly with x, it is clear that

$$\Delta\alpha = \frac{1 - \text{AVR}}{2\text{AVR}}\frac{\tan\beta_1}{\sec^2\beta_1}(1 - \cos\theta) \qquad \text{(D-9)}$$

[D-2] The analysis is based on the fact that each infinitesimally small blade element in the cascade sees a different change in angle of incidence ($\Delta\alpha$) and velocity (ΔV_m) due to change in axial velocity. The values vary from zero at the leading edge to full value at the trailing edge; hence, $d\gamma$, $\Delta\alpha$, and ΔV_m are all functions of x or θ.

$$\Delta V_m = (\Delta V_m)_{TE} \frac{1 - \cos \theta}{2} \tag{D-10}$$

Substituting equations (D–7) through (D–10) in equation (D–5) and integrating the expression between $x = 0$ and $x = c$, the following expression is derived for total change in circulation

$$\frac{\Delta \Gamma}{S V_{x_1}} = \Pi K \sigma \frac{V_m}{V_{x_1}} \frac{1 - AVR}{4AVR} \frac{\tan \beta_1}{\sec^2 \beta_1} + \Pi K \sigma \left(\frac{G}{c} + \frac{\alpha}{4}\right) \left(\frac{\Delta V_m}{V_{x_1}}\right)_{TE} \tag{D-11}$$

Substituting equations (D–3) and (D–7) in (D–11) and rearranging, the following expression can be derived for the change in the deviation angle due to axial velocity change

$$AVR \frac{\Delta \delta^*}{AVR - 1}$$

$$= \cos^2 \beta_2 \left\{ \tan \beta_2 + \frac{\left(\dfrac{\Pi K \sigma [(G/c) + (\alpha/4)] \cos \beta_m [(AVR+1)^2 - 4]}{AVR - 1} - \dfrac{2\Pi K \sigma \tan \beta_1}{AVR \cos \beta_m \sec^2 \beta_1}\right)}{8 + \Pi K \sigma [(\alpha/4) + (G/c)] \cos \beta_m [(AVR+1) \tan \beta_2 + 2 \tan \beta_1]} \right\} \tag{D-12}$$

Equation (D–12) provides deviation values which are better than those of either of the two theories (see discussion of this paper by Horlock and Gostelow) for the cascades of Pollard and Gostelow (ref. D–6), Heilmann (ref. D–7), and Schulze (ref. D–9) as shown in table D–I.

It is not clear why the approximate theory developed above has better agreement with experimental values than the theories developed by the authors and Pollard-Horlock-Shaalan (refs. D–1 and D–2). One possible source of error may be the numerical method. The numerical solution adopted by the authors is not capable of predicting extremely small change in angles. One way to overcome this is to solve directly for the perturbed flow, as shown in this discussion, rather than to solve for the entire cascade flow.

It should be emphasized here that all the theories, including that of the discussor, are strictly valid for small changes in AVR (possibly for $0.9 < AVR < 1.1$) and small flow turning. At higher values of AVR and θ, the three-dimensional effects are important and the flow cannot be considered quasi-two-dimensional.

TABLE D-I.—*Comparison Between Predicted and Experimental Values of* $\Delta(\delta^*/\theta)/(AVR-1)$

Cascade	Parameters	Experimental value	Predicted BL	M/A/W	P/H/S (refs. D-1 and D-2)
Pollard and Gostelow (ref. D-6) 10/C430 C50	$\lambda = 36°$, $\sigma = 1.14$ $\beta_1 = 52°50^1$, $\beta_2 = 31°$ $G/c = 0.065$, $K = 0.8$ $\theta = 30°$, $\alpha = 16°50^1$	0.33	0.42	0.13	0.09
Heilmann (ref. D-7) NACA 65(12A$_2$I$_{8b}$)10	$\lambda = 25.5°$, $\sigma = 1.5$ $\beta_1 = 45°$, $\beta_2 = 19°$ $G/c = 0.073$, $K = 0.65$ $\theta = 31°$, $\alpha = 19°30^1$	0.15	0.18	0.062	0.04
Schulze, et al. (ref. D-9) NACA 65(11)10	$\lambda = 40.5°$, $\sigma = 1.00$ $\beta_1 = 52°30^1$, $\beta_2 = 35°$ $G/c = 0.06$, $K = 0.87$ $\theta = 28°$, $\alpha = 12°$	0.37	0.49	0.175	

WILSON, MANI, AND ACOSTA (authors): In view of the spirited discussion of our paper at the symposium, a thorough review was carried out of all aspects of the calculations. As a result, a rather subtle but important error has been uncovered in our procedure of evaluating deviation and incidence angles once the circulation has been determined. We regret this error[D-3] deeply but, as this closure demonstrates, once this error is rectified, our results for deviation angles are in much better agreement with those of other investigators.

Having obtained the total circulation Γ around each airfoil, we assumed previously that the row of infinite vortices would contribute tangential velocities $\pm\Gamma/2s$ on the downstream/upstream side, where s is the transverse spacing between adjacent airfoils. This result is indeed

---

[D-3] These corrections have been incorporated in the final version of the paper published in these symposium proceedings.

true in the two-dimensional problem. It has turned out to be erroneous to $O(\alpha)$ in the quasi-two-dimensional problem. We have calculated anew these tangential velocities by summing the fundamental solution v_v spelled out in Appendix 1 of reference 4 of our paper. The correct result was found to be that the tangential velocity (due to the vortices) downstream is

$$\frac{-\Gamma}{2s}\left(1+\frac{\alpha}{2}E\right)$$

where α is the contraction parameter and E is the extent of contraction. The tangential velocity due to the vortices upstream is

$$\frac{\Gamma}{2s}\left(1-\frac{\alpha}{2}E\right)$$

Note that the difference of these tangential velocity contributions is still Γ/s (as it should be), but the contraction introduces an asymmetry whereby the downstream contribution is enhanced by a factor $1+(\alpha/2)E$ and the upstream contribution is reduced by a factor of $1-(\alpha/2)E$. We thereby calculate the inlet flow angle with the equation

$$\tan\beta_1 = \frac{\sin(\lambda+\alpha_m)+\frac{1}{2}\Delta V_t[1-(\alpha/2)E]}{(1-\alpha\cos\lambda)\cos(\lambda+\alpha_m)}$$

and the outlet flow angle by

$$\tan\beta_2 = \frac{\sin(\lambda+\alpha_m)-\frac{1}{2}\Delta V_t[1+(\alpha/2)E]}{(1+\alpha\cos\lambda)\cos(\lambda+\alpha_m)}$$

where ΔV_t is still Γ/s.

As can be readily appreciated, correction of this error has the effect of decreasing (at fixed mean angle of attack) both incidence and deviation angles. Two sets of computations were performed with the corrected equations to demonstrate the vastly improved agreement of our results with those of other investigators.

First, in figure D–4, we plot the δ^*-i curves for a zero-thickness, parabolic camber line cascade with $\lambda=45°$, $\sigma=1.25$, $\theta=35.314°$, $E/2\cos\lambda=1.1$, and $\alpha=0.1$. Dr. L. H. Smith of General Electric Company, Cincinnati, Ohio, referred our paper originally to his colleague, Dr. D. C. Prince, Jr. Dr. Prince performed computations based on a finite difference method and kindly supplied us with results for the effect of the contraction on the δ^*-i curves, based on his program. Dr. Prince was among the first to express strong reservations about our results, indicating that the deviation angles may sometimes increase (due to speeding of the flow). The figure is largely self-explanatory, and it is seen that our corrected
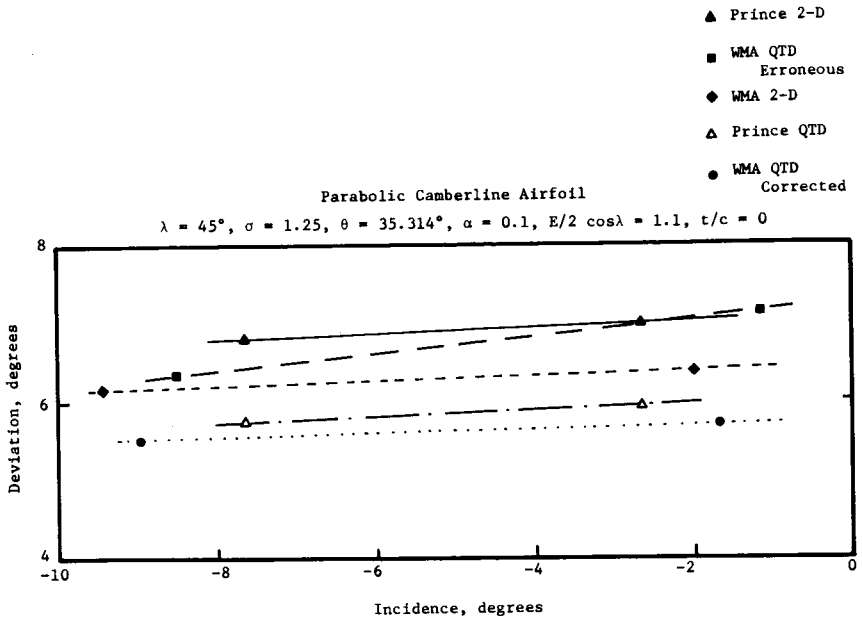
FIGURE D–4. — *Deviation angles for parabolic camber airfoil.*

results are in much better agreement with those of Dr. Prince. Our analysis predicts a drop of around 0.7° due to axial acceleration, while Dr. Prince's estimates are closer to 1° to 1.1°.

The second set of computations pertains to calculations carried out by Professor Lakshminarayana in his discussion of the paper. He considers two cases: first, a cascade with $\lambda = 36°$ and $\sigma = 1.14$ and, second, a cascade with $\lambda = 25.5°$ and $\sigma = 1.5$. By interpolation from our new (corrected) figure 7, the following results were obtained:

The table follows the notation of Professor Lakshminarayana's discussion.

It is seen that the agreement with Professor Horlock's results is now much better. A discrepancy of even 0.04 in the value of the predicted parameter with $\theta = 35°$ and $AVR = 1.15$ corresponds to a discrepancy in $\Delta\delta^*$ itself of only 0.21°. Considering that these results have been derived by interpolation, the agreement seems satisfactory. Professor Lakshminarayana's predictive procedure, of course, would appear to fit the experimental data the best of all. Perhaps most important, corrected results of the present paper seem to fall in line with those of other investigators in that deviation angles would appear to be always reduced due to axial acceleration for decelerating ($\lambda > 0$) cascades.

It is worth emphasizing that, in all these corrected calculations, the value of Γ used was the same as obtained previously. No errors were

TABLE D–II.—*Comparison Between Predicted and Experimental Values of* $\Delta(\delta^*/\theta)/(AVR-1)$

Cascade	Experimental value	Predicted			
		BL	WMA, old, erroneous	WMA, new, corrected	P/H/S
Pollard and Gostelow____	0.33	0.39	−0.05	0.13	0.09
Heilmann_____	0.15	0.16	−0.13	0.062	0.04

found in the basic theory itself; namely, in the singular solutions or the setting up and solving of the integral equation.

All graphs, tables, equations, and conclusions presented in this final version of this paper have been corrected from the earlier version.

In conclusion, we wish to express our sincerest gratitude to several individuals, notably Drs. L. H. Smith and D. C. Prince, Jr., and Professors Horlock and Lakshminarayana, for their sustained interest in our work.

REFERENCES

D–1. POLLARD, D., AND J. H. HORLOCK, A Theoretical Investigation of the Effect of Change in Axial Velocity on the Potential Flow Through a Cascade of Aerofoils. A.R.C. CP 619, 1963.

D–2. SHAALAN, M. R. A., AND J. H. HORLOCK, The Effect of Change in Axial Velocity on the Potential Flow in Cascades. A.R.C. R and M 3547, 1968.

D–3. HAWTHORNE, SIR WILLIAM, private communication.

D–4. HONDA, M., Theory of Shear Flow Through a Cascade. Proc. Roy. Soc. (London), Ser. A, Vol. 265, 1961, pp. 46–70.

D–5. HOWELL, A. R., The Present Basis of Axial Flow Compressor Design: Part I, Cascade Theory and Performance. A.R.C. R and M 2095, 1942.

D–6. POLLARD, D., AND J. P. GOSTELOW, Some Experiments at Low Speed on Compressor Cascades. Trans. ASME, J. Eng. Power, Vol. 427, July 1967.

D–7. HEILMANN, W., Experimentelle und grenzschichttheoretische Untersuchungen an ebenen Verzögerungsgittern bei kompressibler Strömung, insbesondere bei Änderung des axialen Stromdichteverhältnisses und der Zuströmturbulenz. D.V.C. Forschungsbericht 67–88, 1967.

D–8. MAREK, Z., AND J. F. NORBURY, The Effect of Axial Velocity Variation on the Performance of a Compressor Cascade. Unpublished report, Liverpool U., 1968.

D–9. SCHULZE, W. M., et al., NACA TN 4130, October 1957.

D–10. SCHOLZ, N., Aerodynamik der Schaufelgitter. Band I, Verlag G. Braun, p. 165.

The Solution of Three-Variable
Duct-Flow Equations

A. R. STUART

University of Aston
Birmingham, England

R. HETHERINGTON

Rolls-Royce Limited and University of Aston

Past effort in computational techniques in internal flow systems has been concentrated on two-variable problems. This paper establishes a numerical method for the solution of three-variable problems and is applied here to rotational flows through ducts of various cross sections.

An iterative scheme is developed, the main feature of which is the addition of a duplicate variable to the forward component of velocity. Two forward components of velocity result from integrating two sets of first-order ordinary differential equations for the streamline curvatures, in intersecting directions across the duct. Two pseudo-continuity equations are introduced with source/sink terms, whose strengths are dependent on the difference between the forward components of velocity. When convergence is obtained, the two forward components of velocity are identical, the source/sink terms are zero, and the original equations are satisfied.

A computer program solves the exact equations and boundary conditions numerically. The method is economical and compares successfully with experiments on bent ducts of circular and rectangular cross section where secondary flows are caused by gradients of total pressure upstream.

The presence of secondary-flow losses is well known. When a shear flow passes through a bend with a vorticity component directed toward the center of curvature, a secondary flow exists, transverse to the mean flow. The vorticity is produced by a velocity gradient in the flow approaching the bend. This velocity gradient may be produced by viscous losses upstream and by nonuniform work being done on the fluid. The losses in a

135

secondary flow are due to the energy contained in the transverse flow, much of which is not recovered. (The presence of secondary flow may also cause subsequent parts entered by that fluid to run partly "off design.")

This attack on the secondary-flow problem solves the fully three-dimensional flow equations. The equations of three-dimensional fluid flow are intractable to analytic solution, even with the inviscid and steady flow assumptions. Until now, they have defied numerical solution due to the insufficient core size and speed of the past-generation computer and the lack of a numerical technique. The development of this three-dimensional method of solution was stimulated by the success of various two-dimensional numerical methods. The method is an extension of the two-variable streamline curvature method (refs. 1 and 2).

Although the method as presented is restricted to enclosed ducts, it is also possible to include repeat boundary conditions, thus enabling solutions of the turbomachinery blade passage flow to be obtained.

DEVELOPMENT OF THE THREE-VARIABLE METHOD

To economize on time and effort during the initial development of a three-variable method and to facilitate a clear understanding of the mechanisms involved, attention was restricted to incompressible flows and a simple geometry, for which experimental data was available (ref. 3). The geometry is shown in figure 1. It consists of a rectangular duct which turns through any number of degrees on constant mean radius R_m. Coordinates x and z are fixed in each plane of cross section and y is measured along the centerline.

An Eulerian approach to the equations is used, since the Lagrangian method, which is used in two-variable streamline curvature methods, is excessively complicated in three variables. It requires the storage and manipulation of expressions for two interacting families of stream surfaces and their interaction with the boundaries.

Basic Equations

Continuity

$$\frac{1}{1+x/R_m}\frac{\partial}{\partial x}\left[\left(1+\frac{x}{R_m}\right)u\right]+\frac{1}{1+x/R_m}\frac{\partial v}{\partial y}+\frac{\partial w}{\partial z}=0 \tag{1}$$

Momentum

$$\frac{u\partial u}{\partial x}+\frac{v}{1+x/R_m}\frac{\partial u}{\partial y}+\frac{w\partial u}{\partial z}-\frac{v^2}{R_m+x}=-\frac{\partial p}{\partial x} \tag{2}$$
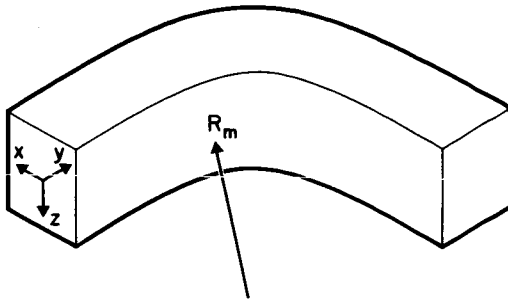
FIGURE 1.—*Geometry of the duct.*

$$\frac{u\partial v}{\partial x}+\frac{v}{1+x/R_m}\frac{\partial v}{\partial y}+\frac{w\partial v}{\partial z}-\frac{vu}{R_m+x}=-\frac{\partial p}{\partial y}\frac{1}{1+x/R_m} \qquad (3)$$

$$\frac{u\partial w}{\partial x}+\frac{v}{1+x/R_m}\frac{\partial w}{\partial y}+\frac{w\partial w}{\partial z}=-\frac{\partial p}{\partial z} \qquad (4)$$

These equations may be verified by considering a simple change of independent variables, $r=R_m+x$ and $\phi=y/R_m$, which yields the well-known inviscid fluid flow equations in cylindrical polar coordinates. The components u, v, and w are physical velocity components normal to the local coordinate surfaces, and the static pressure p is understood to include the specific volume $1/\rho$, which is constant. The term $1/R_m$ is zero outside the bend region, corresponding to infinite radius of curvature.

Manipulation of Equations

Following usual streamline curvature procedure, the u and w velocity components are replaced by new dependent variables λ and μ

where

$$u=\lambda v \qquad (5)$$

and

$$w=\mu v \qquad (6)$$

(Most authors use tan λ and tan μ, but this is not necessary for the present analysis.) The "in-plane" components u and w, which are expected to be relatively small in an enclosed duct, are expressed as fractions of the dominating velocity component v, normal to the planes of cross section. No approximation is here implied, but the transformations (5) and (6) are singular when v is zero, a condition which must be avoided. Using (5) and (6), equations (1) through (4) become

$$\frac{1}{1+x/R_m}\frac{\partial}{\partial x}\left[\left(1+\frac{x}{R_m}\right)\lambda v\right]+\frac{1}{1+x/R_m}\frac{\partial v}{\partial y}+\frac{\partial}{\partial z}\,(\mu v)=0 \tag{7}$$

$$\lambda v\,\frac{\partial}{\partial x}\,(\lambda v)+\frac{v}{1+x/R_m}\frac{\partial}{\partial y}\,(\lambda v)+\mu v\,\frac{\partial}{\partial z}\,(\lambda v)-\frac{v^2}{R_m+x}=-\frac{\partial p}{\partial x} \tag{8}$$

$$\lambda v\,\frac{\partial v}{\partial x}+\frac{v}{1+x/R_m}\frac{\partial v}{\partial y}+\mu v\,\frac{\partial v}{\partial z}+\frac{\lambda v^2}{R_m+x}=\frac{-1}{1+x/R_m}\frac{\partial p}{\partial y} \tag{9}$$

$$\lambda v\,\frac{\partial}{\partial x}\,(\mu v)+\frac{v}{1+x/R_m}\frac{\partial}{\partial y}\,(\mu v)+\mu v\,\frac{\partial}{\partial z}\,(\mu v)=-\frac{\partial p}{\partial z} \tag{10}$$

Bernoulli's equation is also derived from equations (8) through (10).

$$\lambda\,\frac{\partial P}{\partial x}+\frac{1}{1+x/R_m}\frac{\partial P}{\partial y}+\mu\,\frac{\partial P}{\partial z}=0 \tag{11}$$

where the total pressure

$$P=p+\tfrac{1}{2}v^2(1+\lambda^2+\mu^2) \tag{12}$$

The five equations (8) through (12) are not independent, as Bernoulli's equation is linearly dependent on the three momentum equations. One equation must be omitted, and (9) is selected since it is identical with (11) in the trivial case $\lambda=\mu=0$.

Still adhering to the two-variable streamline curvature method, the $\partial v/\partial y$ terms are eliminated from equations (8) and (10) with the aid of (7) to obtain

$$v^2\left[\frac{1}{1+x/R_m}\frac{\partial\lambda}{\partial y}+\mu\,\frac{\partial\lambda}{\partial z}-\frac{1+\lambda^2}{R_m+x}-\lambda\,\frac{\partial\mu}{\partial z}\right]=-\frac{\partial p}{\partial x} \tag{13}$$

and

$$v^2\left[\frac{1}{1+x/R_m}\frac{\partial\mu}{\partial y}+\lambda\,\frac{\partial\mu}{\partial x}-\frac{\lambda\mu}{R_m+x}-\mu\,\frac{\partial\lambda}{\partial x}\right]=-\frac{\partial p}{\partial z} \tag{14}$$

However, p is related to v^2 and P by (12). Using this equation in (13) and (14)

$$\tfrac{1}{2}(1+\lambda^2+\mu^2)\,\frac{\partial}{\partial x}\,(v^2)=\frac{\partial P}{\partial x}+v^2\left[\frac{1}{1+x/R_m}\frac{\partial\lambda}{\partial y}-\frac{1+\lambda^2}{R_m+x}\right.$$

$$\left.-\lambda\,\frac{\partial\lambda}{\partial x}-\mu\,\frac{\partial\mu}{\partial x}+\mu\,\frac{\partial\lambda}{\partial z}-\lambda\,\frac{\partial\mu}{\partial z}\right] \tag{15}$$

and

$$\tfrac{1}{2}(1+\lambda^2+\mu^2)\,\frac{\partial}{\partial z}\,(v^2) = \frac{\partial P}{\partial z}+v^2\left[\frac{1}{1+x/R_m}\frac{\partial\mu}{\partial y}-\frac{\lambda\mu}{R_m+x}\right.$$

$$\left.-\lambda\frac{\partial\lambda}{\partial z}-\mu\frac{\partial\mu}{\partial z}+\lambda\frac{\partial\mu}{\partial x}-\mu\frac{\partial\lambda}{\partial x}\right] \qquad (16)$$

There are now four equations, (7), (11), (15) and (16), for the four dependent variables λ, μ, v, and P. Boundary conditions are required to close the system.

Boundary Conditions

It is necessary to appeal to the physics of the problem to obtain the correct boundary conditions. Some of these are obvious: $\lambda=0$ at the walls given by $x=$ constant and $\mu=0$ at the walls given by $z=$ constant (the no-flow conditions). Upstream conditions are easily come by: straight shear flow where the static pressure is constant and either v or P is specified at the inlet cross section. However, the conditions downstream are not so evident, being complicated by the presence of secondary flow. Two different downstream boundary conditions have been tried, both of which are sufficient to close the system of equations and boundary conditions from a numerical or computational point of view. The first condition is $\partial\lambda/\partial y=\partial\mu/\partial y=0$; the second is $\partial v/\partial y=0$. The latter is a little more symmetric and converges faster, but both produce near-identical flow fields except over the last few computing planes. If, far downstream, there is a uniform swirling flow pattern, repeated at all subsequent planes of cross section, both boundary conditions are correct.

Method of Solution of the Equations

The extent to which the two-variable procedure may be followed has now been reached. Examination of the equations indicates the following:

(1)   Bernoulli's equation (eq. (11)). Given values for λ and μ throughout the flow field, P may be calculated from the starting values at the inlet cross section.

(2)   The momentum equations (eqs. (15) and (16)). Either of these may be integrated for v when λ, μ, and their derivatives are known.

(3)   The continuity equation (eq. (7)). Assuming that v is given throughout the flow field, this equation may be integrated for λ if μ is known or for μ if λ is known.

These integrations will be for *linear, first-order, ordinary differential equations* with *nonconstant coefficients*. Bernoulli's equation is written

$DP/Dt = 0$ along a streamline to fit this classification. It is inconvenient, though, to have two equations, either of which may be solved explicitly for v, and only one equation to solve for both λ and μ. Two methods of solution have been tried.

First Method of Solution

A pattern similar to that proposed by Wu (ref. 4) was followed. Separate sets of two-dimensional solutions were sought, with an iterative procedure connecting them as shown in figure 2. This did not work. Alternating between one set of two-dimensional solutions and the other is not sufficient to produce convergence since neither solution "realizes" that it is not the same as the other. The information conveyed between the solutions is not sufficient to produce convergence.

Although Wu's proposals differ in that his two-dimensional solutions are calculated on S_1 and S_2 stream surfaces using two stream functions, the method follows the pattern suggested by Wu. A few variations on this method have also been tried, but without success. This suggests that for a method to have any chance of success it must "know" about the "error" or difference between separate two-dimensional solutions, $v^x - v^z$ for example, and act on this information until the error is reduced to zero.

Second Method of Solution

Let the result of integrating equation (15) in the x-direction be v^x, and the result of integrating equation (16) in the z-direction be v^z. The error $v^x - v^z$ is related to a static pressure difference by equation (12). Physically, this pressure difference will change the curvature of the streamlines, and thus λ and μ must be influenced by $v^x - v^z$. The best choice seems to be the replacement of the continuity equation (eq. (7)) by the two equations,

$$\frac{\partial}{\partial x}\left[\left(1+\frac{x}{R_m}\right)\lambda v^x\right] + \frac{\partial v^x}{\partial y} + \left(1+\frac{x}{R_m}\right)\frac{\partial}{\partial z}(\mu v^z) = \beta(v^x - v^z) \qquad (17)$$

and

$$\frac{\partial}{\partial x}\left[\left(1+\frac{x}{R_m}\right)\lambda v^x\right] + \frac{\partial v^z}{\partial y} + \left(1+\frac{x}{R_m}\right)\frac{\partial}{\partial z}(\mu v^z) = \beta(v^z - v^x) \qquad (18)$$

where β is a constant. In these equations, the right-hand sides represent source/sink terms and each reduces to the continuity equation (eq. (7)) when $v^x = v^z$. One additional equation and one additional unknown have been introduced and now (17) is integrated directly for λ, (18) for μ, (15) for v^x, (16) for v^z, and (11) for P. In (17) and (18), v^x and v^z are selected appropriately to make the boundary conditions for the velocity

integrations explicit. The essential feature of these equations is that when $v^x = v^z$ they reduce to the physically correct equations.

START
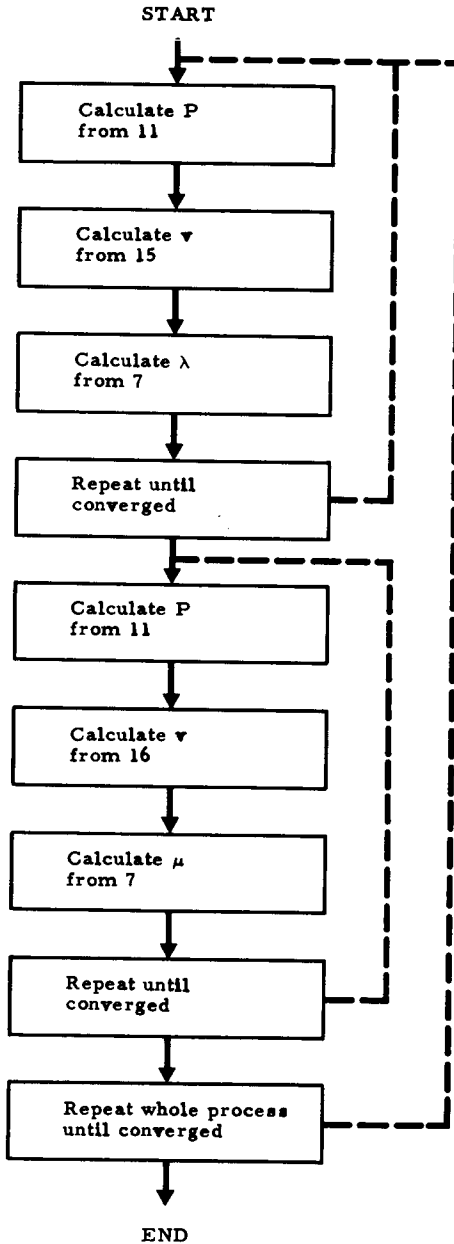
FIGURE 2.—*Iterative procedure for Method 1.*

Revised Boundary Conditions

Although the boundary conditions described are sufficient to determine a solution, they do not lend themselves to an easy integration of the equations in their present form. First, (17) and (18) are first-order equations; each requires only one boundary condition for λ and μ and there are two for each. Second, (15) and (16) also require one boundary condition each for v^x and v^z and there are none. This matter is rectified by the requirements that two boundary conditions may be satisfied by each of the first-order pseudo-continuity equations (eqs. (17) and (18)). These requirements are found as follows. Equations (17) and (18) are integrated, first with respect to x from $x = -\frac{1}{2}X$ across the duct to $x = \frac{1}{2}X$ and then with respect to y from $y = 0$ at the inlet to some station y', to yield

$$\int_{-1/2X}^{1/2X} v^x \, dx + \int_0^{y'} \int_{-1/2X}^{1/2X} \left(1 + \frac{x}{R_m}\right) \frac{\partial}{\partial z} (\mu v^z) \, dx \, dy = 0 \qquad (19)$$

and

$$\int_{-1/2X}^{1/2X} v^z \, dx + \int_0^{y'} \int_{-1/2X}^{1/2X} \left(1 + \frac{x}{R_m}\right) \frac{\partial}{\partial z} (\mu v^z) \, dx \, dy = 0 \qquad (20)$$

where the $\beta(v^x - v^z)$ terms have been omitted, and the boundary conditions $\lambda = 0$ at $x = \pm \frac{1}{2}X$ have been incorporated. Alternatively, a repeat condition, $\lambda(-\frac{1}{2}X, y, z) = \lambda(\frac{1}{2}X, y, z)$ and $v^x(-\frac{1}{2}X, y, z) = v^x(\frac{1}{2}X, y, z)$, yields the same results. The requirement (19) is used as a boundary condition for equation (15). The procedure is repeated with the roles of x and z interchanged to obtain a similar requirement for the other pseudo-continuity equation and a boundary condition for (16).

In general, sets of coupled partial differential equations cannot be put into explicit form, so it is necessary to select one variable in an equation and guess or assume values for all others. Each of the variables must take its turn as the unknown in one of the equations. When all variables have been found, the equations are solved again and this iterative procedure is continued until convergence is obtained.

Iterative Scheme

Figure 3 shows the iterative scheme. Each block represents the integration of the appropriate equation for the unknown variable throughout the entire flow field. In each integration, the most up-to-date values are used for all other variables. This scheme is chosen for its simplicity and because it also simplifies the boundary conditions of (19) and (20). Between the calculation of μ and the next calculation of λ, v^z remains unchanged; hence, on subtracting equations (19) and (20)

$$\int_{-1/2X}^{1/2X} v^x \, dx = \int_{-1/2X}^{1/2X} v^z \, dx \qquad (21)$$

This is the boundary condition used for v^x. Similarly, the boundary condition for v^z is

$$\int_{-1/2Z}^{1/2Z} v^z \, dz = \int_{-1/2Z}^{1/2Z} v^x \, dz \qquad (22)$$

The right-hand sides of these equations are known from previous calculations.

START

Bernoulli
P from 11

First Momentum
v^x from 15

First Pseudo-Continuity
λ from 17

Second Momentum
v^z from 16

Second Pseudo-Continuity
μ from 18

Test   ($v^x - v^z$)

Converged

END
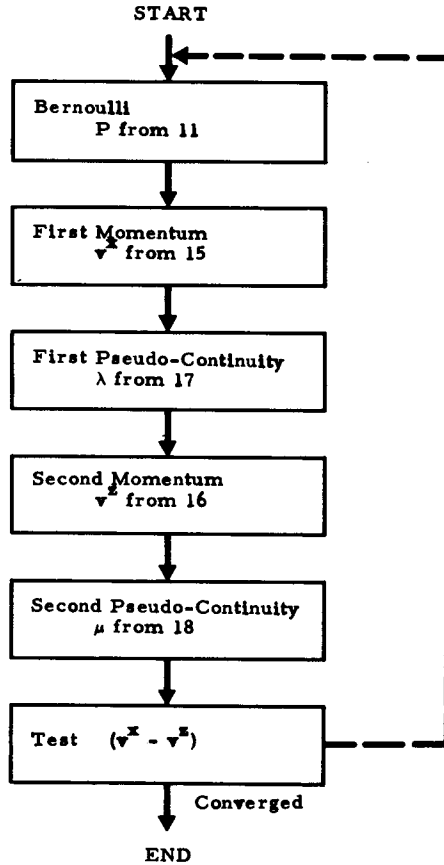
FIGURE   3.—*Iterative   procedure   for
Method 2.*

Uniqueness

These boundary conditions for the velocity are not of a familiar type, and the existence of a unique solution must be explored. Equation (15) is like the equation

$$\frac{d}{dx} v^2 = v^2 g(x) + f(x) \tag{23}$$

A solution is sought, subject to the condition

$$\int_0^1 v \, dx = Q \tag{24}$$

If two solutions, v_1 and v_2, exist then

$$\frac{d}{dx} (v_1{}^2 - v_2{}^2) = (v_1{}^2 - v_2{}^2) \, g(x) \tag{25}$$

subject to

$$\int_0^1 (v_1 - v_2) = 0 \tag{26}$$

The solution of (25) is

$$v_1{}^2 - v_2{}^2 = E \exp \left(\int_0^x g(s) \, ds \right) \tag{27}$$

where E is determined by (26) as follows

$$E \int_0^1 \frac{\exp \left(\int_0^x g(s) \, ds \right)}{v_1 + v_2} \, dx = 0 \tag{28}$$

The further restriction that $v \geq 0$ is necessary for uniqueness. Now, the integrand of (28) is always positive; whence $E = 0$ and $v_1 = v_2$.

Stability

Theoretically, it is only possible to perform a stability analysis for trivial flows where the total pressure is constant, but the resulting criterion is found to have general application. A straight flow without shear is considered, where $v^x = v^z = V$ and $\lambda = \mu = 0$ is the required solution. Small perturbations from this trivial solution are examined and the following stability criterion is obtained

$$\left\{ 1 - r \left[1 + 2 \left(0.63 \frac{X}{\Delta y} \right)^2 \right] \right\}^2 + \left[\frac{3}{\pi} \left(0.63 \frac{X}{\Delta y} \right)^2 r\beta \right]^2 < 1 \tag{29}$$

where X is the duct width, Δy is the grid spacing in the y direction, and r is the relaxation factor on the velocity.

A computer program has been written in FORTRAN IV to solve the problem as outlined. An experiment with a 5-inch by 5-inch 90° bend on a 15-inch mean radius, where the velocity varied across the duct from about 30 feet/second to 80 feet/second at inlet, was simulated. The results, in the form of P_0 contours, are presented for comparison with experiment. The small discrepancies can be accounted for by the presence and separation of the boundary layer. Otherwise, an adequate prediction of the flow is obtained.

Comparison With Experiment

Numerical computations have been carried out for the experiments of Joy (ref. 3) for ducts of rectangular cross section bending through 90° and subject to substantial inlet total head variations across the duct. A comparison has also been made with ducts of circular cross section (Eichenburger reported in ref. 5). The theory presented in this paper is directly applicable to the rectangular duct but requires modification to the circular geometry although the equations are of a similar form.

In figure 4 the total pressure contours at inlet to the duct are presented. In figures 5, 6, and 7 the computed contours are compared with experiment at three stations down the duct.

Station 1	6 inches upstream of the bend
Station 2	30° of turning
Station 3	60° of turning
Station 4	90° of turning

The duct is 5 inches by 10 inches in cross section with a mean radius of 15 inches. For consistency with Joy, the total pressure contours are labelled as velocity contours computed on the assumption of constant static pressure. Similar comparisons are shown for the circular-cross-sectioned duct in figures 8, 9, and 10. The duct is of 6 inches diameter and 30 inches mean radius.

In general, the experimental contours are predicted by the theory. For the circular duct, the agreement is particularly good except in the immediate vicinity of the wall where the viscous forces in the boundary layer are dominant, causing reductions in total pressure. The discrepancies in predictions for the rectangular duct near the inside of the bend are probably due to the occurrence of separation of the boundary layer near Station 3.

A measure of the convergence of the numerical procedure for the rectangular bend is presented in figure 11 showing good convergence after 58 cycles. This procedure took 14 minutes on an IBM 360/65.

LIST OF SYMBOLS

p Static pressure

P_0 Total or stagnation pressure

u, v, w Velocity components

x, y, z Coordinates

β Strength of source/sink distribution

λ, μ Flow directions as defined

ρ Density

15″ x 90° BEND

STATION I - LOOKING UPSTREAM

VELOCITY CONTOURS F.P.S.
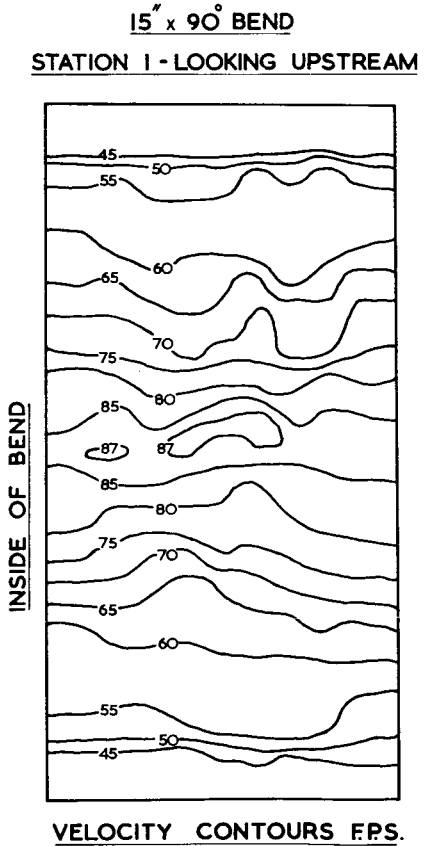
FIGURE 4.—*Velocity contours in rectangular duct.*
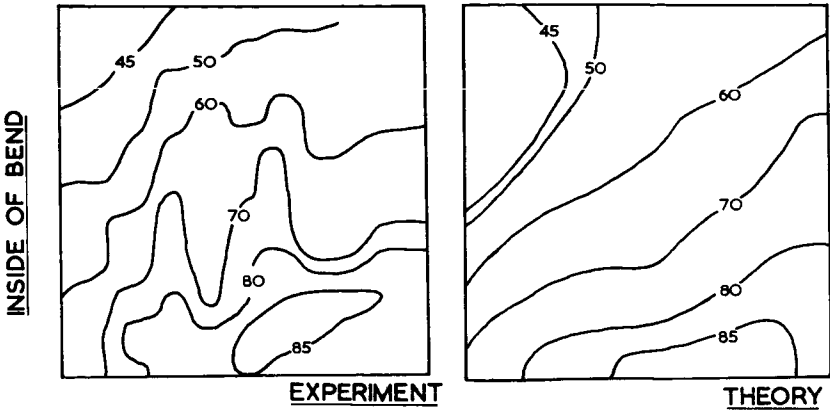
FIGURE 5.—*Velocity contours in rectangular duct; comparison between theory and experiment.*

FIGURE 6.—*Velocity contours in rectangular duct; comparison between theory and experiment.*

15″ x 90° BEND

STATION 4 - LOOKING UPSTREAM
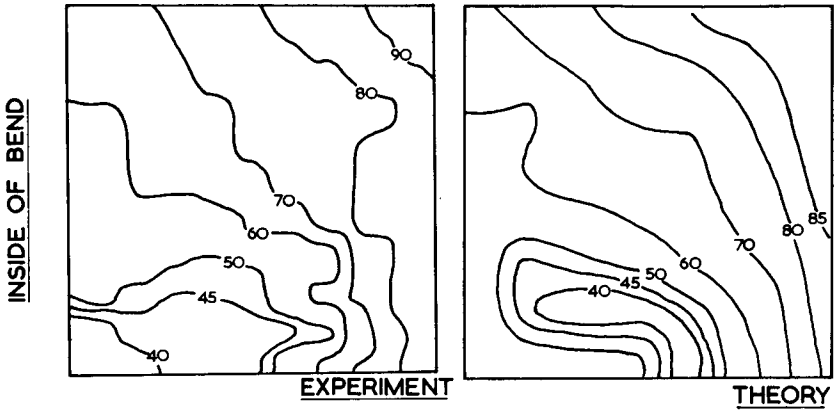
FIGURE 7.—*Velocity contours in rectangular duct; comparison between theory and experiment.*

Total pressure Contours, due to EICHENBURGER, in a 6-inch-diameter circular duct, bent on a mean radius of 30 inches.
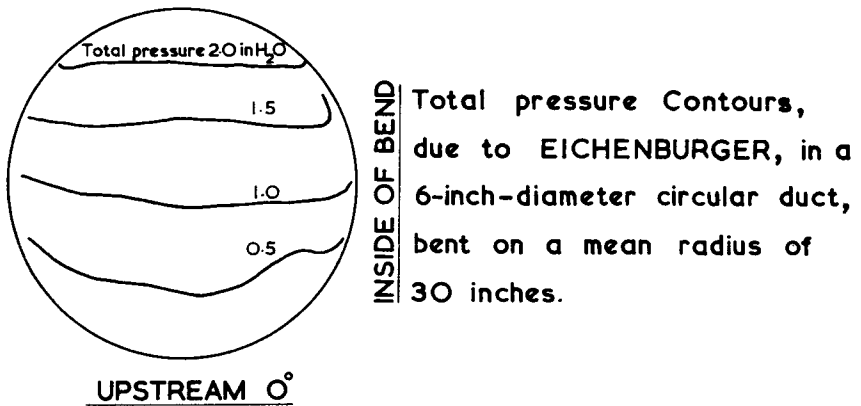
FIGURE 8.—*Total pressure contours in circular duct.*
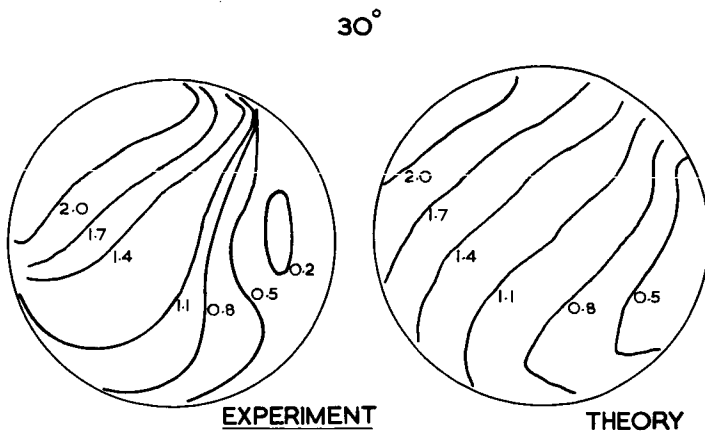
FIGURE 9.—*Total pressure contours in circular duct; comparison between theory and experiment.*
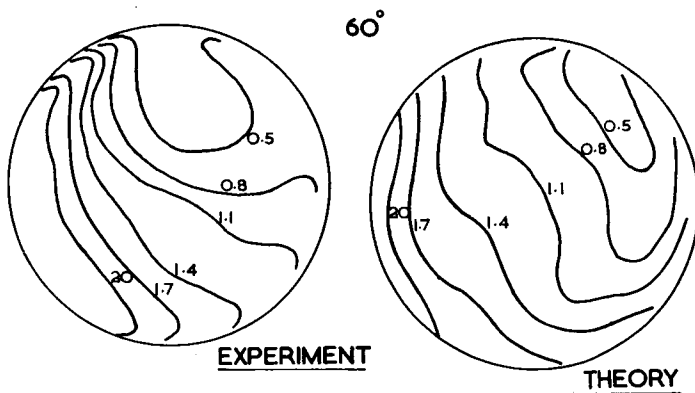
FIGURE 10.—*Total pressure contours in circular duct; comparison between theory and experiment.*

FIGURE 11.—*Convergence of computing scheme.*
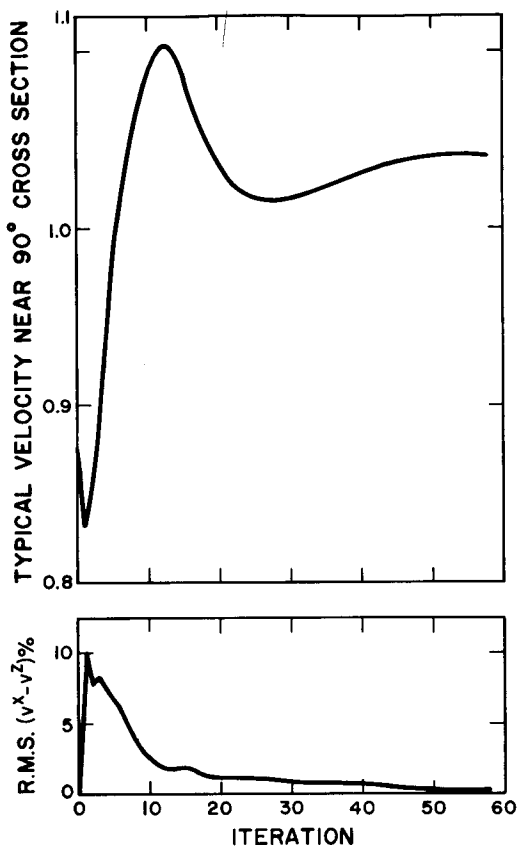
REFERENCES

1. SMITH, L. H., The Radial-Equilibrium Equation of Turbomachinery. *Trans. ASME, J. Eng. Power*, January 1966.
2. SILVESTER, M. E., AND R. HETHERINGTON, Three-Dimensional Compressible Flow Through Axial Flow Turbomachines. *Numerical Analysis: An Introduction*, J. Walsh, ed., Academic Press, 1966.
3. JOY, W., *Experimental Investigation of Shear Flow in Rectangular Bends*. M.S. thesis, M.I.T., 1950.
4. WU, C. H., *A General Theory of Three-Dimensional Flow in Subsonic Turbomachines of Axial, Radial and Mixed Flow Types*. NACA TN 2604, 1952.
5 HAWTHORNE, W. R., Secondary Circulation in Fluid Flow. *Proc. Roy. Soc. London*, Vol. 206, 1951, pp. 374–387.

DISCUSSION

H. MARSH (Cambridge University): The authors have successfully solved a major problem in the calculation of internal flows, namely the three-dimensional flow in a duct. Until recently, it has not been possible to solve this problem due to the lack of adequate computing facilities. It would be interesting to know the computer storage requirements for this program.

Two methods of solution have been examined, but only the successful second method is described in detail. The first method is similar to that proposed by Wu (ref. 4). Until now, this has been considered a viable method for calculating the full three-dimensional flow field. The authors have investigated this technique and have found that they could not obtain convergence. This negative result is extremely important and it deserves a more detailed discussion. Smith (ref. D–1) has described the methods which are available for calculating the two separate two-dimensional flow fields. Until now, it has been assumed that by alternating between the two solutions, the full three-dimensional flow field might be calculated. It would be helpful if the authors would give more details of the basis for their conclusion that the first method of solution does not work.

In the second method of solution, the error $v^x - v^z$ is related to a static pressure difference, but it is not clear why this term should have any physical significance. The replacement of the continuity equation by two equations with source/sink terms is a numerical technique which is used in order to obtain a convergent solution. It is therefore unlikely that the intermediate values of the error $v^x - v^z$ have any physical meaning.

In the derivation of the boundary conditions, the authors have omitted the source/sink term but have not discussed this point. Perhaps they would outline their argument for neglecting these terms. It is possible to argue that any convenient boundary condition can be used, provided that it approaches the true boundary condition as the solution converges.

This is a major contribution to methods of flow calculation and the authors must be congratulated on their presentation in this paper. If this work can be extended to include compressibility, then it would provide a single comprehensive technique for calculating inviscid three-dimensional duct flows.

W. R. HAWTHORNE (Cambridge University): I agree with what Mr. Stuart says. I think the work of Rowe (ref. D–2) should be referred

to in this excellent paper which seems to me to be a substantial break-through on three-dimensional and secondary flow calculations. But I also want to raise the question of getting the right downstream boundary conditions. It isn't clear from what the author was saying how and where the boundary conditions were established. Were they established at 30°, 40°, or down the bend? In one case, he showed a section 1 foot downstream from the bend. How far downstream could you go before you get the right downstream conditions?

STUART AND HETHERINGTON (authors): In reply to H. Marsh, we would like to state the following:

(1)   The computations were performed on an IBM 360/65 and re-quired between 120 000 and 180 000 bytes (depending on whether the program was overlayed or not). Typical execution times were 10 to 14 minutes CPU.

(2)   The conclusion that simple alternation between two separate two-dimensional solutions does not produce the required three-dimen-sional flow field is based on our failure to make such methods produce identical fields for the axial velocity from both two-dimensional solutions, in the absence of the $\beta(v^x - v^z)$ terms in equations (17) and (18). For test computations with $\beta = 0$, convergence has not been obtained, and over a considerable portion of the flow field (about half), near the start of the bend, the secondary flow turned in the wrong direction. This even propagated upstream where no secondary flow is to be expected.

(3)   We agree that physically no terms $\beta(v^x - v^z)$ exist. The argument for the use of such a term as a numerical device is as follows: Physically, fluid will tend to flow from *high* pressure toward *low* pressure regions until the pressure gradient is balanced by acceleration. Now, an imbalance may exist between the pressure gradient of one two-dimensional solution and the acceleration or curvature terms of the other (since these balance their own pressure gradient, which is not necessarily identical to that of the first solution). This imbalance between respective pressure gradients is related to $v^x - v^z$, which term or "error" is used to change λ and μ ac-cordingly in the psendo-continuity equations (17) and (18).

(4)   The neglect of some terms $\beta(v^x - v^z)$ in the derivation of the revised boundary conditions is justified as follows: In practice, the pseudo-continuity equations (17) and (18) are solved with additional source and sink terms $S^x(y,z)$ and $S^z(x,y)$ to allow for the effect of the terms omitted. Now, it must be shown that these terms vanish when convergence is obtained. If the two solutions v^x and v^z converge (remember that these are both the axial velocity, and *not* components in the x and z directions), then subtracting equation (17) from equation (18) yields, at most

$$S^x(y,z) = S^z(x,y) = f(y)$$

Integrating equation (17) or (18) over a plane of cross section yields

$$f(y) \int dx \, dz = \frac{dQ}{dy}$$

where Q is the mass flow. Since Q is constant, $f(y) = 0 = S^x = S^z$.

(5)   In its present form, the method has been extended to compressible flows (Mach number less than 0.98) and the computer program can handle the following problems:

(a)   Bent rectangular ducts
(b)   Bent circular ducts, including S-bends
(c)   Three-dimensional flow through a turbomachinery blade passage specified by random points, including rotors.

Arbitrary values for total temperature, total pressure, and static pressure, varying across the inlet section may be specified as input data to the program. Future work in the Department of Mathematics at the University of Aston will attempt to extend the method further, to include viscous and turbulent flows.

As regards the right boundary conditions mentioned by Sir William Hawthorne, we would like to offer the following reply.

The computing mesh is usually extended two or three planes further downstream of the region of interest (there being expense involved in using too many), but from the calculations we have done, the condition downstream does not have much effect two or three planes upstream (i.e., about three pipe diameters) of where the downstream boundary condition is applied. The flow fields for the two different downstream boundary conditions described were within 0.1 percent of being identical two planes upstream of where the conditions were established.

REFERENCES

D-1. SMITH, D. J. L., Computer Solutions of Wu's Equations for the Compressible Flow Through Turbomachines. In *Fluid Mechanics and Design of Turbomachinery*, Int. Symp., Penn. State U., September 1970. NASA SP-304, 1973.
D-2. ROWE, M., Measurements and Computation of Flow in Pipe Bends. *J. Fluid Mech.*, Vol. 43, Part 4, 1970.

PRECEDING PAGE BLANK NOT FILMED

Three-Dimensional Flow in Transonic Axial Compressor Blade Rows[1]

J. E. McCune

Massachusetts Institute of Technology

Olufemi Okurounmu

University of Lagos
Lagos, Nigeria

Recent developments in the three-dimensional aerodynamic theory of inviscid flow in transonic axial compressors are reviewed briefly. Emphasis is placed on the newly completed lifting surface theory of a transonic ducted rotor. The relationship between the lifting surface theory and axisymmetric through-flow theories of turbomachines is illustrated; a few examples of the additional information obtainable from the new theory are then given. Quasi-two-dimensional cascade theory can also be extracted from the present analysis and the relevance of cascade theory to the actual three-dimensional problem assessed. Details are reported elsewhere, but some of the qualitative conclusions are discussed here. Even moderate departure from uniform spanwise loading of the rotor blades, for example, leads to a rather profound influence of the downstream wakes, suggesting the need for considerable care in applying cascade data on a direct quasi-two-dimensional basis.

The inviscid, three-dimensional, compressible flow through an axial compressor rotor or ducted fan can be described in terms of the perturbation of the incoming flow by the rotor and its wake. If the incoming flow is sufficiently uniform and regular, and if stator interference can be neglected as a first approximation, then the flow is steady in coordinates fixed in the rotor. If, moreover, the perturbations induced by the rotor are "small" they can be described by a velocity potential which satisfies the convected wave equation.

For steady flow in rotor coordinates, when the relative Mach number is everywhere small, the governing equation for the velocity potential reduces to Laplace's equation. In this paper, however, we will be concerned with transonic rotors (i.e., rotors operating with subsonic axial Mach numbers), while the relative Mach numbers at the tip may be supersonic. The relative Mach number at the hub is usually subsonic and, therefore, the flow will generally be of a mixed type. The governing (linear) equation changes from elliptic to hyperbolic type at the "sonic cylinder," $r = r_s$, where $\omega^2 r_s^2 + U^2 = a^2$. Because of three-dimensional effects, however, the linear theory does not exhibit the degeneracy for relative Mach numbers approaching unity which occurs in two-dimensional theory.

The coordinate system we use in this paper is fixed in the rotor (fig. 1); ω is the angular velocity of the rotor, U the (purely axial) velocity far upstream, a the (undisturbed) speed of sound and r the radius; x is the axial coordinate, θ the azimuthal. The corresponding dimensionless variables are $(z,\theta,\sigma) \equiv (\omega x/U, \theta, \omega r/U)$.

In this paper we will be concerned primarily with the lifting problem. The thickness problem was treated earlier (see refs. 1 and 2). In those papers, source-type singular solutions (B radial source "spikes", where B is the number of blades in the rotor) were constructed by superposition of the acoustic eigenmodes of the system in a straight annular duct of infinite extent. These source spikes, of arbitrary strength, $Q(r)$, were then
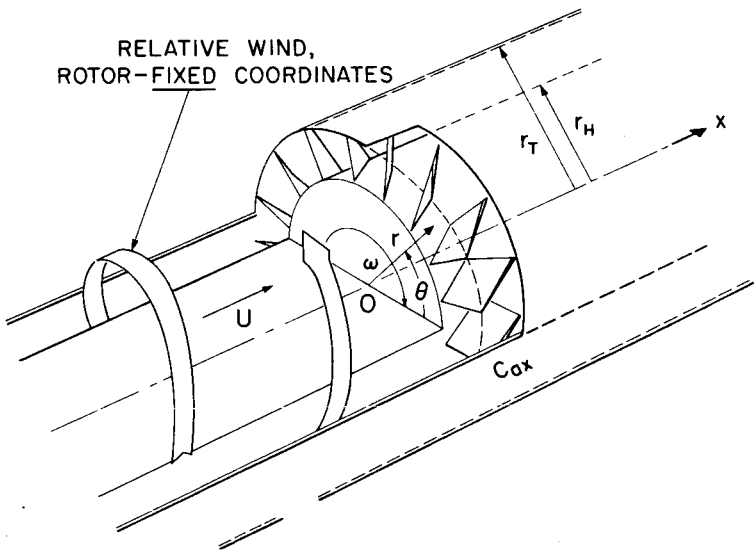

FIGURE 1.—*Geometry and coordinate system fixed in rotor. ω is the angular speed of the rotor relative to the shroud.*

distributed over helical surfaces of finite chord approximating the blades, thus representing blades of arbitrary thickness distribution (with the limitation, of course, that the thickness-to-chord ratio remain small). The camber line of the blades was left free in that study so that the "rotor" produced no lift and hence no positive work. Attention was thus focused on the effects of blade thickness in three dimensions.

The conditions under which quasi-two-dimensional cascade theory could be recovered from the three-dimensional theory were delineated in reference 1, while it was shown in reference 2 that large departures from quasi-two-dimensionality are to be expected in the transonic regime because of an acoustic resonance of certain eigenmodes. It was also shown that the wave drag due to thickness should be considerably smaller than that corresponding to quasi-two-dimensional (strip) theory.

Reference 3 describes experiments on a "free-wheeling" transonic rotor undertaken in part to verify the latter theoretical result. In this regard, the experiment was somewhat inconclusive, partly due to the difficulty of identifying and separating out the various types of drag and/or losses and partly due to the fact that any actual (rigid) rotor, of course, produces lift, varying from hub to tip. For a free-wheeling rotor (zero torque input) the result is that vorticity is shed downstream, adding substantially to the drag.

In order to complete the three-dimensional potential theory, the basis elements of the theoretical *lifting problem* were set up in reference 3. Following the general procedure of superposing the appropriate eigenmodes to construct singular (Green's function) solutions, B bound *vortex* spikes were constructed, having arbitrary strength $\Gamma(r)$. (The method is almost identical to that used in ref. 4, except that a finite hub-to-tip ratio was included and an important error occurring in ref. 4 was removed.)

The most important new feature of the lifting problem, relative to the thickness problem, is the necessity of including the downstream wakes of shed vorticity (one helical wake for each blade) with strength proportional to $d\Gamma/dr$, the rate of change of bound circulation along the span. This is done by a slight modification of the method of Reissner (ref. 5), to allow for the presence of the hub and shroud. Thus, a "wake potential" is included in the downstream flow, added to the acoustic eigenmodes, and construction of the bound vortices at the blades proceeds as before, with the wakes now included. It is interesting to observe that the wakes themselves excite acoustic modes, except when $\Gamma(r) = $ constant.

The acoustic eigenmodes mentioned above are versions of the familiar "spinning" modes associated with cylindrical geometry (refs. 6 and 7). If the relative Mach number at the tip exceeds unity, some of these modes propagate undiminished in strength (in the inviscid, linear theory) upstream and downstream, while the remaining modes die out exponentially at large distances from the rotor. The propagating modes are said

to be above "cut-off"; modes near cut-off can set up the acoustic reso-
nances mentioned above. One effect of such resonances is to create a
significant spanwise flow, yielding strong communication between hub and
tip. Under these conditions (which require supersonic tip Mach numbers),
a *hub* section with a subsonic relative Mach number can nevertheless
have a pressure distribution over the blade which is more typical of
supersonic flow than subsonic flow (refs. 1, 2, and 8).

In reference 9, the lifting theory was refined and extended. In that
paper, the blades were characterized by their total bound vorticity,
$\Gamma(r)$, and the first-order static pressure rise across the rotor, the turning
angles, the torque required, etc., were determined as functions of Γ. For
example, the first-order static pressure rise was found to be

$$C_{p_\infty} \equiv \frac{\langle p_\infty \rangle - \langle p_{-\infty} \rangle}{\rho_{-\infty} U^2/2} = -\frac{2\sigma_T}{\beta^2}\left(\frac{2}{1-h^2}\int_h^1 \eta \, d\eta \, \frac{\Gamma(\eta)}{UL_T}\right) \equiv \frac{-2\sigma_T}{\beta^2}\frac{\overline{\Gamma}}{UL_T} \quad (1)$$

where $\eta \equiv r/r_T = \sigma/\sigma_T$, $h = r_H/r_T$, $< >$ denotes the azimuthal average of a
given quantity, $\beta^2 \equiv 1 - U^2/a^2 \equiv 1 - M^2$, and $L_T \equiv 2\pi r_T/B$, the blade
spacing. The subscripts T and H denote tip and hub, respectively. The
sign convention on Γ is such that it is negative for lifting blades. The
corresponding torque required, to first order, is

$$T^{(1)} = -\rho_{-\infty} U^2 r_T^2 B \int_h^1 \eta \, d\eta \, \Gamma \quad (2)$$

By extending these calculations consistently to second order (a procedure
analogous to the computation of induced drag and wave drag in ordinary
wing theory), the losses due to energy stored in the wakes of shed vorticity
(when $\Gamma(r) \neq$ constant) as well as those due to acoustic radiation (for
supersonic relative tip Mach numbers) were estimated. These are pre-
sented in figure 2 for a typical rotor ($B = 40$, $h = 0.8$), in terms of a
dimensionless efficiency decrement. Since these results are essentially
"integral relationships" (i.e., obtained from momentum balances, etc.)
we expect them to carry over without change to the lifting surface theory,
which will be the main subject of our discussion. Despite the linearizing
assumptions inherent to the theory, we estimate that these results will be
accurate up to static pressure ratios across the (single) rotor of about 1.3
(see eq. (1)). It should be noted that the "concentrated bound vortex
solution" of reference 9 is *not* a lifting-line theory in the sense of Prandtl,
since no quasi-two-dimensional assumptions were used.

The lifting *surface* theory, in analogy to the procedures described in
reference 1, can be constructed from the concentrated bound vortex
solution by distributing the bound vorticity, with its associated wakes,
over helical surfaces representing the blades. Details will be made avail-
able shortly in reference 10. In the next sections, we describe the salient
features of the theory and some of its more interesting results.

B = 40, h = 0.8, C_{ax}/L_T = 1.06

$\frac{\Gamma}{UL_T}$ = a + bη, D = $(\Gamma_T - \Gamma_H)/\bar{\Gamma}$

FOR M = 0.6 σ_s = 1.333

M = 0.5 σ_s = 1.732
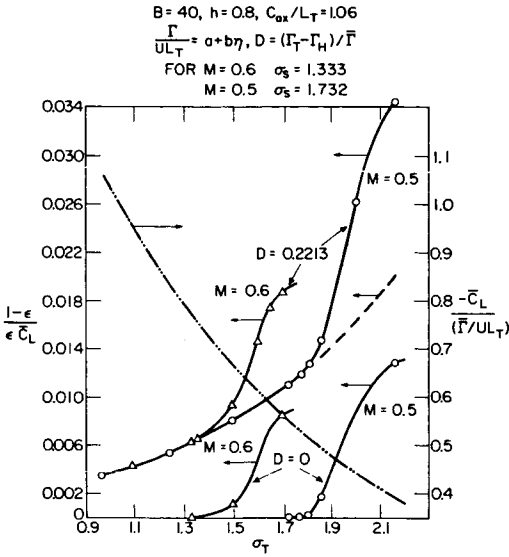
FIGURE 2.—*Losses for a typical rotor configuration as caused by (1) energy stored in wakes (D ≠ 0) and (2) acoustic radiation ($\sigma_T > \sigma_s$). Solid lines (left-hand scale) give values of the efficiency decrement, normalized to $\bar{C}_L$, an average (over the span) sectional lift coefficient. The relation between $\bar{C}_L$ and $\bar{\Gamma}$, defined in the text, is shown, for this rotor geometry, by the broken line (right-hand scale). The sharp increase in losses due to acoustic radiation as σ_T exceeds σ_s is readily observable for both D = 0 and D = 0.2213. In the latter case, the efficiency decrement associated with non-uniform loading is comparable to the acoustic radiation loss. (Figure taken from ref. 9.)*

LIFTING SURFACE THEORY

The velocity potential obtained by distributing bound vorticity, in the manner described, over the helical surfaces representing the rotor blades can be written

$$\phi(x,\theta,r) = \frac{B}{2\pi\beta^2} \left(\int_0^{\hat{x}} \delta\phi^d \, d\xi + \int_{\hat{x}}^{c_{ax}^{(max)}} \delta\phi^u \, d\xi \right) \tag{3}$$

where ξ labels the *axial* location of the bound vortex filaments while

$$\hat{x} \equiv x \qquad\qquad 0 \le x \le c_{ax}^{(max)}$$

$$\hat{x} \equiv 0 \qquad\qquad x \le 0$$

$$\hat{x} \equiv c_{ax}^{(max)} \qquad\qquad x \ge c_{ax}^{(max)}$$

If we denote by $\varphi(r) \equiv \tan^{-1}\sigma = \tan^{-1}(\omega r/U)$ the complement of the stagger angle at each radius, the axial projection of the local chord is $c_{ax}(r) = c \cos\varphi$, and in (3) $c_{ax}^{(max)}$ is the maximum of this quantity along the span. The elemental potentials $\delta\phi^u$ and $\delta\phi^d$ are, respectively, the upstream and downstream velocity potentials associated with B radial strips of concentrated bound vorticity located on the helical surfaces $x = \xi$, $\theta = \omega\xi/U + l\pi/B$, $l = \pm1, \pm3, \pm5, \ldots$. Each strip has elementary chord $d\xi/\cos\varphi$ and strength $\gamma(\eta,\xi)\, d\xi/\cos\varphi$. Their associated wakes of free vorticity, proportional to $\partial/\partial\eta(\gamma/\cos\varphi)$, are included in $\delta\phi^d$. The

total bound vorticity (per blade) at each radial station is the local blade circulation:

$$\Gamma(r) = \Gamma(\eta r_T) = \int_0^{c_{ax}(r)} \gamma(\eta,\xi)\ d\xi/\cos\varphi \tag{4}$$

The elemental potentials occurring in (3) can be expressed as follows (ref. 10; real part implied)

$$\delta\phi^u(z,\theta,\sigma;\xi) = -\sum_{k=1}^{\infty} \frac{\gamma_{0k}(\xi)}{2\lambda_{0k}} \exp\left[\lambda_{0k}\left(z-\frac{\omega\xi}{U}\right)\right] R_0\left(\kappa_{0k}\frac{\sigma}{\sigma_T}\right)$$

$$+ \sum_{n=1}^{\infty}\sum_{k=1}^{\infty}\left\{(-1)^n \frac{h_{nk}(\xi)}{\lambda_{nk}} + i\frac{\beta^2(-1)^n}{nB}\left[h_{nk}(\xi)+\gamma_{nk}(\xi)\right]\right\}$$

$$\times \exp\left[inB\left(\theta-\frac{\omega\xi}{U}\right)\right]$$

$$\times \exp\left[\left(\frac{inBM^2}{\beta^2}+\lambda_{nk}\right)\left(z-\frac{\omega\xi}{U}\right)\right] R_{nB}\left(\kappa_{nk}\frac{\sigma}{\sigma_T}\right) \tag{5}$$

$$\delta\phi^d(z,\theta,\sigma;\xi) = \bar{\gamma}(\xi)\left(z-\frac{\omega\xi}{U}\right) + \beta^2 \frac{\gamma(\eta,\xi)}{\cos\varphi(\sigma)}\zeta_l$$

$$+ \sum_{n=1}^{\infty} \frac{2i\beta^2}{nB}(-1)^n\chi_n(\eta,\xi)\ \exp(inB\zeta)$$

$$- \sum_{k=1}^{\infty} \frac{\gamma_{0k}(\xi)}{2\lambda_{0k}} \exp\left[-\lambda_{0k}\left(z-\frac{\omega\xi}{U}\right)\right] R_0\left(\kappa_{0k}\frac{\sigma}{\sigma_T}\right)$$

$$+ \sum_{n=1}^{\infty}\sum_{k=1}^{\infty}\left\{\frac{(-1)^n h_{nk}(\xi)}{\lambda_{nk}} - i\beta^2\frac{(-1)^n}{nB}\left[h_{nk}(\xi)+\gamma_{nk}(\xi)\right]\right\}$$

$$\times \exp\left[inB\left(\theta-\frac{\omega\xi}{U}\right)\right]$$

$$\times \exp\left[\left(\frac{inBM^2}{\beta^2}-\lambda_{nk}\right)\left(z-\frac{\omega\xi}{U}\right)\right] R_{nB}\left(\kappa_{nk}\frac{\sigma}{\sigma_T}\right) \tag{6}$$

In these expressions, the "radial eigenfunctions" $R_{nB}(\kappa_{nk}\sigma/\sigma_T) \equiv R_{nB}(\kappa_{nk}\eta)$ are orthonormal combinations of Bessel and Neumann functions whose

properties, including the radial eigenvalues κ_{nk}, are determined by the requirement of vanishing radial velocity at hub and shroud. Details are available in references 1 and 3. The quantities λ_{nk}, determining the *axial* behavior of the acoustic modes, are given by

$$\lambda_{nk} = \frac{nB}{\beta\sigma_T} \sqrt{\frac{\kappa_{nk}^2}{n^2 B^2} - \frac{\sigma_T^2 M^2}{\beta^2}}$$

$$\left. \begin{array}{c} \\ \\ \\ \\ \\ \end{array} \right\} \qquad (7)$$

$$\lambda_{0k} = \frac{\kappa_{0k}}{\beta\sigma_T}$$

These quantities are either pure real (yielding axial decay) or pure imaginary (yielding propagating, "spinning" modes). Since the κ_{nk} are all greater than $|nB|$ (ref. 11), the latter possibility occurs only if $\sigma_T > M/\beta = \omega r_s/U$, and then only for a finite number of modes at each n; $k = 1, 2, \ldots k_n^*$. The condition $\sigma_T > \sigma_s$ implies supersonic relative Mach numbers at the tip.

In (6), the variable $\zeta \equiv \theta - \omega x/U = \theta - z$ is the helical coordinate used by Reissner (ref. 5) and the (generalized) function ζ_l is a "sawtooth function," the essential properties of which are that $\partial \zeta_l/\partial \theta = 1$, $\partial \zeta_l/\partial z = -1$ *everywhere*, while the function itself is discontinuous (by an amount $\mp 2\pi/B$) at $\zeta = \pm\pi/B, \pm 3\pi/B, \ldots$. The combination of the second and third terms in (6) makes up the wake potential mentioned earlier, representing the free vorticity shed in the wakes and the induced flow between them. The wake functions, $\chi_n(\eta,\xi)$, can be written in terms of modified Bessel functions of the first and second kind:

$$\chi_n(\eta,\xi) \equiv \chi_{nB}(nB\eta\sigma_T,\xi) = \alpha_n(\xi) I_{nB}(nB\sigma) + \beta_n(\xi) K_{nB}(nB\sigma)$$

$$+ I_{nB}(nB\sigma) \int_{\sigma_H}^{\sigma} \frac{d}{d\sigma'} K_{nB}(nB\sigma')\sigma' \frac{\partial}{\partial\sigma'} \left[\frac{\gamma(\sigma'/\sigma_T,\xi)}{\cos\varphi(\sigma')} \right] d\sigma'$$

$$- K_{nB}(nB\sigma) \int_{\sigma_H}^{\sigma} \frac{d}{d\sigma'} I_{nB}(nB\sigma')\sigma' \frac{\partial}{\partial\sigma'} \left[\frac{\gamma(\sigma'/\sigma_T,\xi)}{\cos\varphi(\sigma')} \right] d\sigma' \qquad (8)$$

where $\alpha_n(\xi)$ and $\beta_n(\xi)$ involve definite (radial) integrals over $\partial/\partial\sigma[\gamma(\eta,\xi)/\cos\varphi]$ and depend on the parameters σ_H and σ_T, as well as nB (refs. 3, 5, 9, and 10). Note that each $\chi_n(\eta,\xi)$ vanishes when $\gamma/\cos\varphi$ is independent of σ (or η); i.e., when $\Gamma = $ constant.

The quantities $\bar{\gamma}(\xi)$, $\gamma_{nk}(\xi)$ and $h_{nk}(\xi)$ are the coefficients of expansions of the functions $\gamma(\eta,\xi)/\cos\varphi$ and $\chi_n(\eta,\xi)$ in terms of the orthonormal radial functions $R_{nB}(\kappa_{nk}\eta)$. Thus,

$$
\left.
\begin{aligned}
\frac{\gamma(\eta,\xi)}{\cos\varphi(\eta\sigma_T)} &= \bar{\gamma}(\xi) + \sum_{k=1}^{\infty}\gamma_{0k}(\xi)R_0(\kappa_{0k}\eta) \\[2ex]
\frac{\gamma(\eta,\xi)}{\cos\varphi(\eta\sigma_T)} &= \sum_{k=1}^{\infty}\gamma_{nk}(\xi)R_{nB}(\kappa_{nk}\eta); \quad n>0 \\[2ex]
\chi_n(\eta,\xi) &= \sum_{k=1}^{\infty}h_{nk}(\xi)R_{nB}(\kappa_{nk}\eta)
\end{aligned}
\right\} \tag{9}
$$

The usual Fourier-Bessel formulas for the expansion coefficients apply; for example

$$
\gamma_{nk}(\xi) = \int_{h}^{1} \eta \, d\eta \, \frac{\gamma(\eta,\xi)}{\cos\varphi(\eta\sigma_T)} R_{nB}(\kappa_{nk}\eta)
$$

while

$$
\bar{\gamma}(\xi) = \frac{2}{1-h^2}\int_{h}^{1} \eta \, d\eta \, \frac{\gamma(\eta,\xi)}{\cos\varphi} \tag{10}
$$

Note that

$$
\int_{0}^{c_{ax}^{(\max)}} d\xi\bar{\gamma}(\xi) = \bar{\Gamma}
$$

as defined in equation (1), and that the coefficients $\gamma_{0k}(\xi)$, as well as the $h_{nk}(\xi)$ vanish whenever $\gamma/\cos\varphi$ is independent of radius.

In the special case for which $c_{ax} = $ constant and $\gamma(\eta,\xi)/\cos\varphi$ is factorizable (i.e., $\gamma/\cos\varphi = \Gamma(\eta)g(\xi)$) we have the especially simple relationships, $\gamma_{nk}(\xi) = \Gamma_{nk}g(\xi)$, $h_{nk}(\xi) = H_{nk}g(\xi)$, $\bar{\gamma}(\xi) = \bar{\Gamma}g(\xi)$, where, from (4),

$$
\int_{0}^{c_{ax}} g(\xi) \, d\xi = 1 \tag{11}
$$

Γ_{nk}, H_{nk} and $\bar{\Gamma}$ are then identical to the corresponding quantities occurring in the concentrated bound vortex solution (refs. 9 and 10), in which the blades are characterized by $\Gamma(r)$.

The three-dimensional lifting surface solution, described formally by equations (3) through (10), has the desired property of producing discontinuities (at the helical surfaces representing the blades) of the velocity component parallel to the blade surface. In fact, if we denote this component by $v_{x'}$, the discontinuity in $v_{x'}$ is $-\gamma(\eta,x)$, and the blade loading is $-\rho_{-\infty}U_r\gamma(\eta,x)$, where $U_r \equiv (U^2+\omega^2r^2)^{1/2}$. The detailed proof that (3) with (5) and (6) has this property is available in reference 10. At the same time $v_{y'}$, the velocity component perpendicular to the helix of advance, is *continuous*, and $v_{y'}/U_r$ defines the slope of the blade camber

line (in the absence of thickness effects) for any loading. As is usual in wing theory, if the blade shape is specified and the loading required, the mathematical problem becomes one of inverting an integral equation—in our case an unusually complicated one.

Actually, if one is given a shape for the rotor blades (desired thickness and camber), the thickness problem must be solved first (refs. 1 and 2) since the distribution of sources used to obtain the desired thickness distribution inevitably produces a camber distribution of its own. This "camber due to thickness" must then be included in the distributed vortex problem if one is to obtain the desired overall camber.

The results given in this paper, however, will be restricted to those for the indirect lifting problem: given the loading, and omitting thickness effects, what is the associated camber line of the blades, how does the flow and pressure field develop, and what is the performance of the rotor? The last of these questions has been substantially answered in reference 9, since most performance characteristics calculable in this theory do not depend on the details of the chordwise loading distribution but primarily on $\Gamma(r)$. This is not to say that the chordwise loading distribution is not important; for example, it will affect boundary-layer behavior, stall margins, etc., of the rotor and is of great interest for these and other reasons.

RELATION TO AXISYMMETRIC "THROUGH-FLOW" THEORY

Let us consider first the mean pressure level (i.e., the azimuthal average pressure) developed by the rotor. We have generally, in the strictly linear approximation,

$$\tilde{p} \equiv p - \langle p_{-\infty} \rangle = -\rho_{-\infty} U \sqrt{1+\sigma^2} v_{x'} \tag{12}$$

where

$$v_{x'} = v_x \cos \varphi + v_\theta \sin \varphi$$

$$= \frac{\omega}{U \sqrt{1+\sigma^2}} \left(\frac{\partial \phi}{\partial z} + \frac{\partial \phi}{\partial \theta} \right) \tag{13}$$

Then for any axial station downstream of the rotor $x > c_{ax}^{(max)}$, using (3)–(6) and averaging over θ, we obtain

$$\langle p(x,r) \rangle^d - \langle p_{-\infty} \rangle$$

$$= -\omega \rho_{-\infty} \left\langle \frac{\partial \phi}{\partial z} + \frac{\partial \phi}{\partial \theta} \right\rangle$$

$$= -\rho_{-\infty} \frac{\omega B}{2\pi\beta^2} \left\{ \bar{\Gamma} + \frac{1}{2} \sum_{k=1}^{\infty} \int_0^{c_{\mathrm{ax}}^{(\mathrm{max})}} d\xi \exp \left[-\lambda_{0k} \left(z - \frac{\omega\xi}{U} \right) \right] \gamma_{0k}(\xi) R_0(\kappa_{0k}\eta) \right\}$$

(14)

Upstream of the rotor $(x < 0)$ the corresponding result is

$$\langle p(x,r) \rangle^u - \langle p_{-\infty} \rangle$$

$$= \rho_{-\infty} \frac{\omega B}{4\pi\beta^2} \sum_{k=1}^{\infty} \int_0^{c_{\mathrm{ax}}^{(\mathrm{max})}} d\xi \exp \left[\lambda_{0k} \left(z - \frac{\omega\xi}{U} \right) \right] R_0(\kappa_{0k}\eta) \gamma_{0k}(\xi) \quad (15)$$

If we recall that all γ_{0k}'s are zero when $\gamma/\cos\varphi$ is independent of η (implying "constant work" design, $\Gamma = \text{constant} = \bar{\Gamma}$), we see from (15) that for a constant work rotor, there is no change in *mean* pressure (starting from upstream) until the rotor itself is reached, while from (14) we see, for the same design, that the entire mean static pressure rise is achieved within the rotor passage and the "far-field" value (compare eqs. (14) and (11)) is already attained at $x = c_{\mathrm{ax}}^{(\mathrm{max})}$.

On the other hand, if $\Gamma(r) \neq \text{constant}$, then the γ_{0k}'s do *not* vanish and there is essentially *exponential* approach, away from the rotor, to the respective upstream and downstream values of the mean pressure level. This type of result is typical of axisymmetric theories of axial compressor flows (ref. 12), but the rate of approach is, of course, sensitive to the assumed area distribution of the flow annulus (ref. 13). For the particular case we have considered $(r_H/r_T = \text{constant})$, the "decay length" for approach to the upstream and downstream values is of order $\beta(r_T - r_H)/\pi$ (see eq. (7) and refs. 11 and 12). At large (subsonic) axial Mach numbers, approach to the asymptotic states is very rapid, as expected (ref. 12).

The result (1) or (14) indicates a constant radial static pressure profile far downstream of the rotor, at obvious variance with the need for a radial pressure gradient to balance the centripetal acceleration associated with the induced tangential velocities (see eq. (18)). This is simply a result of the linearization used throughout the present theory (for example, eq. (12)). However, comparisons between appropriate azimuthal averages of the results from the present three-dimensional (but linear) theory and higher-order (but two-dimensional) "actuator disc" results are expected to suggest means of identifying and including the more important nonlinear effects. We have already shown (ref. 9) that the second-order calculations, used in that paper to compute losses, are consistent with "radial equilibrium". It should be possible to include certain nonlinear effects, such as centrifugal effects, consistently in a modified three-dimensional theory. Further work in this direction is underway.

The results (14) and (15) can be understood in terms of the mean (azimuthally averaged) stream-surface deflections associated with non-uniform loading. (Note that the wake functions themselves, depending

only on ζ and η, yield zero first-order pressure perturbations.) If $\Gamma(r)$ increases from hub to tip, more work is done by the rotor at the tip than at the hub. This appears initially (just behind the rotor) as a higher pressure near the tip than at the hub. In fact, using (7) and evaluating (14) for $x \approx c_{ax}^{(max)}$ with the assumption $c_{ax}^{(max)}/r_T \ll 1$, we find, immediately behind the rotor,

$$\langle p(c_{ax},r)\rangle^d - \langle p_{-\infty}\rangle \cong -\rho_{-\infty}\frac{\omega B}{4\pi\beta^2}\left(\Gamma(\eta)+\bar{\Gamma}\right) \tag{16}$$

where we have used the first of equation (9) and also equation (4). The higher (lower) pressure at the tip (hub) must relax to the constant value given by the linear theory far downstream of the rotor. Moreover, the azimuthally averaged flow is effectively subsonic if $M < 1$ (ref. 12). This means contraction of the outermost streamtubes and expansion of those near the hub. The stream surfaces must, therefore, be deflected outwards. In fact, we find

$$\delta(\eta)_{\langle\psi\rangle=\text{const}} \cong \frac{\sigma_T\bar{\Gamma}}{UL_T\eta}\int_h^\eta \eta\,d\eta\left(1-\frac{\Gamma}{\bar{\Gamma}}\right) \tag{17}$$

provided $\Gamma - \bar{\Gamma} \ll \bar{\Gamma}$. These average radial stream-surface deflections are zero, as required, at $\eta = h$ and $\eta = 1$ and are positive if Γ increases radially and negative if Γ decreases radially. There is no (average) streamline deflection if $\Gamma = \text{constant} = \bar{\Gamma}$.

Associated with (14), (15), and (17) are certain azimuthally averaged tangential, axial, and radial velocity profiles. Downstream of the rotor (see also ref. 9), these are given by

$$\langle v_\theta\rangle^d = \frac{B\Gamma(\eta)}{2\pi r} \tag{18}$$

$$\langle v_x\rangle^d = \frac{\omega B}{2\pi U\beta^2}\left\{\bar{\Gamma}-\beta^2\Gamma(\eta)\right.$$

$$\left.+\frac{1}{2}\sum_{k=1}^{\infty}\int_0^{c_{ax}^{(max)}}d\xi\exp\left[-\lambda_{0k}\left(z-\frac{\omega\xi}{U}\right)\right]\gamma_{0k}(\xi)R_0(\kappa_{0k}\eta)\right\}+U \tag{19}$$

$$\langle v_r\rangle^d = \frac{-\omega B}{4\pi\beta U}\sum_{k=1}^{\infty}\int_0^{c_{ax}^{(max)}}d\xi\exp\left[-\lambda_{0k}\left(z-\frac{\omega\xi}{U}\right)\right]\gamma_{0k}(\xi)R_0'(\kappa_{0k}\eta) \tag{20}$$

The actual velocity field derivable from (3)–(6), of course, is curl-free except at the B helical sheets (wakes) of concentrated shed vorticity, this vorticity having strength proportional to $d\Gamma/d\eta$ and being oriented so as to lie in the helical sheets representing the wakes.

By contrast, the vorticity of the (mean) downstream velocity field defined by (18)–(20) is

$$\Omega^{\langle v \rangle} \equiv \text{curl } \langle v \rangle^d = \frac{\Gamma'(\eta)}{L_T r} \left(1, \frac{\omega r}{U}, 0 \right) \tag{21}$$

Thus, since $\Omega_\theta^{\langle v \rangle} / \Omega_x^{\langle v \rangle} = \omega r / U$, an important effect of defining an "equivalent axisymmetric" flow (through averaging the more detailed three-dimensional theory) is to replace the original concentrated vorticity by an equal total amount of vorticity which is, however, distributed uniformly over the flow annulus, yet still oriented along the zeroth-order streamlines. This distributed downstream vorticity is an important feature of axisymmetric through-flow theories (ref. 12); results such as (21), (19) and (14) help to establish connection between the latter theories and that described here.

It should be clear from the preceding that the three-dimensional (but linearized) potential theory contains many important elements of the axisymmetric theories and has, in addition, the capacity to describe azimuthal variations superposed on those results. Some interesting examples of the latter are given in the following section.

THREE-DIMENSIONAL PRESSURE FIELD (LIFTING PROBLEM)

The azimuthally-averaged pressure fields (14) and (15) are the same, regardless of whether the compressor is transonic or not (ref. 12). But the azimuthal *variations* about these mean levels are vastly different, depending on (1) whether or not the tip relative Mach number is supersonic and (2) whether or not the rotor is uniformly loaded (along the blade span).

The latter observation comes from consideration of the conditions under which transonic "acoustic resonance" (see the introduction) can occur for the strictly lifting problem. As mentioned earlier, when $M_{rT}^2 \equiv M^2(1 + \sigma_T^2) > 1$, some of the quantities λ_{nk} (eq. (7)), as determined by the linear inviscid theory, can vanish. A glance at equations (5) and (6) shows that when this happens some of the acoustic eigenmodes can be amplified indefinitely unless the corresponding $h_{nk}(\xi)$ are identically zero. This is the "resonance" to which we have referred. However, we have already noted that the $h_{nk}(\xi)$ are, in fact, zero if the spanwise loading is constant at each ξ. Thus a constant work rotor with similar chordwise loading profiles (i.e., $\gamma(\eta, \xi)/\cos \varphi = \bar{\Gamma} g(\xi)$) excites no transonic resonance. A more general way of saying this is that any (purely lifting) transonic rotor which sheds wakes of free vorticity can excite acoustic resonances of spinning modes and otherwise not. (Finite values of h_{nk}

can be regarded as representing excitation of acoustic modes by the wakes.) Of course, the finite thickness of the blade of any real rotor will always induce transonic resonances (ref. 2).

If transonic resonance is excited, one or several acoustic modes will be singled out and tend to dominate the pressure field, although the (linear) azimuthal average of the pressure fields will vanish. Naturally, the resonant modes do not attain infinite amplitudes; their finite amplitudes are easily predicted by including either viscous effects (as in refs. 1 and 2) or certain nonlinear effects (as in ref. 10) or both. In the following, we present typical numerical results extracted from reference 10; included are pressure-field results for a typical rotor ($B = 40$, $h = 0.8$) operating both subsonically ($M_{rr} = 0.9$) and transonically ($M_{rr} = 1.054$). In reference 10, both a uniformly loaded rotor ($\Gamma = \bar{\Gamma}$) and a rotor with linearly increasing $\Gamma(\eta)$, characterized by an increase of approximately 20 percent in Γ from hub to tip, were analyzed. However, for lack of space we present here only the results for a uniformly loaded rotor. The axial Mach number in the examples discussed is $M = 0.5$. The specific loading distributions used in the calculations were of the factorizable type $\gamma/\cos\varphi = \Gamma(\eta)g(\xi)$, where

$$g(\xi) = \frac{8}{\pi c_{ax}^2} \sqrt{\xi(c_{ax} - \xi)}$$

Note that this chordwise loading distribution is symmetric about the midchord, nonsingular, and satisfies the Kutta condition and the normalization (11).

Our first example (fig. 3) shows the "near field" subsonic upstream pressure fluctuation, at $x/c_{ax} = -0.1$, over an azimuthal period $\Delta\theta = 2\pi/B$ (corresponding to a single blade passage). Five radial stations are indicated. The tip Mach number being 0.9, we have $\sigma_T = 1.46$. The pressure side of the airfoil corresponds to the smaller values of $B\theta/2\pi$. For the solidity noted in figure 3, the projection of the helix of advance forward from $x = 0$ (for which $B\theta/2\pi = \frac{1}{2}$ is the blade leading edge) to $x/c_{ax} = -0.1$ corresponds to $B\theta/2\pi = 0.35$. Note that the high- and low-pressure regions remain relatively well identified just upstream of the airfoil (typical of subsonic flow). The fluctuating signal is superposed on a zero mean pressure level, in agreement with (15) for a uniformly loaded rotor. This pressure signal is almost entirely dominated here by the ($n = 1$, $k = 1$) eigenmode, not because of any resonance effect, but because the exponential decay of this mode (for $B = 40$) is significantly slower than that of the remaining modes.

Let us contrast this behavior (fig. 4) with the same rotor of the same solidity, but at the transonic state of $M_{rr} = 1.054$. In this case, $\sigma_T = 1.84$, and the angle ($B\theta/2\pi$) of projection of the leading edge is approximately 0.3. The fluctuating pressure signal is significantly distorted, relative to

FIGURE 3.—*Pressure variation just upstream of typical uniformly loaded rotor operating at subsonic tip Mach numbers. Angular range corresponds to one full blade passage.*

UNIFORM LOADING, D = 0

$B = 40, \; h = .8, \; C_{ax}/L_T = 1.06, \; M = .5, \; M_T = .9, \; \sigma_T = 1.46, \; X/C_{ax} = -0.1$

UNIFORM LOADING, D = 0

$B = 40, \; h = .8, \; C_{ax}/L_T = 1.06, \; M = .5, \; M_T = 1.054, \; \sigma_T = 1.84, \; X/C_{ax} = -0.1$
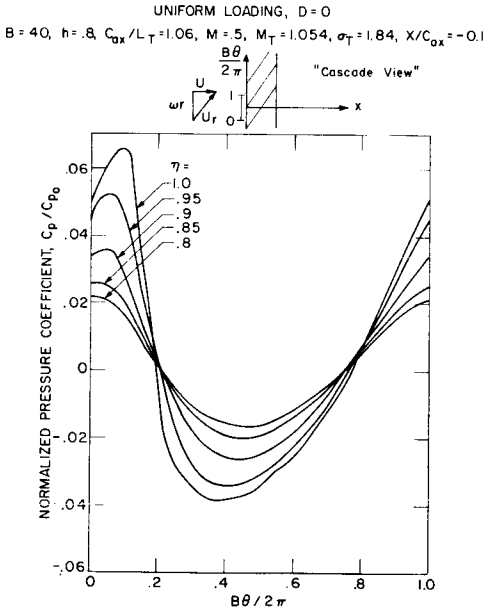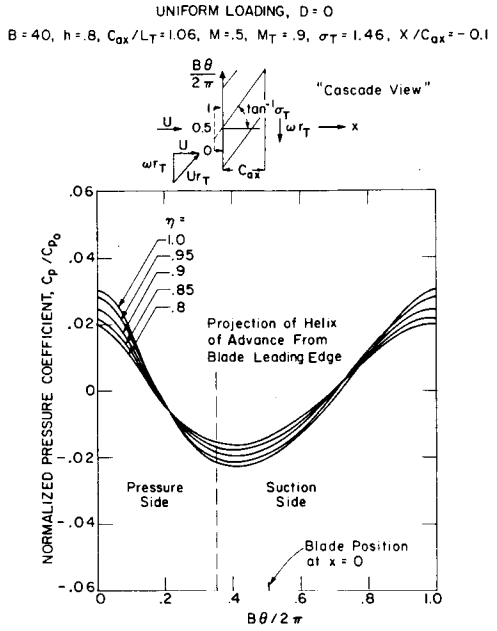
FIGURE 4.—*Pressure variation just upstream of typical uniformly loaded rotor operating at supersonic tip Mach numbers. Note distortion due to modes above cut-off.*

the subsonic case, by the presence of a large number of modes which are now above cut-off and therefore propagate. (For example, the $k = 1$ modes for all n are above cut-off at this tip Mach number; the (7,2) mode is also

above cut-off, etc.) The shift toward smaller angles of the expansion region just ahead of the blade is consistent with the expected formation (for the specified loading) of an expansion fan emanating from the leading edge of the blade tip ($\eta = 1$), but the flow field is still predominantly subsonic in character over the whole annulus. Hence, no really clear-cut development of a quasi-two-dimensional type flow field can be identified in this region.

A clearer distinction between hub and tip section contributions to the pressure pattern seems to develop just behind the rotor (figure 5) indicating some semblance of quasi-two-dimensional behavior. Here, the pressure signal oscillates about the uniform downstream level given by (1) or (14) at each η (because of the uniform loading) but a fairly strong local compression followed by an equally strong expansion fan seems to be emanating from the aft portions of the blade tips.

The results available in reference 10 indicate similar behavior for the nonuniformly loaded rotor, except that the near-field upstream and downstream pressure signals oscillate about different mean levels for each η, in accord with (15) and (14). One other major difference occurs for the case of nonuniform Γ, however; namely, the expected transonic resonance appears (see earlier discussion). For $M_{rT} = 1.054$ the (1,1) mode is the one nearest resonance, and the relative fluctuations in the near-field pressure that it produces are noticeably larger than for the constant-Γ case. The radial structure of this resonant mode also makes it more difficult to separate hub and tip behavior in the strip theory sense.

Far-field pressure signals (for example, at $x/c_{ax} = -5.0$, $x/c_{ax} = +6.0$) were also computed in the work reported in reference 10. As expected, essentially no pressure fluctuation about the azimuthal mean is observed

UNIFORM LOADING, D = 0
B = 40, h = .8, C_{ax}/L_T = 1.06, M = .5, M_T = 1.054, σ_T = 1.84, X/C_{ax} = 1.10
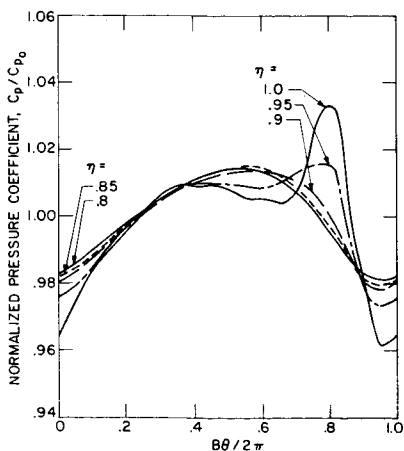
FIGURE 5.—*Pressure variation just downstream of the same rotor as in figure 4. Note development of a semblance of a quasi-two-dimensional pattern.*

at subsonic tip Mach numbers, while substantial fluctuations, comparable to the near-field values, are found to be present as soon as M_{rT} exceeds unity.

CONCLUDING REMARKS

In this paper, we have discussed some of the aspects of the three-dimensional aerodynamic theory of an axial compressor rotor. Our main emphasis has been on the newly developed lifting-surface (distributed-vortex) theory which forms the complement to the previously developed (distributed-source) theory for blade thickness effects.

In the third section, we showed that the present theory contains many aspects of the axisymmetric through-flow or actuator-disc theories, while in the fourth section we gave examples of the type of additional information that the three-dimensional theory offers.

It may be recalled that in reference 1 the relationship between three-dimensional and quasi-two-dimensional cascade theory was emphasized. Not surprisingly, in the lifting problem just as in the thickness problem, cascade theory, and corrections to it, can be derived readily from the three-dimensional theory. The techniques involved are similar to those in reference 1; details and some examples are available in reference 10.

We find, in short, for the purely lifting case, that quasi-two-dimensional cascade theory is an excellent approximation, at least within and near the blade passage, for uniformly loaded rotors, even in the transonic regime. However, for a rotor with only moderate variations in spanwise loading, we find that the wake-induced velocities have a surprisingly large effect on the effective incidence of the blades. Much work remains to be done, therefore, before the complete relationship between cascade theories (and/or data) and the aerodynamics of three-dimensional compressor rotors will be fully understood. Our expectation is that the present theory, despite the limitations imposed by our assumption of small disturbances, neglect of viscosity, etc., will be a useful key in relating all the various approximate theories to the full three-dimensional problem. It has pieces of each part of the puzzle.

REFERENCES

1. McCune, J. E., *J. Aerospace Sci.*, Vol. 25, No. 9, 1958, p. 544.
2. McCune, J. E., *J. Aerospace Sci.*, Vol. 25, No. 10, 1958, p. 616.
3. Okurounmu, O., *Wave Drag in Transonic Axial Compressors*. Sc.D. dissertation, M.I.T., November 1967.
4. Davidson, R. E. *Linearized Potential Theory of Propeller Induction in a Compressible Flow*. NACA TN 2983, 1953.
5. Reissner, H., *J. Aeron. Sci.*, Vol. 5, No. 1, 1937, p. 1.

6. TYLER, J. M., AND T. G. SOFRIN, preprint 345 D, SAE Aeronautic Meeting, 1961;
   MORFEY, C. L., *J. Sound Vib.*, Vol. 1, No. 60, 1964; SLUTSKY, S., AFOSR-
   UTIAS Symposium on Aerodynamic Noise (Toronto), May 1958.
7. MORSE, P. M., AND K. U. INGARD, *Theoretical Acoustics*. McGraw-Hill Book Co.,
   Inc. (New York), 1968.
8. SPARIS, P., AND D. OLIVER, private communication. Nonlinear numerical studies,
   currently underway, of sheared flow past a nonlifting wing in a rectangular
   duct, with the inflow Mach number varying from subsonic to supersonic along
   the wing span, indicate similar effects at the "subsonic" sections.
9. OKUROUNMU, O., AND J. E. McCUNE, Three-Dimensional Vortex Theory of Axial
   Compressor Blade Rows at Subsonic and Transonic Speeds. To be published,
   AIAA J., 1970.
10. OKUROUNMU, O., AND J. E. McCUNE, *Transonic Lifting Surface Theory of Axial
    Flow Compressors*. To be published as United Aircraft Research Laboratories
    Report, East Hartford, Connecticut, 1970.
11. WATSON, G. N., *A Treatise on the Theory of Bessel Functions*. Second Ed., Mac
    Millan, 1944.
12. MARBLE, F. E., Three-Dimensional Flow in Turbomachines. Princeton Series on
    High Speed Aerodynamics and Jet Propulsion, Vol. 10, Sec. C, Princeton U.
    Press, 1964, pp. 83–166.
13. OATES, G. C., *Theory of Throughflow in Axial Turbomachines With Variable Wall
    Geometry*. AFOSR TN 59–680, August 1959.

DISCUSSION

J. C. VRANA (McGill University) : Do you find that, as blade number is increased, the 3-dimensional solutions converge toward the infinitely bladed 2-dimensional approximations, regardless of circulation distribution? Going now in the opposite direction (as I have been mostly involved with low aspect ratios) would you agree that below a certain number of blades (10 to 12) it becomes impossible to design them for a prescribed variation of circulation (say 20 percent variation in circulation from mean)?

McCUNE (author): With regard to the first question, the 3-dimensional solutions converge, provided you are not in the transonic regime, to the 2-dimensional cascade solutions in the limit of large blade number and hub tip ratio approaching unity. This we showed for the thickness case in 1956 (refs. 1 and 2) and for the lifting case in reference 9 of the paper. On the other hand, for the "infinitely bladed" 2-dimensional approximation, by which I take it you mean the axisymmetric through-flow theory emphasized in the present paper, the 3-dimensional solutions will converge to *that* 2-dimensional approximation as $B \rightarrow \infty$, regardless of regime. These are, however, formal mathematical results; I believe that in almost any practical case 3-dimensional effects play a role.

Going in the other direction, the answer would have to depend on what you mean by "impossible". With *present* theory, insofar as it does not include induced velocity effects, I think it would be impossible to correctly design the blades, even for blade numbers as high as 40 or 80 (let alone 10 or 12), with 20 percent variation in circulation from mean. This is especially true in the transonic regime. While the theory presented in our paper is limited by the linearizing assumptions, it is intended as a step in the direction of making such design possible. We intend to pursue it. An important step is to include thickness effects (ref. 1) since they induce camber of themselves.

Secondary Vorticity in Axial Compressor Blade Rows

S. L. Dixon

University of Liverpool

A theoretical investigation of secondary flow in compressor blade rows is presented. Formulas for calculating secondary flows in annular cascade blade passages are derived. The influence of the relative rotation vector on secondary velocity perturbations, using recent developments in shear-flow theory, is examined. A method of calculating the flow through successive blade rows is given and a comparison is made with experimental results.

The prediction of axial-flow compressor and turbine performance using mathematical modeling has long been a desired goal of turbomachinery analysts. Methods available at present for designing compressors and turbines are usually based on the assumption of inviscid flow. Several attempts have been made to predict the performance of axial compressor stages in which secondary-flow theory has been utilized (e.g., Horlock (ref. 1) and Dixon and Horlock (ref. 2)).

Horlock established that realistic estimates of the swirl angle distributions in the flow on and near the annulus walls may be made, provided that the entering vorticity was known and the secondary vorticities traced through successive blade rows. With the flow angle distributions known, the axial velocity profiles may then be calculated using three-dimensional inviscid analysis. Dixon and Horlock applied a simple secondary-flow theory to the calculation of the flow angles and velocity distributions through a compressor stage. Fairly close agreement with experimental values was obtained for the guide vanes. Comparison of calculated and experimental values for the heavily loaded rotor was rather poor and strongly influenced by "corner stall."

In the present paper, recent developments in the theory of shear flow by Hawthorne and Novak (ref. 3) are incorporated into a more accurate three-dimensional flow model to remove some of the approximations of references 1 and 2. It is now possible to calculate the secondary flow in an

annular cascade of low hub/tip radius ratio and with comparatively few blades instead of using a two-dimensional approximation. In reference 1, secondary vorticity was calculated using the approximation derived by Squire and Winter (ref. 4) and in reference 2 an approximation to a formula of Smith (ref. 5) was employed. In this paper, secondary vorticity has been determined more accurately by means of Hawthorne and Novak's analysis (ref. 3). It is assumed that the flow is inviscid in all calculations and the fluid rotation is prescribed by the flow at entry to the guide vanes.

VARIATION OF VORTICITY ACROSS A BLADE ROW

An extensive literature has accumulated on the subject of secondary vorticity in cascades and blade rows. Review papers are available by Lakshminarayana and Horlock (ref. 6) and by Hawthorne (ref. 7). A discussion of the relative merits and differences between some of these theoretical treatments of secondary flow, although of great interest, is not possible in a short paper.

Recently, Hawthorne and Novak (ref. 3) have considered the transport of vortex filaments in a weakly sheared flow through a plane stationary blade cascade. In their treatment, vortex filaments were transported by a plane primary flow which was *irrotational*. They obtained an expression for the streamwise component of vorticity at exit, which is responsible for producing secondary flow, from the distortion and stretching of the vortex filaments by the primary flow.

A similar result is obtainable for the flow through an annular cascade for which the primary flow is irrotational. In this analysis, the stream surfaces of the primary flow are not necessarily at the same radius before and after the cascade (e.g., the annulus walls may be conical). Figure 1a shows the vorticity vectors lying on the development of a stream surface upstream and downstream of the cascade. For the assumed inviscid, incompressible flow, vorticity vector ω_1, at inlet is convected through the blade passage to become ω_2 at outlet. The change in orientation of the vector is caused by blade-passage-induced distortion of the primary flow, which can be determined approximately.

At exit, the streamwise component of vorticity is

$$\omega_{s2} = \frac{\overline{GD}\omega_{n2}}{p_2 \cos \beta_2} - \omega_{n2} \tan \beta_2 \tag{1}$$

where

$$\overline{GD} = \overline{AF}\frac{W_2}{W_1} + W_2 \int \frac{ds}{W_s}$$
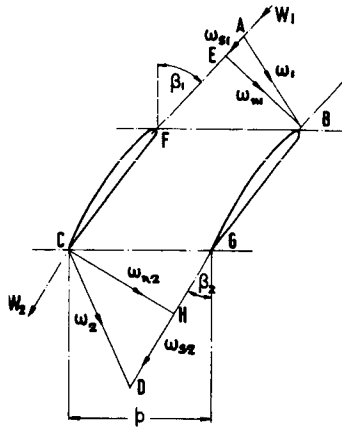
FIGURE 1a.—*Illustration of vorticity vector changes through a blade passage.*
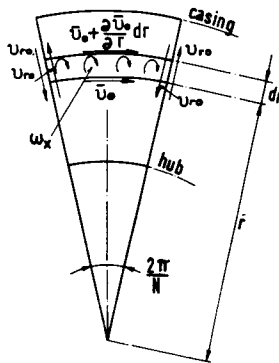
FIGURE 1b.—*Axial projection of blade passage showing passage and wake vorticity.*

$$\overline{AF} = p_1 \left(\frac{\sin \beta_1 + \cos \beta_1 \omega_{s1}}{\omega_{n1}} \right)$$

The integral $\int ds/W_s$ is taken around the surface of an airfoil. It represents the difference in the transit time of a particle traveling from the leading to the trailing edge of the airfoil when passing along the suction surface and when passing along the pressure surface. The integral is not readily evaluated, but may be approximated by an expression given by Smith (ref. 5)

$$\int \frac{ds}{W_s} \doteqdot \frac{\Gamma}{W_\infty^2} \tag{2}$$

where W_∞ is the vector mean of the inlet and exit velocities and Γ is the blade circulation, i.e.

$$\Gamma = \frac{2\pi}{N}\,(r_1 V_{\theta 1} - r_2 V_{\theta 2}) = \text{constant}$$

Using Crocco's equation, grad $I = \mathbf{W} \times \boldsymbol{\omega}$, where I is relative stagnation pressure/density, a useful relation between the normal components of vorticity is obtained

$$W_1 \omega_{n1} = W_2 \omega_{n2} \tag{3}$$

Substituting the preceding expressions into equation (1), the outlet streamwise vorticity is found from

$$\frac{\omega_{s2}}{\omega_{n1}}\cos\beta_2 = \frac{r_1}{r_2}\left(\sin\beta_1 + \cos\beta_1\,\frac{\omega_{s1}}{\omega_{n1}}\right) + \frac{W_1}{p_2}\int\frac{ds}{W_s} - \sin\beta_2\,\frac{W_1}{W_2} \tag{4}$$

By a fairly trivial extension, changes in density can be included in the analysis so that it can apply to compressible flow.

For a flow at constant radius, $r_1 = r_2 = r$ and equation (4) reduces to

$$\omega_{s2} = \omega_{s1}\,\frac{\cos\beta_1}{\cos\beta_2} + \omega_{n1}\left(\frac{\sin\beta_1}{\cos\beta_2} - \frac{\sin\beta_2}{\cos\beta_1} + \frac{W_1}{p\cos\beta_2}\int\frac{ds}{W_s}\right) \tag{5}$$

This is essentially the result obtained by Hawthorne and Novak (ref. 3) for a plane flow in a stationary coordinate system. The streamwise component of vorticity at inlet ω_{s1} has been included in the above analysis from the outset. It is most important to realize that ω_{s1}, which is an axisymmetric vorticity, directly influences the magnitude of the passage (i.e., streamwise) vorticity ω_{s2} at outlet and therefore contributes to the secondary motion of the fluid.

The effect of the angular rotation vector $\boldsymbol{\Omega}$ on the production of secondary vorticity is considered in the following section.

ROTOR SECONDARY FLOW[1]

The calculation of the secondary flow in a rotor raises a fundamental point concerning the effect of rotor relative rotation on the vorticity used to determine the secondary velocities. Several writers (refs. 8, 9, and 10) have proposed flow models in which the angular rotation vector $\boldsymbol{\Omega}$ is subtracted from the absolute vorticity entering the rotor and have then used the resulting relative vorticity to determine the relative secondary

---

[1] The analysis of this section was carried out in collaboration with Professor Sir William Hawthorne.

flow. At exit from the rotor, the angular rotation vector is then added to the relative vorticity, which now includes the rotor secondary vorticity, to give the absolute vorticity at entry to the following stator row. It is shown in the following that the relative rotation vector plays no part in the calculation of secondary vorticity and only the absolute vorticity is relevant.

Hawthorne (ref. 11) demonstrated that in the case of a general rotational *steady* flow of an inviscid, incompressible fluid, the velocity of a fluid particle is represented by

$$\mathbf{V} = \text{grad } \phi - t \text{ grad} \left(\frac{p_o}{\rho} \right)$$

in which ϕ is a potential function, t is the drift time of the particle, p_o is the stagnation pressure, and ρ is the density. In this flow, vortex filaments lie along the intersection of surfaces of constant t and constant stagnation pressure, the latter being also stream surfaces.

By means of an extension of this theory, it can be shown that in a rotating system of coordinates the *relative* velocity of the flow is

$$\mathbf{W} = \text{grad } \phi - t\nabla I - \boldsymbol{\Omega} \times \mathbf{r} \tag{6}$$

where I is relative stagnation pressure/density.

In the theory of shear flow, Hawthorne (ref. 11) used a *small shear* approximation to deal with the large disturbance type of flow such as the secondary flow in blade passages. The flow is assumed to be composed of a primary flow, fully described by a potential function ϕ_0 satisfying the boundary conditions on the walls and blade surfaces, and perturbations to take account of the rotationality of the flow. The velocities induced by rotationality are small, by hypothesis, compared with the primary flow so that the associated vortex filaments are convected by the primary flow.

Writing,

$$\phi = \phi_0 + \phi_1 + \phi_2 + \cdots$$

$$t = t_0 + t_1 + t_2 + \cdots$$

where ϕ_1/ϕ_0, t_1/t_0 are of first order of smallness and ϕ_2/ϕ_0, t_2/t_0 are of second order of smallness, then, using equation (6), the relative velocity is

$$\mathbf{W} = (\nabla\phi_0 - \boldsymbol{\Omega} \times \mathbf{r}) + (\nabla\phi_1 - t_0\nabla I) + (\nabla\phi_2 - t_1\nabla I) + \cdots \tag{7}$$

Bracketed terms in equation (7) are in descending orders of magnitude from the left. The primary flow relative velocity is

$$\mathbf{W}_p = \nabla\phi_0 - \boldsymbol{\Omega} \times \mathbf{r} \tag{8}$$

and the velocity of the secondary flow, which is convected by the primary flow, is

$$\mathbf{W}_s = \nabla\phi_1 - t_0\nabla I \qquad (9)$$

It should be noted that t_0 is the drift time of the primary flow. The primary flow has zero absolute vorticity so that, to the first order, the vorticity is

$$\boldsymbol{\omega} = \text{curl } \mathbf{W}_s = \nabla I \times \nabla t_0 \qquad (10)$$

using equation (9). Thus, from equation (9), the fundamental point is established that the secondary velocities within a rotor should be obtained from the absolute vorticity resolved in the relative flow direction. $\boldsymbol{\Omega}$, the relative rotation vector, does not enter into the calculation, except insofar as it appears implicitly in ∇I.

SECONDARY VELOCITIES IN BLADE PASSAGES

Formulas for calculating the two-dimensional solution of the secondary flow in cascade blade passages have been given by Hawthorne (ref. 12). More recently, the more difficult problem of secondary flow in a stationary annular cascade was investigated by Hawthorne and Novak (ref. 3) but the final solution was not derived. This annular cascade analysis is summarized below and is followed by a solution which can be adapted easily to the computation of secondary velocities.

In the case of a weakly sheared flow, the primary flow may be assumed to lie on cylindrical surfaces of constant radius and there is, therefore, no radial component of vorticity. At outlet from the blades, only ω_{s2}, the streamwise vorticity, contributes to the secondary flow, the effects of ω_{n2} being found from axisymmetric flow analysis. Referring to figure 2, the velocity perturbations induced by ω_{s2} have components v_r, v_θ, and v_x and the vorticity components are

$$\omega_{\theta 2} = \omega_{s2} \sin \alpha_2 = -\frac{dv_x}{dr}$$

$$\omega_{x2} = \omega_{s2} \cos \alpha_2 = \frac{1}{r}\left[\frac{\partial}{\partial r}(rv_\theta) - \frac{\partial v_r}{\partial \theta}\right]$$

Noting that $v_x = v_x(r)$ only, and using the continuity condition, $\text{div}(\mathbf{v}) = 0$, a Stokes' stream function can be defined,

$$v_r = \frac{1}{r}\frac{\partial \psi}{\partial \theta}$$

$$v_\theta = v_x \tan \alpha_2 - \frac{\partial \psi}{\partial r} \qquad (11)$$
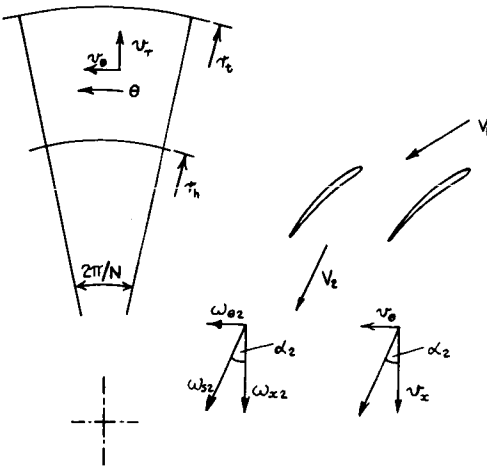
FIGURE 2.—*Vorticity and velocity perturbations in an axial projection of a blade passage.*

After substituting v_θ, v_r and $\omega_{\theta 2}$ into $\omega_{x 2}$, the following differential equation is derived,

$$\nabla^2\psi = \frac{\partial^2\psi}{\partial r^2} + \frac{1}{r}\frac{\partial\psi}{\partial r} + \frac{1}{r^2}\frac{\partial^2\psi}{\partial\theta^2} = \frac{v_x}{r}\frac{d}{dr}(r\tan\alpha_2) - \omega_{s2}\sec\alpha_2 = F(r) \qquad (12)$$

Using equation (11), a mean value of v_θ can be derived and the mean flow angle perturbation obtained,

$$\Delta\alpha_{2s} = -\frac{N\cos^2\alpha_2}{2\pi V_x}\int_0^{2\pi/N}\frac{\partial\psi}{\partial r}\,d\theta \qquad (13)$$

where V_x is the primary flow axial velocity component, which can be replaced with small error by $\bar{V}_x$ (i.e., mean V_x), and N the number of blades.

A solution of equation (12) must satisfy the boundary values $\psi = 0$ at $r = r_h$, r_t and also at $\theta = 0$, $2\pi/N$, $4\pi/N$, etc. The Kutta condition at the trailing edge is then also satisfied, as $v_\theta = v_x\tan\alpha_2$ at $\theta = 0$, $2\pi/N$, etc.

Hawthorne and Novak's equations, as given in the preceding paragraphs, are now solved. Writing

$$F(r) = F(r)\sum_{n\ \text{odd}}^{\infty}\frac{4}{n\pi}\sin k_n\theta$$

and

$$\psi = \sum_{n\ \text{odd}}^{\infty}\psi_n\sin k_n\theta \qquad (14)$$

equation (12) is reduced to

$$\frac{d^2\psi_n}{dr^2}+\frac{1}{r}\frac{d\psi_n}{dr}-\frac{k_n{}^2}{r^2}\,\psi_n=\frac{4}{n\pi}\,F(r) \tag{15}$$

where $k_n=nN/2$. The boundary conditions at $\theta=0$, $2\pi/N$, etc., have now been satisfied through equation (14).

Nondimensionalizing throughout (using r_t and $\bar{V}_x$) and solving for the mean flow angle perturbation $\Delta\alpha_{2s}$, using equation (14), gives

$$\Delta\alpha_{2s}=-\frac{2}{\pi}\cos^2\alpha_2\sum_{n\ \mathrm{odd}}^{\infty}\frac{1}{n}\,y_n{}' \tag{16}$$

and equation (15) becomes

$$y_n{}''+\frac{1}{\rho}\,y_n{}'-\frac{k_n{}^2}{\rho^2}=\frac{4}{n\pi}\,\frac{r_t}{\bar{V}_x}\,F(r)=\Re(\rho) \tag{17}$$

where

$$\rho=r/r_t,\ y_n=\psi_n/(r_t\bar{V}_x),\ y_n{}'=dy_n/d\rho,\ \mathrm{etc.}$$

The solution of equation (17) must satisfy the boundary conditions $v_r=0$ at $\rho=\rho_h$ and $\rho=1$. Solving equation (15) by variation of parameters, the complete solutions for y_n and $y_n{}'$ are

$$2k_ny_n=\frac{(\rho^{k_n}-\rho^{-k_n})}{(1-\rho_h{}^{2k_n})}\int_{\rho_h}^{1}\rho\Re\left[\left(\frac{\rho}{\rho_h}\right)^{k_n}-\left(\frac{\rho}{\rho_h}\right)^{-k_n}\right]\rho_h{}^{k_n}\,d\rho$$

$$+\rho^{-k_n}\int_{\rho}^{1}\Re\rho^{1+k_n}\,d\rho-\rho^{k_n}\int_{\rho}^{1}\Re\rho^{1-k_n}\,d\rho \tag{18}$$

$$2\rho y_n{}'=\frac{(\rho^{k_n}+\rho^{-k_n})}{(1-\rho_h{}^{2k_n})}\int_{\rho_h}^{1}\rho\Re\left[\left(\frac{\rho}{\rho_h}\right)^{k_n}-\left(\frac{\rho}{\rho_h}\right)^{-k_n}\right]\rho_h{}^{k_n}\,d\rho$$

$$-\rho^{-k_n}\int_{\rho}^{1}\Re\rho^{1+k_n}\,d\rho-\rho^{k_n}\int_{\rho}^{1}\Re\rho^{1-k_n}\,d\rho \tag{19}$$

For a typical blade row in which, for example, $N\geq30$ and $\rho_h\leq0.9$, such that $\rho_h{}^{2k_n}\ll1$, a slightly more compact form of these expressions can be obtained. By combining equations (16) and (19), the average flow angle perturbation across the blade passage may be computed as a function of radius. Another useful result is the radial velocity perturbation v_{r_0} at the boundary $\theta=0$, $2\pi/N$, etc. From equation (14)

$$v_{r_0}=\frac{\bar{V}_x}{\rho}\sum_{n\ \mathrm{odd}}^{\infty}k_ny_n \tag{20}$$

where k_ny_n is obtained using equation (18).

In the third section, it was demonstrated that in a rotating coordinate framework, the secondary velocities relate to *absolute* vorticity, not relative vorticity. Thus, the solutions may also be applied to rotor rows, replacing α_2 by the rotor exit flow angle β_2 where required.

DERIVATION OF AXISYMMETRIC FLOW CONDITIONS DOWNSTREAM OF THE BLADE ROW

The calculation of the axial velocity distribution downstream of a blade row really presents a difficult problem unless the flow can be reasonably assumed to be axisymmetric. In the shear flow theory, the vorticity is assumed to be weak and the secondary velocities are then small in comparison with the primary flow velocities. Thus, under these conditions it would seem justifiable to assume that at entry to the following blade row, the flow is steady, or nearly so, the vorticity being distributed circumferentially.

Hawthorne (ref. 13) has shown for the nonuniform flow through a cascade that, in the streamwise direction, there are three components of vorticity downstream of the trailing edge plane. The first is the distributed passage vorticity ω_{s2} already considered in the second section; the second and third are the trailing shed vorticity and trailing filament vorticity, both of which lie along the wake. Now, trailing shed circulation is caused by a gradient in circulation along the blade length and it is easily demonstrated that the contributions of both the primary and perturbation flows are already included in the analysis.

Trailing filament circulation arises in the "wakes" from the cellular motion induced in the blade passage by the secondary streamwise vorticity. The contribution made to the net vorticity by the trailing filament vorticity was shown by Smith (ref. 14) to be small for boundary layers which are thin compared with the blade spacing but appreciable when the boundary-layer thickness/blade spacing ratio is of order unity.

To show how the trailing filament modifies the distributed passage vorticity, consider first the axial component of passage vorticity,

$$\omega_x = \omega_{s2} \cos \alpha_2 = \frac{1}{r} \frac{\partial}{\partial r} (r v_\theta) - \frac{1}{r} \frac{\partial v_r}{\partial \theta}$$

Referring to figure 1*b* and applying Stokes' theorem to the fluid element of area $(2\pi r/N) \, dr$, excluding the blade wake, gives

$$\omega_x = \frac{1}{r} \frac{d}{dr} (r\bar{v}_\theta) + \frac{v_{r_0} N}{\pi r} \tag{21}$$

where $\bar{v}_\theta$ is the averaged perturbation in tangential velocity and v_{r_0} is the radial velocity perturbation at $\theta = 0, 2\pi/N$, etc. Again, applying Stokes'

theorem to the fluid element, but this time including a blade wake, gives

$$\omega_{zA} = \frac{1}{r}\frac{d}{dr}(r\bar{v}_\theta) \tag{22}$$

which is the axial component of the combined secondary and trailing filament vorticities. Combining equations (21) and (22), ω_{zA} can be found

$$\omega_{zA} = \omega_{s2}\cos\alpha_2 - v_{r_0}\frac{N}{\pi r} \tag{23}$$

v_{r_0} being computed from equations (18) and (20).

Now,

$$\omega_\theta = \omega_x\tan\alpha_2 = -\frac{dv_x}{dr}$$

and it is deduced that

$$\omega_{\theta A} = \omega_{zA}\tan\alpha_2$$

if the primary flow direction is not changed by the secondary flow. That this is so can be deduced from Crocco's equation,

$$1/\rho\ \text{grad}\ p_o = \mathbf{V}\times\boldsymbol{\omega}$$

i.e., ω_{n2} is of fixed magnitude and the head of the *resultant* vorticity vector ω_{2A} must lie along the line AB in figure 3. A change in the axial velocity perturbation v_x must occur, consistent with the reduction of ω_θ to $\omega_{\theta A}$. This change in v_x is assumed to be completed far downstream of the trailing edge plane (i.e., as in actuator disc theory).

With the resultant axisymmetric vorticity known, the secondary flow in the following blade row can now be determined using the components of this vorticity resolved parallel and normal to the relative primary flow of that row.

For computing axial velocity profiles, the flow angle of the primary flow is added to the perturbation flow angle $\Delta\alpha_{2s}$ to give the flow angle in the trailing edge plane. All variations in v_x are assumed to occur downstream of this plane.

PERFORMANCE PREDICTION OF A COMPRESSOR STAGE

A revised theoretical model for predicting the performance of an axial-flow compressor based on inviscid secondary flow is now available. It is assumed that the velocity profile upstream of the inlet guide vanes is known and the primary flow (i.e., no secondary flow) efflux angles can be found for each blade row from cascade data.
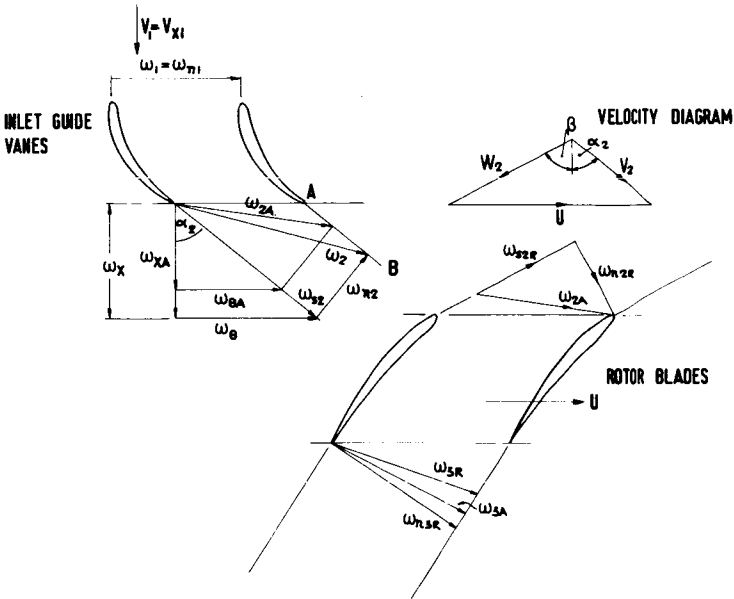
FIGURE 3.—*Vorticity vectors traced through two blade rows of a compressor.*

Referring to figure 3, the steps in the calculation of the flow are summarized as follows.

(1)   Using equation (5), the passage vorticity ω_{s2} at exit from the inlet guide vanes is determined, ω_{s1} and α_1 being generally zero for this flow.

(2)   With ω_{s2} known, the mean flow angle perturbation $\Delta\alpha_2(r)$ is calculated using equations (16) and (19). This distribution is added to the primary flow angle $\alpha_2(p)$, giving the total exit angle $\alpha_2(r)$ to be used in the axisymmetric flow calculation.

(3)   The axial velocity distribution downstream of the guide vanes $V_{x2}(r)$ is calculated using $V_{x1}(r)$ and $\alpha_2(r)$ in an axisymmetric flow equation; e.g., equation (8) in Horlock (ref. 1).

(4)   A modified axial component of the streamwise vorticity is calculated using equation (23); in this calculation v_{r_0} is obtained from equations (18) and (20). The resultant vorticity ω_{2A} can now be found, noting that ω_{n2}, the normal component of vorticity, must remain constant. The vorticity ω_{2A} could also be obtained from the downstream solution for axial velocity but this is less direct and is intrinsically less accurate, as one step in the computation involves differentiation.

(5)   Resolving ω_{2A} into components parallel (ω_{s2R}) and normal (ω_{n2R}) to the *relative* flow at rotor entry, equation (5) is employed to determine the *absolute* streamwise vorticity (ω_{s3R}) at rotor exit. The streamwise

vorticity at entry will strongly influence the magnitude and direction of ω_{3R}.

(6)   The flow angle perturbation $\Delta\beta_{3s}$ at rotor outlet is determined from ω_{s3R} and added to the primary flow angle $\beta_{3(p)}$ to give the rotor exit flow angle for determining the axial velocity distribution far downstream.

(7)   Repeat the sequence, from step (3).

It will be noticed that at rotor (and stator) entry the streamwise vorticity relative to the blades is, in general, nonzero. This was pointed out by Horlock (ref. 1) who observed that the "conventional" direction of secondary rotation may be reversed because of the streamwise vorticity at entry. In inlet guide vanes, for which $\omega_{s1} = 0$, the secondary rotation may produce *overturning* of the flow at the blade ends. For rotors and stators, secondary rotation produces *underturning* of the flow at the blade ends because of the inlet streamwise vorticity. Experimental results and theoretical calculations both show that this is a normal feature of the flow through rotors and stators. It is worth observing that the net effect of secondary vorticity and trailing filament vorticity is to produce a resultant vorticity which remains close to the tangential direction. This feature strongly influences the turning direction at the blade ends.

COMPARISON WITH EXPERIMENTAL RESULTS

Calculations based on the method summarized in the preceding section are still rather limited in scope. So far, only the flow through a set of inlet guide vanes has been determined but the results show a closer fit of experimental data than the earlier attempt described by Dixon and Horlock (ref. 2). The method of determining the secondary flow in reference 2 was of a more approximate nature and the theory was very much simplified.

The test results relate to a low-speed experimental compressor with a hub/tip ratio of 0.8 and with 60 inlet guide vanes having a blade outlet angle of 60°. The space/chord ratio (s/l) was 0.943 at the mean radius and the blade chord was constant (0.7 in.), so that s/l varied from 0.84 at the root to 1.05 at the tip. From this information, the primary flow angle at outlet from the vanes was estimated, using the deviation angle rule

$$\delta = 0.17\theta \frac{s}{l}, \quad \text{deg}$$

where θ is the camber angle of the vanes.

Figure 4 shows the axial velocity distribution at entry to the compressor which was used in all the calculations. The exact form of the velocity profile was not known and the equilibrium velocity profile
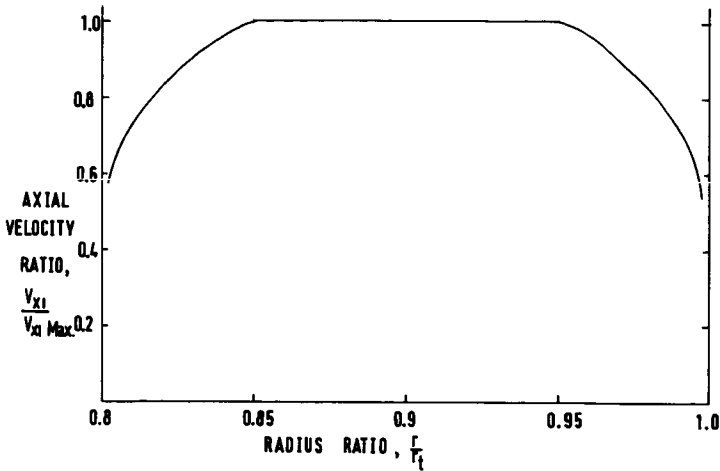
FIGURE 4.—*Axial velocity distribution at entry to inlet guide vanes.*

described by Coles (ref. 15) was used. This profile gives a good match with earlier experimental results by Horlock obtained on a similar compressor entry. The velocity distribution V in the annulus wall boundary layers as a fraction of the mainstream velocity V_1 is

$$\frac{V}{V_1} = \frac{V_{r1}}{KV_1}\left[\ln\left(\frac{\delta_1 V_{r1}}{\nu}\right) + \ln\,\eta + 2 + \Pi_x(1 - \cos\,\pi\eta)\right]$$

where K and Π_x are constants having values of 0.4 and 0.55, respectively; V_{r1} is a "friction velocity"; δ_1 is the boundary-layer thickness; ν is the kinematic viscosity; and η is the distance from the wall as a fraction of δ_1.

The calculated distribution of α_2 based on the theory is shown in figure 5, together with the experimental values. Agreement between calculated and measured values appears to be very good. The corresponding variation in radial velocity perturbation along the blade wake (i.e., at $\theta = 0$) is given in figure 6 as a fraction of the mean axial velocity, which indicates the rather high velocity perturbation caused by secondary flow. The radial velocity perturbation is of most use in determining the resultant vorticity of the axisymmetric flow. Figure 7 shows the axial component of the streamwise vorticity at outlet ω_x, together with the radial velocity correction $v_{r_0}N/\pi r$, both in a nondimensional form. The difference between the two curves results in the net axial component of streamwise vorticity. It is of interest to note that the radial velocity contribution to vorticity predominates over the secondary vorticity toward the boundary-layer edge.

The axial velocity distribution downstream of the guide vanes was calculated using the flow angle distribution of figure 5 and the inlet
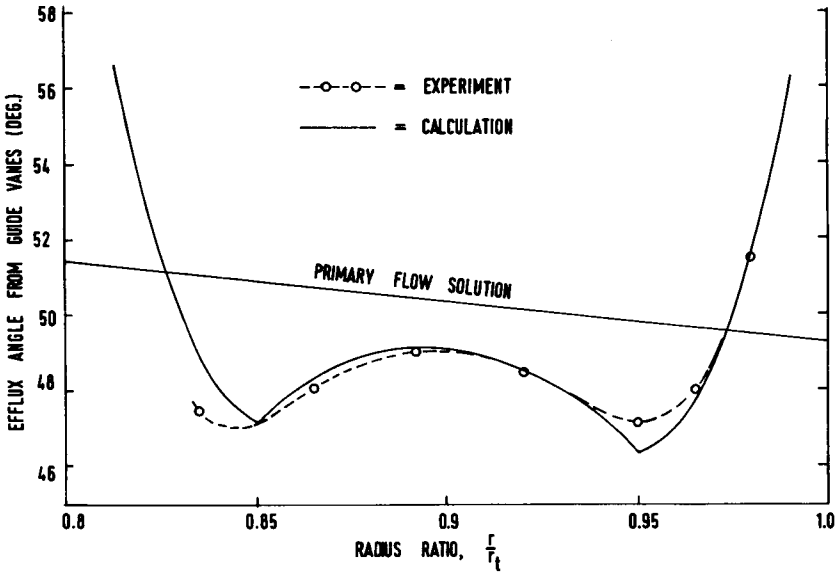
FIGURE 5.—*Flow angles at exit from guide vanes.*
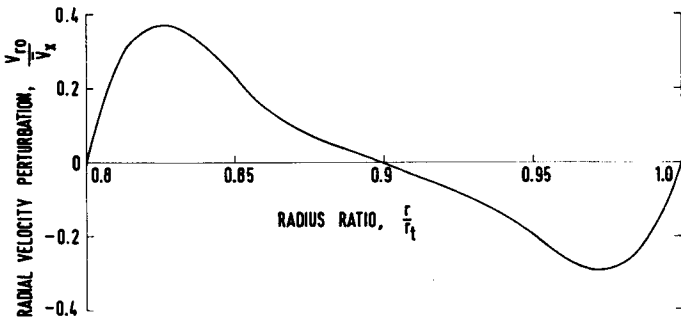
FIGURE 6.—*Variation of radial velocity at exit from guide vanes for $\theta = 0$.*

velocity profile of figure 4. As the hub/tip ratio was high and the blade aspect ratio (the ratio of blade height to distance between centerlines of adjacent blade rows) was small (less than 2), the axisymmetric flow calculations were based on simple radial equilibrium between blade rows. The blade row was replaced by an actuator disc located at the midchord position and interference effects from other blade rows were neglected. Figure 8 shows the calculated axial velocity profile which can be compared with an experimentally derived profile. Agreement between the curves is very good except toward the hub where, as it turns out, the flow angle prediction also differs from the experimental values.
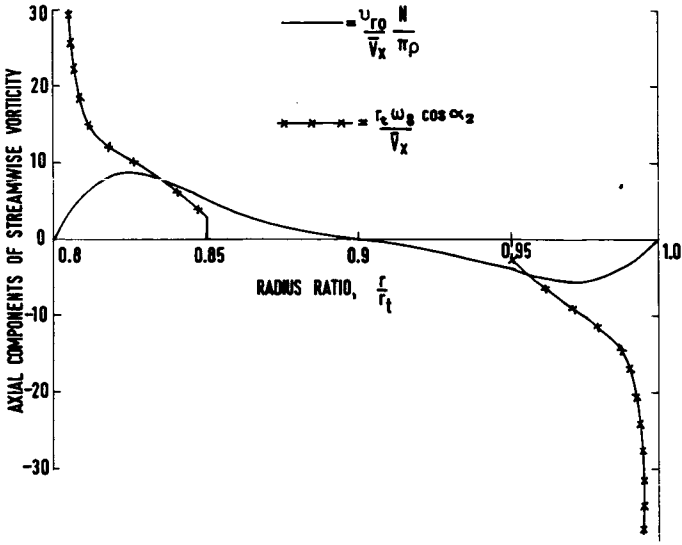
FIGURE 7.—*Axial components of streamwise vorticity at exit from guide vanes.*
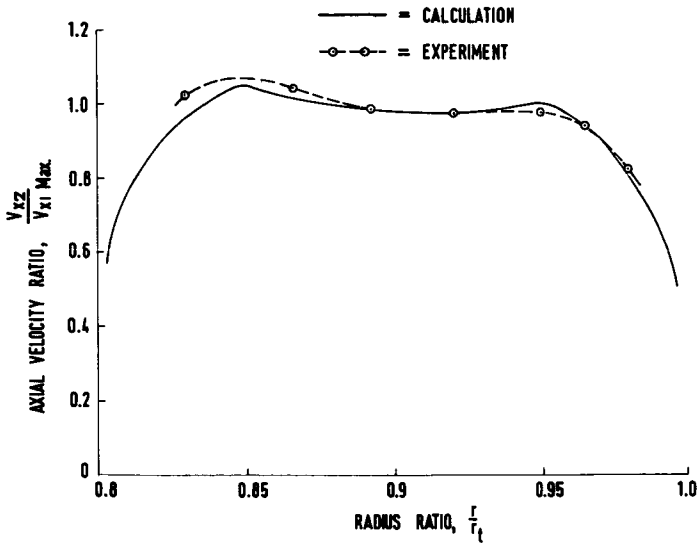
FIGURE 8.—*Axial velocity distribution downstream from guide vanes.*

The calculation of the flow in the following rotor row using the procedure given in this paper has not yet been attempted. However, flow calculations of the rotor have been made by means of a similar but less advanced theory. A fairly crude approximation was used to determine the

secondary vorticity and secondary velocities were obtained from a simple two-dimensional model. Nevertheless, valuable conclusions can be drawn from these results, which are presented here.

The rotor blades had the same space/chord values as the guide vanes and comprised constant section blades (10C5/20C50 profiles) set at 50° stagger. From experimental data available, it was noticed that at the particular test conditions being considered the blades operated close to the peak pressure rise. A primary flow angle at rotor exit was estimated based on the maximum unstalled deviation of the blades. Figure 9 shows the calculated distribution of the flow angle, β_3, at rotor exit, together with experimental values. The results can be seen to be qualitatively similar, the discrepancies between the two curves being due probably to the approximate nature of the theory and the assumption of constant boundary-layer thickness.

Figures 10 and 11 show a series of axial velocity distributions calculated systematically for the rotor with prescribed conditions. In figure 10, both sets of calculations, A and B, employed the previously calculated rotor exit angles shown in figure 9. However, for curve B the measured total pressure losses in the rotor were included in the axisymmetric flow calculation, whereas for curve A they were ignored. Comparing these calculated results with experiment, a very marked improvement in the accuracy of curve B is evident. In figure 11, the measured rotor exit flow angle was
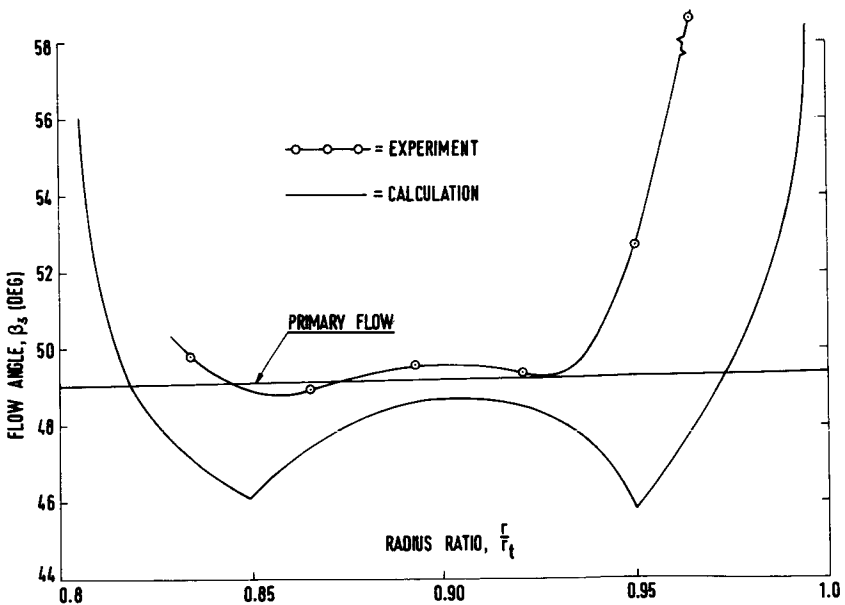
FIGURE 9.—*Flow angle distribution at exit from rotor blades.*
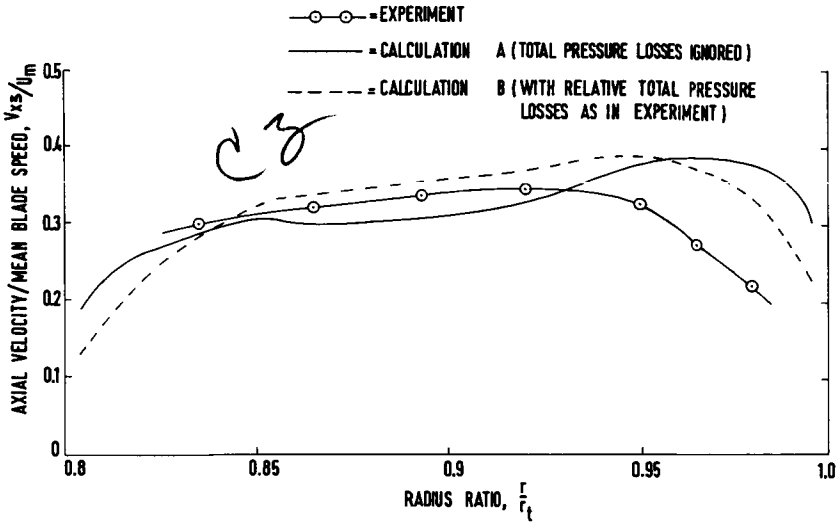
FIGURE 10.—*Axial velocity distributions downstream of rotor row using calculated flow angle distribution.*
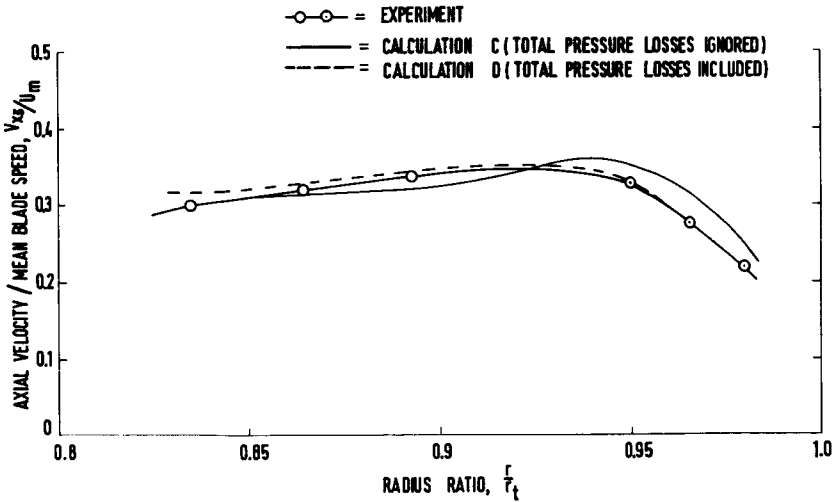
FIGURE 11.—*Axial velocity distributions downstream of rotor row with experimental flow angle distribution.*

used in both calculations, C and D. For the former, the relative total pressure losses were ignored and for the latter, they were included. It is clear from curves C and A together that having the correctly calculated flow angle distribution is vital for accurate performance prediction in

compressors. However, it is evident from curve D that account must be taken also of the "losses," at least in diffusing blade rows.

CONCLUSIONS

A comprehensive theoretical analysis is presented for calculating the secondary flow through the successive rows of axial-flow turbomachines, based on a known inlet velocity distribution. The controversial relative rotation vector is shown in the analysis to be irrelevant to the calculation of secondary vorticity. Application of the analysis to the inlet guide vanes of an axial-flow compressor predicts an exit flow angle distribution which is very close to the measured distribution. Subsequent calculation of the downstream axial velocity distribution using the predicted flow angles gives close agreement with the measured axial velocities. Thus, it is concluded that for guide vanes, at least, the exit flow is fairly accurately predicted by assuming inviscid loss-free flow with no growth in boundary-layer thickness across the row.

The prediction of flow through the rotor, which employed a simplified, more approximate treatment than that given in the paper, showed only a moderate agreement with experiment. The rotor was heavily loaded and relative total pressure losses were significant. These calculations emphasize the importance of the accurate prediction of both outlet angle and pressure loss distributions in the calculation of axial velocity distributions. It should now be possible for a more accurate assessment of rotor outlet angles to be made with the theory given in this paper.

ACKNOWLEDGMENT

REFERENCES

1. HORLOCK, J. H., Annulus Wall Boundary Layers in Axial Compressor Stages. *Trans. ASME, J. Basic Eng.* Vol. 85, 1963.
2. DIXON, S. L., AND J. H. HORLOCK, *Velocity Profile Development in an Axial Flow Compressor Stage.* Gas Turbine Collaboration Committee, Paper 624, 1968.
3. HAWTHORNE, W. R., AND R. A. NOVAK, The Aerodynamics of Turbomachinery. *Ann. Rev. Fluid Mech.*, Vol. 1, 1969.
4. SQUIRE, H. B., AND K. G. WINTER, The Secondary Flow in a Cascade of Aerofoils in a Non-Uniform Stream. *J. Aeron. Sci.*, Vol. 18, 1951.

5. SMITH, L. H., Secondary Flow in Axial-Flow Turbomachinery. *Trans. ASME*, Vol. 77, 1955.

6. LAKSHMINARAYANA, B., AND J. H. HORLOCK, Review: Secondary Flow and Losses in Cascades and Axial-Flow Turbomachines. *Int. J. Mech. Sci.*, Vol. 5, 1963.

7. HAWTHORNE, W. R., The Applicability of Secondary Flow Analyses to the Solution of Internal Flow Problems. *Fluid Mechanics of Internal Flow*, Gino Sovran, ed., Elsevier Publ. Co., 1967.

8. SMITH, A. G., On the Generation of the Streamwise Component of Vorticity for Flows in Rotating Passages. *Aeron. Quart.*, Vol. 8, 1957.

9. NORBURY, J. F., Contribution to a paper by J. H. Horlock, Annulus Wall Boundary Layers in Axial Compressor Stages. *Trans. ASME, J. Basic Eng.*, Vol. 85, 1963.

10. HORLOCK, J. H., AND S. L. DIXON, Contribution to the discussion of Reference 1. *Trans. ASME, J. Basic Eng.*, Vol. 89, 1967.

11. HAWTHORNE, W. R., *On the Theory of Shear Flow*. Gas Turbine Laboratory Report 88, M.I.T., October 1966.

12. HAWTHORNE, W. R., *Some Formulae for the Calculation of Secondary Flow in Cascades*. Brit. Aeron. Res. Council, Report 17519, 1955.

13. HAWTHORNE, W. R., Rotational Flow Through Cascades: Part I, The Components of Vorticity. *Quart. J. Mech. Appl. Math.*, Vol. 8, Part 3, 1955.

14. SMITH, JR., L. H., Contribution to the discussion of Reference 1. *Trans. ASME, J. Basic Eng.*, Vol. 85, 1963.

15. COLES, D., The Law of the Wake in the Turbulent Boundary Layer. *J. Fluid Mech.*, Vol. 1, 1956.

DISCUSSION

W. R. HAWTHORNE (Cambridge University) : The author's solution of equation (12) given in equations (18) and (19), although correct, is somewhat difficult to evaluate. It is easier to reduce equation (12) to a rectangular coordinate system by writing

$$r/r_h = \exp\left(\frac{2\pi z}{N}\right)$$

and

$$\theta = \frac{2\pi y}{N}$$

Then the author's equation (12) becomes

$$\frac{\partial^2\psi}{\partial z^2} + \frac{\partial^2\psi}{\partial y^2} = \left(\frac{2\pi r}{N}\right)^2 F(r) = G(z)$$

with boundary condition $\psi = 0$ at $y = 0$ and $y = 1$ and at $z = 0$ and $l = (N/2\pi) \log_e (r_t/r_h)$.
Writing

$$G(z) = G(z) \sum_{1,3,5}^{\infty} \frac{4}{n\pi} \sin n\pi y$$

and

$$\psi = \sum_{1,3}^{\infty} \psi_n \sin n\pi y$$

we obtain

$$\frac{d^2\psi_n}{dz} - n^2\pi^2\psi_n = \frac{4}{n\pi} G(z)$$

By the method of variation of parameters, we obtain

$$\psi_n(z) = -\frac{4/n^2\pi^2}{\sinh \pi nl}\left[\sinh n\pi z \int_z^l G(t) \sinh n\pi(l-t)\, dt\right.$$

$$\left. + \sinh n\pi(l-z) \int_0^z G(t) \sinh n\pi t\, dt\right]$$

and

$$\frac{d\psi_n}{dz} = \frac{4/n\pi}{\sinh n\pi l} \left[\cosh n\pi(l-z) \int_0^z G(t) \sinh n\pi t \, dt \right.$$

$$\left. - \cosh n\pi z \int_z^l G(t) \sinh n\pi(l-t) \, dt \right]$$

The author refers to an extension of my representation of velocity in the steady rotational flow of an inviscid, incompressible fluid, namely

$$\mathbf{V} = \nabla\phi - \frac{t\nabla p_o}{\rho}$$

to a rotating coordinate system. To complete the record it is desirable to give a derivation of the author's equation (6), since it has not been published elsewhere. If $\mathbf{W}$ is the velocity relative to a coordinate system rotating with angular velocity $\mathbf{\Omega}$, then Euler's equation for steady relative flow is

$$(\mathbf{W}\cdot\nabla)\mathbf{W} + 2\mathbf{\Omega}\times\mathbf{W} + \mathbf{\Omega}\times(\mathbf{\Omega}\times\mathbf{r}) = \frac{1}{\rho}\nabla p$$

where $\mathbf{r}$ is a position vector and p and ρ are pressure and density, respectively. It may be transformed to

$$\mathbf{W}\times(\nabla\times\mathbf{W} + 2\mathbf{\Omega}) = \nabla\left[\frac{p}{\rho} + \tfrac{1}{2}(W^2 - \Omega^2 r^2)\right]$$

where r is the radius from the rotating axis. The term

$$p_R = p + \tfrac{1}{2}\rho(W^2 - \Omega^2 r^2) = \rho I$$

is better called the relative Bernoulli pressure to avoid confusion, since stagnation pressure could be written $p + \tfrac{1}{2}\rho W^2$. The term

$$\nabla\times\mathbf{W} + 2\mathbf{\Omega} = \boldsymbol{\omega}$$

is the absolute vorticity. Now Clebsch (ref. D–1) has shown that it is possible to represent the absolute velocity in a three-dimensional flow as

$$\mathbf{V} = \nabla\phi - \tau\nabla\sigma$$

where ϕ, σ, and τ are scalars which may be chosen arbitrarily. The relative velocity may then be written

$$\mathbf{W} = \nabla\phi - \tau\nabla\sigma - \mathbf{\Omega}\times\mathbf{r}$$

and the absolute vorticity

$$\boldsymbol{\omega} = \nabla\sigma\times\nabla\tau$$

Now we choose $\sigma = I$, so that

$$\nabla \sigma = \nabla I = \mathbf{W} \times \boldsymbol{\omega}$$

Hence

$$\boldsymbol{\omega} = (\mathbf{W} \times \boldsymbol{\omega}) \times \nabla \tau$$

$$= (\mathbf{W} \cdot \nabla \tau) \boldsymbol{\omega} - (\boldsymbol{\omega} \cdot \nabla \tau) \mathbf{W}$$

The second term

$$\boldsymbol{\omega} \cdot \nabla \tau = \nabla \sigma \times \nabla \tau \cdot \nabla \tau = 0$$

hence

$$\mathbf{W} \cdot \nabla \tau = 1$$

or

$$\tau = \int \frac{ds}{W}$$

where the integral is taken along a streamline of the relative flow and s is the distance along the streamline. If, at any instant, one of the surfaces $\tau = $ constant is identified, then, at a time t later, the fluid particles will have drifted a distance downstream such that

$$t = \int \frac{ds}{W}$$

Hence, we may write

$$\mathbf{W} = \nabla \phi - t \nabla I - \boldsymbol{\Omega} \times \mathbf{r}$$

and

$$\boldsymbol{\omega} = \nabla I \times \nabla t$$

The author has adopted the approximation in which the stagnation pressure gradients are small but the disturbance from the upstream flow is large.

There is the possibility of some confusion in the use of the terms "primary flow" and "secondary flow." In all the methods given in the literature on the secondary-flow approximation, the stagnation pressure gradient, $\nabla p_o / \rho$ (or its equivalent, ∇I, in a rotating coordinate system) is assumed to be small of $O(\epsilon)$. We determine the components of vorticities in the flow by considering their convection by a flow of $O(1)$ for which $\nabla p_o / \rho = 0$ (or $\nabla I = 0$) and which satisfies the boundary conditions. This flow of $O(1)$ has frequently been described as the primary flow.

Writing the total velocity as

$$\mathbf{V} = \mathbf{V}_0 + \mathbf{v}$$

where $\mathbf{V}_0$ is the primary flow and $\mathbf{v}$ is $O(\epsilon)$

$$\nabla \times \mathbf{V} = \nabla \times \mathbf{V}_0 + \nabla \times \mathbf{v}$$

Now

$$\mathbf{V}_0 \times (\nabla \times \mathbf{V}_0) = 0$$

because the primary flow has no gradient of p_o. Hence, the primary flow must either be a potential flow, $\nabla \times \mathbf{V}_0 = 0$, or a Beltrami flow with

$$\omega_0 = \nabla \times \mathbf{V}_0 = \lambda \mathbf{V}_0$$

where λ is a scalar which is constant along a streamline of the primary flow. The only component of the vorticity ω_0 is ω_{0s} in the direction of $\mathbf{V}_0$, such that $\omega_{0s}/V_0 = \lambda = $ constant along a streamline. Beltrami flows are found downstream of rows of twisted blades around which the circulation varies along the span when the fluid is ideal and the flow upstream of the blades is irrotational. For such a flow, we may define ω_0 as the primary vorticity and note that it may be $O(1)$. Then $\nabla \times \mathbf{v}$ of $O(\epsilon)$ is the secondary vorticity. If the Beltrami flow is weak so that λ is $O(\epsilon)$, then we may choose a potential flow as the primary flow and incorporate the velocities induced by the vorticity ω_{0s} in the velocity $\mathbf{v}$.

This result may be extended to flows in rotating coordinate systems by noting that in the primary flow

$$\mathbf{W}_0 \times \omega_0 = 0$$

so that

$$\omega_0 = \lambda \mathbf{W}_0$$

where λ is now constant along a streamline of the relative flow. When λ is $O(\epsilon)$, it is possible to define a primary flow

$$\mathbf{W}_0 = \nabla \phi_0 - \boldsymbol{\Omega} \times \mathbf{r}$$

for which the absolute velocity is irrotational.

Hitherto, I have been discussing the definition of the primary flow used in calculating the vorticity convection. Some confusion has, perhaps, arisen because when considering the computation of the velocity components through cascades, it has been convenient to split the flow into two parts—namely, a flow which can be computed by axisymmetric methods (L. H. Smith calls this the primary flow) and a flow component which requires blade-to-blade analysis and in which the effects of the passage vorticity are obtained from equations such as the author's equations (16) and (19). In this latter calculation and in the axisymmetric calculations, we assume that the Kutta condition is adequately satisfied, in the latter case by using a blade element or potential flow theory.

For flows in which $\omega_{s1} = 0$ there appears to be agreement, supported by experimental data, that the actuator disc or axisymmetric approach combined with a passage vortex computation is satisfactory (Hawthorne and Novak, ref. 3).

When $\omega_{s1} \neq 0$ or in the extreme case when the approaching flow is a Beltrami flow, some question arises as to the adequacy of the method assumed for satisfying the Kutta condition in the axisymmetric or actuator-disc computations. It is not obvious that the blade element theory can adequately predict the outlet angle for such flows. Work is proceeding on this point, which is of considerable importance in step (6) of the sixth section of the paper. At the moment, all we can say is that step (6) contains the best assumptions that are available.

The most rigorous attempt to satisfy the Kutta condition for the secondary flows has been given by M. Gomi (ref. D–2).

J. H. HORLOCK (Cambridge University) : With Dr. Dixon, I have for some years followed, and participated in, discussions between Dr. L. H. Smith and Sir William Hawthorne on the problem of secondary flow in stationary and rotating rows of blades. This introduction to the discussion is an attempt to summarize the position, to draw attention to differences in two approaches to the problem, and to pose some questions to which I still do not know the answers. These differences and questions are illustrated by some simple flows, concentrating first on the secondary flows in stators and later on the secondary flows in rotors. Much of the work presented here is not my own, but is drawn from correspondence between the four of us and notes of the discussions that have taken place.

A critical difference between the approaches of L. H. Smith on one hand and of Hawthorne and Dixon on the other lies in their definitions of secondary flow. Smith defines the secondary (passage) vorticity as the difference between the *actual* streamwise vorticity leaving the blade row (ω_s) and the "primary" vorticity that would exist downstream of the blade row if there were an infinite number of blades (ω_{s_0}). Hawthorne and Dixon define the secondary vorticity as the actual streamwise vorticity in the channel (ω_s). In my opinion, neither of these approaches is incorrect for stationary coordinates—it is simply a question of definition.

Let us first summarize the various equations that have been derived (table D–I) for secondary flow of an incompressible fluid, expressed in stationary coordinates. We shall use the notation of Dixon's figure 3 for the flow through the stationary row, working in absolute velocities and vorticities in the first instance, but using z instead of r (implying that the radius of the machine is very large, and we can work in Cartesian coordinates). Subscripts s and n mean parallel and normal to the absolute velocity, respectively.

We shall consider the use of these equations in two flows through stationary blade rows. In the first case there is no secondary vorticity at entry $(\omega_{s_1} = 0, \omega_{n_1} \neq 0)$ and in the second case there is no normal vorticity at entry $(\omega_{n_1} = 0, \omega_{s_1} \neq 0;$ a Beltrami flow). We compare the Hawthorne equation (D–3) with the Smith equation (D–5) in each case.

TABLE D–I.—*Equations for Secondary Flow (Stationary Coordinates)*

Equation	Reference and notes
$$\bar{V} \cdot \nabla \left(\frac{\omega_s}{V} \right) = -\frac{1}{V^4} \left[2\bar{V} \times \nabla \left(\frac{p_0}{\rho} \right) \right] \cdot (\bar{V} \cdot \nabla)\bar{V} \qquad \text{(D–1)}$$	Hawthorne (ref. 13)—general equation
$$\omega_{s2} - \omega_{s1} = -2\epsilon\omega_{n1} \qquad \text{(D–2)}$$	Squire and Winter (ref. 4)—small deflection
$$\delta\Gamma_s = \omega_{s2}\sigma \cos \alpha_2$$ $$= \frac{dV_1}{dz}\left[-V_1 \int \frac{ds}{V} + \frac{\sigma \cos \alpha_2}{2} \times \left(\frac{\sin \alpha_2}{\cos \alpha_1} - \frac{\sin \alpha_1}{\cos \alpha_2} \right) \right] \qquad \text{(D–3)}$$	Hawthorne (ref. 13)—$\omega_{s1}=0$
$$\omega_{s2} = \left(\frac{\nabla p_0}{\rho} \right) \times (\nabla t_0) \qquad \text{(D–4)}$$	Hawthorne and Novak (ref. 3) —$\omega_{s1}=0$
$$\delta\Gamma_s = (\omega_s - \omega_{s0})_2 \cos \alpha_2$$ $$= \left(\omega_{n1} \frac{V_1\Gamma_{VA}}{V_\infty{}^2} + \frac{d\Gamma_V}{dn_1} \right) \frac{dn_1}{dn_2} \qquad \text{(D–5)}$$	L. H. Smith (ref. 5)—general
$$\delta\Gamma_s = -V_1 \frac{dV_1}{dz} \frac{\Gamma_{VA}}{V_\infty{}^2} + \frac{d\Gamma_V}{dz} \qquad \text{(D–6)}$$	L. H. Smith (ref. 5)—special case with $dn_1 = dn_2$ $$\omega_{n1} = -\frac{dV_1}{dz}$$
Γ_{VA} = actual (primary + secondary) circulation Γ_V = primary circulation n = distance normal to axisymmetric streamline	

The first case is as follows:

$$\omega_{s1} = 0$$

$$\omega_{n1} = -\frac{dV_1}{dz}$$

Hawthorne's equation (D–3) may be written as

$$\delta\Gamma_s = -\frac{dV_1}{dz}\left(V_1 \int \frac{ds}{V} \right) - \frac{dV_1}{dz}(\sigma \sin \alpha_1) + \frac{dV_1}{dz}\left(\sigma \frac{V_1}{V_2} \sin \alpha_2 \right) \quad \text{(D–3a)}$$

Smith's equation (D–6) may be written as

$$\delta\Gamma_s = -\frac{dV_1}{dz}V_1\frac{\Gamma_{VA}}{V_\infty{}^2} - \frac{d\Gamma_V}{dz} \qquad \text{(D--6a)}$$

The first two terms are clearly equivalent. Smith also shows that in the primary flow

$$-\frac{d\Gamma_V}{dz} = -\sigma\frac{d}{dz}(V_{\theta_1} - V_{\theta_2})$$

$$= -\sigma\left(\sin\alpha_1\frac{dV_1}{dz} - \sin\alpha_2\frac{dV_2}{dz}\right)$$

and since

$$\frac{dp_{o1}}{dz} = \frac{dp_{o2}}{dz}$$

$$\frac{dV_2}{dz} = \frac{V_1}{V_2}\frac{dV_1}{dz} = \frac{\cos\alpha_2}{\cos\alpha_1}\frac{dV_1}{dz}$$

so that

$$\frac{d\Gamma_V}{dz} = \sigma\left(\sin\alpha_1\frac{dV_1}{dz} - \sin\alpha_2\frac{V_1}{V_2}\frac{dV_1}{dz}\right) \qquad \text{(D--7)}$$

which establishes the identity of the other terms in the equations.

It is important to note here that in Smith's primary flow for this example there is no streamwise vorticity, so that there is no conflict in the definition of the secondary flow in this case.

Let us now examine the second case

$$\omega_{n_1} = 0 \qquad \omega_{s_1} \text{ finite}$$

Consider this Beltrami flow moving through a cascade of twisted flat plates that receive the flow at zero incidence and do not deflect it at all.

We cannot use Hawthorne's equation (D--3), which was derived for $\omega_{s_1} = 0$, but the general equation (D--1) shows that with no change in velocity, $(\bar{V}\cdot\nabla)\bar{V} = 0$ and

$$\omega_{s_2} = \omega_{s_1}$$

Thus, on Hawthorne's definition, the secondary vorticity at exit is equal to that at entry. It is from this total secondary vorticity that we may calculate the total flow velocity perpendicular to the vorticity vector.

From Smith's equation, since $\Gamma_{VA} = \Gamma_V = 0$, $\delta\Gamma_s = 0$; so, on Smith's definition, there is no secondary flow $(\omega_s - \omega_{s_0})_2 = 0$. However, primary vorticity $(\omega_{s_0})_2 = (\omega_{s_0})_1$ exists, so that there is vorticity $\omega_{s_2} = (\omega_{s_0})_1$ along the streamline in the total flow, as in Hawthorne's calculation.

This example illustrates the important difference in definition of secondary flow.

It appears then, from these examples, that the expressions given for secondary flow through stators are entirely consistent, provided the difference in definition is appreciated.

We now try to make a similar comparison for a rotating blade row and again consider a number of examples to which the various approaches must provide a solution. Equations now available are presented in table D–II, with $\bar{W}$ now the relative velocity.

We may at this stage note that A. G. Smith has simplified his equation to the form

$$\left(\frac{\omega_W}{W}\right)_2 - \left(\frac{\omega_W}{W}\right)_1 = \int_1^2 2 \frac{\nabla I}{\rho} \frac{\sin \gamma}{W^2} d\epsilon_R$$

$$+ \int_1^2 \frac{2\Omega}{W^3} \frac{\nabla I}{\rho} \cos \delta \, ds \qquad (D–12)$$

where δ is the angle between $\nabla I/\rho$ and Ω and is usually nearly $\pi/2$, so that the second term may be considered second-order for the purposes of this discussion; γ is the angle between $(\nabla I/\rho) \times \bar{W}$ and the direction of curvature of the relative streamline, which is also approximately $\pi/2$; and ϵ_R is the relative deflection. Thus

$$\left(\frac{\omega_W}{W}\right)_2 - \left(\frac{\omega_W}{W}\right)_1 = \int_0^{\epsilon_R} 2 \frac{\nabla I}{\rho} \frac{d\epsilon_R}{W^2} \qquad (D–13)$$

But $\nabla I/\rho = \bar{W} \times \bar{\omega}$; thus, if the *absolute* vorticity perpendicular to the relative stream line is $\omega_{R_{p1}}$ and the velocity changes little in a small relative deflection of the flow, then

$$\omega_{W_2} - \omega_{W_1} = -2\epsilon_R \omega_{R_{p1}} \qquad (D–14)$$

The present paper argues that the perturbations in the relative flow arise as a result of the absolute vorticity $\bar{\omega}$, but L. H. Smith again argues that the vorticity that should be used is the difference between the total absolute vorticity and the absolute vorticity in the primary flow $(\bar{\omega} - \bar{\omega}_0)$. This argument may be illustrated by a statement of the various velocities and their curl.

	Velocity	Curl
Absolute primary flow	$\bar{V}_0$	$\nabla \times V_0 = \bar{\omega}_0$
Disturbed total absolute flow	$\bar{V} = \bar{V}_0 + \bar{v}'$	$\bar{\omega} = \nabla \times V = \bar{\omega}_0 + \bar{\omega}'$
Disturbance flow (absolute)	$\bar{V} - \bar{V}_0 = \bar{v}'$	$\bar{\omega}'$
Relative primary flow	$\bar{W}_0 = \bar{V}_0 - \bar{\Omega} \times \bar{r}$	$\nabla \times \bar{W}_0 = \bar{\omega}_0 - 2\bar{\Omega}$
Disturbed total relative flow	$\bar{W} = \bar{V}_0 + \bar{v}' - \bar{\Omega} \times \bar{r}$	$\nabla \times \bar{W} = \bar{\omega}_0 - 2\bar{\Omega} + \bar{\omega}'$
Disturbance flow (relative)	$\bar{W} - \bar{W}_0 = v'$	$\nabla \times (\bar{W} - \bar{W}_0) = \bar{\omega}'$

TABLE D–II. *Equations for Secondary Flow (Rotating Coordinates)*

Equation	Reference and notes
$$(\vec{W}\cdot\nabla)\frac{\omega_W}{W}=\frac{1}{W^4}\left[2\left(\frac{\nabla I}{\rho}\right)\times\vec{W}\right]\cdot(\vec{W}\cdot\nabla)\vec{W}+\frac{2}{W^2}\left[\bar{\Omega}\cdot\left(\frac{\nabla I}{\rho}\right)\right]$$ $$(D\text{-}8)$$ where subscript w indicates resolution along the lines of the relative velocity, but ω is still the absolute vorticity. $$\omega_W=\nabla I\times\nabla t_0 \qquad (D\text{-}9)$$	A. G. Smith (ref. 8) Dixon (present paper)—presumably for $\omega_1=0$ only (potential flow at entry)
where, from Hawthorne's discussion of the present paper, $$t_0=\int\frac{ds_R}{W} \qquad (D\text{-}10)$$ $$(\omega_W-\omega_{W_0})=\left(W_{1\omega_{Rp1}}\frac{\Gamma_{VA}}{W_\infty^2}+\frac{d\Gamma}{dn_1}\right)\frac{dn_1}{dn_2} \qquad (D\text{-}11)$$ where ω_{Rp1} is the absolute vorticity, resolved normal to the relative streamlines at entry.	L. H. Smith (ref. 5)

In his derivation, Smith employs the Helmholz laws to determine how the absolute vorticity changes as the flow passes through a blade row, which may be rotating or stationary. He defines the secondary vorticity as the difference between the actual absolute vorticity and the absolute vorticity of the primary flow. His reason for using the difference between two absolute vorticities to obtain flow perturbations in the rotating coordinate system is illustrated in the paragraphs following Equation (D–14) of this discussion.

Thus, the disturbance flow is calculated from $\bar{\omega}'=\bar{\omega}-\bar{\omega}_0$, the difference between the total absolute vorticity and the absolute vorticity in the primary flow.

In Dixon's example in the paper, the primary flow is potential, so that $\bar{\omega}_0=$ zero, and both Dixon and L. H. Smith give the same answer.

We again consider a number of examples of flows through rotors in order to establish whether the various approaches give the same result.

We shall first consider A. G. Smith's example of uniform flow at the entry to a rotor.

If the entry flow is axial and uniform ($V_1=$ constant, $\omega_1=0$), then

$$\nabla\left(\frac{I_1}{\rho}\right)=\frac{\nabla p}{\rho}+\nabla\left(\frac{V_1^2+U^2}{2}\right)-\nabla\left(\frac{U^2}{2}\right)=0$$

It is then evident from A. G. Smith's equation that no *absolute* vorticity ω_W (resolved in the relative direction) can be developed along the streamline, even if the relative flow is deflected. The Hawthorne/Dixon equations imply that no absolute secondary vorticity (ω) can be generated since $\nabla I \times \nabla t_0$ is zero, and the primary flow is potential.

Consider the rotor to be made up of helical plates which do not deflect the flow and have no lift or circulation.

Both A. G. Smith's equations and the Dixon/Hawthorne equations show that the absolute vorticity (ω_W) does not change along the relative streamline in this case. ω_W is zero at entry and at exit. The primary flow also has zero vorticity $\omega_{W_0} = 0$ and the difference $\omega_W - \omega_{W_0} = 0$. There is no secondary flow.

L. H. Smith's equation shows that $\omega_W = \omega_{W_0}$ is zero since $\Gamma_{VA} = \Gamma_V = 0$.

We now consider a forced vortex flow entering a rotor; the entry tangential velocity is everywhere equal to the blade speed, but the entry axial velocity is uniform. The entry vorticity is in the axial direction, so that

$$\frac{\nabla I_1}{\rho} = \bar{W}_1 \times 2\bar{\Omega} = 0$$

The relative velocity and absolute vorticity vectors are parallel—a kind of rotating Beltrami flow. The Dixon/Hawthorne equation cannot strictly be used in this case since the entry flow is not potential.

Consider next this flow moving through rotating flat plates, aligned in the axial direction, operating at zero incidence with zero circulation and zero deflection. A. G. Smith's equations give the absolute vorticity $\omega_W = 2\Omega$ as unchanged. However, the primary flow also has vorticity $\omega_{0W} = 2\Omega$, so the difference $\omega_W - \omega_{W_0}$ is zero, and there is no secondary flow. (Note that 2Ω is subtracted from ω_W here, not because it is the curl of the blade speed but because it is the vorticity in the primary flow.)

L. H. Smith's equation (15) also gives $\omega_W - \omega_{W_0}$ as zero although the primary flow has leaving vorticity 2Ω.

The discussor's tentative conclusions are

(1)   The equations of Hawthorne and L. H. Smith are consistent for flow through stators, if account is taken of the different definitions of secondary flow.

(2)   The Dixon/Hawthorne equation (10) refers only to perturbations of a primary potential flow.

(3)   A. G. Smith's equation accurately describes the change in total absolute vorticity resolved along the relative streamline.

(4)   To determine the secondary flow in rotors, either L. H. Smith's equation or A. G. Smith's equation may be used, as long as the primary vorticity is first subtracted from the absolute vorticity in the latter case. The secondary perturbation flow is calculated from $\bar{\omega}_W - \bar{\omega}_{W_0}$.

B. LAKSHMINARAYANA (The Pennsylvania State University): The secondary flow approximations (namely, small shear and large disturbance) are inadequate for application to annulus wall or hub wall boundary layers. The Bernoulli surface rotation and viscous effects tend to reduce the development of secondary flow. This was indicated by B. Lakshminarayana and J. H. Horlock in reference D–3 where they adequately demonstrated that Bernoulli surface rotation and boundary-layer growth through the blade row should be taken into account for accurate prediction of secondary velocities and outlet angles, especially near the wall. In view of this work, it is somewhat surprising that the author was able to predict the outlet angles accurately (fig. 5) ignoring these effects. The radial or spanwise velocities plotted in figure 6 indicate that the distortions of Bernoulli surfaces in the author's inlet guide vanes are not negligible. The author's conclusion that the outlet angle predictions are good is based on only two experimental points inside the annulus wall boundary layer (fig. 5). It would be useful if the author could provide a few more data points, especially near the wall, and indicate whether the predictions are good in this region.

With regard to the rotor secondary flow, the components ω_{s2R} and ω_{n2R} at the inlet to the rotor (fig. 3) will vary through the boundary layer due to change in relative flow direction. This effect has been neglected in this paper, thus leading to inaccurate estimation of the streamwise vorticity downstream and the resulting perturbations. Inclusion of these effects is essential if accurate prediction near the wall is sought. I have illustrated this effect, quantitatively, for an isolated rotor with axial entry and neglecting the contributions to the downstream streamwise vorticity of the wake vortex sheets.

Using A. G. Smith's equation (eq. D–13 in the discussion by Horlock), the streamwise vorticity in the relative flow direction can be written as

$$\frac{\omega_{W_2}}{\Omega} = \sin \beta_1 - 2\epsilon \cos \beta_1$$

where Ω is the inlet absolute vorticity for axial entry of the absolute flow.

If $\Delta\beta$ is the change in relative flow direction at any location inside the boundary layer and $\epsilon_o + \Delta\beta$ is the corresponding turning angle of the relative flow, the following expression can be derived on the assumption that $\cos \Delta\beta \simeq 1$ and $\sin \Delta\beta \simeq \Delta\beta$

$$\frac{\omega_{W_2}}{\Omega} = \sin \beta_{1_o} - 2\epsilon_o \cos \beta_{1_o} + \Delta\beta(r) \sin \beta_{1_o}[2\epsilon_o + 2\Delta\beta(r) - \phi]$$

where subscript o refers to free-stream values and $\phi = \cot \beta_o$. The last term in the equation represents the error in neglecting the change in β_1 through the boundary layer. $\Delta\beta(r)$ can be derived from the known

absolute velocity distribution in the boundary layer. For example, for $\phi = 0.5$, $\epsilon_o = 25°$ and at the location where the absolute velocity is 60 percent of the free-stream velocity, the effect of neglecting this effect results in 20 percent error in the estimate of ω_{W_2}/Ω at this location. The magnitude of this error depends on the values of ϕ and ϵ; the error is largest for low-speed, large-turning or high-speed, low-turning blade rows. A similar correction can be incorporated in the author's general equation (5).

Thus the author's poor predictions for the rotor (fig. 9) may be due to

(1)   Neglect of the variation in ω_{s2R} and ω_{n2R} through the annulus wall boundary layer

(2)   Tip clearance effect, which has a tendency to underturn the relative flow (This effect has been neglected in this analysis.)

(3)   Boundary-layer growth through the rotor

S. L. DIXON (author): In the discussions presented by Professors Hawthorne and Horlock, the main point at issue is the effect of the streamwise vorticity entering a blade row on the secondary motion generated at exit. The extreme case of a Beltrami flow passing through a blade row poses some presently unanswerable questions on the flow angle leaving the blades. In this paper, I have been concerned with weakly sheared flow in which vorticity is *convected* by a primary potential flow. This potential flow *could* convect a Beltrami flow provided that, in the notation used by Hawthorne,

$$\lambda = \frac{\omega_{0s}}{W} = O(\epsilon)$$

Horlock has considered a forced vortex flow entering a rotor with a tangential velocity equal to the blade speed and having uniform absolute velocity in the axial direction. For this "rotating Beltrami flow," the primary flow has vorticity $O(1)$ and there is *no* transportation of secondary vorticity—at least not in the sense of the paper. The vorticity is an *integral* part of the primary flow. We could replace this flow by a primary potential flow convecting another flow whose vorticity is 2Ω. However, the theory is not valid for flows in which the vorticity is $O(1)$ and should not be applied to such an extreme case.

More light may be thrown on the way Beltrami flows behave by an extension of some analysis due to Hawthorne (ref. 11). We note that for a Beltrami flow in rotating coordinates

$$\omega = \lambda \mathbf{W} \qquad\qquad (D-15)$$

where λ is a scalar. By taking the curl of both sides of equation (D–15) and noting that div $\mathbf{W} =$ curl $\Omega = 0$, we find

$$\nabla^2 \mathbf{W} + \nabla\lambda \times \mathbf{W} = -\lambda \text{ curl } \mathbf{W} \qquad\qquad (D-16)$$

If we consider the special class of flows where $\lambda = \omega/W = \text{constant}$, then $\nabla\lambda = 0$ and

$$\nabla^2 \mathbf{W} = -\lambda \, \text{curl} \, \mathbf{W} = -\lambda(\omega - 2\Omega) \tag{D-17}$$

Using equation (D–15) in equation (D–17), we get

$$(\nabla^2 + \lambda^2)\mathbf{W} = 2\Omega\lambda \tag{D-18}$$

For the special case in which $\omega = 2\Omega$ (Horlock's "rotating Beltrami flow"), equation (D–17) gives us

$$\nabla^2 \mathbf{W} = 0$$

for which the only solution is $\mathbf{W} = \text{constant}$ (i.e., no secondary flow). When $\omega \neq 2\Omega$, equation (D–18) may be solved provided sufficient boundary conditions are known.

Professor Lakshminarayana has rightly mentioned that boundary-layer growth effects should be included in the method. In addition to this, I would include the changes in outlet angle due to flow separation. However, at present no reliable analytical method for predicting these changes is known. Whenever such a method becomes available its inclusion should significantly improve the accuracy of the predicted axial-velocity profiles after diffusing blade rows.

It is no longer possible to obtain any further experimental data from the original source.

The reason why directional changes of the vorticity vector induced by the vorticity itself have been neglected in the analysis is bound up with the nature of the approximations made in the secondary-flow theory. Hawthorne (ref. 3) has indicated that for small vorticity the primary flow may be assumed to remain on cylindrical surfaces of constant radius. If there is a distortion of these surfaces of $O(\epsilon)$, the effect on the vorticity components is $O(\epsilon^2)$ and may be neglected. The analysis given in the paper is based on the assumption of small vorticity, so that it would be incorrect to attempt the higher-order approximations suggested by Professor Lakshminarayana.

REFERENCES

D-1. CLEBSCH, A., *J. Reine. Angew. Math.*, Vol. 54, 1857, pp. 293–312. See also H. Lamb, *Hydrodynamics.* Sixth ed., Cambridge U. Press, 1932, p. 248.

D-2. GOMI, M., *Bull. Japan Soc. Mech. Engrs.*, Vol. X, No. 37, 1967, pp. 86–99.

D-3. LAKSHMINARAYANA, B., AND J. H. HORLOCK, Effect of Shear Flows on Outlet Angle in Axial Compressor Cascades—Methods of Prediction and Correlation With Experiments. *J. Basic Eng.*, March 1967, p. 191.

SESSION II

Two- and Three-Dimensional Viscid Flows

Chairman: J. P. JOHNSTON

PRECEDING PAGE BLANK NOT FILMED

The Effects of Rotation on Boundary Layers in Turbomachine Rotors[1]

JAMES P. JOHNSTON

Stanford University

The boundary layers in turbomachine rotors are subject to Coriolis forces which can (1) contribute directly to the development of secondary flows and (2) indirectly influence the behavior of boundary layers by augmentation and/or suppression of turbulence production in the boundary layers on blades. Both these rotation-induced phenomena are particularly important in the development of understanding of flow and loss mechanisms in centrifugal and mixed flow machines. The primary objective of this paper is to review the information available on these effects.

Prediction of the behavior of the fluid boundary layers in the rotors of a turbomachine is largely based on information derived from experience with stationary systems. Nevertheless, when viewed from stationary (inertial) coordinates, rotor flow is periodically unsteady, and when viewed from rotor attached (rotating) coordinates, although the relative flow is steady,[2] Coriolis and centrifugal accelerations must be included in the dynamic equations of motion (see Appendix I). No matter how one tries, dimensional analysis (see Appendix II) shows that a rotation parameter, in addition to the standard parameters—Mach number, Reynolds number, specific heat ratio, etc.—is required to fully specify gross flow conditions in a rotor. There is then no assurance that stationary flow results will provide an adequate basis for rotor flow analysis. Investigation of the important effects of rotation on boundary layers is the main theme of this paper.

---

[2] Unsteadiness due to pressure fields of adjacent stators and stationary blade wake effects are not considered in this paper.

The most appropriate rotation parameter depends on the particular application. The well-known Ekmann and Taylor numbers (see Appendix II) are sometimes useful, but in turbomachine applications we have found the rotation number, $Ro = 2\omega L/U$, which expresses, in a general way, the ratio of Coriolis to inertial forces in the relative flow, to be most useful. Ro is the inverse of the well-known Rossby number, $Ros = Ro^{-1}$, of geophysical applications. For example, in consideration of the general circulation of ocean basins or the earth's atmosphere an important characteristic is $Ros \ll 1$ and $Ro \gg 1$. However, for rotor flows, the opposite is generally the case, $Ros > 1$ and $Ro < 1$; that is, Coriolis accelerations in rotor boundary layers are generally small, but, as will become evident, not always unimportant.

Probably the most significant rotation number for a boundary layer is formed from δ, a boundary layer thickness, and a characteristic relative free-stream velocity, U_∞. In these terms Ro becomes, with the further insertion of rotor parameters,

$$Ro \triangleq \frac{2\omega\delta}{U_\infty} = 2\frac{u_{\text{tip}}}{U_\infty}\frac{\delta}{r_{\text{tip}}}$$

In most applications u_{tip}/U_∞ is limited to a range of magnitudes from 10 to 1. Thus, the maximum value of Ro is roughly

$$(Ro)_{\max} \approx 20\frac{\delta}{r_{\text{tip}}}$$

In turbine rotors, boundary layers are very thin, $\delta/r_{\text{tip}} < 10^{-3}$. Hence $(Ro)_{\max} < 10^{-2}$, and neglect of rotation effects is probably justified. At the other end of the spectrum are the layers in centrifugal compressors and pump impellers, where δ/r_{tip} may be as large as 10^{-1} and $(Ro)_{\max} \lesssim 1$ indicating the relatively large influence of Coriolis forces. In most applications, values of $Ro \lesssim 10^{-1}$ are more common. However, it has already been pointed out by Dean (ref. 11) that one cannot hope to understand the fluid dynamics of centrifugal rotor flow without an understanding of the effects that arise from system rotation.

Rotation manifests its influence on rotor boundary layers primarily through its effects on (1) *secondary flow*, and (2) *stability*, in the broadest sense. Each effect is considered briefly in the context of a radial-flow compressor, or pump, impeller passage.

Figure 1 illustrates a typical impeller and shows some characteristic relative velocity profiles inside, but near, the impeller exit plane. Profiles of this type have been shown experimentally a number of times (refs. 20, 16, 14, 33, 15, and 25) and may be inferred from other experiments (refs. 13 and 1, for example). The real relative velocity profiles always appear to be grossly different from those expected on the basis of inviscid
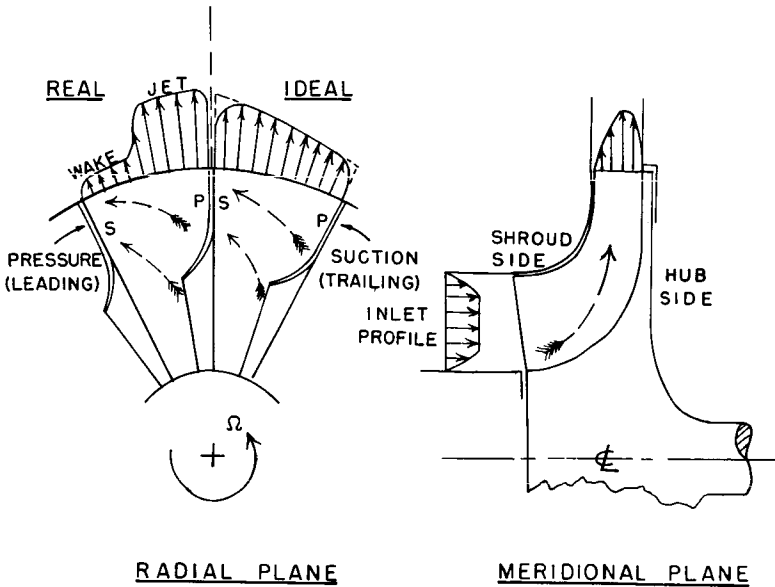
FIGURE 1.—*Centrifugal impeller flow. Dashed arrows indicate secondary flows.*

theory and normal boundary layer methods. It is common to find a thick wakelike region[3] near the blade trailing (suction) surface. This wake may result from more than one cause—certainly the deceleration of the trailing surface boundary layer contributes to the wake. However, secondary flows that arise from local layer growth and inlet total head deficits on the hub and shroud feed "tired" fluid into the trailing surface layer and thereby enhance the growth of the wake.

Secondary flow in the hub and shroud layers in the straight radial section of an impeller is a direct consequence of rotation. These low-speed layers are driven toward the trailing (suction) surface by the primary blade-to-blade tangential pressure field required to balance the Coriolis acceleration in the high-speed, relative, through flow. The qualitative aspects of secondary flows in centrifugal impellers are well illustrated in the visual studies of Senoo, et al. (ref. 42).

Although little work has been published to date on the effects of rotation on laminar boundary layer stability and the consequences of the stabilizing effects of rotation on turbulence, the idea that rotation can affect stability is not new; e.g., the classic study of G. I. Taylor (ref. 45) in 1932. Of more direct interest are the pioneering studies of Trefethen

---

[3] The consequences of the wake-jet effect on downstream flow and stage losses are discussed in references 11, 26, and 41.

(refs. 47 and 48) on laminar, transitional, and turbulent flow in long tubes that rotated about an axis perpendicular to the tube axis. In addition to noting the importance of secondary flows, he recognized that the transverse pressure gradients induced by Coriolis acceleration could affect the process of transition to turbulence by a mechanism similar to those operating in horizontal shear layers with density stratification.

The basic stabilizing mechanism is relatively easy to understand for a simple shear layer in a plane that rotates about an axis perpendicular to the plane of flow (fig. 2). A mean pressure gradient, $d\overline{p^*}/dy$, is required to balance the local mean Coriolis force, $2\rho\Omega\bar{u}$. Assume that a fluid particle is perturbed in the y direction to an adjacent layer (layer 1 to 2, fig. 2) while retaining its original mean velocity. The particle will be dynamically out of balance with the local mean pressure field at layer 2 and will tend to be accelerated away from its equilibrium layer, layer 1, if Ω is a positive number. In this crude sense, the flow is said to be destabilized by rotation. If Ω were negative, the particle would tend to return to its original position and the flow would be stabilized by rotation. From arguments of this type, one may derive a local profile stability parameter,

$$S = \frac{-2\Omega}{d\bar{u}/dy} \tag{1}$$

Positive values of S indicate stability and negative values instability. More exact reasoning, based on analogy to flows with mean streamline curvature[4] and horizontally stratified shear layers with vertical density gradients where centrifugal or buoyancy forces produce normal pressure gradients, led Bradshaw (ref. 7) to conclude that the proper local stability
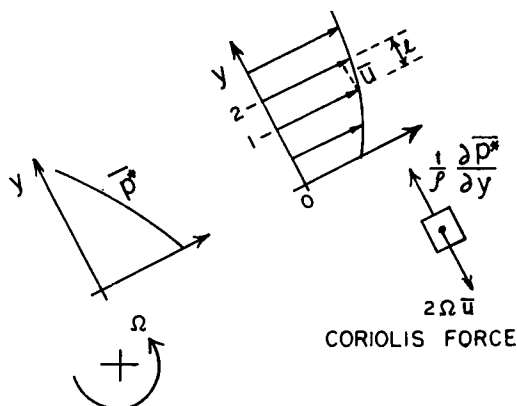

FIGURE 2.—*Pressure and velocity profiles in plane rotating shear flow.*

---

[4] See the classical inviscid stability analysis of Rayleigh (ref. 40) for curved flow.

parameter for plane rotating shear layers is the gradient Richardson number

$$Ri = \frac{-2\Omega[(d\bar{u}/dy)-2\Omega]}{(d\bar{u}/dy)^2} = S(1+S) \tag{2}$$

where $Ri > 0$ indicates the tendency for rotation to stabilize, and $Ri < 0$ to destabilize, the flow. The term

$$2\Omega - \frac{d\bar{u}}{dy} = \bar{\xi}_{abs} \tag{3}$$

is the absolute vorticity and should appear in a parameter of this type. Flow with zero absolute vorticity, whether rotating or stationary, should be neutrally stable to transverse perturbations (ref. 40). In conclusion, it must be recognized that this stability criterion takes no account of viscous effects which may increase, or decrease, the stability of the flow.

For our centrifugal impeller flow, figure 1, the trailing (suction) side boundary layers should be stabilized by rotation as $Ri > 0$. Conversely, on the leading (pressure) side they should be less stable than in similar, but nonrotating, flows. If the main core of the flow is induced from an isothermal, stationary atmosphere, it will be irrotational, $\bar{\xi}_{abs} = 0$, and neutrally stable even though $S < 0$ in this region. In real flows, the shear layer separating the trailing side wake from the main flow (jet) should be more than normally stable because $Ri > 0$ in this region.

The consequences of these stabilizing effects on centrifugal impeller flow are incompletely understood, but Dean (ref. 11) has elucidated them in part. In the stabilized, trailing side layer and the wake-jet shear layer, transition to turbulence may be inhibited and/or the normal turbulent mixing processes reduced in magnitude and effect. On the leading side the opposite effects can occur. The stabilized trailing side layer, under an adverse streamwise pressure gradient, may incur premature separation as a result of reduced turbulent stress levels. The reduction of mixing effectiveness in the wake-jet shear layer may contribute to the sometimes rather steep velocity gradients.

The computation of real flows in real centrifugal impellers is not possible today, in part due to lack of knowledge of the quantitative effects of rotational stabilization and in part due to the complex geometry of the blade passages. The basic theory of secondary flow in viscous boundary layers is known[5] for rotational flows as well as stationary flows, but the geometric complications (e.g., corners) and the interaction of the growing layers with the core flow, especially if stall occurs in a blade passage,

---

[5] The exception is turbulent layers in corners. Theory for three-dimensional thin turbulent layers on essentially flat walls is currently developing rapidly.

make direct application of theory problematical. Only for very simplified geometries and conditions has progress been made in the quantitative aspects of the problems. The remainder of this report will deal primarily with these simple cases in the hope that some better understanding of the phenomena may be attained.

ROTATION-INDUCED SECONDARY FLOWS

It is relatively easy to understand the qualitative behavior of rotation-induced secondary flows. However, the quantitative calculation of such flows starting from the boundary layer equations is generally not simple. In many cases, sufficient understanding may be gained from use of inviscid secondary flow theory. For example, in centrifugal rotors the major secondary flows often result from shroud boundary layers generated in the inducer section and/or other axial velocity profile nonuniformities (primary vorticity) that enter the impeller from upstream. When such effects are present, the streamwise (secondary) vorticity that develops downstream in the rotor depends to only a negligible extent upon local viscous effects.

It is not the intent of this paper to review inviscid theory in detail. Kramer and Stanitz (ref. 30) and Smith (ref. 44) develop the basic theory for application to incompressible fluids in rotating coordinates while Howard (ref. 24) extends it to simple compressible fluids. Application of the theory to real rotor flows appears to be rare, but there are useful exemplary calculations in references 30 and 44 and some attempts at prediction of real flows in centrifugal impellers in references 24 and 25.

In strictly axial-flow impellers, inviscid and viscous theory shows that coordinate rotation has no effect on the development of secondary vorticity in end-wall boundary layers. End-wall secondary flows develop due to the pressure field caused by turning the relative flow. However, secondary (radial) flows may develop on axial rotor blading as a consequence of coordinate rotation. In the latter case, because the layers generally start thin and grow in the chordwise direction, the full equations rather than inviscid theory should be employed.

The simplest case of rotation-induced secondary flow is the radial outflow in the boundary layer on a rotating disk. The laminar solution is well known, and since the classic stability and transition studies of Gregory, et al. (ref. 18), increasingly sophisticated solutions of the turbulent problem have become possible. The references to this problem are too numerous to list here, but useful solutions of the turbulent disk problem start with von Karman's paper (ref. 27) in 1921. A recent study on this topic, Cham (ref. 8), compares a variation of Head's entrainment method for solution of the three-dimensional turbulent boundary layer to

experiment. In comparison to the laminar flow solution, the most striking feature of the turbulent disk flow is the relatively small values of the secondary radial flow velocities.

Axial Rotor Blade Boundary Layers

Closely related to the simple disk flow problem are problems concerning boundary layers on axial-flow rotor and propeller blades. Because un-stalled, axial rotor blade layers remain very thin, it has usually been assumed that the radial, secondary flows developed therein may be neglected. One of the first examinations of this rotational effect appears to be that of Banks and Gadd (ref. 2) who considered laminar and tur-bulent layers on rotating, helical surfaces, and the limiting case of sectors of flat circular disks, in an attempt to study viscous flow effects on ship propellers. Lakshminarayana (ref. 31) and Horlock (ref. 23) have recently reported work in progress for similar geometries. Figure 10 in reference 23 gives some calculated results for a segment of a disk where the boundary layer grows from its leading edge. It is shown there, as for full disk flows, that the secondary skewing of a turbulent layer is much less than that of a laminar layer. Similar results in reference 2 confirm this conclusion and, in addition, it is pointed out that unless the tangential flow tends to separate, or the tangential velocity profiles become quite distorted as a result of axial (chordwise) adverse pressure gradients, the radial flows will be very small for the turbulent case. For normal blade chord lengths and non-separating turbulent conditions, the conventional neglect of this effect may indeed be justified.

On the other hand, if the flow is separating, or close to two-dimensional stall, the radial secondary flows may be important. Banks and Gadd (ref. 2) note the possibility that, as the chordwise profiles distort, the development of larger radial flows leads to a chordwise component of Coriolis force[6] that may be capable of "bucking" the adverse, chordwise pressure gradient and perhaps cause delay of two-dimensional, profile separation compared to an otherwise equivalent nonrotating flow. This rather surprising idea appears not to have been pursued too far in turbo-machine flow research, although the authors of reference 2 say that the experiments of reference 22 on propeller lift coefficients tend to confirm this conclusion. It is believed that further work on this phenomenon could be justified. Experimental work would need to be done in a rotor as there appears to be no way to model the effect in a stationary system; i. e., a cascade.

---

[6] Believed to be the "coupling" effect mentioned by Horlock (ref. 23) as now under study.

Radial Passages, Tubes, and Ducts

Compared to axial flow rotors, blade passages in centrifugal impellers are more nearly like long ducts; that is, passages whose lengths are at least several times greater than their hydraulic diameters. As a consequence, boundary layers tend to be relatively thick compared to passage sectional dimensions and the secondary flows developed therein of considerable importance. In this section, we shall briefly review some basic results on flow in long tubes and ducts that rotate steadily about axes perpendicular to the main flow, x, direction (see fig. 3). Most studies that are of more than qualitative value have confined consideration to very long ducts where the flow is fully developed, or nearly so. The recent study by Moore (ref. 37) is a notable exception and will be discussed at the end of this section.

Laminar flow in long, rotating ducts has been analyzed for two limiting cases: (1) very small rotational speed ($Ro \ll 1$) and (2) large rotational speeds ($Ro \gg 1$). The latter case (see refs. 5 and 6) is of little interest in turbomachine applications, but the former, studied by Barna (ref. 3) and Benton (ref. 4), is of interest. For case (1), when the channel rotation number, $Ro_c \triangleq 2\omega D/\bar{u}_m$, or tube number, $Ro_d \triangleq \omega d/\bar{u}_m$, is small, the experimental results of Trefethen (refs. 47 and 48) on round tube flows and the recent work by Moore (ref. 36) on turbulent flow in rectangular ducts may profitably be reviewed.

As shown in references 3 and 4, the fully developed, laminar flow in round tubes is a small perturbation on Hagen-Poiseuille flow for $Ro \ll 1$. Counter-rotating, secondary flows develop above, and below, the plane which divides the tube and is perpendicular to the axis of rotation. The
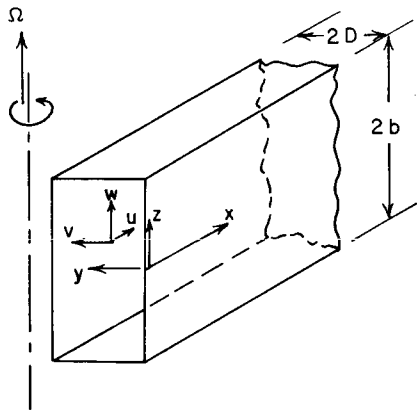

FIGURE 3.—*Rotating rectangular channel.*

additional dissipation engendered by the secondary motions results in an increase of the friction factor, $\hat{f}$. To first order, the ratio $\hat{f}/\hat{f}_0$ (friction factor to the zero-rotation friction factor) was found to be simply related to the parameter $Re_h\sqrt{Ro_d}$. Experimentally, Trefethen (refs. 47 and 48) essentially confirmed this result, but best agreement with his data that span the range $2\times10^2 < Re_h\sqrt{Ro_d} < 3\times10^3$ fits the formula

$$\frac{\hat{f}}{\hat{f}_0} = 0.20\,(Re_h\sqrt{Ro_d})^{0.4}$$

The data become nearly tangent to Barna's linearized theory for $Re_h\sqrt{Ro_d} = 3\times10^3$. Clearly, the secondary flows generated by rotation can significantly affect laminar friction factors in long, round tubes.

In most rotor flows the small rotation condition, $Ro < 1$, should hold, but laminar flow is unlikely because of the high Reynolds numbers. Furthermore, passages are generally rectangular rather than round. Turbulent friction factors for round tubes are presented in references 47 and 48 and by Moore (ref. 36) for rectangular ducts (fig. 3) of aspect ratios: $AS\triangleq b/D = \frac{1}{2}:1$, $1:1$, $4:1$ and $7\frac{1}{3}:1$. These results show that for values of $Ro_c\lesssim0.05$, which are typical in practice, the rotation may increase friction factors by ~20 percent at most. Moore's results for $AS = 1:1$, as one might expect, were consistent with those for round tubes. However, the uncertainty in the data is too high to allow recommendation of formulas for $\hat{f}/\hat{f}_0$.

Moore's results (ref. 36) and similar related experiments (refs. 21 and 35) contain measurements of mean velocity profiles, wall shear stress, and turbulence, $\overline{u'^2}$, profiles measured at the duct center plane (see ¢ in fig. 4) in addition to friction factor data. Only the wall skin friction coefficient, c_f, data at the symmetry plane will be discussed. These data were obtained by the Preston tube method for a range of Reynolds numbers, $Re_h\approx1.3$ to 3.9×10^4 and rotation numbers up to $Ro_c\approx0.05$ for each of the four channels. The data are plotted in figure 5 as $c_f/(c_f)_0$ versus channel aspect ratio. Channel trailing (suction) side wall stress is seen to be lower, and leading (pressure) side stress higher than the no-rotation stress at the same aspect ratio and Reynolds number. The effect of rotation decreases with increase of aspect ratio, but at all aspect ratios except $1:1$ on the trailing side, increasing rotational speed increases the deviation of c_f from its no-rotation value.

As pointed out by Moore (ref. 36), these trends appear to be primarily associated with the secondary flow patterns developed in the channel. Figure 4 indicates typical qualitative secondary streamline patterns for ducts of low and high aspect ratio. Clearly the flow of energy-deficient fluid from the end walls to the trailing surface and the return flow near the channel center plane should be more important at low than at high aspect ratios. End wall regions are a less important fraction of the flow
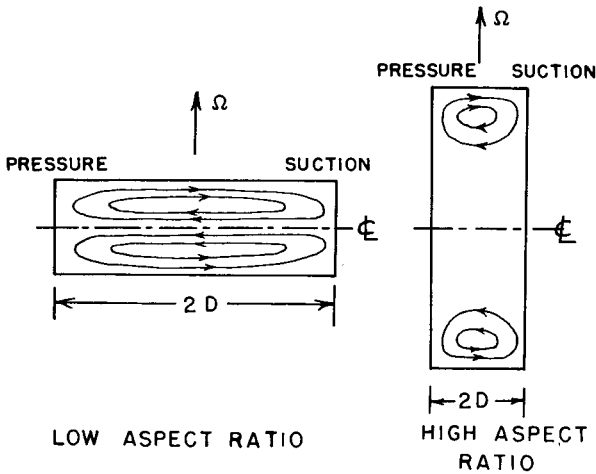
FIGURE 4.—*Secondary-flow streamlines in long rotating channels.*
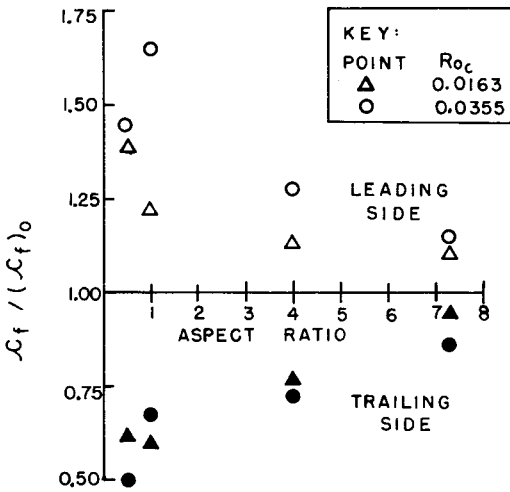
FIGURE 5.—*Skin friction coefficient versus channel aspect ratio; data of reference 36, figure 18.*

field and further removed from the center plane at high aspect ratio. In the limit, as $AS \to \infty$, secondary flow theory would result in the prediction that $c_f/(c_f)_0 = 1$ independent of channel rotational speed. Moore's results (those of fig. 5 and others) are clear proof that rotation-induced secondary flow plays a very important role in the fluid dynamics of turbulent passage flows, particularly in ducts of low aspect ratio. However, the effects of stability must also be considered. It is my belief that at $AS = 7\frac{1}{3}:1$ the

effects noted by Moore are dominated by the stability of the flow and hardly influenced by secondary flow except near the duct end walls. Demonstration of this conclusion will be discussed in the section on turbulent channel flow–experimental results.

The only known complete study of the effects of secondary flow in a passage that is in any way closely comparable to a radial-flow centrifugal impeller passage is that of Moore (ref. 37). He conducted low-speed, air-flow experiments centered on study of the developing side-wall turbulent boundary layers in a rotating, radial, two-dimensional diffuser of 15° included angle between the leading and trailing sides. Boundary layers were thin at channel inlet on all walls, and the core of the flow was irrotational in stationary coordinates; i.e., $\bar{\xi}_{abs} = 0$. In addition, he computed the end-wall and side-wall layers using a known turbulent layer method[7] modified to include the rotation-driven secondary flows. His procedure included a simple momentum transport theory for the corner regions and simultaneous computation of the core flow. The results indicate that secondary flow from pressure to suction side significantly alters the development of all boundary layers. The pressure (leading) and end-wall layers are thinned and the suction-side layer thickened even though the potential core flow region imposes more adverse pressure gradient on the pressure-side layer than on the suction-side layer. A large "wake" region develops downstream on the suction side. It appears to be fed by the end-wall cross flows and has little or no backflow. In addition, the wake shear layer seems to be unusually quiescent with little mixing as might be expected from the stabilizing influence of rotation.

The agreement between theory and experiment in this case (ref. 37) is quite reasonable and leads one to hope that one may eventually apply three-dimensional turbulent boundary layer theory to more realistic impeller design problems. Of course, in many real situations the inlet conditions and channel geometry will considerably complicate the situation (see the introduction to this section).

BOUNDARY LAYER STABILITY AND TURBULENCE

To limit discussion, the remarks of this section will be confined to flows that are incompressible, steady and two-dimensional in the time mean, and in which the mean relative velocity lies in planes perpendicular to the axis of system rotation. Three-dimensional fluctuation and steady perturbations that do not arise as a consequence of end walls must, however, be allowed. In addition the mean flow will be assumed parallel, or

---

[7] Similar to the Moses method (see ref. 49).

nearly parallel (boundary layer), shear flow (see fig. 2). The Cartesian components of velocity are

$$u = \bar{u} + u'$$

$$v = \bar{v} + v'$$

$$w = \bar{w} + w'$$

Here $\bar{v} \ll \bar{u}$ and $\partial(\overline{\quad})/\partial x \ll \partial(\overline{\quad})/\partial y$ are the boundary layer assumptions. $\bar{w} = 0$ and $\partial(\overline{\quad})/\partial z = 0$ limit the mean flow to be two-dimensional.

The time mean boundary layer equations obtained from equations (22) and (28) and these assumptions are

$$\bar{u}\frac{\partial \bar{u}}{\partial x} + \bar{v}\frac{\partial \bar{u}}{\partial y} = -\frac{1}{\rho}\frac{\partial \overline{p^*}}{\partial x} + \nu\frac{\partial^2 \bar{u}}{\partial y^2} + \frac{1}{\rho}\frac{\partial(-\rho\overline{u'v'})}{\partial y} \tag{4}$$

in the x-direction, and

$$2\Omega\bar{u} = -\frac{1}{\rho}\frac{\partial \overline{p^*}}{\partial y} - \frac{\partial(\overline{v'^2})}{\partial y} \tag{5}$$

in the y-direction. The time mean continuity equation is

$$\frac{\partial \bar{u}}{\partial x} + \frac{\partial \bar{v}}{\partial y} = 0 \tag{6}$$

If $\overline{p_a^*}$ is the value of $\overline{p^*}$ at a plane $y = a$ where $\overline{v'^2} = \overline{v_a'^2}$, equation (5) can be integrated at any x-station to obtain

$$-\frac{1}{\rho}\overline{p^*} = -\frac{1}{\rho}\overline{p_a^*} + 2\Omega\int_a^y \bar{u}\, dy + (\overline{v'^2} - \overline{v_a'^2})$$

This equation is then differentiated with respect to x and substituted into equation (4) to give

$$\bar{u}\frac{\partial \bar{u}}{\partial x} + \bar{v}\frac{\partial \bar{u}}{\partial y} = -\frac{1}{\rho}\frac{d\overline{p_a^*}}{dx} + 2\Omega\int_a^y \frac{\partial \bar{u}}{\partial x}\, dy - \frac{d\overline{v_a'^2}}{dx}$$

$$+ \frac{\partial \overline{v'^2}}{dx} + \nu\frac{\partial^2 \bar{u}}{\partial y^2} + \frac{1}{\rho}\frac{\partial}{\partial y}(-\rho\overline{u'v'}) \tag{7}$$

which reduces the mathematical description to two equations, (6) and (7). For a boundary layer, $\overline{p_a^*}$ and $\overline{v_a'^2}$ are presumably given functions of x in the free stream, or at a wall. For turbulent flow, additional input is, of course, required to describe $\overline{v'^2}$ and $\overline{u'v'}$.

Before proceeding to the discussion on fully turbulent and relaminarizing flows in rotating channels, it will be useful to review briefly some laminar flow stability results obtained by linearized small disturbance theory.

It is hoped thereby to demonstrate the pertinence and utility of the Richardson number and other rotation parameters.

Laminar Stability

The stability of plane, rotating, laminar shear flows has been examined by several investigators (refs. 10, 34, and 39) and is currently under investigation by our group (ref. 50). All this work utilizes linear stability theory and hence the results do not purport to predict laminar-turbulent transition.

In an early effort, Conrad (ref. 10) investigated the stability of the Blasius boundary layer on curved or flat rotating surfaces. He recognized, as did Mellor (ref. 34), that the system rotation and wall curvature terms that enter the linearized stability equations (Orr-Sommerfeld type) have no effect on the growth or decay of pure, two-dimensional disturbances such as Tollmien-Schlichting (T-S)[8] waves. However, the stability of the flow to longitudinal vortex cells of the Taylor-Görtler (T-G)[8] type is affected by rotation. Conrad assumed disturbances of the T-G type and obtained a solution that was unstable to cells of all wave lengths, λ, but most unstable to those of $\lambda \to \infty$. Considering only layers on flat rotating walls, the Reynolds numbers required for instability were found to be

$$Re_\delta \gtreqqless \frac{8.8}{\sqrt{Ro_\delta}}$$

where the thickness δ in the parameters is the 99 percent boundary layer thickness of a Blasius layer. It is now known that this solution is valid only for $|Ro_\delta| \ll 1$, as terms required for complete solution were dropped before linearization of the stability equations. A leading side flow corresponds to positive values of Ro_δ and may be unstable to T-G disturbances, but a trailing side flow is stable as shown by the solution above where only imaginary Reynolds numbers result when Ro_δ is negative.

Recently, Potter and Chawla (ref. 39) have investigated the stability of the Blasius layer on flat rotating walls using a general disturbance perturbation containing both T-S waves and T-G cells. Their work complements and extends Conrad's work, although they did not examine the pure T-G cell problem.

We have found a simpler problem for which the T-G disturbance solution is completely known for all values of Ro: the simple Couette flow between flat, parallel walls, one of which is sliding at speed U (see fig. 6). The exact analogue of this problem is the thermal instability problem of Bénard as solved in reference 9. From that solution, the most unstable

---

[8] For brevity, the abbreviation T-S will be used for Tollmien-Schlichting waves and T-G for Taylor-Görtler cells.

FIGURE 6.—*Couette flow between rotating channel walls.*
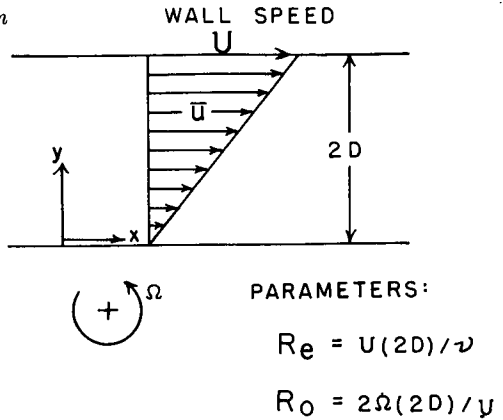
T-G cell has a wave length $\lambda = 2.02$ $(2D)$ for which the critical Reynolds number $(Re \triangleq 2DU/\nu)$ is

$$(Re)_{\text{crit}} = \frac{41.3}{\sqrt{Ro(1-Ro)}} = \frac{41.3}{\sqrt{-Ri}}$$

where $Ro \triangleq 2\Omega(2D)/U$. For this flow the local profile stability parameter, the gradient Richardson number, is a constant as $Ro = -S$ and hence $Ro(1-Ro) = -Ri$. The flow is always stable for $Ri > 0$, and tends to be unstable for $Ri < 0$. For the particular condition where $Ro = -S = \frac{1}{2}$, Ri obtains its minimum value of $-\frac{1}{4}$, for which the minimum value of the critical Reynolds number becomes 82.6. At all other positive values of Ro, values of Re larger than 82.6 are required for instability.

We (ref. 50) have also examined the stability of laminar, fully developed flow in a rotating channel (fig. 7). The mean profile is parabolic and unaffected by rotation in this case (see the section on turbulent channel flow—theoretical considerations). The linear stability equations contain all rotation effects in a gradient Richardson number term, but, as $d\bar{u}/dy$ varies with y, the Richardson number is not a constant for the flow. With the assumption of T-G cell disturbances, numerical solution has yielded a minimum critical Reynolds number of $(Re)_{\text{crit}} = 88.7$ at a channel rotation number of $Ro_c = 0.5$. The Reynolds number is defined here as $Re = 2D\bar{u}_m/\nu$. The critical wavelength of the cell was computed as $\lambda = 1.28D$. The equations show that complete stability must occur for $Ro_c \geqq 3$, in which case the gradient Richardson number is greater than or equal to zero at all points in the flow.

As already pointed out, rotation does not affect stability of the flow to purely two-dimensional disturbances such as waves of the T-S type. If

FIGURE 7.—*Fully developed, laminar flow in a rotating channel.*

PARAMETERS:

$R_e = \bar{u}_m (2D)/\nu$

$Ro_c = 2 \omega D / \bar{u}_m$

$|\Omega| = \omega$
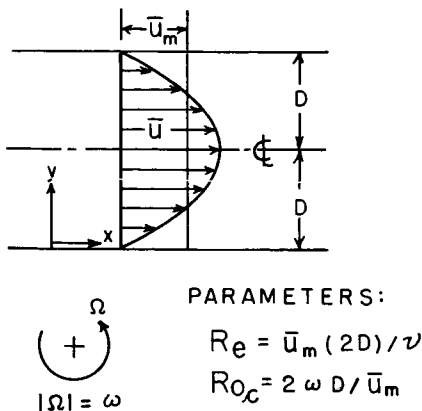
rotational speeds are very high, the Taylor-Proudman theorem indicates that three-dimensional disturbances are not possible. For example, T-G-type cells should be highly damped for large values of Ro. Hence, one might conclude that, even though two-dimensional disturbances may amplify in a rotating shear flow, the three-dimensionality required for breakdown of the flow to turbulence may be inhibited by rotation. If Ro is large enough, true turbulence may never occur in rotating flow. Certainly, one can expect to see a significant effect of rotation on the laminar-turbulent transition. Linear stability theory provides at least a guide and some feeling for the important physical parameters such as the gradient Richardson number which may, in part, control the transition process.

Turbulent Channel Flow—Theoretical Considerations

Under the conditions stated in the introduction to this section, the appropriate boundary layer equations are (6) and (7). If, in addition, the flow is fully developed between the parallel side walls of a channel where the end walls are very far apart ($b \rightarrow \infty$, fig. 3) then $\bar{v} = 0$ and $\partial \bar{u}/\partial x = 0$, etc. From equation (7) we obtain

$$\frac{d\overline{p_a^*}}{dx} = \frac{d\tau}{dy} = \text{constant} \tag{8}$$

where the total fluid shear stress

$$\tau = \nu\rho \frac{d\bar{u}}{dy} + (-\rho\overline{u'v'}) \tag{9}$$

Equation (8) shows that τ is a linear function of y as it is in stationary coordinates.[9] However, as will become evident shortly, the linear τ function is not generally symmetrical about the channel centerline, and we can expect $|\tau_T|$, the trailing (suction) side wall shear stress magnitude, to be less than $|\tau_L|$, the leading (pressure) side wall shear stress magnitude (see fig. 8). For small Ro_c, experiments (ref. 19) on turbulent channel flow indicate that the slope of the τ function is not affected by rotation and hence the channel pressure drop is dependent on Reynolds number alone, even though the wall stresses depend on rotation. In this section, qualitative explanation of these phenomena will be attempted.

Our approach is to start from the equations for the rate of generation (evolution or advection) of components $\overline{u'^2}$, $\overline{v'^2}$, and $\overline{w'^2}$ of the turbulence energy, $2\overline{q'^2}$, and Reynolds stress, $-\rho\overline{u'v'}$, as one follows a mean streamline; i.e., the equations for

$$\frac{D(\overline{u_i'u_j'})}{Dt} \triangleq \frac{\partial(\overline{u_i'u_j'})}{\partial t} + \bar{u}_l \frac{\partial(\overline{u_i'u_j'})}{\partial x_l} \tag{10}$$

in their special form for channel flow. Townsend (ref. 46) derived these equations for zero rotation and they were extended by Halleen and Johnston (ref. 19) to rotating flows. The extended equations differ from
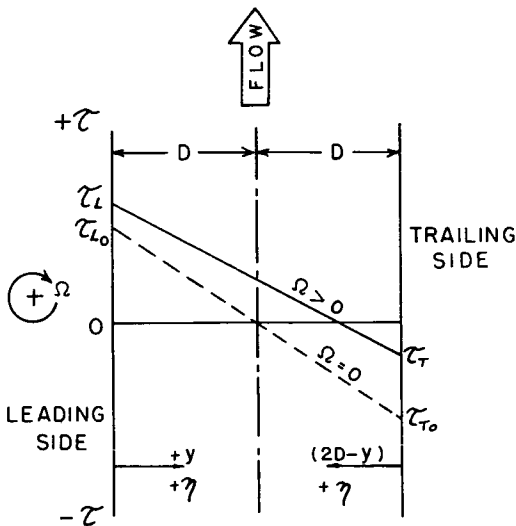

FIGURE 8.—*Shear stress distributions in fully developed channel flow; solid line for turbulent or mixed flow; dashed line also valid at all Ω with plane laminar flow.*

those of Townsend only by an additional rotation-induced turbulence production term. The total, general rate of production of turbulence term is

$$P_{ij} = (-\overline{u_i'u_l'}) \frac{\partial \bar{u}_j}{\partial x_l} + (-\overline{u_j'u_l'}) \frac{\partial \bar{u}_i}{\partial x_l} - [\overline{u_i'f_j'} + \overline{u_j'f_i'}] \qquad (11)$$

f_i' and f_j' are the fluctuating parts of the Coriolis acceleration term (see eq. 24). Hence, the rotational production terms are those in the square set of brackets. The full equations are shown as (12) in table I, as are their special forms for fully developed channel flow, equations (13) through (17).

First, consider equation (13) for $\overline{u'^2}$ and equation (14) for $\overline{v'^2}$. For positive rotation Ω and stress $-\overline{u'v'}$, production of the streamwise component $\overline{u'^2}$ is inhibited by rotation, whereas production of the transverse component $\overline{v'^2}$ is enhanced. This set of circumstances occurs near the leading (pressure) side of the channel. The reverse situation holds near the trailing (suction) side where $-\overline{u'v'}$ is negative (see fig. 8). Although the rotation Ω does not appear explicitly in the turbulence energy equation (eq. (16)) that is obtained by summing equations (13), (14), and (15), the fact that it affects the production rates of the components of $\overline{q'^2}$ shows that rotation plays a role in the establishment of the turbulence field.

The direct influence of rotation on turbulent stress $-\rho\overline{u'v'}$ is seen in equation (17), the equation for $-\overline{u'v'}$. Bradshaw (ref. 7) indicates that the effects of rotation are best illustrated by taking the ratio of (minus) the rotation production induced by $\overline{u'^2}$ to the production induced by $\overline{v'^2}$ This ratio, called the stress Richardson number, is

$$Ris = \frac{\overline{u'^2}}{\overline{v'^2}} \frac{-2\Omega}{(d\bar{u}/dy) - 2\Omega} = \frac{\overline{u'^2}}{\overline{v'^2}} \frac{S}{S+1} \qquad (18)$$

Except for the factor $\overline{u'^2}/\overline{v'^2}$, which in a boundary layer is roughly equal to or less than 4, Ris is equal to a flux Richardson number obtained by forming (minus) the ratio of total production of $\overline{v'^2}$ (eq. (13)) to total production of $\overline{u'^2}$ (eq. (14)); i.e.,

$$Rif = \frac{-2\Omega}{(d\bar{u}/dy) - 2\Omega} = \frac{S}{S+1} \qquad (19)$$

Both these ratios, in a sense, express the ratio of $-\overline{u'v'}$ production due to rotation to that caused by absolute vorticity, ξ_{abs}. Hence, in a region where $\xi_{abs} = 0$ all production, if any, is caused by system rotation. Close to

TABLE I.—*Turbulence Energy Equation in Rotating Frame for General and Fully Developed Channel Flow Case*

Equation number	Generation along mean streamline	Turbulence production		Turbulent field convective transport (diffusion)	Turbulent velocity pressure fluctuation interaction (pressure-strain)	Viscous turbulent field interaction (shear work) and (dissipation)	Description of terms
		(Mean flow shear production)	+ (Rotation induced production)				
(12)	$\dfrac{D(\overline{u_i'u_j'})}{Dt}$ (equation (10)) $=$	$(-\overline{u_i'u_l'})\dfrac{\partial \overline{u_j}}{\partial x_l}$ $+(-\overline{u_j'u_l'})\dfrac{\partial \overline{u_i}}{\partial x_l}$	$+\;-[\overline{u_l'f_j'}+\overline{u_j'f_i'}]$	$-\dfrac{\partial}{\partial x_l}(\overline{u_i'u_j'u_l'})$	$-\dfrac{1}{\rho}\left(\overline{u_i'\dfrac{\partial p'}{\partial x_j}}+\overline{u_j'\dfrac{\partial p'}{\partial x_i}}\right)$	$\nu\left(\overline{u_i'\dfrac{\partial^2 u_j'}{\partial x_l^2}}+\overline{u_j'\dfrac{\partial^2 u_i'}{\partial x_l^2}}\right)$	General equation for $\rho=$ constant Newtonian fluid with steady Ω

Equations for fully developed channel flow

Equation number	Generation along mean streamline	Turbulence production		Turbulent field convective transport (diffusion)	Turbulent velocity pressure fluctuation interaction (pressure-strain)	Viscous turbulent field interaction (shear work) and (dissipation)	Description of terms
(13)	0	$2(-\overline{u'v'})\dfrac{d\overline{u}}{dy}$	$-4(-\overline{u'v'})\Omega$	$-\dfrac{d}{dy}(\overline{u'^2 v'})$	$-\dfrac{2}{\rho}\,\overline{u'\dfrac{\partial p'}{\partial x}}$	$\nu\dfrac{d^2\overline{u'^2}}{dy^2}-2\nu\overline{\left(\dfrac{\partial u'}{\partial x_l}\right)^2}$	Equation for $\overline{u'^2}=\overline{u_{11}^2}$ (streamwise)
(14)	0	0	$+4(-\overline{u'v'})\Omega$	$-\dfrac{d}{dy}(\overline{v'^3})$	$-\dfrac{2}{\rho}\,\overline{v'\dfrac{\partial p'}{\partial y}}$	$\nu\dfrac{d^2\overline{v'^2}}{dy^2}-2\nu\overline{\left(\dfrac{\partial v'}{\partial x_l}\right)^2}$	Equation for $\overline{v'^2}=\overline{u_{22}^2}$ (transverse)

(15)	0	0	0	$-\dfrac{d}{dy}\overline{(w'^2v')}$	$-\dfrac{2}{\rho}\,\overline{w'\dfrac{\partial p'}{\partial z}}$	$\nu\dfrac{d^2\overline{w'^2}}{dy^2}-2\nu\overline{\left(\dfrac{\partial w'}{\partial x_l}\right)^{2}}$
(16)	0	$(-\overline{u'v'})\dfrac{d\bar u}{dy}$	0	$-\dfrac{d}{dy}\overline{(q'^2v')}$	$-\dfrac{1}{\rho}\dfrac{d}{dy}\overline{(p'v')}$	$\nu\dfrac{d^2\overline{q'^2}}{dy^2}-e$
(17)	0	$\overline{(v'^2)}\dfrac{d\bar u}{dy}$	$(\overline{u'^2}-\overline{v'^2})2\Omega$	$-\dfrac{d}{dy}\overline{(u'v'^2)}$	$\left(\overline{u'\dfrac{\partial p'}{\partial y}+v'\dfrac{\partial p'}{\partial x}}\right)\dfrac{1}{\rho}$	$-\nu\dfrac{d^2\overline{(u'v')}}{dy^2}+2\nu\overline{\left(\dfrac{\partial u'}{\partial x_l}\right)\left(\dfrac{\partial v'}{\partial x_l}\right)}$

Column descriptions:

- (15): Equation for $\overline{w'^2}=\overline{u_{33}'^2}$ (spanwise)
- (16): Turbulence energy equation
- (17): Principal Reynolds stress equation $(-\overline{u'v'})=(-\overline{u_1'u_2'})$

the walls, in the inner layers where

$$\left|\frac{d\bar{u}}{dy}\right| \gg |\ 2\Omega\ | \qquad \text{or} \qquad S \ll 1$$

one can conclude that $Ri s \approx 4S$, $Ri f = S$, and in addition the local stability parameter, the gradient Richardson number, $Ri = S$. Hence, in the wall layers, production of turbulent stress is enhanced by rotation where flow instability ($Ri < 0$) is indicated and reduced where stability ($Ri > 0$) is indicated by rotation.

These conclusions do not prove that shear stress magnitude will be greater near the leading side of the channel than near the trailing side. However, the demonstrated tendency of rotation to modify stress production in localized regions of the flow indicates that some excess, or deficit, of $-\rho \overline{u'v'}$ may occur in the layers where production is greater, or less, than that occurring under equivalent zero-rotation conditions.

Turbulent Channel Flow—Experimental Results

At Stanford, we have been studying the effects of rotation on turbulent, fully developed flow of water in a long channel of high aspect ratio, $AS = 7\frac{1}{3}:1$. The first results were reported by Halleen and Johnston (ref. 19). These consisted principally of dye flow visualization of the wall (sub)-layer structure (e.g., see ref. 29), measurements of wall shear stress, primarily by the Preston tube method, and measurement of the mean velocity profiles at the channel centerline (see ¢ in fig. 4). Recent work includes continued analysis of these earlier results and extensive new flow visualization work using the hydrogen bubble technique (ref. 50).

The results to be discussed were obtained far enough downstream in the channel ($x/D = 58$ and $x/D = 68$) so that the flow was quite close to fully developed. Reynolds numbers, Re_h, from 5×10^3, where fully turbulent flow is barely maintained at zero rotation, up to 6×10^4 were used, and a range of rotation numbers, Ro_c, as high as 0.2 at low Reynolds number and 0.08 at $Re_h = 6 \times 10^4$ were achieved in these studies.

Early in the program, the visual studies of the wall layers showed that the flow in the central regions of the wide ($2b = 11$ inches) side walls was not significantly affected by secondary flows from the narrow ($2D = 1.5$ inches) end walls. Hence, the conclusions and results to be discussed below are felt to be essentially independent of end-wall effects.

The two principal conclusions of the visual studies[10] are

(1)   Rotation suppresses turbulence production on the trailing (suction) side of the channel as anticipated. At sufficiently high Ro_c, complete laminarization of the trailing side wall layers was observed.

---

[10] See Fluid Mechanics Research Film No. J–1, by Halleen and Johnston, Engineering Societies Library, New York.

(2)   On the leading (pressure) side, it was difficult to observe the predicted increase of small-scale turbulence, but a new, large-scale structure in the form of Taylor-Görtler-like cells with their axes aligned in the mean flow direction was seen to appear at higher rotational speeds.[11]

Some of the evidence for these conclusions and some other observations are presented below.

Figure 9 shows a sequence of photographs of hydrogen bubble timelines generated on a wire mounted very close and parallel to the trailing wall and perpendicular to the oncoming mean flow (left to right). The Reynolds number was fixed at $Re_h = 1.5 \times 10^4$, and each picture represents conditions at successively higher Ro_c values. As Ro_c increases, the trailing wall layer structure progresses from a fully turbulent streak structure (see ref. 29) at $Ro_c = 0$ to a partly laminar structure at $Ro_c = 0.107$.

Visual data of this type, and the earlier dye studies, allowed the construction of a flow regime map for the trailing side (fig. 10). In the region below the band of points, the flow was judged to be fully turbulent, but for Ro_c values at, and just above, the band the wall layer is so stable that
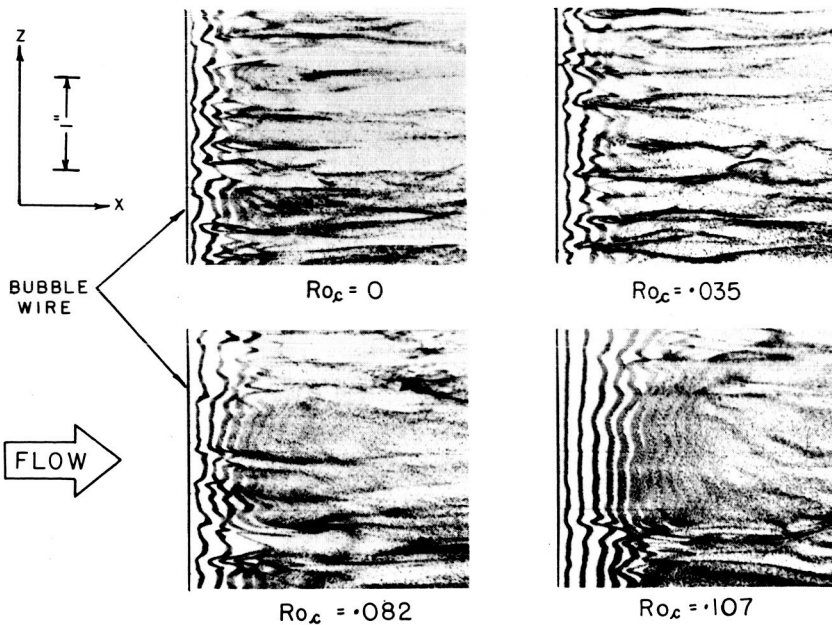
FIGURE 9.—*Hydrogen bubble time lines on channel trailing side*, $Re_h = 15\ 000$, *by D. K. Lezius in 1969. (ref. 50)*.

---

[11] T-G-type vortices have been observed in other turbulent flows such as cases with wall curvature (refs. 28, 38, and 43).
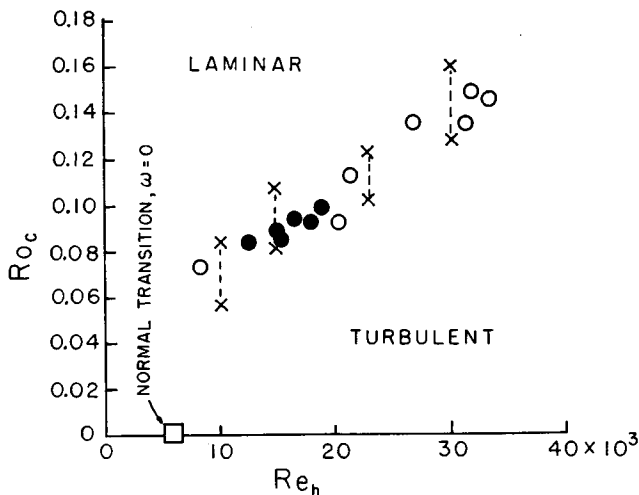
FIGURE 10.—*Wall-layer flow regime line on trailing side—circles from dye studies (ref. 19), open points stationary observer, closed points rotating observer; cross points from film scenes of H_2 bubbles by D. K. Lezius in 1969. (ref. 50).*

it could be called "laminarized." For very large Ro_c the wall layers on the trailing side were completely laminar.

Figure 11 is an attempt to qualitatively illustrate the leading side flow regime. In the early work (ref. 19) the existence of the vortex cells was deduced from the observation of regions of dye concentration (re-collection) near the center of the channel. The dye was injected slowly and uniformly along a spanwise slot at the wall, swept in the wall layers toward the region adjoining two cells, and then ejected away from the wall to form the region of re-collection above the cells. This vortex cell structure has been confirmed in recent hydrogen bubble pictures. It should be noted that these cells are not stationary in time and space once formed, but they shift sideways, disappear, and reform in an irregular way if the flow is viewed for a sufficient period of time.

Mean velocity profiles from reference 19 are shown in figures 12 and 13 for $Re_h \approx 6 \times 10^4$ and figure 14 for $Re_h \approx 2 \times 10^4$ on the trailing side. The considerable reduction in velocity gradients on the trailing side, and increase on the leading side, as rotation number increases is evident. As will be shown shortly, these changes are not just due to rotation-induced changes in shear stress, but also result from changes of mixing length (or eddy viscosity). At the lower Reynolds number (fig. 14), the shapes of the trailing side mean velocity profiles for $Ro_c \gtrsim 0.111$ show no resemblance to the standard turbulent law of the wall profile. At the highest Ro_c, the profile is nearly like the parabolic shape characteristic of laminar
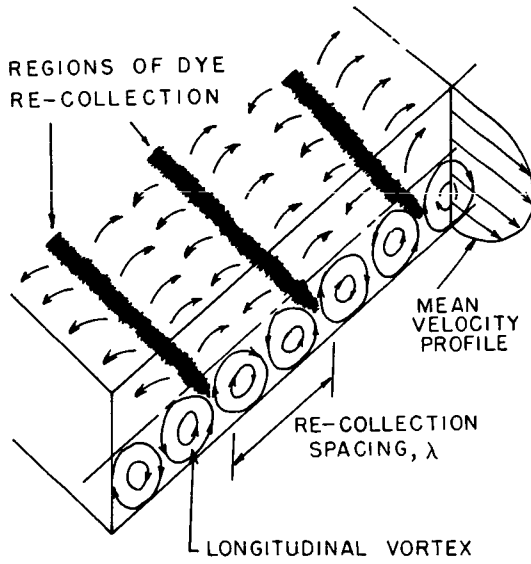
FIGURE 11.—*Longitudinal large vortex structure near leading wall; from reference 19.*
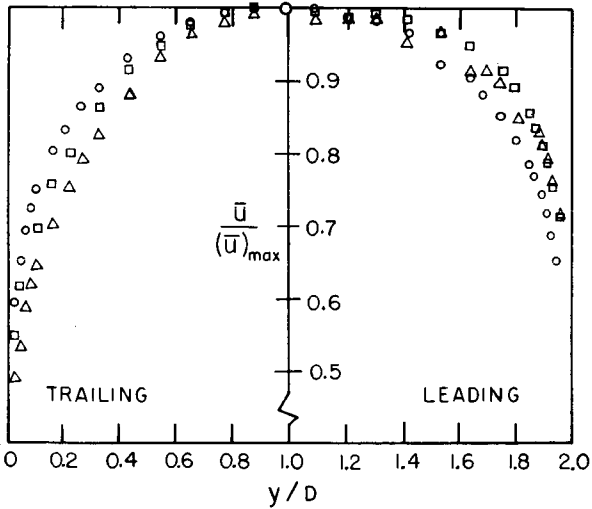
KEY:	POINT	Ro_c	Re_h	x/D
	O	0	57,200	68
	□	0.044	57,700	68
	△	0.083	60,400	68

FIGURE 12.—*Mean velocity profiles; rotating channel flow data of reference 19.*
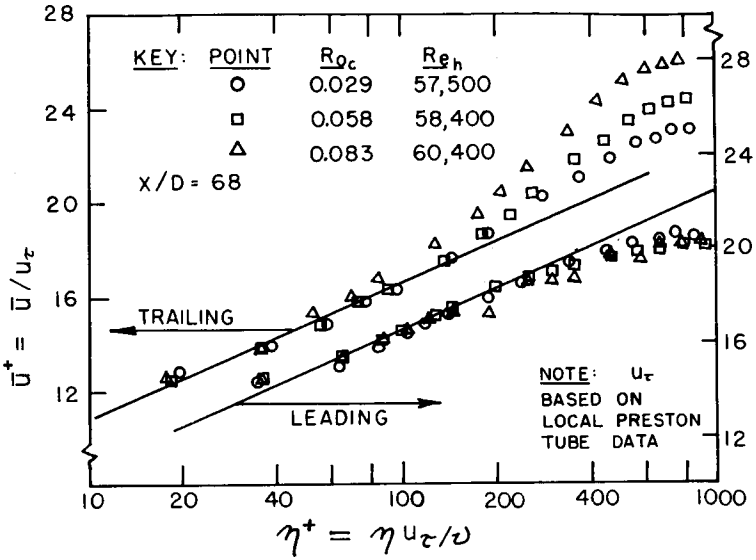
FIGURE 13.—*Mean velocity profiles; rotating channel flow data of reference 19; lines are 5.8 log$_{10}$ η^++5.0 fit to data at* Ro$_c$=0.
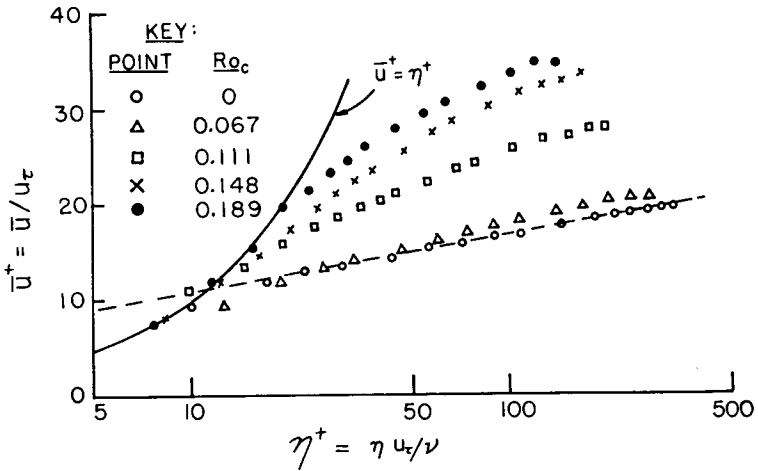
FIGURE 14.   *Mean velocity profiles on trailing side of rotating channel,* Re$_h$≈20 000, *x/D =68; data of reference 19.*

flow. This is further confirmation of the trailing side "laminarization" noted in the visual studies.

The Preston tube measurements of wall shear stress expressed as the ratio of wall shear velocity to zero-rotation wall shear velocity are plotted against rotation number in figure 15. Moore's data (ref. 36) for his $7\frac{1}{3}$:1
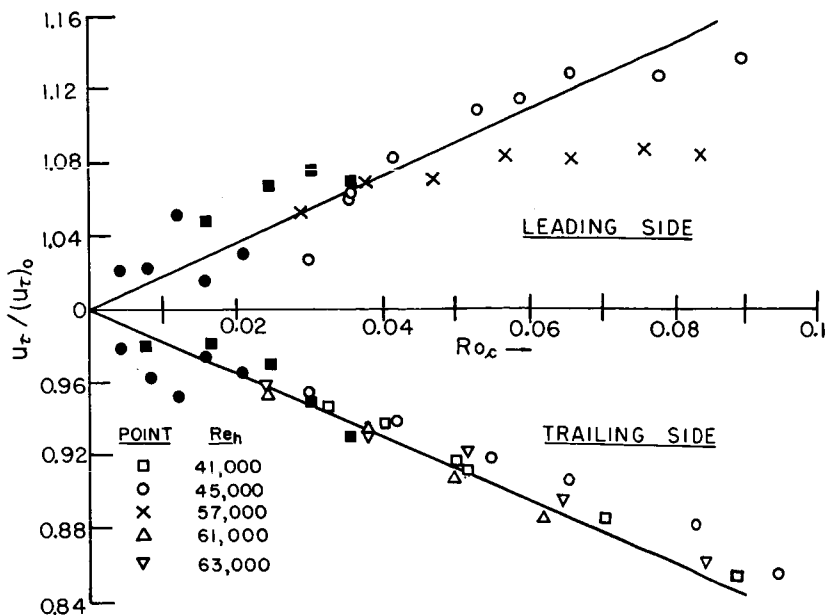
FIGURE 15.—*Ratio of wall shear velocity to zero-rotation wall shear velocity; open symbols from reference 19, closed symbols from reference 36.*

aspect ratio channel are also presented and appear to be in fair agreement with the data of reference 19. Since it has been shown that rotation changes the turbulence structure significantly for the Halleen and Johnston data, and that end-wall secondary flow was probably not significant in the region of measurement, the results of figure 15 bear up the previous conclusion that, at the higher aspect ratios, Moore's results reflect the effect of structure change rather than secondary flow.

An interesting feature of figure 15 is the apparent leveling out of the leading side u_τ values above some moderate value of Ro_c. This effect is believed to be a reflection of the onset of the large-scale longitudinal vortex structure on the leading side of the channel, but the matter is still under investigation.

The experimental data of Halleen and Johnston (ref. 19) are sufficient for the determination of the distribution of mixing length, l (or eddy viscosity), distribution for the channel. Mixing length was determined from these data, using the definition of l

$$l \triangleq \frac{\sqrt{\tau/\rho}}{(d\bar{u}/d\eta)}$$

where the τ-distribution for fully developed flow (fig. 8) was assumed to

fit between the measured values of wall shear stress. $d\bar{u}/dy$ was determined graphically from the measured mean velocity profiles.

The zero-rotation mixing lengths, l_0, are plotted in figure 16. At $Re_h = 2 \times 10^4$, it became evident from comparison of results at $x/D = 58$ and $x/D = 68$ that the flow in the channel was probably not quite fully developed. Hence, the results shown in figures 17 and 18 were only plotted for points of η less than ~0.04 ft, where the shear stress distribution assumption was felt to be valid.

The ratio l/l_0 is plotted as a function of gradient Richardson number, Ri, with Ro_c and Re_h as parameters in figures 17 and 18. The only data shown are for. the case where the whole channel flow was turbulent. Furthermore, no data points for η^+ less than ~50 were included, as these points lay in, and close to, the wall layers which could be partially laminar.

These figures show clearly that mixing length (and eddy viscosity) is reduced near the trailing wall (fig. 17) and increased near the leading wall (fig. 18). Although the accuracy of the results is not better than ±10 percent, it is believed that, at least near the trailing side, the separate influence of the global parameter Ro_c as well as the local variable Ri can be seen.
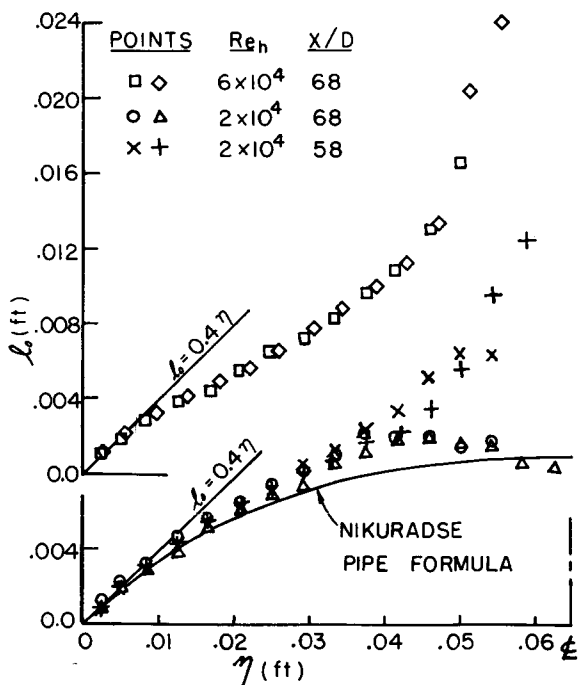
FIGURE 16.—*Zero-rotation mixing length profiles from data of reference 19.*
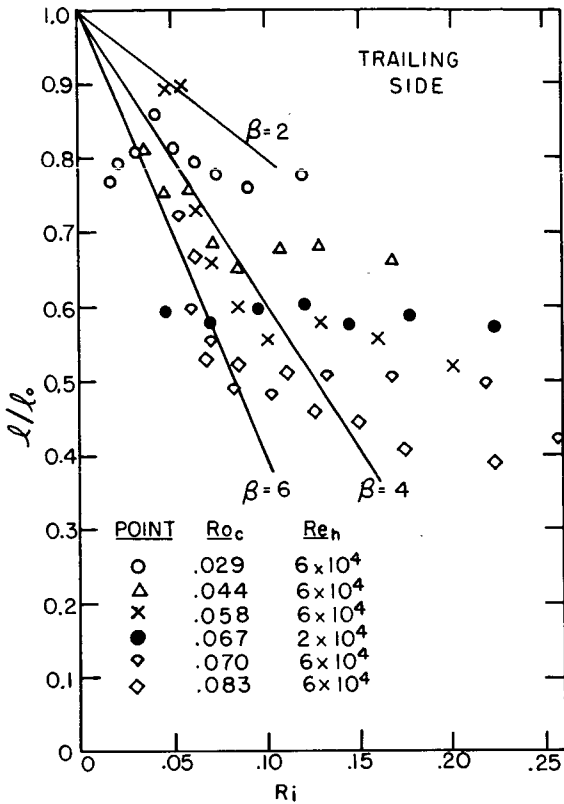
FIGURE 17.—*Mixing length ratio versus local gradient Richardson number on trailing side of channel; from data of reference 19.*

For small Ri, Bradshaw (ref. 7) suggests that a "Monin-Oboukhov" formula of the type

$$\frac{l}{l_0} = 1 - \beta Ri \tag{20}$$

might be useful to represent mixing length in flows with body force stabilization. This formula is plotted in figures 17 and 18 for values of $\beta = 2$, 4 and 6. Values of β from 4 to 6 may be acceptable for very small Ri, but the uncertainty in the data is too high to draw a firm conclusion.

The Monin-Oboukhov type of formula was originally developed to represent l in density-stratified, atmospheric, turbulent shear flow for regions of approximately constant Ri. In nearly normal, turbulent boundary layers, Ri is not a constant and the use of this simple representation for most cases of practical interest will be, at best, a crude approximation.
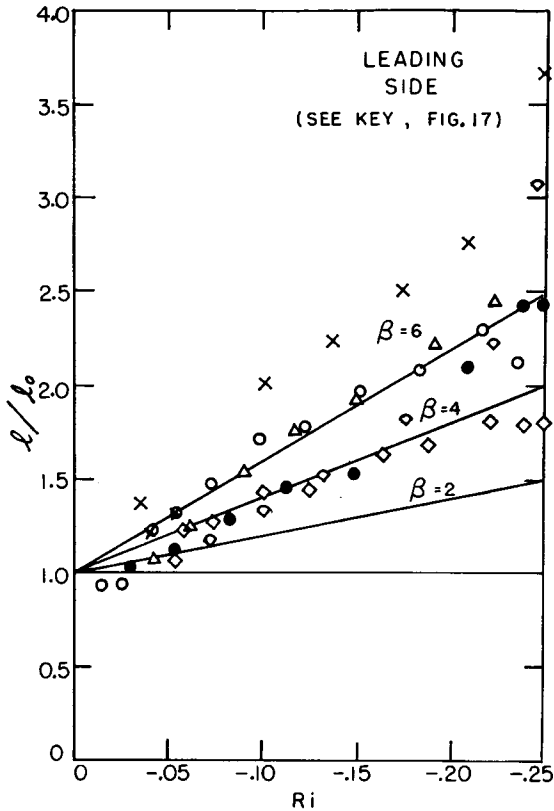
FIGURE 18.—*Mixing length ratio versus local gradient Richardson number on leading side of channel, from data of reference 19.*

Concluding Remarks

If the results of this section are to be employed in new boundary-layer computation methods, much remains to be done. To date, the ideas have only been used qualitatively in practice. For example, the two-dimensional, turbulent boundary-layer calculations shown by Litvai (ref. 32) for trailing side flow on a centrifugal impeller blade do not account for the effects of rotation on structure. His calculated results disagree with his measured results in a manner that tends to show that the experimental boundary layer remains transitional or laminar far downstream of the normal transition point. Qualitatively, this effect is to be expected from the results of this section. The influence of rotation on mixing in the shear layer above the trailing side wake region in Moore's recent experiments (ref. 37) on a rotating radial diffuser has already been quoted as a specific

qualitative example of the stabilizing influence of rotation on turbulence (see the section on radial passages, tubes, and ducts).

The successful inclusion of effects of rotation on turbulent structure in turbulent boundary-layer theory is most likely to be achieved in methods that attempt solution of the differential equations rather than momentum—or other—integral equation methods (see ref. 49) because of the greater ease of interpretation of the physical phenomena in the former methods. In the differential methods, direct use may be made of the equations for the components of Reynolds stress (e.g., table I) and/or simple equations such as the Monin-Oboukhov type of formula for mixing length may be employed.

ACKNOWLEDGMENT

The assistance of the author's past and present associates, in particular Mr. J. M. Kuhne, Dr. R. M. Halleen, and Mr. D. K. Lezius, is gratefully acknowledged.

LIST OF SYMBOLS

English Letters

AS	Aspect ratio, b/D
b	Half depth of duct between walls perpendicular to Ω
c_f	Skin friction coefficient, $\tau_w/(\rho/2)U^2$
D	Half width of duct between walls parallel to Ω
d	Diameter of round tube
d_h	Hydraulic diameter
e	Rate of viscous dissipation of turbulence energy, $\overline{q'^2}$ (see eq. (16))
f_i	Rectangular components $(i=1, 2, 3)$ of Coriolis acceleration vector (see eq. (24))
$\hat{f}$	Friction factor for tube or duct flow
L	Characteristic spatial dimension
l	Mixing length, $\sqrt{\tau/\rho}/(d\bar{u}/d\eta)$
P_{ij}	Total rate of production of turbulent energy and/or stress
p	Static pressure
p^*	Reduced static pressure, $p-\omega^2r^2/2+\Phi$
q'^2	Instantaneous turbulence energy, $(u'^2+v'^2+w'^2)/2$
Re	Reynolds number, UL/ν
Re_δ	Boundary layer thickness Reynolds number, $U_\infty\delta/\nu$
Re_h	Tube or duct Reynolds number, $\bar{u}_m d_h/\nu$
Ri	Gradient Richardson number, $S(1+S)$
Ro	Rotation number, $2\omega L/U$

Ro_δ Boundary layer rotation number, $2\Omega\delta/U_\infty$

Ro_c Channel (rectangular duct) rotation number, $2\omega D/\bar{u}_m$

Ro_d Round tube rotation number, $\omega d/\bar{u}_m$

Ros Rossby number, $U/\omega L$

r Radial distance from axis of rotation

r_{tip} Impeller tip radius

S Local mean profile parameter, $-2\Omega/(\partial\bar{u}/\partial y)$

U Characteristic relative velocity

U_∞ Free-stream relative velocity

u, v, w Components of relative velocity in x, y, z coordinate directions

u_i Rectangular components of relative velocity $(i = 1, 2, 3)$

$\bar{u}^+$ Wall shear normalized mean velocity, $\bar{u}/u_\tau$

u_τ Wall shear velocity, $\sqrt{\tau_w/\rho}$

u_{tip} Impeller tip speed

x, y, z Rectangular Cartesian coordinates used where Ω along z axis

x_i Rectangular Cartesian coordinates $(i = 1, 2, 3)$

Greek Letters

β A parameter (see eq. (20))

δ Boundary layer thickness

η Distance normal to a wall

η^+ Law of the wall coordinate, $\eta u_\tau/\nu$

λ Disturbance wave length

ν Kinematic viscosity

$\bar{\xi}_{abs}$ Absolute mean vorticity for two-dimensional shear flow, $2\Omega - (\partial\bar{u}/\partial y)$

ρ Fluid density

τ Fluid shear stress, $\nu\rho(\partial\bar{u}/\partial y) + (-\rho\overline{u'v'})$, in two-dimensional shear flow

τ_w Wall shear stress

Φ Scalar potential for conservative body force

Ω Coordinate rotation vector for case of Ω along z axis

Ω_i Rectangular components of Ω $(i = 1, 2, 3)$

ω Coordinate rotational speed (magnitude)

Superscripts and Subscripts

$'$ Fluctuating component of a nonsteady quantity; i.e., $u = \bar{u} + u'$

$-$ Time mean value of a quantity

m Mass average across flow of a quantity

0 Quantity evaluated at zero-rotation condition with all other conditions and parameters held fixed

T Wall value of quantity on trailing (suction) side

L Wall value of quantity on leading (pressure) side

APPENDIX I

Equations of Motion in Steadily Rotating Coordinates

The continuity equation and the dynamic equations of motion for a fluid in motion relative to observer coordinates rotating at a steady rate $\Omega_i (d\Omega_i/dt = 0)$ about an axis fixed in inertial space will be displayed and discussed briefly for the general case and the case of constant density and constant viscosity Newtonian fluids. Cartesian subscript notation, including the repeated dummy index convention to indicate summation, will be used. However, the general vector notation will be used, where convenient, to increase understanding. For example, the system rotation vector is $\Omega_i = \mathbf{\Omega}$, and the fluid velocity vector, relative to the rotating system, is denoted by $u_i = \mathbf{u}$.

The *continuity* equation in the rotating system is no different than in inertial coordinates,

$$\frac{\partial \rho}{\partial t} + \frac{\partial}{\partial x_j} (\rho u_j) = 0 \tag{21}$$

For constant density fluids, it is

$$\frac{\partial u_j}{\partial x_j} = 0 \qquad \text{or} \qquad \mathbf{\nabla} \cdot \mathbf{u} = 0 \tag{22}$$

The *dynamic equations* of motion contain two additional inertia terms, the Coriolis and centrifugal acceleration terms. The *Coriolis acceleration* vector is

$$\mathbf{f} = 2\mathbf{\Omega} \times \mathbf{u} \tag{23}$$

or, in Cartesian tensor notation,

$$\mathbf{f} = f_i = 2e_{ijk}\Omega_j u_k \tag{24}$$

where e_{ijk} is the unit cyclic coefficient.[12] The *centrifugal acceleration* caused by system rotation is $\mathbf{\Omega} \times (\mathbf{\Omega} \times \mathbf{r}_0)$ where $\mathbf{r}_0$ is a position vector originating at a fixed point 0 on the axis of rotation. If r is defined as the radial distance from the axis to any coordinate point x_i in the rotating system, this term is expressed as

$$\mathbf{\Omega} \times (\mathbf{\Omega} \times \mathbf{r}_0) = -\omega^2 r \frac{\partial r}{\partial x_i} = -\frac{\partial (\omega^2 r^2/2)}{\partial x_i} \tag{25}$$

---

[12] $e_{ijk} = 0$ unless $i \neq j \neq k$; $e_{ijk} = 1$ if ijk in cyclic order $(1231\ldots)$; $e_{ijk} = -1$ if ijk in anticyclic order $(3213.\_.\_.)$.

where ω is the constant magnitude of $\mathbf{\Omega}$. Using this equation, the dynamic *equations of motion* are

$$\frac{Du_i}{Dt}+f_i-\frac{\partial\left(\omega^2 r^2/2\right)}{\partial x_i}=-\frac{1}{\rho}\frac{\partial p}{\partial x_i}+X_i+\frac{\partial \tilde{\sigma}_{ij}}{\partial x_j} \tag{26}$$

where

$$\frac{Du_i}{Dt}=\frac{\partial u_i}{\partial t}+u_j\frac{\partial u_i}{\partial x_j}$$

is the acceleration of a fluid particle relative to the rotating coordinate system; p is the fluid static pressure; X_i the sum of all externally imposed body forces; and $\tilde{\sigma}_{ij}$ is the deviatoric stress tensor. The left-hand side of equation (26) is the absolute acceleration of the particle with respect to inertial space.

It is noted that the centrifugal acceleration term is the gradient of a scalar potential, $-\omega^2 r^2/2$. If all body forces are conservative, and if the fluid may be assumed of constant density, it is convenient to define a *reduced pressure*

$$p^*\triangleq p-\frac{\rho}{2}\,\omega^2 r^2+\Phi \tag{27}$$

where Φ is the scalar potential of the body forces $X_i=-\partial\Phi/\partial x_i$. A single term, $\partial p^*/\partial x_i$, can then replace three terms in equation (26). Further, if we are dealing with a Newtonian fluid of constant kinematic viscosity, ν, equation (26) reduces to the rotational form of the *Navier-Stokes equations* for constant ρ and ν.

$$\frac{Du_i}{Dt}+f_i=-\frac{1}{\rho}\frac{\partial p^*}{\partial x_i}+\nu\,\frac{\partial^2 u_i}{\partial x_j\partial x_j} \tag{28}$$

Euler's equations for constant density are obtained by setting $\nu=0$. The primary advantage of using these forms which utilize p^* rather than p is to show, for constant density flow, that the rotation-induced centrifugal term plays no essential role in determination of the u_i field in flows without free surfaces where boundary and initial conditions are specified in terms of conditions on u_i (no slip condition, etc.). Equations (22) and (28) form a complete set in the variables u_i and p^*.

APPENDIX II

Elementary Dimensional Analysis

All considerations in this section assume that ρ and ν are constant; hence equations (22) and (28) are used. Assume that L is the relevant scale size of the flow field, U the relative velocity scale, and ω the dimensional rotary speed of the observational coordinates. If each term in equations (22) and (28) is appropriately nondimensionalized in terms of L, U, and ω so that

$$\hat{u}_i = U u_i \qquad \hat{p}^* = \rho U^2 p^*$$

$$\hat{x}_i = L x_i \qquad \hat{t} = Lt/U$$

$$\hat{\Omega}_i = \omega \Omega_i$$

where hatted variables are dimensional, then equations (22) and (28) become, when normalized

$$\frac{\partial u_j}{\partial x_j} = 0 \tag{29}$$

and

$$\frac{\partial u_i}{\partial t} + u_j \frac{\partial u_i}{\partial x_j} + \frac{1}{Ros} e_{ijk}\Omega_j u_k = -\frac{\partial p^*}{\partial x_i} + \frac{1}{Re} \frac{\partial^2 u_i}{\partial x_j \partial x_j} \tag{30}$$

$Re = UL/\nu$ is the Reynolds number and $Ros = U/2\omega L$ is the Rossby number which expresses the ratio of inertial to Coriolis accelerations.

If $Ros \gg 1$, Coriolis effects should be small, but if $Ros \ll 1$, the inertial acceleration terms in equation (30) are generally neglected. If both $Ros \ll 1$ and $Re \gg 1$, the geostrophic approximation, pressure terms are said to just balance the Coriolis accelerations; i.e., Du_i/Dt and $\partial^2 u_i/(\partial x_j \partial x_j)$ may be neglected in equations (30) and (28).

Many other methods of normalization exist in the literature of rotating flows. The normalizing definitions, depending on how they are to be used, lead to various useful parameters and simplifications of the basic equations. For example, if equation (30) is multiplied by Ros, another parameter, $E = Ros/Re = \nu/2\omega L^2$, representing the ratio of viscous to Coriolis forces, appears. The inverse of the Ekmann number is a special form of the Taylor number, $Ta = E^{-1}$. Only in certain very special cases may rotating flows be characterized in terms of a single dimensionless parameter. The Ekmann boundary layer (ref. 12) is an example where E is the single controlling parameter, rather than E and Ros. In turbomachines, we have generally found Re and the Rotation number, $Ro = Ros^{-1}$, to be the most useful. For example, Ro is convenient in presentation of results, since $Ro \to 0$ as $\omega \to 0$ whereas $Ros \to \infty$, and the case of $Ro < 1.0$ (or small Ro) is the most common situation.

REFERENCES

1. ACOSTA, A. J., AND R. D. BOWERMAN, An Experimental Study of Centrifugal Pump Impellers. *Trans. ASME*, Vol. 79, No. 8, 1957, pp. 1821–1839.

2. BANKS, W. H. H., AND G. E. GADD, *A Preliminary Report on Boundary Layers on Screw Propellers and Simpler Rotating Bodies.* Aeronautical Research Council ARC 23,423, FM3150, 1962.

3. BARNA, S. N., Secondary Flow in a Rotating Straight Pipe. *Proc. Roy. Soc. London,* Ser. A, Vol. 227, 1954, pp. 133–139.

4. BENTON, G. S., The Effects of the Earth's Rotation on Laminar Flow in Pipes. *Trans. ASME, J. Appl. Mech.,* Vol. 23, 1956, pp. 123–127.

5. BENTON, G. S., AND D. BOYER. Flow Through a Rapidly Rotating Conduit of Arbitrary Cross-Section. *J. Fluid Mech.,* Vol. 26, Part 1, 1966, pp. 69–80.

6. BOYER, D. L., *Flow Through a Rapidly Rotating Rectangular Channel.* Ph.D. dissertation, Johns Hopkins U., 1965.

7. BRADSHAW, P., The Analogy Between Streamline Curvature and Buoyancy in Turbulent Shear Flow. *J. Fluid Mech.,* Vol. 36, Part 1, 1969, pp. 177–191.

8. CHAM, T., AND M. R. HEAD, Turbulent Boundary Layer Flow on a Rotating Disc. *J. Fluid Mech.,* Vol. 37, Part 1, 1969, pp. 129–148.

9. CHANDRASEKHAR, S., *Hydrodynamic and Hydromagnetic Stability.* Oxford U. Press, 1961, Chapter II and pp. 36–42.

10. CONRAD, P. W., *The Effects of Rotation on the Stability of Laminar Layers on Curved Walls.* Report FLD 9, Mech. Eng. Dept., Princeton U., August 1962.

11. DEAN, R. C., JR., *On the Unresolved Fluid Dynamics of the Centrifugal Compressor.* Presented at ASME Gas Turbine Division Conference (Washington, D.C.), March 17–21, 1968.

12. EKMANN, V. W., On the Influence of the Earth's Rotation on Ocean Currents. *Arkiv Mat. Astr. Fys.,* Vol. 2, November 11, 1905.

13. FISCHER, K., AND D. THOMA, Investigation of Flow Conditions in a Centrifugal Pump. *Trans. ASME,* Vol. 54, pp. 141–155.

14. FOWLER, H. S., *Some Measurements of the Flow Patterns in a Centrifugal Compressor Impeller.* ASME Paper 65-WA/GTP-7, 1965.

15. FOWLER, H. S., The Distribution and Stability of Flow in a Rotating Channel. *Trans. ASME,* Ser. A., Vol. 90, July 1968, pp. 229–236.

16. FUJIE, K., Three-Dimensional Investigation of Flow in Centrifugal Impeller With Straight-Radial Blades. *Bull. Japan Soc. Mech. Eng.,* Vol. 1, No. 1, 1958, pp. 42–49. See also Vol. 1, No. 3, 1958, pp. 275–282, and Vol. 4, No. 13, 1961, pp. 94–101.

17. GÖRTLER, H., *On the Three-Dimensional Instability of Laminar Boundary Layers on Concave Walls.* Translated from original in NACA, TM 1375, June 1954.

18. GREGORY, N., J. T. STUART, AND W. S. WALKER, On the Stability of Three-Dimensional Boundary Layers With Application to the Flow Due to a Rotating Disc. *Phil. Trans. Proc. Roy. Soc. (London),* A 248, 1955, p. 155.

19. HALLEEN, R. M., AND J. P. JOHNSTON, *The Influence of Rotation on Flow in a Long Rectangular Channel—An Experimental Study.* Report MD-18, Thermoscience Division, Dept. Mech. Eng., Stanford U., May 1967.

20. HAMRICK, J. T., J. MIZISIN, AND D. J. MICHEL, *Study of Three-Dimensional Internal Flow Distribution Based on Measurements in a 48-Inch Radial-Inlet Centrifugal Impeller,* NACA TN 3101, February 1954.

21. HILL, P. G., AND I. M. MOON, *Effects of Coriolis on the Turbulent Boundary Layer in Rotating Fluid Machines.* Gas Turbine Lab. Report 69, M.I.T., June 1962.

22. HIMMELSKAMP, H., *Profiluntersuchungen an Einem Umlaufenden Propeller.* Mitt. Max-Planck-Inst. 2, 1950.

23. HORLOCK, J. H., Boundary Layer Problems in Axial Turbomachines. *Flow Research on Blading.* (Proc. Brown Boveri Symposium), L. S. Dzung, ed., Elsevier Press, 1970.

24. HOWARD, J. H. G., Analytical Theory of Secondary Flow in a Centrifugal Impeller. *Trans. Eng. Inst. Canada,* Vol. 9, No. B-1, Paper No. EIC-66-Mech 4, April 1966.

25. HOWARD, J. H. G., AND E. LENNEMANN, *Measured and Predicted Secondary Flows in a Centrifugal Impeller.* ASME Paper 70-GT-55, ASME Gas Turbine Conference, May 1970.

26. JOHNSTON, J. P., AND R. C. DEAN, JR., Losses in Vaneless Diffusers of Centrifugal Compressors and Pumps. *Trans. ASME,* Ser. D, Vol. 88, No. 1, 1964, pp. 49–62.

27. VON KÁRMÁN. T., Über Laminare und Turbulente Reibung. *Z. Angew. Math. Mech.,* Vol. 1, 1921, p. 233.

28. KAYE, J., AND E. C. ELGAR, Modes of Adiabatic and Diabatic Fluid Flow in an Annulus With an Inner Rotating Cylinder. *Trans. ASME,* Vol. 58, 1958, pp. 753–765.

29. KLINE, S. J., W. C. REYNOLDS, F. A. SCHRAUB, AND P. W. RUNSTADLER, The Structure of Turbulent Boundary Layers. *J. Fluid Mech.,* Vol. 30, Part 4, 1967, pp. 741–773.

30. KRAMER, J. J., AND J. D. STANITZ, *A Note on Secondary Flow in Rotating Radial Channels.* NACA Report 1179, 1954.

31. LAKSHMINARAYANA, B., *Investigations and Analysis of Flow Phenomena of Secondary Motions in Axial Flow Inducers.* Dept. Aerospace Eng., Penn State U., May 1968.

32. LITVAI, E., *Discussion in Flow Research on Blading.* L. S. Dzung, ed., Elsevier Press, 1970, p. 392.

33. LOHMANN, R. P., An Investigation of the Influence of the Boundary Layers on the Performance of Centrifugal-Compressor Impellers. *Trans. ASME,* Ser. D., Vol. 88, No. 1, 1966, pp. 71–81.

34. MELLOR, G., Laminar Flow and Transition. *Effect of Curvature and Rotation on Boundary Layer Development, Part I.* Ingersoll-Rand Co., Advanced Eng. Dept., TM66, February 1961.

35. MOON, I. M., *Effects of Coriolis Force on the Turbulent Boundary Layer in Rotating Fluid Machines.* Gas Turbine Lab Report 74, M.I.T., June 1964.

36. MOORE, J., *Effects of Coriolis on Turbulent Flow in Rotating Channels.* M.I.T., Gas Turbine Lab Report 89, January 1967.

37. MOORE, J., *The Development of Turbulent Layers in Centrifugal Machines.* M.I.T., Gas Turbine Lab Report 99, June 1969.

38. PATEL, V. C., *Measurements of a Secondary Flow in the Boundary Layers of a 180 Degree Channel.* ARC 30428, FM 3975, 1968; available as AD 679430 from Clearinghouse, DDC.

39. POTTER, M. C., AND M. D. CHAWLA, *The Stability of Boundary Layer Flow Subject to Rotation.* Private communication, 1970. See also M. D. Chawla, Ph.D. dissertation, Michigan State U., 1969.

40. RAYLEIGH, J. W. S., On the Dynamics of a Revolving Fluid. *Proc. Roy. Soc. (London).* Vol. 6A, 1916, pp. 148–154.

41. SENOO, Y., AND R. C. DEAN, JR., Rotating Wakes in Vaneless Diffusers. *Trans ASME,* Ser. D, Vol. 82, 1960, pp. 563–574.

42. SENOO, Y., M. YAMAGUCHI, AND M. NISHI, A Photographic Study of the Three-Dimensional Flow in a Radial Compressor. *Trans. ASME,* Ser. A, Vol. 90, No. 3, 1968, pp. 237–244.

43. SHIH-I, PAI, *Turbulent Flow Between Rotating Cylinders.* NACA, TN 892, 1939.

44. SMITH, A. G., On the Generation of the Streamwise Component of Vorticity for Flows in Rotating Passages. *Aeron. Quart.*, Vol. 8, November 1957, pp. 369–383.

45. TAYLOR, G. I., Stability of a Viscous Liquid Contained Between Two Rotating Cylinders. *Phil. Trans. Roy. Soc. (London)*, Ser. A, Vol. 223, 1923, pp. 289–343.

46. TOWNSEND, A. A., *The Structure of Turbulent Shear Flow*. Cambridge U. Press, 1956, Chapter 2.

47. TREFETHEN, L., Fluid Flow in Radial Rotating Tubes. *Actes, IX⁰ Congrés International de Méchanique Appliquée*, Vol. II, Bruxelles U., 1957, pp. 341–350.

48. TREFETHEN, L., *Flow in Rotating Radial Ducts*. General Electric Engineering Laboratory, Report 55GL350-A, August 1957.

49. KLINE, S. J., G. SOVRAN, M. V. MORKOVIN, AND D. J. COCKRELL, eds., *Proc., Computation of Turbulent Boundary Layers-1968 AFOSR-IFP-Stanford Conference*. Thermosciences Div., Dept. of Mech. Eng., Stanford U.

50. LEZIUS, D. K., AND J. P. JOHNSTON, *The Structure and Stability of Turbulent Wall Layers in Rotating Channel Flow*, Rept. MD-29, Thermosciences Div., Dept. Mech. Eng., Stanford U., 1971.

DISCUSSION

J. GRUBER (Technical University of Budapest): First of all, I should like to congratulate the author on his excellent paper dealing with some extremely important problems in the field of turbomachinery. His statements concerning the Coriolis forces which influence the stability of the boundary layer seem especially valuable. According to his statements, the rotation modifies the law of the wall. The experiments carried out in the Laboratory of Fluid Mechanics of the Technical University of Budapest support these findings (refs. D–1, D–2, and D–3). The developing turbulent boundary layer on the blading of a centrifugal impeller has been studied, and the research has been extended to the law of the wake too.

In my opinion, the feasibility of accurately measuring the wall shear stress will have a definite importance in further research, and therefore I have two questions in connection with the author's paper:

(1) Does the author intend to repeat the wall shear stress measurements with the Ludwieg method, applying a flush-mounted, quartz-coated, heated film probe, in addition to the Preston tube method?

(2) Did the author consider extending the law of the wall for a stationary flow to a rotating case as follows?

$$\bar{u}^+ = \frac{u}{u_\tau} = F\left[\left(\frac{\eta u_\tau}{\nu}\right), \left(\frac{\Omega \eta}{u_\tau}\right)\right]$$

(The designations are the same as those of the author.)

P. G. HILL (Queen's University): The writer would like to express appreciation for the comprehensive and valuable review Dr. Johnston has given of Coriolis effects in channel flows.

The effects of rotation on channel flow are difficult to discern and categorize, not only because of instrumentation problems, but especially because of the problems of designing a controlled experiment. In general, the boundary conditions (e.g., relative rotationality of the inlet flow) are naturally affected by rotation, so that as the rotational speed of the experimental channel is changed, the problem itself is altered. The effect of rotation on separation, for instance, could be as strongly dependent on change of inlet boundary condition as on either the secondary flow or the stabilizing/destabilizing mechanism. Such effects could of course be understood by the results of inviscid flow calculations if they occurred in

isolation. However, in channels of low aspect ratio with thick boundary layers, there is generally a strong interaction between these mechanisms.

Adding somewhat to the general problem of sorting out what is going on is the difficulty of deciding when secondary flow may be neglected. In constant-area channels at high aspect ratio (e.g., 7:1) it appears, as Dr. Johnston has noted, that secondary flow is negligible at the midplane for quite large values of the rotation parameter. However, for diffusing flows, even at high aspect ratio, this is probably far from realistic. At aspect ratios typical of centrifugal machine impellers (i.e., of order unity) there seems little doubt that secondary flows are very important, if not dominant.

The significance of the work of Moore (ref. 37) in this connection appears to be in demonstrating that (albeit with a very approximate model) stationary flat-plate, three-dimensional boundary-layer techniques can provide a physically realistic description of the flow without direct inclusion of the effects of Coriolis force on turbulence quantities. Although this result suggests that secondary-flow effects are dominant, it does not rule out the possibility that the effect of Coriolis force on turbulence may have a significant effect on separation and mixing losses in impellers. The effect of Coriolis force on turbulence production has been shown in a most interesting way in the film by Johnston and Halleen and commented on in this paper with respect to the turbulent energy equation. It would be of great interest if the author would give his views on the need for, and possible means of, incorporating these effects into turbulent boundary-layer calculation procedures.

A. S. MUJUMDAR (Carrier Corporation): Litvai and Preszler (ref. D-3) have recently published some data on the velocity profile of the turbulent boundary layer on rotating impeller bladings which indicate that the law of the wall holds in the case of a rotating system as well. Using the conventional notation, the law of the wall may be expressed as

$$u^+ = A \log y^+ + B \qquad (D\text{-}1)$$

The constants A and B were correlated in terms of a rotation parameter, Ω, defined by

$$\Omega = 2\omega(u^+)^2 \qquad (D\text{-}2)$$

where ω is the rotational speed. The major effect of rotation was assumed to be confined to A.

The effect of rotation on the slope in the universal velocity distribution was determined by considering the turbulent boundary-layer flow as a damped, forced vibrating system. The stabilizing (damping) effect of the Coriolis forces was regarded as essentially a change in the spring constant of the system. After a series of approximations, the authors derived the

following formula for the slope of the logarithmic velocity profile:

$$A = A_0(1+a\Omega)^{1/2} \tag{D-3}$$

where A_0 is the slope in the absence of rotation and a is a constant which may be determined experimentally. In spite of rather large scatter in the data, equation (D-3) indicates the correct trend; i.e. for $\Omega > 0$, which corresponds to the suction side of the blade, the slope of the velocity profile is steeper. The converse is also true.

It may be noted that the data are limited to very low rotational speeds, the maximum shaft speed being only 18 rpm.

J. MOORE (General Electric Co.): Dr. Johnston has given a stimulating description of the studies of simplified flows which sheds some light on the flows in turbomachine rotors. It is, however, sobering to read Dean's description (ref. 11) of the real situation in centrifugal impellers and compare the unknowns with the mostly qualitative explanations.

Dean has provided several observations of rotational effects for quantitative explanation and prediction.

(1)   A relatively quiescent wake on the suction (trailing) side of an impeller passage, which may contain as much as 20 percent of the through flow.

(2)   The relative absence of turbulent mixing between the wake and the rest of the flow, which flows as a "jet" along the pressure side.

(3)   The violent turbulence generated on the pressure surface of the blades above design incidence.

(4)   Blades operating at $-25°$ incidence without any steady pressure side stalling.

These observations, as well as Dean's overall description of separation within the passage, provide challenges for the boundary-layer predictor.

Moore (ref. 37) has made a start towards predicting the occurrence and development of the "wake" and has shown that three-dimensional, integral boundary-layer techniques can give a quantitative description of the secondary-flow effects on all the boundary layers. It may well be, however, that "separation" within an impeller passage is not always governed by secondary flows, and it certainly seems to be often three-dimensional. But one can say that, if the flow in an impeller ever knows about the Taylor-Proudman theorem, it does so near the wall in the wake on the suction side.

The quantitative description of Coriolis stability effects by Bradshaw (ref. 7) is an encouraging start towards the solution of the differential equations. However, as Bradshaw points out, the linear Monin-Oboukhov formula applies only for the inner layer of the boundary layer which ends at $u_\tau y/\nu = 200$. Certainly the absence of turbulent mixing between the jet and wake occurs in the outer layer, and Dean's pressure side observations

may also be outer-layer phenomena. It seems that the Coriolis stability effects in the outer layer (in particular the "wake") should receive more experimental attention.

One hopes that more studies of simplified flows will be undertaken to shed light on these still dimly lit phenomena.

JOHNSTON (author): Of the various points raised in discussion at least two require some additional comment. Both of the following remarks relate to the effects of Coriolis stabilization on two-dimensional turbulent boundary layers. The first, prompted by Professor Gruber's and Mr. Mujumdar's discussions, concerns the law of the wall for the inner, fully turbulent parts of the layer, whereas the second is made in connection with Dr. Moore's comments on the outer layer and the turbulent free-shear layers that occur on the edge of separated regions.

Dimensional analysis gives the general form of the law of the wall. Professor Gruber presents it in the form

$$\bar{u}^+ = F(\eta^+, \Omega^+\eta^+) \qquad\qquad (D\text{-}4)$$

Ω^+ is the wall-layer rotation parameter $(\Omega^+ = \Omega\nu/u_\tau^2)$ and η^+ is the dimensionless distance from the wall $(\eta^+ = \eta u_\tau/\nu)$. Ω, and hence Ω^+, is negative for trailing (suction) surface layers and positive for leading (pressure) side layers. The data of Gruber, Litvai and Preszler (refs. D–1, D–2, and D–3) and that of Halleen and Johnston (ref. 19) suggest that $\bar{u}^+$ is higher than its zero-rotation value for given η^+ when Ω^+ is negative (suction side) and vice versa for positive Ω^+ (pressure side) conditions; see figure 13, for example.

The wall layer parameter Ω^+ may be related to the stability parameters S and Ri by application of basic definitions, e.g.

$$S = -\frac{2\Omega}{\partial\bar{u}/\partial\eta} = -\frac{2\Omega l}{\sqrt{\tau/\rho}} \qquad\qquad (D\text{-}5)$$

If it is assumed, as is commonly done in the wall layer region, that fluid shear stress τ equals the wall shear stress, $\tau_w = \rho u_\tau^2$, equation (D–5) becomes

$$S = -2\Omega^+\frac{lu_\tau}{\nu} \qquad\qquad (D\text{-}6)$$

Furthermore, in the turbulent part of the wall-layer region the zero-rotation mixing length l_0 is approximately $\kappa\eta$ where $\kappa \approx 0.4$ is the Karman constant. Thus equation (D–6) reduces to

$$S = -2\kappa\Omega^+\eta^+\frac{l}{l_0} \qquad\qquad (D\text{-}7)$$

By assuming that a relation such as the "Monin-Oboukhov" formula (eq. (20)) holds for the turbulent law of the wall regions, it is now seen from equations (D-7) and (2) that $\Omega^+\eta^+$ is directly related to S or Ri and at least two empirical constants K and β. This relationship can be expressed in the explicit form

$$Ri = S = -2\kappa\Omega^+\eta^+ \qquad (D\text{-}8)$$

for the limiting conditions of very small rotation effects; i.e., when $Ri \approx S$ and $l/l_0 \approx 1$ or, alternatively, when $[\Omega^+] \ll 1$. Note that this limiting case is independent of β, whose value is not yet well established.

Two specific forms for the turbulent region law of the wall have been proposed for rotationally stabilized flows: that of Bradshaw (ref. 7) and that of Litvai and Preszler (ref. D-3).

Bradshaw used the "Monin-Oboukhov" formula and the assumptions $\tau = \tau_w$ and $Ri = S$ (small rotation effects) to obtain the formula

$$\bar{u}^+ = \frac{1}{\kappa} \ln \eta^+ + B - 2\beta\Omega^+\eta^+ \qquad (D\text{-}9)$$

He found that this form fit Halleen's data quite well for $\eta^+ \lesssim 500$ with a value of $\beta \approx 4$ for $S > 0$ (stable conditions) and $\beta \approx 2$ for $S < 0$ (unstable conditions). The values of Ω^+ were small, in the range from 0.003 to 0.012, for all the data he used (that shown in fig. 13) in checking equation (D-9).

The formulation by Litvai and Preszler (ref. D-3) is presented by Mujumdar in his discussion. It may be recast in the form

$$\bar{u}^+ = \frac{1}{\kappa} (1 + \gamma S)^{1/2} \ln \eta^+ + B \qquad (D\text{-}10)$$

if one notes that α, the turbulence frequency used in reference D-3, may be expressed as $\gamma\alpha = \partial\bar{u}/\partial\eta$. γ is a dimensionless factor of proportionality that allows α to equal $\partial\bar{u}/\partial\eta$, the local scale of turbulence frequency in a shear layer. γ should be of unity order of magnitude and, as we shall try to show, should be closely related to the factor β of equation (20). The formula shown above seems much more satisfactory than the original as *all* parameters and variables are now dimensionless and S, the stability parameter, appears explicitly.

The formulas given in equations (D-9) and (D-10) may be directly compared for the case of small rotation effects if the term $(1 + \gamma S)^{1/2}$ in equation (D-10) is expanded in a binomial series and terms of order $(\gamma S)^2$ and smaller are neglected. When equation (D-8) is used to replace S in the expanded result, equation (D-10) becomes

$$\bar{u}^+ = \frac{1}{\kappa} \ln \eta^+ + B - \gamma\Omega^+\eta^+ \ln \eta^+ \qquad (D\text{-}11)$$

Since the rotation terms in equations (D–9) and (D–11) are small, the resulting fit of available data to either expression would be equally good if γ were taken to be a constant. The ratio $2\beta/\gamma = \ln \eta^+$ is not too far from constant (3.9 to 5.3) over the range of η^+ values (50 to 200) where data are normally expected to fit a turbulent law of the wall. Furthermore, for the range of probable β values (2 to 4, according to Bradshaw), γ is seen to be close to unity in value. Finally, there are still too few accurate velocity profile data to attempt to formulate more accurate law of the wall equations than those reviewed here. In fact, the need for a better formulation is not yet established.

I should like now to discuss briefly some new, preliminary observations that bear directly on the questions raised by Moore concerning the importance of Coriolis stabilization on the outer layers of turbulent boundary layers, and on free-shear layers in particular. In either case the magnitudes of the Richardson numbers can become quite large as $\partial \bar{u}/\partial \eta$ becomes small near the edge (or edges) of a shear layer. In particular, the value of Ri may be very large and positive in the free-shear layer separating the trailing side wake from the through-flow jet in separated centrifugal impeller flow (see Dean, ref. 11). The high degree of stability implied by such large positive Richardson numbers might indeed completely suppress turbulent transition in the wake-jet shear layer.

We have recently tried to examine the stability of the mixing layer formed over the separated flow that forms behind a backward facing step placed in our rotating channel apparatus. The low-speed ($\sim$1 ft/sec) water flow was observed using the hydrogen bubble technique with the generating wire placed in the free-shear layer and close to the step.

With positive Ω and thus negative (destabilizing) Richardson numbers, the mixing process was turbulent in the layer and qualitatively the same as at zero rotation; that is, two-dimensional, Kelvin-Helmholtz waves formed right behind the step and rapidly degenerated into fully three-dimensional turbulence a short distance downstream of the step. However, at the same unit Reynolds number, with the direction of rotation reversed so that Ω became negative and the Richardson number positive (stabilization) there was clear visual evidence that breakdown of the two-dimensional Kelvin-Helmholtz waves was severely retarded. At high negative rotational speeds, no ordinary turbulence was noted within the observable region of the shear layer that extended 3 to 4 inches downstream of the step.

In conclusion, our new observations tend to confirm those of Dean (ref. 11) and Moore (ref. 37) and lend credence to the idea of a quiescent wake mixing layer in separated centrifugal impeller flows. The full implications of these very preliminary investigations are yet to be appreciated. There certainly must, in addition, be important outer layer effects of rotation on unseparated turbulent boundary layers as pointed out by

Moore in his discussion. Much more research will be required to untangle these phenomena.

Finally, I wish to thank all the discussors for their generous and interesting comments and I am sorry that space does not permit comment on all points raised in discussion.

REFERENCES

D-1. GRUBER, J., AND E. LITVAI, An Investigation of the Effects Caused by Fluid Friction in Radial Impellers. *Proc. III Conf. on Fluid Mech. and Fluid Machinery.* Akadémiai Kiadó (Budapest), 1969, p. 241.

D-2. LITVAI, E., AND L. PRESZLER, The Velocity Profile of a Turbulent Boundary Layer on the Blading of Radial Impellers. *Proc. III Conf. on Fluid Mech. and Fluid Machinery,* Akadémiai Kiadó (Budapest), 1969, p. 348.

D-3. LITVAI, E., AND L. PRESZLER, On the Velocity Profile of the Turbulent Boundary Layer on Rotating Impeller Bladings. *Periodica Polytechnica, Mech. Eng.* (Budapest), Vol. 13, 1969, p. 215.

Prediction of Turbulent Shear Layers in Turbomachines

P. BRADSHAW

Imperial College, London

Turbulent shear layers in turbomachines differ from turbulent boundary layers on airfoils in at least seven important respects.
(1) Stronger three-dimensional effects
(2) High rates of heat transfer at comparatively low Mach numbers
(3) Larger camber
(4) Stronger accelerations and changes of direction
(5) Lower Reynolds number
(6) High free-stream turbulence
(7) Interaction of two shear layers
We have been working on several of these problems as part of an exploration of the limits of boundary-layer theory. The objects are to extend boundary-layer prediction methods to the special cases that we call real life and to use these special cases to test hypotheses used in simpler flows more severely than existing experimental data for the simpler flows permit. Results of the work are presented as part of a discussion of turbomachine problems.

Most present-day prediction methods for turbulent flow, such as those discussed at the 1968 Stanford meeting (ref. 1), refer to rather idealized cases, although several of the methods have been extended to compressible or three-dimensional flow to make them more directly useful to the aircraft industry. Moderate three-dimensionality of the mean flow does not seem to have much effect on the behavior of the turbulence, which is itself always three-dimensional, and there is now adequate evidence that the effects of compressibility on turbulence are small if the density fluctuation is a small fraction of the mean density (but see ref. 1a).

In turbomachine boundary layers, three-dimensionality is more pronounced and density fluctuations due to heat transfer can be much larger than those due to high Mach number. These are obvious and important effects; however, there are several more subtle phenomena to be found in turbomachines and I believe that we ought to take notice of them even at

this early stage. The list of "special effects" given in the abstract is obvious enough—the subtlety is in the way they modify the behavior of the turbulence.

To show that I am not wasting your time with academic trivia, table I shows the conditions under which some of these special effects produce a 10-percent change in surface shear stress or in distance to separation.

The amount of heat transfer or three-dimensionality needed is rather large, but the quoted values of camber, Reynolds number, and free-stream turbulence are typical, or even conservative, figures for turbomachines. Several of these less obvious special effects may occur simultaneously; with good luck they may cancel—with bad luck they will not.

A few recent references have been inserted in this published version, but the text is otherwise that presented at the symposium.

TABLE I.—*Strength of Special Effects Needed to Change Surface Shear Stress or Distance to Separation by 10 Percent*

Special effect	Order of magnitude
Sweepback (with given chordwise pressure gradient)_____	$=45$ deg
Heat transfer_____	$T_w/T = 0.7$
Longitudinal curvature (camber)_____	$\delta/R = 1/80$ or 35 degrees turning angle
Rotation (component about spanwise axis)__	$\Omega\delta/U = 1/80$
Low Reynolds number (C_f compared with Schoenherr value)_____	$U_\infty\theta/\nu = 650$ $(U_\infty x/\nu \ 3\times10^5)$
Free stream turbulence (small scale)_____	3%
Free stream unsteadiness (large scale: $\omega\delta/2\pi U = 0.1$)_____	30% (changes *mean* C_f by 10 percent) 3.5% (minimum C_f 10 percent below mean C_f)

THREE-DIMENSIONAL BOUNDARY LAYERS

If we postpone discussion of flows near streamwise corners and edges where several different Reynolds stress components contribute to the acceleration of the fluid, we can pose the problem of three-dimensional boundary layers as, "What is the direction of the Reynolds shear stress?" People who use mixing-length or eddy-viscosity concepts in three-dimensional flow implicitly assume that the answer is, "The same as the direction of the mean shear" (components $\partial U/\partial y$ and $\partial W/\partial y$, where y is the direction normal to the surface). Figure 1 shows the directions of the velocity, shear stress, and mean shear in a mildly three-dimensional boundary layer with about 3.5 degrees of crossflow (ref. 2) relaxing back to a two-dimensional state. Note that the *difference* between the directions of shear stress and of mean shear is comparable with the mean crossflow angle, except near the surface where the flow is in local equilibrium and the mixing-length formula, with $l=Ky$, is expected to hold. This mild three-dimensional flow can be predicted to within the rather
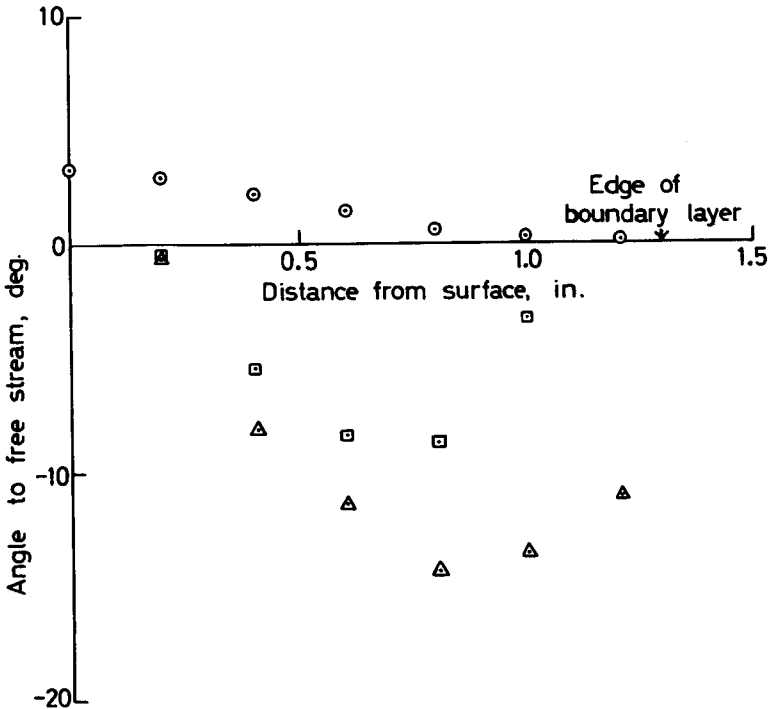

FIGURE 1.—*Measured directions of velocity vector (circled points), shear stress (squared points), and mean shear (triangular points) in the boundary layer on a 45-degree swept wing.*

poor experimental accuracy by an extension (ref. 3) of the boundary-layer calculation method we developed at the NPL (See fig. 2; the calculations are somewhat more plausible than the experiments.)

A more strongly three-dimensional flow investigated by J. P. Johnston (ref. 4) shows some very curious effects: the boundary layer is initially two-dimensional, but on application of a strong pressure gradient the shear stress vector, far from following the mean shear vector, actually yaws in the opposite direction. It is very hard to reconcile this with any of our current ideas about turbulence, but the hot-wire measurements of shear stress are not infallible. All we can safely conclude is that the prediction of three-dimensional effects stronger than those normally occurring on a moderately swept wing must be treated with caution. For practical purposes, many two-dimensional or three-dimensional flows subjected to sudden pressure changes can be predicted by using the mixing-length formula in the inner layer and Bernoulli's equation in the outer layer.

EFFECTS OF STREAMLINE CURVATURE ON TURBULENCE

Several experiments (refs. 5, 6, and 7; see also the paper by J. P. Johnston in this session, and for a recent review see ref. 7a) have shown that longitudinal surface curvature, or a component of rotation in the direction of the mean vorticity vector, can have a large effect on turbulence, quite apart from any extra terms that may appear in the mean-motion equations. Since Professor Johnston is dealing with the case of rotation, I will confine myself to curvature effects. Roughly, the analysis for one can be applied to the other by reading Ω for U/R. Highly cambered airfoils, particularly turbomachine blades, can suffer appreciably from curvature effects. ("Suffer" is the word, because turbulent shear stress is reduced on convex surfaces, leading to premature upper-surface separation, and increased on concave surfaces, leading to greater lower-surface drag and heat transfer.)

I drew a first-order analogy between the effect of centrifugal or Coriolis forces and the effect of buoyancy, relying on the experimental fact that the correlation between the velocity fluctuation u and the density fluctuation ρ' in a heated shear flow is very strong, so that there should also be a strong correlation between the separate effects of the fluctuating centrifugal force $2Uu/R$ and the fluctuating buoyancy force $-g\rho'$. A first-order formula for the effect of curvature, suggested in reference 8 on the basis of the Monin-Oboukhov meteorological formula, is

$$l/l_{Ri=0} = 1 - \beta Ri \qquad (1)$$
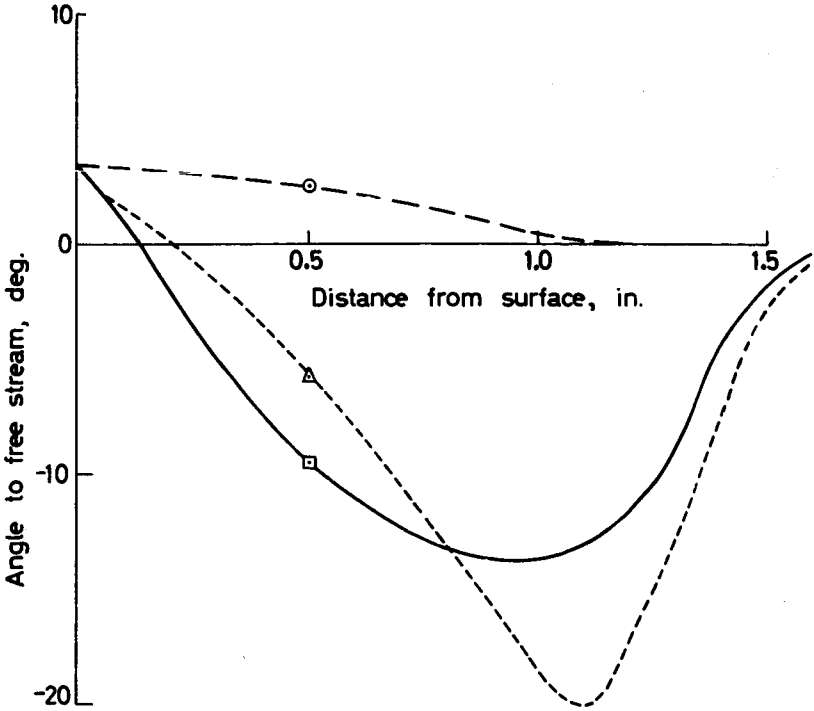
FIGURE 2.—*Calculations for the boundary layer of figure 1 (same notation).*

where the "apparent mixing length," l, is defined as $\sqrt{(\tau/\rho)}/(\partial U/\partial y)$ and is not ascribed any physical significance; $Ri = 2(U/R)/(\partial U/\partial y)$ is a first approximation to an equivalent Richardson number; and β is a constant, equal to about 7 on a convex surface ($Ri > 0$, stable conditions) and about 4 on a concave surface (unstable conditions). Typically, in the outer part of a turbulent boundary layer on a convex surface, $l/l_0 = 1 - 40\delta/R$. Thus, taken at face value, the analogy suggests that turbulence might die away altogether ("relaminarization") at values of δ/R typical of highly cambered blades; however, this crude analogy can scarcely be expected to work if the turbulence structure is radically changed by strong body forces, and we need something better for turbomachine blades. Relaminarization has been observed by Halleen and Johnston (ref. 6) in a rotating flow; also, Patel (ref. 4) commented that his velocity profiles on a highly convex surface were similar to those he found in relaminarization (ref. 10), but this effect can be explained by the Monin-Oboukhov formula.

In a study of rapid distortion of turbulent shear flow, my doctoral student, Mr. I. P. Castro, has made some measurements in the mixing

layer of an impinging jet. It can be seen from figure 3 that the growth of the shear layer is retarded by strong (stabilizing) curvature. The quantity plotted is a rather arbitrary geometrical width (corrected for slight three-dimensional effects) and not a true mass flow, so that its behavior in the region of strong distortion should not be taken too seriously. The surprising thing is that the growth rate returns to normal rather quickly. (There is a hint of an *overshoot* in growth rate, so that things may be more complicated than they seem; see Discussion and ref. 10a.)
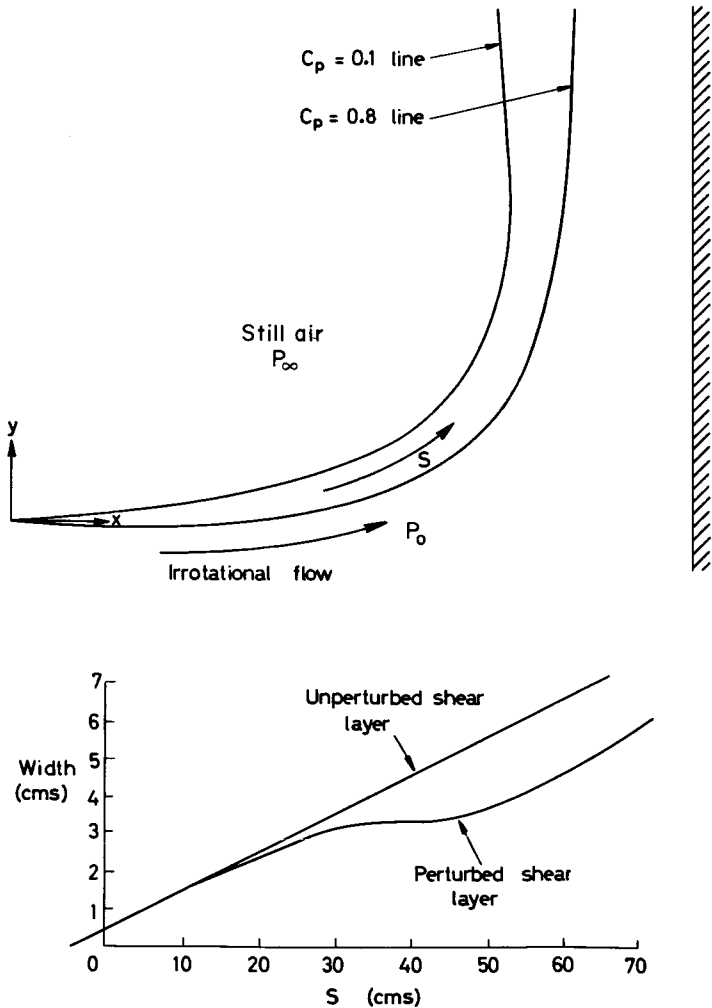

FIGURE 3.—*Flow in deflected mixing layer.* C_p *is total-pressure coefficient,* $(P-p_\infty)/P_0-p_\infty)$; *"Width" is distance between points where* C_p *is 0.8 and 0.1.*

BOUNDARY LAYERS AT LOW REYNOLDS NUMBERS

Coles (ref. 11) has shown, by a painstaking analysis of data, that the velocity defect law in a constant-pressure turbulent boundary layer, usually written as

$$\frac{U_\infty - U}{u_\tau} = f\left(\frac{y}{\delta}\right) \tag{2}$$

depends on Reynolds number if $U_\infty \theta/\nu < 5000$. (Roughly, $U_\infty x/\nu = 2.5 \times 10^6$, a high Reynolds number by turbomachine standards.) There remains a small probability that this "Reynolds number" effect may, in fact, be caused by disturbances arising in the transition region but, in any event, Coles' correlation seems to be a universal one, valid for different transition positions and transition devices.

Coles' analysis relies on the constancy of K in the "mixing-length" formula in the inner layer

$$\partial U/\partial y = \sqrt{(\tau/\rho)}/Ky \tag{3}$$

or, more specifically, on the constancy of K and A in the logarithmic velocity profile

$$\frac{U}{u_\tau} = \frac{1}{K}\left[\log\left(\frac{u_\tau y}{\nu}\right) + A\right] \tag{4}$$

Recently, Simpson (ref. 12) has suggested, on the basis of his measurements in transpired boundary layers, that K may be a function of Reynolds number. Simpson's results could be explained almost equally well in terms of Coles' suggested defect-law behavior; however, incontrovertible evidence of Reynolds number effects on the inner layer velocity profile in pipe and duct flow has been presented by Patel and Head (ref. 10) and merits some discussion.

The changes in the logarithmic law found by Patel and Head can be correlated in terms of an inner-layer parameter, the dimensionless shear stress gradient, $\partial \tau^+/\partial y^+ = (\nu/\rho u_\tau^3)\partial \tau/\partial y$, which has been used by several workers to correlate relaminarization effects in accelerated flows. Even at the lowest Reynolds numbers at which turbulent flow is possible, the values of $\partial \tau^+/\partial y^+$ found in a *constant-pressure* boundary layer are very much smaller than those associated with inner-layer changes in pipe flow. Therefore, Patel and Head's measurements actually contradict Simpson's suggestion and imply that the inner layer in a low-Reynolds-number boundary layer follows the usual logarithmic law if the pressure gradient is small. It follows that the defect-law changes observed by Coles are probably real and necessarily caused by viscous effects in the outer region of the boundary layer. In order to predict low-Reynolds-number boundary layers we need more data on these viscous effects, although both Herring .

and Mellor (ref. 13) and I (unpublished) have inserted an empirical Reynolds number dependence into the specification of shear stress in the outer layer. (The change in total shear stress is *many times* larger than the viscous shear stress in the outer layer.)

The photographs of a smoke-filled boundary layer at low Reynolds number published by Fiedler and Head (ref. 14) suggest that the interface between the turbulent and nonturbulent fluid has more large-scale irregularities than at high Reynolds number. There is no evidence for instability of the viscous superlayer but, since the defect law in a pipe or duct seems to be independent of Reynolds number everywhere outside the viscous sublayer, it seems that the Reynolds-number dependence of the defect law in a boundary layer must be associated with the presence of a free boundary.

In the analysis of Patel and Head's measurements mentioned above (carried out by Dr. G. D. Huffman of Allison while in our department, ref. 16a) it was found that the detailed profiles could be well represented by the mixing-length formula (eq. (3)) with the van Driest mixing-length specification

$$1 = Ky[1 - \exp(-\sqrt{\tau/\rho}\, y/\nu A^+)] \tag{5}$$

with A^+ a function of $\partial \tau^+/\partial y^+$, chosen to optimize the fit. This seems to be a satisfying demonstration of the wide applicability of inner-layer similarity ideas and strongly supports the view that viscous effects in the inner layer depend only on the local turbulence Reynolds number, $\sqrt{\tau/\rho}\, y/\nu$. There is just one difficulty: the values of A^+ in the pipe and in the duct are different for a given value of $\partial \tau^+/\partial y^+$. It can be seen from figure 4 that the values of A^+ that give the best fit to Patel and Head's duct measurements agree fairly well with the empirical relations suggested by several authors for other plane flows. The pipe measurements stand apart. The only possible conclusion is that transverse curvature affects the viscous sublayer even when the sublayer thickness (to $y^+ = 30$) is less than 10 percent of the radius. The sense of the difference between pipe and duct indicates that concave transverse curvature (as in the streamwise corner between a blade and a hub) tends to suppress the Reynolds stress in the sublayer. One hopes that the effect of transverse curvature is confined to the viscous sublayer. If curvature also affects the inner layer ($30\nu/u_\tau < y < 0.2R$, for instance) then the coincidence of the logarithmic laws in pipe and duct (at high Reynolds numbers) takes a great deal of explaining. However, it is very difficult to see why transverse curvature *should* affect the viscous sublayer and not the fully turbulent flow. The small amount of data on the axial flow over a cylinder (convex curvature) shows that the effect on A^+ is of sign opposite to that in a pipe, as one would expect; the effect may, however, be smaller. Again, the inner layer seems unaffected by curvature as such.
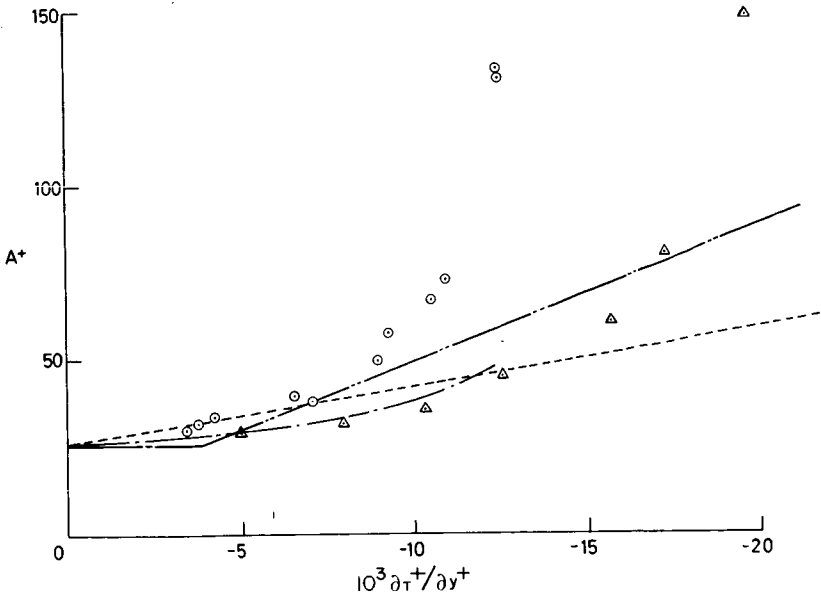
FIGURE 4.—*Variation of best-fit value of Van Driest parameter A^+ (eq. (5)) with dimensionless shear-stress gradient. Data of Patel and Head (ref. 10) for pipe (circled points) and duct (triangular points).*

FREE-STREAM "TURBULENCE"

The word "turbulence" appears in quotation marks because the unsteady free stream in a turbomachine consists partly of true turbulence and partly of nonrandom fluctuations caused by the relative motion of the blades and their wakes. The boundary layer beneath any unsteady stream with typical wavelengths large compared to the boundary layer thickness can be treated by simple extensions of calculation methods for steady flows. If one ignores streamwise "history" effects on the turbulent shear stress in steady flow one can evidently ignore timewise history effects of similar magnitude in unsteady flow. However, it is more satisfying to analyze the effects of unsteadiness by extending a steady-flow method that takes streamwise history into account. As an example, the calculation method we developed at NPL uses an empirical equation for the rate of change of turbulent shear stress along a streamline, expected to be valid if that rate of change is not too large compared to the rates of production or dissipation of turbulent energy. Exactly the same equation can be used in unsteady flow (ref. 15) simply by noting that the rate of change of shear stress along a streamline now contains $\partial \tau / \partial t$ as well as

spatial derivatives. The equation is again expected to be valid if the total (temporal and spatial) rate of change of shear stress along a streamline is not too large compared to the rate of production or dissipation of turbulent energy. The equations for steady and unsteady flow are identical if we use the notation D/Dt for rate of change along a streamline. Of course, the numerical calculations are more difficult in unsteady flow, but no new physics is required. The same simple extension could be made for any other method using a differential equation for shear stress. Figure 5 shows some calculations by the NPL method for the simple case of an unsteady flow over an infinite plate (independent variables y, t only). This graph is included to show that time-dependent flows can behave rather unexpectedly. Both flows have the same value of $\partial U/\partial t$ as seen by an observer moving with the free stream but the pressure rise to separation is very different. Dr. V. C. Patel of the Lockheed-Georgia Company has programmed our method for two-dimensional unsteady flow (independent variables x, y, t: see ref. 15a).

If the wavelength of the free-stream fluctuations is of the same order as the wavelength of the boundary-layer turbulence, rates of change of
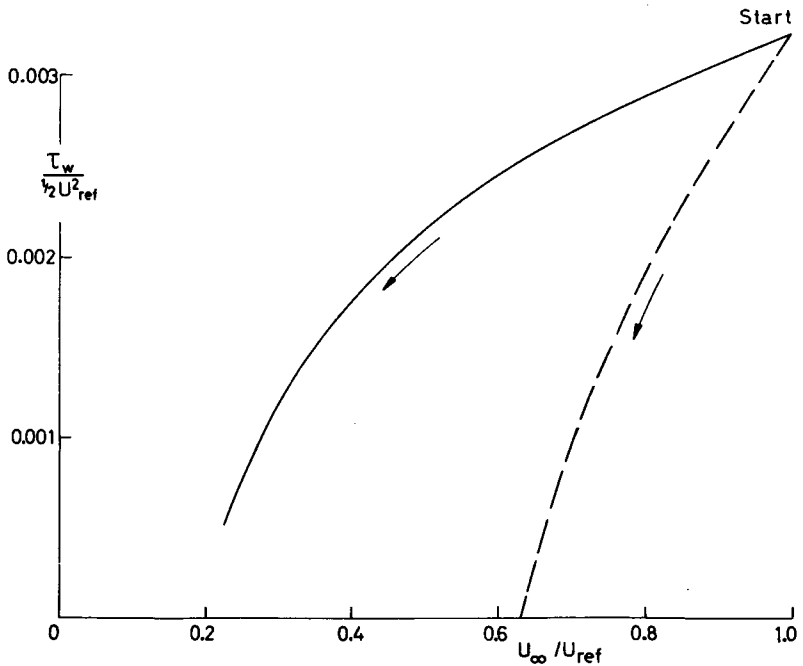

FIGURE 5.—*Comparison of calculations for time-dependent and space-dependent boundary layers with the same free stream acceleration. Solid curve: time-dependent, $U = U_{ref} \exp (-0.25\ U_{ref}t/l)$. Dashed curve: space-dependent, $U = U_{ref} (1 - 0.25\ x/l)$.*

shear stress along a streamline may be large; the above-mentioned calculation method then fails, like all others, and we have to consider the effects of the free-stream fluctuations on the turbulence structure. At present, we have no quantitative ideas about what happens. Qualitatively, we can see that free-stream fluctuations will further distort the irregular "superlayer" boundary between the boundary-layer turbulence and the external stream, leading to increased entrainment, so that there may be some similarity between the effects of small-scale free-stream turbulence and viscous effects in the outer layer at low Reynolds numbers. (Coles' paper shows that the two produce similar changes in the mean velocity profile.) We need more data. For recent work see refs. 16a to 16e, D-18 and D-19.

INTERACTING SHEAR LAYERS

A problem which is harder to solve than that of free-stream turbulence, but perhaps easier to study, is that of interaction between two turbulent shear layers. Examples include the flow near the centerline of a wake or jet or in the entrance region of a duct; the effect of a wing or blade wake on a slotted flap or a following blade, respectively; the wall jet; and the boundary layer in a streamwise corner. The last-named is a three-dimensional problem and, on a fundamental level, much harder than the others, although it may be easier to cope with empirically than the blade-wake problem because fewer parameters are involved.

As an example, let us look at the simplest problem, the flow near the centerline of a "two-dimensional" duct. As the growing boundary layers on the two walls approach the centerline, occasional tongues of turbulent fluid from one boundary layer, bearing (say) a positive shear stress, will cross the centerline and enter the negative velocity gradient of the other boundary layer. The turbulent fluctuations in the tongue will be attenuated because the rate of production of turbulent energy (shear stress times velocity gradient) in the tongue will be negative. As the boundary layers continue to grow, the number and intensity of these "frontier violations" will increase, significantly altering the turbulence in the outer part of each boundary layer. Not only will the turbulent intensities and shear stress be changed, but typical eddy length scales and structural coefficients like the energy diffusion coefficient, $\overline{q^2 v}/(\overline{q^2})^{3/2}$, may also change. The effects of the interaction on the turbulence seem to penetrate as close to the surface as 0.2 of the half-width of the duct and, of course, the interaction eventually stops streamwise change altogether. In an asymmetrical flow (such as a curved duct or a duct with one rough and one smooth wall (ref. 17)), there is a region in which the net shear stress and velocity gradient have different signs and so the net rate of production

of turbulent energy will be negative. This phenomenon has attracted some attention, but it is merely an overt sign of what goes on in secret in a symmetrical interaction.

The main question to be answered is, "Does the interaction seriously change the turbulence structure?"—meaning the dimensionless properties like the diffusion coefficient mentioned above, rather than dimensional quantities like the intensity. If each of the boundary layers that meet to form a duct flow continued to behave like a boundary layer (with an effective thickness somewhat larger than the half-width of the duct) then we could calculate the flow development by using ordinary boundary-layer methods on each, predicting the two shear stress profiles separately (but combining them in the mean motion equation). We cannot possibly hope that matters are as simple as this, but (refs. 17a and 17b) the effects of the interaction on the turbulence structure are small enough for multiple shear layers to be treated as separate layers, slightly modified by their
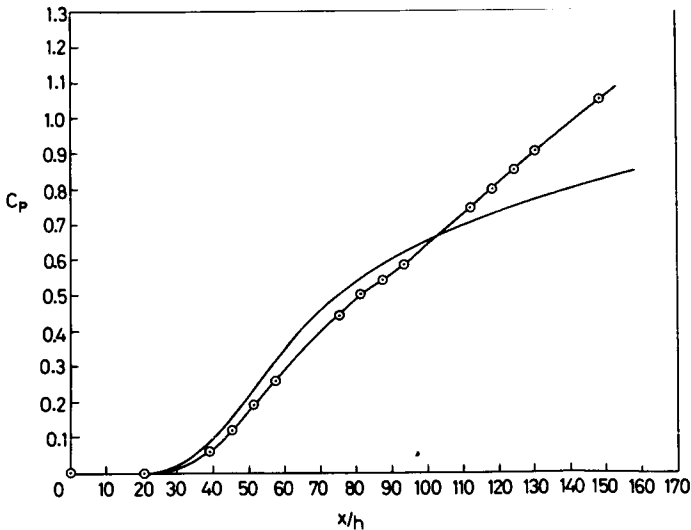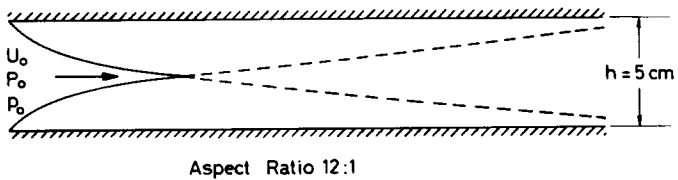

FIGURE 6.—Total-pressure loss on centerline of developing duct flow. C_p is total-pressure loss coefficient, $(P_0-P)/(P_0-p_0) \odot$; measurement is denoted by the circled points, and extrapolation of boundary-layer growth, neglecting interaction, is denoted by the solid curve.

neighbors, rather than as one impossibly complicated mess. A simple piece of evidence for this is shown in figure 6. Here we have plotted the total-pressure deficit on the centerline of a duct, compared with *twice* the total-pressure deficit that would occur at the same distance from the surface in a boundary layer growing unimpeded (i.e., we are adding together the total-pressure deficits in the two boundary layers, pretending that they do not interact at all). Of course, the two curves in figure 6 diverge eventually because the boundary layers do *not* continue to grow unimpeded, but at least we can see that nothing very spectacular happens to the shear-stress-producing part of the turbulence when the boundary layers meet. A similar behavior was found by Knystautas (ref. 18) in interfering jets. My doctoral student, Mr. R. B. Dean, whose results are shown in figure 6, is now looking at the details of the turbulence in the interaction region of the duct (ref. 19).

REFERENCES

1. KLINE, S. J., M. V. MORKOVIN, G. SOVRAN, AND D. J. COCKRELL, eds., *Proc. Computation of Turbulent Boundary Layers—1968 AFOSR-IFP-Stanford Conference*, Vol. 1, Thermosciences Div., Stanford U., 1969.

1a. BRADSHAW, P., *Anomalous Effects of Pressure Gradient on Supersonic Turbulent Boundary Layers.* Imperial College Aero. Rept. 72-21, 1972.

2. BRADSHAW, P., AND M. G. TERRELL, *Response of a Turbulent Boundary Layer on an "Infinite" Swept Wing to the Sudden Removal of Pressure Gradient*, NPL Aero. Report 1305, ARC 31514, 1969.

3. BRADSHAW, P., Three-Dimensional Flow. *Calculation of Boundary Layer Development Using the Turbulent Energy Equation, Part VII*, NPL Aero. Report 1286, ARC 30910, 1969; see also *Part IX, Summary*, NPL Aero. Report 1287, ARC 30909, 1969.

4. JOHNSTON, J. P., Measurements in a Three-Dimensional Turbulent Boundary Layer Induced by a Swept, Forward-Facing Step. *J. Fluid Mech.*, Vol. 42, Part 4, 1970, p. 823.

5. WYNGAARD, J. C., H. TENNEKES, J. L. LUMLEY, AND D. P. MARGOLIS, Structure of Turbulence in a Curved Mixing Layer. *Phys. Fluids*, Vol. 11, 1968, p. 1251.

6. HALLEEN, R. M., AND J. P. JOHNSTON, *The Influence of Rotation on Flow in a Long Rectangular Channel—An Experimental Study.* Thermosciences Div., Stanford U., Report MD–18, 1967.

7. PATEL, V. C., *Measurements of Secondary Flow in the Boundary Layers of a 180-Degree Channel.* ARC 30428, 1968.

7a. BRADSHAW, P., *Effects of Streamline Curvature on Turbulent Flow.* AGARDograph 169, 1973.

8. BRADSHAW, P., The Analogy Between Streamline Curvature and Buoyancy in Turbulent Shear Flow. *J. Fluid Mech.*, Vol. 36, 1969, p. 177.

9. PATEL, V. C., *The Effect of Curvature on the Turbulent Boundary Layer.* ARC 30427, 1968.

10. PATEL, V. C., AND M. R. HEAD, Some Observations on Skin Friction and Velocity Profiles in Fully-Developed Pipe and Channel Flows. *J. Fluid Mech.*, Vol. 38, 1969, p. 181.

10a. CASTRO, I. P., *A Highly Distorted Turbulent Free Shear Layer.* Ph.D. Thesis, Imperial College, London, 1973.

11. COLES, D., *The Turbulent Boundary Layer in a Compressible Fluid.* Rand Report R-403-PR, 1962.

12. SIMPSON, R. L., Characteristics of Turbulent Boundary Layers at Low Reynolds Numbers With and Without Transpiration. *J. Fluid Mech.,* 1970.

13. HERRING, H. J., AND G. L. MELLOR, *A Method of Calculating Compressible Turbulent Boundary Layers.* NASA CR-1144, 1968.

14. FIEDLER, H., AND M. R. HEAD, Intermittency Measurements in the Turbulent Boundary Layer. *J. Fluid Mech.,* Vol. 25, 1966, p. 719.

14a. HUFFMAN, G. D., AND BRADSHAW, P., A Note on Von Karman's Constant in Low Reynolds Number Turbulent Flows. *J. Fluid Mech.,* Vol. 53, 1972, p. 45.

15. BRADSHAW, P., Unsteady Flow. *Calculation of Boundary Layer Development Using the Turbulent Energy Equation, Part VI,* NPL Aero. Report 1288, ARC 30912, 1969.

15a. PATEL, V. C., AND NASH, J. F., In *Recent Research on Unsteady Boundary Layers* (E. A. Eichelbrenner, Ed.), Laval University Press, 1972.

16. KLINE, S. J., A. V. LISIN, AND B. A. WAITMAN, *Preliminary Experimental Investigation of Effect of Free-Stream Turbulence on Turbulent Boundary Layer Growth.* NASA TND-368, 1960.

16a. CHARNAY, G., COMTE-BELLOT, G., AND MATHIEU, J., Development of a Turbulent Boundary Layer on a Flat Plate in an External Turbulent Flow. *AGARD Conf. Proc.* 93, 1972.

16b. ROBERTSON, J. M., AND HOLT, C. F., Stream Turbulence Effects on the Turbulent Boundary Layer. *Proc. ASCE.,* J. Hydr. Div., Vol. 98, 1972, p. 1095.

16c. PICHAL, M., Die Turbulente Grenzschicht bei Hochturbulenter Aussenströmung, *ZAMM,* Vol. 52, 1972, p. T407.

16d. HUFFMAN, G. D., ZIMMERMAN, D. R., AND BENNETT, W. A., *The Effect of Free Stream Turbulence Level on Turbulent Boundary Layer Behavior,* paper presented at AGARD Specialists Meeting "Boundary Layer Effects in Turbomachines," Paris, Apr. 1972.

16e. GREEN, J. E., *On the Influence of Free Stream Turbulence on a Turbulent Boundary Layer, as it Relates to Wind Tunnel Testing at Subsonic Speeds.* RAE TR 72201, 1972.

16f. EVANS, R. L., *Stream Turbulence Effects on the Turbulent Profile Boundary Layer in a Compressor Cascade,* ARC paper 34587, 1973.

17. HANJALIC, K., AND B. E. LAUNDER, Fully Developed Asymmetric Flow in a Plane Channel. *J. Fluid Mech.,* Vol. 51, 1972, p. 301.

17a. BRADSHAW, P., DEAN, R. B., AND McELIGOT, D. M., Calculation of Interacting Turbulent Shear Layers. Duct Flow. *J. Fluids Engg.,* Trans. ASME, Vol. 95, 1973, p. 214.

17b. MOREL, T., AND TORDA, T. P., *Calculation of Free Turbulent Mixing by Interaction Approach.* A.I.A.A. Paper 73–649, 1973.

18. KNYSTAUTAS, R., The Turbulent Jet From a Series of Holes in Line. *Aeron. Quart.,* Vol. 15, 1964, p. 1.

19. DEAN, R. B., *An Investigation of Shear Layer Interaction in Ducts and Diffusers,* Ph.D. Thesis, Imperial College, London, 1973.

DISCUSSION

J. H. HORLOCK (Cambridge University): As usual, Mr. Bradshaw has provided a stimulating contribution in his excursion into turbomachinery fluid mechanics. At Cambridge, we are fortunate to have close collaboration with his group at Imperial College, so we have been given early warning on several of the points he raises and have had early opportunity to use his latest ideas.

Mr. Bradshaw's special points about boundary layers in turbomachines are not equally important for the thin boundary layers growing on successive profiles and the thicker annulus wall layers growing continuously through the (axial) machine. It appears, mainly from calculations, that three-dimensional effects on profile boundary layers are small (see ref. D–1), but they are obviously large in annulus wall layers, and this is where the main emphasis of our work at Cambridge lies. Camber effects on turbulence structure are large on profile layers but small on wall layers (δ/R is small). Strong accelerations apply equally to both, but rapid changes of direction are more important near the annulus walls. Low-Reynolds-number effects apply to the profiles but not the walls and high free-stream "turbulence" to both types of layer. I should like to comment on several of these effects in more detail.

(1)   I think that the interaction of the "inviscid" secondary flows (which are controlled largely by entry shear and blade geometry) with the viscous regions are probably more important than the "isotropy" of eddy viscosity or mixing length. Perkins (ref. D–2), studying the three-dimensional boundary layer just outside a corner boundary layer, finds the isotropic eddy viscosity concept quite reasonable, but I am bound to say that in our three-dimensional integral methods of calculating the annulus boundary layers where we use the Prandtl-Mager model for the crossflow (thereby avoiding the use of mixing length *or* eddy viscosity) it is the crossflow that is poorly predicted (Horlock and Hoadley, ref. D–3).

(2)   The camber effects are undoubtedly important, but in direct measurements of shear stress in three-dimensional boundary layers developing over cylindrical hubs of diffusers Hughes (ref. D–4) finds no evidence *as yet* that shows β is as large as 7. Hughes has also devised an experiment in which we can compare directly shear stresses with and without Coriolis effects.

(3)   Rapid accelerations worry us a great deal in our boundary-layer calculations. Applying the integral method of reference D–3 to the flow through a set of inlet guide vanes of large camber, we find that the streamwise boundary layer (assumed to be described by a Coles profile) is subject to such an enormous acceleration that the value of π becomes negative. This is not an unknown phenomenon in conventional aerodynamics, but if $\pi < -1$, then the method loses validity. Surprisingly, the negative π profiles compare reasonably well with experiment, with a "hump" in the velocity profile. At present, Marsh and Daneshyar at Cambridge University are planning an experiment in which we can provide rapid acceleration, but not through turning the flow—simply by measuring the wall boundary-layer flow through thick uncambered blades. We are thus attempting to separate the acceleration from the three-dimensional effects due to turning.

(4)   The R_θ effects are intriguing and undoubtedly relevant to profile boundary layers. However, I think the main problem relating to these layers is the question of transition, especially in an unsteady environment or one with high free-stream turbulence. At Cambridge, Evans has shown that when the latter is increased, Thwaite's prediction of the laminar separation point becomes pessimistic.

(5)   In our group, Daneshyar and Mugglestone have also programmed the unsteady Bradshaw method and we look forward to comparing results with Patel. We have also developed an unsteady version of the integral method described in reference D–5 for comparison with the more accurate Bradshaw method. This is a general point of some importance. Our philosophy is that it is unlikely that the Bradshaw type of calculation will be used directly in turbomachine work because it requires even further complications in these real situations (effect of body forces, unsteadiness, three-dimensionality, etc). We feel that simple integral methods may still have uses if they compare reasonably with Bradshaw's method in some trial situations.

(6)   The interaction of the shear layers is a new one which I have not thought of before, but obviously of importance in turbomachines, particularly in the effect of a blade wake on a following row. Our only contribution here is the work of Perkins referred to above. Here, the lesson appears to be that if the Reynolds stress distributions can be described with fair accuracy (by correlation of experimental data) the overall parameters such as displacement and momentum "areas" may be predicted and the nature of the secondary flows explained.

I should like to congratulate Mr. Bradshaw on his stimulating paper and look forward to further contributions from him in this area. Perhaps I might emphasize once again that boundary-layer phenomena in turbomachines are also closely related to "inviscid" phenomena such as

secondary and tip clearance flows, but it is very useful to have a new "viscous" recruit to the internal flow area.

H. McDONALD (United Aircraft Research Laboratories): In addition to the seven points of difference between conventional airfoil boundary layers and those encountered on the blades of turbomachinery listed by Mr. Bradshaw, I would like to add two additional points, one on transition and one on separation, and comment upon the low Reynolds number remarks made by Mr. Bradshaw as point (5).

First, experimental evidence obtained by the Pratt & Whitney Division of United Aircraft (ref. D–6) shows clearly that at the low Reynolds numbers typical of turbine blade operation the effect of the high free-stream acceleration on the suction side is to inhibit the transition to fully turbulent flow, in spite of the very high levels of free-stream turbulence induced by the upstream combustion process. In figure D–1, a typical result from reference D–6 is reproduced, illustrating the foregoing remark, and it can be clearly seen that over most of the chord the boundary layer is transitional. It is apparent from figure D–1 that some means of predicting the behavior of transitional boundary layers must be evolved before the heat transfer to the suction side of a turbine can be predicted to an acceptable level of engineering accuracy.
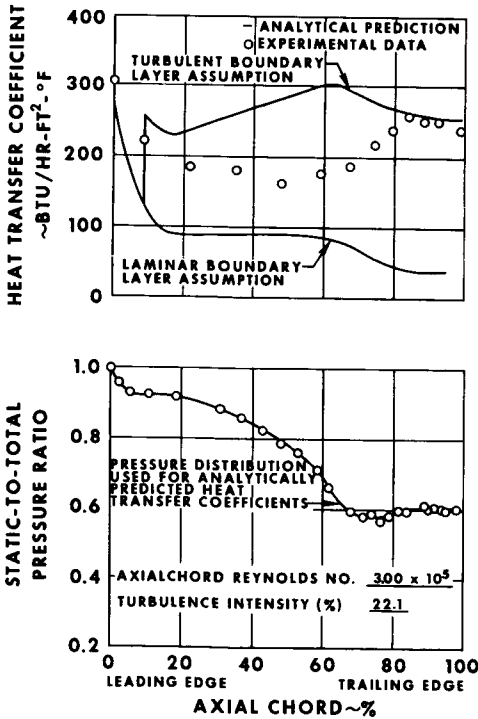

FIGURE D–1.—*Experimental heat-transfer coefficient and pressure distribution for a typical turbine vane. (United Aircraft Research Laboratories)*

Second, as a result of the low Reynolds numbers commonly encountered in turbomachinery, boundary-layer separation occurs very readily. Conventional separation near the trailing edge usually occurs without reattachment of the boundary to the airfoil surface and often such a separation generates large increases in the loss level. Near the leading edge, separation is usually followed by subsequent reattachment, forming a separation bubble, probably with comparatively little change in the overall loss level. Sometimes, in a poorly designed, highly loaded airfoil, separation can occur near the gauge point. Separation bubbles can, of course, give rise to unexpected Reynolds number effects and, in addition, usually play havoc with boundary-layer prediction methods. Since, with an arbitrary, prescribed pressure distribution, the boundary-layer equations of motion are, in fact, singular at a point of zero wall stress, the more accurately a prediction procedure treats the boundary-layer equations the more likely it is to fail at a separation point. The only rigorous course of action appears to be to use the full Navier-Stokes equations in the region of the bubble. Recently, a study has been completed at United Aircraft Research Laboratories utilizing a finite difference procedure for computing the Navier-Stokes equations in the region of the bubble (ref. D–7). These calculations have shown a considerable upstream influence of the separation process. Future work in this area will involve incorporation of a turbulence model into the procedure.

Concerning the direct effect of Reynolds number, the structure of the low Reynolds turbulent boundary layer has been evaluated recently at United Aircraft Research Laboratories from the equations of mean motion (ref. D–8) using Coles' velocity profile (ref. 11). It was found that the disappearance of the wake component as the Reynolds number is reduced, observed by Coles, is consistent with a large increase in normalized eddy viscosity or mixing length. (At $R_\theta = 500$ the normalized mixing length was double what it was at $R_\theta = 5000$.) Use of a normalized eddy viscosity or mixing length which does not vary with Reynolds number causes the skin friction to be underpredicted by about 10 percent. The variation of eddy viscosity derived from Coles' profile was in fair agreement with the suggestion of Herring and Mellor (ref. 13).

Finally, although the blade profile boundary layers seem amenable to treatment by modest developments of conventional boundary methods, the annulus boundary layer seems particularly troublesome. In addition to being strongly three-dimensional, as Mr. Bradshaw points out, the annulus boundary seems capable of interacting strongly with the "free" stream and distorting the inviscid flow by an appreciable amount. As is well known, this coupling between the annulus boundary layer and the inviscid flow results in both displacement thickness effects and secondary flows, and it would be mandatory to take these effects into account in any stage loss calculation procedure based on boundary-layer theory.

G. L. MELLOR (Princeton University): Professor Bradshaw's paper is an interesting one and I find myself in general agreement with the conclusions expressed there. I will, therefore, attempt to add a corroborative point or two.

(1)   Mr. Ronald So of our laboratory has just completed some interesting measurements on wall curvature illustrating the dramatic effect of, for instance, $\delta^*/R \simeq .01$; going from a flat surface to a convex surface, the Reynolds stress in the outer 60 to 70 percent of the layer is virtually "turned off". First indications are that this effect appears to be quantitatively deducible from a Prandtl-Rotta type boundary-layer model.

(2)   Mr. Luc Bissonnette of our laboratory has also completed measurements of an axisymmetric boundary layer on a rotating cylinder. We find that the simple eddy viscosities differ by about 30 percent in the axial and circumferential directions.

(3)   Characterization of the inner viscous layer is functionally equivalent using either Van Driest's formula (eq. (5)) or the one we used,

$$\frac{\nu_t}{\nu} = \frac{\chi^4}{\chi^3 + (6.9)^3}$$

where $\nu_t = -\overline{u'v'}/(\partial \bar{u}/\partial y)$ and $\chi \equiv u(y/\nu)\sqrt{\tau/\rho}$. When Van Driest's function is mapped onto ours or vice versa, the detailed distributions do differ in what one would think to be an unimportant way. However, in the case of wall suction or blowing it appears that A^* in Van Driest's equation must be adjusted as a function of blowing rate, whereas our formula does not seem to require adjustment. This must currently be considered fortuitous; however, I mention it since the same situation might prevail with regard to the effect of $\partial \tau^+/\partial y^+$.

Speaking in general terms, it is my feeling that the most important turbulent boundary layers in a turbomachine are the annulus wall layers, which probably defy description even in terms of the seven attributes listed in the author's abstract.

J. M. ROBERTSON (University of Illinois): This review, and especially the quantification embodied in table I, indicates serious additional problems imposed on boundary-layer type flow analyses when turbomachinery applications are involved. For several years we have had a number of these under study, as motivated by machinery interests, together with the unlisted one of the turbulent near wake of blades. The present remarks pertain to items (3), (5), and (6) of table I of the authors' listing.

The discussion of streamline curvature effects suggests an increased likelihood of separation on convex surfaces due to a reduction in turbulent shear stress. A study of the boundary layer on the upper surface of a simulated turbomachinery blade by Dr. R. C. Hansen (ref. D–9) indi-

cated turbulent separation much ahead of the locale predicted by analysis. It has been supposed that the breakdown in analysis may be due to a variation in pressure across the layer under appreciable streamline curvature, as such variation is not ordinarily included in boundary-layer analyses. Other studies in our laboratory (refs. D–10 and D–11) of flows approaching turbulent separation have evidenced such a breakdown in the basic boundary-layer premise of constant pressure across the layer. An experiment, in which the turbulent layer developed along a flat plate is sent along the outer surface of a circular cylinder, has been set up to study this occurrence under more controlled conditions. Although only preliminary measurements are available, it is found that already at the point of tangency a pressure change of $0.05\rho U^2/2$ occurs across the layer.

A low-Reynolds-number defect in frictional formulation is suggested in table I. To this writer, this appears to be a matter of what C_f formulation is employed; a local friction factor formulation drawn from the Schoenherr average C_f relation does not seem too appropriate. The 1953 relation of D. Ross (ref. D–12)

$$C_f = (4.4 + 3.8 \log R_\theta)^{-2}$$

where $R_\theta = \theta U/\nu$ has been well verified for flat-plate boundary-layer flows and agrees with Cole's tabulation within a few percent. For adverse-pressure-gradient flows, the Ludwieg and Tillman formulation in terms of R_θ and H ($H = \delta^*/\theta$, ratio of displacement to momentum thicknesses) is almost universally accepted; however, several years ago our calculations suggested that this yielded poor values at low Reynolds numbers. The predictions were checked in the flat-plate case where H is well established (refs. D–12 and D–13) as a unique function of R_θ. The Ludwieg and Tillman formulation was found to be 19-percent low at $R_\theta = 300$, about the smallest turbulent-layer Reynolds number to be expected. In the spirit of the Ludwieg and Tillman formulation, the following expression was developed to circumvent the error.

$$C_f = \frac{\exp\left[1.8(H_0 - H)\right]}{(4.4 + 3.8 \log R_\theta)^{-2}}$$

where

$$H_0 = 1.09 + \frac{0.40}{0.72 \log R_\theta - 1.0}$$

is the flat-plate turbulent-layer shape factor (ref. D–14) formulation based on a large number of observations (refs. D–12 and D–13).

For some time, we have been studying the effect of free-stream turbulence on the turbulent boundary layer. This has the effect of increasing the lateral momentum transfer, thus making the velocity profile more uniform over most of the layer; the shape factor H is thus reduced in

magnitude, while G ($G = \delta/\theta$, ratio of layer disturbance thickness (locale of $0.99U$) to momentum thickness) and C_f are increased by the turbulence. In an attempt to quantify these occurrences beyond the rather scattered data available in the literature, we have been studying the turbulent layer on a flat plate downstream of various turbulence-producing grids (up to 10-percent turbulence intensity). Comparison of the changes in the boundary-layer parameters versus those expected in nominally low-level turbulence indicates appreciable changes at intensities up to about 5 percent and then some leveling off. The author's estimate of a 3-percent turbulence level producing a 10-percent increase in C_f is rather well verified; at this level, the shape factor H is reduced by some 4 percent.

A. S. MUJUMDAR (Carrier Corporation): I just wish to point out a few recent papers that would complement the excellent review made by Professor Bradshaw.

Chin, Hulschos, and Hunnicutt (ref. D–15) have reported on their experimental investigation of the effect of lateral curvature on the characteristics of turbulent boundary layers, while Willmarth and Chi (ref. D–16) more recently considered the effect of transverse curvature on wall pressure fluctuations and the turbulence microstructure. From the spectral and cross-correlation measurements of reference D–16, it appears that the turbulence structure of the boundary layer, primarily that of the viscous sublayer, is affected by the transverse curvature. An interesting analytical study of the effect of longitudinal (streamwise) surface curvature on the turbulent boundary layer has been reported recently by Dr. Neal Tetervin (ref. D–17). Although his equations do not give accurate quantitative results, they show that if the concave curvature increases the shear sufficiently, separation is delayed despite the boundary layer thickening. The converse is also true; i.e., convex curvature hastens separation even though the boundary layer is thinned. An important indication from his calculations, which is of special interest to turbomachine designers, is that when the curvature increases in the streamwise direction, separation is hastened on a surface of concave curvature and is delayed on a surface of convex curvature.

Regarding the effect of free-stream turbulence on turbulent boundary layers, there has been some work in this area since the pioneering work of Kline et al. Kestin and his co-workers at Brown University (ref. D–18) and Junkhan and Serovy (ref. D–19) at the Iowa State University have made some valuable contributions in this area.

BRADSHAW (author): I am grateful to the discussors for their comments. In particular, Professor Horlock's second paragraph clarifies the relative importance of the different effects I mentioned, and all of the discussors mention additional effects.

The paragraph numbers below refer to the numbered list in the Abstract.

(1)   The effects of anisotropy of eddy viscosity in three-dimensional flow may well be negligible in flows dominated by pressure gradients or viscous inviscid interactions (see the last sentence of the section on three-dimensional boundary layers); however, if the Reynolds stresses outside the local-equilibrium inner layer are important, anisotropy of eddy viscosity is likely to be important also (see figure 2).

(3)   Further work on curved flow by my student, Mr. Ian Castro, agrees with So's work mentioned by Professor Mellor. Figure D-2 (also see figure 3) shows the response of $\overline{u^2}$ in a suddenly deflected shear layer. The maximum δ/R is about 0.025, about the same as Professor Robertson's and roughly one-third of So's. It is notable that the decrease in $\overline{u^2}$ (taken as the maximum value at a given station and measured in the direction of the local mean velocity) lags behind the increase in curvature. If the subsequent increase of $\overline{u^2}$ above its initial value is genuine (and it does not seem to be caused by large-scale unsteadiness of the shear layer), one is led to suspect that the recovery of the turbulence from its partly damped state resembles laminar-turbulent transition, in which intense well-organized disturbances appear. I hope the experiments mentioned by the
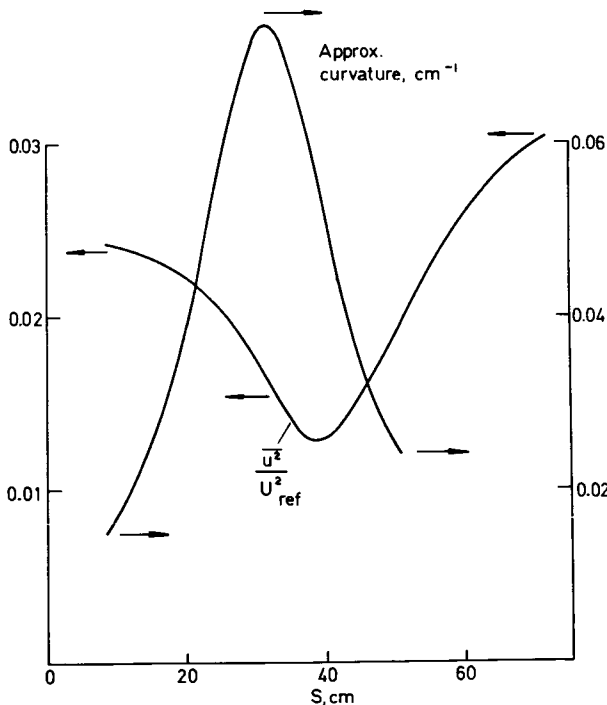

FIGURE D-2.—*Deflected shear layer (Castro); see figure 3 of paper.*

discussors will help us to represent curvature effects more accurately in shear-layer calculation methods, but I wish to point out that the partly-stabilized state (δ/R of order .01) is more important for blade and airfoil calculation than the "turned off" state, and the latter may not throw much light on the former. Incidentally, I gather that Professor Horlock's student, Mr. Hughes, has now found $\beta \approx 6$ to 7 in a flow with an effective δ/R of about 0.007.

(5) I agree with Professor Robertson that one can find a better C_f law than Schoenherr for low Re; the point is that Schoenherr is based on the log law and the defect law, and so a failure of Schoenherr implies a failure of the log law or the defect law, which merits investigation in its own right.

As mentioned in the paper, I am fairly confident that, at least in moderate pressure gradients, it is only the outer layer (*defect* law) that alters, owing to viscous effects.

Dr. J. E. Green of R.A.E., Bedford, has also deduced mixing length and eddy viscosity in the outer layer from Coles' low Re profiles; his results agree with Mr. McDonald's in showing large changes.

Figure D–3 shows the final results of Dr. David Huffman's data analysis for strong negative shear stress gradients (or pressure gradients); transverse curvature affects the sublayer behavior for a given $\partial \tau^+/\partial y^+$. This result is qualitatively independent of the sublayer model used, so replacement of Van Driest's formula by Professor Mellor's formula would not collapse the curves, though it would be interesting to see if the duct (flat surface) results were better represented by the latter formula than by Van Driest's formula with constant A^+.

Of course I agree that, as Professor Horlock and Mr. McDonald say, transition is an important low-Reynolds-number effect; I said nothing about it in the paper because I had nothing to say. The effect of turbulence changes at low Re on $\int C_f \, dx$, integrated from the leading edge to where $Re_\theta = 5000$, is about the same as a change in transition Re_θ from 400 to 300—not negligible compared to the actual uncertainty of transition position.

(6) Professor Robertson's measurements of the effects of free-stream turbulence are very welcome (not only because they confirm my rough estimate). I hope he or others will look at the effects on the turbulence structure of the shear layer itself. In this connection, the latest measurements in a duct entry region by my student, Mr. Bruce Dean, show that the "non-interaction" (superposition) hypothesis works quite well for $\overline{u^2}$, as well as for total pressure P (figure D–4). The difference between this curve for "non-interaction" C_p and that shown in figure 6 results from a change in our method of extrapolating the boundary-layer growth from data upstream of the interaction region; this is surprisingly critical.

I don't think "non-interaction" can be trusted too far (in its simplest form it would imply no effect of free-stream turbulence) but it is a useful concept when dealing with minor interactions.
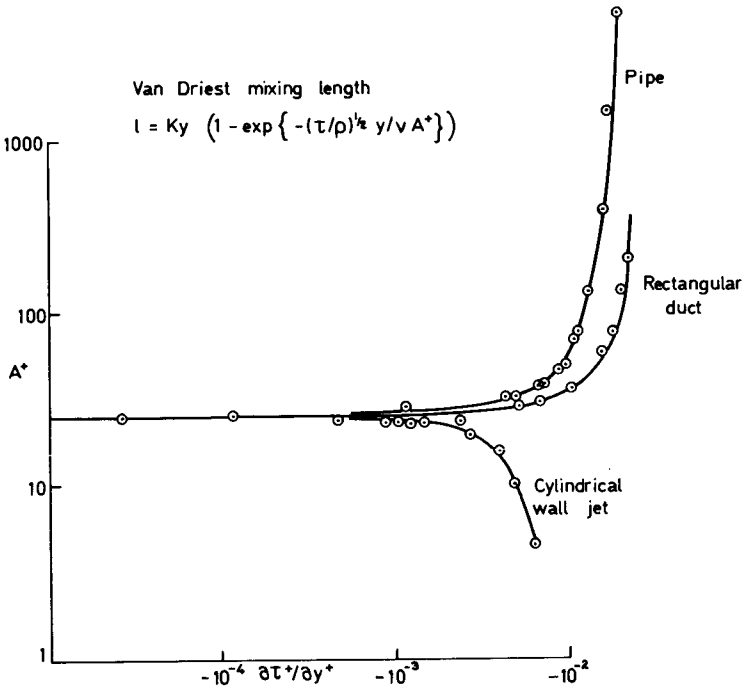

FIGURE D-3.—*Sublayer behavior (Huffman); effect of transverse curvature; see figure 4 of paper.*
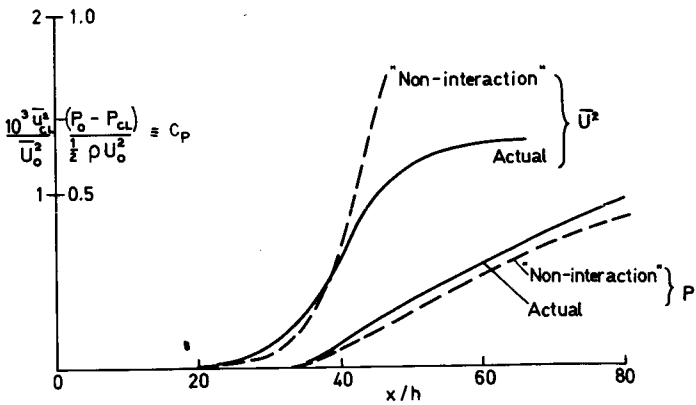

FIGURE D-4.—*Duct entry length (Dean); see figure 6 of paper.*

The comments about annulus boundary layers made by the discussors emphasize the need to treat viscous/inviscid and viscous/viscous interactions. I hope that people who work on these important problems will not ignore all the knowledge we have gained on thin shear layers; a lot of it will still be usable, provided we have the patience to treat the interaction as an interaction (solution by matching) and do not try to find a complete field solution in one go.

I would change the emphasis of Mr. McDonald's remarks about singularities at separation and say that the less accurately a prediction method treats the physics of the flow the less suitable it will be in calculations of viscous/inviscid interactions. Undoubtedly, one will have to admit elliptic behavior of the pressure and also normal Reynolds stress gradients, but I would not expect any large changes in the turbulence unless the rate of strain changed appreciably from a simple shear.

Finally, I would like to comment on (5) of Professor Horlock's remarks. He rightly points out that real life leads to extra complications in calculation methods and implies that methods like ours, which are already quite complicated, may become intractable, so that integral methods may be preferable. I don't want to argue about the merits of our method in particular, but I think Professor Horlock's "general point" may not be quite as general as he implies.

Let us distinguish between two sorts of turbulence model:

(1) "No history"—local equilibrium between turbulence and mean flow, leading to algebraic equation for shear stress

(2) "History"—differential equation for shear stress and two sorts of solution procedure:

(3) "Integral" method—otherwise, Method of Integral Relations

(4) "Differential" method—finite differences in all independent variables

(3) does not necessarily go with (1) or (4) with (2). At least three people have produced "integral" versions of our calculation method and our "differential" program has built-in options to simulate the input and output of an integral method working on Re_θ, H and C_f. The fastest of the integral versions runs at only five times the speed of the differential program and suffers noticeably from using too crude a velocity profile family. Therefore, I do not think we should reject (4) in favor of (3); computing times for given accuracy will not be an order of magnitude less. Programming time matters only to the originator, not the user. There are some cases where "history" effects are unimportant. In such cases, our method reduces to the mixing-length formula, for which Patankar and Spalding have a program which runs about twice as fast as ours; again, this is not a significant saving unless a vast amount of computing is to be done because the cost of a run is less than a dollar.

Even in three-dimensional (swept wing) flow, the computing time for our method would be only about $2 \times$ (number of spanwise stations) $\times$ (two-dimensional computing time); roughly the same factor of increase would apply to any other method. The only case which is really daunting is the two-dimensional time-dependent calculation. Unless one uses a method that is implicit in time, solutions for a typical flow whose period of oscillation is many times greater than a typical turbulence time scale are exceedingly lengthy, as Professor Horlock's colleagues have found. With an integral method, one can take larger time steps.

Turning from arithmetical complication to physical complication, the turbulence models used in "history" methods are—or can be—nearer to real life than those used in no-history methods. Therefore, they are *easier* to extend to complicated cases. For instance, extension of our model to time-dependent flow is immediate (see the section of the paper on free-stream "turbulence"); extension to three-dimensional flow requires only a plausible hypothesis based on the observation that turbulence is always three-dimensional; and our present knowledge of the effect of body forces can be included very simply. Therefore, I think that Professor Horlock's view may be slightly colored by his experience with the particularly unpleasant case of unsteady flow, and, while he undoubtedly has a point, it would be a pity if his remarks discouraged turbomachine engineers from trying more complicated turbulence models—they are all much less complicated than turbulence itself.

REFERENCES

D–1. HORLOCK, J. H., Boundary Layers in Axial Turbomachines. *Flow Research on Blading,* L. Z. Dzung, ed., Elsevier Press, 1969.

D–2. PERKINS, H., *The Boundary Layer Flow in a Corner.* Ph.D. dissertation, Cambridge U., 1970.

D–3. HORLOCK, J. H., AND D. HOADLEY, *Calculation of the Annulus Wall Boundary Layers in Axial Flow Turbomachines.* Aero. Research Council Report 31.955, 1970.

D–4. HUGHES, D. W., *Swirling Flow in an Annular Diffuser With a Rotating Centre-Body.* Ph.D. dissertation, Cambridge U., 1972.

D–5. LEWKOWICZ, A. K., D. HOADLEY, J. H. HORLOCK, AND H. J. PERKINS, A Family of Integral Methods for Predicting Turbulent Boundary Layers. *AIAA J.,* Vol. 8, No. 1, 1970, pp. 44–51.

D–6. LANDER, D. E., *Evaluation of the Effect of Free Stream Turbulence on the Heat Transfer to Turbine Airfoils.* Air Force Aero Propulsion Lab Report TR-69-70, September 1969.

D–7. BRILEY, W. R., *A Numerical Study of Laminar Separation Bubbles Using the Navier-Stokes Equations.* United Aircraft Research Laboratories Report J110614-1, July 1970, and *J. Fluid Mech.,* Vol. 47, 1971, p. 713.

D–8. McDONALD, H., *Mixing Length and Kinematic Eddy Viscosity in a Low Reynolds Number Boundary Layer.* United Aircraft Research Laboratories Report J214453-1, July 1970.

D-9. HANSEN, R. C., *Blade Channel Flow in a Simulated Radial-Flow Turbomachine.* Ph.D. dissertation, Illinois U., 1967.

D-10. MUELLER, T. J., AND J. M. ROBERTSON. A Study of the Mean Motion and Turbulence Downstream of a Roughness Element. *Devel. in Theoretical and Appl. Mech.*, Vol. I, 1963, pp. 326–340.

D-11. ROBERTSON, J. M., AND D. B. TAULBEE, Turbulent Boundary Layer and Separation Flow Ahead of a Step. *Devel. in Mech.*, Vol. 5, 1969, pp. 171–190.

D-12. ROSS, D., A New Analysis of Nikuradse's Experiment on Turbulent Flow in Smooth Pipes. *Proc. Third Midwest Conf. on Fluid Mech.*, 1953, pp. 651–667. See also Turbulent Flow in the Entrance Region of a Pipe. *Trans. ASME*, Vol. 78, 1956, pp. 915–923.

D-13. ROBERTSON, J. M., *A Turbulence Primer.* Circular No. 79, Illinois U., Eng. Exp. Station, 1963.

D-14. ROBERTSON, J. M., Growth of the Turbulent Flat-Plate Boundary Layer. *ASEE Monograph Series*, Mon. M-1, 1969, pp. 14–21.

D-15. CHIN, Y. T., J. HULSCHOS, AND G. H. HUNNICUTT, *Proc. 1967 Heat Transfer Fluid Mechanics Institute* (San Diego), 1967, pp. 394–407.

D-16. WILLMARTH, W. W., AND YANG, C-S., Wall Pressure Fluctuations Beneath Turbulent Boundary Layers on a Flat Plate and a Cylinder. *J. Fluid Mech.*, Vol. 41, 1970, p. 47.

D-17. TETERVIN, NEAL, U. S. NOLTR Report 69-22, February 1969.

D-18. KESTIN, J., *Advances in Heat Transfer*, Vol. III, Academic Press (New York) 1966.

D-19. JUNKHAN, G. H., Ph.D. dissertation, Iowa State U., 1966.

PRECEDING PAGE BLANK NOT FILMED
Boundary Layer Separation and Reattachment[1]

V. A. SANDBORN

Colorado State University

A review of recent developments in a new model for boundary-layer separation will be presented. The separation model encompasses time-varying as well as steady-flow conditions. Engineering criteria in terms of calculable pressure gradients are obtained for both laminar and turbulent boundary-layer separation. These criteria, together with limited information on time-dependent separations, should be of value in predicting flows in turbomachinery. The reattachment of boundary layers is also shown to fit within the separation model.

Boundary-layer separation is a limiting factor in the performance of nearly all fluid-flow devices. In turbomachinery, turbulent separation is encountered in the diffuser flow, and laminar separation can be encountered on the compressor and turbine blades. The problem of boundary-layer separation in turbomachinery can be further complicated due to unsteady or time-varying flow conditions. It is readily apparent that an understanding of boundary-layer separation can be applied directly to improvement of the operation of several components in turbomachines.

Prandtl (ref. 1) first advanced a model of a zero wall-shear stress, laminar, separation boundary layer. Prandtl's model is adequate for an ideal flow in which the boundary layer has sufficient time to adjust to the separation conditions. However, for turbulent boundary layers, and also for laminar boundary layers where separation occurs rapidly, the layer cannot adjust to the ideal conditions required by Prandtl.

Sandborn and Kline (ref. 2) proposed a boundary-layer separation model which incorporated the Prandtl "steady separation" and also an "unsteady separation." This model suggested a separation region in which the boundary layer "transitioned" to the separation conditions. The recent experimental measurements by Liu (refs. 3 and 4) for turbulent

boundary-layer separation confirmed the general concept of the transition region. It has, however, become increasingly apparent that the concept of "steady" and "unsteady" separation, suggested by Sandborn and Kline, is not an adequate description for all boundary-layer separations.

The present paper presents a more general model for boundary-layer separation. The new model is based on the concept of an adjustment time for the boundary layer. It is now possible to include time-dependent boundary layers in the model. Based on these new concepts, an engineering criterion for a wide range of boundary-layer separation is constructed.

BOUNDARY-LAYER SEPARATION MODEL

The definition of boundary-layer separation is usually associated with zero wall shear stress or in terms of a limiting streamline (ref. 5). Such a definition, while exact, appears too idealized for general engineering applications. Separation must be defined mainly as an unwanted viscous region, where mass and heat transfer at the surface are greatly reduced.

A general definition of boundary layer separation is *the removal of viscous restraints at the wall*. This definition is intended to imply that the wall shear has a negligible effect on the further development of the flow characteristics in the separation region. It does not necessarily require that the wall shear vanish. The wall shear may be positive, negative, or zero, as long as it is small compared to inertia terms. The definition is necessarily vague in order to encompass both time-average and time-dependent boundary-layer evaluations.

The flow visualization studies of Kline (ref. 6) were instrumental in showing that turbulent separation began as an unsteady, three-dimensional phenomenon. The separation was seen to develop into what was thought to be a statistically "steady" type of separation. Thus, the Sandborn-Kline model assumed that a transition region existed where the flow changed from the "unsteady" to the "steady" type separation. Liu (ref. 4) was able to experimentally demonstrate the existence of the transition region. However, it was readily apparent that conditions were certainly far from steady at any point in the transition process.

It is now realized that the original Sandborn-Kline model is too restricted. The transition region should be viewed as a region over which the flow adjusts to the removal of viscous restraints at the wall. Figure 1 is a sketch of the separation transition region. The extent of the region depends directly on the body geometry and the free-stream conditions. At the start of the region, boundary conditions are such that viscous effects at the surface are negligible. At the end of the region, the complete velocity distribution has adjusted to the surface condition. If a laminar boundary layer approaches separation in a sufficiently mild, adverse,

Velocity Distribution
Unadjusted to the
Separation Conditions
at the Surface

Velocity Distribution
Adjusted to the
Separation Conditions
Imposed at the Start
of the Transition

Start

Transition Region

End
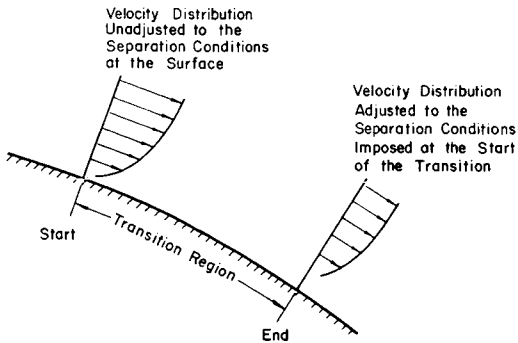
FIGURE 1.—*Sketch of the proposed separation model.*

pressure-gradient flow, the whole layer can adjust to the boundary conditions. Thus, for some laminar separation cases the transition region reduces to a point. On the other hand, if the approach to separation is very rapid, the velocity distribution cannot adjust to the wall conditions and a transition region exists. The nature of the turbulent boundary layer is such that a transition region would be expected.

The adjustment time required depends on how quickly the outer flow in the boundary layer comes to equilibrium with the separation boundary condition. For a turbulent boundary layer, it is well known that the outer part of the layer is inertia dominated and responds very slowly to changes in the inner region of the boundary layer. It is possible for the inner region to "so to speak" vanish completely, with only a secondary effect on the outer region. Thus, the adjustment time of a turbulent boundary layer to a viscous condition at the surface is quite long. The laminar boundary layer is much thinner, so it can adjust to boundary conditions at the surface in a shorter time.

Measurements for turbulent boundary layers at the start of the separation transition region indicate a small positive mean wall-shear stress (ref. 4). Only at the end of the transition region does the mean wall-shear stress appear to be zero. This residual shear is thought to be due to the unsteady nature of the flow. The description of "steady" separation for the end of the transition region, employed by Sandborn and Kline, now appears to be misleading. For the time-varying free-stream flows it is found that the wall-shear stress may vary from zero to a negative value as the velocity profile adjusts. Thus, specification of the wall-shear stress in the separation region is quite subjective. It appears that the wall-shear stress may be of only secondary importance in defining the separation region.

The empirical velocity profile parameter correlations developed by Sandborn and Kline (ref. 2) are employed to identify the beginning and end of the separation transition region. Figure 2 is a plot of the velocity profile form factor versus the ratio of displacement to boundary-layer
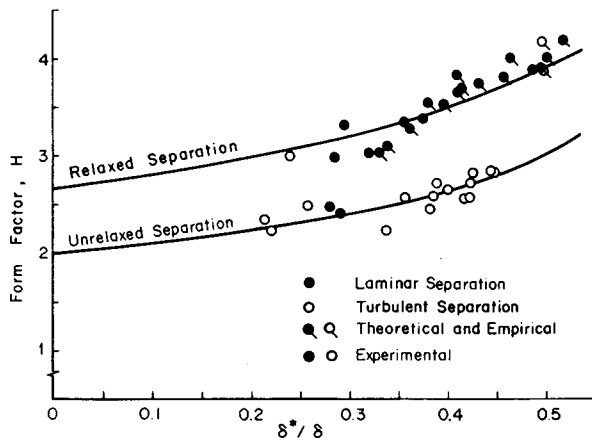
FIGURE 2.—*Boundary-layer separation correlations.*

thickness. The empirical correlation curves identified as "relaxed" and "unrelaxed" separation are those originally given by Sandborn and Kline and identified as "steady" and "unsteady" separation. The words "relaxed" and "unrelaxed" are presently thought to be a better technical description of the boundary layer than "adjusted" and "unadjusted". All available identified separation velocity profiles are included in figure 2. The profiles are identified according to whether they are laminar or turbulent boundary layers. Points are also identified as either experimental or analytical.

In general, laminar boundary-layer separations are found to be near the relaxed separation limit. This is in keeping with the classical separation model of Prandtl. The turbulent boundary-layer separations are likely to be identified with the unrelaxed separation limit. The obvious exceptions are

(1)   Liu's measured turbulent boundary layer profile at the point of relaxed separation ($H = 3.0$, $\delta^*/\delta = 0.24$) (ref. 7)

(2)   Coles' "law" of the wake turbulent separation profile ($H = 4.1$, $\delta^*/\delta = 0.5$) (ref. 8)

(3)   Two measured laminar separation bubble profiles ($H = 2.49$, $\delta^*/\delta = 0.286$ and $H = 2.48$, $\delta^*/\delta = 0.282$) (ref. 9)

The concept of boundary-layer adjustment distance implies that partially relaxed separations should also be found. It is suspected that the two laminar separation bubble measurements, shown in figure 2 at $H = 3.05$, $\delta^*/\delta = 0.325$ and $H = 3.00$, $\delta^*/\delta = 0.290$ may indicate partially relaxed separation. The analytical points at $H = 3.10$, $\delta^*/\delta = 0.341$ and $H = 3.05$, $\delta^*/\delta = 0.332$ computed by Liu (ref. 7) may also represent partially relaxed separation. Evidence of partially relaxed separation will

also be demonstrated in the sections on time varying flows and reattachment of boundary layers.

The present model of boundary-layer separation assumes that the velocity distributions for laminar and turbulent flows are similar. The analysis of Sandborn and Liu (ref. 4) demonstrated that the similarity at the relaxed separation location could be justified by considering the equations of motion. At the location of relaxed separation, the equations reduced to the inertia terms equal to the pressure force over the major part of the layer. The shear forces were only important in matching the pressure force at the surface. For unrelaxed separation, it does not appear possible to make a specific statement about the magnitudes of the inertia and shear terms. The magnitudes will depend on how rapidly the separation is approached. Thus, the shear terms may range in importance from that of a flat plate flow to negligible values compared to the inertia terms.

ENGINEERING CRITERIA FOR BOUNDARY-LAYER SEPARATION

The correlations shown in figure 2 imply that one-parameter families of velocity profiles exist at separation. This model may prove too simple to cover all possible separation cases; the time-varying flow cases may be exceptions. However, as a first approximation it is possible to construct engineering criteria based on the results of figure 2. The three parameters employed in figure 2 are not readily computed in boundary-layer prediction methods. Thus, it is necessary to recast the correlations in terms of a calculable pressure-gradient parameter. The analysis of Sandborn and Kline (ref. 2) led to a criterion for laminar relaxed separation in terms of the pressure-gradient parameter

$$\lambda_\delta \equiv \frac{\delta^2}{\nu} \frac{dU_1}{dx}$$

The recent analysis of Liu and Sandborn (ref. 3) produced a criterion for laminar separation in terms of the velocity profile form factor, H, versus the pressure-gradient parameter

$$\lambda_\theta \equiv \frac{\theta^2}{\nu} \frac{dU_1}{dx}$$

Figure 3 shows the criterion given by Liu and Sandborn. Experimental and analytical data points are included in figure 3. The laminar curve is shown dashed out to include the turbulent relaxed separation point measured by Liu (ref. 4). It appears reasonable to identify the laminar criterion with relaxed separation. Table I lists the coordinates for the curves of figure 3.
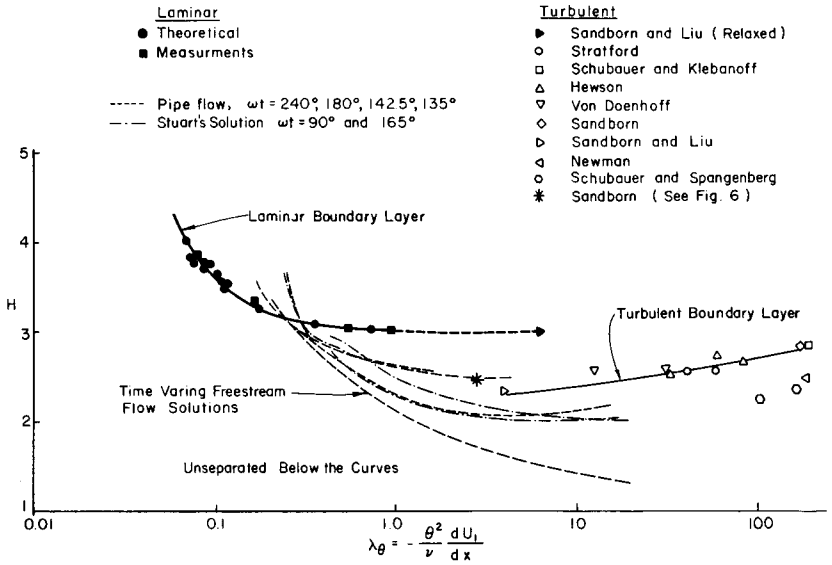
FIGURE 3.—*Boundary separation criteria.*

The pressure-gradient parameter, λ_θ, can be computed for laminar boundary layers, once the external velocity distribution is specified, by employing Thwaites' relation (ref. 10) for momentum thickness:

$$\theta^2 = 0.45\nu U_1^{-6} \int_0^x U_1^5 \, dx \tag{1}$$

This relation was demonstrated by Liu and Sandborn to be an accurate prediction of θ for the analytical laminar boundary-layer solutions included in figure 3. The x-location of the separation can be estimated from the simple relation given by Stratford (ref. 11)

$$x_s^2 C_p \left(\frac{dC_p}{dx}\right)^2 = \text{constant} \tag{2}$$

Stratford gave the constant as 7.64×10^{-3}. Curle and Skan (ref. 12) suggested a value of 1.04×10^{-2} for the constant. The recent calculations by Liu and Sandborn indicate that a constant midway between the constant of Stratford and that of Curle and Skan may be the best. Thus, the separation criterion of figure 3 is a quick means of evaluating H or δ^* at separation, once θ and x_s are computed from equations (1) and (2).

An engineering criterion for the unrelaxed separation case may also be expected in terms of H and λ_θ. Included in figure 3 is a plot of unrelaxed turbulent boundary-layer separation profile parameters. Much of this

TABLE I.—*Separation Criteria*

Laminar separation				Turbulent separation[1]			
Curve		Plotted Points		Curve		Plotted Points	
λ_θ	H	λ_θ	H	λ_θ	H	λ_θ	H
.06	4.29			4.0	2.30		
.08	3.86	0.007	4.03	5.0	2.32	3.95	2.36
.10	3.62	0.0725	3.83	6.0	2.34	12.6	2.59
.12	3.51	0.0750	3.8	7.0	2.36	31.5	2.58
.14	3.40	0.08	3.80	8.0	2.375	32.5	2.50
.20	3.22	0.08	3.88	9.0	2.385	43.0	2.57
.30	3.12	0.09	3.79	10	2.40	58.5	2.56
.40	3.10	0.096	3.78	12	2.42	59	2.74
.50	3.08	0.092	3.75	15	2.45	83	2.66
.60	3.07	0.0875	3.73	20	2.485	170	2.83
.70	3.06	0.105	3.67	25	2.515	180	2.46
.80	3.05	0.108	3.60	30	2.54	192	2.84
.90	3.04	0.115	3.54	35	2.56	102	2.25
1.00	3.03	0.120	3.535	40	2.58	167	2.35
		0.117	3.51	50	2.61		
		0.167	3.36	60	2.635		
		0.178	3.26	70	2.66		
		0.360	3.10	80	2.675		
		0.545	3.05	90	2.69		
		0.725	3.05	100	2.71		
		0.9425	3.01	120	2.74		
				150	2.77		
				200	2.82		
				250	2.86		

[1] Approximate formula (straight line) $y = 2.12 + 0.306 \log_{10} x$.

data is now available in tabular form (ref. 13), so that parameters such as λ_θ can be determined in a uniform manner.

The curve through the turbulent data in figure 3 was drawn to agree in placement with the way in which the data points lie about the unrelaxed separation curve in figure 2. The coordinates of this unrelaxed separation curve are listed in table I.

The variation of H with λ_θ for the unrelaxed turbulent separation is opposite to that found for laminar flow. This trend of H increasing with λ_θ is not understood at present. Turbulent separation measurements are always subject to question due to secondary-flow effects. However, secondary flow acts to make θ larger than it would be in two-dimensional

flow. Corrections for secondary flow would be expected to reduce the range of λ_θ.

The "partially relaxed" curves shown in figure 3 will be discussed in the section on time-varying flows. Figure 4 demonstrates that the unrelaxed separation correlation also may be applied to axisymmetric boundary layers. The axisymmetric profile parameters are defined (ref. 14) as

Outside Curvature   Inside Curvature

$$
\left.
\begin{aligned}
\delta_{3-d}^* &= \frac{1}{R} \int_R^{R+\delta} \left(1 - \frac{U}{U_1}\right) r\, dr \qquad & \delta_{3-d}^* &= \frac{1}{R} \int_{R-\delta}^R \left(1 - \frac{U}{U_1}\right) r\, dr \\[2ex]
\theta_{3-d} &= \frac{1}{R} \int_R^{R+\delta} \frac{U}{U_1}\left(1 - \frac{U}{U_1}\right) r\, dr \qquad & \theta_{3-d} &= \frac{1}{R} \int_{R-\delta}^R \frac{U}{U_1}\left(1 - \frac{U}{U_1}\right) r\, dr
\end{aligned}
\right\} \quad (3)
$$

a.—*Relaxed.*
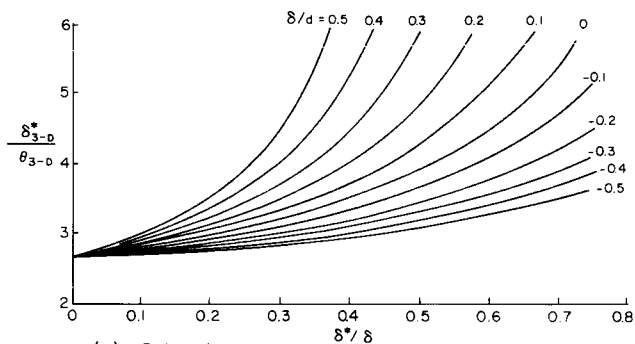
(a)   Relaxed

b.—*Unrelaxed.*
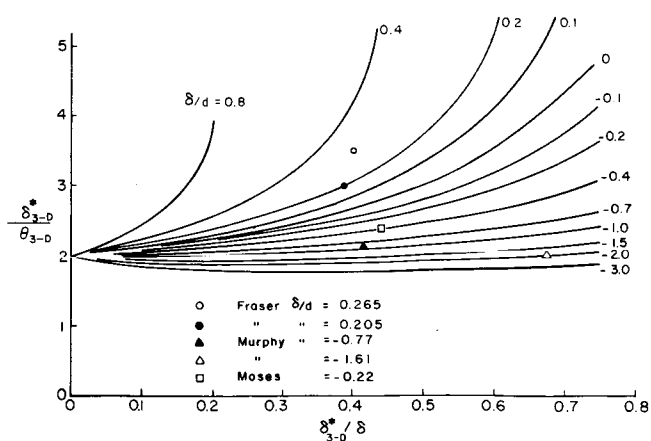
FIGURE 4.—*Axisymmetric boundary-layer separation correlation.*

where d is the diameter and R is the radius of the body at the point of separation. In figure 4, positive values of δ/d are for internal conduits, such as diffusers, and negative values of δ/d are for external curvature, such as cones or cylinders. The data of Murphy (ref. 15), shown in figure 4, are for ogive cylinders. For the ogives, the local curvature at the point of separation was employed to specify d. Correlations of H_{s-d} in terms of $\lambda_{\theta_{s-d}}$ have not been determined, since only limited measurements are available.

Although a criterion for turbulent separation is given in figure 3, it is of limited value at present. The difficulty encountered is that predictions of the boundary layer do not agree with the experimental data near separation. Figure 5 compares the calculations presented at the Stanford Conference on Computations of Turbulent Boundary Layers (Vol. I of ref. 13) for the Schubauer-Klebanoff flow. The measured separation point and separation criterion are also noted in figure 5. In no case do the predictions appear to approach the separation criterion. Prediction of the Schubauer-Spangenberg and Newman separation points, shown in figure 3, is somewhat better. Unfortunately, these results do not appear to belong with the other measured separation flows.

TIME-VARYING FLOW

An important problem in boundary-layer separation is that of a time-varying free-stream flow. This type of flow is characteristic of that encountered by blades in turbomachines. Analytical treatment of this type of flow is extremely limited. The relaxation or adjustment time
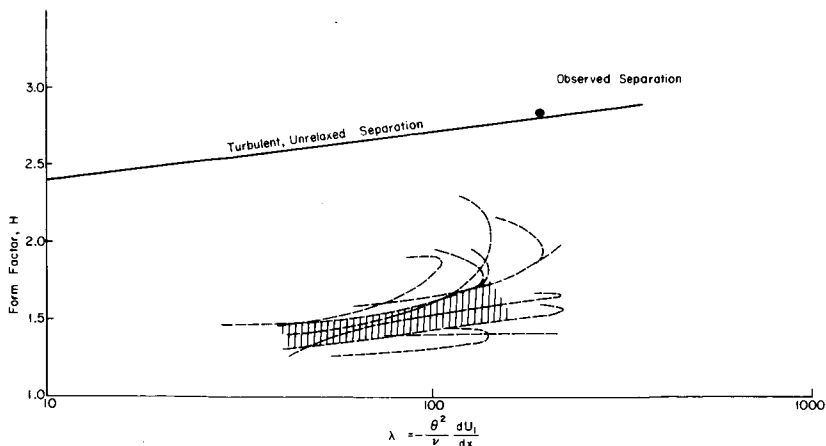
FIGURE 5.—*Comparison of turbulent separation criterion with boundary-layer predictions of the Schubauer-Klebanoff flow (ref. 13).*

concept for boundary-layer separation makes it possible to take time-varying flows into account. The degree to which a boundary layer can adjust to the boundary conditions will depend on the frequency and amplitude of the free-stream velocity. This section examines both turbulent and laminar flows with varying free-stream velocities. The specific point where $\tau_w(t) = 0$ is evaluated with respect to the separation criteria. This zero wall-shear point is only part of the general separation model; however, it does give some insight into conditions for these special flows.

Measurements in a turbulent boundary layer with a pulsing free-stream flow were made by the author and C. Feiler at the NASA Lewis Research Laboratory. The physical setup and heat transfer measurements for this flow were reported by Feiler (ref. 16). A siren was employed to produce a pulsing free-stream velocity, such as that shown in figure 6a. The free-stream velocity was of the order of 6 feet per second in order to produce an approximate pure velocity pulse. The hot-wire anemometers were employed to measure the boundary-layer velocity distribution along a flat plate. One wire was fixed in the free stream and the second wire was traversed through the layer. At each height, an oscilloscope trace was recorded to obtain the instantaneous variation in wire voltage. Typical hot-wire traces are shown in figure 6a. From these traces, it was possible to compute the boundary-layer velocity at each instance in the pulse. Complete boundary-layer velocity profiles are computed in this manner. The faired boundary-layer velocity distributions are shown in figure 6b.

The measurements, while subject to considerable scatter, give an accurate picture of a transient turbulent boundary layer approaching separation. Figure 6c is a plot of the velocity profile form factor H versus δ^*/δ for boundary-layer development from "reattachment" to "separation." The point D represents the instant of time when it appeared the flow very near the surface reversed direction or stopped. The point F indicates where the flow near the surface appeared to again reverse direction or stop. Thus, the "separation" and "reattachment" points are taken as points where $\tau_w(t) \simeq 0$. The faired velocity profiles at "separation" and "reattachment" were found to fall on the unrelaxed separation correlation curve. These results are very much in keeping with the concept that the boundary layer is unable to adjust to the separation condition. The relation

$$\frac{\theta}{\delta} = \frac{\delta^*}{\delta} - \frac{9}{5}\left(\frac{\delta^*}{\delta}\right)^2 \tag{4}$$

very closely fits the parameter development to the separation region. This relation comes from a simple velocity profile approximation (ref. 17)

$$\frac{U}{U_1} = 1 - \zeta(t)\left(1 - \frac{y}{\delta}\right)^m \tag{5}$$
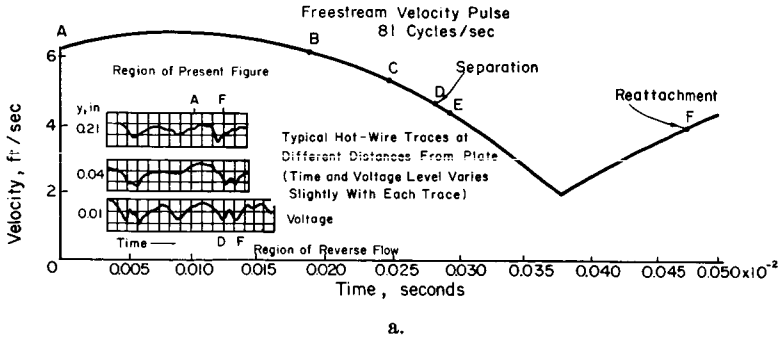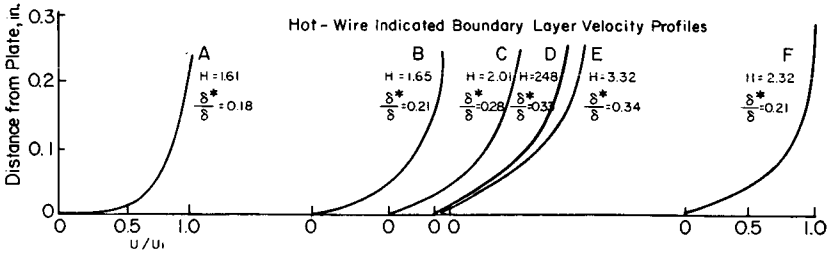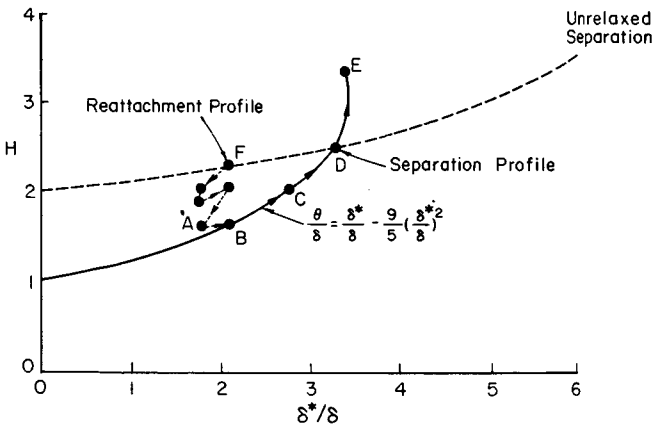
FIGURE 6.—*Turbulent boundary-layer development in a pulsing flow.*

where $\zeta(t)$ is a function that may be related to the wall-shear stress. At unrelaxed separation it is required that $\zeta(t) = 1$. For the constant $\frac{9}{5}$ in equation (4), it is required that $m = 2$. If m is a constant, this implies that the shape of the outer region of the velocity profile is similar. Similarity

of the outer region of the velocity profile is equivalent to the requirements for an unrelaxed separation.

Recently, Chou and Sandborn (ref. 18) have evaluated the properties of two special laminar flows with time-varying free-stream velocity. Exact solutions exist for transient Poiseuille flow (ref. 19) and a special suction-type boundary layer studied by Stuart (ref. 20). Figure 7 is a
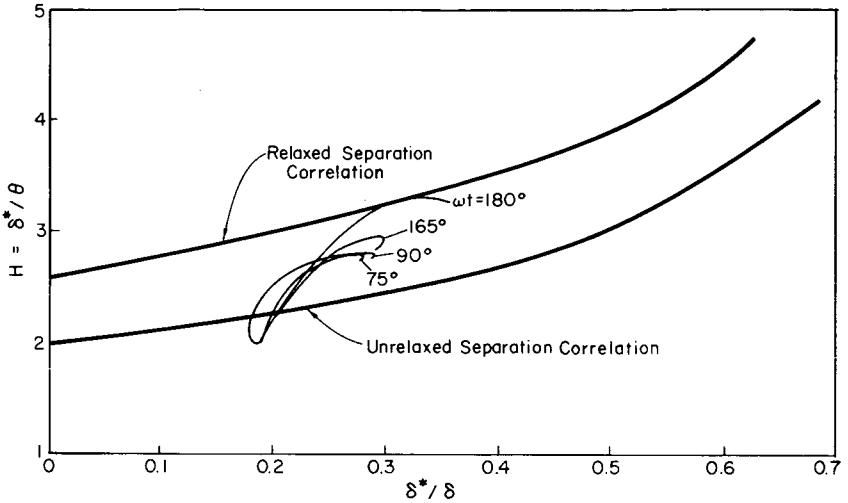
a.—*Stuart's suction boundary layer.*
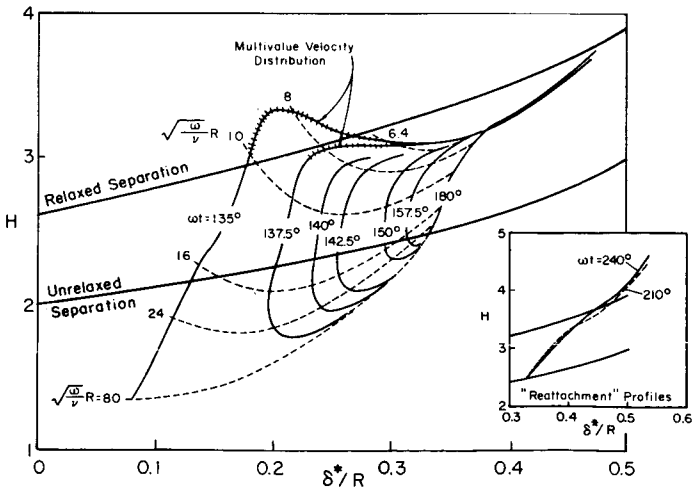
b.—*Transient Poiseuille flow.*

FIGURE 7.—*Variation of transient flow separation parameters.*

plot of the velocity profile form factor, H, versus δ^*/δ or δ^*/R for families of possible separation profiles. Figure 7a is for the flow studied by Stuart and figure 7b is for the transient Poiseuille flow. The parameter ωt is a frequency-time parameter for the free-stream flow. Variation along an ωt line represents a variation in amplitude of the free-stream velocity. These curves are for "separation" cases ($\tau_x(t) = 0$) in which no reversal of flow occurs. For boundary-layer consideration, it appears that velocity distributions with multivalued velocities should also be excluded. Some multivalued distributions are noted in figure 7b, and others have not been plotted. Curves for constant values of ωt are also included in figure 3 in terms of H versus λ_θ. Further analysis is still required to fully evaluate the limits indicated by the laminar time-varying flows. The curve for $\omega t = 135°$ in figure 7b was the lowest value for which a reasonable separation occurred. The limit, $\sqrt{\omega/\nu R} = 80$, was the largest value of the special Bessel function computed in the study. The range of possible separation velocity distributions far exceeds the unrelaxed and relaxed separation limits proposed for boundary-layer data. These theoretical solutions indicate that the assumption of a one-parameter family of profiles at the separation limits may be too restricted.

REATTACHMENT OF BOUNDARY LAYERS

Boundary-layer reattachment is found to be basically the reverse of separation. Sandborn and Liu (ref. 4) demonstrated that a number of reattachment profiles that have been reported belong to the relaxed separation family of profiles. No doubt a region should be postulated where the reattachment profile "relaxes" back to a boundary-layer profile. This relaxation in reverse has not been explored. The reattachment profile for the pulsing free-stream flow, shown in figure 6, was found to fall on the unrelaxed separation correlation curve. The insert in figure 7b shows parameters for reattaching velocity distributions in transient Poiseuille flow ranging over the complete region from a point which is greater than the relaxed separation value of H to the unrelaxed separation correlation curve.

An interesting evaluation of a set of laminar separation bubble and reattachment measurements reported by Gault (ref. 9) is shown in figure 8.[2] It is assumed that the separation bubble is a region detached from the main flow, so that only the flow above the bubble is considered. The "edge" of the bubble is taken where $U = 0$ for $y > 0$. The parameters for the velocity distributions above the bubble were computed and are

---

[2] This evaluation was made by Dr. A. T. Roper in May 1965 as part of a class assignment for the author.
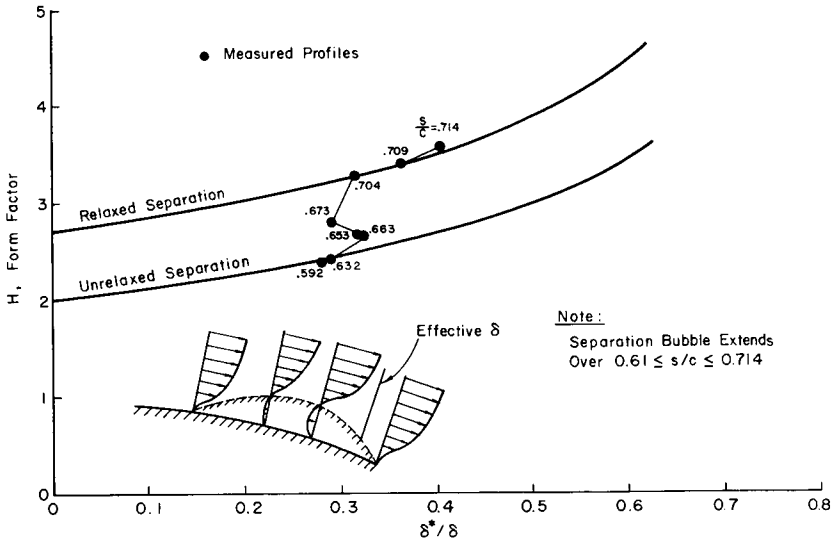
FIGURE 8.—*Profile form factor variation above a separation bubble region.*

plotted in figure 8. This particular flow was for a case where the laminar separation was of an unrelaxed type. As can be seen by the variation of the form factor, H, the velocity distribution relaxed to the relaxed separation curve. Once the profile reached the relaxed condition, it remained on the curve until reattachment occurred. This behavior of an experimental boundary layer is taken as a demonstration of the present model boundary-layer separation.

CONCLUSIONS

An improved model for boundary-layer separation has been proposed. This new model is an updating and improvement of the model proposed by Sandborn and Kline. The major new step is the introduction of a boundary-layer adjustment or relaxation time, rather than the steady and unsteady description employed in the earlier model. The relaxation time or distance concept allows the inclusion of transient boundary-layer separation in the model.

Engineering criteria for laminar and turbulent separation are presented. These criteria fit within the framework of the proposed model. However, the curves presented were determined from available experimental data and analytical solutions.

Several cases of time-dependent free-stream flows were evaluated. These flows demonstrate the concept of a relaxed model for boundary-layer

separation. The theoretical solutions for laminar time-varying free-stream flows appear to produce a more complex picture of separation than that of the proposed model.

Boundary-layer reattachment is found to follow the same model as separation. It is demonstrated that one set of laminar separation bubble data gives a graphic representation of the proposed model.

REFERENCES

1. PRANDTL, L., The Mechanics of Viscous Fluids. *Aerodynamic Theory, Vol. III, Div. G.*, W. F. Durand, ed., Durand Reprinting Committee (Pasadena, Calif.), 1943.
2. SANDBORN, V. A., AND S. J. KLINE, Flow Models in Boundary Layer Stall Inception. *Trans. ASME, J. Basic Eng.*, Ser. D, Vol. 83, 1961, p. 317.
3. LIU, C. Y., AND V. A. SANDBORN. Evaluation of the Separation Properties of Laminar Boundary Layers. *Aeron. Quart.*, Vol. XIX, 1968, p. 235.
4. SANDBORN, V. A., AHD C. Y. LIU, On Turbulent Boundary Layer Separation, *J. Fluid Mech.*, Vol. 23, 1968, p. 293.
5. MASKELL, E. C., *Flow Separation in Three Dimensions.* Report Aero. 2565, British RAE, 1955.
6. KLINE, S. J., Some New Conceptions of the Mechanism of Stall in the Turbulent Boundary Layer. *J. Aeron. Sci.*, Vol. 24, 1957, pp. 470–471. See also, On the Nature of Stall. *Trans. ASME, J. Basic Eng.*, Ser. D., Vol. 81, 1959, p. 305.
7. LIU, C. Y., *Boundary Layer Separation.* Ph.D. dissertation, Colorado State U., 1967.
8. COLES, D. E., The Law of the Wake in the Turbulent Boundary Layer. *J. Fluid Mech.*, Part 2, Vol. 1, 1956, p. 191.
9. GAULT, D. E., *An Experimental Investigation of Regions of Separated Laminar Flow.* NACA TN 3505, 1955.
10. THWAITES, B., Approximate Calculation of the Laminar Boundary Layer. *Aeron. Quart.*, Vol. I, 1949, p. 245.
11. STRATFORD, B. S., Flow in the Laminar Boundary Layer Near Separation. ARC R&M 3002, 1957.
12. CURLE, N., AND S. W. SKAN, Approximate Methods for Predicting Separation Properties of Laminar Boundary Layers. *Aeron. Quart.*, Vol. VIII, 1957, p. 257.
13. COLES, D. E., AND E. A. HIRST, *Proc., Computation of Turbulent Boundary Layers-1968. AFOSR–IFP–Stanford Conference,* Vol. II, Compiled Data, Thermoscience Div., Dept. Mech. Eng., Stanford U., 1969.
14. ROBERTSON, J. M., AND J. W. HALL, Effects of Adverse Pressure Gradients on Turbulent Boundary Layers in Axisymmetric Conduits. *J. Appl. Mech.*, Vol. 24; *Trans. ASME,* Vol. 79, 1957.
15. MURPHY, J. S., *The Separation of Axially Symmetric Turbulent Boundary Layers— Part I.* Douglas Aircraft Co. Report ES 17513, 1955.
16. FEILER, C. E., AND E. B. YEAGER, Effect of Large-Amplitude Oscillations on Heat Transfer. NASA TR–R–142, 1962.
17. SANDBORN, V. A., An Equation for the Mean Velocity Distribution of Boundary Layers. NASA Memo 2–5–59E, 1959.
18. CHOU, F. K., AND V. A. SANDBORN, *Flow Separation in Time Varying Flow.* Colorado State U. Eng. Res. Center Report CER69–70FKC–VAS23, 1969.

19. UCHIDA, S., The Pulsating Viscous Flow Superposed on the Steady Laminar Motion of Incompressible Fluid in a Circular Pipe. *ZAMP*, Vol. VII, 1956, p. 403.

20. STUART, J. T., A Solution of the Navier-Stokes and Energy Equations Illustrating the Response of Skin Friction and Temperature of an Infinite Plate Therometer to Fluctuations in the Stream Velocity. *Proc. Roy. Soc.* (*London*), Ser. A, Vol. 231, 1955, p. 116.

DISCUSSION

G. SOVRAN (General Motors Research Laboratory): In spite of the universal recognition of the vital role that boundary-layer separation plays in the operation of high-performance turbomachinery, this discussor is amazed at how few investigators have the fortitude to tackle this very challenging problem. The author is to be complimented for his continuing efforts to develop understanding of this exceedingly complex fluid-mechanical phenomenon.

In this latest in a series of papers, the author introduces the concept of a boundary-layer adjustment or relaxation time into his separation model, as well as the new general definition of boundary-layer separation as "the removal of viscous restraints at the wall." I find these to be very interesting ideas, but since this is a turbomachinery symposium I would like to direct my comments in another direction. The companion papers in this session, particularly the one by Peter Bradshaw, point out the great differences that exist between the extremely complex boundary layers found in turbomachines and the much simpler two-dimensional ones that have been studied in research facilities. In addition, the turbomachine boundary layers are primarily *turbulent* in nature. Furthermore, the turbomachinery designer's game with separation is one of brinksmanship. He cannot make competitive fluid-mechanical designs if he avoids it by too great a margin; nor can he afford the consequences of inadvertently triggering it while attempting to achieve maximum performance. However, he has little interest in the details of separation once it occurs— he just wants to avoid it.

In view of these facts, and recognizing the author's own statement that "the criterion for turbulent separation given in figure 3 is at present of limited value," how would he interpret the significance of his separation model and correlations to the particular problem of turbomachinery design? How would he decide, in an a priori manner, whether a particular turbulent boundary layer would be subject to the relaxed or unrelaxed separation criterion?

Finally, the origin of the unrelaxed curves of figure 4b is not clear. Was the separation velocity profile corresponding to the unrelaxed *plane* boundary layers of figure 2 formally applied to axisymmetric flow geometries? If so, what about the effects of transverse wall curvature on this velocity profile?

J. M. ROBERTSON (University of Illinois) : The author's contribution to our understanding of complex separation occurrences is a subject in need of considerable elucidation. The concept of the boundary layer at separation being inertia controlled and thus the separation velocity profile being essentially the same whether the layer from which it developed was laminar or turbulent seems well established. That the laminar layer developing towards separation is less likely to encompass appreciable lengths of adjustment seems rational; in fact, this writer doubts that the laminar layer will involve appreciable "unrelaxed separation." Interpretation of laminar velocity-profile measurements near separation is fraught with uncertainty due to the scarcity of measurement points in the very thin layers usually encountered, so that verification of laminar occurrences is difficult.

For the past half-dozen years, the writer has been working on the problem of calculating the boundary-layer growth on turbomachinery blading. Separation-flow considerations must be considered in the overall analysis of such flows and, in general, I have found that our understanding of these is hardly sufficient to permit adequate calculation. As the flow proceeds along the blade surface, the first question which appears is that of transition versus separation of the laminar layer which must perforce precede the more common turbulent layer, if only for a short distance. The question is one of the laminar separation occurrence and where it is likely to occur, as well as whether the subsequent flow will reattach as the "short bubble" or stay separated as "stall." The contributions of I. Tani (ref. D–1) and others (such as A. Roshko and J. C. Lau, ref. D–2) to these questions are most useful but still leave something to be desired for one attempting boundary-layer predictions. Assuming that a short bubble occurs, the next question is how the reattached turbulent layer, with its excess turbulence, relaxes back to the more-normal turbulent layer otherwise characteristic of that locale on the blade surface. Should the laminar layer simply have transitioned, rather than separated, the initial condition for the turbulent layer is merely one of equivalence of the momentum thickness at the transition "point." As the layer further develops along the blade, the possibility of turbulent separation raises its ugly head. Ultimately, no matter how the layer reaches the end of the blade (i.e., as separated or not), the final separated flow problem is one of analyzing the development of the turbulent wake, as has been noted elsewhere (ref. D–3).

The writer finds some difficulty in accepting the phenomenon of appreciable adjustment between the two separation curves for the laminar layer near separation. Such an occurrence seems to be predicated upon just two laminar layer measurements having H values slightly less than 2.5. In view of the fact that the surface pressure distribution near and ahead of the separation region for these flows was not changing rapidly, the

approach to separation can hardly be classed as rapid. It seems hard to conceive of the flow development in these cases being such that the shape factor could fall below the zero-pressure-gradient (flat-plate) value of 2.596. As may be seen in figure D–1, the laminar flat-plate occurrence appears slightly above the author's "unrelaxed separation" curve. This writer suggests that boundary-layer development from the flat-plate condition towards separation should appear simply—as without reversal in trend—on such a plot as this; thus the suggested trends are indicated in the figure for the laminar and turbulent cases from the established flat-plate locales. Also shown in this figure is the laminar separation "point" ($H = 3.889$, $\delta^*/\delta = 0.500$, and $\lambda_\theta = -0.0992$) given by the laminar velocity-profile formulation of B. E. Launder (ref. D–4) which, when used with the Karman momentum-integral equation, we have found much superior to other rather quick methods[D-1] of laminar-layer calculation. Separation locale prediction by this analysis has been found to agree with about 12 observations recorded in the literature at about 95 percent (with a scatter of about 5 percent) of the distance from the locale of minimum pressure on the blade surface.

If the difficult question of whether the separated laminar layer after transition as a free shear layer will reattach to form the short bubble is answered affirmatively, the analyst is then faced with the problem of how
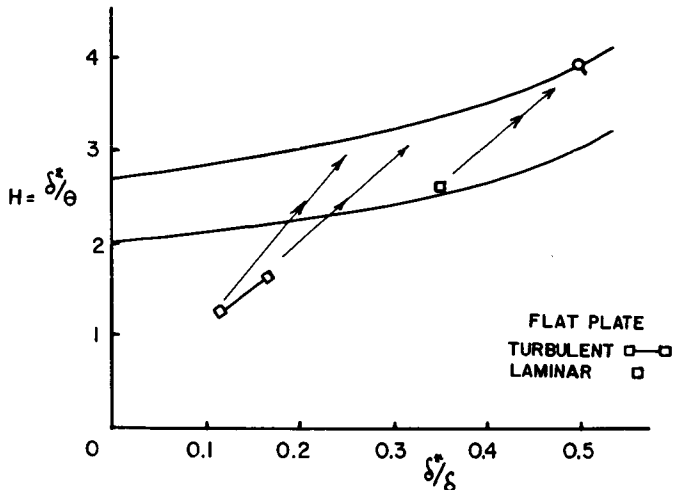
FIGURE D–1.—*Possible development of boundary layer from flat-plate condition toward separation.*

[D-1] Thus the quadrature method of Waltz, Tani, and Thwaites (1941, 1949).

the turbulent layer redevelops from its disturbed condition back into a more proper layer. After noting this problem the author gives it short shrift, presumably deferring it to later analysis. The writer is currently in the throes of developing the analysis for this occurrence. Measurements of redeveloping flow on a flat plate reported by T. J. Mueller and J. M. Robertson (ref. D–5) are quite suggestive in this regard. At reattachment, the skin friction was approximately zero and H had a value of the order of 4.0. Subsequent redevelopment of the turbulent layer towards the normal flat-plate condition extended over a distance of about 30 times the height of the bubble. However, initial changes were rapid and in 10 heights the friction factor was within 25 percent of the flat-plate value and H was less than 10-percent larger than the corresponding flat-plate value. The early decay in H from the high reattachment value was roughly as the logarithm of the distance from reattachment. From this decay rate and appropriate formulations for C_f in terms of the momentum-thickness Reynolds number and H, it seems possible to predict the increase in C_f for redeveloping flows. Then boundary-layer development prediction via the momentum integral equation follows simply. Verification studies of this approach are underway.

SANDBORN (author): The author would like to thank the reviewers for their comments. The reviewers point out the extreme difficulty that still exists in an adequate engineering prediction of boundary-layer separation. As noted by the reviewers, the present separation model is still limited in its engineering application. The present discussion is intended mainly as a starting point from which engineering analysis can proceed. The model presented suggests a "one parameter" pressure-gradient type of engineering criterion for both laminar and turbulent separation. Unfortunately, methods of calculating turbulent boundary layers up to separation are not sufficiently accurate to make the turbulent separation criterion usable. Improvements in boundary-layer calculation techniques are necessary in order that the turbulent separation criterion (fig. 3) can be of engineering value.

In answer to Dr. Sovran's question about a turbulent boundary layer being subject to the relaxed or unrelaxed separation criterion, it appears that the turbulent boundary layer always separates along the unrelaxed curve. For turbulent separation the relaxed separation criterion may not be of major engineering importance, since the unwanted effects of separation are present at the unrelaxed separation point.

The axisymmetric separation correlation curves shown in figure 4 were obtained by applying the definitions of equation (3) to the empirical velocity profile of Sandborn (ref. 17). The agreement of experimental measurements with the curves of figure 4b suggests that the transverse wall curvature does not produce a major effect on the integral boundary-layer parameter.

Dr. Robertson has pointed out the difficulties involved if laminar separation bubbles are encountered. The present model for separation is unable to produce information on whether the laminar flow will reattach. It is pointed out by Dr. Robertson that a reattaching boundary layer will, so to speak, "unadjust" to the turbulent boundary layer again. This suggests that the words used in the present model may still be subject to change.

For most laminar flows, one may suspect that separation occurs along the relaxed correlation curve. However, the two cases shown in figure 2 are definitely exceptions to the rule. For these two cases, the free-stream turbulence level had been increased. The point raised by Dr. Robertson that unrelaxed separation is not necessarily related to a rapid approach to separation may well be valid. It would appear that free-stream turbulence level as well as pressure gradient can be a factor for laminar separation. Certainly, for the time-dependent free-stream flows, the concept of a rapid change in pressure gradient can produce the unrelaxed types of laminar separation.

A recent look at turbulent separation profiles suggests that the major relaxation process in the region from unrelaxed to relaxed separation takes place near the wall. The outer profile is nearly wakelike at the point of unrelaxed separation, and the inner flow adjusts to the zero wall-shear stress condition over the transition region. This relaxation process appears to be just the reverse of that observed for time-dependent free-stream flows.

REFERENCES

D–1. TANI, ITIRO, Low Speed Flows Involving Bubble Separations. *Progress in Aeron. Sci.*, Vol. 5, 1964, pp. 70–103.

D–2. ROSHKO, A., AND J. C. LAU, Some Observations on Transition and Reattachment of a Free Shear Layer in Incompressible Flow. *Proc. 1965 Heat Trans. and Fluid Mech. Inst.*, pp. 157–167.

D–3. ROBERTSON, J. M., Turbulent Wake of a Body of Revolution. *Trans. ASME, J. Basic Eng.*, Vol. 90D, 1968, pp. 637–638.

D–4. LAUNDER, B. E., An Improved Pohlhausen-Type Method of Calculating the Two-Dimensional Laminar Boundary Layer in a Pressure Gradient. *Trans. ASME, J. Heat Trans.*, Vol. 86C, 1964, pp. 360–364.

D–5. MUELLER, T. J., AND J. M. ROBERTSON, A Study of the Mean Motion and Turbulence Downstream of a Roughness Element. *Dev. in Theor. and Appl. Mech.*, Vol. I, 1963, pp. 326–340.

PRECEDING PAGE BLANK NOT FILMED

Boundary Layers in Centrifugal Compressors

ROBERT C. DEAN, JR.

Creare Incorporated
Hanover, New Hampshire

The objective of this paper is to demonstrate the utility of boundary-layer theory in the design of centrifugal compressors. Boundary-layer development in the diffuser entry region is shown to be important to stage efficiency. The result of an earnest attempt to analyze this boundary layer with the best tools available is displayed. Acceptable prediction accuracy was not achieved. The inaccuracy of boundary-layer analysis in this case would result in stage efficiency prediction as much as four points low. Fluid dynamic reasons for analysis failure are discussed with support from flow data. Empirical correlations used today to circumnavigate the weakness of the theory are illustrated.

In centrifugal compressors, there are two key boundary-layer situations which powerfully influence stage efficiency. They are diffusion in the impeller of the inlet relative velocity and diffusion (pressure recovery) in the diffuser (stator).

Figures 1a and 1b illustrate the influence on stage efficiency of these two diffusion processes. The impeller diffusion is measured by the ratio DR of the inlet relative velocity over the relative velocity at the separation point in the impeller. After this point, no further relative diffusion is possible.

The diffuser (stator) diffusion is measured by its pressure recovery coefficient C_p, which is the static pressure rise from impeller tip to the stage outlet plenum divided by the difference between stagnation and static pressure at impeller tip.

Figures 1a and 1b have been constructed from our detailed centrifugal analysis methods, which agree well with the actual test points spotted on the curves. One can see that, in order to reach the ultimate performance discussed below, improvement in DR and C_p will be about equally important and for both pressure ratio 3 and 10 stages.

Impeller diffusion involves complex flow situations that are very inadequately understood today. These include boundary-layer separation

and free-shear flow under the influence of Coriolis forces, separated flow in a rotating coordinate system, transonic flow over the blades and tip leakage, and secondary flow. Johnston (ref. 1) has surveyed the slight knowledge of the Coriolis effects.

Today so little is known fundamentally about most of these impeller flow situations that little can be said positively about boundary-layer analysis in the impeller. We choose, therefore, to discuss here the region between the impeller tip and diffuser throat. Boundary-layer growth there has a direct and serious influence on diffuser recovery.

Before proceeding to the fluid dynamics, it is valuable to sketch the context of the problem, in order to put the specific matter in proper focus.
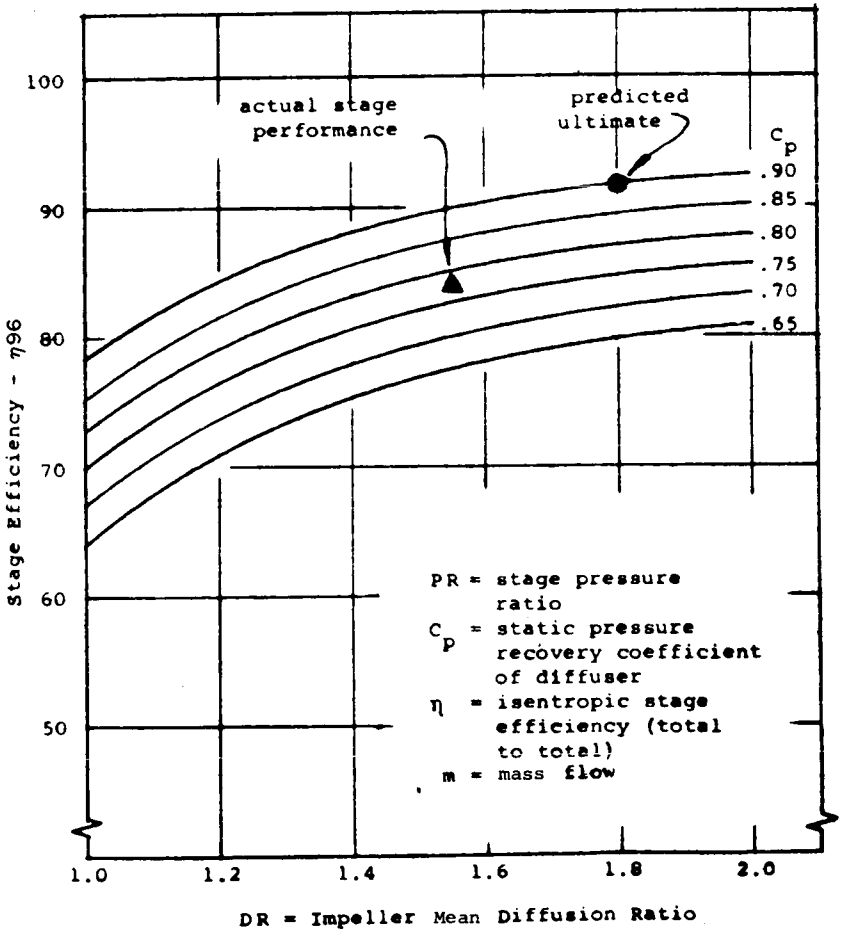
FIGURE 1a.—*Effect of impeller mean diffusion ratio on stage efficiency, for P.R.=3, m=3 lb/sec.*

CONTEXT

For years, the centrifugal compressor has been out of favor in many circles for use in high-performance gas turbines; but, within the past 10 years, the military small gas turbine has advanced so much in specific power that its dropping flow rate per unit power again favors the centrifugal compressor. Today, axicentrifugal machines with two to six axial stages ahead of a pressure ratio 3 to 6 centrifugal stage are common. Within 5 years, new engine designs may incorporate only a single centrifugal stage operating at pressure ratio 10 to 15 or with one or two axial
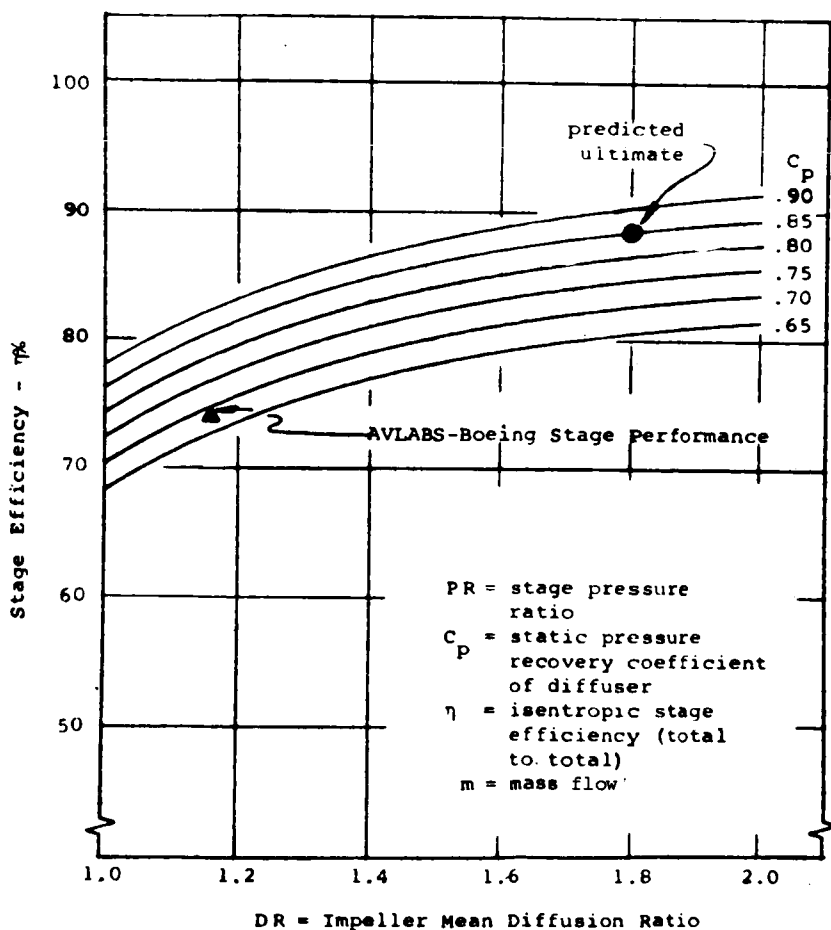
FIGURE 1b.—*Effect of impeller mean diffusion ratio on stage efficiency, for P.R. = 10, m = 2 lb/sec.*

precompression stages giving overall compressor pressure ratios of $20X$ to $30X$.

By 1980, small gas turbine engines should be demonstrated with centrifugal compressors of 12 to 15 pressure ratio and 80- to 85-percent total-to-static stage efficiency. A forecast comparing 1970 and 1980 engines is shown below.

Expected Performance of Demonstration Engines

	1970	1980
pr	15–20	20–30
pr_{cent}	3–6	12–15
η_{cent}	80–83	80–85
TIT	2000–2200	2500–3000
sfc	0.5	0.35
swt	0.3	0.2
SHP	200–250	250–300

where   pr = pressure ratio
    TIT = turbine inlet temperature, °F
    η_{cent} = centrifugal compressor total-to-static adiabatic efficiency
    sfc = engine specific fuel consumption, lbm/hp–hr
    swt = engine specific weight, lbm/hp
    SHP = specific power = engine hp/air-flow rate, hp/lbm/sec

These prospects have focused considerable technical attention on the small centrifugal compressor. Of prime interest has been the helicopter engine. The U.S. Army Aviation Materiel Laboratories (AVLABS) lately has been the principal sponsor of research and advanced concept demonstration.

Recently, Dean, Wright, and Runstadler (ref. 2) have critically reviewed contemporary fluid design methods and sought means to reach ultimate performance. This paper is based on that work.

IMPORTANCE OF THE DIFFUSER

Figure 2 presents the state of the art for small centrifugal compressors and shows our forecast of ultimate performance (ref. 3). The forecast is not a guess, but is based on detailed calculations and performance attained with other related flow devices.

Figures 1a and 1b show the importance of diffuser performance in reaching the ultimate performance of machinery. Figure 3 displays the
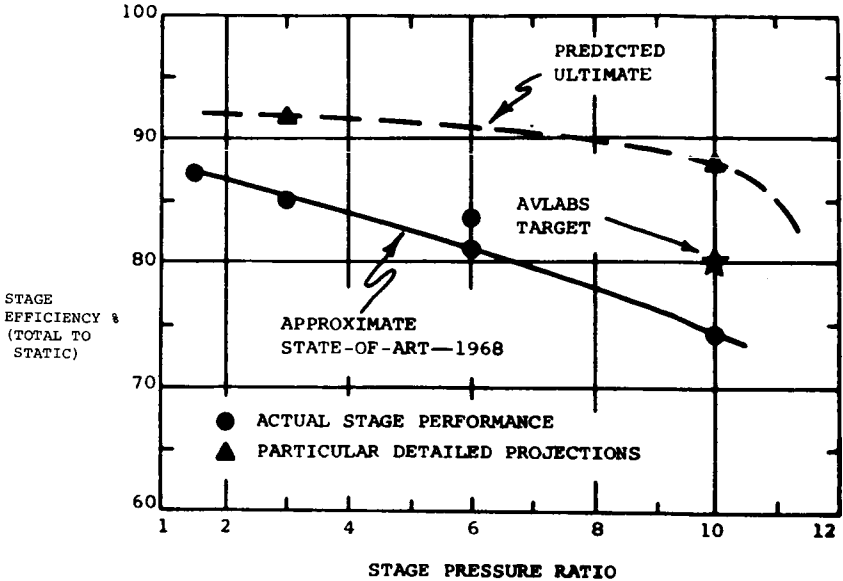
FIGURE 2.—*State-of-art centrifugal compressor performance and predicted ultimate (from ref. 3).*

state of the art of diffuser performance and our forecast of ultimate recovery, again based on detailed calculations and related flow data.

A study of this set of graphs proves that diffuser recovery must advance quite a lot before the ultimate centrifugal stage will be realized. A 1-point gain in C_p (e.g., 0.75 to 0.76) is worth about $\frac{1}{3}$-point gain in compressor efficiency (for pressure ratio = 10). In turn, a $\frac{1}{3}$-point gain in compressor efficiency gives about a 1-percent reduction in fuel consumption. So, even small gains in diffuser performance lead to attractive gains in engine performance.

The sizable gains needed in the diffuser must be won from a difficult flow device with very shallow passages (aspect ratio $\frac{1}{10}$ to $\frac{1}{20}$), large viscous effects, shocks, and unsteady and three-dimensional transonic flow.

DIFFUSER FLOW MODEL

Before we consider the entry boundary layer, it is necessary to appreciate the rudiments of diffuser flow and the model we shall use to predict it.

An analytical model is essential in this complex flow situation before any real understanding can be had. No significant models existed in the

VANED DIFFUSER PERFORMANCE
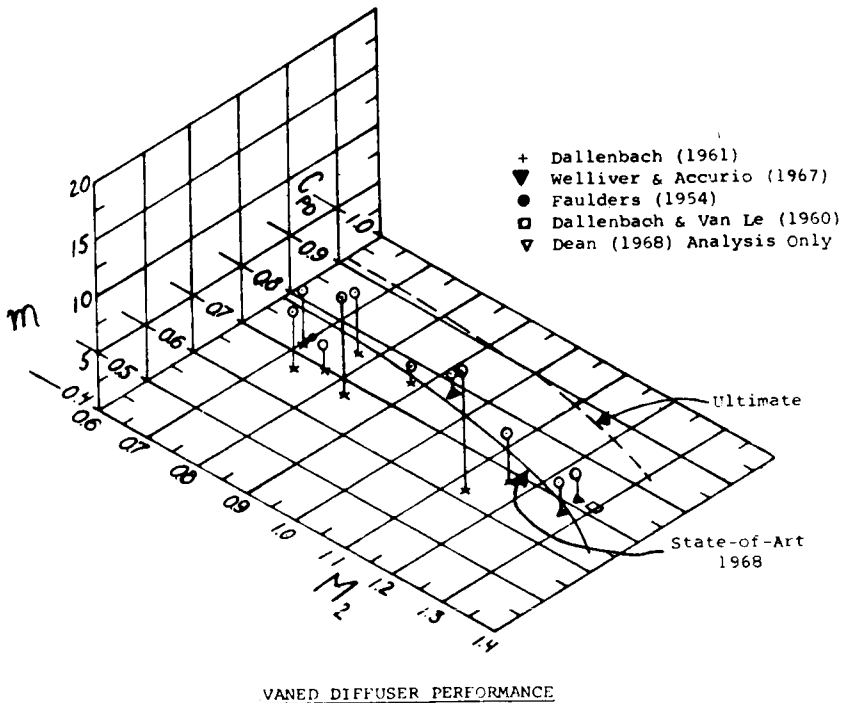
FIGURE 3.—*State-of-art centrifugal compressor diffuser performance and projected ultimate (from ref. 3).*

literature before Welliver and Acurio (ref. 4) published the model we use here. They also published the first extensive set of high-quality data on the centrifugal diffuser; this alone was a major contribution. Dean, Wrignt and Runstadler (ref. 2) used these data in their analysis.

The Welliver and Acurio diffuser data have a number of striking features. First, there is a shock at channel diffuser entry, as many schlieren pictures like figure 4 and wall pressure data revealed. This shock appeared when the impeller tip discharge Mach number rose just above 1.0. Secondly, there was always a remarkable pattern in the isobaric plots made from many taps on both walls.

Note in figure 5 that the isobarics roughly parallel the swirling streamlines in the vaneless and semivaneless spaces up to just ahead of the entry shock. This means that little supersonic diffusion occurred.[1] Indeed, only 10 percent of the diffuser's pressure recovery was gained up to the shock.

---

[1] With a much larger vane leading-edge radius ratio (to impeller tip radius), supersonic diffusion will occur to subsonic values and without an entry shock.
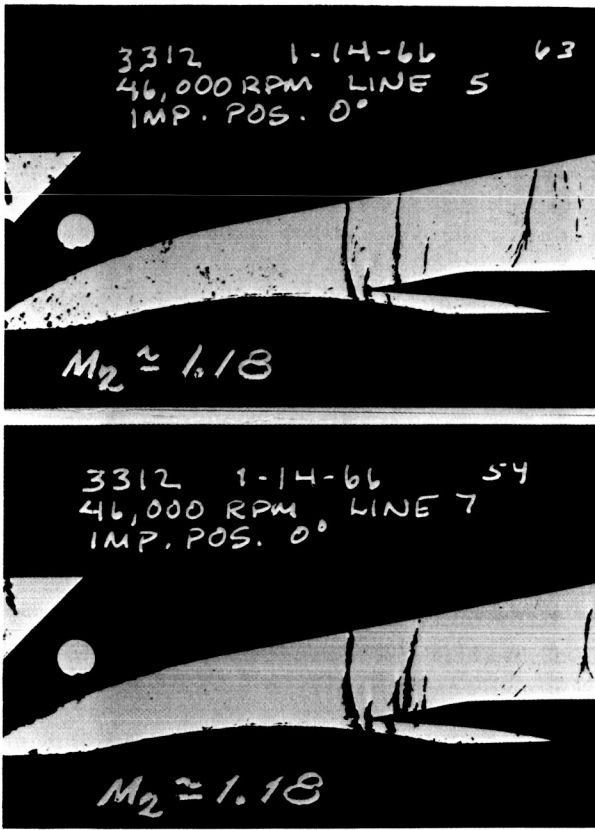
FIGURE 4.—*Schlieren photographs of high-Mach-number centrifugal compressor diffuser flow (from ref. 4).*
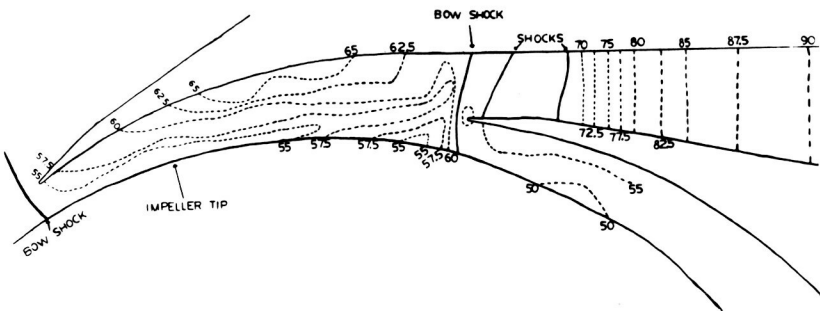
FIGURE 5.—*Isobarics measured in high-Mach-number flow of centrifugal compressor vane-island diffuser (numbers on contours are pressures, psi) (from ref. 4).*

Just ahead of the shock there is a zone of very rapid adjustment. Here the flow Mach number decreased or increased suddenly to produce a normal-like shock of proper strength to match the subsonic throat conditions downstream. This zone of rapid adjustment was accompanied by sharp streamline curvature near the vane leading edges. The shock typically gave 30 percent of the overall pressure recovery.

Behind the shock, the flow pattern becomes one-dimensional immediately. Note, in figure 5, that the isobarics are perpendicular to the passage centerline even within a fraction of a throat width downstream of the channel entry. The flow pattern changes in less than a throat width from a swirling flow to a straight flow; this seems remarkable to us. This characteristic is not a supersonic phenomenon; subsonic relaxation solutions produce the same pattern, without the shock, of course. Apparently, this flow pattern is a dominant characteristic of the peculiar geometry of such compressor diffusers.

In the diverging channel diffuser, the flow is so one-dimensional that one immediately thinks of modeling this region as a simple isolated straight diffuser. This is what was done in the model.

The channel diffuser gave typically 55 percent of the overall pressure recovery. At the end of the channel, the flow was dumped into a collector in Welliver and Acurio's case. No pressure recovery occurred because of the large dump area ratio.

This diffuser flow was modeled for analysis as shown in figure 6. First, there is a region of mixing of the impeller's (r,θ) plane distorted discharge flow. This region was assumed to be of zero radial extent, in accord with the theoretical results in Johnston and Dean (ref. 5). The mixed-out flow properties are computed by a compressible version of the Dean and Senoo (ref. 6) theory.[2]

No meridional mixing is assumed. To date, backflow into the impeller, which has been observed in the data, has not been specifically incorporated into the diffuser model.

After the thin (r,θ) plane mixing region, the flow is assumed to proceed with constant stagnation temperature and pressure on the passage centerstream surface right through the shock (with a shock Δp_o correction) to the diffuser throat. The centerline flow Mach number is assumed to be constant up to just ahead of the shock when it suddenly changes to give a shock strength that satisfies throat conditions. The shock is assumed to be thin and "normal".[3]

Flow centerline properties after the shock are taken equal to throat centerline properties unless the throat is of finite length. In that case, the

---

[2] Found in reference 2, Appendix II.

[3] I.e., one-dimensional, normal shock theory.
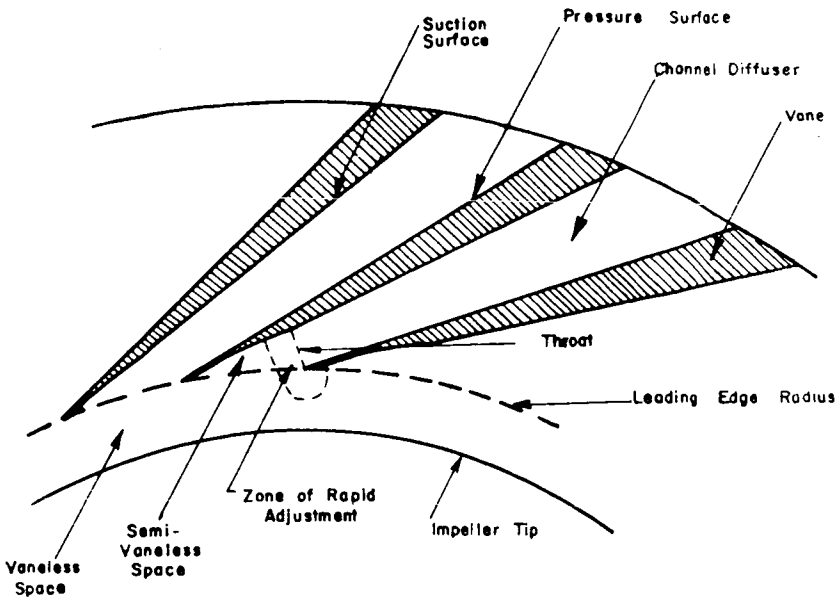
FIGURE 6.—*Principal flow regions in high-Mach-number vane-island diffuser flow (from ref. 2).*

one-dimensional duct flow relations with wall friction (e.g., Shapiro, ref. 7) are used to calculate the centerline Mach number and other flow properties at the entrance to the diverging channel.

As we shall show shortly, boundary-layer blockage in the diffuser throat is a key variable. In the model, blockage was to be predicted by two-dimensional, compressible, turbulent boundary-layer theory starting at zero thickness at the impeller tip.[4] This paper is concerned primarily with the success of this last feature of the model. Before we review that, we must appreciate how sensitive performance predictions and design optimization are to the precision of the boundary-layer theory results. According to the flow model, the only element affected is the channel diffuser.[5]

CHANNEL DIFFUSER CHARACTERISTICS

Once the flow model was put together, Welliver and Acurio proceeded to test it. Channel diffuser data was produced by Runstadler (ref. 14) on

---

[4] See reference 2 for further details and discussion of the assumptions.

[5] Boundary-layer growth has a nil continuity effect in the semibounded space ahead of the channel entry.

simple laboratory diffusers which correlated very well with data from the Boeing compressors as shown in figure 7. This early data showed that throat blockage B_4 was the most powerful variable governing maximum attainable C_p (with complete flexibility in choosing channel diffuser L/W and 2θ). Throat Mach number was a weak variable until well into the supercritical range (throat centerline Mach number $=1.0$), when the channel shock[6] separated the diverging passage.

The success of the model for the channel diffusers caused AVLABS to commission us to produce a full range of transonic and subsonic data for simple, flat symmetrical diffusing passages. This work is reported by Runstadler (ref. 8). With 2300 tests, he covered a wide range of Mach number, Reynolds number, throat boundary-layer blockage, throat aspect ratio, length-over-throat-width ratio and divergence angle. Typical maps are shown in figures 8a, 8b, and 8c. The agreement of the laboratory and compressor diffuser data is shown in figures 9a, 9b, and 9c. In general, the compressor diffuser performed a little better than the laboratory diffuser. We consider the agreement to be good despite the large uncertainty band of the compressor data.
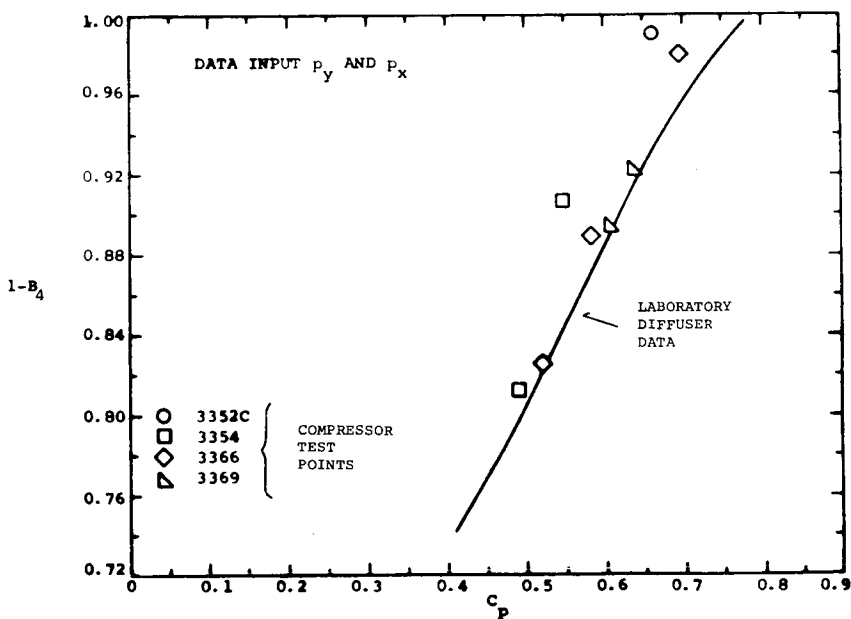
FIGURE 7.—Comparison of pressure recovery for compressor channel with laboratory diffuser data (from ref. 2).

[6] A second shock which appears as the back pressure is lowered. The entry shock remained fixed in position over the full compressor flow range.
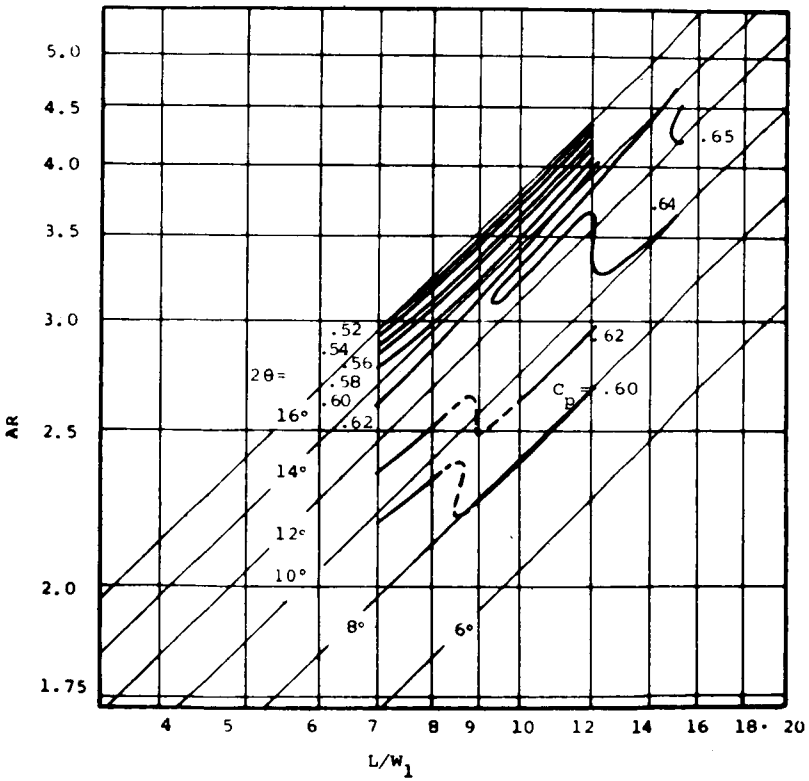
FIGURE 8a.—*Straight-channel diffuser performance (from ref. 8).*
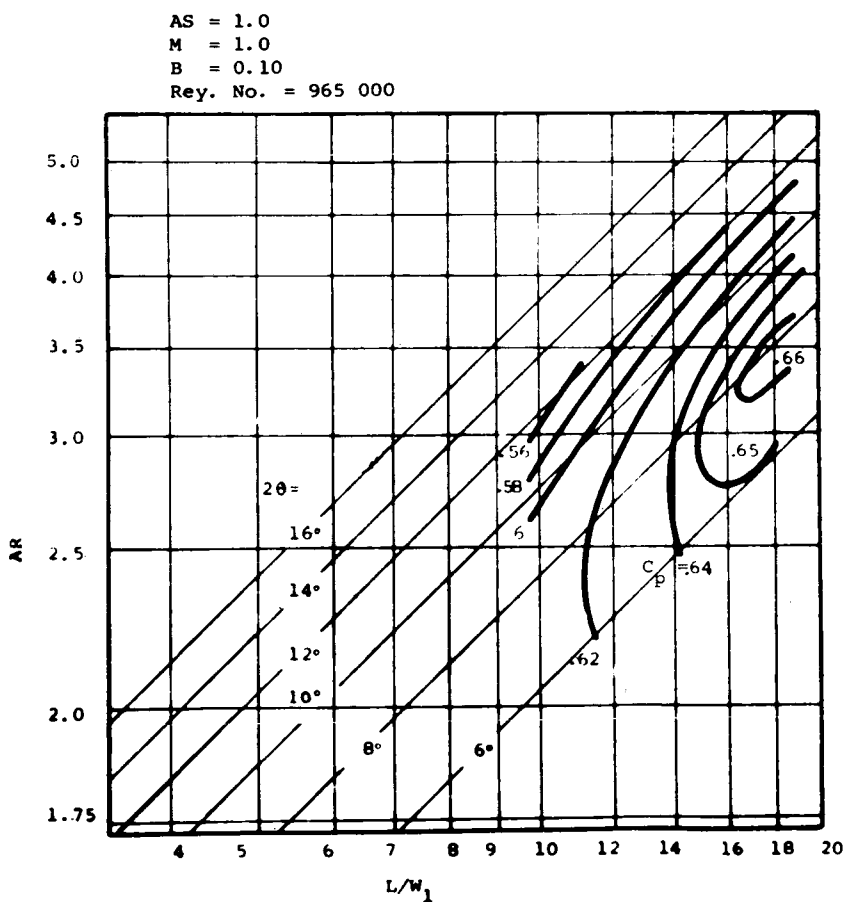
FIGURE 8b.—*Straight-channel diffuser performance (from ref. 8).*

AS = 5.0
M = 1.0
B = 0.10
Rey. No. = 740 000
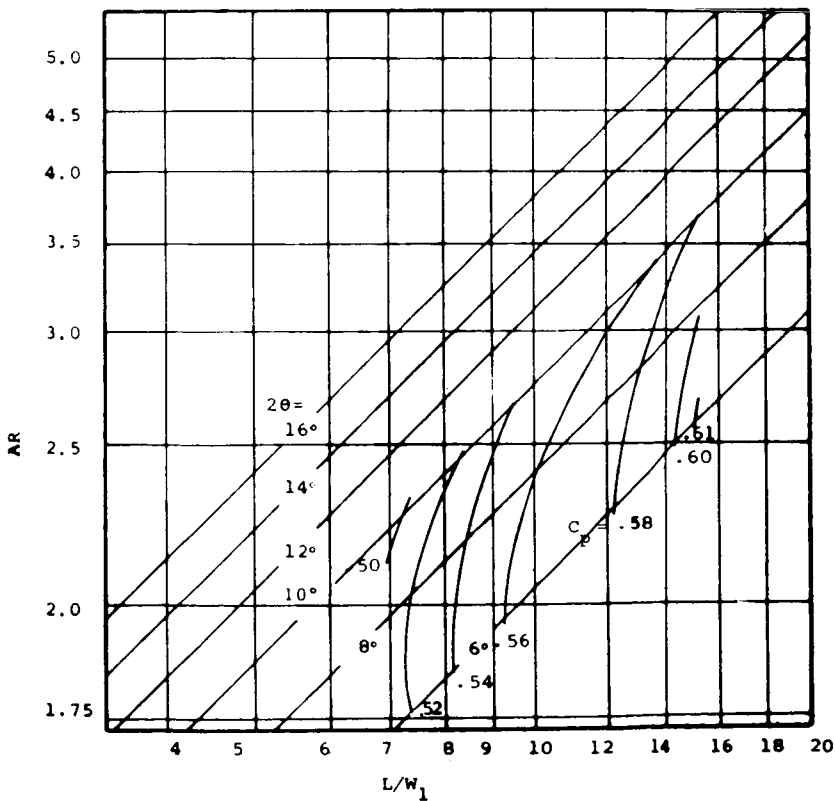
FIGURE 8c.—*Straight-channel diffuser performance (from ref. 8).*
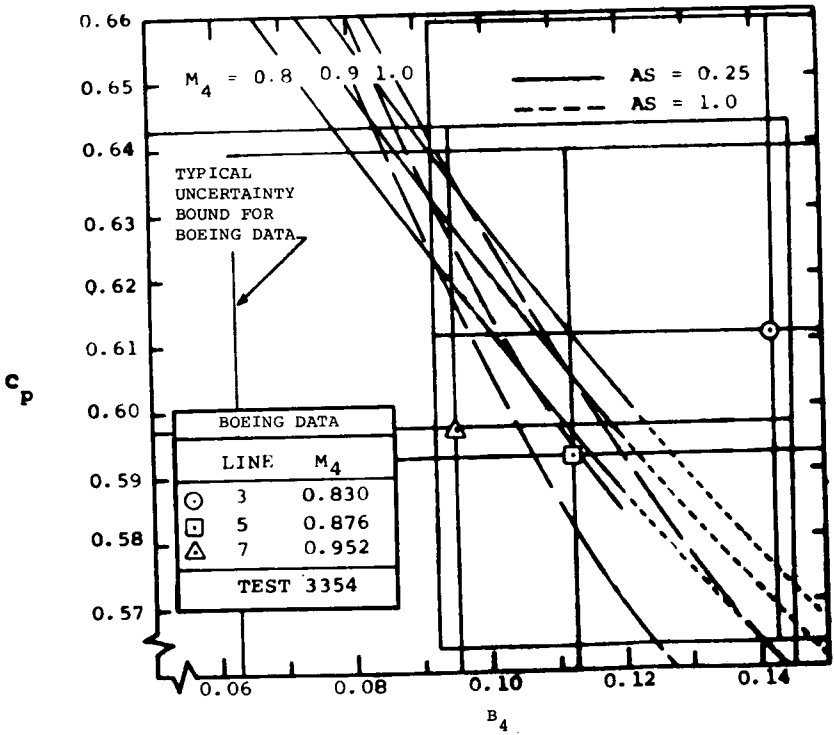
FIGURE 9a.—*Comparison between Boeing-AVLABS channel diffuser data from compressors with Creare-AVLABS straight-channel diffuser data. Pressure recovery* C_p *versus throat blockage* B_4 *and Mach number* M_4 *(from ref. 2).*
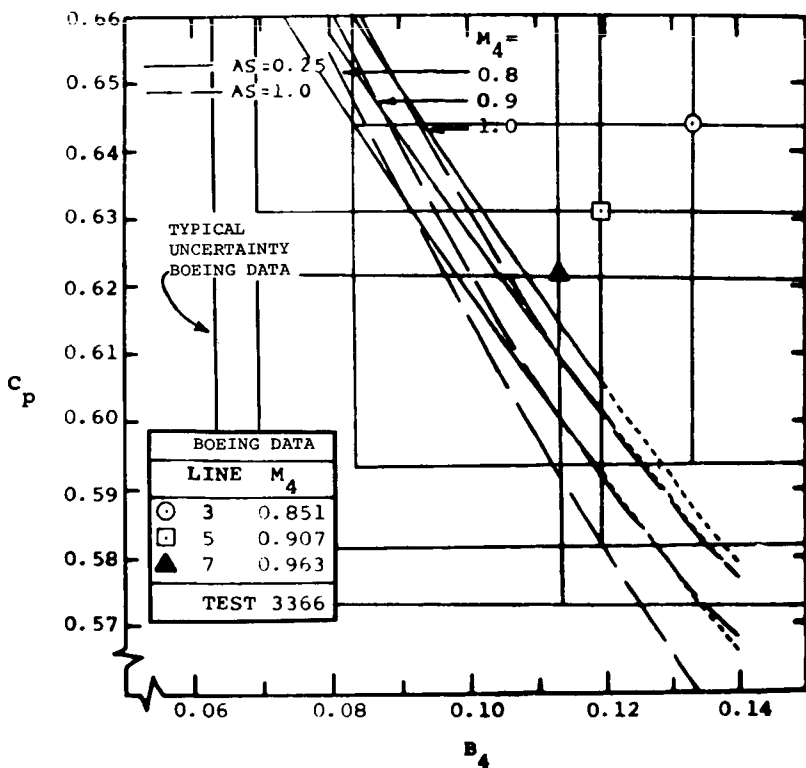
FIGURE 9b.—*Comparison between Boeing-AVLABS channel diffuser data from compressor with Creare-AVLABS straight-channel diffuser data. Pressure recovery* C_p *versus throat blockage* B_4 *and Mach number* M_4 *(from ref. 2).*
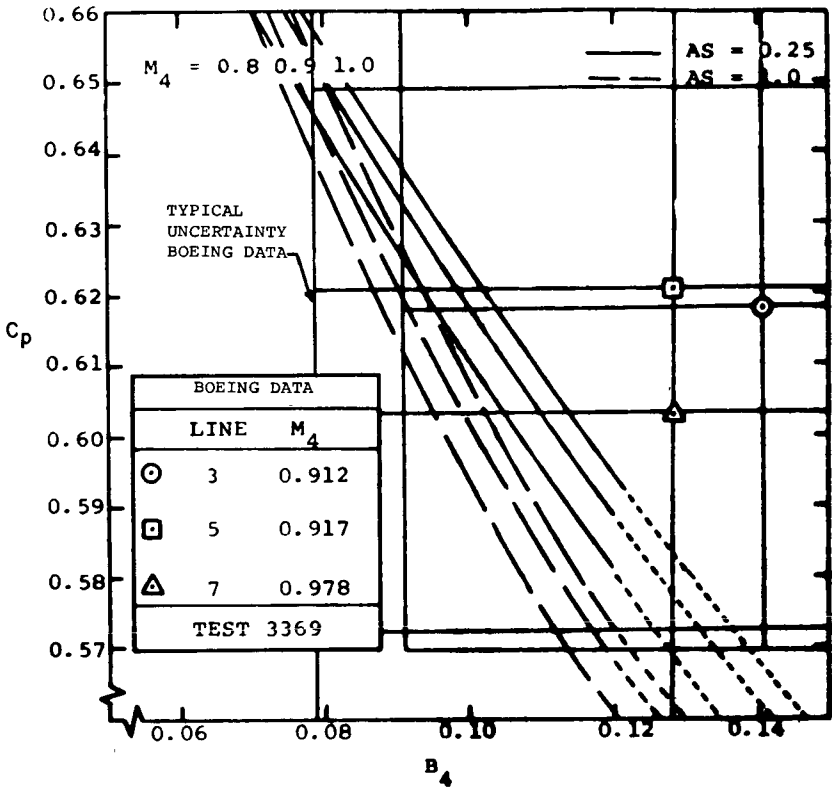
FIGURE 9c.—*Comparison between Boeing-AVLABS channel diffuser data from compressors with Creare-AVLABS straight-channel diffuser data. Pressure recovery* C_P *versus throat blockage* B_4 *and Mach number* M_4 *(from ref. 2).*

The strongest characteristics of these maps are shown in figures 10a, 10b, and 10c. Throat blockage, B, and aspect ratio, AS, have the greatest effect on maximum attainable channel diffuser pressure recovery (the peak of the "hill" on the maps of figure 8). Mach number up to 1.0 had little effect, as can be seen in figure 10. Dean (ref. 3), Runstadler and Dean (ref. 9), Runstadler (ref. 8) and Dean, Wright, and Runstadler (ref. 2) discuss at length the implications of these empirical findings in centrifugal diffuser design and optimization.

The important aspect for our purposes here is the dependence of channel diffuser and overall diffuser performance on throat boundary-layer blockage. This variable is what the boundary-layer theory, applied from impeller tip to throat, attempts to predict. If that prediction is inaccurate, figure 10 shows the consequences. Remember that the channel diffuser gave 55 percent of the overall recovery and that 1-point variation in
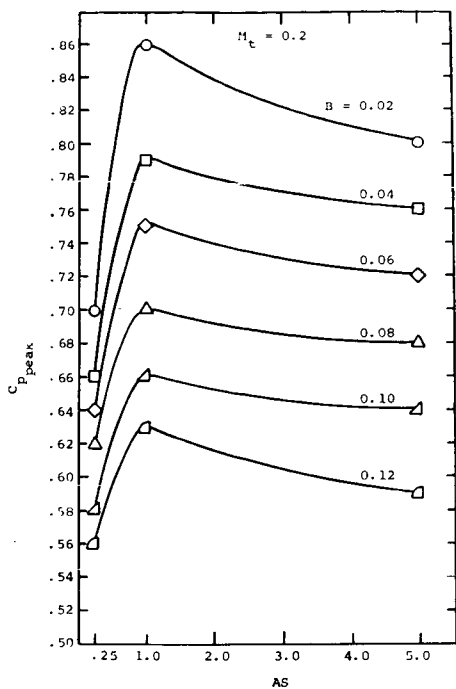
FIGURE 10a.—*Peak pressure recovery versus aspect ratio; Mach number =0.2 (from ref. 8).*
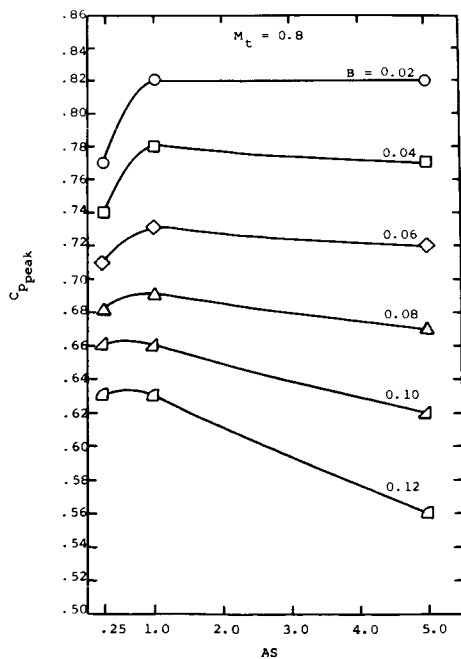
FIGURE 10b.—*Peak pressure recovery versus aspect ratio; Mach number =0.8 (from ref. 8).*
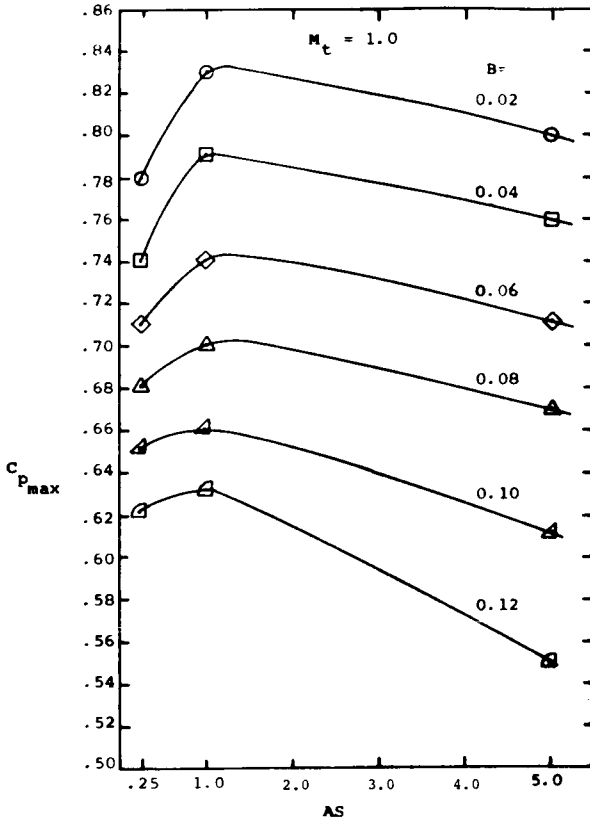
FIGURE 10c.—*Peak pressure recovery versus aspect ratio; Mach number = 1.0 (from ref. 8).*

overall C_p amounts to $\frac{1}{3}$-point in stage efficiency and about 1-percent variation in engine fuel consumption.

BOUNDARY-LAYER ANALYSIS AND RESULTS

In order to predict throat blockage, we attempted a wide variety of theoretical attacks using two- and three-dimensional turbulent boundary-layer theory and shock/boundary-layer interaction theory. Both Mellor (Princeton) and Johnston (Stanford) concluded that three-dimensional theory was too weak to handle the complex flows discussed here. So we used the method of Englert (ref. 10) which appeared to be the most competent available for transonic flow on the basis of the Stanford Conference (1968) results.

The measured pressure distributions of Welliver and Acurio were employed as input. Because initial conditions at impeller tip were very uncertain, the starting boundary-layer thickness and shape factor were varied over wide ranges. The details will not be repeated here; they are fully presented in reference 2.

After due consideration of the use of various shock/boundary-layer interaction theories, all of which have been developed for external flow, they were abandoned. This was because of the shallow passage and thick boundary layers in the compressor. Instead, the Englert calculations were pressed right on through the measured shock pressure rise to the throat.

The results of all of this calculation are discouraging. They are shown in figure 11. Note that the "best" boundary-layer theory results gave throat blockage values for various tests that were about *two times* higher than the measured data as reduced both by Boeing and by us. This error is of grave consequence. Note, in figure 10, that a theoretical blockage of 0.20, compared to the measured value of 0.10, would give about 20 points (estimated) lower channel diffuser recovery, which would amount to a reduction in stage efficiency of about 4 points. One probably would not


Calculation Scheme	3354--7**	3366--5	3369--5
From Boundary Layer Calculation	0.2	0.23	0.27
Boeing Best Estimate Using $P_{o_{4CL}}$, P_y, Data	0.096	0.111	0.126
From $P_{o_{4CL}}$, P_4, Data	0.095	0.119	0.128

* Theoretical and Measured
** Supercritical Case
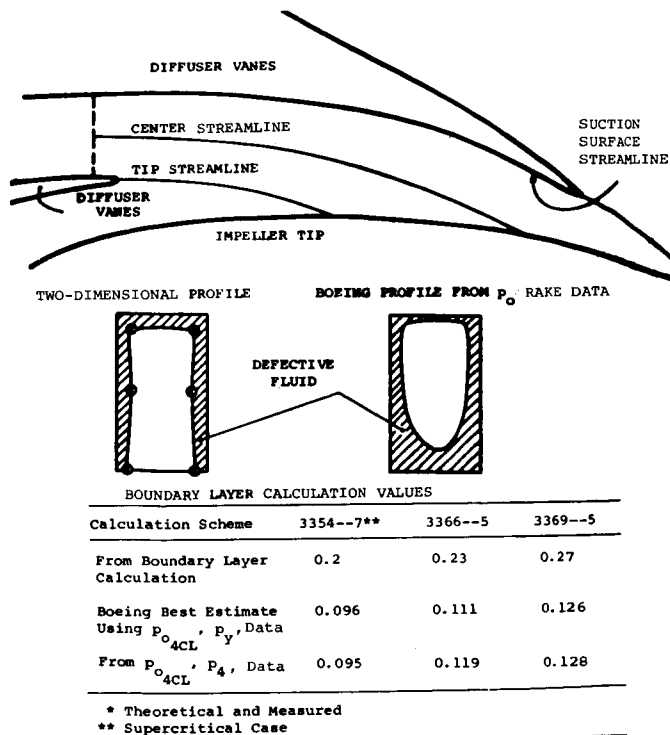
FIGURE 11.—*Throat blockage comparison (from ref. 2).*

even build the compressor if one believed the boundary-layer theory results.

We conclude that the two-dimensional boundary-layer theory is unsatisfactory for this work. Why does it fail?

THE FLUID MECHANICS OF THE DIFFUSER ENTRY REGION

In order to understand why the theory fails, we must understand the flow. That is very difficult today for many reasons.

First, there is little good data. Even the "good" data is highly suspect for reasons considered in detail in reference 2. The principal reasons are the narrow passages (order 0.2 inches deep in the Boeing compressor), instrument distortion of the flow, gross unsteadiness, high oscillation frequencies (blade passing frequency≃20 KC), distorted flow from the impeller, three-dimensional shear flow, strong mixing, shocks, transonic flow, etc. Proven stagnation temperature measurement errors were on the order of 20° F. Backflow was suggested by a compendium of all the data, but could not be resolved by the instruments. The best modern instrument practice was used by Welliver and Acurio, with uncertain data results.
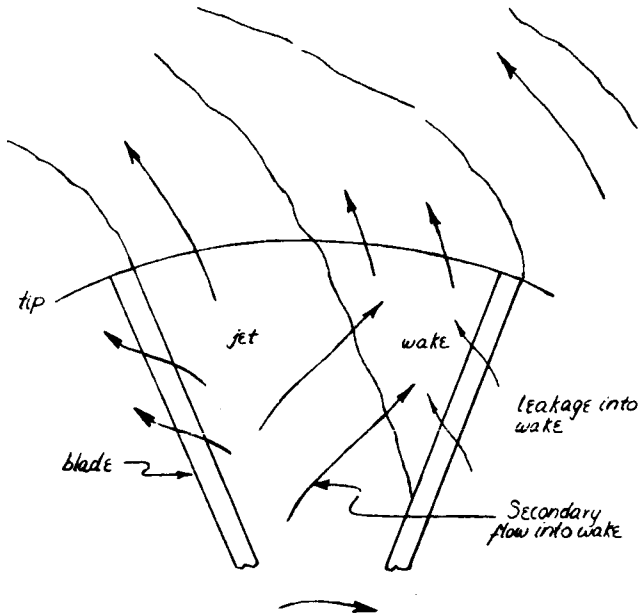

FIGURE 12.—*Wake-jet flow pattern at exit of centrifugal impeller.*

Despite the paucity of data, there are certain flow characteristics that we can deduce. The full diagnosis is displayed in reference 2. Here, we will repeat only the essential conclusions.

The flow from the Boeing impeller was separated grossly in the blade-to-blade plane. The wake width, figure 12, was about 75 percent and the jet velocity about 900 fps.[7] This discharge pattern leads to a very unsteady absolute flow as shown by hot-wire traces in figure 13 from another, low-speed, and much less separated impeller.

The weakness of the radial outflow in the wake region encourages back-flow off the diffuser sidewalls as suggested in figure 14. Such backflow has
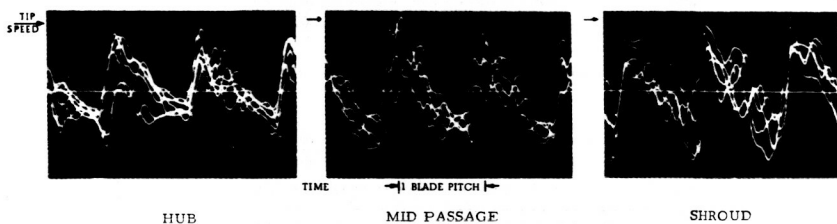

FIGURE 13.—*Typical radial hot-wire anemometer traces for a particular impeller passage measured at impeller tip (multiple traces superimposed) illustrating relative unsteady flow. (Approximately three channels are shown).*
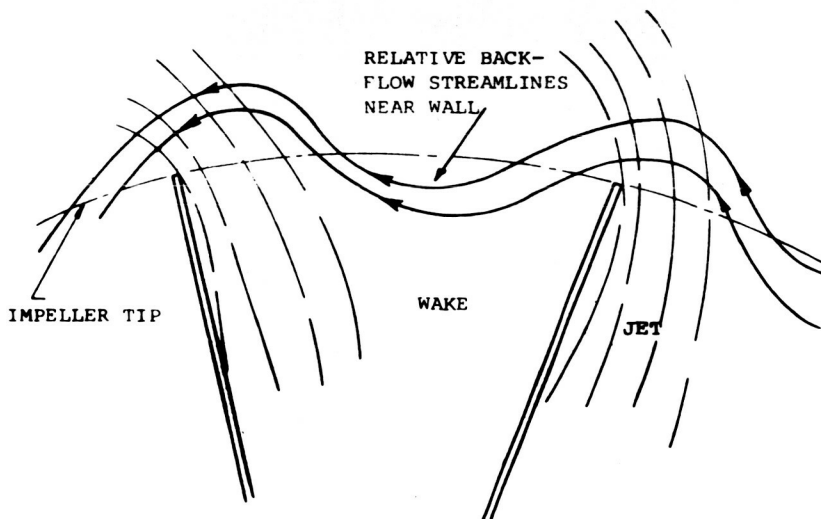
FIGURE 14.—*Schematic of backflow pattern in rotor space.*

---

[7] Tip speed approximately 2000 fps.

been seen by many observers. For instance, Faulders (ref. 11) and Johnston (ref. 1) observed it plainly in a static diffuser rig as shown in figures 15 and 16. In the Boeing case, time-average wall traces, shown in figure 17 by oil streaks in the schlieren windows, suggest mild backflow. We feel the time-average streaks are meaningless because the backflow is probably transient in stator coordinates as the wakes move past and travel through the strong pressure fields of the diffuser vanes (fig. 18). There may be important acoustic wave and resonance phenomena acting


FIGURE 15.—*Limiting wall streamline traces from vaned diffuser flow (from ref. 15).*
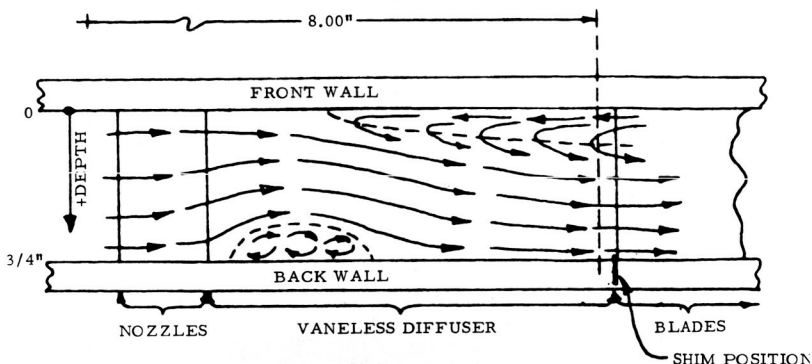
FIGURE 16.—*Flow in vaneless region of vaned diffuser (from ref. 15).*
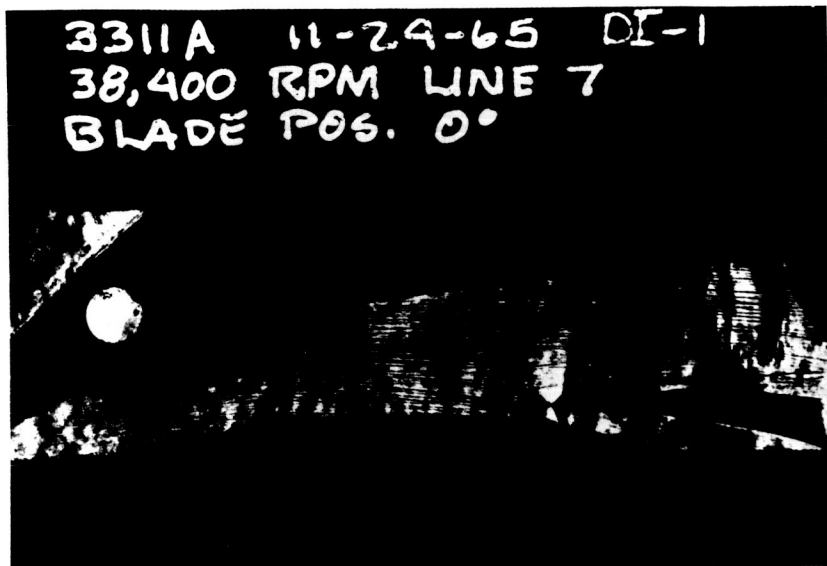
FIGURE 17.—*Oil traces in vaneless region of vaned diffuser flow (from ref. 2).*

in the impeller and diffuser channels. It should be mentioned that the diffuser shock pattern was unaffected by the impeller blade position relative to the diffuser vanes (see ref. 4), but, plainly, the flow conditions at the impeller tip are very unsteady.

We conclude that the boundary layer on the diffuser sidewalls was flowing backwards at certain times in an unsteady, three-dimensional way. Perhaps this backflow, and consequent mixing with and energizing of the return flow by the outflow, can account for the large prediction error of the two-dimensional boundary-layer theory.
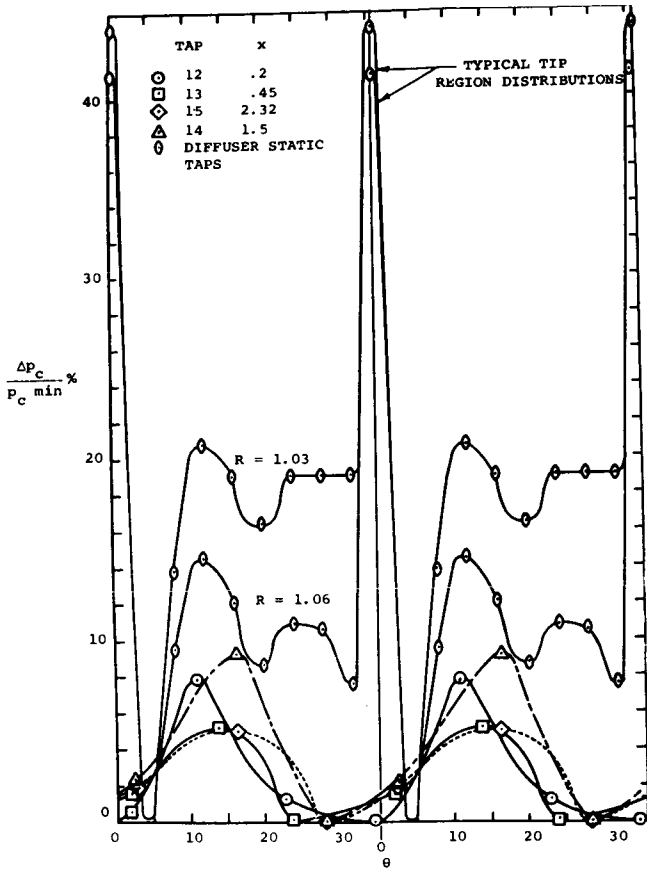
FIGURE 18.—*Tangential variation of cover pressure (from ref. 2).*

In addition to this, there is strong three-dimensional mixing occurring in the entry region. This is driven by the (r,θ) plane mixing of the impeller discharge jet-wake pattern. The fluid near the sidewalls will move at a lower tangential velocity than the core flow. Thus the (r,θ) plane distortion results in an (x,θ) plane distortion and shear, shown schematically in figure 19 for the (r,θ) plane and figure 20 for the (x,θ) plane. We think this (x,θ) distortion leads to the rollup of eddies which cause strong momentum transport perpendicular to the diffuser sidewalls. The consequence of this action should be a loss in core stagnation pressure, while the profile should be flattened at the same time. Then p_o would be lowered in the throat along with a blockage decrease. We could not prove a p_o loss on the centerline in the entry region, although the data diagnosis is quite uncertain. This question is examined in detail in reference 2.
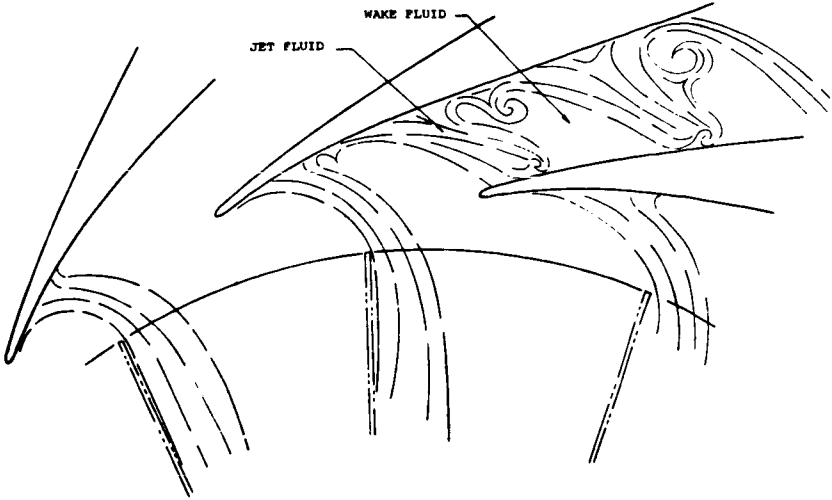
FIGURE 19.—*Schematic of the progression through the diffuser of wakes and jets from the impeller (from ref. 2).*
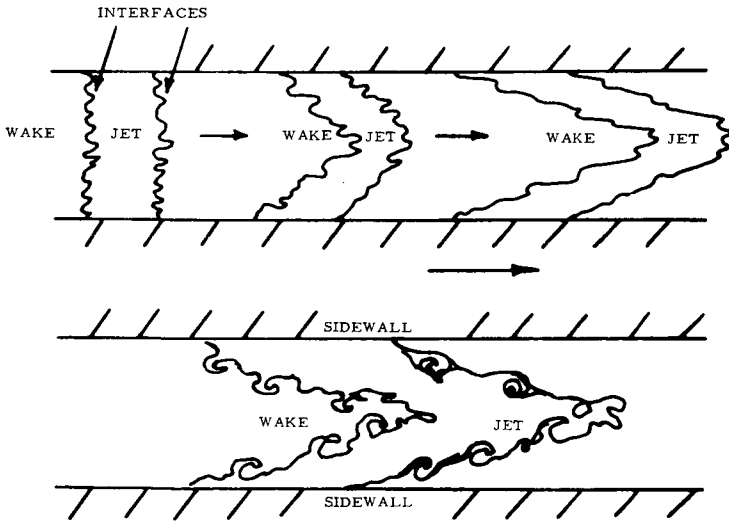

FIGURE 20.—*Schematic of vortex roll-up on interfaces between jet and wake (from ref. 2).*

According to Bradshaw (ref. 12) the very strong turbulence and mixing and gross unsteadiness of the free stream probably obviates the validity of the usual boundary-layer theory. This too may be a cause of the prediction inaccuracy.

Finally, the entry shock may not affect the boundary-layer thickness as a simple boundary-layer theory would claim. In deducing the possible shock effect on blockage, we note from Welliver and Acurio that the shock produced approximately the simple normal-shock pressure rise. That the data are somewhat uncertain on this point must be noted, however. The principal difficulty was that the taps were not spaced closely enough to detect always the minimum pressure at the foot of the shock in the zone of rapid adjustment. Yet, despite the uncertainties, there is enough data to conclude that the shock upstream Mach number and the pressure rise across the sometimes spread-out shock correspond to simple normal-shock theory. This is the same behavior observed by Neumann and Lustwerk (ref. 13; see Shapiro, Vols. I and II) for very spread-out shocks in constant-area ducts.

Given "normal-shock" behavior, we expect to be able to apply the simple normal-shock theory in the core of the flow. Across the shock, the mass flux per unit area ρC is constant. Therefore, for the compressor diffuser entry shock, continuity asserts that the area of the core flow must be constant. Because the passage geometrical area does not change much across the shock, then the boundary-layer flow area must be constant, too, or since

$$\rho C (A - \delta^*) = \text{constant}$$

$$\frac{\partial \rho C}{\rho C} + \frac{\partial A - \partial \delta^*}{A - \delta^*} = 0$$

with

$$\partial \rho C = \partial A = 0$$

Then

$$\partial \delta^* = 0$$

This result says that the throat blockage should equal the blockage *ahead* of the entry shock. Also it says that increasing shock strength will not increase blockage, contrary to the assumptions in the Welliver and Acurio flow model. They claimed (with our support) that surge occurs because the entry shock strengthens with decreasing mass flow, making the throat blockage so high that the channel diffuser characteristic assumes an unstable positive slope $(\partial C_p / \partial m)$.

Actually, measured shock strength and throat blockage do rise with decreasing flow and surge does seem to occur when the measured diffuser $\partial C_p / \partial m$ goes positive. So whether the shock does or does not materially increase δ^* is not plain from the evidence. Perhaps the real case lies between a duct shock and a shock on an external surface. The partial confinement by the vane of the region in which the shock lies might be responsible for intermediate behavior.

Table I presents throat blockage calculated from the computed displacement thickness of the entry boundary layers at a station just *ahead* of the measured shock location. The agreement with the data is quite good for the three cases computed.

The shock/boundary-layer interaction argument presented above may resolve the discrepancy between boundary-layer theory and measurements. At this point we have too little reliable data to be sure. If this is indeed the answer to the dilemma, then the Welliver and Acurio surge model is incorrect in format. However, the diffusion from impeller tip to channel throat does rise as the flow is reduced (because throat Mach number drops) so δ^* and blockage will rise even if the shock is ignored.

Perhaps the true resolution of the difficulty with the entry boundary-layer prediction lies in a combination of some or all of the effects discussed above. All would tend to reduce blockage below that predicted by two-dimensional theory, but the sum effect we cannot calculate.

CORRELATIONS

At this impasse the designer still must design and as accurately as possible ($\pm\frac{1}{2}$-point uncertainty in stage efficiency prediction is desirable), so we have resorted to correlation of throat blockage versus diffusion from impeller tip to throat (fig. 21). The amount of good data available for making this correlation is woefully inadequate but it does give a better prediction than theory. We believe, but cannot prove, that the correlation can be scaled with streamline length $Rey^{1/5}$.

TABLE I.—*Diffuser Throat Blockage (Measured Versus Calculated) With Two-Dimensional Turbulent Boundary-Layer Theory, Illustrating the Effect of Entry Shock on Calculated Blockage*

|	Boeing test number		
	3354	3366	3369
Boundary layer calculation without shock____	0.108	0.098	0.120
Data from figure 11_____	0.095	0.118	0.128
Boundary layer calculation including shock___	0.2	0.23	0.27
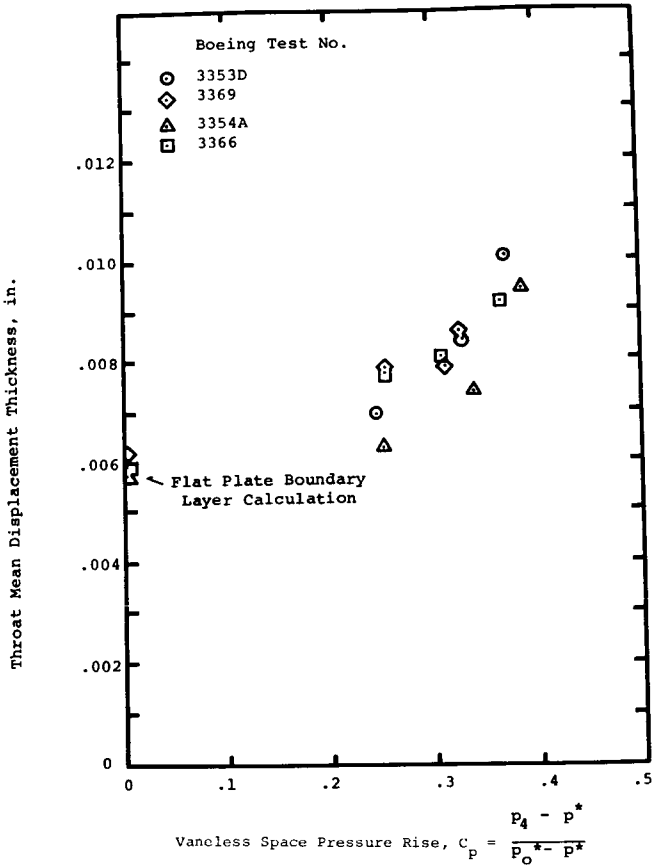
FIGURE 21.—*Correlation of throat blockage versus diffusion from impeller tip for the channel diffuser throat.*

CONCLUSION

We have now laid out our dirty linen and confessed we cannot make boundary-layer theory work for us for a vital prediction in the centrifugal compressor. Yet we are certain that achieving the ultimate compressor performance forecast in figure 2 will require powerful fluid dynamic tools. We do not think that boundary-layer theory will grow in competence to help much here in the next 10 years. The fact that the simple diffuser has defied analysis and that the shock in the duct problem has not even been explained experimentally discourages much hope of analyzing theoretically such a very complex flow as in the diffuser entry; that is,

within the next decade. Yet we are convinced that the small centrifugal compressor will be pushing its ultimate limits by 1980, even without much more than qualitative assistance from boundary-layer theory.

LIST OF SYMBOLS

A Flow area (normal to mean velocity vector, specifically defined)

AR Channel diffuser area ratio

AS Channel diffuser throat aspect ratio

B Boundary-layer blockage,

$$B \equiv 1 - \frac{A_{\text{effective}}}{A_{\text{geometrical}}}$$

C Absolute velocity (relative to a Newtonian frame; e.g., compressor casing)

C_p Pressure recovery coefficient,

$$C_p \equiv \frac{p_{\text{exit}} - p_{\text{ref}}}{\cdot (p_o - p)_{\text{ref}}}$$

where measuring and reference states and stations must be specifically defined

C_{p_D} Pressure recovery coefficient,

$$C_{p_D} \equiv \frac{p_{\text{coll}} - p^*}{p_o{}^* - p^*}$$

where $* \equiv$ mixed-out state (must be specifically defined)

DR Diffusion ratio,

$$DR = V_1 / V_{\text{sep}}$$

h Static enthalpy/unit mass

h_o Stagnation enthalpy/unit mass

L Diffuser centerline length (from throat to exit plane)

M Mach number

m Mass flow rate

p Static pressure

pr Pressure ratio,

$$pr \equiv p_{\text{coll}} / p_{oi}$$

R Radius ratio, r/r_2

r Radius from impeller centerline

V Relative velocity (in coordinate system rotating steadily in Newtonian space)

W	Diffuser throat width (in principal plane of divergence)
W_x	Shaft work per unit mass of fluid
x	Axial coordinate
δ^*	Boundary-layer displacement thickness
η	Efficiency (total to static),

$$\eta = \frac{h_{o_s} - h_{o_i}}{W_x}$$

θ	Tangential angular coordinate
2θ	Diffuser divergence angle
ρ	Density

Subscripts

1, 2, 3, 4	Stations in the stage
CL	Centerline
c	Cover
coll	Collector station (receiving volume after diffuser)
i	Inlet or impeller
o	Stagnation
s	Indicates that process follows an isentropic path
sep	Flow separation value
t	Tip or throat
x	Upstream of shock (e.g., M_x) or axial component
y	Downstream of shock (e.g., M_y)

REFERENCES

1. JOHNSTON, J. P., *The Effects of Rotation on Boundary Layers in Turbomachine Rotors*. Report MD–24, Dept. Mech. Eng., Stanford U., May 1970.
2. DEAN, R. C., JR., D. D. WRIGHT, AND P. W. RUNSTADLER, JR., *Fluid Mechanics Analysis of High-Pressure-Ratio Centrifugal Compressor Data*. Report 69–76, U.S. Army Aviation Materiel Laboratories, February 1970.
3. DEAN, R. C., JR., *The Unresolved Fluid Dynamics of Centrifugal Compressors*. To be published by ASME.
4. WELLIVER, A. D., AND J. ACURIO, *Final Report on AVLABS Contract DAA–177–AMC–173(T)*. U.S. Army Aviation Materiel Laboratories, Reports 67–47 and 67–30, Vols. I and II, published September 1967 and August 1967, respectively.
5. JOHNSTON, J. P., AND R. C. DEAN, JR., *Losses in Vaneless Diffusers of Centrifugal Compressors and Pumps*. ASME Paper 65–FE–1, *J. Basic Eng.*, 1965.
6. DEAN, R. C. JR., AND Y. SENOO, Rotating Wakes in Vaneless Diffuser. *Trans. ASME, J. Basic Eng.*, September 1960.
7. SHAPIRO, A. H., *The Dynamics and Thermodynamics of Compressible Fluid Flow, Vols. I and II*. The Ronald Press Co. (New York), 1953.
8. RUNSTADLER, P. W., JR., *Pressure Recovery Performance of Straight-Channel Single-Plane Divergence Diffusers at High Mach Numbers*. U.S. Army Aviation Materiel Laboratories, Report 69–56, October 1969.

9. RUNSTADLER, P. W., JR., AND R. C. DEAN, JR., Straight Channel Diffuser Performance at High Inlet Mach Numbers. *Trans. ASME, J. Basic Eng.*, Ser. D, Vol. 91, September 1969.

10. ENGLERT, G. W., *Estimation of Compressible Boundary Layer Growth Over Insulated Surfaces With Pressure Gradient.* NACA Tech. Note 4022, June 1951.

11. FAULDERS, C. R., *An Aerodynamic Investigation of Vaned Diffusers for Centrifugal Compressors.* M.I.T., Gas Turbine Lab, January 1954.

12. BRADSHAW, P., *Prediction of Turbulent Shear Layers in Turbomachinery.* Presented at the International Symposium on Fluid Mechanics and Design of Turbomachinery, Penn State U., August–September 1970.

13. NEUMANN, E. P., AND F. LUSTWERK, Supersonic Diffusers for Wind Tunnels. *J. Appl. Mech.*, Vol. 16, No. 2, 1949.

14. RUNSTADLER, P. W., JR., *Straight Diffuser Performance at High Inlet Mach Numbers.* Creare TN–60, September 1966.

15. JOHNSTON, J. P., Experimental Data on Three-Dimensional Flow in a Centrifugal Compressor Diffuser. Gas Turbine Lab, M.I.T., December 1954.

DISCUSSION

H. LINHARDT (Airco Cryogenics): I find your enthusiasm for the high-pressure-ratio compressor very interesting; however, I do believe, as far as industrial application is concerned and also in some aircraft applications, a new material has to be invented before you can draw 15-to-1 pressure ratio because of the high tip speed you're talking about. The other problem with the high-pressure-ratio compressor is the small performance range between the choke and surge, and I do not believe that there is any reasonable application for such a device.

A. D. WELLIVER (Boeing Co.): Dr. Dean made a comment that he would try to design the impellers so they separate, and I would like to clarify that point just a little bit. It's the one point which I have run into over the years that people seem to get more confused over than any other. It has something to do with the fact that many of the people who have designed centrifugals have designed for relatively low pressure ratio and we, on the other hand, were striving for a centrifugal of a fairly high pressure ratio. We designed some centrifugals and had them running at a pressure ratio of 6 and 87 percent total-to-static efficiency with reasonably good range (15 percent). But the flow models that we used seem to run out at this pressure ratio with respect to prediction of static pressure rise and performance that we actually measured in the compressor. It was for this reason that we started looking for a better flow model as we pushed to higher pressure ratio. Now, as far as the separation concept goes, I believe that our experience at both low and high pressure ratio is that if you have a lower pressure ratio design, you can afford to have little or no separation. You must design for the static pressure rise that you might get from one of the potential flow concepts or potential flow programs and you cannot tolerate having large flow separation. As you go to higher pressure ratio, you will find you're allowed to separate earlier in the machine and the mixing loss, which is really a loss of the relative pressure, doesn't have such a dire effect on the machine, and so pressure ratios of say at least 10 to 1 at 80 percent might still be quite feasible and we're getting closer all the time.

Now the other point I wanted to make is quite practical to the compressor designer. What happens when you move across the speed line? It's all well and good to design a compressor that has one point but, as H. Linhardt pointed out, if you have zero surge margin you can't fit that in

inches. Now one of the things that we have learned is that the vaneless space (the area right ahead of the shock system) appears to be what I would call a great adjustor of the flow and, in many cases, the streamlines actually curve far up towards the upper wall and then come down almost in front of the diffuser vane. The amount of curvature varies as you move from the maximum air flow towards the surge line. Actually, as you get closer and closer to the surge line this flow straightens out and finally you go into surge.

G. F. WISLICENUS (Arizona): I like optimism. We all know that in the incompressible field we built centrifugal pumps a long time ago that were 90-percent efficient. To some extent I share the optimism, but I do not understand why we have to live with separation in the impeller. I do not think we had separation in the impeller of the centrifugal pump— not major separation. I cannot understand the author's optimism about the future efficiencies unless he can avoid major separation in the impeller. I do not as yet understand why he feels that the violent unsteady flow which he would get would be helpful and, incidentally, I believe you can avoid the separation in the compressor.

J. L. DUSSOURD (Ingersoll-Rand Research): It seems to me we've missed one important word here in this question of separating and non-separating impellers. That's the simple word "specific speed." If you have an impeller which has a very low specific speed, it simply means that the amount of kinetic energy which is tied in with the V^2 coming into the impeller is smaller compared to the total amount of work which the impeller is putting into the stream. This means that if you don't diffuse this kinetic energy very efficiently, you're not really hurting the performance of the impeller too much. On high-pressure-ratio machines with very high tip Mach number, we are forced to have a comparatively low inducer-to-tip-diameter ratio and therefore a low specific speed. Otherwise your inducer Mach number becomes extremely high. So you can afford, with this kind of a machine, to have a relatively inefficient recovery of the V^2. If you have a high-specific-speed impeller, which is more common perhaps at low pressure ratio, you cannot afford to do that.

DEAN (author): The vigorous discussion of this paper when presented was appreciated; it illuminates the depth and breadth of concern today for the centrifugal compressor.

The following comments are in reply to verbal discussions offered at the meeting.

H. Linhardt commented that strength of materials limitations would prevent the attainment of 15:1 pressure ratio in a single centrifugal stage. I agree that sufficiently strong materials are not available today. However, pressure ratio 12:1 has been achieved at 2200 fps. In the paper, I have called for 15:1 pressure ratio after 10 years or more development.

This prognostication does not seem unrealistic when only 300 fps must be added to tip speed in order to generate 15:1 pressure ratio. With the emergence of new composite materials, fiber reinforcement, control of microstructure from forging powder metallurgy preforms, etc., the needed gain does not seem improbable.

Linhardt also commented that high-pressure-ratio centrifugals were unattractive because of the small range between choke and surge. In reply, I point out that the Boeing experience showed a much broader range (on the order of 10 percent) than had been expected previously. As was mentioned in the paper, we attribute compressor surge to diffuser flow instability. At the moment, there is no understanding of diffuser and stage stability. I have never seen any adequate experimental work on this subject. Appropriate theoretical work is just starting (e.g., Ehrich, ref. D–1). With this lack of attention and knowledge, how can one expect good range or damn the machine with the stigma of poor range?

Our research suggests that the diffuser's throat conditions control stability and surge. We are developing means for controlling surge, but it is too early to report with any certainty. However, the early results encourage the prediction that high-pressure-ratio, high-efficiency centrifugal compressors with excellent range will be developed within 10 years.

Mr. Linhardt also commented on the virtues of the United Aircraft of Canada "pipe" diffuser versus the two-dimensional type used by Boeing and employed for illustration in this paper. We are not championing any particular type of diffuser (other than a well-designed one). However, it is still not plain that the "pipe" diffuser has any distinct advantage over the two-dimensional channel diffuser. No one, including United Aircraft of Canada, has offered hard evidence of superiority. The first order of business today is to get the general diffuser geometry close to an optimum configuration regardless of the details of the diffuser type. Guiding principles for that have been discussed by Dean (ref. D–2) and Dean, Wright and Runstadler (ref. D–3).

By his discussion, A. D. Welliver of the Boeing Company helped to clarify the controversial question of designing a centrifugal compressor with a separated impeller. This matter has been widely misinterpreted by people who do not read carefully what we have said on the matter. So here again we shall repeat. *It is not true, ipso facto, that an optimum centrifugal stage will have an unseparated impeller.*

Under certain conditions, the optimum design proves to be unseparated but, in many other cases, the optimum design proves to have a certain degree of separation at the impeller tip. As we have pointed out repeatedly (e.g., Johnston and Dean, ref. D–4) the degree of separation should not exceed about 40 percent of the passage area because the consequent mixing loss begins to soar with further increases in wake width.

Below 40 percent, the losses due to separation usually are not very serious.

Dr. Wislicenus commented that a separated machine could never be an optimum design. He is stating this as a matter of faith. We do not subscribe to this faith for the centrifugal compressor and, I might point out, some supersonic axial compressor designers do not either. Likewise, if one examines many successful transonic axials, one can only conclude that the blading is heavily separated at the blade row exit. In all these cases, the designers strove for optimum performance.

These situations are much like the simple two-dimensional diffuser. For it, many workers (e.g., Kline, et al., at Stanford) have established that optimum pressure recovery occurs in a stalling diffuser. If one insisted, along with Dr. Wislicenus, that the diffuser should be unseparated, one could not achieve maximum static pressure recovery. On the other hand, if one's objective is to design a diffuser for minimum stagnation pressure loss, then an unseparated design would be optimum.

There are plenty of instances in the design of fluid dynamic systems where separation has been purposely incorporated in order to achieve optimum performance. E. S. Taylor (MIT) distinguished these by saying they are "separated, but not stalled." The centrifugal compressor happens to be a member of this set, in spite of the intuitive repulsion for this set evidenced by most experts.

While it was not a subject of this paper, it is interesting to mention that the paper and motion picture presented by Dr. Johnston at this conference demonstrate in the open literature for the first time a major reason why separation of the centrifugal compressor impeller does not lead to major losses.

When Dr. Johnston and I were together at the Ingersoll-Rand Company circa 1958, we observed through the use of flow visualization with milling yellow aniline dye that the boundary layer on the suction surface of a centrifugal compressor passage was highly stabilized by Coriolis forces. On the other hand, the boundary layer on the driving or pressure side was destabilized. In the last sequence in Johnston's motion picture shown here, bursts of turbulence off the driving face of the passage were seen plainly. We observed the same thing in 1958.

We also observed that the bounding surface between the through-flow jet in the separated impeller and the wake region was unusually quiescent under the influence of the same Coriolis acceleration. Most telling was the occasional observation of a Karman vortex street running from the separation point along the jet-wake interface nearly to the tip of the impeller. If there were turbulent mixing there, as one would expect in stationary coordinates, the pattern of the Karman vortex street would never persist for such a long distance (order 20 times the street width).

Theoretical reasoning about the effect of Coriolis acceleration and these empirical observations have led us to the conclusion that mixing losses due to separation *within* the centrifugal impeller are greatly attenuated by the Coriolis acceleration. Thus one can have separated flow inside the impeller with a relatively small internal loss penalty compared to what would be suffered in the absence of Coriolis acceleration (e.g., axial turbomachine or stationary coordinates). The internal flow in impellers has been discussed at length in Dean (ref. D–2) and Dean, Wright, and Runstadler (ref. D–3).

Dr. J. L. Dussourd questioned our emphasis on impeller diffusion. Of course, we agree with him that there are cases where the relative kinetic energy of the inlet flow is very small compared to the work addition. If this kinetic energy were lost by irreversible mixing, not much influence on stage efficiency would accrue. On the other hand, there are many practical cases where this is not so. We have analyzed a few of them in the paper and have shown in figure 1 the gains which can be made by improving internal diffusion in the impeller. These figures plainly show that internal diffusion is significant for these cases. Perhaps Dr. Dussourd wants to challenge our calculations; but if he accepts their validity, then he must accept the conclusion.

In many cases of high-performance compressors, where overall size is important, the inducer tip relative Mach number is pushed up toward or even beyond 1.0. Centrifugal stages have been designed up to 1.4. Even for a pressure-ratio-10 machine, such as the Boeing compressor which had a relative Mach number of 0.84, internal diffusion was important in order to prevent severe impeller discharge mixing losses. The jet relative velocity leaving the impeller was calculated to be about 700 fps. Losing that much kinetic energy, even at a tip speed of 2000 fps, leads to several points loss in stage efficiency.

Obviously, specific speed is not the important parameter in determining whether internal diffusion is important or not. Rather, it is the ratio of inducer tip relative velocity over impeller tip speed, all squared. This parameter represents the potential loss in kinetic energy compared to the work input of the impeller (when slip factor is close to 1.0). For a design where this parameter is only a few percent, impeller diffusion is not important. However, in a case like the Boeing design (with even a low inducer tip relative Mach number compared to others), the ratio was on the order of 0.20 and impeller internal diffusion was important. See Dean, Wright, and Runstadler (ref. D–3) for extensive discussion of this point and a detailed examination of the Boeing RF–2 data.

Unfortunately, none of the discussors really talked about the main subject of the paper, which was boundary-layer behavior in the diffuser entry region of centrifugal compressors. However, their comments did bring out important background information, which was not presented

due to a lack of time. For those who are deeply interested, we suggest consulting our other recent works mentioned in the references here and those of the paper.

REFERENCES

D-1. EHRICH, F. F., Aerodynamic Stability of Branched Diffusers. Paper 70-GT-27, ASME Gas Turbine Conference, (Brussels), May 24-28, 1970.

D-2. DEAN, R. C., JR., The Unresolved Fluid Dynamics of The Centrifugal Compressor. *Advanced Centrifugal Compressors*, ASME publication, 1971.

D-3. DEAN, R. C., JR., D. D. WRIGHT, AND P. W. RUNSTADLER, JR., *Fluid Mechanics Analysis of High-Pressure-Ratio Centrifugal Compressor Data.* Technical Report 69-76, USAVLABS.

D-4. JOHNSTON, J. P., AND R. C. DEAN, JR., Losses in Vaneless Diffusers of Centrifugal Compressors and Pumps. ASME Paper 65-FE-1, *J. Basic Eng.*, May 1965.

SESSION III

Cavitation

Chairman: J. W. HOLL

Physical Effects in Cavitating Flows

Milton S. Plesset

California Institute of Technology

A discussion of the physical effects in cavitation naturally divides itself into a part concerned with microscopic aspects and a part concerned with macroscopic aspects. The microscopic features of cavitating flows are related to the properties of nuclei in liquids and to the moderate tensile strengths which are usually encountered in flows. The macroscopic features are concerned with the growth of vapor or gaseous cavities from a small initial size and with their eventual collapse. The growth and collapse of vapor or gaseous cavities are macroscopic problems of a transient nature. There are macroscopic problems of a quasi-steady nature which are encountered in cavity flows—or in supercavitating flows, as they are sometimes called. We shall not consider these quasi-steady flows in any detail here.

TENSILE STRENGTH OF LIQUIDS

As is well known, the theoretical tensile strength of a liquid free of contaminants is very large—much larger than is ever observed. The theory of this tensile strength is statistical in nature so that one determines the probability of appearance of a small vapor bubble under a given tension (ref. 1). The formation of a bubble of radius R_0 requires an increase in free energy of $4\pi R_0^2 \sigma$ where σ is the surface tension. As was recognized a long time ago by Gibbs, the pressure within the bubble exceeds the pressure in the liquid by $2\sigma/R_0$ so that the net increment in free energy is reduced to $4\pi R_0^2 \sigma/3$. The probability, P, of appearance of a bubble is dominated by this free energy:

$$P \sim e^{-4\pi R_0^2 \sigma/(3kT)} \tag{1}$$

In equation (1), k is the Boltzmann constant and T is the absolute temperature. It is apparent that this probability is very small even for large tensions. For example, with $\sigma = 72$ dynes/cm (water at 27° C), $\ln P = -73$ when $R_0 = 10^{-7}$ cm; the corresponding tension is 1400 atm.

While there is some reduction in the macroscopic value of the surface tension constant when the radius of curvature becomes very small (ref. 2), this reduction is not significant unless R_0 is less than 10^{-7} cm. We must conclude, therefore, that a homogeneous, pure liquid should have tensile strengths of the order of several thousand atmospheres. It is pertinent to remark that this large tensile strength would be predicted for liquids containing dissolved gases, so long, of course, as the gas is truly dissolved— that is to say, so long as the gas is distributed through the liquid on a molecular scale.

The conventional resolution of the disagreement between the theory of the tensile strength of a liquid and the experimental findings of much lower values is made with the introduction of "nuclei" in the liquid. Various properties of these nuclei have been proposed and we shall wish to discuss some of these here, but their function is to provide sites at which bubbles may grow from some effective size, R_0, which is large enough to give a moderate value of $2\sigma/R_0$. In the statistical theory of the strength of a pure liquid, a cavity of radius R_0 must be formed where no nucleus exists through a statistical fluctuation. Such fluctuations are most improbable unless the spherical cavity is of the order of molecular dimensions. If the cavity in the liquid already exists at a larger radius, the corresponding tensile strength will be reduced.

One model which has been suggested for nuclei is that they are solid particles such as dust particles. It is easy to show (ref. 1) that such solid particles must not be wetted by the liquid if they are to serve as sites at which a macroscopic cavity is to grow. For water one would expect an abundance of hydrophobic dust particles, and, to give agreement with observations, "ordinary" water should have such particles with sizes at least as large as $R_0 \sim 10^{-4}$ cm; very carefully prepared "clean" water should have particles no larger than $R_0 \sim 10^{-5}$ cm or 10^{-6} cm.

Solid particles will tend to settle out from the liquid so that there should be some tendency for the tensile strength of ordinary water, for example, to rise with time if the sample is quiescent and protected from the atmosphere. Such an "aging" effect has been observed (ref. 3). It must be admitted, however, that this aging effect could be explained by undissolved air bubbles rising out of the liquid. The tensile strengths of very clean liquids should not show a significant aging effect since very small nuclei, say $R_0 \sim 10^{-6}$ cm, can be maintained in suspension by the mechanism of Brownian motion. In a macroscopic flow, much larger particles will be effectively maintained in the liquid since their settling velocities are so small.

So far we have not considered any effects of dissolved gases on the tensile strength of the liquid. In the application of a single tension pulse, or of a steady tension, this picture of the tensile strength as being determined by suspended, solid nuclei would indicate that there should be no

significant effect from dissolved gases. An increase in the effective size of solid nuclei by layers of gas adsorbed from solution would be unimportant since such a layer would have a thickness determined by the range of intermolecular forces. This range is of the order of 10^{-7} cm. There is, however, a macroscopic mechanism whereby dissolved gases can play a significant role; this mechanism is the surface tension resultant at the interface of three media: liquid, gas, and solid. The surface tension forces can be annulled, or even reversed, for such combinations so that undissolved pockets of gas can be stabilized in crevices of solid nuclei.

Undissolved bubbles of gas have been considered as possible nuclei from which macroscopic cavities can grow under reduced pressure. Such gas bubbles are, however, unstable. In an undersaturated solution the bubbles dissolve; even in a saturated solution gas bubbles will dissolve because of surface tension (ref. 4). In a sufficiently supersaturated solution, gas bubbles will grow indefinitely. While it must be acknowledged that the mass diffusion process which leads to collapse or growth of these gas bubbles is very slow compared with the dynamic process of vapor-bubble growth or collapse, it is difficult to explain a long-term modest tensile strength by means of undissolved gas bubbles unless they are attached to a solid surface. Such attachment of air bubbles with dimensions less than 10^{-4} cm has indeed been observed to exist on a rather permanent basis on hydrophobic particles in water (ref. 5).

There is a mechanism whereby the time required for the dissolution of very small free bubbles might be increased. Impurities, dissolved or distributed in the liquid, could tend to deposit on the surfaces of gas bubbles. This process would decrease the effective surface tension constant of the gas/liquid interface and would thereby represent a configuration of greater stability since the free energy would be decreased. The decrease in the surface tension would in itself lengthen the time for disappearance of the bubble and, in addition, could decrease the diffusion rate of gas through the bubble boundary into the liquid. An anomalous behavior in small oscillating gas bubbles has been observed (ref. 6) which might be due to such an adsorbed film. Some anomalous persistence of small bubbles has also been claimed (ref. 7) and might be similarly explained.

A liquid should show the same tensile strength for a single pulse of tension or for any nonrepetitive tension regardless of whether the nucleus is a solid, nonwetted particle or happens to be a small gas bubble. The growth from a nucleus to a macroscopic cavity under these conditions is so rapid that diffusion of dissolved permanent gas into the bubble from the solution does not take place.

If there are sufficiently long times available, diffusion of dissolved gases can play a central role in increasing the size of nuclei. Such long times are produced when a liquid is exposed to oscillating pressure fields. If the liquid has a concentration of dissolved gas, c_∞, which is the equilibrium

value for the liquid pressure P_0, then a bubble of radius R_0 can gain mass when the liquid pressure undergoes periodic oscillations with angular frequency ω:

$$P(t) = P_0(1 + \epsilon \sin \omega t)$$

This process is known as rectified diffusion, and the rate of increase of mass in the bubble averaged over many oscillation cycles is (ref. 8)

$$\frac{dm}{dt} = \frac{8\pi}{3} Dc_\infty R_0 \epsilon^2$$

where D is the coefficient of diffusivity of the gas in the liquid. Clearly, rectified diffusion can stabilize a gas bubble which would otherwise dissolve. A gas bubble of radius R_0 in a liquid at pressure P_0, with equilibrium-dissolved concentration c_∞, will lose mass at the following rate (ref. 4):

$$\frac{dm}{dt} \simeq -4\pi D \frac{2\sigma}{P_0} c_\infty$$

The threshold pressure amplitude for rectified diffusion which would just balance this loss is

$$\Delta P = P_{max} - P_0 = P_0 \left(\frac{3}{2} \frac{2\sigma}{P_0 R_0}\right)^{1/2}$$

If ΔP exceeds this value, the bubble will grow—but at the slow rate characteristic of diffusion processes.

Another situation in which the long times required for the diffusion process are available is familiar in the flow of water over a submerged body so that the static pressure is reduced. The liquid may then be appreciably supersaturated, and a small bubble may grow on the surface. Such bubble growth has been observed in the boundary layer of a model in the working section of a water tunnel. When the bubble has become large enough, it leaves the surface of the body, enters the flow, and may serve as the nucleus for formation of a macroscopic vapor bubble.

It may be of interest to note that Einstein gave a theoretical connection between gas diffusivity in a liquid and the liquid viscosity:

$$D = \frac{kT}{6\pi\mu a}$$

where a is the radius of the diffusing molecule, T is the absolute temperature, and μ is the coefficient of viscosity. From this relation it is evident that a highly viscous liquid like glycerol should have a coefficient of

diffusion which is approximately 10^{-3} times that of water. The implications of such a small diffusion coefficient in a viscous liquid for gaseous cavitation are indeed interesting.

To summarize our view of the effective tensile strength of liquids, the small observed tensile strengths are due to the presence of nuclei which should for the most part consist of nonwetted solid particles. Dissolved gases should play only a secondary part in tensile strength and cavitation except where slow processes can be effective, and typical of these is rectified diffusion with oscillating pressures or the flow of supersaturated dissolved gas into a bubble attached to a solid.

DYNAMICS OF CAVITATION BUBBLES

Growth of Vapor Bubbles

In the growth of a vapor bubble, we may suppose that the rate of growth gives bubble boundary velocities which are small compared with the speed of sound in the vapor. It follows that the pressure within the bubble will be close to the equilibrium vapor pressure corresponding to the temperature in the liquid at the boundary. As the bubble grows, the latent heat of evaporation must be supplied at the liquid boundary. The associated cooling will reduce the vapor pressure and may therefore affect the rate of growth. We may easily find the conditions under which this cooling effect becomes important.

Let us suppose that a vapor bubble grows to a macroscopic size, R, in a time τ from some initial size $R_0 \ll R$. Then the total mass of vapor which is evaporated into the bubble is $(4\pi/3)R^3\rho'$ where ρ' is the vapor density. If L is the latent heat of evaporation per gram, then the total heat required is

$$Q = (4\pi/3)R^3\rho'L$$

This heat is taken out of a liquid layer around the bubble which has an effective thickness determined by the thermal diffusivity of the liquid, κ,

$$\kappa = \frac{k}{\rho c}$$

where k is the thermal conductivity, ρ is the density, and c is the specific heat of the liquid. The thickness of the liquid layer is given approximately by

$$d \simeq (\kappa\tau)^{1/2}$$

We see that the estimate of the thickness is not sensitive to the choice of τ. The volume of the liquid layer is then of the order of magnitude

$4\pi R^2 d$, and the corresponding mass of liquid is $4\pi R^2\rho d$. The temperature drop in this mass of liquid, ΔT, is then

$$\Delta T \simeq \frac{(4\pi/3)R^3\rho'L}{4\pi R^2\rho c d} = \frac{R}{3d}\frac{\rho'}{\rho}\frac{L}{c}$$

The drop in vapor pressure, Δp_v, associated with this temperature decrease may be estimated from the Clausius-Clapeyron equation, which gives

$$\frac{dp_v}{dT} \simeq \frac{LM}{BT^2}p_v$$

where M is the molecular weight of the vapor, B is the perfect gas constant, and T is the absolute temperature. This expression for the rate of change of vapor pressure with temperature comes from supposing that the vapor behaves like an ideal gas and, further, that $\rho \gg \rho'$. Both these approximations are fairly accurate. It follows that

$$\Delta p_v \simeq \left(\frac{dp_v}{dT}\right)\Delta T$$

and finally

$$\frac{\Delta p_v}{p_v} \simeq \frac{LM}{BT^2}\frac{R}{3d}\frac{\rho'}{\rho}\frac{L}{c} \tag{2}$$

The condition for a negligible effect from cooling by evaporation is that

$$\frac{\Delta p_v}{p_v} \ll 1$$

When this condition is satisfied, thermodynamic effects are unimportant in cavitation bubble growth. We then say that we have bubble growth in a "cold" liquid since it is evident that both ρ' and (dp_v/dT) decrease rapidly with temperature.

In a cold liquid, since thermodynamic effects are unimportant, we may disregard the energy equation and consider only the momentum equation. Since we have already supposed that the bubble growth rate is small compared with the speed of sound in the vapor, it will certainly be slow compared with the speed of sound in the liquid. The flow in the liquid is then essentially incompressible, and if, in addition, we take the growth to be spherically symmetric, the momentum equation integrates to the Bernoulli equation. From the Bernoulli equation one gets the equation of motion of the bubble boundary

$$R\ddot{R} + \frac{3}{2}\dot{R}^2 = \frac{p(R) - P_0}{\rho} \tag{3}$$

where P_0 is the pressure in the liquid at infinity and $p(R)$ is the pressure in the liquid at the bubble boundary. The boundary condition of continuity of stress across the bubble boundary gives

$$p(R) = p_v - \frac{2\sigma}{R} - 4\mu \frac{\dot{R}}{R} \tag{4}$$

The problem of spherical growth in a cold liquid is thus completely determined. We may observe that the left side of equation (3) may be written in the form

$$\frac{1}{2R^2\dot{R}} \frac{d}{dt} (R^3\dot{R}^2)$$

and one can easily get the asymptotic growth velocity for fixed P_0:

$$\dot{R} \sim \left[\frac{2}{3} \frac{(p_v - P_0)}{\rho} \right]^{1/2} \tag{5}$$

since for large R the terms $2\sigma/R$ and $4\mu\dot{R}/R$ in $p(R)$ become unimportant.

When the condition $\Delta p_v \ll p_v$ is not met, the dynamics of vapor-bubble growth are strongly coupled to the energy equation, or the heat-flow equation. The physical situation now corresponds to tension in a "hot" liquid. We consider, for simplicity, the case in which the static pressure at infinity, P_0, is constant, and we assume further that the temperature in the liquid is T_0. The liquid must be superheated if a vapor bubble is to grow; that is, the vapor pressure at the liquid temperature, $p_v(T_0)$, exceeds the ambient pressure. We introduce the temperature T_b, which is the "boiling" temperature for the ambient pressure P_0; that is, T_b is the temperature such that $p_v(T_b) = P_0$. Then

$$p_v(T_0) > p_v(T_b) = P_0$$

We characterize the "hot" liquid case as that in which the cooling effect lowers the temperature in the bubble so that it approaches T_b as the bubble grows. When the cooling effect is so large, we have the limiting case in which inertial effects are unimportant so that the growth is controlled entirely by the rate of heat flow. Clearly, the cooling effect can never lower the temperature, T, within the bubble so far that $p_v(T) < P_0$. Growth cannot then proceed, and the heat inflow would cease together with any cooling. In the asymptotic case, we can expect that the temperature T within the bubble would exceed T_b by only a small amount, so that we may estimate the heat inflow requirement approximately by taking $T \simeq T_b$. The temperature in the liquid rises from its value at the bubble wall to T_0 in a distance of the order of magnitude $(\kappa t)^{1/2}$ at the time t. This distance is the heat diffusion length. The temperature

gradient in the liquid, then, is approximately $(T_0-T_b)/(\kappa t)^{1/2}$, and the heat inflow into the bubble is

$$\dot{Q} \simeq 4\pi R^2 k \frac{(T_0-T_b)}{(\kappa t)^{1/2}} \tag{6}$$

where $R = R(t)$. Now the heat requirement per unit time for evaporation is

$$\dot{Q} = L \frac{d}{dt}\left(\tfrac{4}{3}\pi R^3 \rho'\right) \simeq 4\pi R^2 \dot{R} L \rho' \tag{7}$$

If we equate these two values of $\dot{Q}$, we find the asymptotic growth speed

$$\dot{R} \simeq \frac{k}{L\rho'} \frac{(T_0-T_b)}{(\kappa t)^{1/2}} \tag{8}$$

We see that the two limiting cases for growing vapor bubbles have very simple behavior described by equations (5) and (8). The intermediate situation of a "lukewarm" liquid does not have this simplicity, although we can be assured that the $R(t)$ trajectory must lie between those specified by the limiting curves just described. An accurate solution of the general case has analytical complications because the heat-flow equation is coupled to the momentum equation. The essential complication comes from the heat flow across a moving boundary $R(t)$, which is implicit in the problem (ref. 9).

Collapse of Vapor Bubbles

When the ambient pressure P_0 exceeds the vapor pressure p_v, so long as these pressures remain constant we may use the momentum equation (3) to determine the collapse velocity. If we suppose, for the moment, that p_v remains constant, and if, in addition, we neglect the effect of viscosity, then we easily find that

$$\dot{R}^2 = \frac{2(P_0-p_v)}{3\rho}\left(\frac{R_0^3}{R^3}-1\right) + \frac{2\sigma}{\rho R}\left(\frac{R_0^2}{R^2}-1\right)$$

It follows that $\dot{R}$ increases in magnitude like $R^{-3/2}$ as R approaches zero. Clearly, many of the simplifying assumptions which have been made cannot remain valid toward the end of the collapse motion.

Even in a cold liquid, a stage in the collapse will be reached in which the heat of condensation will produce a temperature rise so that p_v will increase. In this case, however, it may be shown by numerical treatment that the time for collapse and the trajectory for $R(t)$ are not greatly affected by this temperature rise. An additional effect which is of particular significance for cavitation or cold bubble collapse is the effect of compressibility, which has been studied by many authors.

There are evidently many complications which appear in the theory of the collapse in addition to the effect of compressibility. Among these are the instability in the spherical shape and the difficulty of determining the equation of state of the compressed vapor. All these difficulties appear only in the last stages of the collapse, when the radius is quite small. It is known, however, that a physical case of particular interest is that of the collapse of cavitation bubbles near a solid boundary. For this physical situation, the presence of a neighboring solid boundary changes the collapse behavior early in the bubble history before the difficulties characteristic of the late stage of collapse can appear. The bubble is deformed, and a jet is formed directed toward the solid boundary (ref. 10). This result not only simplifies the theoretical analysis by making it possible to avoid these difficulties, but also has important implications for the mechanism of cavitation damage.

REFERENCES

1. PLESSET, M. S., Tensile Strength of Liquids. *Cavitation State of Knowledge*, ASME Symposium, June 1969, p. 15.
2. KIRKWOOD, J. G., AND F. P. BUFF. Statistical Mechanical Theory of Surface Tension. *J. Chem. Phys.*, Vol. 17, 1949, p. 338.
3. STRASBERG, M., Onset of Ultrasonic Cavitation in Tap Water. *J. Acoust. Soc. Am.*, Vol. 31, 1959, p. 163.
4. EPSTEIN, P. S., AND M. S. PLESSET, On the Stability of Gas Bubbles in Liquid-Gas Solutions. *J. Chem. Phys.*, Vol. 18, 1950, p. 1505.
5. LIEBERMANN, L., Air Bubbles in Water. *J. Appl. Phys.*, Vol. 28, 1957, p. 205.
6. EXNER, M. S., AND W. HAMPE, Air Bubbles in Water. *Acoustica*, Vol. 3, 1953, p. 17.
7. TURNER, W. R., Microbubble Persistence in Fresh Water. *J. Acoust. Soc. Am.*, Vol. 33, 1961, p. 1223.
8. HSIEH, D–Y., AND M. S. PLESSET, Theory of Rectified Diffusion of Mass into Gas Bubbles. *J. Acoust. Soc. Am.*, Vol. 33, 1961, p. 206.
9. PLESSET, M. S., AND S. A. ZWICK, The Growth of Vapor Bubbles in Superheated Liquids. *J. Appl. Phys.*, Vol. 25, 1954, p. 493.
10. PLESSET, M. S., AND R. B. CHAPMAN, Collapse of a Spherical Vapor Cavity Near a Solid Boundary. *J. Fluid Mech.*, Vol. 47, 1971, p. 283.

DISCUSSION

J. M. ROBERTSON (University of Illinois) : In turbomachinery flows with liquids, cavitation may enter to cause noise, loss of machine effectiveness, vibration, or material erosion damage. The designer is faced with the questions of when and where cavitation will appear, how the flow is modified, and the nature of the cavity collapse. A clear and lucid picture has been given of the matter of tensile strength of liquids relevant to cavitation occurrence and to subsequent consideration of the transient dynamics of cavitation bubbles, both growth and collapse, as related to damage. And, through concentration on the basic physics, this presentation has been achieved without recourse to a single figure or complex mathematics.

In the matter of tensile strength, the author's review brings this matter down from the large values of pure liquids to the rather small values usually encountered in engineering. Concerning "dissolved gas" effects, I request the author's interpretation of the rather well-known experiments in which pressurization of nonpurified water led to much larger tensile strengths. My rough interpretation is that although the gas in the sample initially was not visually evident, it was only dissolved on pressurization.

The author suggests that often for cavitation to appear with oscillation, and in body flows, time must be available for gas diffusion into bubbles to occur. He notes that with highly viscous glycerol the diffusion would be significantly less than with water, thus implying a delay in cavitation occurrence. Cavitation experiments have dealt with glycerol, but concern was not with the initial appearance of cavitation. An even more viscous fluid (pluracol) was used by S. Sundaram (ref. D–1) for studies of cavitation inception (actually desinence) for a friction-type valve. The cavitation number was found to decrease by a factor of two with a doubling of the Prandtl number, which is directly proportional to viscosity.

In view of the use of fluids other than water in some machines, the discussion of bubble growth in "hot" liquids versus that in "cold" liquids and the resulting thermodynamic effect is germane to a host of turbomachinery flows. In an extensive review of cavitation damage, A. Thiruvengadam (ref. D–2) made a suggestive comparison of several fluids on this basis.

R. HICKLING (General Motors Research Laboratories) : Professor Plesset has given a succinct summary of our present understanding of

some of the physical effects involved in the formation, growth, and collapse of bubbles. The theory that he presents allows a clear conceptualization of the processes involved.

The assumption of a uniform equilibrium behavior of the vapor inside the bubble permits considerable simplifications of the theory, but, in some cases, these may not be entirely realistic. It should be emphasized here that by a *non*equilibrium behavior we mean deviations from the Clausius-Clapeyron equation—i.e., the assumption that the liquid and vapor phases are continuously in equilibrium with each other. Calculations for a bubble containing a permanent gas (ref. D–3) have shown that significant thermal gradients develop in the gas next to the cavity wall, even when the bubble wall is moving relatively slowly. A similar situation is expected to occur with a vapor. Such nonuniformity of temperature naturally has associated with it a nonequilibrium behavior in the vapor, and, under certain conditions, the interaction could become quite pronounced.

It has been argued that, because the thermal diffusivity of the vapor in the bubble is much greater than that of the surrounding liquid, the liquid presents a kind of thermal barrier to the flow of heat in and out of the bubble. It is reasoned that the vapor responds relatively quickly to thermal changes and consequently has a more uniform temperature distribution, while the liquid responds relatively slowly and has steep temperature gradients in the region close to the bubble wall. Surely this argument does not completely prove its case. It is indeed true that the thermal diffusion length of the vapor is an order of magnitude greater than the diffusion length in the liquid. However, the thermal capacity (density times specific heat) of the vapor is *two* orders of magnitude less than that of the liquid. Thus the temperature variations in the liquid phase should be an order of magnitude less than the temperature variations in the vapor. Therefore, one would expect the principal temperature gradients at the interface to lie within the vapor phase rather than the liquid. A nonuniform temperature in the vapor would appear to be the rule rather than the exception.

Having raised the specter of a nonuniform, nonequilibrium state inside the bubble, one next wonders what to do about it. Clearly this has to be considered if improvements are to be made in the theory. Recent attempts at this have involved rather gross assumptions and do not appear to be an advance on the basic work reported in Professor Plesset's paper.

PLESSET (author): Professor Robertson has asked me to comment on the "dissolved gas" effect which is found when a liquid is subjected to high pressure. After a liquid such as water has been so treated and when it is then tested under ordinary pressure, it shows a large tensile strength. This large tensile strength, however, gradually disappears as the liquid returns to its normal low tensile strength. I believe that this phenomenon is not primarily due to undissolved gas in the usual sense. I think that,

rather, it is due to the presence of solid particles which are not wetted by the liquid. These particles under ordinary conditions act as holes in the liquid and will therefore serve as "nuclei" or sites at which cavities can form with moderate tensions. When, on the other hand, the liquid is put under high pressure, the liquid will be forced into the surface of the solid particles, which will then no longer be unwetted and will no longer act as nuclei. Such particles, of course, may have originally stable layers of gas adsorbed on their surfaces, but such gas layers would be expected to be only a few molecules thick. Upon pressurization, this gas will also be forced into the surface of the solid with some liquid and may in this sense be dissolved. The gradual return to low tensile strength is to be interpreted as the diffusion of liquid out of the solid particles so that it again acts as a nucleus.

While Dr. Hickling has raised some subtle and interesting points in his discussion of my paper, I believe that his reservations regarding the present treatments of thermal problems in bubble dynamics are not justified. He suggests that nonequilibrium behavior in the liquid/vapor system will occur even when the interface moves slowly. This question has been considered in detail, and it has been shown that the vapor pressure at a liquid interface will have its equilibrium value (the "Clausius-Clapeyron" value) when the motion of the interface is small compared with the characteristic vaporization velocity c^* where

$$c^* = \frac{c}{(2\pi\gamma)^{1/2}}$$

Here c is the velocity of sound in the vapor and γ is the ratio of specific heats for the vapor. When the liquid interface is moving into the vapor with a velocity $\dot{R}$, the pressure in the vapor adjacent to the liquid, p', is above the equilibrium value and is given by

$$p' = p_{eq}\frac{c^*}{c^* - \dot{R}}$$

where p_{eq} is the Clausius-Clapeyron value. When the interface is moving away from the vapor, one has

$$p' = p_{eq}\frac{c^*}{c^* + \dot{R}}$$

These expressions, which are accurate when $\dot{R}$ is less than c^*, show that the deviations of p' from p_{eq} are unimportant for interface motions that are characterized by small Mach numbers. These slow motions are typical of those encountered in most cavitation and boiling situations.

We can also easily answer the question of the spatial variations in vapor pressure throughout a bubble of radius R. The vapor pressure at a bubble

wall, as we see from the expressions above, is the equilibrium vapor pressure corresponding to the liquid temperature at the wall, provided that $\dot{R}$ is small compared to c^*. But this condition is a statement that the bubble wall has a motion with small Mach number. Such a motion of the vapor is essentially subsonic, incompressible motion. In this approximation it follows that the pressure in the vapor cannot have any appreciable spatial variation. The conclusion is that a bubble which has a moderate radial velocity, $\dot{R}$, has a spatially uniform vapor pressure which is given by the equilibrium vapor pressure corresponding to the temperature of the liquid interface.

We cannot yet conclude that the vapor density and vapor temperature are uniform throughout the bubble. Although the vapor pressure is uniform in the bubble, the vapor density and temperature in the interior of the bubble do not necessarily have the values that they assume at the boundary. It is clear, however, that both of these latter quantities must be spatially uniform if one of them is uniform, since the pressure, density, and temperature are connected by the equation of state. We can readily see that the vapor temperature is uniform for the moderate values of $\dot{R}$ of present concern. This conclusion follows because the diffusion length will then be greater than R, and the temperature in the bubble, while it may vary with time, will not have appreciable spatial variation. Dr. Hickling is aware that the diffusion length will be large compared with R. It is of course well known that the coefficient of thermal diffusion is the only physical parameter which appears in the equation for heat flow, and, as Dr. Hickling points out, the thermal diffusivity of the vapor is much larger than that of the liquid, although the thermal conductivity of the vapor is appreciably less than that of the liquid. The only way that the thermal conductivity of the vapor or the liquid can enter into a problem, however, is through boundary conditions, and the boundary conditions should be considered with care since this is where Dr. Hickling is in error in his view of the problem. On the liquid side of the interface the heat flow per unit time is

$$-k_L 4\pi R^2 \left(\frac{\partial T}{\partial r}\right)_L$$

where k_L is the thermal conductivity of the liquid, $(\partial T/\partial r)_L$ is the temperature gradient in the liquid at the bubble wall, and $4\pi R^2$ is the area through which the heat flows. The boundary condition on the vapor side of the interface is *not*

$$-k_v 4\pi R^2 \left(\frac{\partial T}{\partial r}\right)_v$$

as Dr. Hickling supposes. Rather, the boundary condition in the vapor is

$$L \frac{d}{dt} \left(\tfrac{4}{3}\pi R^3 \rho_v \right)$$

where L is the latent heat of evaporation or condensation. We see that the heat flow into an expanding bubble needed for latent heat of evaporation is supplied by a temperature gradient in the liquid, but we also see that no gradient is developed in the vapor. In the same way, for a shrinking bubble the latent heat of condensation of vapor is conducted away by a suitable gradient in the liquid without the development of a gradient in the vapor. Our conclusion is, finally, that a vapor bubble which expands or contracts at moderate rates will have a spatially uniform interior: uniform in vapor pressure, density, and temperature.

Dr. Hickling has also made reference to permanent gas bubbles in a liquid and again expresses concern that large temperature gradients are to be expected in the gas near the bubble boundary. As in the condensible vapor case, the thermal diffusivity of permanent gas is much larger than that of the liquid, so that the diffusion length may be much larger than that of the liquid. The physical situation is straightforward. When the diffusion length is large compared with the bubble radius—that is, for slow processes—the bubble temperature will remain isothermal. The fact that the thermal conductivity of the gas is small compared to that of the liquid is immaterial, since the temperature gradients in the liquid and in the gas are both essentially zero. The boundary condition at the bubble wall becomes trivial. The case of rapid motions of a permanent gas bubble is perhaps outside the scope of this discussion, but it may have some interest nevertheless. If the diffusion length in the gas becomes appreciably smaller than the bubble radius, the bubble motions will become adiabatic in some average sense. So far as the boundary condition in the liquid at the bubble wall is concerned, the temperature gradient is negligible; no appreciable heat flows into or out of the bubble. Gradients develop in the gas, and it is for this reason we must speak of an adiabatic behavior in an average sense.

I hope that these comments represent a clarification of a problem which has been beset by difficulties in understanding.

REFERENCES

D–1. SUNDARAM, S., Some Cavitation Scale Effects in a Plug Valve. *Proc. 1969 Cavitation Forum*, ASME, pp. 13–14.

D–2. THIRUVENGADAM, A., On Modeling Cavitation Damage. *J. Ship Res.*, September 1969, pp. 220–233.

D–3. HICKLING, R., *J.A.S.A.* Vol. 35, No. 7, 1963, pp. 967–974.

Some Effects of Applied Stress on Early Stages of Cavitation Damage[1]

DALE J. KEMPPAINEN

General Electric Company

FREDERICK G. HAMMITT

University of Michigan

The problem of material attrition due to the phenomenon of cavitation has become increasingly important in recent years. Methods of alleviating cavitation damage have been suggested, including the use of externally applied stresses. The possible presence of inherent tensile or compressive stresses in fluid system components causes concern regarding their effect on the longevity of the components of the system as a whole when exposed to cavitation. Previous work from this laboratory (ref. 1) indicated that the effect of stress upon cavitation damage rates depended strongly upon the material. In general, compression, if applied parallel to the surface, tended to reduce the damage, while tension tended to increase it. The present paper considers particularly the initial phases of damage and the effect of these external stresses on the extent to which damage is incurred.

EXPERIMENTAL FACILITIES

General

Three experimental facilities were used to procure the data required for this study. These were (1) water loop with venturi, (2) mercury loop with venturi, and (3) vibratory facility (stationary specimen, nonflow system). Each of these facilities has been extensively discussed elsewhere (refs. 2–5). A short description of each system is given here only for clarification of test conditions. Reference 2 presents full details.

Water Loop

The water loop, a multiple, closed-loop system, is shown in figure 1. One of the available loops was operated at a venturi throat velocity of 50 ft/sec at 75° F in the ½-in.-diameter throat.

Mercury Loop

The mercury loop (fig. 2) is a single-loop venturi system. A throat velocity of 30 ft/sec at 75° F in the ½-in.-diameter throat was used.
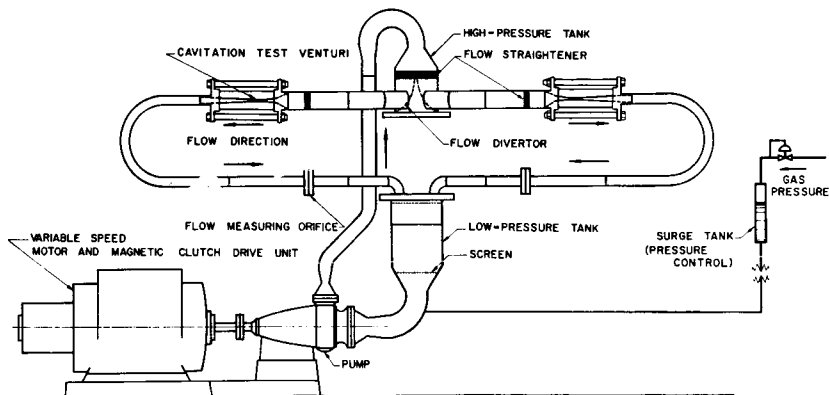
FIGURE 1.—*Schematic of water cavitation damage facility (only two of the four loops shown).*
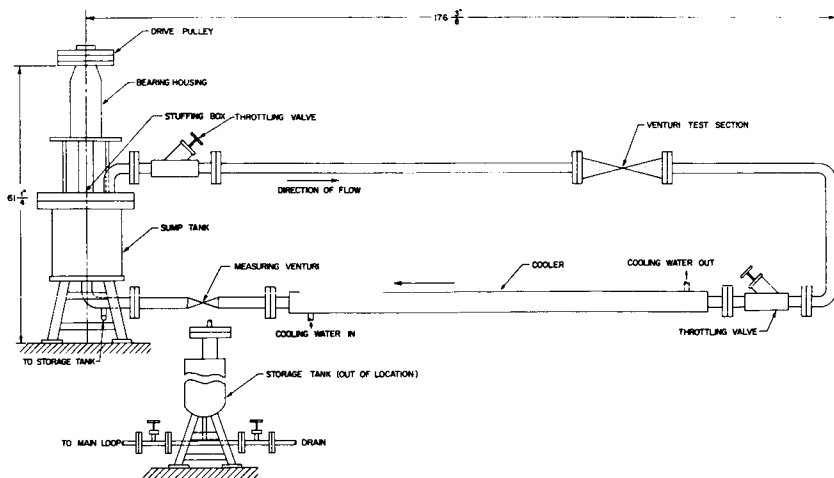
FIGURE 2.—*Schematic drawing of overall mercury facility layout.*

Vibratory Facility

A standard exponential horn (20 kHz, 2 mil) was used. The test specimens were held stationary in the cavitation field about 18 mils from the oscillating horn tip. Figure 3 is a schematic diagram of one of the arrangements used, and figure 4 illustrates the other.
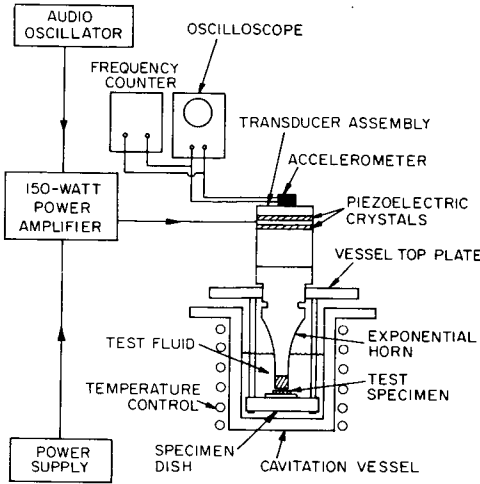
FIGURE 3.—*Schematic representation of the stationary-specimen vibratory cavitation test facility.*
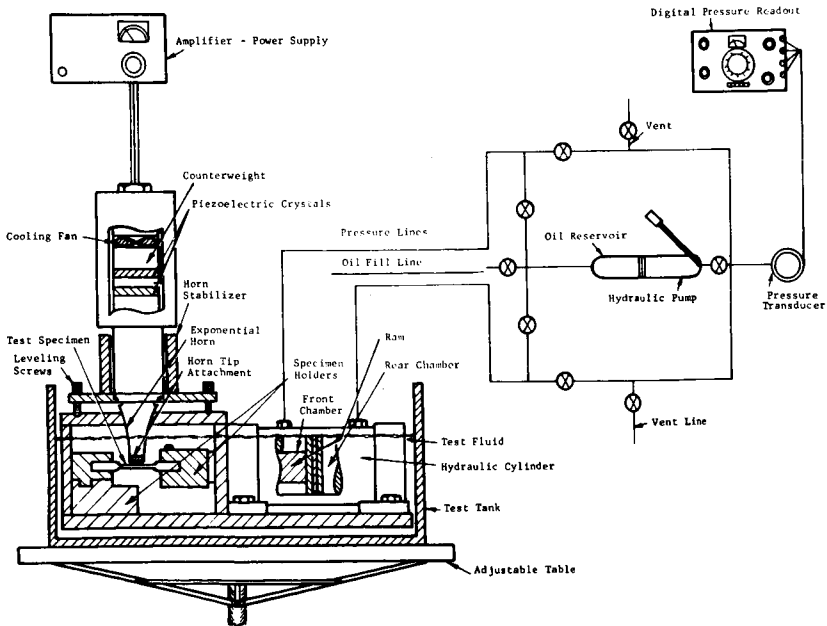
FIGURE 4.—*Schematic diagram of test facility.*

Specimen Placement

In both flowing systems a cylindrical specimen (fig. 5) was used. The specimen was placed across the fluid stream in the venturi diffuser (fig. 6), slightly downstream from the venturi throat exit.

Two types of specimens were used in the vibratory facility, depending on the method used to provide the applied stress: (1) 1.25-in.-diameter slugs placed parallel to the face of the vibratory horn or (2) a specimen of dumbbell shape closely resembling a tensile test specimen (fig. 7). Figure 4 shows the specimen arrangement. These tests were run in distilled water at 73° F.
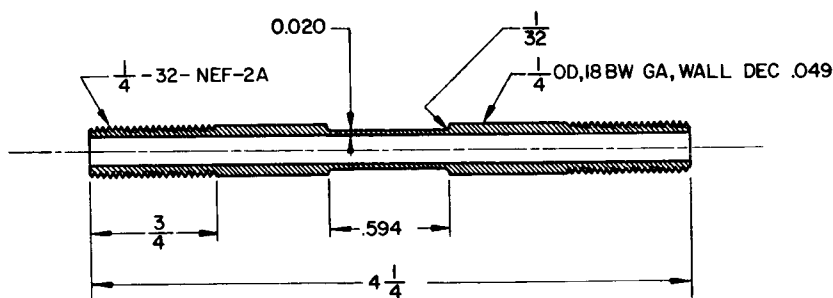
FIGURE 5.—*Drawing of tubular test specimen (pin).*
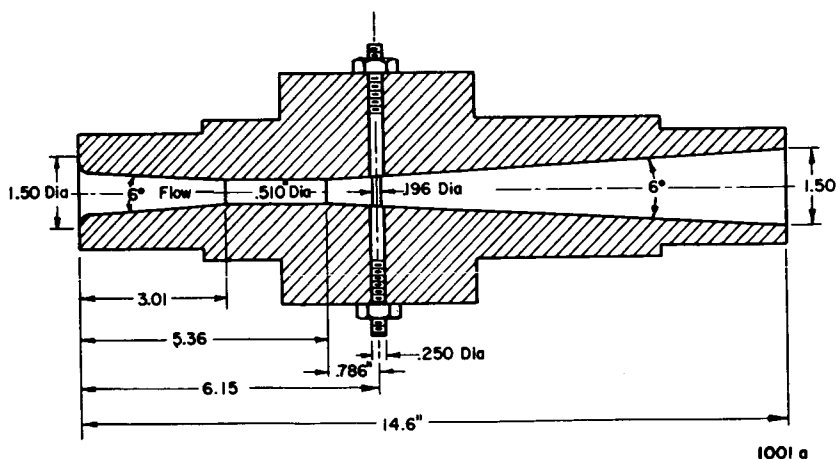
FIGURE 6.—*Assembly drawing of tension-test venturi.*
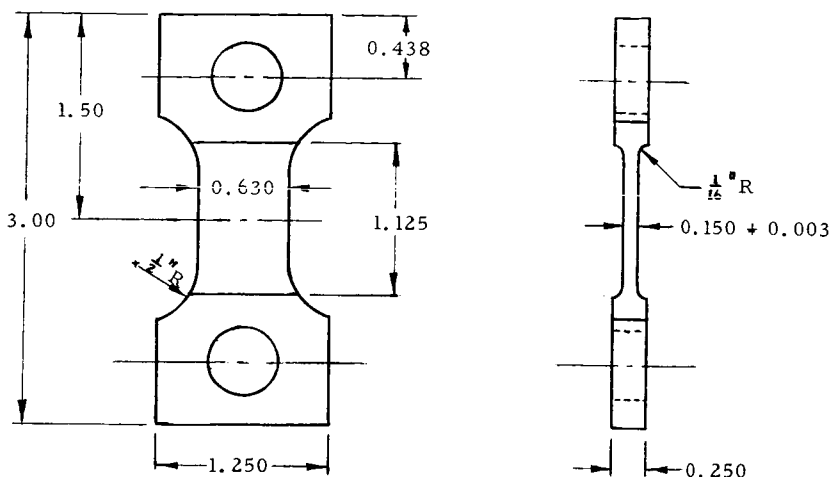
FIGURE 7.—*Dimensional drawing of tension/compression specimen.*
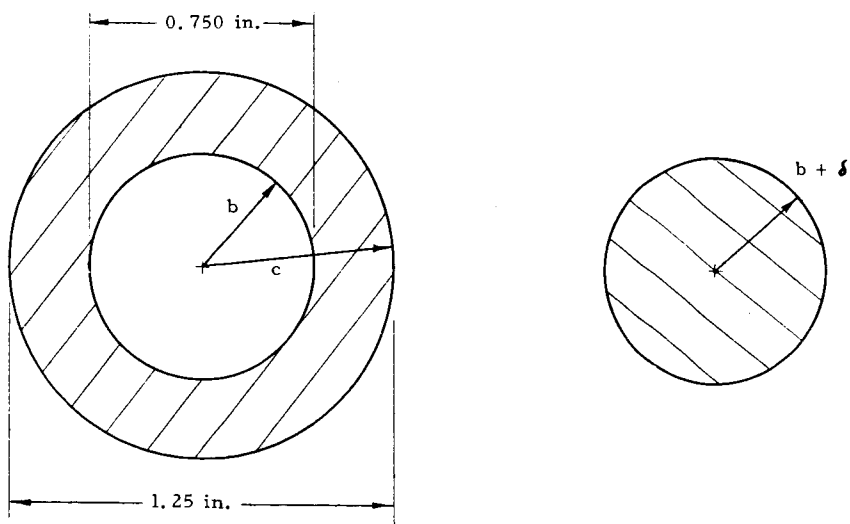
FIGURE 8.—*Test specimen and ring.*

Effect of Radially Symmetric Compressive Stress (Arrangement No. 1)

The first arrangement provides a radially symmetric compressive surface stress which corresponds to the radially symmetric flow of the fluid imposed by the oscillating horn tip (ref. 2). This stress field was provided by shrink-fitting an outer ring around the metal center (fig. 8).

The test specimen consisted of a solid cylindrical center section nominally 0.25 in. thick and 0.7500±0.0005 in. in diameter of the material to be tested. The outer ring was of type 304 stainless steel. By adjusting the radial interference, δ, the calculated specimen stress is varied according to the relationship:

$$P_{sf} = \frac{\delta/b}{1/E_0\{[1+(b/c)^2]/[1-(b/c)^2]+\nu_0\}+[(1-\nu_I)/E_I]}$$

where P_{sf} = compressive stress on the specimen material
E_0 = elastic modulus of the ring material
E_I = elastic modulus of the test material
ν_0 = Poisson's ratio for the outer material
ν_I = Poisson's ratio for the test material
$b+\delta$ = test specimen radius
δ = radial interference
c = outside radius of the outer ring
b = inside radius of the ring

The specimen and ring combinations were selectively paired according to the difference of fit, δ, after accurate measurement of the diameters, thus providing the desired surface compressive stress to the inner slugs.

Materials

Test materials were chosen which exhibited good reproducibility and availability, ease of fabrication, and relatively low damage resistance. Two materials, chosen to obtain rapid damage to investigate the feasibility of the test, were O.F.H.C. (oxygen-free high-conductivity) copper and 2024 aluminum. Control specimens of these materials were also made to the same diameter as the total test/slug/ring combination. Thus the same flow conditions were maintained for both the controls and the compressively loaded specimens.

TEST RESULTS

Damage Rates

Figure 9, which shows test data obtained for the shrink-fit specimens, indicates that the cavitation damage resistance of both the O.F.H.C. copper and the 2024 aluminum are decreased by the impressed radially symmetric compressive stress. This comparison, made on the basis of maximum volumetric loss rates, shows a 19.3-percent increase in damage over the nonstressed control for the copper and a 7.1-percent increase for the aluminum. However, the initial damage rate (i.e., that between time zero and 15 minutes) for the aluminum of the compressed specimen was
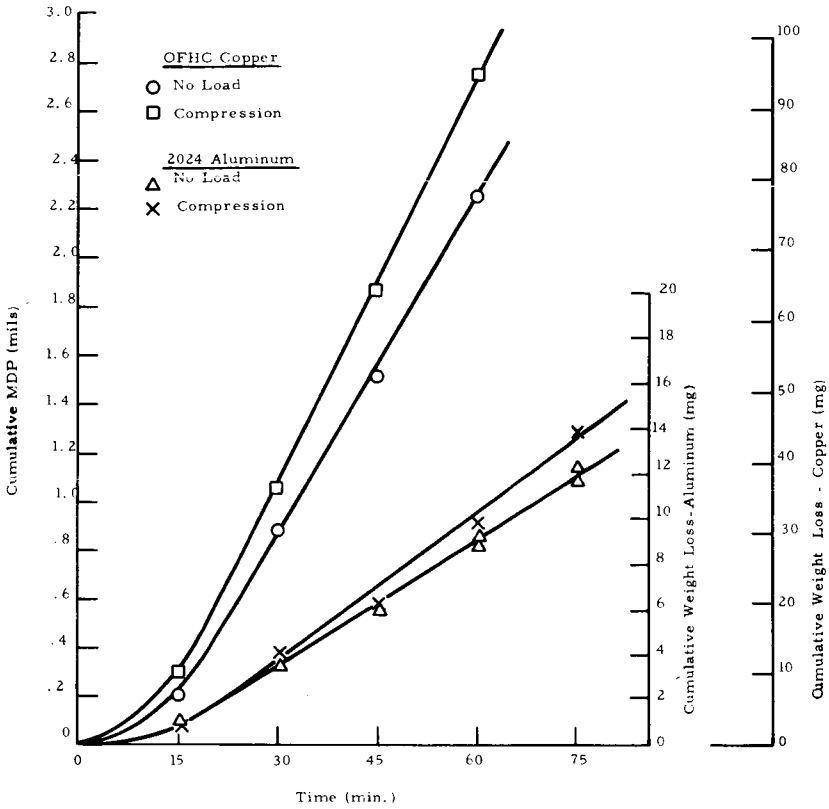
FIGURE 9.—*Effect of compressive stress on cumulative damage of O.F.H.C. copper and 2024 aluminum shrink-fit specimens.*

less than that for the nonstressed specimen. This same effect was reported earlier (refs. 1 and 2) for a number of other materials stressed only in the axial direction. For this particular material, in this test, for a mean depth of penetration (MDP[1]) less than 1 mil, the effect of the radially symmetric compressive stress was thus to inhibit the amount of cavitation damage. For greater MDP the damage rate increases, indicating that after

---

[1] MDP = mean depth of penetration (i.e., the volume loss per unit area, or an equivalent damage depth if volume loss were uniform across the entire area).

$$\text{MDP} = \frac{W}{\rho A}$$

where W = weight loss
ρ = density
A = damage area over which weight loss occurs

the initial damage period the inhibiting effect of the compressive stress decreases and then becomes negative. Thus the compressive stress appears to be detrimental once the surface of the material has been broken.

These same trends were not seen in the copper. However, no measurements for less than 0.1 mil MDP were made.

Photographic Investigation of Short-Duration Damage Tests

The results of a photographic investigation of specimens under the three load conditions of tension, compression, and zero applied load are shown in figure 10. These three series of photographs are a composite of 10-degree segments of a cylindrical specimen of type 304 stainless steel (fig. 5) run in the mercury loop (fig. 2). The test duration was 1.5 minutes with a throat velocity of 30 ft/sec and a pressure drop across the venturi of 71 psi. The pitting density changes which are evident from sector to sector are due to the distribution of the cavitation field which surrounds the specimen in this configuration (ref. 6). Figure 10a shows a polished 304 stainless-steel specimen tested with zero applied stress. Figure 10b shows the same material tested under a compressive load parallel to its
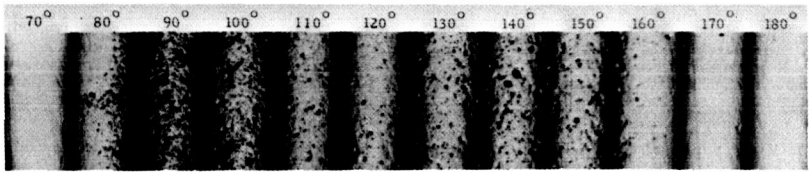
a.—*No applied force.*
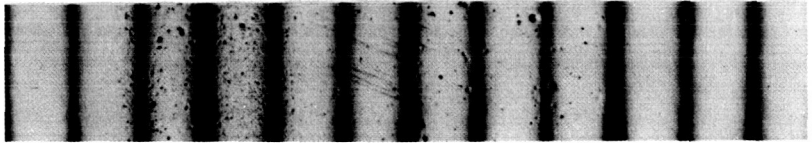
b.—*Compressive force.*
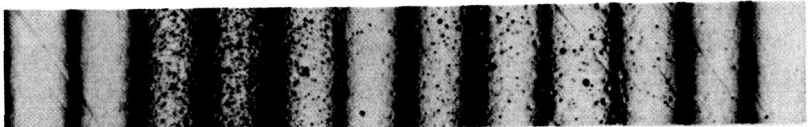
c.—*Tensile force.*

FIGURE 10.—*Effect of surface stress on damage for short-duration tests.*

axis of 88 percent of its yield strength, while figure 10c is for an impressed tensile load of 88 percent of the yield strength.

Comparing the photo for the imposed compressive force (fig. 10b) to that for zero force (fig. 10a) shows a very significant reduction in the number of smaller size pits and some reduction for all pits for compressive load. There are, however, still some very large pits visible in the compressive specimen. The tensile specimen (fig. 10c) and the zero-force specimen (fig. 10a) appear to be quite similar in pit-number densities of all sizes.

Three highly polished brass (65/35) specimens were run in the vibratory rig under conditions of tensile, zero, and compressive external applied load. The test duration in each stress mode was 10 seconds. The results are shown in figure 11. As in figure 10, there is markedly less pitting for compressive applied load than for other conditions. Under microscopic
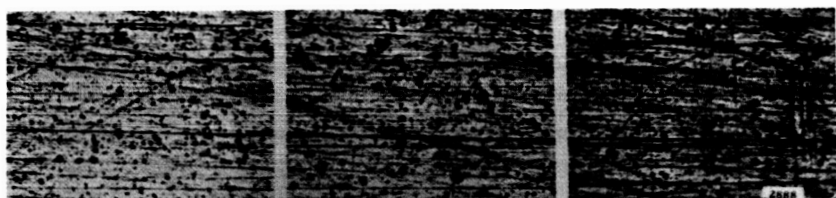
a.—*Tension* (*100*×).

b.—*Zero load* (*100*×).

c.—*Compression* (*100*×).

FIGURE 11.—*Cavitation damage in brass vibratory specimens after 10-second exposure.*

examination, all specimens showed approximately uniform radial damage distribution over the damaged area. For comparison, figure 12 shows a heavily damaged specimen. Proficorder traces across its damaged area indicate that damage depth is again approximately uniform (ref. 2).

Comparing the short-duration specimens in detail, the pit-number density is greatest for the tension specimen (fig. 11a). There is a greater number of small pits than of large ones, as is typical in cavitation tests. The specimen with zero applied load (fig. 11b) has a somewhat larger number of small pits than the tension specimen, but the number and size of large pits are about the same. The compressive specimen (fig. 11c), however, shows a definite decrease in the number of both small and large pits.

Comparing the results from the vibratory facility with those from the mercury loop, the effects of externally applied stress are about the same even though specimen shape, material and fluid properties, and cavitation field differed drastically. In both tests the effect of the compression on damage in the early stages is to strongly decrease the number of small pits, with less effect on larger pits. Even in the early stages, however, the compressive force does not totally alleviate the damage. Rather, it appears to increase the threshold bubble energy required for creating a pit, thereby decreasing most strongly the number of small pits. The material is still vulnerable to higher energy bubble collapses, which cause the larger pits. It thus appears that the "incubation period" is increased by a compressive preload.
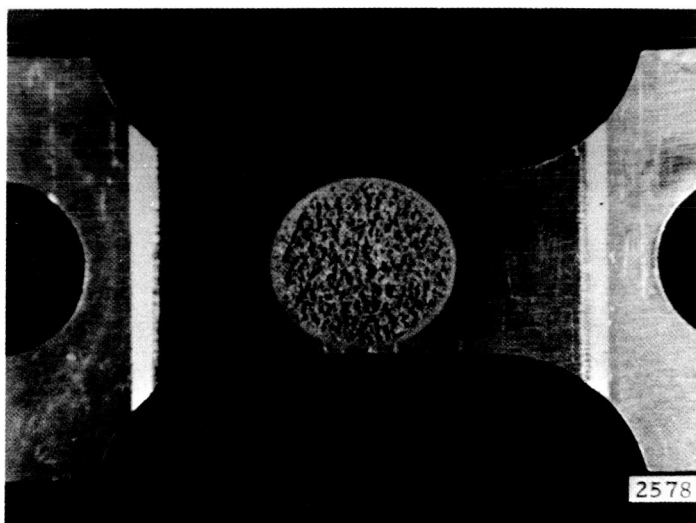

FIGURE 12.—*Center damage area of a specimen with a reduced cross section prior to tensile pull.*

Additional examples of early damage on metallic specimens were obtained using a plated specimen of 304 stainless steel. This experiment was suggested by the previous work of Noell (ref. 6) and Wood (ref. 7), who used a lacquer film coating to quickly indicate areas of maximum vulnerability to cavitation damage. Our water loop and associated test venturi were used in this investigation. Venturi throat velocity was 50 ft/sec with the cylindrical specimen (fig. 5) placed across the venturi. Several lacquer coatings were investigated. However, since these did not provide adequate bonding to the 304 stainless-steel specimen, electroplated cadmium films of various thicknesses were tried. These plated specimens were exposed to the cavitation field of the venturi for a 15-minute duration and then examined microscopically. As in the previously described mercury tests, the damage appeared on the sides and downstream portions of the cylinders. Pressure profiles and flow-regime photographs which enabled prediction of these damage areas were reported previously (refs. 2 and 6). Unlike the specimen from the mercury loop, only a small number of distinct circular holes or pits were found. Figure 13 shows the effect of varying thickness of the cadmium plate. A complete removal of cadmium at the pit center occurred for the thinner platings (fig. 13a, b). For thicker plating (fig. 13c), the damage does not extend completely through the plating.

In figure 13b a raised rim around the circular damaged area appears. Figure 13c shows areas where the cadmium has been partially dislodged. Close examination of these pits (fig. 13c) shows small circular areas (indicated by arrows and outlined in black ink for easier visualization) near the center of the damaged areas suggesting a very local circular area of most intense attack, as if the surface had been impacted by a microjet of liquid.

Figure 14 shows more detail of the pits in the thinner platings. The central area of each pit, void of all plating material, is surrounded by an outer area from which only a minor portion of the plating has been removed. Figure 14a is an enlarged photo of the most central pit in figure 13a. Its diameter is 0.6 μm. The complete symmetry of this central region from which the cadmium has been removed is shown. Such excellent symmetry strongly indicates that the material removal has been accomplished by a single (rather than multiple) impact.

These pictures strongly substantiate the theory that cavitation damage even in a flowing system may be created by liquid microjets generated during bubble collapse, rather than by spherical shock waves radiating from the bubble collapse center. The type of damage shown cannot easily be attributed to such shock waves, which would merely press the cadmium plate into the surface (as was demonstrated by impacting steel shot against a similar surface) rather than "washing it off." This damage is much more easily understood as the result of the radial velocity from a

high-velocity impacting liquid jet. Selected pictures of this type have been published previously by this laboratory (ref. 9) in support of this theory.

Metallurgical Examination of Damage Pits

A metallurgical examination of the region of the damaged surfaced area of the tension and compression specimens was made. SAE 660, a cast

a.—*Coating thickness: 2.5×10⁻⁵ inches (120×).*
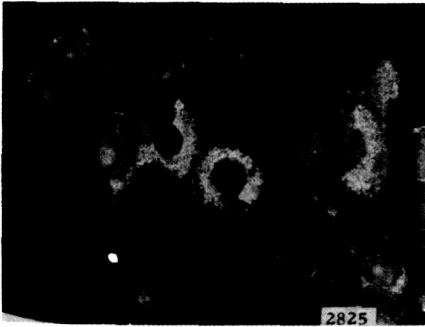
a.—*Coating   thickness: 2.5×10^{-5} inches (120×).*

b.—*Coating thickness: 5×10^{-5} inches (note raised rim) (120×).*
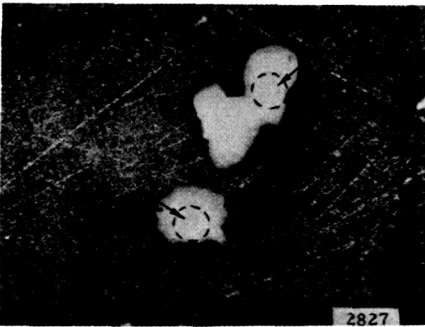
c.—*Coating   thickness: 5.5×10^{-4} inches (small circles marked by arrows indicate a point of impact of a central jet) (120×).*

FIGURE 13.—*Effect of increasing cadmium coating thickness of stainless steel tubular pin specimens on water-loop cavitation pits.*

bearing bronze, and O.F.H.C. copper were tested for this purpose in the vibratory rig. Test duration was sufficient to provide relatively large MDP. Figure 15 illustrates the method of sectioning. The specimens were polished, etched, and then photographed at 400 diameters.

Figure 16 is four photomicrographs of a damaged SAE 660 specimen, showing both transverse and longitudinal sections. The interior "holes" are porosity in the cast material. This specimen had been tested under

a.—*Coating thickness: 2.5×10⁻⁵ inches (enlargement of central pit) (500×).*
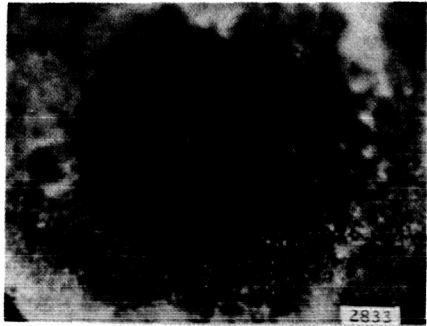
b.—*Coating thickness: 5×10⁻⁵ inches (120×).*

c.—*Coating thickness: 5×10⁻⁵ inches (note difference in area around pits) (120×).*
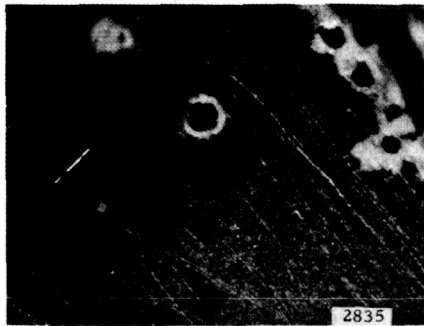
FIGURE 14.—*Cavitation pits in coated specimens showing material removal.*

FIGURE 15.—*Cutting directions on damaged specimens.*

a.—*Transverse (400×).*
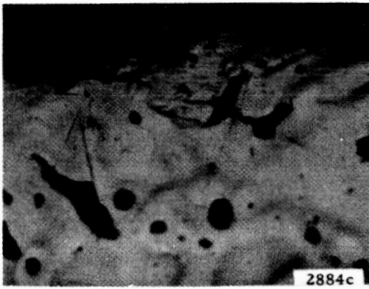
b.—*Transverse (400×).*

c.—*Longitudinal (400×).*

d.—*Longitudinal (400×).*

FIGURE 16.—*Photomicrographs of cavitation damage area of zero-load SAE 660 vibratory specimens.*

zero applied load. In the section in the transverse direction (fig. 16a, b) only a few cracks are visible. Slip lines, however, can be seen in photograph a at the base of the pit on the top right. Slip lines are also visible in photographs b, c, and d, indicating that the material adjacent to the pits has experienced considerable cold work. In photographs a and b, the slip lines appear almost perpendicular to the pit apex.

The longitudinal photographs (fig. 16c, d) show some evidence of microcracks at the base of the pits. In the center of photograph d, a large pit has at its apex a number of microcracks emanating in different directions. There are also slip lines on either side of the pitted region, particularly to the right of the apex, indicating that considerable cold work was done in this region. In figure 17, a and b are photomicrographs of SAE 660
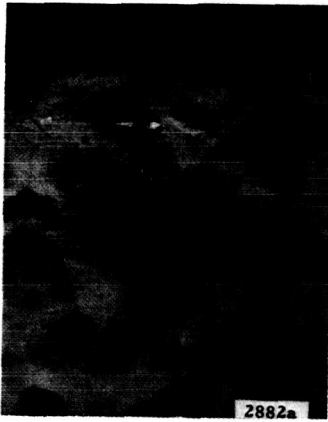
a.—*Compression—longitudinal* (*400*×).
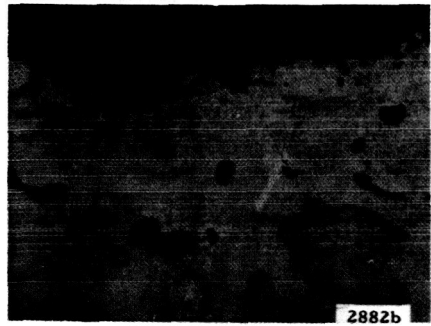
b.—*Compression—transverse* (*400*×).

c.—*Tension—transverse* (*400*×).

d.—*Tension—longitudinal* (*400*×).

FIGURE 17.—*Photomicrographs of cavitation damage area of tension and compression SAE 660 vibratory specimens.*

specimens tested under compressive load, while c and d are for a tensile specimen. In both stress modes the longitudinal pictures (a, d) show the microcracks from the area of the pit apex running vertically to the surface, and the transverse pictures (b, c) show the microcracks angled off from the pitted surface. None of these photos show slip lines, and there is no apparent difference between specimens tested under compressive or tensile load.

In figure 18, photos a and b show a copper specimen damaged with zero applied force, and photos c and d show a copper specimen damaged under
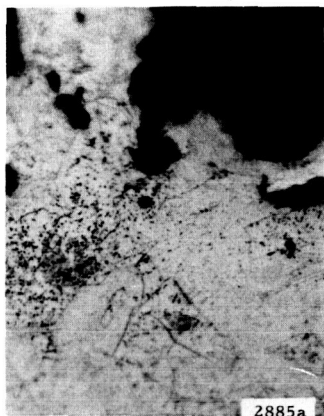
a.—*No force—transverse* (400×).

b.—*No force—longitudinal* (400×).
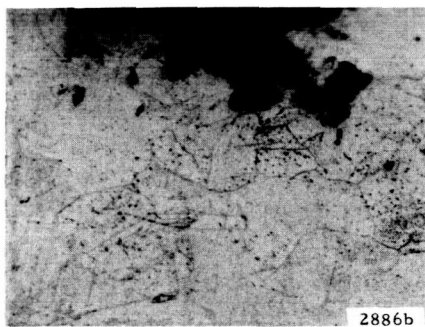
c.—*Tension—transverse* (400×).   d.—*Tension—longitudinal* (400×).

FIGURE 18.—*Photomicrographs of cavitation damage area of tension O.F.H.C. copper vibratory specimens* (400×).

tensile load. In a and b there appears to be no difference between the transverse direction (a) and the longitudinal direction (b). There are, however, a few small microcracks at or near the apex of the damage pits. There are no discernable slip lines in these photographs, perhaps indicating little or no work hardening of the damaged surface.

Photos c and d of figure 18 also show no slip lines. However, both the transverse (c) and longitudinal (d) directions show larger, more prominent microcracks emanating from the base of the damage pits. As for the SAE 660, the cracks in the longitudinal direction appear to come away from the pits at an angle almost perpendicular to the centerline of the pit.

Figure 19 shows both the transverse (a) and longitudinal (b) directions of a copper specimen cavitated in compression. Close examination of the photographs reveals a number of microcracks at the base of the damage pits. These seem to start at the apex of the pit and continue until they intersect a grain boundary, at which point they terminate. The longitudinal picture again shows the direction of the cracks to be perpendicular to the surface.

Photomicrographs for brass specimens (not shown) give results similar to those for copper. There were, in all cases, microcracks in the region of the damage pits, but no slip lines. The damage is thus accompanied by two possible effects: (1) microcracks emanating from the base of the damage pits and (2) cold work or strain-hardening, depending on the material just below the damage surface. There appears to be no difference in the number of microcracks or their appearance in specimens tested.

a.—*Transverse* ($400\times$).   b.—*Longitudinal* ($400\times$).

FIGURE 19.—*Photomicrographs of cavitation damage area of compression O.F.H.C. copper vibratory specimens.*

under compression, tension, or zero load for these relatively heavily damaged specimens. This is consistent with the previously stated finding that after the surface has been broken the effect of the externally applied compressive stress is diminished.

CONCLUSIONS

In the early portion of a test when the materials were subjected to an external compressive stress, a substantial decrease in the number density of small pits was found. In tests run under compression, there was little difference between the mercury facility and the vibratory facility. The application of a tensile load in both the mercury facility and the vibratory facility produced very little or no difference in the amount of damage compared to that incurred under zero load.

Photographic investigation of individual pits shows that they are approximately circular. Such photographs strengthen the hypothesis that these pits are caused by the impact of liquid microjets generated during bubble collapse rather than by spherical shock waves radiating from the center of collapse.

Photomicrographs of different materials indicate two manifestations of damage immediately beneath the surface: (1) microcracks emanating from the apex of the pit and (2) areas of cold work just adjacent to the pit, depending on the material used.

The effect of an externally applied compressive stress appears to diminish after the damage has initially disrupted the surface. This is apparent because little or no difference in the microstructure below the pits was seen for the different stress modes after substantial damage was incurred.

REFERENCES

1. KEMPPAINEN, D. J., AND F. G. HAMMITT, Effects of External Load on Cavitation Damage. *Proc. IAHR Symposium* (Kyoto, Japan), September 1969; also available as ORA Technical Report 01357–5–T, Mech. Eng. Dept., Michigan U.
2. KEMPPAINEN, D. J., *Prestress Conditioning and its Effects on Material Attrition in a Cavitating Environment.* Professional Engineering Degree dissertation, Nucl. Eng. Dept., Michigan U., June 1969; also available as ORA Technical Report 01357–7–T, Michigan U.
3. GARCIA, R., *Comprehensive Cavitation Damage Data for Water and Various Liquid Metals Including Correlations with Material and Fluid Properties.* Ph.D. dissertation, Nucl. Eng. Dept., Michigan U., August 1966; also available as ORA Technical Report 05031–6–T, Michigan U.
4. ROBINSON, M. J., *On the Detailed Flow Structure and Corresponding Damage to Test Specimens in a Cavitating Venturi.* Ph.D. dissertation, Nucl. Eng. Dept., Michigan U., August 1965; also available as ORA Technical Report 03424–16–T, Michigan U.

5. HAMMITT, F. G., AND D. J. KEMPPAINEN, Cavitating Flow Past Transverse Cylinder in Venturi Diffuser with Water and Mercury. *Proc. 3rd Conference on Hydraulics and Hydraulic Machinery* (Budapest, Hungary), September 1969, pp. 255–264.
6. NOELL, G. L., *Cavitation Sensitive Coating Evaluation.* Pratt and Whitney Aircraft-CANAL, Technical Memorandum No. 878, June 1965.
7. WOOD, G. M., R. S. KULP, AND J. V. ALTIERI, JR., Cavitation Damage Investigations in Mixed Flow Liquid Metal Pumps. Pratt and Whitney Aircraft-CANAL, *Proc. Symposium on Cavitation in Fluid Machinery,* Winter Annual Meeting ASME (Chicago), November 1965.
8. HAMMITT, F. G., J. F. LAFFERTY, R. CHEESEWRIGHT, M. T. PITEK, D. J. KEMPPAINEN, AND T. M. MITCHELL, Laboratory Scale Devices for Rain Erosion Simulation. *Proc. 2nd Meersburg Conference on Rain Erosion,* March 1967; also available as ORA Technical Report 08153–3–T, Nucl. Eng. Dept., Michigan U.

DISCUSSION

F. GILMAN (Worthington Corporation): I discovered a paper which was not referenced by the authors; the mechanism involved may not be very closely related, but the subject is the effect of shot peening the surface of metals in an attempt to improve cavitation resistance. The paper is by Nicholas Grossman and appeared in ASTM Bulletin No. 183 of July 1952. The end of the abstract states, "In the present study the effect of shot peening on the rate of cavitation damage is investigated. Two types of steel and one of brass were tested. It was found that the damage which was measured by rate of weight loss per unit time was decreased by shot peening. The amount of decrease varied from 7 to 58 percent for the different materials."

J. DUSSOURD (Ingersoll Rand): I have always been a little skeptical of the damage theory which is the result of the physical impact of high-velocity jets, and I tend to be in favor of also viewing the importance of the electrochemical effect. I would like to raise some questions concerning some of the data. For example, the last slides show no effect of work-hardening on the surface, but you show deep penetration of the damage inside the structure. It seems that this would suggest that there are some effects which are not necessarily mechanical in nature. One is prone to think that maybe some other effects are really more important than we may believe. Also, it is disturbing that there are many bubbles but very few make individual pits.

D. REEMSNYDER (NASA Lewis Research Center): Although this paper contains some interesting data on cavitation damage, the results are somewhat confusing.

It would be helpful if the authors would comment in more detail on the discrepancy between the effects of compressive stress on long-term damage results observed in this investigation and those observed in previous work (ref. 1). For the long-term vibratory specimens of this investigation, the cavitation damage resistance of both copper and aluminum decreased due to the impressed radially symmetric compressive stress. However, the long-term cavitation damage resistance increased for the materials of reference 1, and the *initial* damage rate of the aluminum specimens *only* increased from that of the nonstressed specimen in this investigation. Why is there a discrepancy in the initial damage

rates of aluminum and copper? Perhaps there are factors other than material and direction of applied stress that affect the cavitation-damage resistance of a material.

The paper indicates that a stationary-specimen vibratory cavitation test facility was utilized in this investigation. A cavitation field is induced on the oscillating exponential horn tip, and the transmission and collapse of this field on the stationary test specimen may be dependent on gap ($\sim$.018 in.), frequency, material, fluid, gas content, pressure level, and/or the distribution of the cavitation field. It would be of interest to have the authors comment on the comparison of cavitation damage results obtained from a stationary-specimen and an oscillating-specimen vibratory test facility.

HAMMITT (author): The authors would very much like to thank the various discussors for their interesting comments. Some of these are actually in the form of supplying additional interesting input, and no reply is required. Others raise issues too complex to be handled briefly. However, we will attempt to summarize our view on some of the issues raised.

We agree that there are no doubt factors other than material and applied stress which affect cavitation damage, and also that such damage is not entirely the result of mechanical effects. However, for the observations discussed in the paper, we believe that mechanical effects predominate. In the field, mechanical effects can be more or less dominant depending on their intensity and the corrosivity of the environment. The latter can certainly be very important in some cases.

The photomicrographs from the present paper showing effects apparently well below the surface are misleading because of their large magnification. Actually, the effects in these tests are concentrated very close to the surface. It has been indicated that sometimes labyrinthine-type damage is found after long exposure in field tests. We agree that corrosive effects may well be very important in these cases.

We also agree with Mr. Dussourd that there are many bubbles and only a few pits. We interpret this as an indication of the very complex chain of events required to make a collapse damaging, involving the correct combination of bubble size, wall distance, velocity and pressure profiles in the flow, etc., necessary to generate a microjet with the correct orientation and intensity. Further light is thrown on this subject by work recently completed in our laboratory (refs. D–1 and D–2).

We believe that in some cases the effects of applied stress on cavitation damage rates can be quite important, while in others they are not. However, this is a factor which should at least be considered, and it may in some cases be possible to significantly inhibit the onset of major cavitation damage in this way.

In the present vibration damage tests, we used the stationary-specimen arrangement because it made feasible the application of applied stress. We have also used this method, as have others, to test materials which by their nature are not suitable for the usual vibratory arrangement. The damage rate does depend on amplitude, frequency, and gap distance, as well as other parameters. For the frequency (20 kHz) and amplitude of our facility (2 mils), we have found that the damage rate peaks at about 18 mils gap distance and, hence, is relatively insensitive to gap distance in this range. There is insufficient data available to allow a meaningful comparison between material rankings obtained in this test and in the conventional vibratory test. There is no reason to believe that the rankings should be widely different except for the fact that, in past experience, almost any change in test parameters for any type of cavitation test has appeared to provoke relatively large differences in relative material damage rates.

REFERENCES

D-1. KLING, C. L., *A High-Speed Photographic Study of Cavitation Bubble Collapse.* Ph.D. dissertation, Nucl. Eng. Dept., Michigan U., 1969.
D-2. KLING, C. L., AHD F. G. KAMMITT, A Photographic Study of Spark-Induced Cavitation Bubble Collapse. *Trans. ASME, J. Basic Eng.*, 1971–1972.

Experimental Studies on Thermodynamic Effects of Developed Cavitation

ROBERT S. RUGGERI

NASA Lewis Research Center

A method for predicting thermodynamic effects of cavitation (changes in cavity pressure relative to stream vapor pressure) is presented. The prediction method accounts for changes in liquid, liquid temperature, flow velocity, and body scale. Both theoretical and experimental studies used in formulating the method are discussed. The prediction method provided good agreement between predicted and experimental results for geometrically scaled venturis handling four different liquids of widely diverse physical properties. Use of the method requires geometric similarity of the body and cavitated region and a known reference cavity-pressure depression at one operating condition.

Because cavitation is a vaporization process that involves heat and mass transfer, the physical properties of the liquid and its vapor and the flow conditions can affect the cavitation process and thus the cavitation performance of hydraulic equipment as well. These combined effects of fluid properties, flow conditions, and heat transfer—termed thermodynamic effects of cavitation—can improve cavitation performance. For example, cavitation studies with pumps and pump inducers (refs. 1 through 6) have shown that, for certain liquids and/or liquid temperature, the net positive suction head (NPSH) requirements can be significantly less than those for room-temperature water. This improvement in inlet pressure requirements is attributed to the varying degrees of evaporative cooling associated with the cavitation process. Because of cooling, the vapor pressure of the liquid adjacent to the cavity and the cavity pressure itself are decreased relative to the vapor pressure of the bulk liquid. This decrease in cavity pressure retards the rate of further vapor formation, thereby allowing lower inlet pressures than are otherwise possible. For a given cavity size at fixed flow conditions, a reduction in cavity pressure allows a corresponding reduction in the inlet pressure requirements. The accurate prediction of the thermodynamic effects of

cavitation is therefore essential to an optimum system designed to operate with cavitation.

The objective of this paper is to summarize the results obtained from theoretical and supporting experimental venturi cavitation studies (refs. 7 through 11) which led to the formulation of a method for predicting thermodynamic effects of cavitation. The method was motivated by, but is an extension of, the B-factor concept of Stahl and Stepanoff (ref. 12). The prediction method accounts for changes in liquid, temperature, flow velocity, and scale. The cavitation data were obtained for Freon-114, liquid hydrogen, liquid nitrogen, and water using two accurately scaled venturis (1.0 and 0.7 scale) as test devices. The liquid hydrogen data were obtained from a NASA-sponsored study conducted at the National Bureau of Standards (ref. 11). The data for the other liquids (refs. 7 through 10) were obtained at the NASA Lewis Research Center.

ANALYTICAL REVIEW

Thermodynamic Effects of Cavitation

Heat is required to generate the vapor within a cavitated region, and this heat of vaporization must be drawn from the surrounding liquid. If the time available for vaporization is short, as is usually the case for flowing systems, the liquid which supplies the heat for vaporization consists of a relatively thin film of liquid adjacent to the cavity. Cooling of this film causes the vapor pressure of both the liquid film and the vaporous cavity to drop from that of the bulk liquid to that corresponding to the reduced local temperature. For a cavity of given size with fixed flow conditions, a reduction in cavity pressure allows a corresponding reduction in the inlet pressure requirements. Thus the inlet pressure requirement for a particular flow device handling liquids which exhibit significant drops in cavity pressure is less than that for liquids which do not exhibit this beneficial effect. In general, cavity-pressure and temperature depressions (thermodynamic effects of cavitation) are a function of fluid properties as well as the body geometry, the flow velocity, and the complex heat and mass transfer mechanisms involved.

Heat Balance

The magnitude of cavity-pressure depression can be estimated by setting up (as an initial step) a heat balance between the heat required for vaporization and the heat drawn from the liquid surrounding the cavity; that is,

$$\rho_v \nu_v L = \rho_l \nu_l c_l (\Delta T) \tag{1}$$

where ν_l represents the volume of the thin layer of liquid that is cooled

during vaporization. Although applied to cavitation in a flowing system herein, the energy balance (eq. (1)) is equivalent to a static model of a simple insulated cylinder-piston model (ref. 13). A given mass of liquid fills the cylinder. With an increase in total volume, achieved by lifting the piston, some of the liquid is vaporized. The heat required to form the vapor that fills the resulting increased volume must be drawn from the remaining liquid, thereby lowering the temperature by some amount ΔT. The primary assumptions associated with the heat balance (eq. (1)) are discussed in reference 8.

By expressing the temperature drop ΔT (eq. (1)) in terms of a vapor-pressure drop Δh_v, through use of the vapor-pressure temperature relations, equation (1) may be expressed in the form

$$\Delta h_v = \frac{\rho_v}{\rho_l} \frac{\nu_v}{\nu_l} \frac{L}{c_l} \left(\frac{dh_v}{dT} \right)$$

(2)

where dh_v/dT is the slope of the vapor-pressure/temperature curve at the temperature of interest. All the terms in equation (2) are fluid properties and are known except the vapor- to liquid-volume ratio ν_v/ν_l. In the experimental case the absolute value of volume ratio cannot be directly determined because ν_l is only that volume of liquid actually involved in the vaporization process. Thus ν_l is only a fraction of the entire liquid stream. However, as shown in equation (2), the parameter Δh_v can be expressed as a function of ν_v/ν_l for any liquid whose fluid properties are known. To account for changes in fluid properties as the temperature decreases due to vaporization, equation (2) may be solved (in terms of Δh_v versus ν_v/ν_l) in incremental form. That is, suitably small increments of Δh_v are assumed, and the results from successive steps are summed to yield ν_v/ν_l. Results obtained in this manner for water, liquid nitrogen, Freon-114, and liquid hydrogen at various initial fluid temperatures are presented in figure 1. The nonlinearity of the curves is due to the change in fluid properties as the equilibrium temperature drops due to vaporization.

For a given value of ν_v/ν_l, the depression in cavity pressure can vary by several orders of magnitude depending on liquid and liquid temperature.

By using the Clasius-Clapeyron equation to approximate the slope of the vapor-pressure/temperature curve, the following useful approximation of equation (2)—and thus the curves of figure 1—is obtained:

$$\Delta h_v \cong J \left(\frac{\rho_v}{\rho_l} \right)^2 \left(\frac{L^2}{c_l T} \right) \left(\frac{\nu_v}{\nu_l} \right)$$

(3)

This expression provides a useful and close approximation of the curves presented in figure 1.

a.—*Water, liquid nitrogen, and Freon-114.*
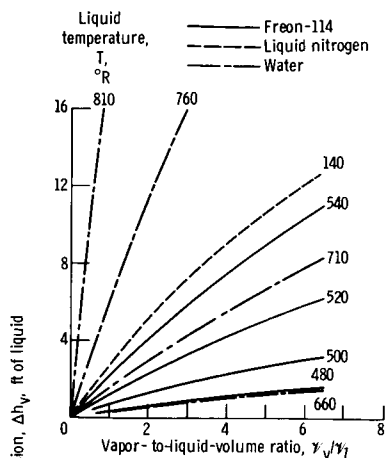
b.—*Liquid hydrogen.*
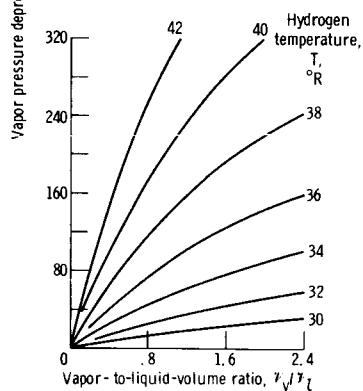
FIGURE 1.—*Vapor pressure depressions for various liquids and liquid temperatures.*

As previously discussed, the vapor-to-liquid-volume ratio ν_v/ν_l in any real flow situation is not known and cannot be measured directly. Thus values of the ν_v/ν_l ratio from figure 1 are used only in a relative sense. However, useful predictions for geometrically similar cavities may be made as follows. By experiment, an effective or reference value of ν_v/ν_l is established through the determination of cavity-pressure depressions Δh_v for one flow devic :, liquid, temperature, and velocity. Then values of ν_v/ν_l for other geometrically similar flow devices, liquids, liquid temperatures, and flow velocities may be estimated relative to this reference value, as described subsequently. With these predicted values of ν_v/ν_l and figure 1, determination of Δh_v relative to reference data is possible.

Estimation of Vapor-to-Liquid Volume Ratio

In the overall systematic study of thermodynamic effects of cavitation, several theoretical analyses for estimating vapor-to-liquid-volume ratio

were made. However, in the interest of brevity, only the pertinent relations and a short discussion of these analyses is presented. Details of the various derivations are presented in the references cited.

The theoretical analysis of reference 8 shows that for one body scale, the vapor-to-liquid-volume ratio v_v/v_l can be predicted for changes in the liquid used, the temperature, the velocity, and the cavity length, provided that a reference value of v_v/v_l is known. Subsequently this study was extended to include the effects of geometric scaling (ref. 9). The combined results from references 8 and 9 led to the following general equation (see ref. 10) for predicting the vapor-to-liquid-volume ratio, relative to a reference value, for changes in liquid, liquid temperature, flow velocity, and model scale:

$$\left(\frac{v_v}{v_l}\right)_{\text{pred}} = \left(\frac{v_v}{v_l}\right)_{\text{ref}} \left(\frac{\alpha_{\text{ref}}}{\alpha}\right)^m \left(\frac{V_0}{V_{0,\text{ref}}}\right)^n \left(\frac{D}{D_{\text{ref}}}\right)^{1-n} \left[\frac{(\Delta x/D)_{\text{ref}}}{\Delta x/D}\right]^p \qquad (4)$$

where α is thermal diffusivity, V_0 is free-stream velocity, D is diameter, and Δx is the axial length of the cavitated region. The exponents m, n, and p depend, at least in part, on the heat transfer process involved and must be determined by experiment. The derivation and use of equation (4) requires, first, that geometric similarity of cavitating flow is maintained for various liquids and flow conditions and, second, that thermodynamic equilibrium conditions exist within the cavitated region. At present, these two requirements can only be assumed for untested liquids.

EXPERIMENTAL VENTURI STUDIES

In order to determine the exponents for the theoretically derived equation (4), it was necessary to conduct cavitation studies in such a way that the temperatures and pressures within cavitated regions of various liquids could be measured directly. Accurately scaled venturis (1.0 and 0.7 scale) were used as test flow devices. In order to provide a wide range of physical properties, Freon-114, liquid hydrogen, liquid nitrogen, and water were used as test fluids. The fluids were studied over a range of approach flow velocities (100 to >200 ft/sec for liquid hydrogen and ~19-50 ft/sec for the other liquids).

Venturis

The venturis, made of transparent acrylic plastic, incorporated a circular arc contour to provide convergence from the approach section to a constant-diameter throat section (fig. 2). The throat section is followed by a conical diffuser. The venturi with the 1.743-inch approach-section diameter is referred to herein as the 1.0-scale venturi, and that

FIGURE 2.—*Venturi test sections (all dimensions in inches).*
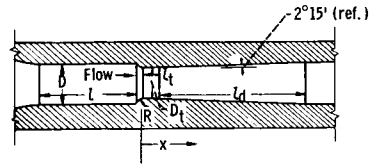
	Venturi scale	
	1.0	0.7
Free-stream diameter, D	1.743	1.232
Throat diameter, D_t	1.377	0.976
Radius of curvature, R	0.183	0.128
Approach-section length, l	4.198	2.964
Throat length, l_t	0.75	0.52
Diffuser length, l_d	4.66	3.26

with the 1.232-inch approach section diameter is referred to as the 0.7-scale venturi. Detailed descriptions of the venturis are given in references 7 through 9. The venturis were mounted either in a small, closed-return hydrodynamic tunnel of 10-gallon capacity (NASA facility, ref. 7) or in an NBS liquid hydrogen blowdown test facility (ref. 11) with the 0.7-scale venturi located between 265-gallon supply and receiver dewars.

The noncavitating wall-pressure distribution for the venturis is presented in figure 3. As stream pressure was lowered, cavitation occurred first at the point of minimum pressure located on the circular arc portion of the venturi. The cavity's leading edge was visually observed to remain fixed at the minimum pressure location for all cavitating conditions studied.
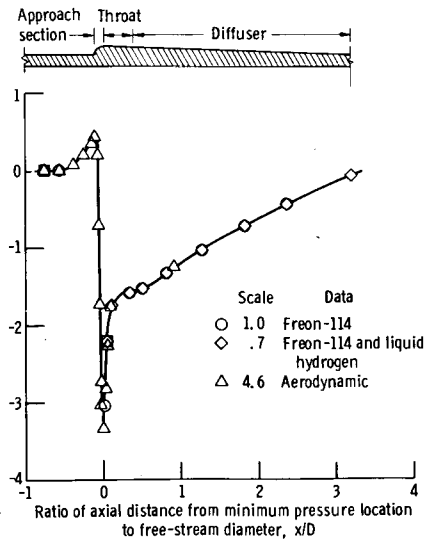

FIGURE 3.—*Wall pressure distribution for venturis.*

Appearance of Developed Cavitation

Photographs showing typical developed cavitation for Freon-114 and liquid hydrogen are presented in figure 4. Although the vapor formation in hydrogen was more homogeneous, the appearance of cavitation for these fluids was similar; that is, the cavities exhibit a uniform peripheral development with the leading edge at a fixed location. Because of this similarity in cavitating flow (a prerequisite in the analysis), the data obtained for both hydrogen and Freon-114 are considered equally valid for determining the exponents in the theoretical prediction equation. Temperatures and pressures within the relatively thin annulus of vapor formed (estimated thickness less than 0.03 inch in the throat) were measured simultaneously by pressure taps and calibrated thermocouples located on the adjacent wall.

RESULTS AND DISCUSSION

Specific trends in temperature and pressure depressions within cavitated regions of Freon-114 and liquid hydrogen are discussed first. Exponents in the theoretical prediction equation are then determined, and, finally, the significance of a developed cavitation similarity parameter $K_{c,min}$ is discussed.

Typical Cavity Pressure and Temperature Distribution

A plot showing typical variations in pressure and temperature depressions within a constant-length cavity (Freon-114) is shown in figure 5. Cavity-pressure depression is presented as a function of x/D measured from the minimum pressure location determined with noncavitating flow. The data are for a cavity length of about 2.75 inches (comparable to that shown in fig. 4d) and a constant approach velocity of 31.8 feet per second. All pressures within the cavitated region are less than vapor pressure based on the free-stream temperature (represented by $\Delta h_v = 0$). The maximum measured cavity-pressure depression always occurred at or near the cavity's leading edge. The point at which the cavity pressure equals the vapor pressure of the bulk liquid ($\Delta h_v = 0$) coincides with the collapse region of cavitation. The open symbols represent cavity pressures measured directly, whereas the solid symbols represent the fluid vapor pressure corresponding to the locally measured temperature. The figures adjacent to the solid symbols represent measured reductions in local cavity temperature below the free-stream temperature. The good agreement between the measured pressures and the vapor pressures based on measured temperature indicate that, for engineering purposes, thermodynamic equilibrium conditions can be assumed to exist within the cavity.

a.—*Liquid hydrogen in 0.7-scale venturi; nominal cavity length, 1.0 freestream diameter.*
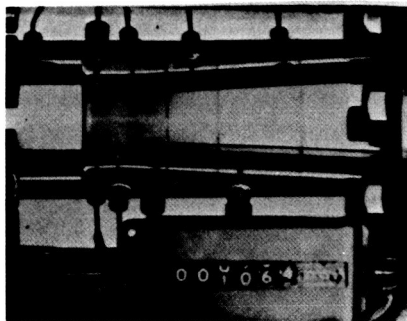
b.—*Liquid hydrogen in 0.7-scale venturi; nominal cavity length, 1.6 freestream diameters.*
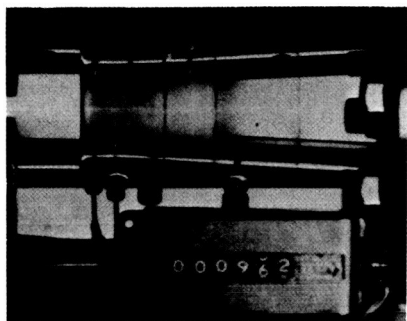
c.—*Freon-114 in 0.7-scale venturi; nominal cavity length, 1.4 freestream diameters.*
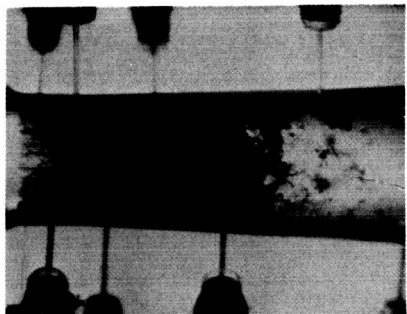
d.—*Freon-114 in 1.0-scale venturi; nominal cavity length, 1.5 freestream diameters.*
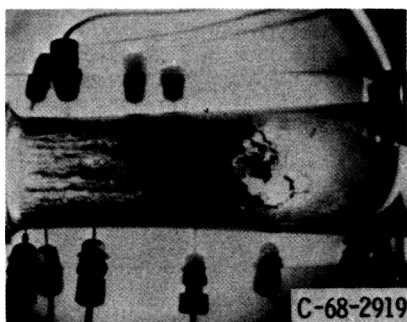
FIGURE 4.—*Typical cavitation in venturis.*

Open symbols denote measured pressure
depression
Solid symbols denote vapor pressure
depression at measured temper-
ature depression
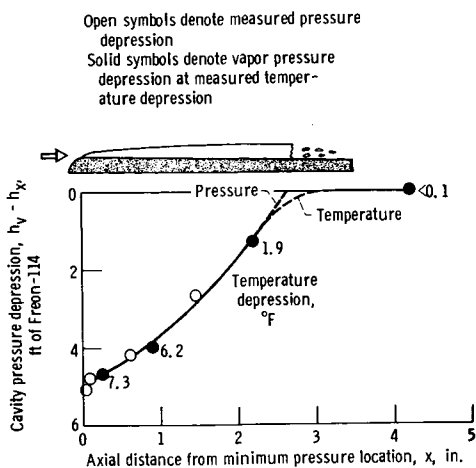
FIGURE 5.—*Typical pressure and temperature depressions within cavitated region. Freon-114; 1.0-scale venturi; velocity, 31.8 feet per second; temperature, 519.1° R.*

Also, the studies showed that for fixed flow conditions and geometrically similar cavities, a change in the maximum cavity depression resulted in an equal change in the inlet pressure requirement (NPSH). This occurred for all liquids and temperatures studied.

Effects of Temperature, Flow Velocity, Cavity Length, and Scale

An increase in bulk liquid temperature caused an increase in cavity-pressure depression along the entire cavity length as illustrated in figure 6. For the conditions shown, the maximum cavity depression is about 8.5 feet of Freon-114 ($\sim$5.5 psi) at 538.8° R, which is about 1.7 times that at 519° R and 4.6 times that at 467.5° R. This trend with temperature was observed for all test liquids at each flow velocity studied. However, for water, over the 500° R to 580° R temperature range studied, the cavity-pressure drop was so small as to be negligible.

An increase in free-stream velocity caused an increase in cavity-pressure depressions. Some typical results are presented in figure 7. As velocity was increased from 22.9 to 44.5 feet per second, the maximum cavity depression increased from about 6.6 feet of Freon-114 to about 11.0 feet.

As cavity length was increased, the cavity-pressure depression increased over the full axial length of the cavity, as illustrated by the liquid hydrogen data (0.7-scale venturi) presented in figure 8. The trend shown is typical for the other liquids tested. For the conditions studied, the measured cavity-pressure depressions for hydrogen were about 50 to 100 times greater (in feet of liquid) than those for Freon-114. Maximum

FIGURE 6.—*Effect of free-stream liquid temperature on cavity pressure and temperature depressions. Freon-114, 1.0-scale venturi; nominal cavity length, 2.75-inches.*
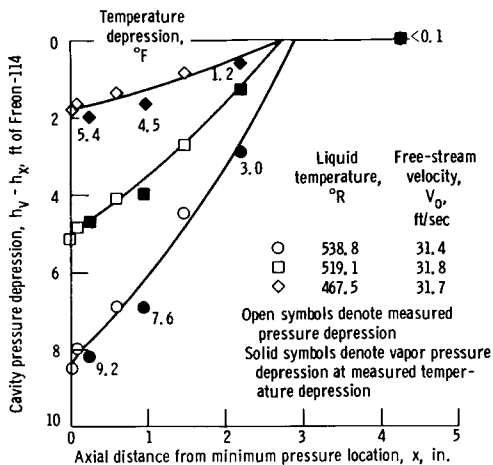

FIGURE 7.—*Effect of free-stream velocity on pressure and temperature depressions within cavitated regions of Freon-114. Venturi scale, 0.7; liquid temperature, 540° R; nominal cavity length, 1.6 inches.*
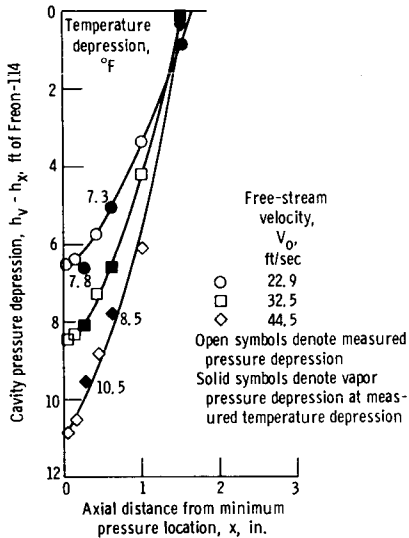
depressions reached as much as 580 feet of hydrogen at the higher free-stream velocities and temperatures studied, compared to about 11 feet for Freon-114.

For geometrically similar cavities ($\Delta x/D = \text{const}$), cavity-pressure depressions over the entire length of the cavity are little affected by model scale, at least for the modest range tested. This is illustrated in figure 9, where Freon-114 data obtained in both the 0.7- and 1.0-scale venturis are compared. Cavity-pressure depression is plotted as a function of the ratio of axial distance to free-stream diameter.
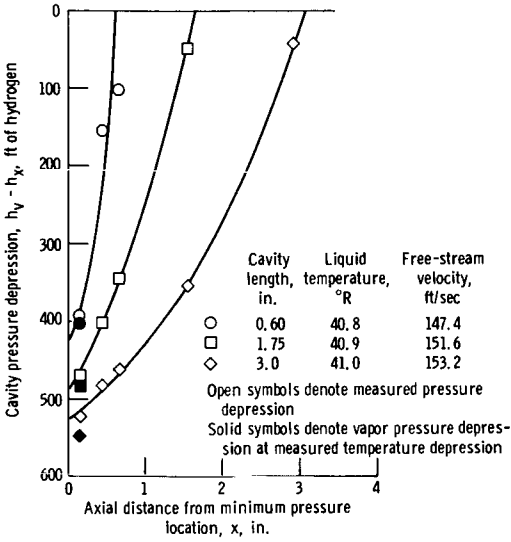
FIGURE 8.—*Effect of cavity length on cavity pressure depression. Liquid hydrogen;   0.7-scale venturi.*

Cavity length, in.	Liquid temperature, °R	Free-stream velocity, ft/sec
○ 0.60	40.8	147.4
□ 1.75	40.9	151.6
◇ 3.0	41.0	153.2

Open symbols denote measured pressure depression
Solid symbols denote vapor pressure depression at measured temperature depression

Axial distance from minimum pressure location, x, in.
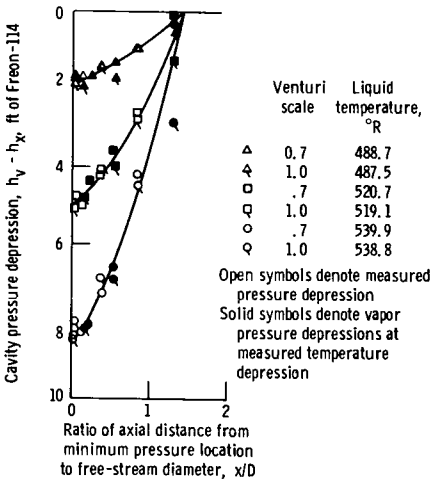
FIGURE 9.—*Effect of venturi scale on pressure and temperature depressions within cavitated regions of Freon-114. Cavity length, 1.4 free-stream diameters.*

Venturi scale	Liquid temperature, °R
△ 0.7	488.7
◬ 1.0	487.5
□ .7	520.7
◩ 1.0	519.1
○ .7	539.9
◔ 1.0	538.8

Open symbols denote measured pressure depression
Solid symbols denote vapor pressure depressions at measured temperature depression

Ratio of axial distance from minimum pressure location to free-stream diameter, x/D

DETERMINATION OF EXPONENTS IN PREDICTION EQUATION

In all instances the maximum measured cavity-pressure depressions were used to determine the exponents for the equation for prediction of vapor-to-liquid-volume ratio ν_v/ν_l (eq. (4)). The Freon-114 data (for both the 1.0- and 0.7-scale venturis) and the hydrogen data (0.7-scale venturi) were used in conjunction with the method of least squares to

solve for all the exponents simultaneously. More than 100 data points were used. The resulting expression with the experimentally determined exponents is

$$\left(\frac{\nu_v}{\nu_l}\right)_{\text{pred}} = \left(\frac{\nu_v}{\nu_l}\right)_{\text{ref}} \left(\frac{\alpha_{\text{ref}}}{\alpha}\right)^{1.0} \left(\frac{V_0}{V_{0,\text{ref}}}\right)^{0.8} \left(\frac{D}{D_{\text{ref}}}\right)^{0.2} \left[\frac{\Delta x/D}{(\Delta x/D)_{\text{ref}}}\right]^{0.3} \quad (5)$$

The exponent for the diameter-ratio term presently comes via theory from the exponent n of the velocity-ratio term (see eq. (4)). Thus additional cavitation studies which use other scale factors are needed to further substantiate the exponent for D/D_{ref}.

From a measured value of Δh_v in a model of given scale, the volume ratio $(\nu_v/\nu_l)_{\text{ref}}$ can be determined from figure 1 (or eq. (2)). Equation (5) can then be used to determine $(\nu_v/\nu_l)_{\text{pred}}$ for the liquid, temperature, velocity, and scale of interest. With this value of $(\nu_v/\nu_l)_{\text{pred}}$, figure 1 can be used again to predict the corresponding value of Δh_v. For the present, equation (5), with the experimentally determined exponents, is offered as the best approach toward generalizing results for different scaled venturis, different liquids and liquid temperatures, and various velocities.

COMPARISON OF PREDICTED AND EXPERIMENTAL RESULTS

The agreement to be expected between experimental and predicted results is presented in figure 10. The complete test range of Δh_v values is presented in figure 10a, which emphasizes liquid-hydrogen data. The low range of values is presented in figure 10b. All points shown in figure 10 are based on a single reference point represented by the solid symbol. The reference value was obtained with 538° R Freon-114 in the 1.0-scale venturi at a free-stream velocity of 19.6 feet per second. The cavity length, $\Delta x/D$, was 0.72. The measured Δh_v was 5.0 feet of Freon-114, and thus the value of $(\nu_v/\nu_l)_{\text{ref}}$ (from fig. 1) was 2.6. Predicted values of ν_v/ν_l were then calculated from equation (5). All predicted Δh_v-values appear to be quite good, considering that predicted values of up to 600 feet of liquid (at $V_0 > 200$ ft/sec), were based on a single reference value of only 5.0 feet at 19.6 feet per second.

It is concluded that the simple static model analysis with experimentally determined exponents provides reasonably good predictions over a wide range of fluid properties and flow conditions, provided that (1) the maximum cavity-pressure depression is known for at least one operating condition, (2) similarity of cavitating flow is maintained, and (3) local equilibrium of temperature and pressure exists at the vapor/liquid interface.
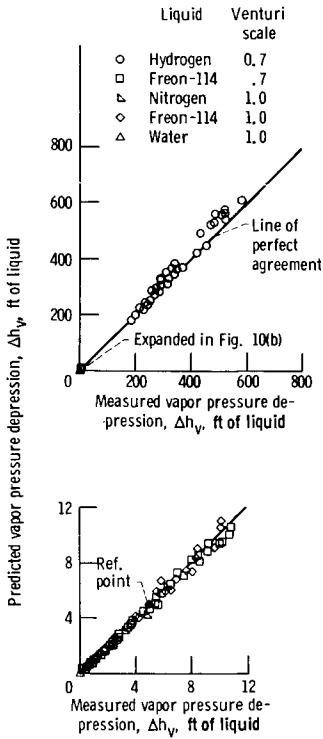
a.—*Complete range of vapor-pressure depressions.*

b.—*Low range of vapor-pressure depressions.*

FIGURE 10.—*Comparisons of measured and predicted vapor-pressure depressions.*

CAVITATION SIMILARITY PARAMETERS

The conventional cavitation parameter is usually expressed as

$$K_v \equiv \frac{h_0 - h_v}{V_0^2/2g} \tag{6}$$

The parameter K_v for developed cavitation is derived from the assumption that Bernoulli's equation for steady ideal flow applies between a free-stream location and the cavity surface and that the cavity surface is at a constant pressure equal to free-stream vapor pressure. However, because of the previously discussed thermodynamic effects of cavitation, the cavity pressure can be significantly less than free-stream vapor pressure and can also vary with axial distance. Thus, a more general expression for the cavitation parameter would have h_v in equation (6) replaced with a more appropriate reference pressure in the cavity. As in references 8 through 10, the maximum cavity-pressure depression is selected as the reference pressure to define the following developed cavitation parameter:

$$K_{c,\min}=\frac{h_0-h_{c,\min}}{V_0^2/2g}=\frac{h_0-h_v}{V_0^2/2g}+\frac{(\Delta h_v)_{\max}}{V_0^2/2g}=K_v+\frac{(\Delta h_v)_{\max}}{V_0^2/2g} \qquad (7)$$

The venturi cavitation studies show that $K_{c,\min}$ is approximately constant over the range of liquids, temperatures, velocities, and venturi scales tested, provided that the geometric similarity of the cavitated region is maintained. The value of K_v however, varied widely.

The degree to which a constant value can be used to represent $K_{c,\min}$ is shown graphically in figure 11, where the numerator of $K_{c,\min}$ is plotted as a function of its denominator. The line shown is for a $K_{c,\min}$ of 2.47. The good agreement between the data and the line indicates that a single $K_{c,\min}$ value of 2.47 can be utilized to represent all the hydrogen and Freon-114 data. This $K_{c,\min}$ value of 2.47 also applies quite well for liquid nitrogen and water. As previously stated, the cavity-pressure depressions for water were practically negligible; thus, the values of $K_{c,\min}$ and the conventional cavitation parameter K_v were essentially the same for the range of water temperatures studied. Although the value of $K_{c,\min}$ remained constant for different cavity lengths, it is possible that for other venturi shapes $K_{c,\min}$ will vary with cavity length.

Prediction of Free-Stream Pressure Requirements

For constant values of $K_{c,\min}$ and V_0 in equation (7), a change in $(\Delta h_v)_{\max}$ results in a corresponding change in h_0-h_v. This pressure
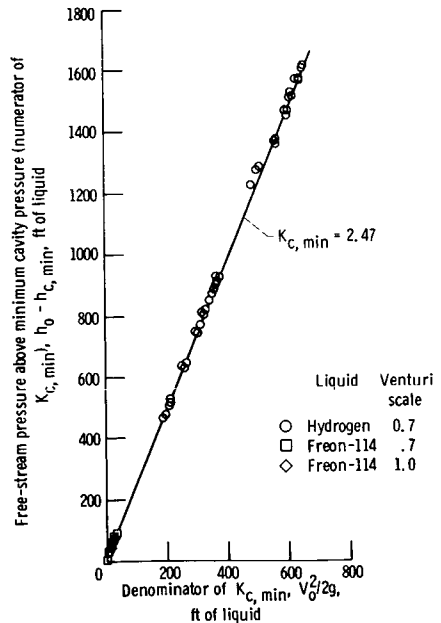
FIGURE 11.—*Effects of venturi scale and liquid on minimum pressure of cavitated region. Various cavity lengths,* $\Delta x/D$.

difference $h_0 - h_v$ is a measure of free-stream pressure requirements to obtain geometrically similar cavities and includes the thermodynamic effects of cavitation. Thus, for the wide range of conditions for which $K_{c,min}$ is constant, it is a most useful cavitation similarity parameter. When at least one value of $(\Delta h_v)_{max}$ (or $h_{c,min}$) is known and used as the reference value for predicting other values of $(\Delta h_v)_{max}$, as previously discussed, the free-stream pressure requirements h_0 for untested conditions can be predicted by equation (7). This equation can be rearranged so that

$$h_0 = \frac{V_0{}^2}{2g} (K_{c,min}) + h_v - (h_v - h_{c,min}) \qquad (8)$$

where $h_v - h_{c,min} = \Delta h_{v_{max}}$.

In the present study the reference value of Δh_v, needed for prediction purposes, was measured directly. However, because $K_{c,min}$ remains constant with geometric similarity of body and cavitated region, it is possible to estimate $(\Delta h_v)_{max=ref}$ without measuring cavity pressure directly. In a given flow device, two different tests are made in which the free-stream pressure requirements $(h_0 - h_v)$ to obtain geometrically similar cavitated regions are measured. These tests need not be for the same liquid, temperature, velocity, or model scale; however, at least one of these tests must yield measurable thermodynamic effects of cavitation $(\Delta h_v > 0)$. From these measured free-stream pressure requirements, it is possible to determine a $(\Delta h_v)_{ref}$ value using an iterative process as described in reference 14.

CONCLUDING REMARKS

A method for predicting thermodynamic effects of developed cavitation in venturis, or other flow devices, has been developed. The prediction method, formulated from simple theoretical analyses and supporting experimental cavitation studies, provided good agreement between predicted and experimental results for geometrically scaled venturis handling liquids of widely diverse physical properties. The prediction method accounts for changes in liquid, liquid temperature, flow velocity, cavity length, and model scale, provided that similarity of the cavitating flow is maintained.

The method requires a known reference value of the maximum cavity-pressure depression at one operating condition, obtained either by direct measurement or from two appropriate tests wherein stream static pressure is measured under conditions of similarity of the cavitating flow. These latter test data need not necessarily be for the same liquid, temperature, velocity, or model scale.

Although the present study is limited to venturis, the basic prediction method has been applied successfully to the prediction of cavitation performance for devices such as pumps and inducers (see ref. 14).

LIST OF SYMBOLS

C_p	noncavitating wall-pressure coefficient, $(h_x - h_0)/(V_0^2/2g)$
c_l	specific heat of liquid, Btu/(lb mass)(°R)
D	free-stream diameter (approach section, fig. 2), in.
g	acceleration due to gravity, 32.2 ft/sec²
$h_{c,min}$	minimum measured pressure in cavitated region, ft of liquid abs
h_v	vapor pressure corresponding to free-stream or bulk liquid temperature, ft of liquid abs
Δh_v	decrease in vapor pressure corresponding to decrease in liquid temperature, ft of liquid
h_x	static pressure at x, ft of liquid abs
h_0	free-stream static pressure (approach section, fig. 2), ft of liquid abs
J	mechanical equivalent of heat, 778 (ft)(lb force)/Btu
$K_{c,min}$	developed cavitation parameter based on minimum cavity pressure, $(h_0 - h_{c,min})/(V_0^2/2g)$
K_v	developed cavitation parameter based on free-stream vapor pressure, $(h_0 - h_v)/(V_0^2/2g)$
k	thermal conductivity of saturated liquid, Btu/(ft)(hr)(°R)
L	latent heat of vaporization, Btu/(lb mass)
NPSH	net positive suction head, ft of liquid
T	liquid temperature, °R
ΔT	decrease in local equilibrium temperature due to vaporization, °R
V_0	free-stream velocity (approach section, fig. 2), ft/sec
ν_l	volume of saturated liquid, cu ft
ν_v	volume of saturated vapor, cu ft
x	axial distance from minimum noncavitating pressure location (also cavity's leading edge) (fig. 2), in.
Δx	length of cavitated region, in.
α	thermal diffusivity, $k/(\rho_l c_l)$, (sq ft)/hr
ρ_l	saturated liquid density, (lb mass)/(cu ft)
ρ_v	saturated vapor density, (lb mass)/(cu ft)

Subscripts

max	maximum
min	minimum
pred	predicted
ref	reference value obtained by experiment

Superscripts

m, n, p exponents (see eq. (4))

REFERENCES

1. SALEMANN, VICTOR, Cavitation and NPSH Requirements of Various Liquids. *J. Basic Eng.*, Vol. 81, No. 2, June 1959, pp. 167–180.
2. SPRAKER, W. A., The Effects of Fluid Properties on Cavitation in Centrifugal Pumps. *J. Eng. Power*, Vol. 87, No. 3, July 1965, pp. 309–318.
3. STEPANOFF, A. J., Cavitation Properties of Liquids. *J. Eng. Power*, Vol. 86, No. 2, April 1964, pp. 195–200.
4. MENG, PHILLIP R., *Change in Inducer Net Positive Suction Head Requirement with Flow Coefficient in Low Temperature Hydrogen (27.9° to 36.6° R)*. NASA TN D–4423, 1968.
5. MOORE, ROYCE D., AND PHILLIP R. MENG, *Cavitation Performance of Line-Mounted 80.6° Helical Inducer in Hydrogen*. NASA TM X–1854, 1969.
6. MENG, PHILLIP R., AND ROBERT E. CONNELLY, *Investigations of Effects of Simulated Nuclear Radiation Heating on Inducer Performance in Liquid Hydrogen*. NASA TM X–1359, 1967.
7. RUGGERI, ROBERT S., AND THOMAS F. GELDER, *Cavitation and Effective Liquid Tension of Nitrogen in a Tunnel Venturi*. NASA TN D–2088, 1964.
8. GELDER, THOMAS F., ROBERT S. RUGGERI, AND ROYCE D. MOORE, *Cavitation Similarity Considerations Based on Measured Pressure and Temperature Depressions in Cavitated Regions of Freon–114*. NASA TN D–3509, 1966.
9. MOORE, ROYCE D., AND ROBERT S. RUGGERI, *Venturi Scaling Studies on Thermodynamic Effects of Developed Cavitation of Freon–114*. NASA TN D–4387, 1968.
10. MOORE, ROYCE D., AND ROBERT S. RUGGERI, *Prediction of Thermodynamic Effects of Developed Cavitation Based on Liquid-Hydrogen and Freon–114 Data in Scaled Venturis*. NASA TN D–4899, 1968.
11. HORD, JESSE, DEAN K. EDMONDS, AND DAVID R. MILLHISER, *Thermodynamic Depressions within Cavities and Cavitation Inception in Liquid Hydrogen and Liquid Nitrogen*. Report 9705, National Bureau of Standards (NASA CR–72286), March 1968.
12. STAHL, H. A., AND A. J. STEPANOFF, Thermodynamic Aspects of Cavitation in Centrifugal Pumps. *Trans. ASME*, Vol. 78, No. 8, November 1956, pp. 1691–1693.
13. HOLLANDER, A., Thermodynamic Aspects of Cavitation in Centrifugal Pumps. *ARS J.*, Vol. 32, No. 10, October 1962, pp. 1594–1595.
14. RUGGERI, ROBERT S., AND ROYCE D. MOORE, *Method for Prediction of Pump Cavitation Performance for Various Liquids, Liquid Temperatures, and Rotative Speeds*. NASA TN D–5292, 1969.

DISCUSSION

J. HORD (National Bureau of Standards): The author and his co-workers are to be commended for extending the B-factor[1] theory and synthesizing previous efforts (refs. 1, 2, 12, D–1, D–2) to develop a practical and effective solution to a complex and difficult problem. The "quasi-static" theory upon which the solution is based is amazingly simple, and one cannot help but wonder why it works so well (ref. 14); nevertheless, it must be concluded that the solution, though simplified, contains the significant groups of dimensionless parameters. A current research program (ref. D–3) is endeavoring to upgrade the thermostatic approach outlined in this paper and account for dynamic effects via entrainment theory. Test results from this program indicate that $K_{c,\min}$ for a zero-caliber ogive varies with cavity length as suspected by Ruggeri.

I feel that the author should warn the reader that equation (3) may be a rather crude expression for relating Δh_v and B when the fluid properties vary appreciably with temperature; as evidenced by the nonlinearity of the curves in figure 1b, this is particularly true for liquid hydrogen. Solution of equation (2) in incremental form as outlined by the author in reference 8 is more appropriate for general use. Still a more direct approach for computing B-factor is given below: Hollander (ref. 13) showed that various B-factor solutions (refs. 12, D–1, D–2) were equivalent and could be represented by a "quasi-static" model; this model features a unit mass of liquid confined in an insulated cylinder with a nonleaking piston. When the piston is lifted, we will assume that the fluid undergoes an isentropic expansion. The mass-entropy balance may be written

$$m_1 s_1 = m_{f2} s_{f2} + m_{v2} s_{v2} \tag{D–1}$$

and conservation of mass requires that

$$m_1 = m_{f2} + m_{v2} \tag{D–2}$$

Combining equations (D–1) and (D–2) and multiplying the result by ρ_{f2}/ρ_{v2}, we obtain

$$B = \left(\frac{\rho_{f2}}{\rho_{v2}}\right)\left(\frac{m_{v2}}{m_{f2}}\right) = \left(\frac{\rho_{f2}}{\rho_{v2}}\right)\left(\frac{s_1 - s_{f2}}{s_{v2} - s_1}\right) \tag{D–3}$$

---

[1] $B = V_v/V_l$

where

m_1 = initial mass of liquid

m_{f2} = mass of saturated liquid at final pressure

m_{v2} = mass of saturated vapor at final pressure

s_1 = specific entropy of saturated liquid at initial pressure

s_{f2} = specific entropy of saturated liquid at final pressure

s_{v2} = specific entropy of saturated vapor at final pressure

ρ_{f2} = density of saturated liquid at final pressure

ρ_{v2} = density of saturated vapor at final pressure

This result does not depend on summation of incremental steps to account for changing fluid properties, vaporization of liquid, recondensation of vapor, and so on. The results are as accurate as the fluid P-V-T data; charts, tables, etc., may easily be developed from appropriate equations of state or tabulated thermodynamic properties.

The author emphasizes that local thermodynamic equilibrium within the cavitated region is a prerequisite for application of the B-factor theory. The "quasi-static" model requires only that thermodynamic equilibrium prevail during the vaporization process; consequently, only the *leading edge* of the developed cavity must be in thermodynamic equilibrium. The central and trailing edges of the cavity, where condensation occurs, may not be in stable thermodynamic equilibrium. Recent experiments at NBS with the 0.7-scale venturi substantiate metastability in the central and aft regions of vaporous hydrogen cavities. The experimentally determined exponents in equation (5) are based on pressures measured within the cavity near the leading edge, where equilibrium prevailed in all fluids tested. It appears that the experimental conditions under which the exponents were determined are compatible with the thermostatic theory, and local equilibrium *throughout* the cavitated region is not required. It also appears plausible that exponents derived in this manner could easily account for slight metastabilities (or perhaps unstable equilibria) within vaporous cavities.

I heartily agree with the author that more data are needed to substantiate the exponent for D/D_{ref} in equation (5). For the scale factor studied, the diameter-dependence is less than 4 percent—combining the last two terms in equation (5). For geometrically similar cavities, the last term in equation (5) goes to unity and the diameter-dependence is still less than 8 percent.

M. L. BILLET and J. W. HOLL (The Pennsylvania State University): The research reported by the author constitutes a valuable contribution to the understanding of thermodynamic effects on developed cavitation. Mr. Ruggeri is to be complimented for his measurement of the effect and its correlation with possible scaling parameters. Also, the corre-

lation of data by means of the B-factor theory is very encouraging. Our comments are primarily restricted to introducing an alternate approach to the B-factor method based on convective heat transfer (ref. D–3).

From the B-factor theory of Stahl and Stepanoff (ref. 12), the temperature depression is given by

$$\Delta T = B \cdot \left(\frac{\rho_v}{\rho_L}\right) \cdot \left(\frac{L}{C_L}\right) \tag{D-4}$$

where B is defined as the ratio of vapor volume to liquid volume and must be determined in terms of scaling parameters of the system. However, the vapor volume is proportional to the product of cavity length and cavity thickness, and also the liquid volume is proportional to the cavity length and thickness of the liquid layer supplying the heat of vaporization. Thus, B must be a function of a maximum cavity diameter divided by the liquid thickness for a body of revolution.

Previous investigators have shown that for water at ordinary temperatures the ratio of maximum cavity diameter to model diameter is solely a function of the cavitation number based on cavity pressure, which in turn is a function of the geometry.

According to the analysis of Gelder, Ruggeri, and Moore (ref. 8), based on the analysis of Eisenberg and Pond (ref. D–4), the liquid thickness is proportional to $\sqrt{\alpha \Delta X / V_0}$. Assuming that the cavities are geometrically similar, the expression for the B-factor for an axisymmetric flow is

$$B = \left(\frac{\Delta X}{D}\right)^{0.5} \cdot \left(\frac{DV_0}{\alpha}\right)^{0.5} C \tag{D-5}$$

where V_0 is the velocity in the uniform stream. It was assumed that C was a universal constant and could be evaluated from a reference state. Denoting the reference state with the subscript "ref," it follows that

$$C = \frac{B_{\text{ref}}}{(V_0 D / \alpha)_{\text{ref}}^{0.5} (\Delta X / D)_{\text{ref}}^{0.5}} \tag{D-6}$$

Employing equation (D–6) in equation (D–5) for C gives

$$B = B_{\text{ref}} \left(\frac{\alpha_{\text{ref}}}{\alpha}\right)^{0.5} \left(\frac{V_0}{V_{0_{\text{ref}}}}\right)^{0.5} \left(\frac{D}{D_{\text{ref}}}\right)^{0.5} \left[\frac{(\Delta X / D)}{(\Delta X / D)_{\text{ref}}}\right]^{0.5} \tag{D-7}$$

Application of equation (D–7) to venturi results indicated that the actual exponents did not agree with theory. Thus, the exponents in equation (D–7) were altered empirically, resulting in equation (5) of the paper.

An alternate approach to correlating data for the thermodynamic effect is the entrainment theory, which is similar to that proposed by Acosta and Parkin (ref. D–5) and later by Plesset (ref. D–6). In this

theory the latent heat requirement is equated to the convective heat transfer at the cavity wall. From this theory, the temperature depression is given by

$$\Delta T = \frac{C_Q}{\mathrm{Nu}} \frac{P_e}{A_w/D^2} \left(\frac{\rho_v}{\rho_L}\right)\left(\frac{L}{C_L}\right) \tag{D-8}$$

where the entrainment coefficient, C_Q, is defined as

$$C_Q = \frac{Q_v}{V_0 D^2} \tag{D-9}$$

and where

A_w = surface area of the cavity through which the heat transfer occurs
Q_v = volume flow rate of the vapor in the cavity
Nu = Nusselt number, $h\Delta X/K$
h = film coefficient for convective heat transfer
P_e = Peclet number, $V_\infty \Delta X/\alpha$

In order to apply equation (D-8), it is necessary to determine the three dimensionless parameters C_Q, Nu, and A_w/D^2.

The cavitation number based on cavity pressure, P_c, is defined as

$$K_c = \frac{P_0 - P_c}{\frac{1}{2}\rho_L V_0^2} \tag{D-10}$$

where P_0 is the free-stream pressure. Similarity for developed cavitation in the absence of significant viscous or gravity effects is provided if the cavitation number is constant. This result has been verified by numerous experiments in water at ordinary temperatures. The similarity law was applied to a zero-caliber ogive model (ref. D-3), and the entrainment coefficient, C_Q, was found by creating a similar ventilated cavity and measuring the volume flow rate. The area coefficient, A_w/D^2, was determined from photographs taken of the ventilated cavity. The Nusselt number was assumed to be of the form

$$\mathrm{Nu} = a R_e^b P_r^c F_r^d \tag{D-11}$$

where R_e, P_r, and F_r are the Reynolds, Prandtl, and Froude numbers, respectively. The constants, a, b, c, and d in equation (D-11) were determined by substituting the measured values of ΔT, C_Q, and A_w/D^2 and equation (D-11) into equation (D-8) and then solving for the constants.

The equation for the temperature depression for the *entrainment theory applied to the zero-caliber ogives* was found to be

$$\Delta T = \text{constant } g^{0.175} \left[\frac{\rho_v}{\rho_L}\right]\left[\frac{L}{C_L}\right]\left[\frac{1}{\alpha}\right]^{0.55}\left[\frac{1}{\nu_L}\right]^{0.10}\left[\frac{\Delta X}{D}\right]^{0.58} V_0^{0.3} D^{0.825} \tag{D-12}$$

The corresponding equation for the *B-factor theory applied to the venturis* as employed in the paper is

$$\Delta T = \text{constant} \left[\frac{\rho_v}{\rho_L}\right]\left[\frac{L}{C_L}\right]\left[\frac{1}{\alpha}\right]\left[\frac{\Delta X}{D}\right]^{0.3} V_0^{0.8} D^{0.2} \qquad \text{(D–13)}$$

The dimensionless constant in equation (D–12) is equal to 0.495×10^{-3}, whereas the constant in equation (D–13) is dimensional.

A comparison of equations (D–12) and (D–13) indicates that the *B*-factor theory applied to the venturis results in $\Delta T \alpha (\Delta X/D)^{0.3} V_0^{0.8}$, whereas the entrainment theory applied to the ogive yields $\Delta T \alpha (\Delta X/D)^{0.58} V_0^{0.3}$. Thus the effect of velocity is greater for the venturis, but the effect of cavity length to diameter ratio, $\Delta X/D$, is greater for the ogive.

Referring to equations (D–12) and (D–13), it is seen that $\Delta T \alpha D^{0.2}$ for the *B*-factor theory applied to the venturis, whereas $\Delta T \alpha D^{0.825}$ for the entrainment theory applied to the ogive. Thus the implication is that the effect of size is greater for the ogive. However, this has not been verified experimentally, since D was not a variable in the ogive test program; thus D enters as a constant in equation (D–12). Nevertheless, in order for equation (D–12) to be dimensionally correct, it is necessary that the exponent for D be 0.825. It is intended that the size effect will be checked in subsequent investigations of the ogives.

Referring to the fluid property effects in equations (D–12) and (D–13), it is seen that the influence of (ρ_v/ρ_L) and (L/C_L) are the same in both cases, but the exponent on α differs. Also, the entrainment theory contains the additional term $(1/\nu_L)^{0.1}$, which arises from the kinematic viscosity appearing in the Reynolds and Prandtl numbers in the assumed relation for the Nusselt number.

In addition to the above-mentioned differences between the results for the venturis and ogives is the variation of cavitation number with $\Delta X/D$. As indicated in the paper, the cavitation number based on minimum cavity pressure is independent of $\Delta X/D$ for the venturis, whereas for the ogives the cavitation number decreases as $\Delta X/D$ increases (ref. D–3).

Equation (D–12), which was obtained from tests with a zero-caliber ogive in water from 80° to 290° F was employed to predict the behavior of a zero-caliber ogive in Freon-113 from 75° to 190° F. The comparisons between equation (D–12) and the experiment were found to be very good (ref. D–3). As indicated in the paper, equation (D–13) has been applied to venturi data obtained with several liquids, and the correlations have been encouraging.

The aforementioned comparisons between the results for venturis and zero-caliber ogives show that the effects of fluid properties are not in complete agreement and that the major differences appear to be in the

effects due to velocity, size, and relative cavity length. This implies a need to emphasize the investigation of the influence of changes in boundary shape and size on the thermodynamic effect.

F. G. HAMMITT (University of Michigan) : I am interested in whether or not the NASA program has included any measurements of void fraction in the cavity. The appreciable pressure drop measured across the cavity length in the venturi tests seems to indicate the presence of considerable liquid within this cavity. I believe such measurements could be obtained fairly easily by gamma-ray (or X-ray) densitometry, as we once did in our laboratory in a cavitating venturi (ref. D–7). More detailed information on the mechanics of the actual flow could be very useful in improving the realism of the model.

RUGGERI (author) : I wish to thank all the discussors for their timely and very worthwhile comments. First, with regard to Mr. Hord's discussion, I completely agree that equation (3) of the paper does not necessarily provide a good approximation of the vapor-to-liquid-volume ratio curves (B-factors), and one should indeed use caution in applying this relation in cases where the physical properties of the liquid and its vapor change significantly with temperature. The method for determining volume ratio, as outlined by Mr. Hord, is more direct and simple and provides ultimate accuracy without the need for solving equations in incremental form to account for changes in fluid properties as the temperature drops due to vaporization. On the question of thermodynamic equilibrium within the cavitated region, it should be pointed out that although the experimentally determined exponents of equation (5) were based on conditions in the cavity's leading-edge region, where equilibrium conditions existed, the final correlations presented in figure 10 included considerable liquid-hydrogen data which exhibited various degrees of metastability in the central and rearward portions of the cavity. No trend was noted in the degree of this metastability. Thus, it appears that conditions of thermodynamic equilibrium need only exist in the leading-edge region to satisfy the present prediction method. This implies that vaporization is confined primarily to the cavity's leading-edge region, with the process for the remainder of the cavity being mostly one of condensation.

Mr. Billet and Dr. Holl are to be commended for their efforts toward the development of a different cavitation model via the entrainment theory. The NASA studies were based on a "quasi-static" conduction model, which admittedly does not properly represent the real flow situation. This may be borne out by the fact that the experimentally determined exponents varied somewhat from the theoretical values based on a pure conduction process. However, it is interesting to note that, with one exception, the parameters for both theories are the same. Nevertheless,

the entrainment theory, which is based on a dynamic—or convective—model, better represents the real flow situation and thus is more sound from a theoretical standpoint. From the standpoint of experimentation, however, the entrainment theory involves certain problems similar to those encountered with the present cavitation model in the determination of absolute rather than effective values of parameters such as C_Q and h. For example, the volume flow rate measured for a ventilated cavity may not necessarily equal the volume flow rate of vapor for a similar vaporous cavity.

The studies of Dr. Holl and his coworkers indicate that for zero-caliber ogives, the value of $K_{c,min}$ changes with cavity length. This is an interesting finding, since, during the venturi studies, it had been suspected that this variance of $K_{c,min}$ with cavity length might occur for different venturis (or body shapes), but it was not verified. Unquestionably, body shape (i.e., noncavitating wall pressure distribution) influences the thermodynamic effects of cavitation in general, and this effect is probably the primary reason for the difference in exponents between the entrainment and modified B-factor theories. The influence of body shape is likely to preclude the prediction of absolute values of thermodynamic effects for arbitrary bodies and liquids for considerable time to come. Much research is needed in this area, but a more immediate need appears to be the influence of body scale on the thermodynamic effects of cavitation.

With regard to Dr. Hammitt's comments, no attempt was made to measure the void fraction in vaporous cavities. Attempts were made to determine whether macroscopic droplets, wall rivulets, etc., were present within the cavity, and, except for isolated instances (particularly for liquid nitrogen), none was found. The axial pressure gradients within vaporous cavities, in my opinion, are due in large part to the velocity (dynamic head) of the vapor, which of course implies very high axial velocities in the extreme leading-edge region and comparatively low velocities in the collapse region. At the time the NASA Lewis program was phased out, plans were to make total and static pressure measurements within vaporous cavities to prove or disprove this concept.

REFERENCES

D-1. Jacobs, R. B., Prediction of Symptoms of Cavitation. *J. Res. Natl. Bur. Std.*, Sec. C., Vol. 65, No. 3, July–September 1961, pp. 147–156.

D-2. Fisher, R. C., Discussion of A Survey of Modern Centrifugal Pump Practice for Oilfield and Oil Refining Services by N. Tetlow. *Proc. Inst. Mech. Engrs.*, Vol. 152, January–December 1945, pp. 305–306.

D-3. Billet, M. L., *Thermodynamic Effects on Developed Cavitation in Water and Freon–113*, M.S. thesis, Aerospace Eng. Dept., Penn. State U., March 1970.

D–4. EISENBERG, P., AND H. POND, *Water Tunnel Investigations of Steady State Cavities*. David Taylor Model Basin Report 668 (Carderock, Md.), October 1948.

D–5. HOLL, J. W., AND G. F. WISLICENUS, Scale Effects on Cavitation. *J. Basic Eng., Trans. ASME*, Series D, Vol. 83, 1961, pp. 385–398. (See discussion by A. Acosta and B. R. Parkin.)

D–6. PLESSET, M. S., *Remarks on Thermal Effects on Cavitation*. Discussion booklet for Symposium on Cavitation State of Knowledge, ASME, 1970.

D–7. SMITH, W., G. L. ATKINSON, AND F. G. HAMMITT, Void Fraction Measurements in a Cavitating Venturi. *Trans. ASME, J. Basic Eng.*, June 1964, pp. 265–274.

PRECEDING PAGE BLANK NOT FILMED

Non-Newtonian Effects on Flow-Generated Cavitation and on Cavitation in a Pressure Field[1]

ALBERT T. ELLIS AND ROBERT Y. TING

University of California, San Diego

Observations are presented which show that the stresses in a flow field of very dilute polymer are not well enough described by the Navier-Stokes equations to accurately predict cavitation. The constitutive equation for the particular polymer and concentration used is needed. The second-order fluid form in which accelerations are relatively important appears capable of explaining observed cavitation suppression by changing the pressure field due to flow.

Bubble dynamics in stationary dilute polymer solutions are also examined and found to be little different from those in water.

In earlier work (refs. 1 and 2), the authors reported the suppression of flow-generated cavitation in dilute polymers on cylinders with hemispherical noses at Reynolds numbers from 7×10^4 to 3.1×10^5. Reduction of the incipient cavitation number to 30 percent of its value for tap water was observed. Flow velocity field visualization was achieved by optical techniques using 1-microsecond light pulses scattered by polymer particles or small polystyrene latex spheres in the flow. Dark field multi-exposure photographs taken at 90 degrees to the direction of the light beam thus provided reliable data on velocity field magnitude and direction and ruled out the possibility of errors due to non-Newtonian effects on pressure taps. Figure 1 shows the results.

POSSIBLE MECHANISMS

While it is believed that incipient flow cavitation suppression by dilute polymers has been shown to be a real effect of considerable magnitude, the correct mechanism involved is still to be proven. The main purpose of
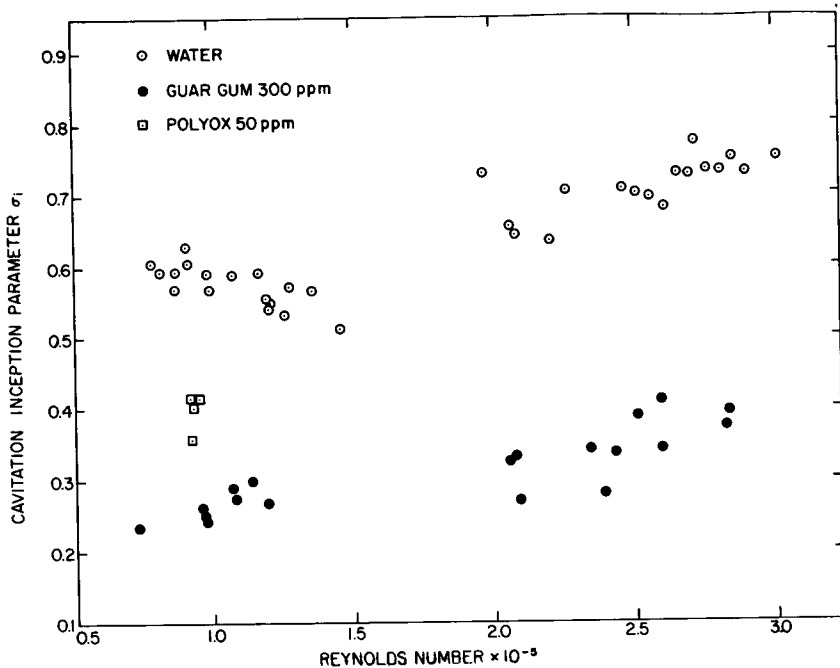
FIGURE 1.—*Cavitation inception parameter versus Reynolds number.*

this paper is to report the results of early stages of a program which, it is hoped, will accomplish this end in a systematic fashion.

It is still the opinion of the authors that cavitation suppression is due to an overpressure existing in the region of the model where the pressure would ordinarily be low enough to permit cavitation in the case of water. This belief is supported by the fact that true velocities—both around the model and along the axial streamline—obtained by the optical method are as much as 10 percent higher than the velocities calculated from the Bernoulli equation on the basis of pressure-tap readings upstream (in the upper tank of the blow-down tunnel where the liquid is quiescent) and flush with the wall of the working section. These details of the facility and instrumentation have been described elsewhere (refs. 2 and 3). The nozzle itself is based on designs of Stewart (ref. 4) and Tsien (ref. 5) to provide a nearly uniform velocity profile across the working section. Optical measurements—not including the boundary layer—indicate that the nozzle apparently does this quite well, so that the flow approaching the model is a uniform potential flow.

The absolute velocities measured by the optical technique show that the pressure at the high-velocity end of the nozzle (measured by the pressure tap flush with the wall at the working section entrance) is

approximately 10 to 18 percent higher than that for water, depending on the kind of polymers used. Over the range of 40 to 70 feet per second, the error is independent of the flow velocity. For the three different sizes of pressure taps tested—$\frac{1}{4}$, $\frac{1}{8}$, and $\frac{1}{16}$ inch in diameter—the error increases very slightly as the sizes of the pressure taps decrease. Samples from the various runs of polymers were monitored for degradation by testing drag reduction in a portable hydrating apparatus kindly supplied by Dr. Hoyt of the U.S. Naval Underseas Research Center, Pasadena. It should be especially noted that the sign of the error is positive rather than negative as has been shown to be the case for pressure-tap error both experimentally and theoretically by Professors Tanner and Pipkin (ref. 6) of Brown University for low-speed polymer flows.

It is believed by the authors that the errors observed in reference 2 are not primarily pressure-tap errors, but, rather, that the Bernoulli equation must contain a correction term. An analysis made by the authors based on the second-order fluid model for the extensional flow along the center streamline through the nozzle gives an expression for the pressure of the form:

$$P = P_N + 2\alpha \left[2 \left(\frac{du}{dx} \right)^2 - u \frac{d^2u}{dx^2} \right] \tag{1}$$

where P is the free-stream pressure and is made up of P_N, the free-stream pressure for water, and a correction term involving α, one of the material constants of the second-order fluid model represented by equation (7), (which may be different for various solutions), the velocity along the central streamline, u, and its spatial derivatives, du/dx and d^2u/dx^2. It should be noted that this correction to the pressure may thus be positive or negative. In our experiment, u, du/dx, and d^2u/dx^2 were such that, if α were given the value of -0.01 dyne sec^2/cm^2 taken as a representative value in the literature, then the pressure correction would be positive, as indicated by our working-section pressure-tap reading. It is not proposed that the second-order fluid is a correct model in all situations, but rather that the truncation in its theoretical derivation permits us to obtain a solution which may be used to explain our experimental results.

The idea that polymers may affect other than turbulent pressure fields has also been advanced by various persons such as Professor John Lumley (ref. 7) and Dr. Arndt in his discussion of the authors' previous work (ref. 2).

It was also suggested by Dr. Fabula in his discussion (ref. 2) as well as by Professor Tanner (ref. 8) that the suppression of cavitation inception might be due to effects of polymers on individual cavitation bubble growth or collapse. This possibility had also occurred to the authors, and it was therefore decided to pursue theoretical and experimental work to assess the validity of this concept. The theoretical study of a perfectly spherical

bubble is obviously attractive because of its symmetry, which greatly simplifies the analytical solution for the bubble radius as a function of time. The solution for water was obtained by Lord Rayleigh in 1917 for the case of a vapor bubble and for one containing an isothermal permanent gas (ref. 9). Many investigators have since covered more complicated aspects of the problem, such as the effect on growth of heat transfer (refs. 10, 11, and 12); the basic stability of the spherical interface (ref. 13); and the formation of jets due to pressure gradients (ref. 14), wall proximity (ref. 15), or both (ref. 16). Fortunately, for the purposes of this paper, it turns out that a spark-generated bubble in a stationary liquid at one atmosphere pressure does remain quite spherical until a rather late stage in its collapse. During this period it follows the simple Rayleigh theory very well, as demonstrated by the experimental part of this paper. Any gas from the spark simply does not have an observable effect until later stages of higher compression are reached. Of course the spark must be of short duration (one microsecond in this case) so that thermal equilibrium is attained when maximum radius is reached. Theoretical curves are not given for the growth phase, since the simple theory used may not apply to the experiments. However, any marked effect due to extensional flow or viscoelastic effects should show up during collapse as well as growth, and the authors have therefore confined their attention to this regime.

THEORETICAL STUDY OF BUBBLE COLLAPSE

Consider the problem of a single bubble collapsing in an incompressible liquid of infinite extent. The vapor bubble is taken to be spherical at all times. Gravity effect is neglected. Thermal equilibrium is assumed such that the vapor pressure inside the bubble is uniform and equal to the equilibrium vapor pressure of the liquid at the liquid temperature. Spherical coordinates are chosen with the origin at the center of the bubble, which is at rest. The radius of the bubble at any time t is $R = R(t)$, and r is the radial distance to any point in the liquid as a spherical coordinate system (r, θ, φ) is taken. The velocity will only have one component in the radial direction, i.e.,

$$V = u e_r \tag{2}$$

For an incompressible liquid, the continuity equation is

$$\frac{\partial u}{\partial r} + \frac{2u}{r} = 0 \tag{3}$$

which gives

$$u = u(r, t) = \frac{f(t)}{r^2} \tag{4}$$

For the bubble dynamics problem it is generally given as

$$u = \frac{R^2(t)\dot{R}(t)}{r^2} \tag{5}$$

The governing equation of motion is

$$\rho \frac{\partial u}{\partial t} + \rho u \frac{\partial u}{\partial r} = -\frac{\partial p}{\partial r} + \frac{\partial \sigma_{rr}}{\partial r} + \frac{2\sigma_{rr} - \sigma_{\theta\theta} - \sigma_{\varphi\varphi}}{r} \tag{6}$$

where p is the hydrostatic pressure and σ_{rr}, $\sigma_{\theta\theta}$, and $\sigma_{\varphi\varphi}$ are the normal stress components of the deviatory stress tensor $[\sigma_{ij}]$, which is related to the strain-rate tensor $[e_{ij}]$ by the specific constitutive equation the liquid obeys.

The dilute polymer solutions of interest may be slightly viscoelastic (ref. 18). To predict their behavior involving viscoelastic effects, two generally accepted models for viscoelastic fluids are analyzed in the following.

Second-Order Fluid Model

A second-order fluid model proposed by Markovitz and Coleman (ref. 19) has the constitutive equation of the form

$$\sigma_{ij} = \mu e_{ij}^{(1)} + \alpha e_{ij}^{(2)} + \beta e_{ik}^{(1)} e_{kj}^{(1)} \tag{7}$$

where μ is the Newtonian viscosity, α and β are material constants, and

$$e_{ij}^{(1)} = v_{i,j} + v_{j,i}$$

$$e_{ij}^{(n)} = \frac{De_{ij}^{(n-1)}}{Dt} + e_{ik}^{(n-1)} v_{k,j} + e_{jk}^{(n-1)} v_{k,i}$$

For the present problem, the strain-rate tensor is

$$[e_{ij}] = \begin{bmatrix} \dfrac{\partial u}{\partial r} & 0 & 0 \\ \\ 0 & \dfrac{u}{r} & 0 \\ \\ 0 & 0 & \dfrac{u}{r} \end{bmatrix} \tag{8}$$

By substituting equation (8) into equation (7), it can be noted that the second normal stress difference vanishes:

$$\sigma_{\theta\theta} - \sigma_{\varphi\varphi} = 0$$

and hence the relation

$$2\alpha + \beta = 0 \tag{9}$$

is used to simplify the analysis (ref. 19). By using equations (4), (7), and (9), equation (6) becomes

$$\rho\frac{\partial u}{\partial t} + \rho u\frac{\partial u}{\partial r} = -\frac{\partial \rho}{\partial r} - \frac{8\alpha}{3}\frac{\partial u}{\partial r}\cdot\frac{\partial^2 u}{\partial r^2} \tag{10}$$

Substituting equation (5) into equation (10) and integrating over (R, ∞), the result is

$$R\ddot{R} + \frac{3}{2}\dot{R}^2 - \frac{16\gamma}{3}\left(\frac{\dot{R}}{R}\right)^2 = \frac{P(R) - P(\infty)}{\rho} \tag{11}$$

where $(\dot{\ }) = d/dt$, $\gamma = \alpha/\rho$ with a dimension of $[length]^2$ and $P(\infty) = P_a$ is the constant pressure at infinity. The hydrostatic pressure $P(R)$ is eliminated by applying the boundary condition at the bubble wall; i.e., at $r = R$,

$$P_v - \frac{2\sigma}{R} = -\sigma_{rr}(R)$$

$$= P(R) - 2\mu\left[\frac{\partial u}{\partial r}\right]_{r=R} - 2\alpha\left[\frac{\partial^2 u}{\partial t\partial r} + u\frac{\partial^2 u}{\partial r^2} - 2\left(\frac{\partial u}{\partial r}\right)^2\right]_{r=R} \tag{12}$$

where P_v is the vapor pressure inside the bubble and σ is the surface tension.

Combining equations (11) and (12), the equation governing the collapsing process of the bubble is obtained.

$$\left(R + \frac{4\gamma}{R}\right)\ddot{R} + \left(\frac{3}{2} + \frac{20\gamma}{3R^2}\right)\dot{R}^2 + 4\nu\frac{\dot{R}}{R} = \frac{P_v - P_a - (2\sigma/R)}{\rho} \tag{13}$$

where $\nu = \mu/\rho$ is the kinematic viscosity of the fluid. For the special case of $\gamma = 0$, equation (13) reduces to the classical bubble equation in a Newtonian fluid (ref. 11).

$$R\ddot{R} + \frac{3}{2}\dot{R}^2 + 4\nu\frac{\dot{R}}{R} = \frac{P_v - P_a - (2\sigma/R)}{\rho} \tag{13'}$$

From the prediction of molecular theory, γ or α is negative (ref. 20). Consequently, equation (13) shows that under the same pressure difference $P_v - P_a$, the bubble in a non-Newtonian fluid obeying the constitutive

relation, equation (7), of the second-order fluid model will collapse more rapidly than in the Newtonian fluid.

Oldroyd Three-Constant Fluid Model

Oldroyd (ref. 21) suggested the following constitutive equation for a viscoelastic fluid:

$$\sigma_{ij}+\lambda_1\left[\frac{\partial\sigma_{ij}}{\partial t}+v_k\frac{\partial\sigma_{ij}}{\partial x_k}-\sigma_{ik}e_{jk}-\sigma'_{kj}e_{ik}\right]=2\mu\left[e_{ij}+\lambda_2\left(\frac{\partial e_{ij}}{\partial t}+v_k\frac{\partial e_{ij}}{\partial x_k}-2e_{ik}e_{kj}\right)\right]$$

(14)

where λ_1 and λ_2 are two material constants, both having the dimension of [time] and a positive sign.

Due to the special form of the strain-rate tensor in this problem, the shear stress components $\sigma_{r\theta}$, $\sigma_{\theta\varphi}$, and $\sigma_{r\varphi}$ vanish, and the normal stress components $\sigma_{\theta\theta}$ and $\sigma_{\varphi\varphi}$ are equal. Using equation (5), the stress components σ_{rr} and $\sigma_{\phi\phi}$ are determined by the following relations:

$$\frac{\partial\sigma_{rr}}{\partial t}+\frac{R^2\dot{R}}{r^2}\frac{\partial\sigma_{rr}}{\partial r}+\left(\frac{1}{\lambda_1}+4\frac{R^2\dot{R}}{r^3}\right)\sigma_{rr}=-\frac{4\mu}{\lambda_1}\cdot\frac{R^2\dot{R}}{r^3}\left[1+\lambda_2\left(\frac{\ddot{R}}{\dot{R}}+\frac{2\dot{R}}{R}+\frac{R^2\dot{R}}{r^3}\right)\right]$$

(15)

$$\frac{\partial\sigma_{\varphi\varphi}}{\partial t}+\frac{R^2\dot{R}}{r^2}\frac{\partial\sigma_{\varphi\varphi}}{\partial r}+\left(\frac{1}{\lambda_1}-2\frac{R^2\dot{R}}{r^3}\right)\sigma_{\varphi\varphi}=\frac{2\mu}{\lambda_1}\cdot\frac{R^2\dot{R}}{r^3}\left[1+\lambda_2\left(\frac{\ddot{R}}{\dot{R}}+\frac{2\dot{R}}{R}-5\frac{R^2\dot{R}}{r^3}\right)\right]$$

(16)

Equations (6), (15), and (16) are thus the governing equations for the bubble-collapsing problem. It was found convenient to introduce the transformation to Lagrangian coordinates (ref. 10):

$$h=\tfrac{1}{3}\left[r^3-R^3(t)\right]$$

(17)

Then equations (15) and (16) become

$$\frac{d\sigma_{rr}}{dt}+\left(\frac{1}{\lambda_1}+4\frac{R^2\dot{R}}{r^3}\right)\sigma_{rr}=-\frac{4\mu}{\lambda_1}\cdot\frac{R^2\dot{R}}{r^3}\left[1+\lambda_2\left(\frac{\ddot{R}}{\dot{R}}+\frac{2\dot{R}}{R}+\frac{R^2\dot{R}}{r^3}\right)\right]$$

(18)

$$\frac{d\sigma_{\varphi\varphi}}{dt}+\left(\frac{1}{\lambda_1}-2\frac{R^2\dot{R}}{r^3}\right)\sigma_{\varphi\varphi}=\frac{2\mu}{\lambda_1}\cdot\frac{R^2\dot{R}}{r^3}\left[1+\lambda_2\left(\frac{\ddot{R}}{\dot{R}}+\frac{2\dot{R}}{R}-5\frac{R^2\dot{R}}{r^3}\right)\right]$$

(19)

which are readily integrated to obtain

$$\sigma_{rr}(h,t)=-\frac{4\mu}{\lambda_1}\int_0^t e^{(\tau-t)/\lambda_1}R^2(\tau)\dot{R}(\tau)\left\{\frac{[3h+R^3(\tau)]^{1/3}}{[3h+R^3(t)]^{4/3}}\right\}\{1+\lambda_2 M_{rr}(h,\tau)\}\,d\tau$$

(20)

$$\sigma_{\varphi\varphi}(h, t) = \frac{2\mu}{\lambda_1} \int_0^t e^{(\tau-t)/\lambda_1} R^2(\tau) \dot{R}(\tau) \left\{ \frac{[3h+R^3(t)]^{2/3}}{[3h+R^3(\tau)]^{5/3}} \right\} \{1 + \lambda_2 M_{\varphi\varphi}(h, \tau)\} \, d\tau$$

(21)

where

$$M_{rr}(h, \tau) = \frac{\ddot{R}(\tau)}{\dot{R}(\tau)} + \frac{2\dot{R}(\tau)}{R(\tau)} + \frac{R^2(\tau)\dot{R}(\tau)}{3h+R^3(\tau)}$$

(22)

$$M_{\varphi\varphi}(h, \tau) = \frac{\ddot{R}(\tau)}{\dot{R}(\tau)} + \frac{2\dot{R}(\tau)}{R(\tau)} - 5\frac{R^2(\tau)\dot{R}(\tau)}{3h+R^3(\tau)}$$

(23)

Substituting equations (20) and (21) into equation (6) written in terms of the new coordinates (h, t), and integrating over the range from $h = 0 (r = R)$ to $h = \infty (r = \infty)$, the result is

$$\rho(R\ddot{R} + \tfrac{3}{2}\dot{R}^2) + 4\mu\frac{\dot{R}}{R} = P_v - P_a - \frac{2\sigma}{R} + \frac{2\mu}{\lambda_1}(\lambda_1 - \lambda_2)$$

$$\times \int_0^t e^{(\tau-t)/\lambda_1} \left[\left(1 + \frac{R^3(\tau)}{R^3(t)}\right) \frac{\ddot{R}(\tau)}{R(t)} + 3\frac{R^2(\tau)}{R^4(t)} \dot{R}(\tau)^2 \right] d\tau$$

(24)

The first term in the integral of equation (24) is integrated by parts, and by using the initial condition

$$\dot{R}(0) = 0$$

(25)

for the bubble-collapse problem, equation (24) reduces to the form

$$R\ddot{R} + \frac{3}{2}\dot{R}^2 + 4\nu\frac{\lambda_2}{\lambda_1}\frac{\dot{R}}{R} + \frac{P_a - P_v + (2\sigma/R)}{\rho}$$

$$= -\frac{2\nu}{\lambda_1}\left(1 - \frac{\lambda_2}{\lambda_1}\right)\int_0^t e^{(\tau-t)/\lambda_1} \frac{\dot{R}(\tau)}{R(t)} \left[1 + \frac{R^3(\tau)}{R^3(t)}\right] d\tau \quad (26)$$

For the Newtonian case, $\lambda_2/\lambda_1 \to 1$ and equation (26) again reduces to equation (13'). In general, λ_2 is less than λ_1. With the appropriate interpretation of the material constants μ, λ_1, and λ_2 (ref. 22), it is shown that the third term on the left of equation (26), the viscous damping term, is not changed with respect to the Newtonian case. The viscoelastic memory integral on the right-hand side then appears to have the effect of slowing down the collapse. However, by a dimensional analysis it can be shown that, in the situation of a collapsing bubble, the magnitude of the viscoelastic correction term—as well as that of the viscous damping term—is too small to affect the collapse process in any significant way.

While the two constitutive relations used give different results, the authors believe that the conclusion deduced from the Oldroyd fluid will be more applicable in a real physical situation in the viscoelastic fluids. It has been suggested that the Oldroyd model is superior to the second-order model at higher strain rates (ref. 23). Indeed, the inadequacy of the second-order fluid model is not surprising, since it is generally known to be a poor model for unsteady flows involving short deformation periods (ref. 24), in which cases the results could lead to paradoxes (ref. 25) and questionable mathematical solutions.

EXPERIMENTAL PROCEDURE

A cubical lucite tank 30 centimeters on a side was used to contain the liquid. The flat walls avoided optical problems, and the tank was large enough that the 1-centimeter-diameter, spark-generated bubbles would not suffer from wall proximity effects. Small tungsten wires were used for the underwater spark gap. These may be seen in the bubble photographs of figure 2. It may be noted that there is negligible departure from a spherical shape. The spark was formed by discharge of a 0.04-μF capacitor charged to 14 000 volts through a 5C22 hydrogen thyratron which allowed current to flow in one direction only, so that there was a single pulse of about a microsecond duration without any subsequent current oscillations. This was important in order to obtain essentially a delta function of heat energy to grow the bubble in a steady one-atmosphere pressure field. These conditions are essential to simplify the analysis. The bubble photographs of figure 2 were taken at a repetition rate of 10 000 per second or 100 microseconds between frames. The bubbles were back-lighted by a xenon flash lamp operating at $\frac{1}{4}$ joule per flash and a 1-microsecond duration. The pulsing was also done by a 5C22 hydrogen thyratron. It was realized that such a slow rate would not give much detail for the radius/time curve, but the high-speed photographic equipment had not yet been reassembled. It was thought that any gross effects caused by the polymer solutions would still be evident.

The spark gap which generated the bubble was fired at random times with respect to the photographic frames, and at least five runs were made for each solution. This is evident from the bright spot caused by the spark at the beginning of each sequence. (Apparent bright spots near the bubbles' centers are due only to the back-lighting.) The pictures were taken on a rotating-drum streak camera without any mechanical shutter or optical compensation for the speed of the moving 35-mm film. As can be seen from these contact prints and the accompanying scale, the film speed was about 12 000 centimeters per second. Tri-X film and D–19 developer were used, and the lens was of 10-inch focal length stopped
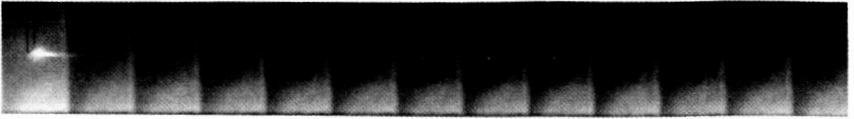
a.—*Water.*

b.—*Fresh 100-ppm Polyox.*
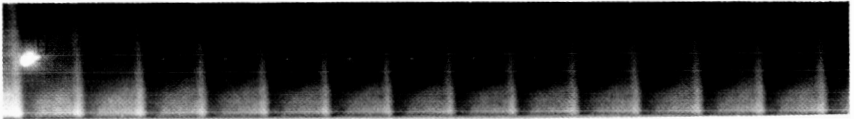
c.—*Aged 100-ppm Polyox.*

d.—*Aged 1000-ppm Polyox.*

e.—*Fresh 300-ppm Guar Gum.*

f.—*Scale in centimeters.*

FIGURE 2.—*Growth and collapse of spark-generated bubbles in various solutions (picture rate is 10 000 per second).*

down to $f16$. All runs were made at one-atmosphere pressure; hence no jet formation was observed, in contrast to earlier work performed by Benjamin and Ellis (ref. 16) at the University of Cambridge. The difference was, of course, due to the lower ambient pressures used in the latter experiments. The ratio of pressure gradient to pressure is the pertinent parameter for jet formation in bubble collapse far from boundaries. Bubble photographs for five runs of each solution (fig. 2 shows representative sequences) were measured on a precision traveling microscope with a readout of 10^{-4} centimeter per division.

RESULTS AND DISCUSSION

The experimental results for the radius/time curves of the different solutions are plotted as points on figures 3, 4, 5, 6, and 7. The dimensionless radius, R/R_0 (where R_0 is the maximum radius), is the ordinate; the dimensionless collapse time, t/τ (where τ is the Rayleigh theoretical collapse time for a bubble of the particular R_0 observed), is the abscissa. The solid lines are theoretical curves obtained on a computer for the second-order fluid model with $\gamma = 0$ (which reduces to the Rayleigh theory) and $\gamma = -0.01$. Time was not available to compute a corresponding curve for the Oldroyd model.

It may be seen that figure 3, the case for water, followed the correct Rayleigh curve quite well, which was taken to be a good check on the


Run		R_0(cm)
1	o	0.548
2	x	0.545
3	△	0.493
4	▼	0.530

$T = 23\,°C$
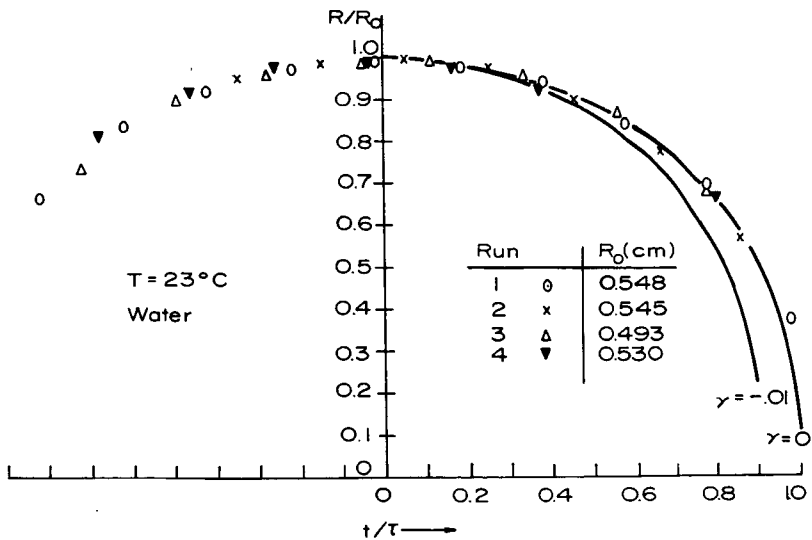
Water

FIGURE 3.—*Experimental points and theoretical dimensionless bubble collapse curves for water under atmospheric pressure.*
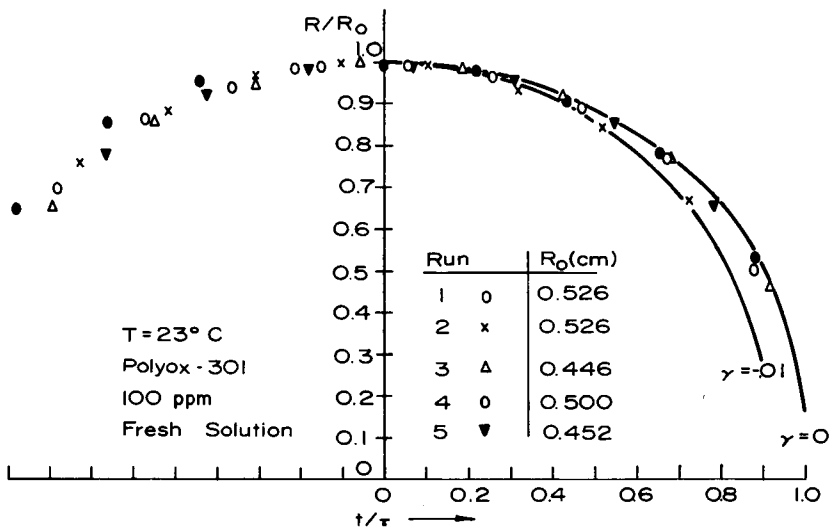
FIGURE 4.—*Experimental points and theoretical dimensionless bubble collapse curves for fresh 100–ppm Polyox under atmospheric pressure.*
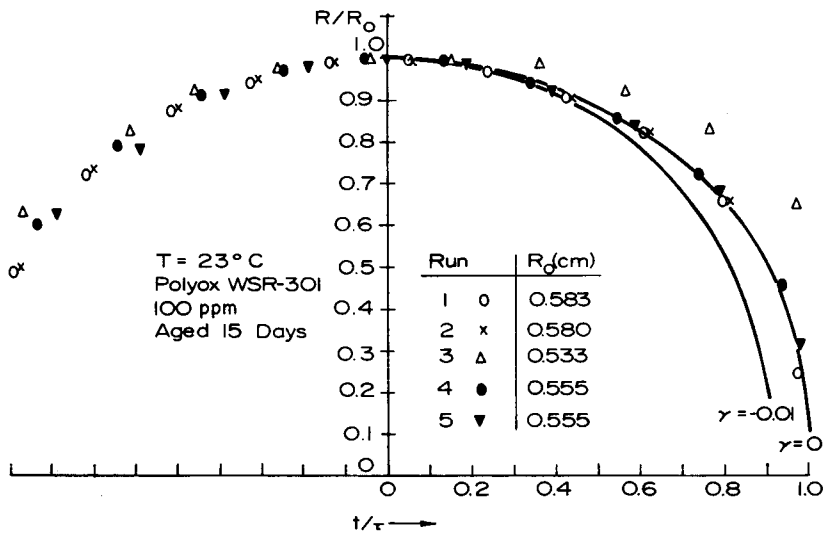

FIGURE 5.—*Experimental points and theoretical dimensionless bubble collapse curves for aged 100–ppm Polyox under atmospheric pressure.*
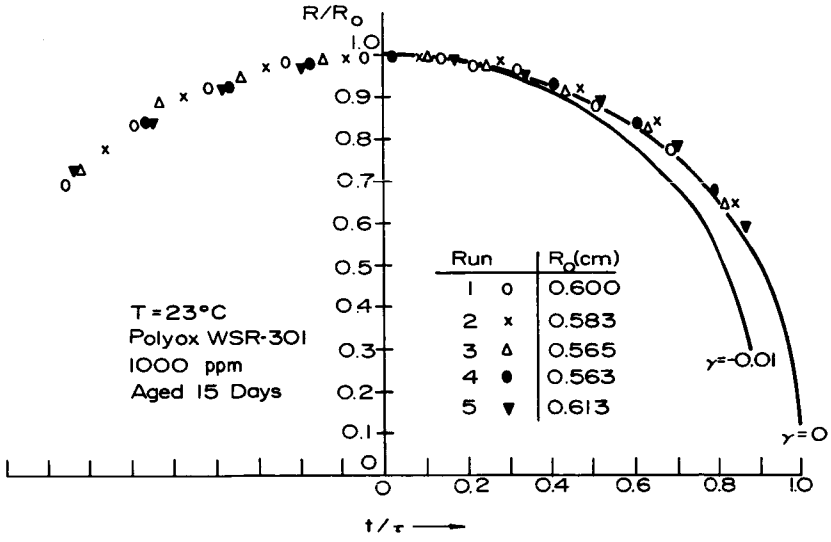
FIGURE 6.—*Experimental points and theoretical dimensionless bubble collapse curves for aged 1000–ppm Polyox under atmospheric pressure.*
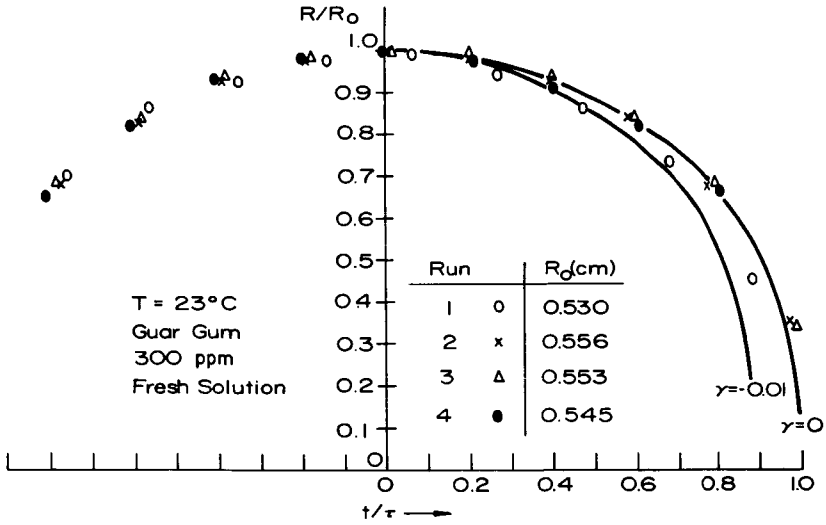

FIGURE 7.—*Experimental points and theoretical dimensionless bubble collapse curves for fresh 300–ppm Guar Gum under atmospheric pressure.*

validity of the experimental method. However, the polymer solutions also seemed to follow this curve fairly well. The exceptions were run 2 of the fresh 100–ppm Polyox series (fig. 4), which collapsed faster in agreement with second-order theory, and run 3 of the aged 100–ppm Polyox (fig. 5), which collapsed more slowly than water. It is regretted that only five runs for each system were made, but time was not available. However, with four runs out of five agreeing, it is felt that these single runs should be discounted.

SUMMARY AND CONCLUSIONS

Theoretical expressions for a spherical cavity collapsing in a stationary infinite fluid are derived for liquid constitutive equations of both the second-order and Oldroyd types. These reduce to the classical Rayleigh result if the non-Newtonian parameters are set to zero. Both models predict that bubble collapse will be different relative to the case for water; however, the difference will be very small due to the low concentrations used.

Experimentally obtained collapse curves show little difference from water and thus indicate that—for the concentrations used and for the resolution of the experiment—the effect of dilute polymers on local bubble dynamics is negligible. It is reasonable to expect normal stress differences to have some effect on bubble dynamics, but preliminary computer results show their maximum magnitude to be only about 1 percent of ambient pressure for these experiments. This tends to support the authors' present view that cavitation suppression by polymers is due to changes of pressure in flow fields. Future work is planned to properly measure the tractions on solid surfaces in flow, since this appears to be of prime importance.

REFERENCES

1. ELLIS, A. T., AND J. W. HOYT, *Some Effects of Macromolecules on Cavitation Inception.* ASME 1968 Cavitation Forum, ASME Fluids Engineering Conference (Philadelphia), May 1968, pp. 2–3.
2. ELLIS, A. T., J. G. WAUGH, AND R. Y. TING, Cavitation Suppression and Stress Effects in High-Speed Flows of Water with Dilute Macromolecule Additives. *Trans. ASME, J. Basic Eng.,* Series D, September 1970, p. 459.
3. ELLIS, A. T., B. S. BARNARD, AND M. E. SLATER, *The Unsteady Flow Cavitation Tunnel at the California Institute of Technology.* ASME Symposium on Cavitation Research Facilities and Techniques, May 1964.
4. STEWART, H. J., unpublished work from Guggenheim Aeronautical Laboratory, Cal Tech, circa 1950.
5. TSIEN, H. S., On the Design of the Contraction Cone for a Wind Tunnel. *J. Aeron. Sci.,* Vol. 10, 1943, p. 68.

6. TANNER, R. I., AND A. C. PIPKIN, Intrinsic Errors in Pressure-Hole Measurements. *Trans. Soc. Rheology*, Vol. 13, No. 4, 1969, p. 471.

7. LUMLEY, J. L., Drag Reduction by Additives. *Annual Reviews of Fluid Mechanics*, W. Sears and M. Van Dyke, eds., Vol. 1, 1969, p. 367.

8. TANNER, R. I., personal communication.

9. RAYLEIGH, The Pressure Developed in a Liquid During the Collapse of a Spherical Cavity. *Phil. Mag.*, 34:94, 1917.

10. EPSTEIN, P. R., AND M. S. PLESSET, Stability of Gas Bubbles in Liquid-Gas Solutions. *J. Chem. Phys.*, Vol. 18, 1950, p. 1505.

11. PLESSET, M. S., AND S. A. ZWICK, On the Dynamics of Small Vapor Bubbles in Liquids. *J. Math. Phys.*, Vol. 33, No. 4, 1955.

12. DERGARABEDIAN, P., Observations on Bubble Growths in Various Superheated Liquids. *J. Fluid Mech.*, Vol. 9, Part 1, 1960, pp. 39–48.

13. PLESSET, M. S., AND T. P. MITCHELL, On the Stability of the Spherical Shape of a Vapor Cavity in a Liquid. *Quart. Appl. Math.*, Vol. 13, 1956, p. 419.

14. MITCHELL, T. P., AND F. T. HAMMITT, *Collapse of a Spherical Bubble in a Pressure Gradient*. ASME Cavitation Symposium, 1970.

15. ELLIS, A. T., AND C. F. NAUDE, On the Mechanism of Cavitation Damage by Nonhemispherical Cavities Collapsing in Contact With a Solid Boundary. *Trans. ASME, J. Basic Eng.*, Vol. 83, 1961, p. 648.

16. BENJAMIN, T. B., AND A. T. ELLIS, The Collapse of Cavitation Bubbles and the Pressures Thereby Produced Against Solid Boundaries. *Phil. Trans. Roy. Soc. London*, Series A, No. 1110, Vol. 260, July 1966, pp. 221–240.

17. PLESSET, M. S., The Dynamics of Cavitation Bubbles. *J. Appl. Mech.*, September 1949, p. 277.

18. METZNER, A. B., AND M. G. PARK, Turbulent Flow Characteristics of Viscoelastic Fluids. *J. Fluid Mech.*, Vol. 20, 1964, p. 291.

19. MARKOVITZ, H., AND B. D. COLEMAN, Incompressible Second-Order Fluid. *Advances Appl. Mech.*, 1964, p. 69.

20. SINGH, K., *Non-Newtonian Effects on the Turbulent Energy Spectrum Function*. Ph.D. thesis, Penn. State U., 1966.

21. OLDROYD, J. G., On the Formulation of Rheological Equations of State. *Proc. Roy. Soc. (London)*, Series A, Vol. 200, 1950, p. 523.

22. LUMLEY, J. L., personal communication.

23. STREET, J. R., The Rheology of Phase Growth in Elastic Liquids. *Trans. Soc. Rheology*, 12:1, 1968, p. 103.

24. METZNER, A. B., J. L. WHITE, AND M. M. DENN, Significance of the Deborah Number. *Am. Inst. Chem. Engrs. J.*, 12:5, 1966, p. 863.

25. COLEMAN, B. D., R. J. DUFFIN, AND V. J. MIZEL, Instability, Uniqueness, and Nonexistence Theorems for the Equation $u_t = u_{xx} - u_{xtx}$ on a Strip. *Arch. Rat. Mech. Anal.*, Vol. 19, 1965, pp. 100.

DISCUSSION

J. L. LUMLEY (The Pennsylvania State University): The authors, Ellis and Ting, are to be commended for a particularly clear combination of calculation and experimental work. I agree fully with the conclusions which they draw therefrom. At the same time, I feel that the analytical basis on which their conclusions rest is somewhat open to question and would not provide a suitable basis for future work.

My comments relate primarily to the choice of constitutive relation. The second-order fluid model used by the authors is likely to be a poor model, since it includes only in a rudimentary way the effect of molecular extension, which seems likely (ref. D–1) to be responsible for the large effects observed in these very dilute solutions. A much better model is provided by the Oldroyd equation (ref. D–2), which can be shown to be based on a dumbbell model of the molecule (the form of the equation quoted by the authors is correct only in an irrotational flow; see ref. D–2 for the complete equations). In this way, the constants used by the author may be identified as

$$\left.\begin{array}{l} \lambda_1 = T \\[2mm] \lambda_2 = T/(1+c[\eta]) \\[2mm] \mu = \mu_0(1+c[\eta]) \end{array}\right\} \qquad \text{(D-1)}$$

where T is the molecular terminal relaxation time, c is the concentration, $[\eta]$ is the intrinsic viscosity, and μ_0 is the solvent viscosity. Substitution of these values into the authors' final form (eq. (26)) indicates that the coefficient of the viscous damping term

$$4\frac{\mu}{\rho}\frac{\lambda_2}{\lambda_1} = 4\frac{\mu_0}{\rho} \qquad \text{(D-2)}$$

is the value for the solvent alone, so that the viscous damping is unchanged. Hence, the only effect lies in the viscoelastic memory integral, having a coefficient of

$$\frac{2\mu_0 c[\eta]}{\rho T} \qquad \text{(D-3)}$$

The authors' conclusion that this would slow the collapse, but is ordinarily

quite small, certainly appears to apply during the early stages of the collapse; as the bubble closes, however, and the strain rate rises to quite large values (relative to $1/2T$), this term may slow the final stages appreciably. Numerical calculations appear to be warranted.

The same remarks relative to the constitutive equation can be made in connection with the authors' calculation of the pressure in a contraction. In the quasi-steady case, using the Oldroyd equation, it is possible (refs. D–3 and D–4) to obtain an analog of the Bernoulli equation applicable on the centerline:

$$P = P_N + \frac{\mu_0 c[\eta]}{T} \left\{ \frac{2ST}{(1-2ST)(1+ST)} + \frac{2}{3} \ln\left(\frac{1-2ST}{1+ST}\right) \right\} \quad \text{(D–4)}$$

where S is the local strain rate $(2ST<1)$ and the additional term can be shown always to be positive, in agreement with the authors' observations. From the derivation of equation (D–4), it appears to be a bound (for an Oldroyd fluid) in the sense that the deviation from P_N cannot be more positive than this.

R. E. A. ARNDT (The Pennsylvania State University): The authors are to be congratulated on presenting an excellent sequel to their original work (ref. 2), which demonstrated a non-Newtonian effect on cavitation in essentially irrotational flow. In the discussion of that previous paper, it was pointed out that the observed delay of cavitation inception could be a result of either a reorientation of the flow field or a change in the bubble dynamics. Apparently this paper is the first in a series of steps toward isolating the one or more mechanisms involved.

With this in mind, one must focus attention on the basic question at hand—namely, what causes the observed reduction in the value of incipient cavitation index based on upstream velocity and pressure? This paper considers the possibility of an effect on the bubble dynamics by polymer addition. Presumably such an effect is small, and this discussant's intuition agrees with the authors' conclusion on the point. This conclusion, however, is based on the evidence that relatively large spark-generated bubbles collapse under atmospheric pressure in a manner which appears to be relatively insensitive to the presence of small quantities of polymer. Two questions immediately arise in extending this result to consideration of cavitation inception: First, is there a "size effect" for the onset of viscoelastic phenomena in bubble dynamics? Second, is there an effect on nuclei distribution with the addition of polymers? What this discussant has in mind is that a spherical bubble expansion or collapse induces an axisymmetric strain, the magnitude of which probably increases with a decrease in bubble size. Presumably a critical value of rate of strain must be reached before viscoelastic phenomena become evident, and experiments with large bubbles may not be in the right size range for

observation of any effect. This second question is not the subject of this paper and will require further investigation. As with any good piece of research, the paper has generated several new questions to be answered.

M. S. PLESSET (California Institute of Technology): Ellis and Ting have given convincing evidence that dilute polymer solutions in water do not have a significant effect on the collapse of cavitation bubbles. It is indeed of interest that their measurements show radius/time curves that are essentially the same as those which they observed in pure water.

Also of importance is the authors' theoretical analysis, which points in the direction of faster collapse than for pure water. Here they do not find experimental evidence that indicates any speeding up of the collapse in the polymer solutions.

It is perhaps not surprising that the dilute polymer solutions show no significant effect in cavity collapse. We are familiar with the fact that ordinary viscous effects are not important for growth or collapse behavior in liquids of low viscosity such as water. It is, however, useful to have this result as well for the non-Newtonian liquids used by the authors.

Some experiments performed in our laboratory at the California Institute of Technology support the conclusion of the present paper. Using some polymer solutions prepared by Dr. Hoyt of the Naval Undersea Research and Development Laboratory, we measured cavitation damage rates in an oscillating magnetostrictive device. We observed no difference between the damage rate with pure water and the damage rate with the dilute polymer solution. In the light of the study of Ellis and Ting this observation is very satisfying. However, our experimental findings with the oscillating magnetostrictive device are not of themselves conclusive, since it is to be expected that the pressure oscillations generated in those experiments would produce some degradation of the drag-reducing additive.

ELLIS AND TING (authors): We agree with Dr. Arndt and Dr. Lumley that the scales in our experiment are not such as to show up non-Newtonian effects until later stages in the collapse, and this is also evident from our theory. However, the assumption of spherical symmetry would be invalid if we observed the collapse at later stages in these experiments.

We also agree that the Oldroyd constitutive equation is more applicable than the second-order fluid model. That is why we derived the bubble collapse equation using the Oldroyd model. The second-order model was also included for comparison in the bubble problem and was used for obtaining the venturi pressure drop. It is agreed that the expression given by Dr. Lumley is probably more accurate, but the qualitative results of both models are the same—including the algebraic sign of the pressure correction term.

It should be pointed out that the rotational terms in the Oldroyd equation are well known, but were not included here because the flow considered is irrotational.

Dr. Lumley, in his discussion, gave an interpretation of μ, λ_1, and λ_2 based on a molecular model which was unknown to the authors at the time the paper was written. This interpretation leads to the conclusion that bubble collapse will be slowed down relative to collapse in water. However, the difference could still be too small for our experiment to detect, and there is no contradiction to the results obtained by Dr. Plesset even if degradation was not present.

REFERENCES

D-1. LUMLEY, J. L., Drag Reduction by Additives. *Annual Review of Fluid Mechanics*, Vol. 1, 1969, p. 367.

D-2. LUMLEY, J. L., *Applicability of the Oldroyd Constitutive Equation to Flow of Dilute Polymer Solutions*. Internal Memorandum, Ordnance Res. Lab, Penn. State U. (to be issued).

D-3. LUMLEY, J. L., *A Centerline Bernoulli Equation for Quasi-Steady Dilute Polymer Flow*. Internal Memorandum, Ordnance Res. Lab, Penn. State U. (to be issued).

D-4. LUMLEY, J. L., *On the Solution of Equations Describing Small Scale Deformation*. Technical Memorandum 503-09, Ordnance Res. Lab, Penn. State U., August 12, 1970.

INDEX OF AUTHORS AND DISCUSSORS*

* Italic page numbers indicate first page of paper.

"*The aeronautical and space activities of the United States shall be
conducted so as to contribute . . . to the expansion of human knowl-
edge of phenomena in the atmosphere and space. The Administration
shall provide for the widest practicable and appropriate dissemination
of information concerning its activities and the results thereof.*"

—NATIONAL AERONAUTICS AND SPACE ACT OF 1958

NASA SCIENTIFIC AND TECHNICAL PUBLICATIONS

TECHNICAL REPORTS: Scientific and
technical information considered important,
complete, and a lasting contribution to existing
knowledge.

TECHNICAL NOTES: Information less broad
in scope but nevertheless of importance as a
contribution to existing knowledge.

TECHNICAL MEMORANDUMS:
Information receiving limited distribution
because of preliminary data, security classifica-
tion, or other reasons. Also includes conference
proceedings with either limited or unlimited
distribution.

CONTRACTOR REPORTS: Scientific and
technical information generated under a NASA
contract or grant and considered an important
contribution to existing knowledge.

TECHNICAL TRANSLATIONS: Information
published in a foreign language considered
to merit NASA distribution in English.

SPECIAL PUBLICATIONS: Information
derived from or of value to NASA activities.
Publications include final reports of major
projects, monographs, data compilations,
handbooks, sourcebooks, and special
bibliographies.

TECHNOLOGY UTILIZATION
PUBLICATIONS: Information on technology
used by NASA that may be of particular
interest in commercial and other non-aerospace
applications. Publications include Tech Briefs,
Technology Utilization Reports and
Technology Surveys.

Details on the availability of these publications may be obtained from:

SCIENTIFIC AND TECHNICAL INFORMATION OFFICE

NATIONAL AERONAUTICS AND SPACE ADMINISTRATION

Washington, D.C. 20546